Transactions of the ASME®

Journal of Engineering for Gas Turbines and Power

Published Quarterly by The American Society of Mechanical Engineers

VOLUME 111 • NUMBER 1 • JANUARY 1989

Technical Editor
G. K. SEROVY
Associate Technical Editors
Advanced Energy Systems
M. J. MORAN
Environmental Control
H. E. HESKETH
Fuels and Combustion Technologies
R. E. BARRETT
Gas Turbine
T. H. OKIISHI
Internal Combustion Engine
J. A. CATON
Nuclear Engineering
S. M. CHO
Power
R. W. PORTER

BOARD ON COMMUNICATIONS
Chairman and Vice-President
R. NICKELL

Members-at-Large
J. LLOYD
R. REDER
F. SCHMIDT
M. FRANKE
M. KUTZ
T. MIN
F. LANDIS
R. ROCKE
W. WINER
R. GENTILE
B. ZIELS
R. MATES

President, **E. L. DAMAN**
Executive Director,
D. L. BELDEN
Treasurer, **ROBERT A. BENNETT**

PUBLISHING STAFF
Mng. Dir., Publ., **JOS. SANSONE**
Managing Editor,
CORNELIA MONAHAN
Sr. Production Editor,
VALERIE WINTERS
Editorial Prod. Asst.
MARISOL ANDINO

Transactions of the ASME, Journal of Engineering for Gas Turbines and Power (ISSN 0022-0825) is published quarterly (Jan., Apr., July, Oct.) for $120 per year by The American Society of Mechanical Engineers, 345 East 47th Street, New York, NY 10017. Second class postage paid at New York, NY and additional mailing offices. POSTMASTER: Send address change to The Journal of Engineering for Gas Turbines and Power, c/o The AMERICAN SOCIETY OF MECHANICAL ENGINEERS, 22 Law Drive, Box 2300, Fairfield, NJ 07007-2300.

CHANGES OF ADDRESS must be received at Society headquarters seven weeks before they are to be effective. Please send old label and new address.

PRICES: To members, $29.00, annually; to nonmembers, $120.00.
Add $12.00 for postage to countries outside the United States and Canada.

STATEMENT from By-Laws. The Society shall not be responsible for statements or opinions advanced in papers or ... printed in its publications (B 7.1, para. 3).

COPYRIGHT © **1989** by the American Society of Mechanical Engineers. Reprints from this publication may be made on condition that full credit be given the TRANSACTIONS OF THE ASME—JOURNAL OF ENGINEERING FOR GAS TURBINES AND POWER, and the author, and date of publication be stated.

INDEXED by Applied Mechanics Reviews and Engineering Information, Inc.

TECHNICAL PAPERS

(Contents continued on p. 23)

Downloaded 03 Jun 2010 to 171.66.16.159. Redistribution subject to ASME license or copyright; see http://www.asme.org/terms/Terms_Use.cfm

(Contents Continued)

ANNOUNCEMENTS

F. W. Staub

S. G. Kimura

C. L. Spiro

Corporate Research and Development,
General Electric Company,
Schenectady, NY 12301

M. W. Horner
Marine and Industrial Engines Projects
Department,
General Electric Company,
Springdale, OH 45246

Coal-Water Slurry Combustion in Gas Turbines

This paper presents preliminary results of a program to investigate the key technologies for burning coal-water slurries in gas turbines. Results are given for slurry atomization and combustion testing and analyses performed at conditions typical for gas turbine applications. Significant progress has been made toward the understanding of slurry combustion and ash deposition phenomena. Confidence has been gained to the extent where elimination of a supplementary pilot fuel can now be projected.

Introduction

Direct combustion of coal in gas turbines was first attempted in the late 1940s as an alternative to coal-fired boilers for locomotive propulsion. More recently, uncertain oil and gas fuel prices, as well as technical innovations in the production of coal-water slurries for their combustion, has rekindled interest in coal as a fuel for gas turbines. Direct injection of the slurry into the gas turbine combustor would retain much of the existing infrastructure for fuel transportation and storage for liquid fuels. Capital costs for these systems may also be attractive compared to potentially more complex alternatives, such as coal gasification.

Earlier research and development programs have shown that fuel atomization and combustion zone mixing are very important to successful combustion of coal-water slurries (Kimura et al., 1987; Horner, 1985; Ross, 1987). In these testing programs, natural gas or fuel oil was used to establish a stable flame and to avoid ignition delay of the slurry fuel droplets. The first attempts at burning coal-water slurries in a 27.9-cm-dia cylindrical can combustor, as reported by Horner (1985), resulted in severe combustion instabilities when slurry flow exceeded 80 percent on a heat input basis. These tests indicated that improved fuel atomization and enhanced recirculation would be needed to reduce the use of auxiliary fuel. The approach taken here for successful combustion of coal-water slurries in gas turbines involves the use of in-line, short residence time combustors typical of present-day gas turbines. Use of near-conventional technology for fuel atomization, fuel-air mixing, liner cooling, air dilution, and overall fabrication techniques improves the reliability of analytical predictions as well as hardware producibility. Benefit is also taken of significant on-going research and development activities toward improvements in the technical performance of these combustion systems for aircraft applications.

This paper describes the results of studies to characterize coal-water slurry (CWS) fuel nozzle performance and to establish predictive combustor performance criteria for coal-water fuels. The nozzle characterization studies employed an optical particle sizer and measured velocity profiles to obtain the spatial and temporal drop size distributions. The combustor performance criteria were developed using a three-dimensional code to predict the fuel drop residence time and combustor velocity field. The performance criteria and model results have been compared with actual combustion performance.

Nozzle Characterization

To achieve carbon burnout in gas turbine combustors using micronized coal-water slurries, minimum atomized drop size is required since the short available residence times, typically 20-30 ms, are of the same magnitude as the time needed for complete carbon utilization. This is especially the case if the micronized slurry droplets burn in the agglomerated manner shown for larger coal particles by Beer (1986). Standard pulverized coal slurries were not considered in view of the need for maximum ash removal from the coal and the fact that the large particle fraction of such coals is too large for the required residence time. To determine whether air atomized nozzles can achieve the needed drop size, a spray tunnel was employed to obtain the spatial and temporal drop size distribution of several candidate nozzle designs. A three-dimensional flow code was then used to model the test combustor flow distribution using the drop size distribution generated by each nozzle, to yield a qualitative measure of the available residence time and the degree of swirl stabilization. These calculated qualitative results were compared with combustor performance to obtain a first-order correlation of the coupled effect of nozzle and swirler design on coal water slurry combustor performance. The nozzle characterization technique is summarized below followed by the combustor evaluation method and the initial results.

Characterization Technique. A schematic of the spray tunnel employed to measure the spray drop size distribution is shown in Fig. 1 and described further by Staub (1986a). The 25-cm-dia tunnel allows a uniform axial velocity environment to 30

Contributed by the International Gas Turbine Institute and presented at the 33rd International Gas Turbine and Aeroengine Congress and Exhibition, Amsterdam, The Netherlands, June 5-9, 1988. Manuscript received by the International Gas Turbine Institute December 1987. Paper No. 88-GT-94.

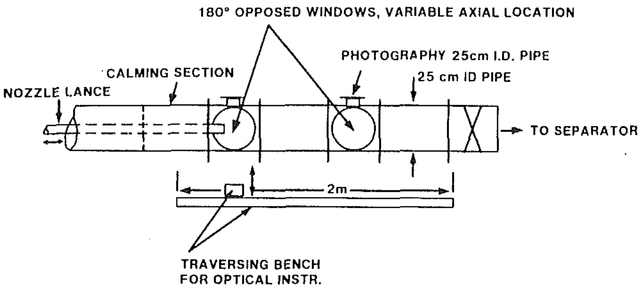

Fig. 1 CRD spray tunnel schematic

m/s at 1 atm and can be operated at pressures to 10 atm, temperatures to 150°C, and at controlled relative humidities between 10 and 90 percent. The spray can be traversed over the tunnel diameter and over an axial distance from the nozzle of 2 m. The opposed windows are optically flat and parallel. A Malvern Mod 2600 HSD optical particle sizer is mounted on the traversing bench shown in Fig. 1. Suitable slurry flushing and separation is provided. The tunnel is operated at a velocity large enough to prevent any recirculation of drops from the spray envelope.

In a prior investigation (Staub, 1986b), a GE CRD (Corporate Research and Development) designed LT nozzle (Fig. 2) was selected for the 15-cm-dia combustor employed here since it provided the desired spray diameter and small drop size. Both water and a micronized coal-water slurry provided by OTISCA were used with the slurry properties given below. The high shear viscosity measurements were carried out by Professor Beer at MIT where the maximum value tested is commensurate with the shear rate encountered in the LT nozzle.

The atomized spray structure can be roughly divided into three regions that more or less overlap. These consist of the initial drop formation region, discussed by Simpkins and Bates (1972) and Chigier (1985a), the relative deceleration region where the spatial size distribution is a strong function of axial distance (Lefevbre and Risk, 1984), and the developed spray region where droplet behavior is dictated by the ambient flow field. Since the tunnel provides a well-defined ambient field, the axial distance selected for the traversing measurements reported here was just beyond the relative deceleration region. The latter was calculated to be about 8 cm at a 1-atm tunnel pressure using a drop tracking model (Staub, 1986a).

Coal-water slurry properties

Particle size Distribution	Viscosity Shear rate, 1/s	 Viscosity, PA·s
1.8 percent > 14.5 μm	10^3	0.8
50 percent > 4.26 μm	10^4	0.55
5 percent < 1.5 μm	10^5	0.20

Average percent solids = 50 Percent ash = 0.78
Density = 1.1 s.g. Percent sulfur = 0.87
Heating Valve = 3800 cal/g of slurry

Selected spatial measurements are reviewed below followed by a brief discussion of the calculation method for the temporal distribution and the verification of this simplified characterization technique.

Results. The original LT nozzle and three added nozzles, the MS, HS, and HH nozzles, were characterized using the above technique. The MS and HH nozzles in Fig. 4 each had successively increased atomizing air swirl at the same (0.039 kg/s) atomizing air flow as the LT nozzle, while the HS nozzle had the same swirl as the HH nozzle but employed an atomizing air flow of 0.035 kg/s. The maximum swirl velocity was increased by 50 percent between the LT and MS nozzles and about 90 percent between the LT and HH nozzles.

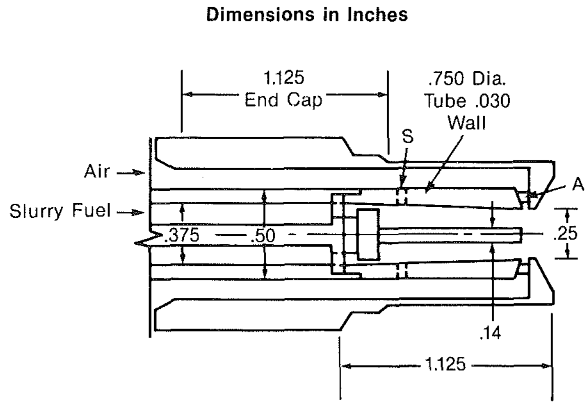

Fig. 2 Schematic of LT nozzle geometry: center 0.14 in. passage for auxiliary fuel; holes at "S" premix air with slurry; vanes at "A" provide swirl

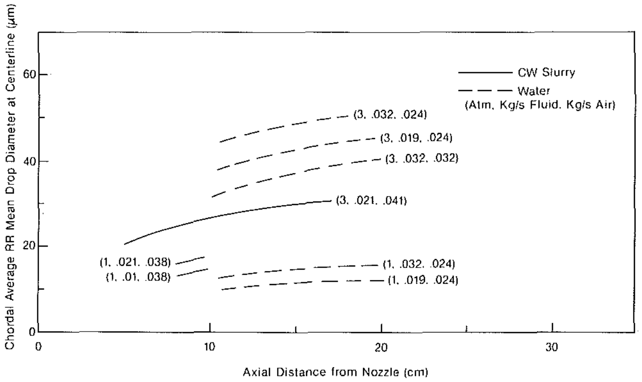

Fig. 3 Average RR mean drop diameters measured at the centerline for the LT nozzle at the indicated conditions

The chordal average Rosin–Rammler (RR) drop diameter measured at the spray centerline using the Malvern Sizer with the LT nozzle is shown in Fig. 3 as a function of the axial distance from the nozzle. The water data are shown to demonstrate that water cannot be employed to model a coal–water slurry. Note the much larger increase in mean size with ambient air density with water compared to that with the slurry. The faster rate of size decrease with decreasing axial distance below 8 cm is primarily due to the influence of the relative deceleration region indicated above. The RR mean size measured 9 cm from the LT nozzle, as well as that measured for the three design changes discussed subsequently, was proportional to the slurry flow rate raised to the 0.51 to 0.65 power and was inversely proportional to the atomizing air flow rate. For coal-water slurry, this drop size was proportional to the tunnel air density raised to the 0.4 power.

As the first step to determine the temporal drop size distribution generated by each nozzle, the multiple chordal scans of both the drop size distribution and their concentration, obtained at 9 cm axial distance, were first transformed to radial distributions (see Chigier et al., 1981, and Cormack, 1963). A set of the radial RR size distributions for each of the nozzles tested is shown in Fig. 4 at 0.023 kg/s fuel and 3 atm tunnel operation pressure. The latter was chosen to obtain the same tunnel density as the average gas density in the combustor spray region. The large beam obscuration encountered near the spray centerline required correction due to multiple scattering effects. The correction relations given by Felton (1985) were employed. When those of Dodge (1984) were used, excessive correction at high obscuration was obtained as evidenced by the fact that the corrected drop sizes were maximum at about half the spray radius, while both the measurements and the drop flow analysis showed that the maximum drops are located at the outer radius of the spray.

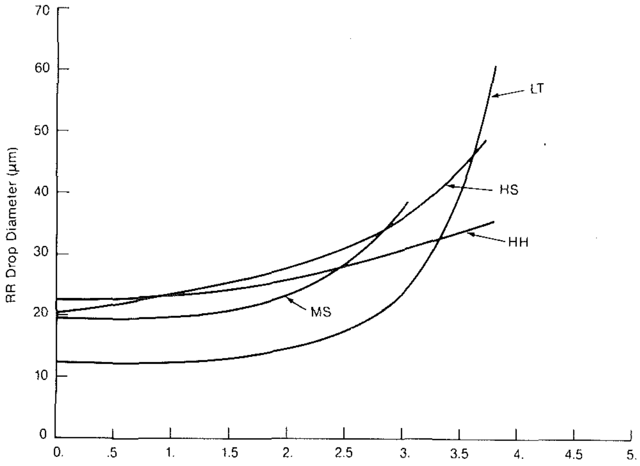

Fig. 4 Radial distribution of Rosin-Rammler drop size as obtained from chordal traverse data with slurry at 0.021 kg/s, atomizing air at 0.041 kg/s, 3 atm ambient pressure, 9 cm from nozzle. See text for nozzle description.

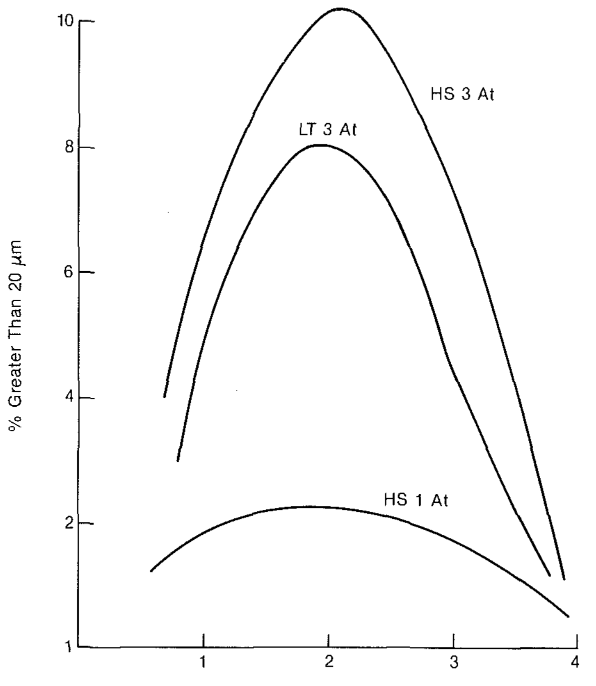

Fig. 5 Temporal distribution of drop size larger than 20 μm in flowing fuel; slurry at 0.021 kg/s, atomizing air at 0.041 kg/s, 9 cm from nozzle

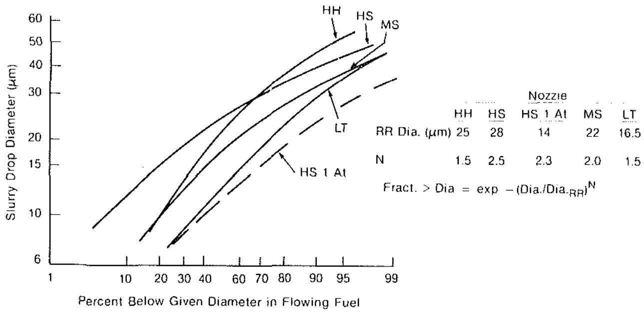

	HH	HS	HS 1 At	MS	LT
RR Dia. (μm)	25	28	14	22	16.5
N	1.5	2.5	2.3	2.0	1.5

Fract. > Dia = exp $-(\text{Dia.}/\text{Dia.}_{RR})^N$

Fig. 6 Temporal drop size distributions generated by CWS nozzles at 0.021 kg/s, air-fuel ratio 1.7; ambient pressure 3 atm unless otherwise noted

The second step to determine the temporal size distribution generated by each nozzle was to measure the axial air velocity distributions at the same measurement location and the same nozzle operating point but without fuel flow. As will be observed subsequently, the assumption of equal axial air and drop velocities over the spray diameter is reasonably justified, within about 15 percent, for these nozzle operating conditions and the selected measurement location. The measured radial velocity distribution, RR drop size distribution, and concentration distribution for each nozzle were used to calculate the temporal (flowing) drop size distribution at the measurement location over the spray radius. Three selected profiles of the temporal drop size distribution are shown as a function of spray radius in Fig. 5. The size fraction above 20 μm shows a peak at roughly one-half the spray radius. The larger drop size at the higher tunnel pressure is clearly evident in Fig. 5. The integration over the radius yielded the RR drop diameter and exponent for the drop size generated by each nozzle as given in Fig. 6. The distributions shown in Fig. 6 are those employed in a combustor model at an axial distance from the nozzle large enough to be past the expected drop formation length, typically 2.5 cm (Chigier, 1984), and where the spray diameter of the nozzle is easily measured to determine the initially uniform atomizing air and drop velocities. This method also assumes that negligible drop agglomeration has taken place between this point and the axial location at which the drop size is measured. A first-order check on these assumptions is given below.

Verification. The above assumptions inherent in this simplified nozzle characterization method require at least first-order verification. Using the measured radial distribution of the axial air velocity and the radial concentration distribution derived from the chordal measurements, the calculated volumetric slurry flow rate was within ±15 percent of the measured flow rate. To obtain an approximate check on the assumption of equal axial air and drop velocities as well as the radial concentration distribution generated by the derived temporal drop size distribution, the FLUENT[1] flow code was employed to model the tunnel and nozzle flow conditions.

In the absence of fuel flow, the measured and calculated axial velocity profiles are shown in Fig. 7 with the LT nozzle at the indicated operating conditions. The angular momentum measured for this nozzle at the 9-cm location was taken to be conserved for the atomizing air flow leaving the nozzle. While the agreement between the measured and calculated axial profiles in Fig. 7 is not exact, it is satisfactory considering the limitations of the k-ϵ turbulence model for swirling flows. The calculated effect of fuel flow on the axial air velocity profile at the 9-cm location is also shown in Fig. 7 and indicates the relatively small effect of fuel-air momentum exchange for this nozzle. The RR parameters for this operating condition were taken at the nozzle discharge with an injected drop size range from 2 μm to 30 μm using FLUENT. A comparison of the maximum drop velocities calculated for each drop size at the 9-cm location with the axial air velocity at the same location yielded the following results:

Drop diameter, μm	Drop velocity, m/s	Air velocity, m/s
2	190	170
9	140	120
23	79	70
30	20	20

The equal velocity assumption thus seems to hold within about 15 percent for this nozzle. As a further check on the temporal drop size distribution, the radial distribution of the drop concentration calculated for this nozzle at the 9-cm location using FLUENT is compared in Fig. 8 with the concentration profile measured by the Malvern Sizer. Again, the agreement is satisfactory within the accuracy of both the model and the ex-

---

[1] CREARE Inc., Hanover, NH.

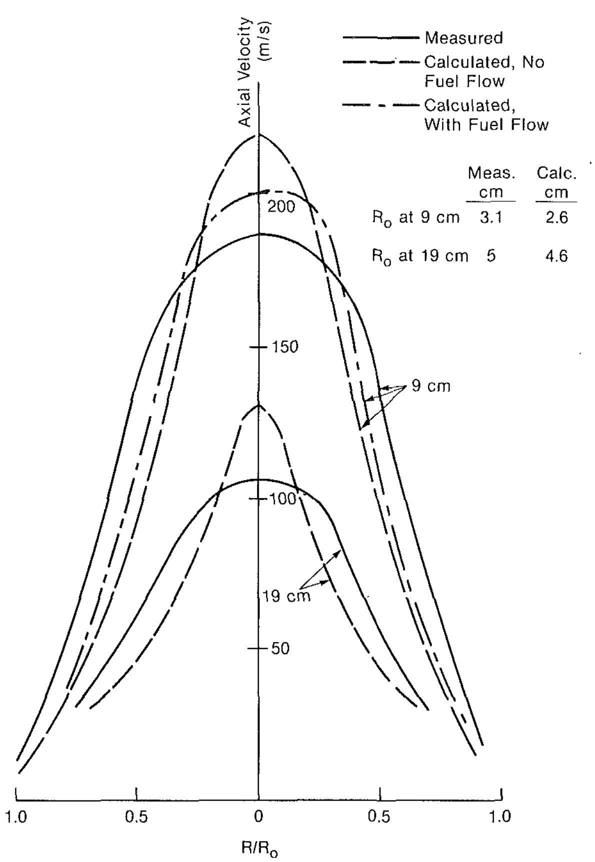

Fig. 7 Comparison of calculated and measured axial air velocity profiles in spray tunnel for LT nozzle at 0.041 kg/s atomizing air, 1 atm ambient pressure, 9 cm and 19 cm from nozzle; calculated effect of slurry flow at 0.021 kg/s; R = spray radius, R_0 = spray outer radius

perimental measurement. The change in drop velocity distribution for each drop size with axial distance from the nozzle is calculated by the model to cause an increase in the spatial RR drop size of 35 percent between the 9-cm and 19-cm positions at the above operating point. The measured spatial RR drop size increased by 40 percent between these locations. This expected behavior, also pointed out by Chigier (1985b), is also predicted by this flow modeling technique.

The above use of a flow model to verify measured information is still an indirect technique that is recommended only for well-defined and controlled flow fields. Direct temporal measurements are preferred. Unfortunately, optical drop velocity measurement methods must be employed with great care to obtain valid data (Dodge, 1986; Chigier, 1985b), and cannot be employed in sprays as dense as those investigated here.

Predictive Combustor Performance Criteria

In recent years the modeling of gas turbine combustor performance has advanced rapidly with increased computational speed. Three-dimensional combustor models have successfully predicted measured performance for standard fuels where rapid fuel evaporation and combustion were obtained. Even where fuel evaporation was not sufficiently rapid, drop tracking models have been employed (Swithenbank, 1985) to obtain improved agreement with measurements. For coal-water slurry combustion, however, the required burning time is over an order of magnitude longer than that of standard fuels. Even the most recent combustion models require several rate constants for each coal and are dependent on whether or not slurry drop breakup takes place. For these reasons, it was decided first to exercise an isothermal model of the combustor of interest, to be followed subsequently by the addition of the slurry combustion model. The isothermal model outlined below was employed to determine the drop residence time and location as well as the gas flow distribution. The former is compared to the expected residence time requirement and the latter was used to evaluate a flame stabilization criterion.

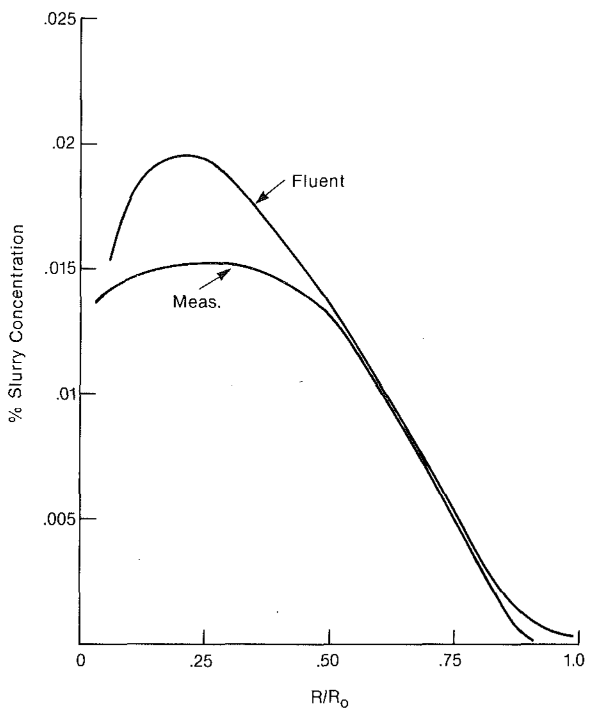

Fig. 8 Comparison of calculated (FLUENT) and measured slurry concentration profiles for LT nozzle with slurry at 0.041 kg/s, atomizing air at 0.021 kg/s, 1 atm ambient pressure, 9 cm from nozzle

A brief description of the combustion experiments is in order prior to the discussion of the flow model.

Combustion Experiments. Coal-water mixture combustion was tested on the LM-500 turbine simulator (Kimura et al., 1987). Three modified LT-type dual fuel nozzles, which had previously been characterized for atomization performance, and five combustion air swirlers were tested for their effect on combustion efficiency and stability.

The LM-500 turbine simulator is a pressurized combustion/deposition test facility in which the combustion exhaust gases pass through a LM-500 gas turbine first-stage nozzle cascade. This facility has been used to study deposition with coal-water mixture fuel (Kimura et al., 1987). Previous testing had all been performed using a single swirler and dual fuel nozzle. Typically, 20 to 25 percent of the fuel input was fuel oil on a heating value basis. Combustion efficiencies, which are based on CO and unburned hydrocarbons in the exhaust gas and residual carbon in collected particulates, were always in excess of 99.5 percent.

The effect of fuel nozzle characteristics and air swirler on combustor stability and efficiency were evaluated for a fuel nozzle/swirler combination by measuring combustion efficiencies over a range of fuel oil flows. The minimum fuel oil flow required to maintain stable combustion was then determined. Nominal operating conditions are shown in Table 1. Otisca-T coal-water mixture was used in all tests.

Combustion tests were performed as follows. Combustion was initiated on distillate oil, and air and fuel flows were increased until the test point was approached. CWM fuel flow was then initiated and increased while decreasing oil flow. When an oil/CWM heating value ratio reached approximately 25 percent and test point conditions achieved, conditions were maintained at steady state. Particulate samples were collected using a quenched, isothermal probe (Kimura et al., 1986), and were analyzed for residual carbon content. The oil/CWM ratio was reduced in approximately 5 percent increments, with gas

Table 1 Operating conditions for combustion tests

Pressure	10 Atm
Combustor exit temperature	1090-1200 °C
Air preheat temperature	400 °C
Fuel input (oil + CWM)	3.7×10^9 J/hr

Table 2 Summary of combustion tests

Fuel Nozzle	Swirler	Minimum Oil for Stable Combustion,%
LT	45*	22
MS	45*	8
HS	45*	8
LT	30	20
LT	38	15
LT	45	10
LT	60	11
HS	30	4
MS	45	>30
LT	60 LF	2

*45 swirler refers to the original swirler, which has considerable bypass.

Table 3 Design point combustor flow rates

Nozzle Air	7.5%
Swirl Air	21.0%
Primary Air	15.0%
Dilution Air	9.0%
Cooling Air	47.5%
Total Air Flow	1.0 Kg/s

Table 4 Calculated coal-water slurry drop residence times required in combustor

Slurry Diameter (μm)	Evaporation (ms)	Devol. (ms)	Char Burnout (ms)	Total (ms)
10	0.7	7.0	1.0	8.7
20	2.0		1.7	10.7
30	2.7		3.6	13.3
50	7.0		10.0	24.0

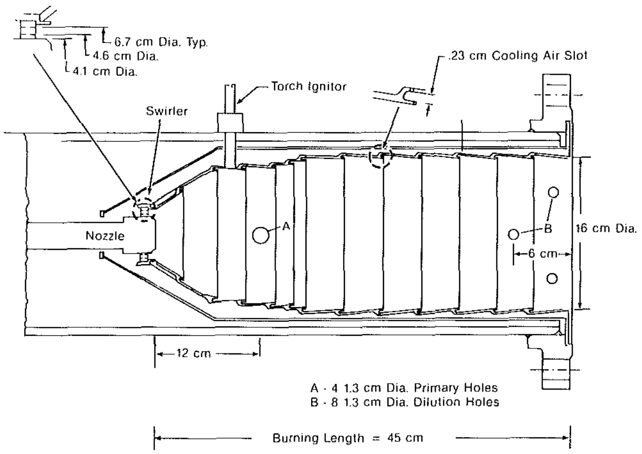

Fig. 9 Schematic of combustor

analysis and particulate sampling at each operating point. When significant reduction in efficiency or an indication of the onset of combustion instabilities was noted, it was judged that the minimum ratio for stable combustion was reached. The atomizing air-to-fuel flow ratio was maintained at about 1.8 for these experiments. These results are summarized in Table 2.

It should be noted that under no circumstances in which stable combustion was maintained did the combustion efficiency drop below 99 percent. There was sufficient variability in CO content in the exhaust gas and residual carbon content in the particulates during the runs to prevent derivation of a clear trend of these variables with auxiliary fuel use.

Flow Model. A three-dimensional, 90 percent sector symmetry FLUENT model of the combustor is shown in Fig. 9. The design point air mass flow rates (see Table 3) were injected through the nozzle swirler, primary hole, and cooling slots. The design fuel flow rate was injected at the nozzle using the characterized RR distribution for the selected nozzle.

The injected nozzle flow rates are at 50°C while the remaining injected flows are at 350°C. The design pressure level is 10 atm. An average gas temperature of 750°C is a compromise between a higher temperature that would more closely approach a mean gas density and a lower temperature that would allow a minimum change in the liner flow areas. Since both the injected air mass flow rates and their total momentum define the flow field, both were matched in the model. This requires a change in the cross-sectional injected flow areas since the injected flow rates are at a lower temperature than the local combustor gas flow. The selection of 750°C required an increase of 26 percent in both these areas and the injection velocities to achieve the desired match. Clearly, the use of an isothermal model provides mostly qualitative information, with quantitative results that should be interpreted with caution.

Slurry Residence Time. The slurry evaporation model given by Abauf and Staub (1985) and the slurry devolatization and char combustion model of Beer (1982, 1986) were employed to estimate the required residence times for this bituminous coal in the test combustor. This model assumes that the drops stay agglomerated as a porous matrix after evaporation. In the primary zone (1400°C) drops larger than 20 μm have diffusion-controlled char burnout while downstream of the primary zone (1250°C) those larger than 30 μm are diffusion controlled. The calculated residence time distributions shown in Table 4 were obtained with these assumptions.

These required residence times imply that the slurry drop in this combustor should not exceed 40 μm in diameter if no drop recirculation takes place.

The combustor flow model was employed to calculate the drop residence times to a point 5 cm downstream of the primary holes where the model no longer predicted gas recirculation. Drop sizes from 5 μm to 60 μm were evaluated using each of the nozzles characterized at the design point.

The calculated effect of nozzle atomizing air swirl and of redistribution of the primary and swirler air flows is shown in Figs. 10 and 11. To obtain the total calculated residence time, 13 ms must be added to the values in Fig. 10 to account for the remaining combustor length. Changing the LT nozzle to the high-swirl HS nozzle more than doubles the gas backflow and increases the 30 μm drop residence time by 50 percent as shown in Fig. 10 at 15 percent primary air flow. The anticipated benefit of this increased residence time was estimated to be greater than the effect of the small increase in maximum drop size produced by the HS nozzle. The calculated 30 μm drop tracks, shown in Fig. 11, also indicate that the increased residence time with the HS nozzle is due to greater circulation in the primary zone near the nozzle. Increasing the primary flow to 30 percent, with a corresponding flow reduction through the swirler, has a weaker effect on gas backflow and residence time (see Fig. 10). Nevertheless, Fig. 10 indicates that the maximum gas backflow for different nozzle air swirl values will take place at different primary/swirler air flow splits so that a change in nozzle swirl may need a change in this flow split to maximize gas backflow.

Although the residence times calculated for the combustor all exceeded the required values, the use of the isothermal model and the lack of combustion rate constant data on this coal limit the quantitative significance of this comparison.

Flame Stabilization Criterion. The use of air swirl to improve combustor stability and efficiency is well documented (Beer et al., 1973, 1969). As swirl is increased, the decreased static pressure near the nozzle yields increased gas backflow in that region. Excessive swirl has also been shown by Beer et al. (1973) and Driscol (1986) to reduce combustor efficiency or even cause flame blow-off. For this reason, the calculated backflow percentage halfway between the nozzle and the primary hole location (6 cm) was selected as a criterion for combustor performance.

The tested combustor configuration corresponds to the 15 percent primary air flow case in Fig. 10 for all cases except one noted below. The design of the original air swirler, which had reduced swirl due to bypass, was changed to a replaceable configuration to allow four swirlers with increasing swirl angle to be evaluated with several nozzles as described in Table 1. The six cases from Table 1 are shown in Fig. 12 where the minimum auxiliary fuel flow is compared with the calculated air backflow. The correlation between increased backflow and decreased need for auxiliary fuel is clear up to about 33 percent backflow. The swirler air swirl numbers, as defined by the ratio of angular-to-axial momentum flux in the swirler flow (Beer, 1973), range from 0.9 for the 30 deg swirler to 2.5 for the 60 deg swirler in Fig. 12. The latter does not include the additional angular momentum of the atomizing air between the LT and HS nozzles. The minimum auxiliary fuel test in Fig. 12 was obtained with the LT nozzle and a 60 deg swirler whose flow rate was about one-half of the design point swirler flow. The primary air flow was increased for this test to yield approximately constant swirler-plus-primary air flow.

With a 45 deg swirler and the MS nozzle, highly unstable combustion ensued that required shutdown. The ratio of angular air momentum to axial fuel momentum exceeds the maximum value above which combustor instability is expected (Driscoll, 1986) only for the 42 percent backflow case in Fig. 12. Although auxiliary fuel was almost eliminated at 33 percent backflow in Fig. 12, further analysis indicated that increased residence time can be obtained, without increasing the backflow above 33 percent, by moving the primary holes 3 cm downstream.

The nozzle characterization technique outlined above permits a reasonable definition of the termporal drop size distribution for combustor analysis. The isothermal combustor model provides guidance on air flow split, angular momentum, and location of the primary air injection. It has already reduced the number of required combustor tests and is expected to shorten further the development path for coal-water slurry combustors as additional variables are included in the correlation between calculated and measured performance. A meaningful quantitative comparison between calculated drop residence time and residual carbon will have to await the inclusion of the slurry combustion model.

Influence of Atomization on Products of Combustion. Atomization and residence time considerations represent two interdependent means to effect combustion efficiencies. As the combustion efficiency changes, so too are the nature and distribution of combustion products. These in turn impact engine performance and longevity through deposition, erosion, and corrosion processes, as well as alter the gaseous and particulate emissions.

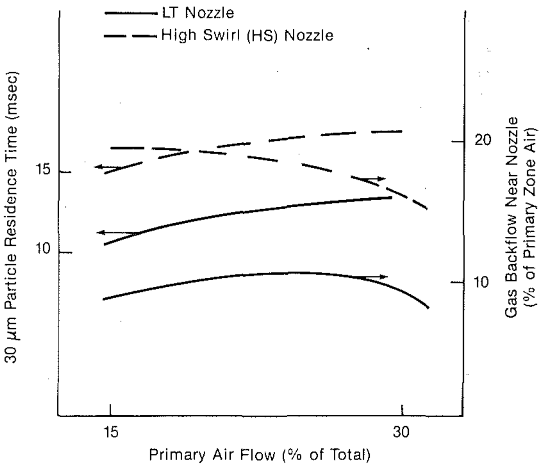

Fig. 10 Calculated 30 μm drop residence time 5 cm downstream of primary holes and gas backflow 6 cm from LT and HS nozzles as function of primary air flow; primary plus swirler air flow held constant

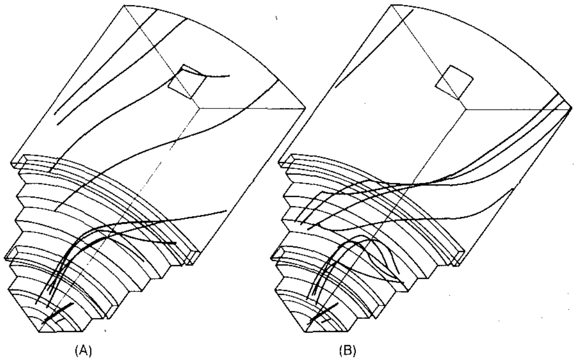

Fig. 11 Calculated mean 30 μm drop tracks for 30 deg swirler with LT nozzle (A) and HS nozzle (B) corresponding to residence time in Fig. 10

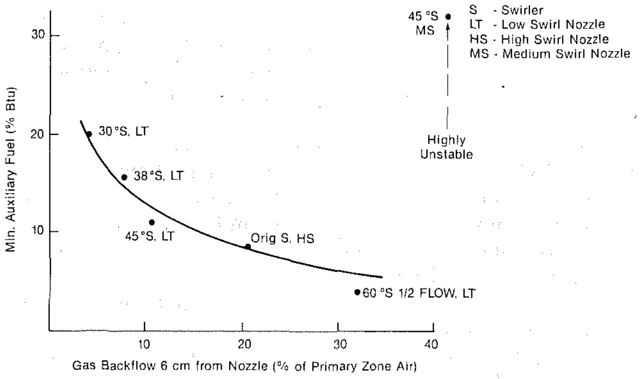

Fig. 12 Comparison of calculated gas backflow with minimum auxiliary fuel combustor operation at 10 atm; 1100°C design point (see text)

As described earlier (Spiro et al., 1987), atomization is followed by water loss and coal pyrolysis. Pyrolizing coal passes through a metastable plastic intermediate in which intradroplet agglomeration and fusion of particles can occur. This is purely an organic chemical phenomenon, unrelated to ash fusion. Atomization therefore is a primary determinant of the resultant char particle size, even nonswelling/nonplastic coals (Dunn-Rankin et al., 1987). During the plastic stage, evolution of gaseous products of pyrolysis causes the particles to balloon into hollow carbonaceous shells, which ultimately solidify when the pyrolysis is near complete. Typical shell diameters ≥ 5 μm have been measured in combustion tests using suction probes. Thus the degree of atomization directly influences the burnout efficiency by altering the resultant char particle size, buoyancy, and surface-to-volume ratio, and less directly, through possible particle recirculation and residence time.

The influence of ash chemistry appears to be primarily a localized phenomenon in which individual mineral grains melt or vaporize. The resultant dense glassy fluids take on a spherical morphology, typically one micron or less in diameter, in order to minimize interfacial tension, and poorly wet the char surfaces. The mobility of these inorganic droplets is not known, though slags are highly viscous even at elevated temperatures (Raask, 1985). Still, some intradroplet ash fusion is anticipated here, as was demonstrated for pulverized coal under boiler conditions (Neville et al., 1981). To the extent that intradroplet ash fusion takes place, atomization will play a role in the resultant ash chemistry. For example, a poorly atomized, large cluster of coal grains will contain several mineral species while a small droplet will contain many fewer.

The first step in deposition/erosion/corrosion phenomena is impact with a turbine component surface. In the event that the particles are larger than one or more micron in diameter, inertial impaction will occur (France et al., 1984) on the leading edge and pressure side surfaces of turbine airfoils. In the event that atomization is extremely poor so that particles are considerably larger than 10 μm and consist mostly of unburned char, erosive impact is likely to predominate with minimal adhesion. The carbon is not likely to be inherently sticky as a solid, though inelastic collision accompanied by fragmentation is possible. In the event that burnouts are sufficiently high that ash makes up a majority fraction of the particulate, a molten and sticky surface will likely impinge on the turbine. Wenglarz (1987) has shown, for example, that for a 0.8 percent ash coal, combustion efficiencies greater than 99.2 percent are required to achieve an ash-predominant POC. Due to the inevitable presence of carbon associated with (and possibly dissolved in) the ash, however, locally reducing conditions will suppress the slag freezing point to that approaching the firing temperature. This raises the possibility of droplet freezing in cooled boundary layers which in turn effects the corrosion mechanism. Thus the degree of atomization, which is a critical parameter in determining combustion efficiency, in turn affects ash composition, deposition rate, adhesion, and the corrosion process.

Conclusions

A simplified nozzle characterization technique has been developed and verified that allows reasonable definition of the temporal drop size distribution. The use of this distribution in an isothermal flow model of the combustor has provided guidance to the selection of the swirler-primary air flow split, the desired angular momentum in the injected air, and the best axial location for the primary air. The best correlating parameter between the calculated flow distribution and the measured combustor performance, as determined by the minimum use of auxiliary fuel, was found to be the percentage of gas backflow near the nozzle based on the total air addition to the primary zone.

The above approach will be applied to shorten the development time in further CWS combustion activities. To permit a quantitative comparison between slurry drop residence time and carbon burnout, a verified slurry combustion model needs to be added to the combustor flow model.

Acknowledgments

The work described in this paper has been largely supported by the U.S. Department of Energy under contract No. DE-AC21-86MC23168, E. L. Parsons, COTR.

References

Abauf, N., and Staub, F. W., 1985, "Drying of Liquid-Solid Slurry Droplets," GE TIS Report No. 85CFD225, Dec.

Beer, J. M., and Chigier, H., 1969, "Stability and Combustion Intensity of Pulverized Coal Flames – Effect of Swirl and Impingement," *Journal of the Institute of Fuel*, Dec., p. 443.

Beer, J. M., and Lee, K. B., 1973, "The Effect of Residence Time Distribution on the Performance and Efficiency of Combustors," *Tenth Int. Symp. on Combustion*, The Combustion Institute, p. 1187

Beer, J. M., and Vermes, G., 1982, "Gas Turbine Combustion for Coal Water Mixtures," *Eng. Found. Conf.*, Santa Barbara, CA, Nov.

Beer, J. M., et al., 1986, "A Mechanistic Model of Coal Water Fuel Combustion," *Twenty-First Int. Symp. on Combustion*, Munich, Federal Republic of Germany, Aug.

Chigier, N. A., et. al., 1981, "Laser Tomographic Investigation of Liquid Fuel Sprays," *Eighteenth Symposium (Int.) on Combustion*, The Combustion Institute, p. 1501.

Chigier, N., and Meyer, P. C., 1984, "Atomization of Coal Water Slurries," *Proc. Sixth Int. Symp. on Coal Slurry Comb. and Technology*, Orlando, FL, June.

Chigier, N., et al., 1985a, "Drop Size Distribution in Air Assist Swirl Atomizer Sprays," *The Combustion Institute Joint Technical Meeting*, San Antonio, TX, Apr.

Chigier, N., et al., 1985b, "The Structure and Characterization of Air-Assisted Swirl Atomizer Sprays," ASME Paper No. 85-WA/HT-45.

Cormack, A. M., 1963, "Representation of a Function by Its Line Integrals With Radiological Applications," *Journal of Applied Physics*, Vol. 34, No. 9, p. 00.

Dodge, L. G., 1984, "Change of Calibration of Diffraction Based Particle Sizers in Dense Sprays," *Optical Eng.*, Vol. 23, No. 5, p. 626.

Dodge, L. G., 1986, "Comparison of Drop Size Measurement in Fuel Sprays: Malvern Diffraction and Aerometrics Phase/Doppler," 1986 Meeting of Central States Section/The Combustion Institute, NASA Lewis Research Center, May.

Driscoll, J. F., 1986, "Scattering Measurements to Study Blow-off of Swirling Flames," AIAA Paper No. 86-0593.

Dunn-Rankin, D., Hoornstra, J., Greulich, F. A., and Holve, D. J., 1987, "Combustion of Coal-Water Slurries; Evolution of Particle Size Distribution for Coals of Different Rank," *FUEL 66*, pp. 1138–1144.

Felton, P. G., et al., 1985, "Measurement of Drop Size Distribution in Dense Sprays by Laser Diffraction," *Proceedings of ICCASS-85, Third Int. Conference on Liquid Atomization and Spray Systems*, Inst. of Energy, London, p. IVA1411.

France, J. E., Grimm, U., Anderson, R. J., and Kovach, J. J., "Deposition and Corrosion in Coal or Coal-Derived Fuel," DOE Report DOE/METC-84-17.

Horner, M. W., 1985, "Combustion of a Coal-Water Mixture in Gas Turbine Combustor," Joint ASME/IEEE Power Generation Conference, Oct.

Kimura, S. G., Spiro, C. L., and Chen, C. C., 1986, "Alkali Species Characterization in Coal-Fired Turbines," *Proceedings of the Third Annual Heat Engine Contractors Meeting*, F. W. Crouse, ed., May.

Kimura, S. G., Spiro, C. L., and Chen, C. C., 1987, "Combustion and Deposition in Coal Fired Turbines," ASME JOURNAL OF ENGINEERING FOR GAS TURBINES AND POWER, Vol. 109, pp. 319–324.

Lefebvre, A. H., and Risk, N. K., 1984, "Influence of Downstream Distance on Simplex Atomizer Spray Characteristics," presented at the ASME Annual Winter Meeting, New Orleans, LA, Dec.

Neville, M., Quann, R. J., Haynes, B. S., and Sarofim, A. F., 1981, "Vaporization and Condensation of Mineral Matter During Pulverized Coal Combustion," *Eighteenth Symposium on Combustion*, The Combustion Institute, pp. 1267–1274.

Raask, E., 1985, *Mineral Impurities in Coal Combustion-Behavior, Problems, and Remedial Measures*, Hemisphere Publishing, Washington, DC.

Ross, K. J., 1987, "Gas Turbine Component Screening Program," Vol. I, DOE/MC21395-2298, Final Report, Mar.

Simpkins, P. G., and Bates, E. L., 1972, "Water Drop Response to Sudden Accelerations," *J. Fluid Mech.*, Vol. 55, Pt. 4, p. 629.

Spiro, C. L., Kimura, S. G., and Chen, C. C., 1987, "Ash Behavior During Combustion and Decomposition in Coal Fueled Gas Turbines," ASME JOURNAL OF ENGINEERING FOR GAS TURBINES AND POWER, Vol. 109, pp. 325–330.

Staub, F. W., 1986a, "Spray Characterization and CW Slurry Atomization," GE TIS Report No. 86CRD123, July.

Staub, F. W., 1986b, "Air Atomized Coal-Water Slurry Nozzle Performance," GE TIS Report No. 86CRD169, Oct.

Swithenbank, J., et al., 1985, "Spray Combustion Modeling," *Calculations of Turbulent Reactive Flows*, ASME, New York, p. 259.

Wenglarz, R., 1987, "Gas Turbine Components Screening," DoE Final Report, Contract DE-AC21-84MC21394, Morgantown Energy Technology Center, Morgantown, WV.

E. Carr
Project Manager Aero Engine Combustion.

H. Todd
Senior Project Engineer.

Aero & Industrial Technology Ltd.,
Combustion Technology Centre (CTEC),
Burnley, Lancashire, United Kingdom

A Methanol/Oxygen Burning Combustor for an Aircraft Auxiliary Emergency Power Unit

The development of advanced single-engine aircraft with reduced stability and "Fly-by-Wire" control systems requires the provision of emergency hydraulic and electrical power from a stored energy system. The desire to achieve this objective using readily available fluids of low toxicity has led to the development of a methanol/oxygen burning combustor to provide a hot gas stream to drive a small turbine. The paper describes the performance of a 300 kW output combustor, which is cooled by the methanol consumed.

Introduction

Modern agile combat aircraft require power for the controls at all times if the pilot is to survive. Three levels of redundancy are typically provided, so that, if the main engine and the APU fail, an additional source of hydraulic and electrical power is available.

Systems powered by hydrazine reactors have been used in the past, but there is a desire to avoid the use of this mono fuel because of its toxicity. Hence there has been a great deal of recent interest in exploring the use of alternative fuels and emergency power unit configurations, as covered by McFadden (1977), Fischer (1985), and SAE report AIR 1467 (1987).

After a review of the possible alternatives by Kirkman (1984) a decision was taken by Lucas to develop a system using methanol and gaseous oxygen as the propellant. The approach adopted was to achieve the required heat release by the combustion of methanol and oxygen and then to dilute the combustion products with methanol to provide a gas stream suitable for driving a small turbine. The methanol and oxygen would be obtained from supplies stored on board the aircraft.

At the concept stage there appeared to be two main problem areas, namely, (*a*) what degree of dissociation of the excess methanol would occur and what would be the resultant exhaust gas properties and temperature rise? (*b*) Would it be possible to cool the combustor adequately using only the methanol supplied to the combustor?

System Requirements

With a view to possible future aircraft applications the following system requirements were selected:

- Operation from sea level up to 20 km altitude.
- Temperature range −40°C to +80°C.
- Full output to be available in less than 0.5 s of initiating a start.
- Rapid response to load change and capability of shutdown and relight during an aircraft mission.
- A total operating life between repair and overhaul of 2 1/2 h.
- Minimum size, weight, and cost.
- High reliability.
- Capability of operating with nitrogen-saturated methanol.

Design Features

At the design stage it was not possible to make a reliable estimate of the level of dissociation of the excess methanol or the magnitude of the cooling system problems. Further, the combustion stability limits for systems of the type being considered were not adequately defined. After a study of the information on oxygen-fed combustion systems given in the references and from knowledge of the performance of air/kerosene combustion systems, a combustion volume of 4.75×10^{-4} m^3 was chosen. Over the target power range this gives combustion loading values of $\Lambda = 4.0$ to 8.8 kg/s m^3 Pa$^{1.8}$, where

$$\Lambda = \frac{Wcc 10^9}{P^{1.8} V e^{T/300}}$$

Wcc = Total methanol and oxygen flow, kg/s
T = Methanol and oxygen temperature, K
P = Combustor operating pressure, Pa
V = Combustor volume, m^3

The combustion temperature of a stoichiometric methanol/oxygen mixture is approximately 3300 K. Design studies showed that the sensible heat of the methanol at +80°C day operating temperature was inadequate to cool the combustor and that the design would have to utilize the latent heat of vaporization in the cooling process.

The arrangement of the combustor is shown in Fig. 1. It comprises a pressure casing, a simple liner, an exhaust gas mixer, and suitable oxygen/methanol injection devices.

Contributed by the International Gas Turbine Institute and presented at the 33rd International Gas Turbine and Aeroengine Congress and Exhibition, Amsterdam, The Netherlands, June 5–9, 1988. Manuscript received by the International Gas Turbine Institute June 7, 1987. Paper No. 88-GT-236.

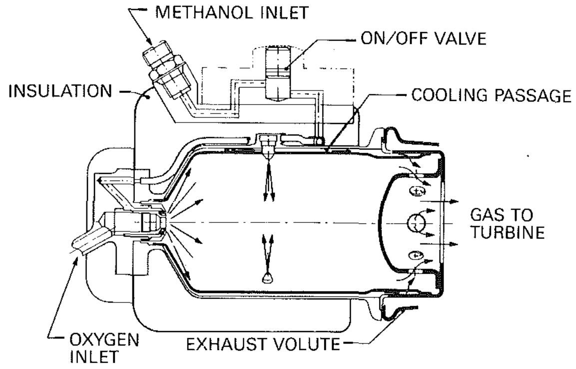

Fig. 1 Combustor arrangement

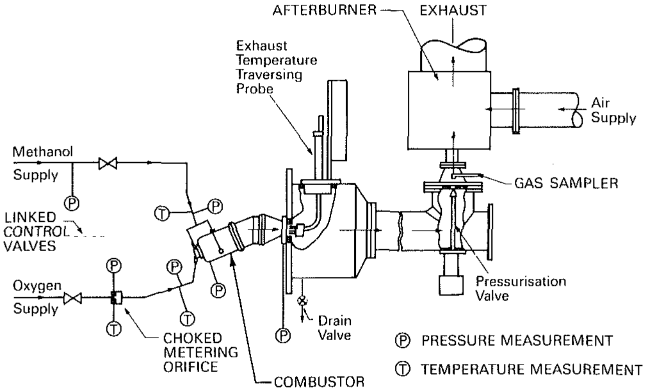

Fig. 2 Test rig arrangement

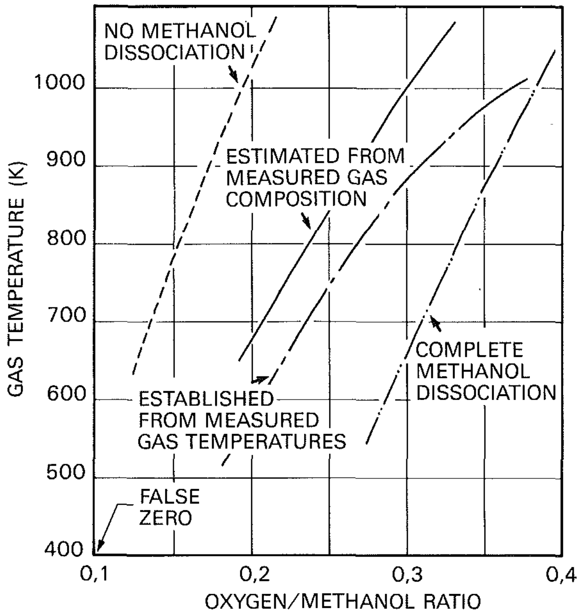

Fig. 3 Variation of gas temperature with oxygen/methanol ratio

The oxygen is injected in the form of a hollow cone at the upstream end of the combustor and the methanol is injected into three separate zones.

A flow mixing device is fitted at the combustor exhaust to mix into the exhaust gas flow any liquid persisting to the liner rear.

In a practical application the methanol fill time would need to be a minimum. To simulate this a methanol ON/OFF valve is mounted directly onto the combustor.

Ignition is by means of a high-energy plug supplied from a 0.4 J exciter box.

Table 1 Maximum and minimum power sea level ISA rig operating conditions

	Oxygen/ methanol ratio	Oxygen flow, kg/s	Methanol flow, kg/s	Combustor pressure, kPa
Maximum power	0.30	0.030	0.100	615
Minimum power	0.22	0.011	0.051	262

Table 2 Exhaust gas composition

Oxygen/ methanol ratio	Percent volume					
	CO_2	CO	H_2	H_2O	CH_3OH	CH_4
0.37	4.90	25.50	33.13	25.60	9.93	0.94
0.22	3.47	18.07	23.46	25.03	29.30	0.67

Test Conditions

The combustor design was based on the assumption that an engine control system would provide a constant methanol supply pressure and control the power output by modulating the oxygen flow rate. Small changes of the methanol flow rate occurred as a result of (*a*) the change of combustor back pressure with change of load, (*b*) change of methanol temperature, and (*c*) the level of nitrogen saturation.

The system has been tested over the full operation envelope, i.e., an altitude range from sea level to 20 km, methanol and oxygen temperatures from −40°C to +80°C, and with nitrogen-free methanol and methanol fully nitrogen saturated.

In order to explore fully the potential of the system, it was evaluated over a range of oxygen/methanol ratios at two methanol flow rates.

The maximum and minimum power conditions covered by the rig tests are given in Table 1.

Test Equipment

The arrangement of the test rig used for the full-pressure calibration is shown in Fig. 2.

Metered methanol and oxygen supplies were provided with provision for heating or cooling and nitrogen saturation as required. The test pressures were controlled by means of an adjustable exhaust valve. Comprehensive instrumentation was fitted for temperature and pressure measurements and exhaust gas sampling. A short circular to sector shaped transition duct was fitted at the combustor exhaust so that a comprehensive exhaust gas temperature traverse could be obtained by means of a movable multiheaded traverse probe.

The rig exhaust pipework was water cooled; hence there was the possibility that any methanol present in the exhaust gas flow could condense out. Provision was made, therefore, for collection of this liquid for inclusion in the overall performance assessment.

An afterburner was fitted to the rig exhaust to burn off the combustible products in the exhaust gas flow before discharge to atmosphere.

For low-pressure lightup and stability testing the test unit was installed in the CTEC Altitude Test Facility.

Performance

Flame observations on an open-ended combustor at atmospheric pressure showed that a satisfactory primary zone stabilizing regime was obtained.

Pressure tests confirmed that a wide combustion stability range was achieved and showed the performance of the system was satisfactory over the full range of test conditions.

Figure 3 shows the temperature rise characteristics obtained and for comparison includes an estimated temperature rise curve based on the measured exhaust gas compositions given in Table 2.

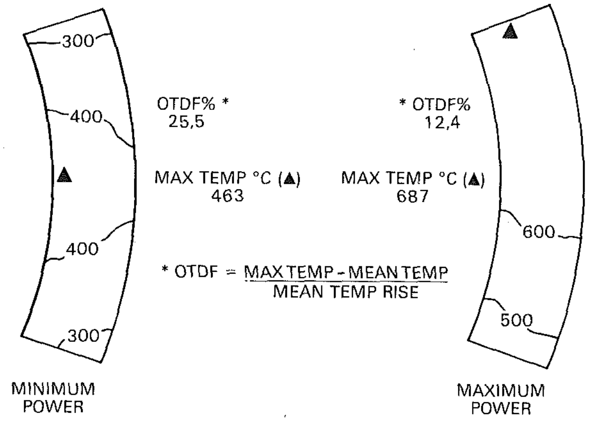

Fig. 4 Exhaust temperature distribution

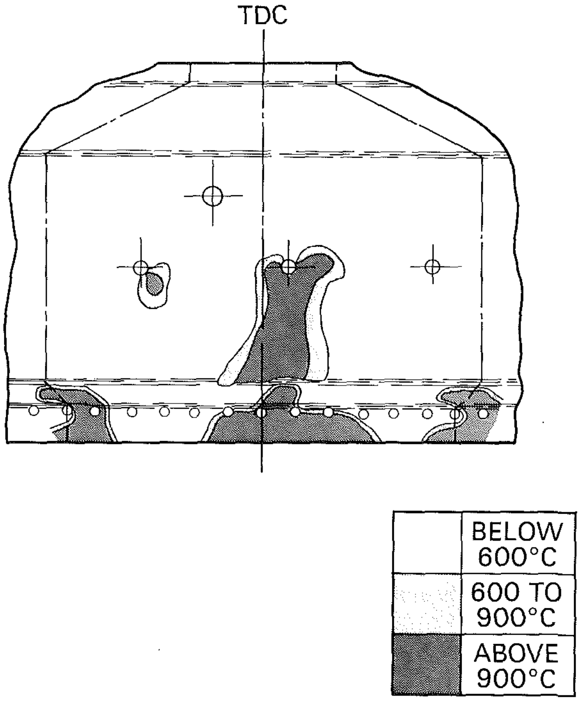

Fig. 5 Developed view of liner showing metal temperatures

Figure 3 shows estimated curves assuming (*a*) the excess methanol undergoes no dissociation and appears as vapor in the exhaust gas products, and (*b*) the methanol completely dissociates to CO and H_2 and minor quantities of other species. It will be noted that the measured temperatures are some 20 percent lower than those estimated from the gas compositions.

Figure 3 shows that the endothermic reaction associated with the dissociation of the methanol to CO and H_2 has a marked effect on the final gas temperature. However, this is not fully reflected as a loss of turbine power output since there is an increase in the gas constant and the ratio of specific heats to provide an increase in enthalpy drop as the gases expand. At this stage we are unable to say whether the obtained gas compositions could be changed by modification of combustor geometry to alter, for example, reactant residence times or local oxygen/methanol ratios.

The measured exhaust gas temperature distribution at both maximum and minimum power conditions are shown in Fig. 4.

The temperature distribution is satisfactory; there were no excessive peak temperatures or values below the saturation temperature that would indicate that liquid methanol was present.

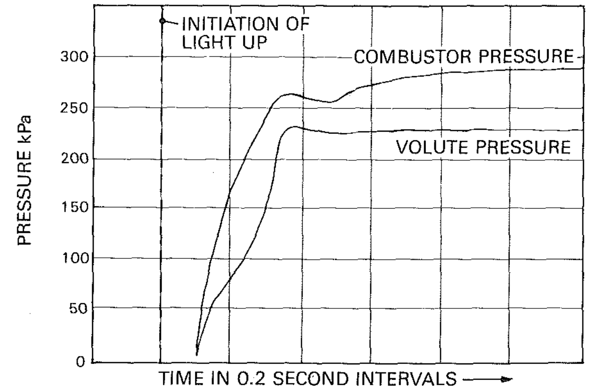

Fig. 6 Combustor pressure after light-up at 20 km altitude and −40°C

Liner metal temperatures were established from liner metal temper colors. Figure 5 shows the temperatures indicated after a test at the most severe conditions. The tests showed that there were no overheating problems.

The tests also showed the combustor to be mechanically sound. The experimental equipment completed more than four times the target life of 2 1/2 h without showing any evidence of damage. The system remained clean and free from carbon deposits during operation.

Tests in the CTEC Altitude Test Facility showed the combustor to light reliably to the maximum altitude of 20 km with methanol and oxygen at −40°C. Lightup was initiated by a single switch that energized the igniter and opened the oxygen and methanol inlet valves. Lightup was detected by pressure transducers recording the sudden rise in combustor pressure occurring as lightup was achieved. An exhaust thermocouple was also used to confirm lightup but because of thermal hysteresis this did not provide an acceptable response rate. As shown by the instrumentation output traces, a typical example of which is reproduced in Fig. 6, the combustion pressure was stable and established within 0.3 seconds of initiation of lightup.

Conclusions

A design standard has been established for a small methanol/oxygen combustor that is suitable for a stored energy emergency power unit.

The combustor gave a satisfactory performance standard and has a mechanical life in excess of possible aircraft requirements.

Acknowledgments

The authors wish to thank the Directors of Lucas Industries plc for permission to publish this paper, and colleagues for helpful discussions.

References

Aerospace Information Report, 1987, "Gas Energy Limited Starting Systems," publication prepared by SAE committee AE-6, Starting Systems, Paper No. AIR 1467.

Fischer, R. L., 1985, "Evaluation of Less Toxic Fuels for Aircraft Emergency Power Systems," *Proceedings, Aerospace Technology Conference and Exposition*, Long Beach, CA, Paper No. 851974.

Kirkman, B. G., 1984, "Auxiliary and Emergency Power System," SAE Technical Paper 841572.

McFadden, B., 1977, "The Super Integrated Power Unit—The Aircraft Power Unit of the Future," *Proceedings, AIAA Conference on the Future of Aerospace Power Systems*, St. Louis, MO, Paper No. 77-502.

An Experimental Data Base for the Computational Fluid Dynamics of Combustors

R. E. Charles

G. S. Samuelsen

UCI Combustion Laboratory,
Department of Mechanical Engineering,
University of California,
Irvine, CA 92717

A model axisymmetric gas-fired can combustor is used to (1) establish the sensitivity of the aerodynamic and thermal structure to inlet boundary conditions, and (2) thereby establish a demanding and comprehensive data base for the computational fluid dynamics of combustors. The parameters varied include fuel injection angle and inlet configuration. Detailed characterizations of the aerodynamic and thermal flowfields are accomplished using two-color laser anemometry and a Type R thermocouple, respectively. Specific results show that the reactor operation is especially sensitive to modest changes in both the inlet geometry and fuel injection angle. For example, the addition of a step expansion significantly alters the size and location of the swirl-induced toroidal recirculation zone. Further, the use of the step expansion, in combination with the injection of fuel matched to the swirl aerodynamics, transforms the recirculation zone to an on-axis structure. The addition of a divergent inlet further enhances the effectiveness of the backmixing by enlarging the recirculation zone. The data base developed for these conditions is carefully documented and provides a comprehensive challenge for the computational fluid dynamics of combustors.

Introduction

The design of gas turbine combustors can be enhanced, and the costs of combustor development reduced, by the successful application of computational fluid mechanics to the prediction of the complex aerothermochemical flow. While substantial progress is being realized in the evolution of applicable codes (Patankar et al., 1987), the development and verification of such codes are compromised by a lack of relevant and/or well-documented experimental data (Mongia et al., 1986).

In recent work (Charles et al., 1987a, 1987b), the sensitivity of flowfield structure to modest changes in inlet boundary conditions was demonstrated. The approach was to vary parameters associated with key inlet boundary conditions systematically and to document the extent to which the parametric variation affects the aerodynamic and thermal structures of an axisymmetric, model laboratory reactor. In the present paper, the data base is expanded and carefully documented in a format following that presented by Faeth and Samuelsen (1986).

The goal of the paper is to provide a collection of detailed data covering a range of conditions and configurations for the purposes of model development, verification, and application. The data presented include mean and rms values of the axial and azimuthal velocities, as well as Reynolds stress ($\overline{u'w'}$) data obtained using two-component laser velocimetry, and mean temperatures from thermocouple measurements.

Experimental Reactor

The model turbulent reactor, presented in Fig. 1 and described in detail elsewhere (Charles and Samuelsen, 1987), consists of an 80 mm i.d. cylindrical stainless steel tube that extends 32 cm from the inlet plane of the reactor. Swirl vanes (57 mm o.d.) are concentrically located within the tube around a 19 mm o.d. centrally positioned fuel delivery tube. The vanes impart an angle of turn to the flow, 60 deg in the present study. Two inlet plane configurations, obtained by changing the step height (h/H), are accommodated (Fig. 1*b*). The angle of this step insert can also be varied and, in the present study, both

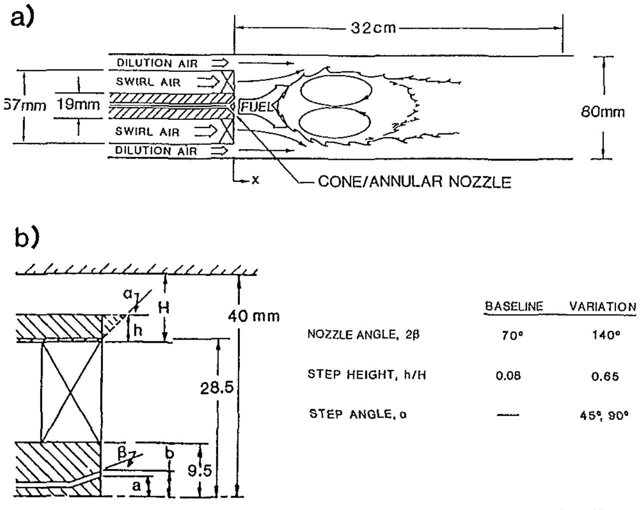

	BASELINE	VARIATION
NOZZLE ANGLE, 2β	70°	140°
STEP HEIGHT, h/H	0.08	0.65
STEP ANGLE, α	—	45°, 90°

Fig. 1 Model laboratory reactor: (*a*) reactor; (*b*) geometric details

---

Contributed by the International Gas Turbine Institute and presented at the 33rd International Gas Turbine and Aeroengine Congress and Exhibition, Amsterdam, The Netherlands, June 5-9, 1988. Manuscript received by the International Gas Turbine Institute September 15, 1987. Paper No. 88-GT-25.

Table 1 Test conditions

Nozzle Angle, 2β	Step Height, h/H	Step Angle, α
70°	0.08	---
70°	0.65	90°
140°	0.08	---
140°	0.65	90°
140°	0.65	45°

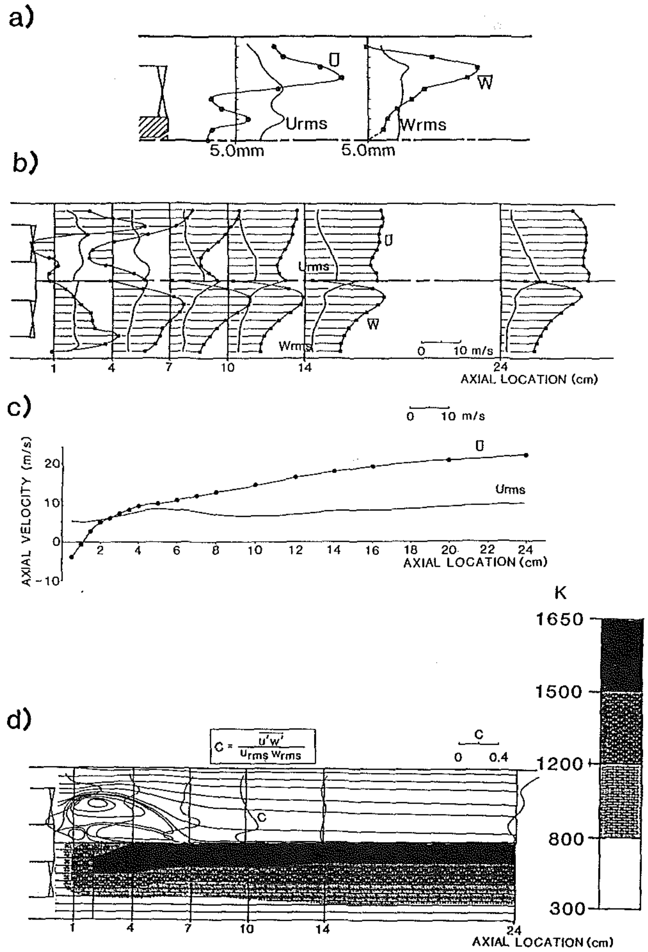

Fig. 2 Basic aerodynamic and thermal structure (baseline: $2\beta = 70$ deg, $h/H = 0.08$): (a) inlet velocity; (b) axial and azimuthal, mean and rms velocities; (c) centerline axial velocity; (d) streamlines and temperature

a 45 and a 90 deg angle are investigated. Fuel (gaseous propane) is introduced through a cone annular nozzle at the end of the central fuel delivery tube. The injection velocity is maintained at 12.4 m/s for two values of injection angle: 70 and 140 deg. Results are reported for an overall stoichiometric ratio, swirl-to-dilution air ratio, and bulk reference velocity of 0.3, 50/50, and 7.5 m/s, respectively.

The aerodynamic field is established using a two-color laser anemometry (LA) system, and the thermal field is established using a type R thermocouple probe mounted on a three-axis positioning traverse, both of which are described elsewhere (Charles and Samuelsen, 1987). Axial and azimuthal velocity and temperature measurements are acquired at eight axial locations, from 0.5 cm to 24.0 cm downstream of the nozzle (0.06 to 3.0 duct diameters), and at 10 uniformly spaced radial locations from the centerline to the outer wall.

Table 1 lists the test conditions being investigated in the present work. The first condition described is a baseline condition consisting of a 70 deg nozzle and a step height of $h/H = 0.08$ (see Fig. 1). This condition was selected using intuitive judgment as to the inlet geometry that would produce satisfactory combustor performance. The combustor is indeed stable for this configuration with a wide turndown ratio. Measurements of axial velocity, however, reveal that, except for the core of the hollow-cone nozzle, the recirculation is off-axis. An exhaustive set of experiments has been conducted to assess the sensitivity of recirculation zone size and location to inlet conditions. Reported here are the parametric variations for which the results are especially profound.

The first variation is a change in the inlet configuration by adding a 90 deg step expansion, such that $h/H = 0.65$. Next, the fuel injection angle is increased to 140 deg, again with a step height of $h/H = 0.08$. The final two variations are the addition of the step expansion with the 140 deg nozzle, and then a modification of the expansion to a divergent exit with a step angle α of 45 deg, still with the 140 deg nozzle. While the full data set is presented for the baseline conditions, only select data are presented for the parametric variations to highlight the more significant effects. Full, tabulated data sets are available for each condition (Charles and Samuelsen, 1987) following a standardized format (Faeth and Samuelsen, 1986), the outline of which is presented in Appendix A.

Results and Discussion

Baseline Condition. The results for the baseline condition are given in Fig. 2. Presented is the full set of data available for this condition including: inlet profile (Fig. 2*a*); mean and rms axial and azimuthal velocity profiles (Fig. 2*b*); centerline axial velocity profile (Fig. 2*c*); streamlines with the Reynolds stress correlation coefficient (*C*) profiles overlaid, and the mean temperature field (Fig. 2*d*) where

$$C = \frac{\overline{u'w'}}{u_{rms}w_{rms}}$$

In the inlet profile, two recirculation zones are evident, the first in the hollow cone of the nozzle, and the second, a toroidal, swirl-generated recirculation zone located off-axis. The development and structure of the aerodynamic flowfield, as documented by the velocity profiles and streamlines (Figs. 2*a*–*d*), are described in more detail elsewhere (Charles et al., 1987a).

The Reynolds stress correlation coefficient *C*, shown overlaid on the streamlines in Fig. 2(*d*), has a maximum value of 0.296 and minimum of −0.385. In general, the regions of strong negative shear stress correspond to the interface between the primary and secondary recirculation zones, and the high positive shear correlates spatially with the outer edge of the primary recirculation zone. The mean temperature field on the bottom half of Fig. 2(*d*) is also described in more detail elsewhere, and provides further evidence of a high-temperature, "diffusion flame" type core, which results from the penetration of a portion of the fuel to the combustor centerline.

Table 2 presents the numerical data for the baseline condition. Included in these data are: mean and rms values of the axial (u) and azimuthal (w) velocity components (m/s); Reynolds stress, $\overline{u'w'}$ (m^2/s^2), when u and w were taken simultaneously and with a sufficient number of samples to suggest convergence; and mean temperature (°F). The axial (x) and radial (y) positions for each station are presented in cm.

90 deg Step Expansion. The centerline axial profile of Fig. 3(*a*) shows that the addition of a step expansion to the inlet plane results in significantly lower velocities in the recirculation zone, thus bringing the zone closer to an on-axis structure. Although not shown here, the inlet profile identifies a secondary recirculation on the face of the step. The step allows the swirling flow to expand upon entering the combustor and thereby produce stronger backmixing and an overall larger recirculation zone. The net result is a thermal field that is

Table 2 Raw data, baseline ($2\beta = 70$ deg, $h/H = 0.08$)

7.5 m/s, phi=0.3 baseline 26,27MAY87

AXIAL (cm)	RADIAL (cm)	U (m/s)	W (m/s)	U' (m/s)	W' (m/s)	U'W' (m^2/s^2)	T (deg F)	COMMENT
5.00E-01	0.00E+00	-5.38E+00		4.59E+00				
5.00E-01	4.00E-01	-4.50E+00		5.36E+00				
5.00E-01	8.00E-01	2.25E+00		8.71E+00				
5.00E-01	1.20E+00	-2.56E+00		6.62E+00				
5.00E-01	1.60E+00	-4.51E+00		6.88E+00				
5.00E-01	2.00E+00	8.09E+00		8.48E+00				
5.00E-01	2.40E+00	2.02E+01		6.83E+00				
5.00E-01	2.80E+00	1.59E+01		4.80E+00				
7.00E-01	3.20E+00	8.87E+00		4.04E+00				
7.00E-01	3.60E+00	7.21E+00		2.12E+00				
5.00E-01	0.00E+00		-5.23E-01		5.43E+00			
5.00E-01	4.00E-01		2.88E+00		5.73E+00			
5.00E-01	8.00E-01		3.48E+00		6.19E+00			
5.00E-01	1.20E+00		5.68E+00		5.96E+00			
5.00E-01	1.60E+00		8.41E+00		6.44E+00			
5.00E-01	2.00E+00		1.06E+01		6.61E+00			
5.00E-01	2.40E+00		1.87E+01		6.15E+00			
5.00E-01	2.80E+00		2.07E+01		7.83E+00			
5.00E-01	3.20E+00		1.20E+01		3.37E+00			
5.00E-01	3.60E+00		-5.38E-01		2.13E+00			
1.00E+00	0.00E+00	-1.25E+00	-8.79E-01	5.19E+00	6.58E+00	5.57E-01	1.53E+03	BASELINE F
1.00E+00	4.00E-01	-1.03E+00	2.71E+00	5.46E+00	6.06E+00	-2.07E+00	1.79E+03	BFP
1.00E+00	8.00E-01	1.14E+00	5.23E+00	7.30E+00	5.50E+00	-1.01E+01	2.08E+03	BFP
1.00E+00	1.20E+00	-1.20E+00	7.31E+00	7.37E+00	5.60E+00	-1.11E+01	2.02E+03	BFP
1.00E+00	1.60E+00	-5.95E+00	9.77E+00	6.58E+00	5.15E+00	-2.60E+00	2.03E+03	BFP
1.00E+00	2.00E+00	-5.98E+00	1.02E+01	6.74E+00	5.34E+00	5.61E-01	1.99E+03	BFP
1.00E+00	2.40E+00	8.92E+00	1.09E+01	8.66E+00	5.36E+00	6.05E+00	1.60E+03	
1.00E+00	2.80E+00	2.33E+01	1.72E+01	5.70E+00	5.30E+00	8.94E+00	6.00E+02	BFP
1.00E+00	3.20E+00	1.54E+01	1.38E+01	6.03E+00	6.69E+00	-1.22E+00	1.70E+02	BFP
1.00E+00	3.60E+00	9.73E+00	-4.19E-01	3.13E+00	3.60E+00	-8.72E-01	1.32E+02	BFP
2.00E+00	0.00E+00	4.77E+00	-1.41E-01	5.81E+00	6.74E+00	1.08E+00	1.88E+03	BFP
2.00E+00	4.00E-01	3.96E+00	4.55E+00	6.20E+00	6.36E+00	-6.58E+00	2.09E+03	BFP
2.00E+00	8.00E-01	6.14E-01	8.32E+00	7.27E+00	6.01E+00	-9.98E+00	2.28E+03	BFP
2.00E+00	1.20E+00	-4.21E+00	1.11E+01	7.85E+00	5.72E+00	-8.53E+00	2.25E+03	BFP
2.00E+00	1.60E+00	-7.92E+00	1.27E+01	6.94E+00	5.23E+00	-2.51E+00	2.25E+03	BFP
2.00E+00	2.00E+00	-7.95E+00	1.24E+01	6.02E+00	5.06E+00	3.02E-01	2.22E+03	BFP
2.00E+00	2.40E+00	3.93E-01	1.12E+01	8.00E+00	5.30E+00	-2.13E+00	1.96E+03	BFP
2.00E+00	2.80E+00	1.87E+01	1.24E+01	7.56E+00	5.33E+00	6.55E+00	1.15E+03	BFP
2.00E+00	3.20E+00	2.20E+01	1.29E+01	5.73E+00	5.89E+00	5.73E+00	2.30E+02	BFP
2.00E+00	3.60E+00	1.38E+01	5.96E+00	4.54E+00	6.46E+00	3.48E+00	1.50E+02	BFP
4.00E+00	0.00E+00	8.82E+00	-6.19E-01	8.14E+00	9.26E+00	-2.07E+00	2.24E+03	
4.00E+00	4.00E-01	5.97E+00	8.12E+00	9.46E+00	8.70E+00	-3.17E+01	2.39E+03	BFP
4.00E+00	8.00E-01	-1.51E+00	1.59E+01	9.23E+00	7.32E+00	-1.97E+01	2.41E+03	BFP
4.00E+00	1.20E+00	-5.84E+00	1.86E+01	6.49E+00	6.16E+00	-2.36E-01	2.36E+03	BFP
4.00E+00	1.60E+00	-4.74E+00	1.76E+01	5.89E+00	5.58E+00	2.99E-01	2.26E+03	BFP
4.00E+00	2.00E+00	7.56E-01	1.52E+01	6.98E+00	5.25E+00	-4.03E+00	2.05E+03	BFP
4.00E+00	2.40E+00	9.56E+00	1.33E+01	6.80E+00	4.81E+00	-1.65E+00	1.74E+03	BFP
4.00E+00	2.80E+00	1.67E+01	1.28E+01	5.04E+00	4.42E+00	1.43E+00	1.18E+03	BFP
4.00E+00	3.20E+00	1.95E+01	1.16E+01	5.08E+00	4.39E+00	-3.03E-01	6.10E+02	BFP
4.00E+00	3.60E+00	2.14E+01	8.91E+00	5.36E+00	4.50E+00	-8.05E-01	3.10E+02	BFP
7.00E+00	0.00E+00	1.26E+01	9.65E-01	8.36E+00	1.35E+01	-7.40E+00	2.34E+03	BASELINE F
7.00E+00	4.00E-01	1.02E+01	1.49E+01	8.29E+00	9.90E+00	-2.28E+01	2.40E+03	BFP
7.00E+00	8.00E-01	8.08E+00	2.07E+01	6.71E+00	6.61E+00	2.07E+00	2.38E+03	BFP
7.00E+00	1.20E+00	7.97E+00	2.05E+01	5.60E+00	5.71E+00	3.86E+00	2.28E+03	BFP
7.00E+00	1.60E+00	9.89E+00	1.75E+01	4.98E+00	4.91E+00	-1.36E+00	2.06E+03	BFP
7.00E+00	2.00E+00	1.24E+01	1.47E+01	4.26E+00	3.89E+00	-1.37E+00	1.67E+03	BFP
7.00E+00	2.40E+00	1.43E+01	1.24E+01	3.88E+00	3.66E+00	-7.45E-01	1.24E+03	BFP
7.00E+00	2.80E+00	1.58E+01	1.06E+01	3.85E+00	3.60E+00	-7.11E-01	8.60E+02	BFP
7.00E+00	3.20E+00	1.74E+01	8.97E+00	3.68E+00	3.74E+00	-2.28E-01	5.55E+02	BFP
7.00E+00	3.60E+00	1.81E+01	8.01E+00	3.75E+00	3.60E+00	4.97E-01	3.90E+02	BFP
1.00E+01	0.00E+00	1.50E+01	1.69E+00	6.77E+00	1.41E+01	1.20E+00	2.39E+03	BFP
1.00E+01	4.00E-01	1.37E+01	1.61E+01	7.21E+00	8.65E+00	-6.44E+00	2.38E+03	BFP
1.00E+01	8.00E-01	1.30E+01	1.98E+01	7.02E+00	5.57E+00	5.13E+00	2.34E+03	BFP
1.00E+01	1.20E+00	1.38E+01	1.91E+01	6.71E+00	5.42E+00	3.34E+00	2.28E+03	BFP
1.00E+01	1.60E+00	1.52E+01	1.65E+01	5.74E+00	4.78E+00	6.29E-01	2.14E+03	BFP
1.00E+01	2.00E+00	1.62E+01	1.35E+01	4.61E+00	3.67E+00	-3.32E-01	1.84E+03	BFP
1.00E+01	2.40E+00	1.68E+01	1.13E+01	3.80E+00	3.11E+00	-5.22E-01	1.46E+03	BFP
1.00E+01	2.80E+00	1.72E+01	9.78E+00	3.29E+00	2.95E+00	-6.94E-01	1.11E+03	BFP
1.00E+01	3.20E+00	1.78E+01	8.96E+00	3.01E+00	2.84E+00	-4.14E-01	8.00E+02	BFP
1.00E+01	3.60E+00	1.81E+01	8.99E+00	3.01E+00	2.78E+00	-3.05E-01	5.00E+02	BFP
1.40E+01	0.00E+00	1.83E+01	2.28E+00	7.75E+00	1.36E+01	7.04E+00	2.40E+03	BFP
1.40E+01	4.00E-01	1.78E+01	1.70E+01	7.87E+00	7.99E+00	-8.86E-01	2.40E+03	BFP
1.40E+01	8.00E-01	1.64E+01	1.99E+01	7.77E+00	4.88E+00	-3.19E-02	2.32E+03	BFP
1.40E+01	1.20E+00	1.69E+01	1.84E+01	7.14E+00	5.03E+00	2.07E-01	2.20E+03	BFP
1.40E+01	1.60E+00	1.81E+01	1.56E+01	6.26E+00	4.34E+00	6.74E-01	2.03E+03	BFP
1.40E+01	2.00E+00	1.86E+01	1.32E+01	5.05E+00	3.31E+00	4.67E-01	1.82E+03	BFP
1.40E+01	2.40E+00	1.86E+01	1.12E+01	4.12E+00	2.54E+00	6.12E-02	1.55E+03	BFP
1.40E+01	2.80E+00	1.90E+01	1.00E+01	3.60E+00	2.14E+00	-1.23E-01	1.22E+03	BFP
1.40E+01	3.20E+00	1.94E+01	9.42E+00	3.07E+00	2.09E+00	1.43E-02	9.60E+02	BFP
1.40E+01	3.60E+00	1.89E+01	9.15E+00	3.17E+00	2.18E+00	2.67E-01	7.00E+02	BFP
2.40E+01	0.00E+00	2.18E+01	6.06E+00	1.02E+01	1.18E+01	-1.17E+01	2.34E+03	BFP
2.40E+01	4.00E-01	2.22E+01	1.83E+01	9.04E+00	5.59E+00	4.82E-01	2.33E+03	BFP
2.40E+01	8.00E-01	2.06E+01	2.00E+01	8.21E+00	3.64E+00	-1.97E+00	2.33E+03	BFP
2.40E+01	1.20E+00	2.07E+01	1.79E+01	7.09E+00	3.96E+00	-1.84E+00	2.20E+03	BFP
2.40E+01	1.60E+00	2.11E+01	1.49E+01	6.30E+00	3.38E+00	4.01E-01	1.99E+03	BFP
2.40E+01	2.00E+00	2.14E+01	1.26E+01	5.32E+00	2.61E+00	9.66E-01	1.81E+03	BFP
2.40E+01	2.40E+00	2.14E+01	1.12E+01	4.67E+00	2.19E+00	8.65E-01	1.59E+03	BFP
2.40E+01	2.80E+00	2.11E+01	9.96E+00	3.61E+00	1.86E+00	3.02E-01	1.30E+03	BFP
2.40E+01	3.20E+00	2.02E+01	9.05E+00	3.01E+00	1.82E+00	6.77E-01	9.10E+02	BFP
2.40E+01	3.60E+00	1.81E+01	8.42E+00	2.98E+00	2.04E+00	1.40E+00	5.60E+02	BFP

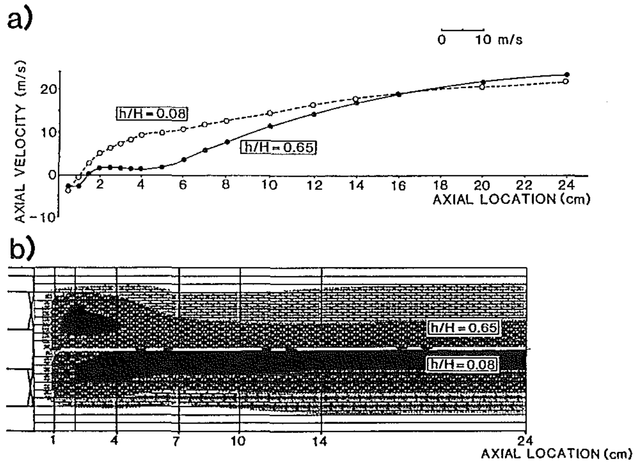

Fig. 3 Inlet configuration change—step expansion ($h/H = 0.65$, 0.08; $2\beta = 70$ deg, $\alpha = 90$ deg): (a) centerline axial velocity; (b) temperature

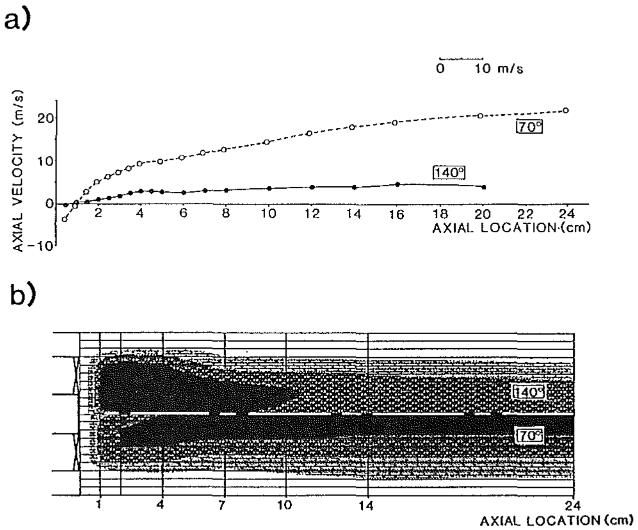

Fig. 4 Nozzle injection angle ($2\beta = 140$, 70 deg; $h/H = 0.08$): (a) centerline axial velocity; (b) temperature

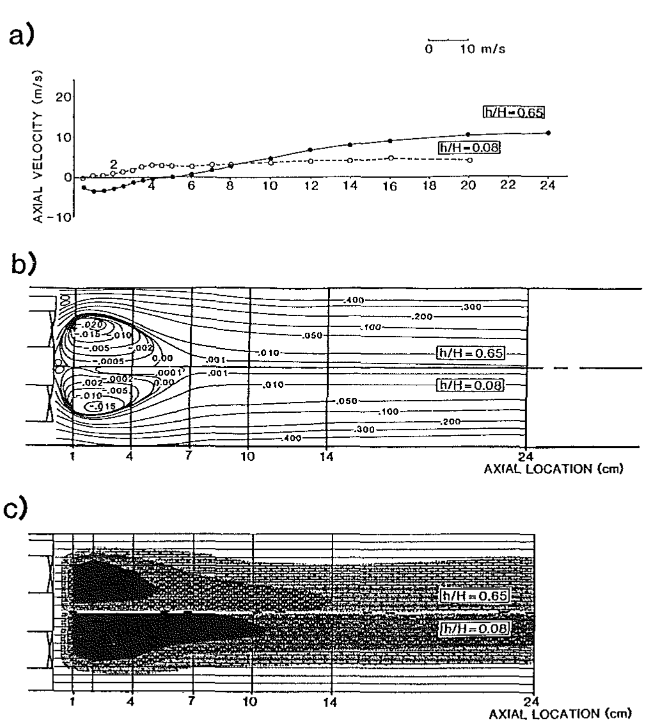

Fig. 5 Inlet configuration change—step expansion ($h/H = 0.65$; 0.08; $2\beta = 140$ deg, $\alpha = 90$ deg): (a) centerline axial velocity; (b) streamline; (c) temperature

devoid of the high temperature "diffusion" core observed for the baseline condition and a more uniform exit plane temperature profile (Fig. 3*b*). This condition is described in more detail elsewhere (Charles et al., 1987a).

140 deg Nozzle With No Step Expansion. This variation was undertaken to match the injection angle of the fuel jet to the structure of the swirl-induced recirculation zone as documented in isothermal measurements. In particular, a wider angle nozzle was employed to direct the fuel into the outer edge of the recirculation zone. This task was accomplished using a 140 deg nozzle with an attendant and dramatic reduction of the positive centerline velocities throughout the combustor (Fig. 4*a*). Figure 4(*b*) shows the thermal field for this condition and the absence of the high-temperature core.

140 deg Nozzle With 90 deg Step Expansion. The centerline axial profile of Fig. 5(*a*) shows that the combination of injecting the fuel to the outer edge of the recirculation zone (using the 140 deg nozzle) and allowing the swirling flow to expand (using the 90 deg step expansion) results in an on-axis swirl-stabilized reaction. Figures 5(*b*) and 5(*c*) present the streamlines (including stream function values) and thermal field for this condition compared to the 140 deg nozzle without a step. (It is worth noting that a preliminary scoping study with a 100 deg nozzle and the step expansion did not result in on-axis recirculation.)

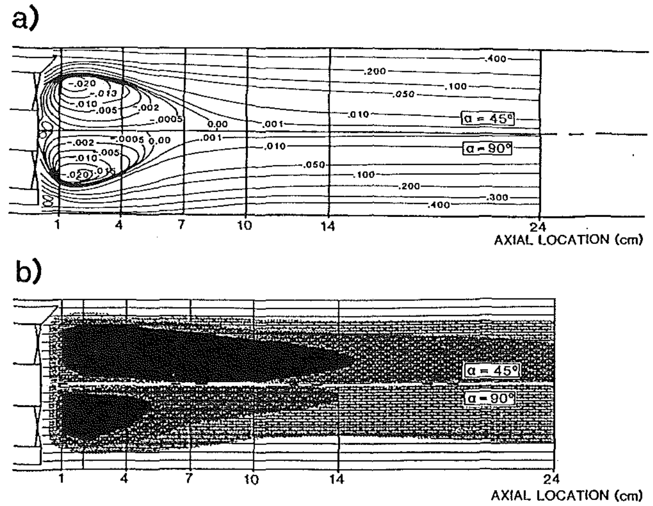

Fig. 6 Inlet configuration change—divergent expansion ($\alpha = 45, 90$ deg; $h/H = 0.65$, $2\beta = 140$ deg): (a) streamlines; (b) temperature

140 deg Nozzle With 45 deg Divergent Expansion. Expanding the inlet geometry from a sudden step (90 deg) to a divergent (45 deg) angle results in a lengthening of the recirculation zone as shown in the streamlines of Fig. 6(*a*). The thermal field exhibits a correspondingly enlarged high-temperature region (Fig. 6*b*). The divergent exit allows the swirl to retain more energy as compared to the step expansion where energy is lost to the corner recirculation zone. The net result is a stronger on-axis recirculation.

Summary and Conclusions

Detailed and well-documented data sets, following the format prescribed in Appendix A, are available for the development and verification of computation codes proposed for gas turbine combustors (Charles and Samuelsen, 1987). The data sets reflect significant changes in the aerodynamic and thermal structure of a swirl-stabilized combustor due to relatively modest changes in the inlet boundary conditions. In particular, the availability of such data should (1) significantly enhance the development of numerical codes that are intended to predict the flowfields of swirl-stabilized reactions, and (2) establish the ability of the codes to reflect the sensitivity to changes in inlet conditions demonstrated in the present model combustor.

Acknowledgments

The efforts of Jacob Brouwer for the collection of detailed laser anemometry and temperature data, support of the UCI Center for Combustion and Propulsion Science and Technology, and Janice Johnson in the preparation of the manuscript are gratefully acknowledged.

References

Charles, R. E., and Samuelsen, G. S., 1987, "Detailed Data Set: Velocity (u, w, $\bar{u}_{rms}$ $\bar{w}_{rms}$) and Temperature (T) Measurements in the Axisymmetric Can Combustor (ASCC) for a Parametric Variation in Inlet Conditions," UCI Combustion Laboratory Report ARTR-87-6, Department of Mechanical Engineering, University of California, Irvine, CA 92717.

Charles, R. E., Brouwer, J., and Samuelsen, G. S., 1987a, "The Sensitivity of Swirl-Stabilized Distributed Reactions to Inlet Flow and Physical Boundary Conditions," presented at the AIAA 25th Aerospace Sciences Meeting, Paper No. AIAA-87-0304; submitted to the *AIAA Journal.*

Charles, R. E., Emdee, J. L., Muzio, L. J., and Samuelsen, G. S., 1987b, "The Effect of Inlet Conditions on the Performance and Flowfield Structure of a Non-premixed Swirl-Stabilized Distributed Reaction," presented at the Twenty-First Symposium (International) on Combustion, The Combustion Institute.

Faeth, G. M., and Samuelsen, G. S., 1986, "Fast-Reaction Nonpremixed Combustion," *Progress in Energy and Combustion Science*, Vol. 12, No. 4, pp. 305-372.

Mongia, H. C., Reynolds, R. S., and Srinivasan, R., 1986, "Multidimensional Gas Turbine Combustion Modeling: Applications and Limitations," *AIAA Journal*, Vol. 24, No. 6, pp. 890-904.

Patankar, S. V., Karki, K. C., and Mongia, H. C., 1987, "Development and Evaluation of Improved Numerical Schemes for Recirculating Flows," presented at the AIAA 25th Aerospace Sciences Meeting, Paper No. AIAA-87-0061.

APPENDIX

Recommended Format for Data Base Documentation (Source: Faeth and Samuelsen, 1986)

1 Experimental Facility
  - general description of facility

2 Experimental Configurations
  - detailed description of experimental configurations; figures

3 Test Conditions
  - identification of test conditions including table listing conditions

4 Inlet and boundary conditions
  - identification and explanation of inlet and boundary conditions including axial pressure gradient

5 Quantities Measured
  - delineation of quantities measured, quantities tabulated, and quantities archived on tape and or disk
  - identification of diagnostic(s) used for each measurement

6 Diagnostics
  - description of diagnostics used; figures of configuration

7 Unusual Measurement Methods
  - description of methodology used in the acquisition of data with attention to techniques unique to the present experiment

8 Experimental Protocol
  - a description of the protocol adopted in the acquisition of the data; the order in which the data were collected; the elapsed period of time

9 Quality Control
  - a delineation of steps taken to assure accuracy of the data; mass balances; repeatability tests; diagnostic(s) performance including seeding uniformity and consistency in the case of laser anemometry, steps taken to assure identical test conditions throughout the duration of the study; tests of sensitivity of experimental to boundary conditions (e.g., exhaust suction)

10 Error Analysis
  - an estimate of the uncertainty (in percent) associated with each measurement due to uncertainty in the measurement method, flow conditions, and so forth

11 Availability of Data
  - explanation of the availability of the data (report number, source, ordering information) and the media (magnetic tape, floppies) on which the data are available

12 References
  - citations of (1) reports and publications referred to in item 11, and (2) references referred to in text

13 Data
  - still photographs of flame for the purposes of (1) identifying the physical nature of the experiment, and (2) the time-averaged structure of the flame
  - presentation of successive frames from a high-speed photographic sequence for the purposes of (1) describing the dynamic behavior of the flame, and (2) providing an indication of the scales of turbulent mixing
  - description of the format in which the data are presented
  - tables of data

Fuel Spray Evolution: Comparison of Experiment and CFD Simulation of Nonevaporating Spray

L. G. Dodge

J. A. Schwalb

Southwest Research Institute,
San Antonio, TX 78284

Detailed spray characteristics were obtained for a small-capacity, pressure-swirl atomizer using an Aerometrics phase-Doppler particle analyzer. Measurements included drop size and velocity distributions, liquid volume fluxes, and air velocities at four axial locations, 25, 50, 75, and 100 mm, with complete radial traverses at each location. Drop size results were compared with measurements from a Malvern laser-diffraction instrument, and integrated liquid volume fluxes were compared with measured flow rates to estimate measurement uncertainties. Drop sizes measured by the two independent techniques and area-weighted-averaged over the radial traverses at each of the four axial stations varied on average by less than 4 percent. Integrated volume flux measurements by the phase-Doppler instrument at four axial stations differed from the nozzle flow rate by at most 19 percent, with some of the difference due to evaporation. The phase-Doppler data were used to begin an evaluation of a commercial two-phase, three-dimensional, CFD code (FLUENT). Using a simplified representation of the spray based on velocity measurements 2 mm from the atomizer, it is shown that the model predicts drop trajectories, velocities, and volume fluxes reasonably well, and air entrainment velocities fairly accurately except on the spray centerline. Drop velocity profiles indicate dense spray effects very close to the atomizer that are not properly predicted by the dilute spray model.

Introduction

At least two significant problem areas remain in the use of two-phase, computational fluid dynamics (CFD) codes to predict the properties of spray flames (El Banhawy and Whitelaw, 1980). One deficiency is in specifying the initial fuel spray drop sizes and velocities with sufficient accuracy to compute spray evaportion and spreading rates. The second deficiency is in the prediction of strongly recirculating flow fields. This paper addresses the first problem area in defining the initial spray characteristics and then comparing the actual spray evolution with that predicted by a commercial CFD code. This work was simplified by studying the spray under almost nonevaporating conditions. These studies will be extended to evaporating conditions using the same spray nozzle and fuel. A realistic gas turbine fuel nozzle and fuel were used in these tests.

The validation of fuel spray submodels in CFD codes requires detailed measurements throughout the spray field. Spray characteristics vary axially and radially even in the axisymmetric case, requiring a series of measurements to represent the spray. Measurements should include drop-size distributions and associated velocity distributions, liquid volume fluxes, and fuel vapor concentrations. Air velocities and turbulence properties are also required to evaluate interphase exchange laws.

Double-pulse spark gaps or lasers have been used to measure drop-size and velocity distributions simultaneously (Mellor et al., 1971). This is clearly a slow, tedious process and requires large depth-of-field corrections to avoid a bias toward the larger drops. Automated video-imaging systems provide similar information at much higher speeds, but are still slow compared with some other drop-sizing instrumentation.

Laser-diffraction instruments (Swithenbank et al., 1977) have been used extensively in recent years to characterize drop-size distributions, but they are not well suited for CFD code verification because the measurements are line-of-sight averages through the spray rather than spatially resolved, and no velocity information is obtained. However, laser-diffraction measured line-of-sight integral results may be converted to spatially resolved data in axisymmetric sprays using Abel inversion schemes (Hammond, 1981). Laser-diffraction instruments that have been "calibrated" (Dodge, 1984) show excellent accuracy when compared with standard reticles (Hirleman and Dodge, 1985), and also show very good agreement between instruments on standard sprays (Dodge, 1987a). Thus, laser-diffraction instruments have the accuracy required for obtaining benchmark-quality drop-size data in some sprays, and the capacity for spatially resolved data in axisymmetric sprays, but do not provide drop velocity information desirable for CFD-type models.

Single-particle-counting instruments that operate on a combination of fringe visibility and scattering intensity (Hess, 1984)

Contributed by the International Gas Turbine Institute and presented at the 33rd International Gas Turbine and Aeroengine Congress and Exhibition, Amsterdam, The Netherlands, June 5-9, 1988. Manuscript received by the International Gas Turbine Institute December 16, 1987. Paper No. 88-GT-27.

or on the phase shift of light refracted through drops (Bachalo et al., 1986) offer the possibility of simultaneously measuring drop size and velocity. In addition, if the probe area is known and if a large majority of drops passing through the probe area can be successfully counted, then the liquid volume flux is easily calculated. Thus, if these instruments can operate accurately at the high counting rates required, they would provide the information required for detailed CFD spray model validation. Intercomparisons among three instruments—a laser diffraction, a phase-Doppler, and a fringe-visibility/scattering-intensity device—on one spray resulted in similar values for average drop sizes, with the laser-diffraction measurements somewhat lower than the other two instruments (Jackson and Samuelsen, 1987). The phase-Doppler instrument has a broader size range than the fringe-visibility/scattering intensity (35:1 versus 10:1) and a higher counting rate, making it more suitable for model validation. Other intercomparisons between phase-Doppler and laser-diffraction instruments on a spray showed drop size measurements to be similar but with the phase-Doppler measurements slightly larger than the laser-diffraction values (Dodge et al., 1987). However, liquid volume flux measurements by the phase-Doppler instrument showed errors by up to a factor of 7, which precluded the use of those data for model validation. After improvements in the phase-Doppler instrument and in operating procedures, those measurements were repeated with significantly improved results for both drop-size and volume flux measurements, as reported in this paper.

In addition to a characterization of the drop properties, detailed spray modeling requires a specification of the air velocity and turbulence properties inside and outside the spray. Characterizing the air flow inside the spray is difficult with a conventional laser-Doppler velocimeter because the scattering cross sections of the drops are much larger than those of the seed particles. However, instruments that simultaneously measure drop size and velocity may be set to measure the velocities of small liquid seed particles while discriminating against signals from the larger drops.

Approaches to modeling fuel sprays have been reviewed by Crowe (1982) and Faeth (1983), among others. Fuel sprays and the corresponding spray models range from dilute sprays characteristic of, for example, spinning disks or pressure-swirl atomizers, to very dense sprays such as those formed by multihole diesel nozzles. In very dense sprays, it is necessary to include drop collisions, coalescence, and breakup, and drop sizes measured downstream may be relatively independent of initial drop sizes due to re-arrangement by these processes (Reitz and Diwaker, 1987). However, in dilute sprays such as the one studied here from a pressure-swirl atomizer, collisions are assumed to be infrequent with those that do occur being between very different sized drops traveling with very different velocities and having minimal impact on either the size of the larger drop or the number density of the smaller drops (Asheim and Peters, 1987).

Comparisons similar to those performed in this work have been reported by several workers. Gosman and Ioannides (1981) compared results from their CFD simulation with the experimental data of Tishkoff et al. (1980) for an *n*-heptane spray from a small-capacity pressure-swirl atomizer. Experimental data were principally cone angle measurements and drop size and volume fraction measured at two axial locations with a laser-diffraction instrument and converted to spatially resolved data by deconvolution. Large discrepancies were reported between predicted and measured liquid volume fractions, with predicted volume fractions peaking near the centerline and measured volume fractions peaking further out radially. Discrepancies for fuel vapor concentration were less dramatic. The discrepancies were attributed to uncertainties in the initial conditions.

The experimental data of Mellor et al. (1971) were compared with computations by the original authors and by two other groups. The experimental measurements were performed with a small-capacity pressure-jet atomizer spraying water. Measurements of drop size, velocity, and angle of trajectory were recorded with double-flash photography at the breakup region and at four axial locations downstream. Air velocity was high (13.9 m/s), minimizing air entrainment effects. Mellor et al. analyzed the spray as single isolated spheres in an infinite atmosphere (no momentum coupling from the drops to the gas). They reported that spray evolution could be predicted more accurately based on initial conditions from the measurements for different drop size classes at the 30-mm axial location rather than the average velocities and trajectories at the sheet breakup location of 7.8 mm.

The experimental data of Mellor et al. were also compared with computed results by Sturgess et al. (1985) using a TEACH code modified to include a second phase. Computed drop velocities agreed fairly well with experimental results, while computed trajectory angles were larger than experimental values and average drop sizes at various radial locations were significantly underpredicted. Asheim et al. (1987) performed similar computations on the same spray using a similar model but with an additional submodel to account for collisions. Even for this seemingly dilute spray, Asheim et al. showed very modest improvements in predicted drop size and velocity distributions when drop collisions were accounted for.

This paper is organized as follows. First the experimental apparatus and spray characterization equipment are discussed. Then the two-phase CFD code used for comparison with experimental measurements is described. The drop size and volume flux data are presented, with at least two independent measurements for each. Then the spray evolution as predicted by the CFD code is compared with the experimental results. Finally, these results are discussed and compared with previous work.

Experimental Apparatus

The atomizer used for this study was a type that was tested by eleven different laboratories in a recent drop-size measurement round robin unofficially organized by ASTM subcommittee E29.04 (Dodge, 1987a). The atomizer was a small pressure-swirl type of peanut style used in gas turbine combustors and was manufactured by Parker Hannifin Corp. as P/N 3030946. The flow number on aircraft fuel system calibration fluid MIL-C-7024 type II (special-run stoddard solvent) was 2.05×10^{-6} kg/s $\sqrt{\text{Pa}}$ (1.35 lbm/h $\sqrt{\text{psid}}$). This fluid was used for all tests, and some of its properties are listed in Table 1. The nominal cone angle was 80 deg. The fluid was maintained at 300 K, and measurements were made at pressure differences across the atomizer of 689 kPa (100.0 psid).

The atomizer was mounted in a spray chamber with a cross section of 0.30 m × 0.41 m and a length of 0.53 m between honeycomb flow-straightener sections. A bellmouth inlet was used in addition to the honeycomb straightener to reduce turbulence levels. A twisted metal screen and settling chamber

Table 1 Selected physical properties of aircraft fuel system calibration fluid

Test	Specification		Actual
	Minimun	Maximum	
Specific gravity	0.765	0.775	0.772
Viscosity, cSt at 25°C	1.12	1.22	1.13
Distillation, °C			
Initial boiling point	149		157
End point		210	200
Recovery, percent volume	98.5		99.0
Molal average boiling point, °C			163
Latent heat of vapor (estimated), kJ/kg			282

followed the outlet honeycomb flow straightener to aid in mist removal. An explosion-proof fan pulled air through the system at a velocity in the test section of 1.6 m/s and a turbulence level of about 2.5 percent. The atomizer was positioned within the chamber by a two-axis, computer-controlled actuator system.

Drop size and velocity distributions and liquid volume fluxes were measured with an Aerometrics phase-Doppler particle analyzer (Bachalo et al., 1986). The same system was used to characterize the air flow, which was seeded with approximately 2-μm diameter drops by vaporizing and coalescing military fog oil. Several changes were made in the instrument and operating procedures to improve performance over that previously reported (Dodge et al., 1987). The receiver lenses were replaced with a more accurately aligned set. The 50-μm-wide slit in the receiver was replaced with a 100-μm slit. The phototubes were replaced with a matched set. The top end of the size range for a given optical arrangement was avoided. Fringe-shifting was avoided except where required. New criteria were developed to set the photomultiplier tube voltages. (The manufacturer was involved and helpful in some of these modifications.) With these improvements, the performance was significantly improved over that previously reported (Dodge et al., 1987). Typically 5000 drops were measured at each location, except in dilute outer regions of the spray, where counts dropped to about 1000.

A laser-diffraction instrument was used for an independent measurement of drop-size distributions and volume fractions with which to compare the phase-Doppler instrument. This Malvern model 2200 particle size was calibrated and gave excellent results when compared with a calibration reticle (Dodge, 1984). To increase the spatial resolution, the laser beam diameter was reduced from 9 to 3 mm. For the receiver, the 300-mm focal length f/7.3 lens was used for all tests. The laser-diffraction drop-size distributions were assumed to be Rosin-Rammler for the line-of-sight data. The line-of-sight integral data were converted to spatially resolved results by deconvolution, or Abel inversion (Hammond, 1981). The size distributions after deconvolution were not assumed to follow any particular function.

Description of Two-Phase CFD Computer Model

The experimental results obtained during this effort were used in the preliminary evaluation of a two-phase, computational fluid dynamics (CFD) code. A commercially available code, the Creare R&D FLUENT code,[1] was used in this evaluation. The FLUENT code was chosen because it is widely available and easy to use for a problem such as the one studied here. It has the disadvantage that the spray submodel does not include some capabilities that would be desirable to evaluate, as described below.

The FLUENT code is a two-phase, three-dimensional, finite difference, CFD code that models the gas phase in an Eulerian frame of reference and the drops in a Lagrangian frame of reference. Turbulence effects are included and were treated with the K-ϵ model. Momentum exchange is computed both ways between both phases with drop drag effects following the treatment by Morsi and Alexander (1972). Evaporation rates are calculated during both the heatup phase and at the final equilibrium temperature using the equations given by Ranz and Marshall (1952). Most of the results presented here were with the evaporation option turned off so that the drops were treated as solid particles to simplify data analysis. Computations with evaporation in operation indicated an evaporation of about 12 percent at the farthest axial location (100 mm). The evaporation model does include the buildup of fuel vapor in the gas phase and the resulting decrease in evaporation rates as the gas phase approaches saturation.

The spray submodel does not include drop breakup, collisions, or coalescence. Also the turbulence damping effects of drops on the gas phase are not included. However, turbulence generation by the drops is included. The experimental data generated in this work will help to evaluate whether these added features are necessary to model this type of spray correctly.

This problem was simulated in two dimensions, assuming axial symmetry and using a cylindrical coordinate system. Staggered grids (25 axial, 20 radial) were employed that concentrated calculations axially close to the atomizer and radially just off the centerline. The corresponding physical domain was about 150 mm wide and 250 mm long. The smallest computational cell measured 2.65 mm axially by 2.81 mm radially. Blockage by the spray nozzle was included in the calculations.

The approach to comparing computational and experimental results was to use the measured axial and radial spray velocities 2 mm downstream of the atomizer to predict spray evolution further downstream. The initial air velocity was based on LDV measurements upstream of the atomizer, while liquid mass flow was the known flow rate to the atomizer, and the drop-size distribution was an area-weighted average of all the radial measurements at a location 50 mm downstream of the nozzle. (Preliminary calculations of drop evaporation indicated that only 5 percent of the liquid had evaporated at that point.) The distribution of sizes was simulated by using 12 discrete drop sizes from 10 to 120 μm. Turbulence effects were included in the calculations with a stochastic particle tracking method similar to that of Gosman and Ioannides (1981), except that eddy lifetimes were assumed to be long relative to the eddy transit times by the drop.

The aircraft fuel system calibration fluid (MIL-C-7024 II) used in the experiments is a multicomponent hydrocarbon similar to jet fuel. A limited number of computer simulations were performed that included evaporation, and the test fluid was simulated by using properties of the single-component hydrocarbon decane that had a similar molal boiling point.

Experimental Results

Drop size measurements made by the phase-Doppler instrument are for a small volume in space (ca. 10^{-5} cm^3), and the response is weighted by the number of drops passing through the sampling area per unit time (referred to as a temporal or flux-weighted sample). The laser-diffraction results are for a line-of-sight average that must be converted to a spatially resolved value by deconvolution (Hammond, 1981) for comparison with the phase-Doppler results. Also the laser-diffraction instrument response is weighted by the number of drops per unit area (referred to as a spatial or number-density-weighted sample). For comparison with the laser-diffraction results, the phase-Doppler measurements were converted from the temporal frequency format to the spatial frequency format by using the average drop velocities (Dodge, 1987b).

Comparison of the Sauter mean diameters or SMD's ($\bar{D}_{32}$) as measured by the two instruments at different radial locations is shown in Fig. 1 for an axial location of 50 mm. Similar agreement was obtained at 25, 75, and 100 mm (Dodge and Schwalb, 1987). Note that the phase-Doppler instrument is based on refraction through the drops (Bachalo et al., 1986) (as used here in 30 deg scattering) while the Malvern instrument relies on diffraction from the edges of the drops (Swithenbank et al., 1977). Thus, the measurement techniques are completely independent. In spite of numerous possible sources of errors or differences between these two measurement techniques (Dodge et al., 1987), these results show excellent agreement, generally with differences within the accuracy of either measurement. Errors in the deconvolution procedure build up toward the centerline, contributing to differences there. Near the edges of the spray, the number densities are low, resulting in poor statistics particularly for the phase-Doppler instrument.

---

[1] Available from Creare R&D Inc., Hanover, NH.

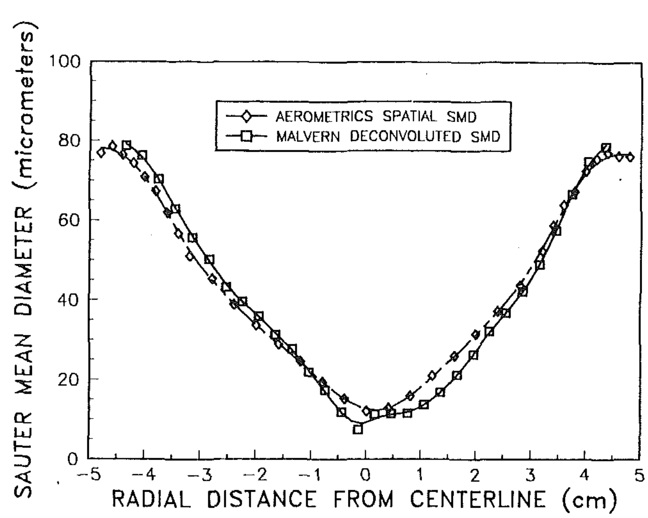

Fig. 1 Comparison of SMD's measured as a function of radial location by Aerometrics phase-Doppler and Malvern laser-diffraction (after deconvolution) instruments at an axial location of 50 mm

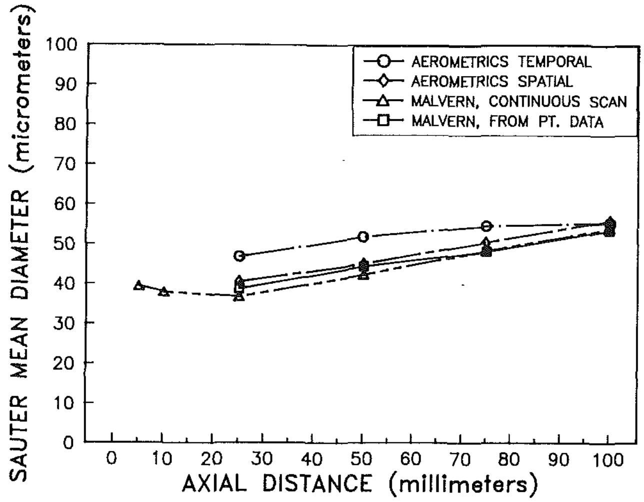

Fig. 2 Comparison of cross-section-averaged SMD's measured by Aerometrics phase-Doppler (temporal and spatial formats) and by Malvern laser-diffraction (from summing deconvoluted point data and from continuous scan method)

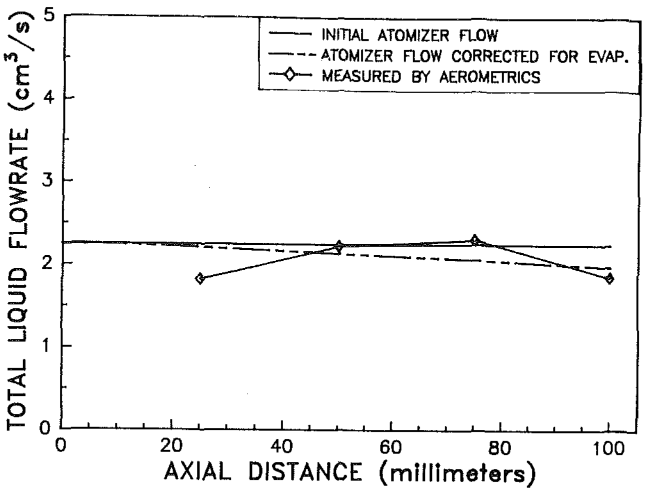

Fig. 3 Compression of integrated volume flux measured by aerometrics phase-Doppler with the flow rate to atomizer (both with and without correction for evaporation)

If the Malvern laser-diffraction instrument is used as a reference based on its accurate measurement of a reticle (Hirleman and Dodge, 1985), then these Aerometrics phase-Doppler measurements appear to be an accurate representation of the spray. The reader is cautioned that results from the phase-Doppler instrument appear to vary somewhat with instrument settings, and poorer performance on the same spray has been demonstrated.

Another approach to verification of the drop size measurements is the summation of the radial measurements into a single cross-section-averaged SMD that is weighted by the number density (number flux for flux-weighted measurements) and the annular ring area for each radial measurement (Dodge, 1987b). For the laser-diffraction instrument, this cross-section-averaged SMD may be computed from the deconvoluted point values by summation, or directly from experiment by scanning the laser beam across the spray continuously while acquiring scattering data. The differences between these two values for the laser-diffraction instrument help to highlight errors in the deconvolution and summation processes.

A comparison of the cross-section-averaged SMD's for the four axial locations is shown in Fig. 2. The Aerometrics phase-Doppler data in the spatial format are directly comparable with the Malvern laser-diffraction data calculated from summing the point data or acquired by the continuous scan method. It may be seen from Fig. 2 that the Aerometrics data differ from the Malvern summed-point-data by an average of only 3.9 percent. Thus, if the laser-diffraction data are used as a reference, the Aerometrics phase-Doppler drop-size data are an accurate representation of the cross-section-averaged drop-size. The cross-section-averaged SMD's for the Malvern calculated from summing the point data and measured by the continuous scan technique differ by an average of only 2.8 percent for the four axial locations shown in Fig. 2. This close agreement serves to help verify both the deconvolution procedure and the summation method.

The Aerometrics data in the temporal format are larger than the other data due to increased weighting of the higher-velocity larger drops close to the atomizer. As all drops decelerate to about the same velocity at the 100-mm location, the differences between the temporal-frequency and spatial-frequency sampling disappear as verified in Fig. 2. In a spray with no evaporation, recirculation, breakup, or coalescence, a temporal frequency measurement of cross-section-averaged drop size should be constant as a function of axial distance from the atomizer (Dodge et al., 1987). The Aerometrics temporal-frequency SMD's shown in Fig. 2 are relatively constant, but show a slight increase with distance, possibly due to coalescence of drops. Further modeling may help to explain the trend.

In previous work at this laboratory, the most serious measurement error with the phase-Doppler instrument has been the liquid volume flux (Dodge et al., 1987). The principal source of error is in the computation of the effective sampling area, which is combined with the drop size measurements and elapsed time to compute the liquid volume per unit time per unit area. Previous work has resulted in integrated liquid volume fluxes measured to be several times larger than the flow rate through the atomizer.

With improvements in instrument design and operation as described in the Experimental Apparatus section, the results obtained here were significantly improved. Figure 3 shows a comparison of the integrated liquid volume flux measured by the phase-Doppler instrument with the liquid flow rate to the atomizer, and with that flow rate corrected for evaporation as estimated from the FLUENT code calculations. These results indicate a maximum error for the integrated measured values of about 19 percent when compared with the flow rate to the atomizer, with somewhat smaller errors (maximum of about 15 percent) if evaporation is accounted for. Since errors in liquid volume flux scale with the cube of errors in size measurement, and are significantly affected by the calculation of

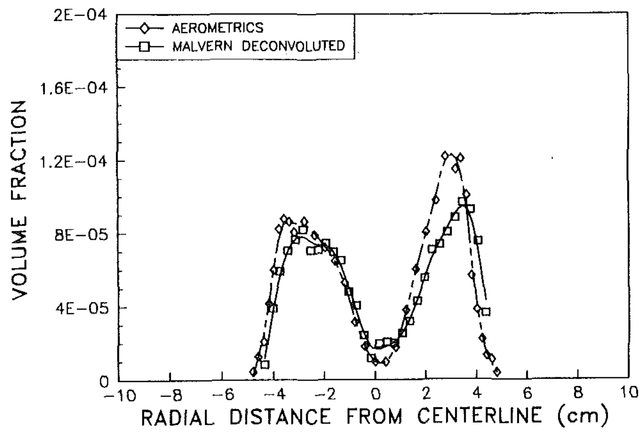

Fig. 4 Comparison of volume fractions measured by Malvern laser-diffraction (after deconvolution) and by Aerometrics phase-Doppler at an axial distance of 50 mm

the effective sampling area, it is not surprising tht volume flux errors are larger than drop size measurement errors.

Integrated liquid volume fluxes were computed from about 30 individual measurements at the same radial locations as shown in Fig. 1, and then weighted by the annular area corresponding to each radius. These integrated volume fluxes then have the units of liquid flow rate. Measurements at individual radial locations probably had larger errors and variability than the integrated values. Some of the variability at individual locations is due to actual variability of the volume flux as seen also in patternator measurements. These sprays tend to be more symmetric in terms of average drop size than in terms of volume flux.

Comparisons were made between volume fluxes measured by the phase-Doppler instrument and a tube-type patternator. However, the patternator had a poor collection efficiency for the small drops in the center of the spray cone due to non-isokinetic sampling conditions at the entrance to the tubes. These comparisons were judged to be unreliable and are not presented here, but do highlight problems associated with using tube-type patternators for collecting fine drops.

The laser-diffraction instrument does not measure a liquid volume flux with which to compare the phase-Doppler measurements. However, it does measure a liquid volume fraction that can be converted from the line-of-sight average measurement to a spatially resolved value by Abel inversion, or deconvolution (Hammond, 1981). The phase-Doppler instrument measures a number flux and a volume mean diameter ($\overline{D}_{30}$) that can be converted to a liquid volume fraction for comparison with the laser-diffraction result. This procedure involves dividing the number flux of each drop size class by the average velocity of the size class to get a number density of each size class. These number densities of each size class are summed over all size classes to get a total number density, which is multiplied by ($\pi/6$) $\overline{D}_{30}^3$ to get the volume fraction ($\overline{D}_{30}$ in spatial-frequency format). It should be noted that the conversion of phase-Doppler measurements to volume fraction is solely for comparison with the laser-diffraction measurement, as the volume flux is more appropriate than volume fraction for comparison with model predictions. Liquid volume flux integrated across a spray cross section is a conserved quantity except for liquid that has evaporated, while volume fraction is not. Therefore, in principle, a measurement of the total liquid volume flux at various axial locations gives a measure of the vaporized fuel at different spray cross sections. In practice, the precision of the volume flux measurements limits this to sprays with reasonably high evaporation rates.

A comparison of the volume fractions as measured by the Aerometrics phase-Doppler and Malvern laser-diffraction instruments is shown in Fig. 4 for an axial location at 50 mm. Similar results were obtained at 25, 75, and 100 mm (Dodge and Schwalb, 1987). Considering the order of magnitude changes in volume fractions through the spray and the differences in the sample volumes for the two instruments, the agreement is considered acceptable.

Having established that the phase-Doppler measurements of average drop size were accurate and the volume flux measurements were reasonably accurate, these data were judged to be suitable for CFD model validation. (The complete set of data, which includes far more information than can be presented here, can be made available on floppy disks to others with similar interest.) In order further to evaluate these results, they were compared with a CFD simulation that employed a fairly basic spray model.

Two-Phase CFD Simulation Results

The experimental results as measured by the Aerometrics phase-Doppler instrument were used in a preliminary evaluation of the Creare R&D FLUENT code. The following comparisons were performed:

- Drop trajectories
- Drop velocities along the trajectories
- Profiles of liquid volume flux
- Profile of axial air velocity and turbulence intensities

Comparing CFD simulation results from the FLUENT code with measurements from the phase-Doppler instrument requires processing both sets of results to arrive at a similar format. Phase-Doppler measurements at one location consist of the velocity components and sizes of a distribution of drops flowing through a small measurement volume. By taking measurements over a range of locations in the spray, a map of drop size and velocity is made for the entire axisymmetric spray region, resulting in an Eulerian frame of reference where each property is known as a function of location, but the paths of individual particles are not known. In contrast, the FLUENT code calculates drop behavior in a Lagrangian reference frame. Also, instead of a continuous distribution of drop sizes, the FLUENT code assumes that a limited number of discrete particle sizes are being injected simultaneously. Each particle size is treated as a separate injection carrying its fraction of the total flow rate.

Drop trajectories are of interest in pressure-swirl atomizers because of the significant segregation of sizes as a function of radial distance from the centerline (e.g., Fig. 1). Using a Lagrangian frame of reference, the FLUENT code naturally provides information on individual droplet positions as they move through the spray. Stochastic particle tracking (Gosman and Ioannides, 1981) was used to include turbulence effects, and 10 trajectories were calculated for each of 12 drop size classes from 10 to 120 μm. However, after obtaining a converged solution, the "average" particle track was computed for each drop size through the previously computed gas flow field with the turbulence contribution to the particle tracks removed, and these results were used for comparison with drop size measurements at various radial locations.

The phase-Doppler measurements do not provide trajectories of individual drops, but do provide average drop sizes as a function of axial and radial location. These measurements were interpolated to determine the locations of the 10, 20, 30, . . . μm diameter drops corresponding to the predicted trajectories. Various measures of average drop size were available, and the SMD (D_{32}) was chosen as the representative diameter for these comparisons (as a flux-weighted or temporal sample). (It would be possible to process the CFD results to predict particle size distributions at any point, but it would require computations for a large number of drop trajectories.)

The initial conditions for the model, which are specified in Table 2, were the measured average axial and radial spray

Table 2 Initial conditions for computer model simulation

Air velocity, m/s	1.60
Air turbulence intensity	.025
Drop velocities, axial, m/s	19.85
radial, m/s	16.10
Flow rate distribution in kg/s among drop sizes (micrometers)*	
5-15	1.178×10^{-6}
15-25	1.089×10^{-5}
25-35	2.157×10^{-5}
35-45	2.686×10^{-5}
45-55	2.998×10^{-5}
55-65	3.452×10^{-5}
65-75	3.946×10^{-5}
75-85	4.017×10^{-5}
85-95	3.285×10^{-5}
95-105	1.985×10^{-5}
105-115	8.359×10^{-6}
115-125	2.237×10^{-6}
Total	2.683×10^{-4}

---

*This is for a one radian slice of the spray cone. The flow rates for the entire spray cone are the above values multiplied by a factor of 2π.

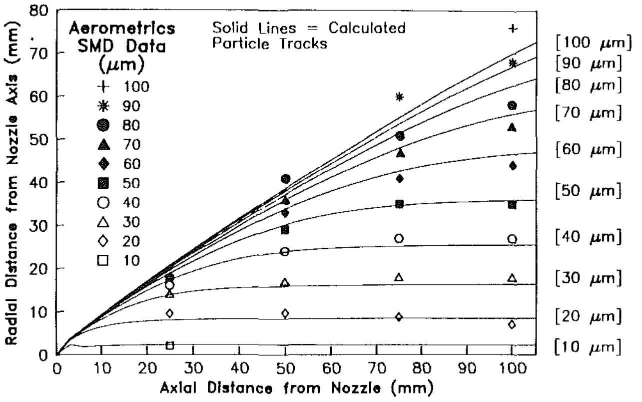

Fig. 5 Comparison of trajectories predicted by FLUENT code with SMD's measured by Aerometrics phase-Doppler

velocities for the larger drops at the peak flux locations 2 mm downstream of the atomizer, the drop-size distribution measured 50 mm downstream of the nozzle, and the air velocity and turbulence intensity measured upstream of the atomizer. All drops were assumed to have the same initial axial and radial velocities, while measurements indicated a range of velocities and angles. However, measurement accuracy of drop sizes and volume fluxes was poor at the 2-mm location due to high spray densities and (probably) incomplete atomization and stabilization of drops.

The trajectories as predicted by the FLUENT code from the initial drop velocities at 2 mm are compared witih the SMD's measured at four downstream axial locations in Fig. 5. It is important to note that the FLUENT code has not been "adjusted" in any way based on the downstream measurements. These results show that predicted trajectories match very well with the actual spray evolution as measured by the phase-Doppler instrument. The only significant discrepancies are at the outer edge of the spray where drop densities were low and measurement statistics also low. Also, the actual size distributions are broader near the edge of the spray, making the choice of which average size to use more critical. Overall, the spray trajectories are predicted accurately, even with the over-simplified initial condition.

The velocity of drops as they travel through the spray may be compared in a similar manner. By virtue of its Lagrangian reference frame, the FLUENT code automatically provides velocities of the selected drop sizes as they move along their trajectories. Interpolation betweeen the radial positions of Aerometrics measurements was performed in the same way as for the drop-trajectory data.

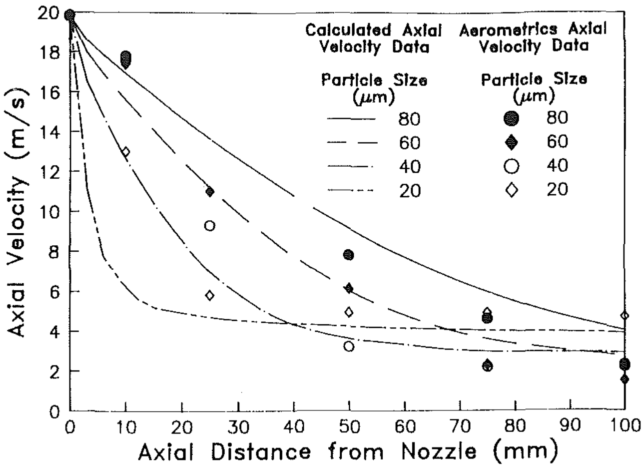

Fig. 6 Comparison of axial drop velocities along trajectories in Fig. 5 predicted by FLUENT code and measured by Aerometrics phase-Doppler

A comparison of axial drop velocities predicted by FLUENT along the trajectories shown in Fig. 5 with those measured by the phase-Doppler instrument at the same locations is shown in Fig. 6. General trends are as expected, with the small drops decelerating due to drag forces more rapidly than the large drops. (The "final" velocities for the different sizes do not approach the same value because the air velocities are different at the different trajectory locations.) The trends observed experimentally are predicted well by the model, but there are noticeable discrepancies. The computed deceleration rates close to the atomizer are much larger than the actual rates, probably due to the finite distance required for sheet breakup and drop formation and other drop interaction and dense spray effects. Smaller computational grid dimensions could possibly increase momentum transfer to the gas in the dense spray region near the nozzle and improve the computed drop velocities in that region. Downstream the FLUENT code predictions seem to overestimate the velocity of the 80-µm drops, but generally predict the velocities fairly accurately including the crossover by the 20-µm drops.

Liquid volume flux in the axial direction is another important spray characteristic, especially for later studies of vaporization of sprays. Volume fluxes, computed directly from the FLUENT code calculations, would be infinite at the computed trajectory locations (see Fig. 5) for test drops (i.e., finite flow rate ÷ zero area), and zero elsewhere. Therefore, to smooth the volume fluxes it was necessary to define computational areas and add up the flow rates for all drop trajectories through those areas. In the two-dimensional space of the computations, those areas became one-dimensional intervals over a range of radial locations at a constant axial location, but represent annular areas in three-dimensional space. The flux computed over each interval was assigned to the midpoint of the interval, and the interval shifted in small steps over all radial locations. A triangular weighting function was used within the interval to preferentially weight the trajectories nearest the midpoint.

The results of those calculations, along with Aerometrics measurements are presented for profiles at 25, 50, 75, and 100 mm downstream of the nozzle in Figs. 7(*a*)-(*d*). The characteristic shape of hollow cone sprays is apparent in both calculated and measured data that show peaks in volume flux at the edge of the spray cone in Fig. 7(*a*). Also of note is the trend for those peaks to become lower and for the flux in the center of the spray to become relatively higher as the profile is moved farther downstream from the nozzle. The two reasons that the peaks on the edge of the spray cone decrease in going downstream can be seen in Fig. 5. First, at the 25-mm axial

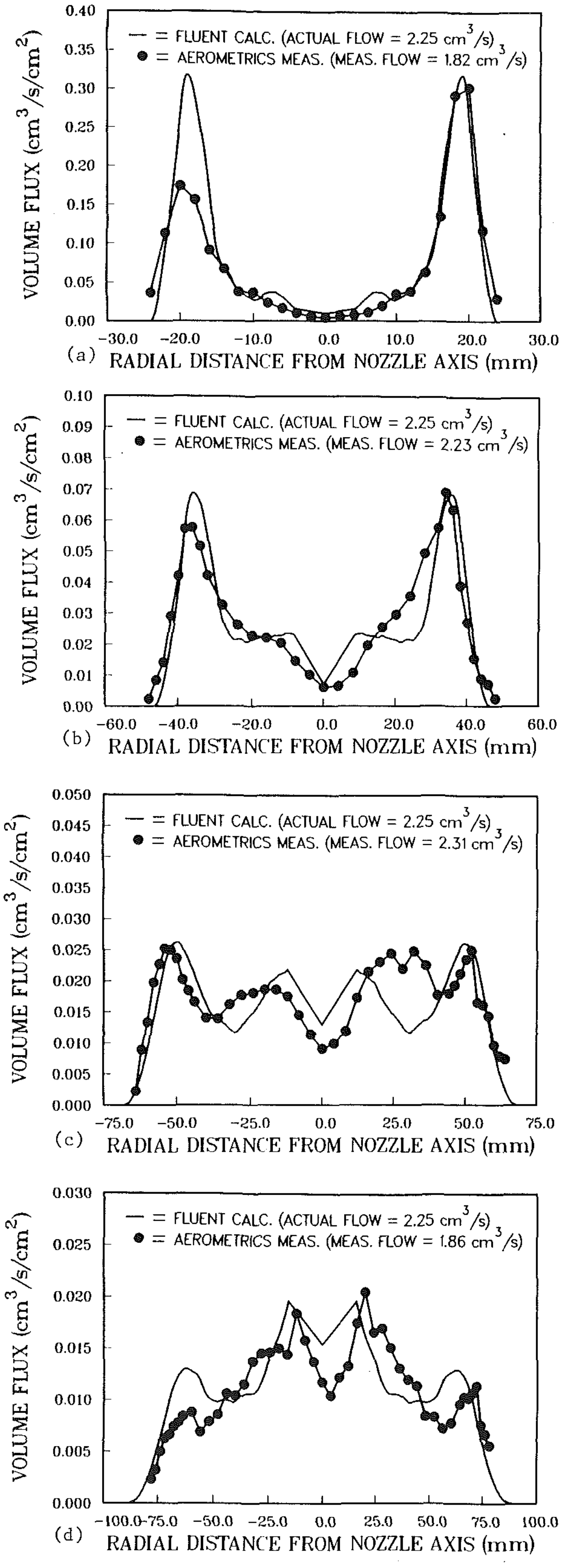

Fig. 7 Comparison of liquid volume fluxes predicted by FLUENT code and measured by Aerometrics phase-Doppler at axial locations of (*a*) 25 mm, (*b*) 50 mm, (*c*) 75 mm, and (*d*) 100 mm

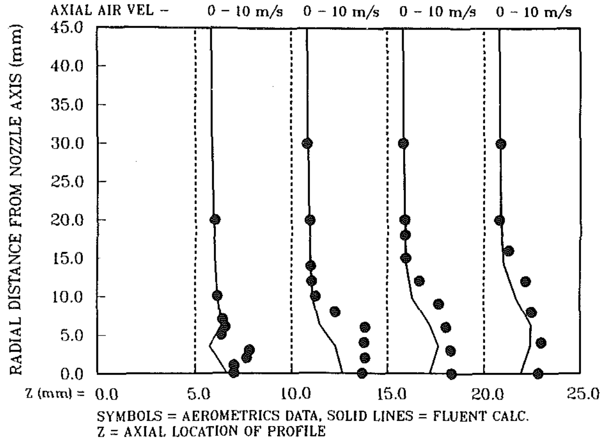

Fig. 8 Comparison of axial air velocities predicted by FLUENT code and measured by Aerometrics phase-Doppler at axial locations of 5 to 20 mm

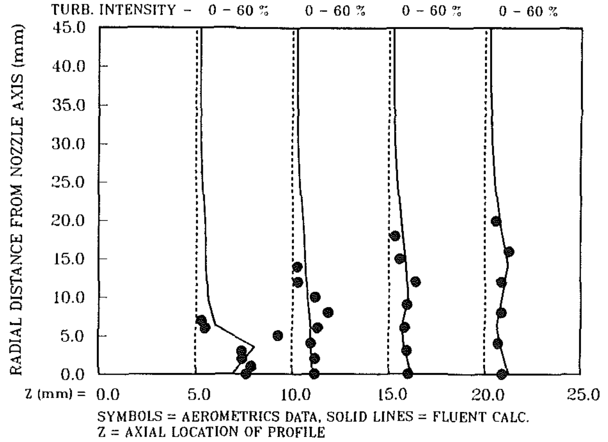

Fig. 9 Comparison of axial component of air turbulence intensities predicted by FLUENT code and measured by Aerometrics phase-Doppler at axial locations of 5 to 20 mm

location, the trajectories for all the drops 40 μm and larger are closely spaced, but the trajectories spread out farther downstream. Second, the annular area corresponding to the edge region increases at greater axial distances due to the increase in radius, and this annular area is in the denominator of the flux calculation. The computed volume fluxes verify that trend in the experimental data.

Considering the simplicity of the assumed initial conditions and the lack of symmetry in the experimental values, the calculated volume fluxes are fairly accurate. If made broad enough, the sliding calculational interval artificially corrects for some of the lack of dispersion in initial drop velocities and angles. For these results, the interval width was chosen to provide the best match with the experimental results at 50 mm, and the same ratio of interval width to the largest radial trajectory value was used for the other three axial locations (ratio = 0.42).

The final comparisons concern the entraining effect the spray has on the air flow. Since, in this case, both Aerometrics phase-Doppler and FLUENT data are provided in an Eulerian frame of reference, no special data processing is necessary other than some interpolation between FLUENT grid points. Air entrainment is strongest close to the atomizer, with axial air velocities at the 5- to 20-mm axial locations shown in Fig. 8, while comparisons for the 25- to 100-mm axial locations are given by Dodge and Schwalb (1987). It appears from these data that the drag forces and momentum exchange between liquid and gas are somewhat underpredicted by the FLUENT code.

Air turbulence intensities (axial velocity component) were measured at the same points with results as shown in Fig. 9 for the 5- to 20-mm axial locations, while comparisons for the

25- to 100-mm axial locations are given by Dodge and Schwalb (1987). Magnitudes were reasonably well predicted, except that they are underpredicted at 5 mm and overpredicted at the 75- and 100-mm axial locations. It is possible that the drops are damping the air turbulence (Mostafa et al., 1987), and this is not accounted for in the FLUENT code.

In conclusion, the FLUENT code successfully predicted the spray evolution of this small-capacity pressure-swirl atomizer, although discrepancies were noted in computed drop drag effects near the atomizer, in air velocities near the centerline, and in turbulence decay. These deficiencies could be related to the oversimplified initial conditions.

Discussion

A relatively new instrument, the Aerometrics phase-Doppler, has been used to acquire these spray data, and the results have been checked against independent measurements by a Malvern laser-diffraction instrument and other instrumentation. Most previous work of this type has been based on double-flash photography (e.g., Mellor et al., 1971). The phase-Doppler instrument used here acquires data much more rapidly than photographic or video systems, so that the overall spray can be mapped more readily. Experimental uncertainties should be easier to evaluate for these data because of the measurement of many of the properties by two independent techniques.

The phase-Doppler system has been used previously to study the evolution of a particle-laden jet (Mostafa et al., 1987). However, the particles in that study were glass beads of known, monodisperse size, so that the problem was essentially different from the one studied here.

Previous work has been performed to establish the accuracy of the Aerometrics phase-Doppler instrument by comparison with other instrumentation on liquid sprays (see Introduction). This work extends those previous efforts.

Mellor et al. (1971) reported problems in trying to predict spray evolution based on measurements close to the atomizer (7.8 mm). Although data were recorded close to the atomizer in this study (10 mm), the integrated volume fluxes did not show a mass balance and were not used to predict downstream size distributions. However, those data are available and could be used for a similar analysis.

The volume flux computations from this study show much better agreement with experiment than those of Gosman and Ioannides (1981) for the experimental data of Tishkoff et al. (1980). Since the spray model in the FLUENT code is similar to that used by Gosman and Ioannides, this work supports their conclusion about the importance of establishing the initial conditions. In the effort here, it was noted that drop-size distributions measured by the laser-diffraction instrument at the 25-mm location in a spatial (or number-density-weighted) format were much broader than comparable measurements expressed in a temporal (or number-flux-weighted) format. Since Tishkoff et al. (1980) used a laser-diffraction instrument while the modeling work requires number-flux-weighted input, it is possible that the width of the distribution was overestimated by Gosman and Ioannides, resulting in an excess of small drops near the centerline, causing the overestimate of volume flux there.

Summary and Conclusions

- Detailed experimental data have been obtained with an Aerometrics phase-Doppler instrument for drop size and velocity distributions and volume fluxes for a pressure-swirl atomizer spraying aircraft fuel system calibration fluid (essentially, a standardized jet fuel) at (almost) nonevaporating conditions. Data were obtained at about 25 radial locations for each of four axial locations. Additional data not presented here were obtained closer to the atomizer.
- The accuracy of the drop size measurements has been established by comparison with measurements using a Malvern laser-diffraction instrument. Cross-section-averaged SMD's measured by the two techniques varied on average by only 3.9 percent.
- The accuracy of the volume flux measurements has been established by comparison with the measured flow rate to the atomizer, and by comparison with volume fraction measurements using a laser-diffraction instrument. Volume fluxes integrated across the spray cross section agreed with flow rates to the atomizer with errors of 19 percent or less. Individual point measurements may have had larger errors.
- These data were used in the preliminary evaluation of the FLUENT code, a commercial, two-phase, three-dimensional, computational-fluid-dynamics code. Drop trajectories were accurately predicted, and drop velocities were computed fairly well except very close to the atomizer. Liquid volume fluxes were predicted reasonably well. Calculated air velocities in the spray were in error near the centerline, but reasonably close to experimental values elsewhere. Turbulence intensities were underpredicted at the atomizer and overpredicted far downstream. The computations were helpful in interpretation of the experimental data.

Acknowledgments

We would like to acknowledge the financial support of the Office of Naval Research, with technical monitor Gabriel Roy. Mike Ryan provided excellent technical support in performing the experimental measurements. Rolf Reitz (General Motors Research Laboratories) and Dan Hirleman (Arizona State University) provided valuable insight into interpretation of the results. Mike Houser and Will Bachalo provided support in the use of the Aerometrics phase-Doppler particle analyzer.

References

Asheim, J. P., Kirwan, J. E., and Peters, J. E., 1987, "Modeling of a Hollow-Cone Liquid Spray Including Droplet Collisions," AIAA Paper No. 87-0135.

Asheim, J. P., and Peters, J. E., 1987, "Alternative Fuel Spray Behavior," *70th Symposium of the Propulsion and Energetics Panel on Combustion and Fuels in Gas Turbine Engines*, Chania (Crete), Greece.

Bachalo, W. D., Houser, M. J., and Smith, J. N., 1986, "Evolutionary Behavior of Sprays Produced by Pressure Atomizers,"AIAA Paper 86-0296.

Crowe, C. T., 1982, "Review—Numerical Models for Dilute Gas-Particle Flows," ASME *Journal of Fluids Engineering*, Vol. 104, pp. 297-303.

Dodge, L. G., 1984, "Calibration of the Malvern Particle Sizer," *Applied Optics*, Vol. 23, No. 14, pp. 2415-2419.

Dodge, L. G., 1987a, "Comparison of Performance of Drop-Sizing Instruments," *Applied Optics*, Vol. 26, No. 7, pp. 1328-1341.

Dodge, L. G., 1987b, "Representation of Average Drop Sizes in Sprays," AIAA Paper No. 87-2133.

Dodge, L. G., Rhodes, D. J., and Reitz, R. D., 1987, "Drop-Size Measurement Techniques for Sprays: Comparison of Malvern Laser-Diffraction and Aerometrics Phase/Doppler," *Applied Optics*, Vol. 26, No. 11, pp. 2144-2154.

Dodge, L. G., and Schwalb, J. A., 1987, "The Physics of Fuel Sprays, 2nd Annual Report," Interim Report No. SwRI-8858/3, Southwest Research Institute, San Antonio, TX.

El Banhawy, Y., and Whitelaw, J. H., 1980, "Calculation of Flow Properties of a Confined Kerosene-Spray Flame," *AIAA Journal*, Vol. 18, No. 12, pp. 1503-1510.

Faeth, G. M., 1983, "Evaporation and Combustion of Sprays," *Progress in Energy and Combustion Science*, Vol. 9, No. 1, pp. 1-76.

Gosman, A. D., and Ioannides, E., 1981, "Aspects of Computer Simulation of Liquid-Fuelled Combustors," AIAA Paper No. 81-0323.

Hammond, D. C., Jr., 1981, "Deconvolution Technique for Line-of-Sight Optical Scattering Measurements in Axisymmetric Sprays," *Applied Optics*, Vol. 20, No. 3, pp. 493-499.

Hess, C. F., 1984, "A Technique Combining the Visibility of a Doppler Signal With the Peak Intensity of the Pedestal to Measure the Size and Velocity of Drops in a Spray," AIAA Paper No. 84-0203.

Hirleman, E. D., and Dodge, L. G., 1985, "Performance Comparison of Malvern Instruments Laser Diffraction Drop Size Analysers," *Proceedings, ICLASS-85, Third International Conference on Liquid Atomisation and Spray Systems*, The Institute of Energy, London, pp. IVA/3/1-14.

Jackson, T. A., and Samuelsen, G. S., 1987, "Droplet Sizing Interferometry: a Comparison of the Visibility and Phase/Doppler Techniques," *Applied Optics*, Vol. 26, No. 11, pp. 2137-2143.

Mellor, R., Chigier, N. A., and Beer, J. M., 1971, "Hollow-Cone Liquid Spray in Uniform Air Stream," *Proceedings of the Symposium on Combustion and Heat Transfer in Gas Turbine Systems*, E. R. Norster, ed., Cranfield International Symposium Series, Vol. 11, Pergamon Press, Oxford, pp. 291-305.

Morsi, S. A., and Alexander, A. J., 1972, "An Investigation of Particle Trajectories in Two-Phase Flow Systems," *Journal of Fluid Mechanics*, Vol. 55, Part 2, pp. 193-208.

Mostafa, A. A., Mongia, H. L. C., McDonell, V. G., and Samuelsen, G. S., 1987, "On the Evolution of Particle-Laden Jet Flows: A Theoretical and Experimental Study," AIAA Paper No. 87-2181.

Ranz, W. E., and Marshall, W. R., Jr., 1952, "Evaporation From Drops, Part I," *Chemical Engineering Progress*, Vol. 48, No. 3, pp. 141-146; "Part II," Vol. 48, No. 4, 1952, pp. 174-180.

Reitz, R. D., and Diwakar, R., 1987, "Structure of High-Pressure Fuel Sprays," SAE Paper No. 870598.

Sturgess, G. J., Syed, S. A., and McManus, K. R., 1985, "Calculation of a Hollow-Cone Liquid Spray in a Uniform Air Stream," *Journal of Propulsion and Power*, Vol. 1, No. 5, pp. 360-369.

Swithenbank, J., Beer, J. M., Taylor, D. S., Abbot, D., and McCreath, G. C., 1977, "A Laser Diagnostic Technique for the Measurement of Droplet and Particle Size Distribution," *Progress in Astronautics and Aeronautics*, Vol. 53, pp. 421-447.

Tishkoff, J. M., Hammond, D. C., Jr., and Chraplyvy, A. R., 1980, "Diagnostic Measurements of Fuel Spray Dispersion," ASME Paper No. 80-WA/HT-35.

Calibration of CFD Methods for High Mach Number Aeroengine Flowfields

J. R. Chawner

G. S. Spragle

R. J. Matus

General Dynamics Fort Worth Division,
Computational Fluid Dynamics Group,
Fort Worth, TX 76101

The design and analysis of scramjet engines relies heavily on the use of Computational Fluid Dynamics (CFD) methods due to the lack of experimental facilities and engineering analysis techniques for high Mach number, high-temperature flows. This emphasis on CFD requires that the methods be calibrated through comparison with existing experimental data to determine their level of capability and range of applicability. At General Dynamics' Fort Worth Division a level of confidence has been established in the use of CFD methods for scramjet flowfields. These methods include a Beam-Warming-based Unsteady Navier-Stokes (UNS) solver, a Beam-Warming-based Parabolized Navier-Stokes (PNS) solver, and a MacCormack-based PNS solver. Specifically, comparisons between CFD flowfields and experimental data for a blunt cone at Mach 10.6, an inlet at Mach 7.4, a combustor at Mach 2.4, and an axisymmetric plug nozzle at Mach 3.2 have been made. These calibrations show good overall agreement for wall pressures, integrated forces, and pressure, Mach number, and chemical species profiles. Examination of the disparities between the CFD and experimental results focuses concern on the treatment of boundary layer turbulence and finite rate chemistry. As a result, further developmental tasks are suggested, which, when complete, will further enhance the applicability of the subject CFD methods.

Introduction

Computational Fluid Dynamics (CFD) has proven to be an invaluable tool in the design process for hypersonic aerospace vehicles. These vehicles will operate across a wide range of Mach numbers and will encounter temperatures high enough to cause nonequilibrium chemical effects in the surrounding gas. This aerodynamic environment will be nowhere more severe than in scramjet engines, where shock wave-boundary layer interactions and hydrogen-air chemical reactions dominate the flowfield. Because of these extremes in aerodynamic environment, the wind tunnel data upon which designers conventionally rely either do not exist or cannot be obtained in today's experimental facilities. Also, the traditional engineering analysis tools are not capable of simulating nonlinear flow phenomena. CFD methods are then the most efficient means of determining the complex flowfields and performance of scramjet engines.

The flowfield associated with scramjets embodies several distinctive features. The forebody flowfield is typified by a strong bow shock at the vehicle nose with subsonic, high-temperature flow immediately behind the shock. The nose shape influences the flow quality many nose radii downstream. Despite the effect of the forebody shock waves, the Mach number at the inlet entrance is still very high, and the boundary layer may be transitional or fully turbulent. The geometry of the inlet itself is complex, with swept ramps, sidewall and ramp compression, and internal struts. In the combustor, turbulent supersonic flow with embedded shock waves is mixed with fuel, resulting in violent chemical reactions and complex wave interactions. As the flow leaves the combustor and enters the nozzle the combustion may not be complete, and chemical reactions are still occurring as the flow is expanded and interacts with the free-stream flow. The result of these geometric and chemical complexities is a truly three-dimensional flowfield in which the likelihood of boundary layer separation is very high.

Fortunately, as pointed out by White et al. (1987), the use of CFD for analysis of the scramjet engine flowfield is developing rapidly. The application of these CFD methods to the scramjet flowfield takes one of two approaches: the global approach or the zonal approach. In the global approach, a single CFD code is used to compute the flowfield throughout the entire engine. This approach is exemplified in a paper by Gielda et al. (1988) in which a Parabolized Navier-Stokes (PNS) code with finite rate hydrogen-air chemistry is used to analyze a generic scramjet. In the zonal approach several different CFD codes are applied in the regions of a flowfield in which they are most applicable. This approach is described in general terms in a paper by Bradley et al. (1987). For example, a PNS code would be used to compute the forebody flow where no separation or appreciable subsonic flow is expected, an Unsteady Navier-Stokes (UNS) code would be used in the inlet where shock wave-boundary layer interactions and flow separation are likely, and so on. There is another factor that

---

Contributed by the International Gas Turbine Institute and presented at the 33rd International Gas Turbine and Aeroengine Congress and Exhibition, Amsterdam, The Netherlands, June 5-9, 1988. Manuscript received by the International Gas Turbine Institute November 18, 1987. Paper No. 88-GT-199.

influences the use of the zonal versus global approach, which is discussed by Bradley et al. (1986). Bradley points out that the development of CFD methods has proceeded along one of two lines: complex geometry and perfect gas, or simplistic geometry and finite rate chemistry. Rephrased in practical terms, there are no codes for the finite rate chemistry analysis of a complex, three-dimensional engine. A final argument for the zonal approach is economics; it is simply less expensive to run a PNS code than a UNS code, making it an attractive alternative in applicable regions. The work in this paper follows the zonal approach.

No matter which of the two approaches one takes to the CFD analysis of a scramjet flowfield, the methods must be calibrated against experimental data to determine their accuracy and range of applicability. These calibrations will shed light on the veracity of future calculations on configurations for which no experimental data are available. Unfortunately, much of the experimental hypersonic data that are available today are for unit problems such as cone flow and simple inlet flow, and very few data are available for combustion processes. Calibration of CFD methods against these limited data will, however, provide insight into the ability of the codes to model the distinctive features of scramjet flow. It is up to the user to extrapolate these simple calibrations to realistic scramjet configurations.

The following sections of this paper described the application of several CFD methods to hypersonic blunt body, inlet, combustor, and nozzle flowfields for which experimental data are available. First, the CFD methods are outlined by reviewing the governing equations, the numerical algorithm, the turbulence model, and the gas state model. Following this, the applications of these codes to the various flowfields are discussed, and comparisons of the CFD results to experimental data are shown. In closing, the accuracy of the CFD results is discussed and suggestions made for areas of improvement and enhancement.

Description of CFD Methods

Descriptions of each of the CFD methods used for the subject calibrations are given in this section. Since the emphasis of this paper is on the results of the calibrations, the reader is directed to the references for a detailed description of each method.

Parabolized Navier–Stokes. Two-dimensional PNS analyses are performed with an integrated package of codes developed by Krawczyk and Harris (1987), Sinha and Dash (1986), and Wolf et al. (1987) and extensively modified by the authors. The package consists of four separate PNS codes, each of which is specialized for a particular region of the vehicle flowfield: SCRAMP for the forebody, SCRINT for the inlet, SCORCH for the combustor, and SCHNOZ for the nozzle. In addition to the PNS codes, the package contains a viscous shock layer (VSL) code for computing the flow about the vehicle nose and cowl leading edge and various auxiliary programs, which are required to interface the PNS codes in the zonal analysis approach. The supplementary programs interpolate the solution from one grid to another, compute species concentrations and gas properties for code input, and perform postprocessing tasks such as calculating performance parameters and making plots. This zonal approach to CFD analyses uses the best-suited code for each part of the flowfield, and produces a relatively inexpensive, quick solution.

While these PNS codes are able to produce a solution in very little time, there are several limitations inherent in PNS methodology that should be noted. First, since the solution is computed in a single pass from nose to tail there is no modeling of upstream influence effects, which may occur near compression corners or separated flow areas. Second, the PNS equations were derived from the UNS equations by neglecting viscous derivative terms in the marching direction. Therefore, if the velocity gradients in the streamwise direction are not small, as may occur in separated regions, the PNS equations are a poor approximation to the actual flow physics. Third, to achieve a stable marching scheme the pressure gradient term in the streamwise momentum equation must be neglected or calculated at a lagged marching step, which restricts the ability of PNS codes to calculate flows with large streamwise pressure gradients. Fortunately, hypersonic vehicles operate in an environment in which the above limitations are usually not experienced so that the PNS assumptions are valid.

The SCRAMP (forebody) and SCRINT (inlet) codes are nearly identical. Forebody and inlet flowfields are dominated by strong shocks, expansions, slip surfaces, and boundary layers, which interact in a complex manner. To model these regions accurately a CFD code has to be robust, to capture the strong shocks, and inexpensive, so that a large number of points may be used to define the sharp gradients in the boundary layer, and obtain good predictions of heat transfer and skin friction. Both SCRAMP and SCRINT are based on a Beam–Warming (1976) implicit algorithm, which requires the addition of smoothing terms to capture strong shocks, but which is able to take relatively large marching steps. This algorithm is a good tradeoff between coding complexity and computational efficiency. At present, both of these codes have the capability to handle either perfect gas or equilibrium chemistry air flows.

The combustor region is characterized by the presence of strong chemical reactions and large mixing regions where the fuel is injected into the flow and is burned. Therefore, the CFD code used in this region has to model finite rate chemistry and turbulent mixing. The SCORCH code is based on a viscous characteristics approach, which splits each marching step into two parts: (1) a parabolic viscous mixing solution of the axial momentum, energy, and species equations with a specified pressure field, and (2) a hyperbolic inviscid wave field solution with the viscous transport terms specified. SCORCH includes a fully coupled chemical kinetics model, and a hybrid k-epsilon/van Driest turbulence model. The viscous mixing, chemical kinetics, and turbulence model steps are treated with an implicit numerical integrator, while the inviscid wave field solution is determined explicitly.

The SCHNOZ nozzle code was not used in the present calibration effort.

Unsteady Navier–Stokes. The UNS code used in the present investigation is the PARC code developed by Cooper (1987) and extensively enhanced by the authors. PARC solves the two-dimensional, Reynolds averaged Navier–Stokes equations in nondimensional, conservation law form. A perfect gas equation of state and Sutherland's laminar viscosity law are used to supplement the governing equations. For turbulent flows the algebraic turbulence model of Baldwin and Lomax (1978) is used for the computation of turbulent viscosity.

A Beam–Warming numerical algorithm is used to solve the discretized form of the governing equations. The combination of this implicit algorithm and spatially varying time steps results in a code that reaches a converged, steady-state solution in a relatively small number of time steps.

By far the most beneficial feature of PARC is the capability for arbitrary boundary condition specification. A unique coding of the Beam–Warming algorithm has resulted in the ability to specify boundary conditions on any grid line throughout the domain. This, in addition to the generality and robustness of the authors' grid generation procedures, allows almost arbitrarily complex geometries to be analyzed. This generality does not come without a price, however. Sufficient resolution of complex geometries usually requires a large

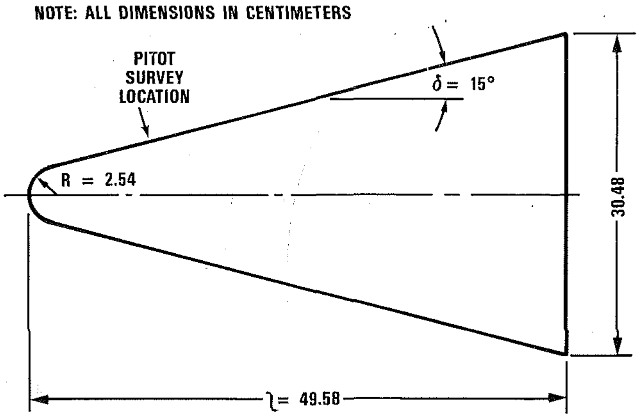

Fig. 1 Schematic diagram of the Cleary cone

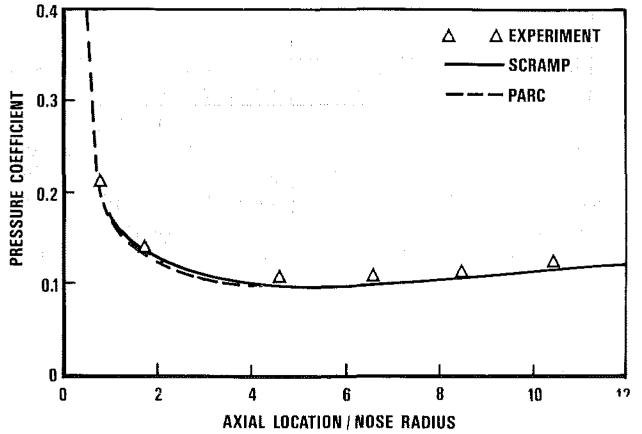

Fig. 2 Comparison of SCRAMP and PARC results to wind tunnel data for surface pressure on the Cleary cone at Mach 10.6

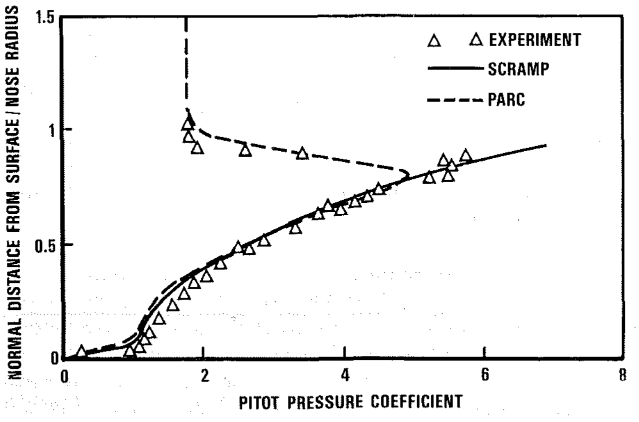

Fig. 3 Comparison of SCRAMP and PARC results to wind tunnel data for pitot pressure profile on the Cleary cone at Mach 10.6

number of grid points, especially when resolution of viscous effects is required. Many grid points and tight clustering result in CRAY run times that greatly exceed those of comparable PNS analyses. Despite this economic drawback it is the ability of the PARC code, and UNS codes in general, to compute reversed, separated, and subsonic flows, which makes their use attractive.

Code Calibrations

This section describes the application of the previously described CFD methods to representative configurations for which experimental data are available. All analyses were performed two-dimensionally. The accuracy of the comparisons between CFD results and experimental measurements is used to identify potential areas of improvements on the CFD methods.

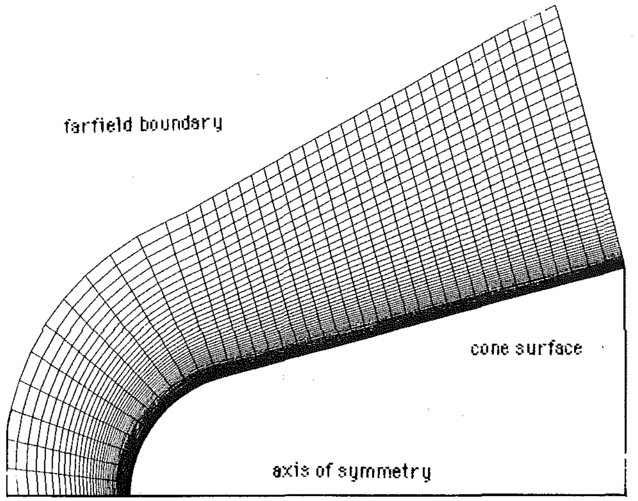

Fig. 4 Computational grid (41×61) used for PARC analysis of the Cleary cone

Blunt Cone. Hypersonic flow about a simple blunted cone is a good test of the ability of a CFD method to capture strong shock waves. A 15 deg cone with a 2.54 cm nose radius, shown in Fig. 1, was tested by Cleary (1965) at Mach 10.6. Both surface pressure and pitot pressure profiles were recorded during the wind tunnel tests. PNS and UNS codes were used to analyze this cone at Mach 10.6, $\alpha = 0$ deg. The wind tunnel Reynolds number was $3.281 \times 10^6 \mathrm{m}^{-1}$, the tunnel total temperature was 1111 K, and the cone surface was maintained at 277.8 K.

PNS. Analysis of the Cleary cone was performed by first solving the spherical nose flowfield using the VSL code, and then spatially marching down the body with the SCRAMP code. Only 30 s of cpu time on a CRAY X/MP® were required to obtain the VSL and PNS solution with a 150×110 grid.

As can be seen in Figs. 2 and 3, respectively, comparisons between the PNS calculation and experiment for axial surface pressure coefficient and radial pitot pressure coefficient were very good. Numerical calculations were within the reported 2 to 4 percent accuracy band of the experimental data. In order to perform the comparison of pitot pressures in Fig. 3 the axis-normal CFD data were conically scaled to coincide with the body normal rake data. Strictly speaking, the conical flow assumption is only valid in the inviscid field, which perhaps contributes to the larger variation between numerical and experimental values near the wall. In the thermal layer near the wall, changes in the chemical composition of the air might also be responsible for some of the differences noted.

UNS. The PARC code also was used to compute the Cleary cone flowfield. Of particular interest was the ability of the centrally differenced PARC to capture the strong bow shock wave. An algebraically generated, body normal, 41×61 point grid was used to model the first 10.16 cm of the body, as shown in Fig. 4. Only 0.1 cpu h on a CRAY-X/MP® were required to obtain the converged solution. The Mach number contours in the flowfield are shown in Fig. 5. The Mach number contours show a thickening of the shock wave as it travels downstream. This thickening is due in large part to the lack of grid clustering away from the body at the aft stations (see Fig. 4). Yet, the normal portion of the bow shock wave near the leading edge is relatively thin. The quality of the solution is revealed through a comparison of the PARC and wind tunnel pitot pressure profiles in Fig. 3. Overall agreement is

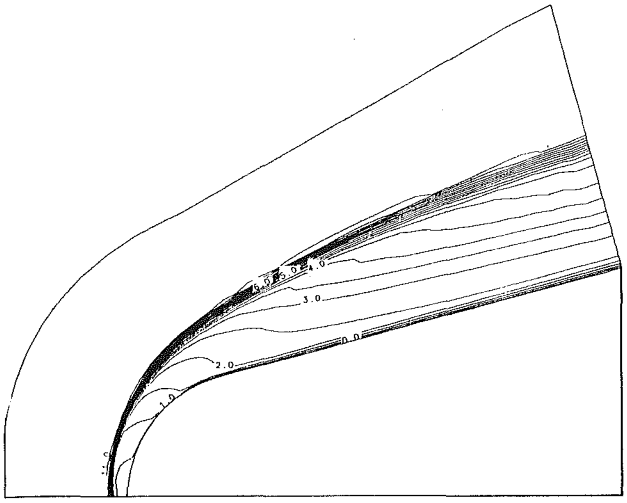

Fig. 5 PARC Mach number contours about the Cleary cone at Mach 10.6

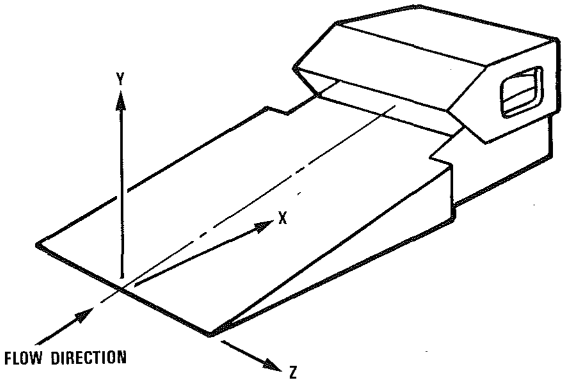

(b) COORDINATE SYSTEM

Fig. 6 Schematic diagram of the P8 inlet

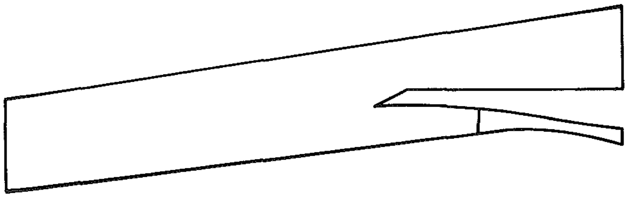

Fig. 7 Cross section of the P8 inlet showing the survey location

good, but the peak pitot pressure is underpredicted by approximately 10 percent. The PARC results are also compared to wind tunnel surface static pressure data in Fig. 2. The agreement between the CFD and experimental results is comparable for both the UNS and PNS codes except near the shock wave. The higher quality of the PNS solution is a direct result of fitting the bow shock as opposed to capturing it.

P8 Inlet. The P8 inlet is a representative internal compression inlet from a Mach 12 cruise vehicle in which oblique shock wave boundary layer interactions dominate the flow. It was tested at Mach 7.4 in the NASA Ames Research Center 3.5 ft tunnel (Gnos et al., 1973). A schematic of this nominally two-dimensional inlet is shown in Fig. 6. Many surface measurements and rake surveys were taken during testing. The resulting data that are available for comparison with CFD results include static pressure, pitot pressure, and Mach number. The survey location at which CFD results were compared to wind tunnel data is shown in Fig. 7. Because the

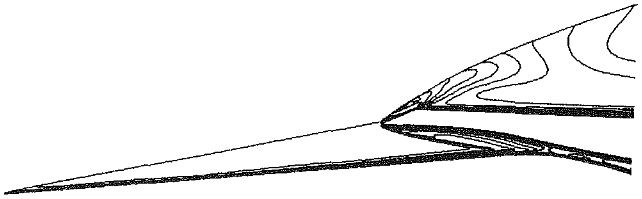

Fig. 8 SCRAMP/SCRINT Mach numbers contours in the P8 inlet at Mach 7.4

boundary layers were relatively thin and no flow separation was noted, both PNS and UNS analyses were performed for this configuration. The tunnel Mach number was 7.4, the total pressure was 4.14 MPa, the total temperature was 811 K, the Reynolds number was 8.86×10^6 m^{-1}, and the inlet wall temperature was approximately 304 K.

PNS. Analysis of the P8 inlet required the use of several CFD methods. The ramp leading edge was assumed to be spherically blunted (radius = 2.54 mm) and the VSL algorithm was used to obtain two planes of starting data for the external PNS code SCRAMP. SCRAMP was then spatially marched to the cowl station. The onset and length of boundary layer transition were deduced from the experimental data and were modeled by the intermittency factor approach of Dhawan and Narashima (1957) coupled with an algebraic turbulence model. For this particular analysis, the inlet cowl lip was determined to be within the forebody shock layer. This condition required determination of the flowfield quantities, including primitive variables and flow angularity, for another VSL solution on the cowl lip. However, no attempt was made to account for the variation of the flowfield along the cowl lip bow shock. Instead, the required reference quantities were held constant, being extracted from a point in the forebody solution that corresponded to the tip of the cowl lip. The resulting VSL solution and the SCRAMP forebody solution were then combined to yield starting solutions for the internal calculation with SCRINT and the external outer cowl calculation with SCRAMP.

Qualitatively, the resulting PNS flowfield looks very reasonable, as can be seen in Fig. 8, a plot of Mach number contours. The internal shock structure, however, does not agree with the experimental Schlieren photos (not shown). The probable causes of this discrepancy are numerous, but inadequate definition of the actual geometry is one major area of concern. Coarse tabular data of the inlet coordinates were fit with a tension spline technique, so the computational geometry was only an approximation of the actual configuration. Minute variations in geometry could drastically alter shock reflections. Other factors that might have contributed to differences include: (1) incorrect cowl shock location and strength due to assuming constant "effective" free stream, (2) upstream blockage effects not modeled with a spatial marching code, (3) nonideal chemistry effects in the air due to the compression and expansion for supersonic tunnel operation, and (4) uncertainty in actual tunnel Mach number, total pressure and temperature, and flow angularity.

Comparisons of surface pressure on the centerbody and inner cowl surface were fair, as can be seen in Fig. 9. The PNS code overpredicts surface pressure slightly on the ramp surface and drastically in post-cowl shock interaction regions. Although the pressure instrumentation is sparse, it seems the cowl shock and its reflection strike the centerbody and lower cowl surface in approximately the same location as the experiment. The Mach number profiles in Fig. 10 show good agreement (within the 3 percent experimental error band), but the numerical calculation demonstrated a curious inflection in the profile that is attributed to the algebraic turbulence model being employed. The PNS pitot pressure profiles in Fig. 11

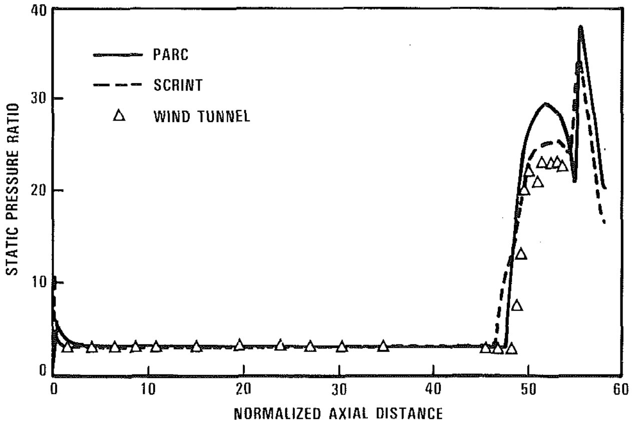

Fig. 9 Comparison of SCRAMP/SCRINT and PARC results to wind tunnel data for static pressure on the P8 inlet Centerbody at Mach 7.4

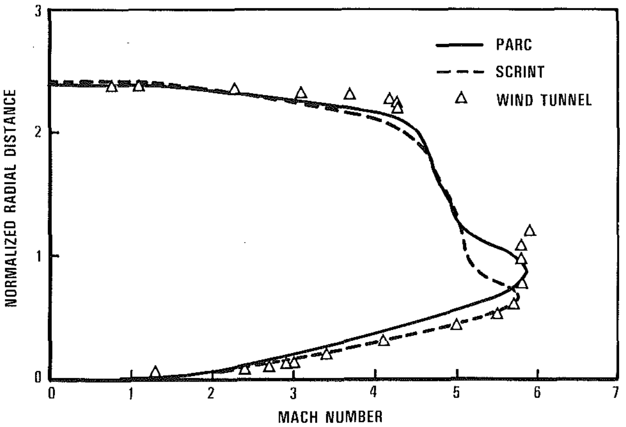

Fig. 10 Comparison of SCRINT and PARC results to wind tunnel data for Mach number profile for the P8 inlet at Mach 7.4

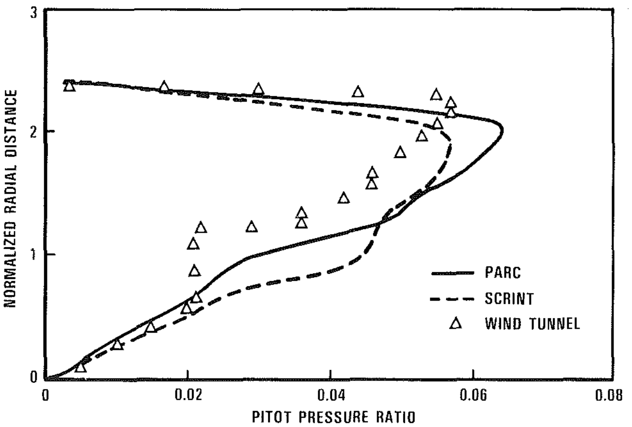

Fig. 11 Comparison of SCRINT and PARC results to wind tunnel data for pitot pressure profile for the P8 inlet at Mach 7.4

showed consistently higher pressures than the experimental values. Investigation of turbulence and chemistry modeling, as well as the uncertainties previously mentioned, will be necessary to quantify differences fully in numerical and experimental results.

UNS. Analysis of the P8 inlet using the perfect gas PARC code required approximately 1 h of cpu time on a CRAY-X/MP® for a 400 × 120 grid. Figure 12 shows the static pressure contours throughout the computational domain from the converged solution. Most noticeable in Fig. 12 are the internal shock wave reflections and the intersection of the external cowl shock wave with the farfield boundary. The farfield boundary condition prevents the cowl shock from passing out of the domain, which results in a nonphysical bending of the shock wave. Although this is incorrect, it was anticipated and the lack of upstream influence prevents this anomaly from affecting the internal flowfield. The UNS surface pressure results are compared to wind tunnel data in Fig. 9. The overall agreement is good but the peaks are shifted axially. In Figs. 11 and 12 the PARC results are compared to wind tunnel data for Mach number and pitot pressure profiles, respectively. The axial location of the profiles is indicated in Fig. 7. The PARC Mach number profiles show overall good agreement with the wind tunnel data, yet the details near the shock wave are smeared. The pitot pressures show much the same trends as the Mach numbers, except that the peaks are overpredicted by PARC. The smearing of the profiles and the overprediction of the levels is indicative of shock wave smearing. This is excepted, to some degree, in a centrally differenced code such as PARC, which employs both second and fourth-order damping. Smearing of the reflected shocks is also a result of improper modeling of the shock wave-boundary layer interactions. Poor resolution of the boundary layer can be caused by two occurrences: The grid clustering in the near wall region is too coarse to resolve the velocity profile, or the turbulence model is inadequate.

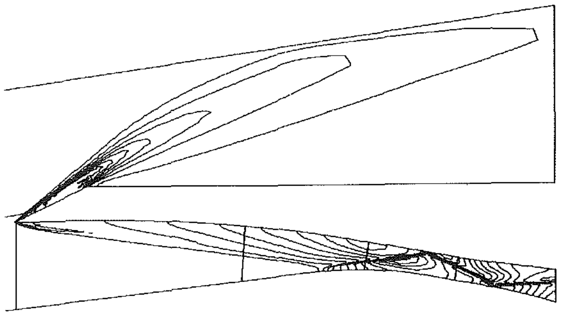

Fig. 12 PARC static pressure contours in the P8 inlet at Mach 7.4

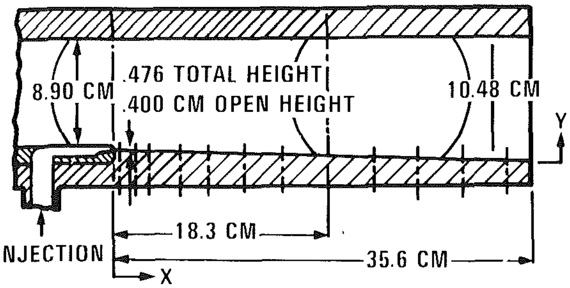

Fig. 13 Schematic diagram of the Burrows and Kurkov combustor

Two-Dimensional Combustor. The ability of the SCORCH code to compute chemically reacting internal flows was verified by solving a supersonic combustion flowfield, which was experimentally measured by Burrows and Kurkov (1973). The experimental geometry is shown in Fig. 13. An airstream at Mach 2.44 enters the test section from the left in the figure, and mixes with hydrogen being injected parallel to the airflow at Mach 1 from a 0.40 centimeter slot. The pressure in the hydrogen flow was approximately equal to the airstream pressure at the injection location. Profiles of species mole fractions were measured at the exit of the test section, 35.6 cm downstream of the hydrogen injection point.

The SCORCH calculation was started at the hydrogen injection point. Experimentally measured profiles of temperature and velocity in the airstream at this point were used to provide

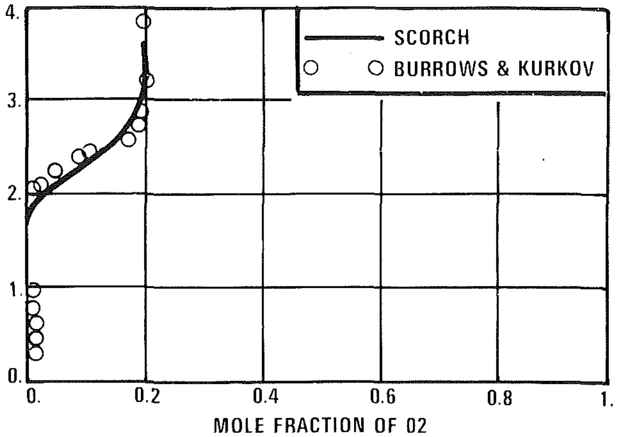

Fig. 14 Comparison of SCORCH results to wind tunnel data for mole fraction profile of molecular oxygen at the exit of the Burrows and Kurkov combustor

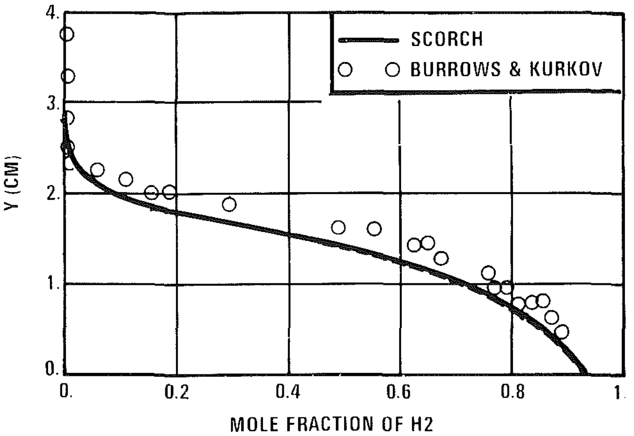

Fig. 15 Comparison of SCORCH results to wind tunnel data for mole fraction profile of molecular hydrogen at the exit of the Burrows and Kurkov combustor

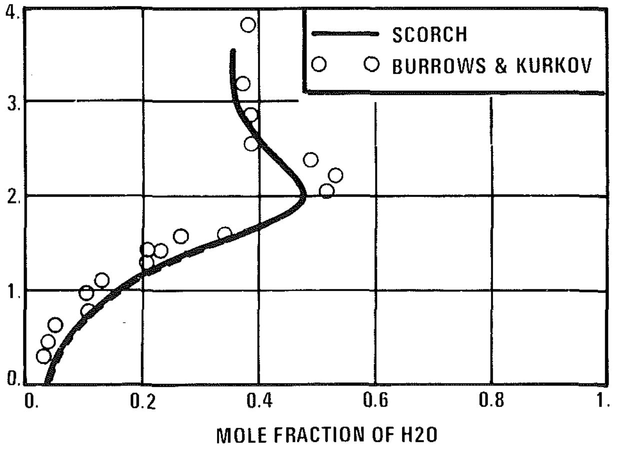

Fig. 16 Comparison of SCORCH results to wind tunnel data for mole fraction profile of molecular water at the exit of the Burrows and Kurkov combustor

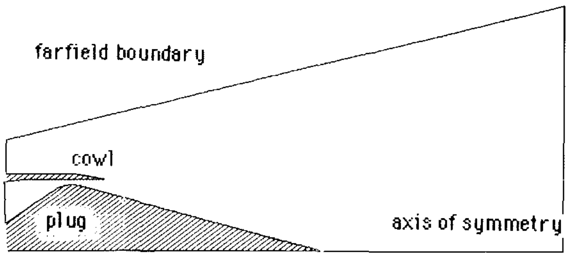

Fig. 17 Schematic diagram of the axisymmetric plug nozzle

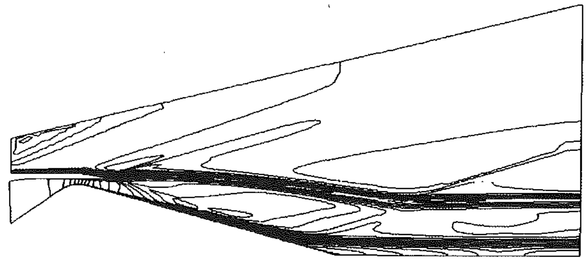

Fig. 18 PARC Mach number contours about the axisymmetric plug nozzle at Mach 3.2 and nozzle pressure ratio 30

a starting solution for the computation, and the properties across the hydrogen stream were assumed to be constant. The turbulent energy and dissipation were determined from the initial velocity profile assuming an equilibrium state. A seven-species chemistry model containing H, H_2, H_2O, N_2, O, OH, and O_2 simulated the burning of the hydrogen in the air. The initial composition of the airstream was approximately 21 percent O_2, 41 percent N_2, and 38 percent H_2O by volume, and the injected flow was assumed 100 percent H_2. The solution was then marched to the test section exit where comparison data were available.

Figures 14, 15, and 16 show profiles of O_2, H_2, and H_2O, respectively, at the test section exit. The experimental and computed species profiles are qualitatively in agreement, but the SCORCH solution shows less spreading of the chemically reacting region than the experiment. In the experimental data the mixing region extends outward to around 3 cm from the lower wall while the numerical results show the mixing only out to approximately 2.8 cm. The extent of the reacting region is highly dependent on the initial velocity profiles, and the reaction spreads quite slowly when uniform initial profiles are used. This dependence on the starting profiles is due to the important role of the shear and turbulence on the mixing, and hence on the spread of the reacting region. It is believed that the numerical solution could be improved by determining the initial velocity, temperature, and turbulent energy and dissipation profiles more accurately.

Axisymmetric Plug Nozzle. The axisymmetric plug nozzle shown in Fig. 17 was tested at Mach 3.2 and a nozzle pressure ratio (NPR) of 30. The data from this test include surface pressure measurements, gross thrust measurement, and shadowgraphs. Even though the Mach number is only high supersonic, the flowfield still contains many of the typical features of a hypersonic afterbody flow. The free-stream conditions were Mach 3.2, static pressure of 7.1 kPa, static temperature of 295 K. The conditions of the exhaust flow were NPR of 30 and total temperature of 311 K.

A 300 × 120 point grid was used for the PARC analysis of the axisymmetric plug nozzle. Approximately 1.0 h of CRAY-X/MP® cpu time was required to obtain the converged solution, which is displayed in Fig. 18 as Mach number contours. The MACH number contours show the detachment of the plume from the plug, which results in the recompression indicated in Fig. 19, a plot of surface pressure along the plug. PARC underpredicts the recompression on the end of the conical plug. This indicates that the shock wave-boundary layer interaction is not being modeled properly. This was also the case in the P8 inlet analysis and again the turbulence model is suspect. As a final comparison, the PARC gross thrust coefficient 0.9112 was compared to the experimentally measured

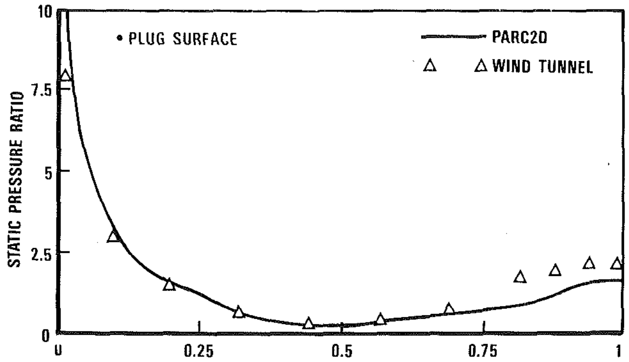

Fig. 19 Comparison of PARC results and wind tunnel data for surface pressure on the plug of the axisymmetric plug nozzle at Mach 3.2 and nozzle pressure ratio 30

gross thrust coefficient 0.9206. The agreement here is excellent, within 1 percent.

Conclusions

The CFD results from the calibration cases are very promising. Admittedly, the routine use of CFD for the analysis of scramjet engines is in its infancy. Despite this, the existing methods have obtained a level of capability. For example, the comparison to surface pressure in all of the calibrations is good. In addition, the profile data for the blunt cone and combustor agree very well with the experimental data. Also, from a practical standpoint the PARC code was able to give a very accurate prediction of thrust for the axisymmetric nozzle. However, there is still considerable room for improvement. Most notable is the need for an accurate turbulence model, as pointed out by the P8 inlet and axisymmetric nozzle calibrations. The authors have already begun work on installing a two-equation turbulence model in the PARC code. A short-term result of this work has been the development of a wall function treatment of the near wall region to replace the no-slip boundary condition. Preliminary results indicate the wall function is as accurate as the no-slip boundary condition. The benefit of the wall function is that it does not require grid clustering to solid walls, which results in enhanced convergence rates. A two-equation turbulence model would also circumvent the difficulties associated with merging algebraic wall and wake turbulence models, as would be the case for the axisymmetric nozzle. The blunt cone and P8 inlet test case also revealed the effect of shock wave smearing on the flowfield solution. An upwind solution algorithm would greatly improve the solution quality and development of UNS and PNS procedures with this feature is underway. Several of the calibrations also pointed out that real gas equations of state would be beneficial for resolving the effects of high-temperature flows. To date, curvefits for equilibrium air chemistry have been included on the PARC, SCRAMP, and SCRINT CFD methods. Work is also under way for installation of finite rate chemistry in the PARC code so that combustor flowfields with large injection angles (resulting in separated flow) can be analyzed. Finally, it should be pointed out that while the SCORCH code provides a very good design capability for turbulent, chemically reacting flows, its geometry is limited to two dimensions. Development of a three-dimensional capability in the combustor area is underway.

Consideration of realistic scramjet configurations indicates that the CFD methods in use today must undergo considerable development before analysis of three-dimensional, chemically reacting flows is performed every day. However, the existing methods have been proven to be viable design tools. The authors have applied these CFD methods to several three-dimensional vehicles in order to estimate vehicle performance. Blunt nose analysis is performed using a three-dimensional VSL code, and a three-dimensional version of the SCRAMP code is used to march downstream on the forebody until the inlet cowl station is reached. At this location the PNS solution is interpolated onto the first plane of a three-dimensional grid of the inlet, which is then analyzed using the PARC code. The PARC solution is then used to start a two-dimensional SCORCH analysis of the combustor. The SCORCH solution is then interfaced to the SCHNOZ code for two-dimensional analysis of the nozzle and afterbody flow. Three-dimensional analysis of the combustor and nozzle/afterbody have been performed with a PNS code that is still under development. These solutions, however, have yet to be integrated into a complete three-dimensional vehicle analysis. Calibration of CFD methods as discussed in this text has identified turbulence modeling, finite rate chemistry, and algorithm technology as areas for development that will allow CFD methods to be used for the analysis of scramjet engines well into the next century.

References

Baldwin, B. S., and Lomax, H., 1978, "Thin Layer Approximation and Algebraic Model for Separated Turbulent Flows," AIAA 16th Aerospace Sciences Meeting, Huntsville, AL, AIAA Paper No. 78-257.

Beam, R., and Warming, R. F., 1976, "An Implicit Difference Algorithm for Hyperbolic Systems in Conservation-Law Form," *Journal of Computational Physics*, Vol. 22, No. 1, pp. 87-110.

Bradley, R. G., et al., 1986, "Current Capabilities and Future-Directions in Computational Fluid Dynamics," compiled by the National Research Councils Committee to Assess Current Capabilities and Future Directions in Computational Fluid Dynamics, R. G. Bradley, Chairman, National Academy Press, Washington, DC.

Bradley, R. G., Bhateley, I. C., and Howell, G. A., 1987, "Computational Fluid Dynamics—Transition to Design Applications," *Supercomputing in Aerospace*, NASA Conference Publication 2454.

Burrows, M. C., and Kurkov, A. P., 1973, "Analytical and Experimental Study of Supersonic Combustion of Hydrogen in a Vitiated Airstream," NASA TM X-2828, Washington, DC.

Cleary, J. W., 1965, "An Experimental and Theoretical Investigation of the Pressure Distribution and Flow Fields of Blunted Cones at Hypersonic Mach Numbers," NASA TN D-2969, Washington, DC.

Cooper, G. K., 1987, "The PARC Code: Theory and Usage," AEDC-TR-87-24, Arnold Engineering Development Center, Arnold Air Force Base, TN.

Dhawan, S., and Narashima, R., 1957, "Some Properties of Boundary Layer Flow During the Transition From Laminar to Turbulent Motion," *Journal of Fluid Mechanics*, Vol. 3, pp. 418-438.

Gielda, T., Hunter, L. G., and Chawner, J. R., 1988, "Efficient Parabolized Navier-Stokes Solutions of Three-Dimensional, Chemically Reacting Flowfields," presented at the 1988 AIAA Aerospace Sciences Conference, Reno, NV, AIAA Paper No. 88-0096.

Gnos, A. V., Watson, E. C., Seebaugh, W. R., Sanator, R. J., and DeCarlo, J. P., 1973, "Investigation of Flow Fields Within Large-Scale Hypersonic Inlet Models," NASA TN D-7150, Washington, DC.

Krawczyk, W. K., and Harris, T. B., 1987, "Analysis of Aerospace Vehicle Scramjet Propulsive Flowfields: 2-D Forebody/Inlet Code Development—Phase 1," NASP Contractor Report 1003.

Sinha, N., and Dash, S. M., 1986, "Parabolized Navier-Stokes Analysis of Ducted Turbulent Mixing Problems With Finite-Rate Chemistry," AIAA Paper No. 86-0004.

White, M. E., Drummond, J. P., and Kumar, A., 1987, "Evolution and Application of CFD Techniques for Scramjet Analysis," *AIAA Journal*, Vol. 3, No. 5, pp. 423-439.

Wolf, D. E., Lee, R. A., and Dash, S. M., 1987, "Analysis of Aerospace Vehicle Scramjet Propulsive Flowfields: 2-D Nozzle Code Development—Phase I," NASP Contractor Report 1005.

A Detailed Characterization of the Velocity and Thermal Fields in a Model Can Combustor With Wall Jet Injection

C. D. Cameron

J. Brouwer

C. P. Wood

G. S. Samuelsen

UCI Combustion Laboratory,
Department of Mechanical Engineering,
University of California,
Irvine, CA 92717

This work represents a first step in the establishment of a data base to study the interaction and influence of liquid fuel injection, wall jet interaction, and dome geometry on the fuel air mixing process in a flowfield representative of a practical combustor. In particular, the aerodynamic and thermal fields of a model gas turbine combustor are characterized via detailed spatial maps of velocity and temperature. Measurements are performed at an overall equivalence ratio of 0.3 with a petroleum JP-4 fuel. The results reveal that the flowfield characteristics are significantly altered in the presence of reaction. Strong on-axis backmixing in the dome region, present in the isothermal flow, is dissipated in the case of reaction. The thermal field exhibits the primary, secondary, and dilution zone progression of temperatures characteristic of practical gas turbine combustors. A parametric variation on atomizing air reveals a substantial sensitivity of the mixing in this flow to nozzle performance and spray symmetry.

Introduction

Gas turbine combustors are receiving increased attention with respect to design, internal flowfield structure, and dome region mixing processes between the fuel and air. A greater understanding of the processes associated with gas turbine engine combustion is required as designers address problems due to increasing demands on combustor performance and the move toward the use of relaxed specification fuels and alternative fuels. Little is understood about the interaction between fuel spray injection and a swirl-induced aerodynamic field or the interaction of wall jets with a swirl-stabilized flowfield.

As an aid to understanding the complex flowfield, in-situ and nonintrusive, spatially resolved measurements of gas velocity, temperature, droplet size, droplet velocity, soot distribution, and species concentration must be provided. Although experimental research has been conducted in both laboratory bench-scale and full-scale hardware (e.g., Brum and Samuelsen, 1987; Gouldin et al., 1985; Lilly, 1985), the required data base is still not available. This is due to several factors. First, the relatively simple model combustors amenable to modeling and optical access for laser diagnostics typically do not exhibit some of the geometrical and operational features characteristic of practical combustors. Second, full-scale combustor beds preclude the use of optical diagnostics, have poorly defined boundary conditions, and have prohibitive operating costs.

In recent work at the UCI Combustion Laboratory, a model gas turbine can combustor has been developed that provides optical access for laser diagnostics and clean boundary conditions amenable to modeling, and also incorporates critical features of practical combustors such as discrete wall jets, swirl-induced flowfield, liquid spray atomization, and elevated pressure operation (Rudoff and Samuelsen, 1986). The primary objective of the present study was to characterize the performance of this model combustor.

Background

The present combustor evolved from a simplified configuration, dubbed the Axisymmetric Can Combustor (ASCC). The ASCC (Fig. 1*a*) is an atmospheric pressure combustor operated at bulk velocities up to 15 m/s. The design was developed in a series of tests (Brum and Samuelsen, 1982) and the module has been used for a number of turbulent transport (Brum and Samuelsen, 1987; LaRue et al., 1985) and fuel effects (Wood and Samuelsen, 1985; Wood et al., 1985; Smith et al., 1985) studies. The dilution air (nonswirling) is introduced through an annular shroud to provide closure to the swirl-generated recirculation zone, retain clean boundary conditions, maintain axisymmetry, and keep the optical windows cool and clean. As a result, the ASCC provides (1) an axisymmetric flowfield amenable to modeling, and (2) optical access. The geometric features of the ASCC result in a representative model of the primary zone of a practical gas turbine combustor: strong swirl, strong backmixing, and liquid fuel spray injection.

Contributed by the International Gas Turbine Institute and presented at the 33rd International Gas Turbine and Aeroengine Congress and Exhibition, Amsterdam, The Netherlands, June 5–9, 1988. Manuscript received by the International Gas Turbine Institute September 15, 1987. Paper No. 88-GT-26.

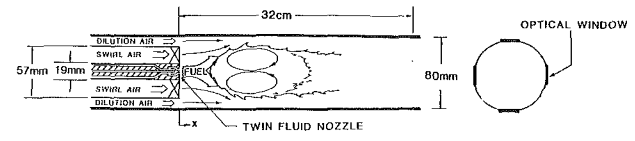

Fig. 1(*a*) The axisymmetric can combustor (ASCC)

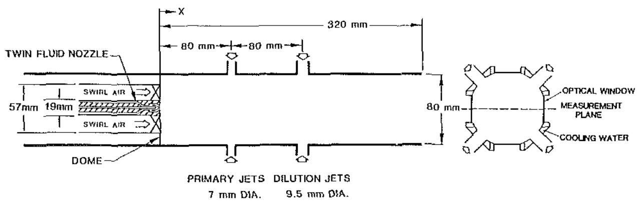

Fig. 1(*b*) The wall jet can combustor (WJCC)

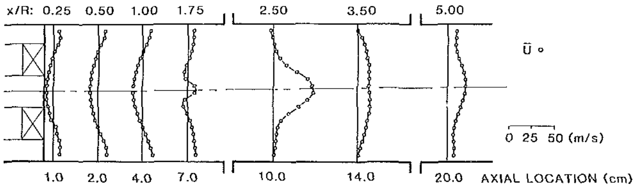

Fig. 2 The isothermal mean axial velocity field (25 percent swirl, 35 percent primary jet air, 40 percent dilution jet air)

The present combustor, the Wall Jet Can Combustor (WJCC), features introduction of primary and dilution air via discrete wall jets. This produces a more accurate representation of the aerodynamics of a practical combustor, namely primary, secondary, and dilution regions.

Major changes in the ASCC design (Fig. 1*a*), which led to the current WJCC design (Fig. 1*b*), were (1) the replacement of the front face injection of dilution air with discrete wall injection, and (2) the replacement of the front face dilution air shroud with a step expansion dome. Design decisions required in the development of the WJCC (e.g., number and location of wall jets, air flow ratios, and dome design) were made with the input from designers of practical combustors and design texts (e.g., Lefebvre, 1983). The design was refined and finalized based on the results of prototype testing (Rudoff, 1986).

The present work reports on a characterization of the WJCC for a select set of parametric variations. In particular, the aerodynamic and thermal fields of this model combustor are presented. Nonintrusive measurements of mean and rms velocity were made via laser anemometry. A thermocouple probe was used to map the average gas temperature inside the combustor. The goals are to (1) establish initial insights into the mixing processes associated with complex flowfields typical of can combustors, and (2) assess the utility of the WJCC for studies of gas turbine combustion processes.

Experiment

Approach. The WJCC was characterized operating at atmospheric pressure with a petroleum derived JP-4. A twin fluid air-assist Parker Hannifin nozzle was used for fuel injection. The combustor air was preheated to 100°C and the bulk flow rate was 163 kg/h. The fuel flow rate was 3.27 kg/h, which corresponds to an overall equivalence ratio of 0.3.

The approach was to characterize the aerodynamic field of the WJCC using laser anemometry to measure the gas mean and rms velocities in the axial and azimuthal direction. Measurements of velocity were made across the full diameter in increments of 4 mm at seven axial locations. A thermocouple was used to obtain the average temperature at the same locations.

Test Bed. The WJCC is an 80 mm stainless steel duct, with an operating length of 32 cm (Fig. 1b). A 57 mm diameter, 100 percent blockage, 60 degree swirler is located at the front face of the combustor. Air flow to the combustor passes through a stainless steel preheater section, where it is preheated to 100°C. After passing through the preheater the flow is split into three separate lines delineated as the swirl, primary jet, and dilution jet air lines. The swirl air is sent through a straightening section before entering the combustor at the inlet plane while the primary and dilution jet flows are sent to the discrete wall jets of the WJCC.

As shown in the end view of Fig. 1(*b*), four ports for diagnostic access are located longitudinally around the combustor. The plane of optical measurements bisects the wall jets through the side ports while the top port is used for thermocouple and radiometer measurements. Also, as shown in Fig. 1(*b*), water cooling is provided to the walls in the nonwindow regions through four channels to preserve the integrity of the combustor and wall jet tubes and to prevent warpage around the window frames.

Two rows of discrete wall jets are included (primary and dilution), each consisting of four orthogonally located jets. They are located one and two combustor diameters downstream from the inlet, respectively. The primary jets have a 7 mm diameter and the dilution jets have a 9.5 mm diameter.

Diagnostics

Laser Anemometer. A two-component, dual-beam laser anemometer (LA) system was used to characterize the axial and azimuthal velocity components of the flowfield. The green beam (514.5 nm) from a dispersion prism was focused by a lens onto a diffraction grating where it was split into ordered pairs. The first-order beam pair was collimated, then focused and crossed into a probe volume by a pair of lenses. Frequency shifting to eliminate directional ambiguity was provided by rotating the diffraction grating. By varying the speed of the precision motor that rotates the grating, shifts of up to 8 MHz were available.

The Doppler bursts were collected 20 deg off axis through a pair of collimating lenses and focused upon a photodetector. Pedestal and high-frequency noise removal were accomplished through adjustable high and low pass filters provided on a Macrodyne counter/processor. Data reduction was performed by an LSI 11/23 minicomputer. All air flows were seeded with nominally 1 μm alumina powder to scatter light while passing through the probe volume.

Thermocouple Probe. Temperature measurements in the WJCC were accomplished with the use of a thermocouple probe using a Type R exposed junction thermocouple. The thermocouple wire diameter was 250 μm. The thermocouple was supported by a 1.6 mm o.d. Inconel tube, 38 mm long, which was in turn mounted on a 6.4 mm o.d. Inconel tube for structural rigidity. Water cooling was provided through the larger Inconel tube to assure the structural integrity of the probe, but only to 41 cm from the thermocouple bead to minimize conduction losses down the length of the probe. The probe is mounted on a three-axis positioning traverse to place the bead in alliance with the beam crossing of the LA system. The probe is then traversed through the entire flowfield using the traverse of the LA system.

Results

Isothermal. The isothermal mean axial velocity field in the combustor module is shown in Fig. 2 for swirl, primary jet, and dilution jet air flows of 25 percent, 35 percent, and 40 percent, respectively. These flow splits are based on design criteria for practical combustors (Rudoff, 1986). A strong on-

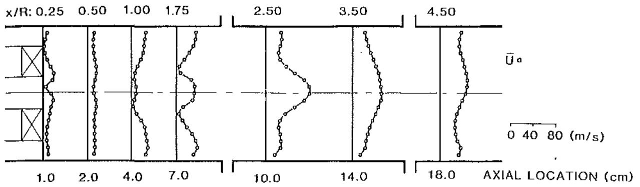

Fig. 3 The mean axial velocity field for a nozzle air-fuel ratio = 1.5 (25 percent swirl, 35 percent primary jet air, 40 percent dilution jet air)

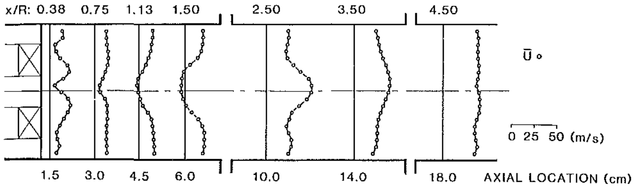

Fig. 4(*a*) Mean velocity

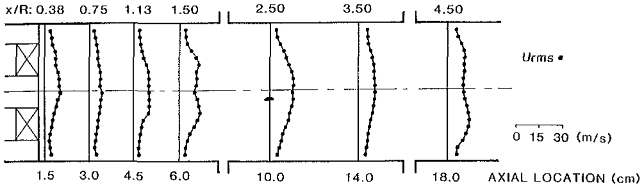

Fig. 4(*b*) Rms velocity

Fig. 4 The axial velocity field for a nozzle air-fuel ratio = 1.5 (45 percent swirl, 30 percent primary jet air, 25 percent dilution jet air)

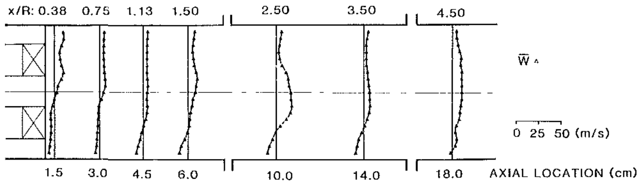

Fig. 5(*a*) Mean velocity

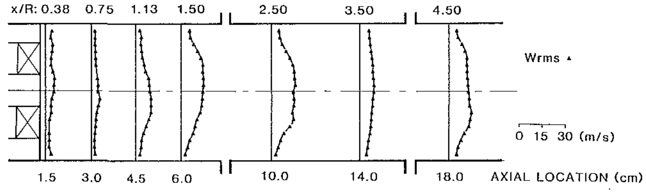

Fig. 5(*b*) Rms velocity

Fig. 5 The azimuthal velocity field for a nozzle air-fuel ratio = 1.5 (45 percent swirl, 30 percent primary jet air, 25 percent dilution jet air)

axis recirculation zone extends from $x/R = 0.25$ to $x/R = 1$. At $x/R = 1.75$, a small off-axis recirculation zone is formed. The strong axial acceleration of the flow along the centerline at $x/R = 2.5$ is due to the primary jet flow. At $x/R = 3.5$, the velocity profile is more uniform due to the on-axis flow of the dilution jets. At $x/R = 5$, a modest centerline acceleration occurs due to the dilution jet flow. The axial velocity profiles exhibit a reasonable degree of symmetry in the measurement plane.

Liquid Injection and Reaction. The mean axial velocity field, shown in Fig. 3, was obtained with the combustor operating on a petroleum-derived JP-4. The flow splits between the swirl and wall jets are identical to those of the isothermal case. The nozzle air-fuel ratio was 1.5 as per the manufacturer's recommended operating range for this atomizer.

The presence of fuel injection and reaction changes the character of the flowfield; notably, no mean on-axis recirculation zone is present.

In addition, the velocity profile displays a slight asymmetry ($x/R = 0.25$, 0.5) with respect to the centerline. This is attributed to a modest asymmetry in the spray produced by the nozzle since the flowfield demonstrates symmetry in the absence of fuel injection and reaction. Noteworthy is that nozzles generally display modest asymmetries (e.g., McDonell et al., 1987; Rosjford, 1987). The present data reflect the probable asymmetries in flowfield properties that can result from these asymmetries in fuel distribution.

Beyond $x/R = 1.75$, the aerodynamics again control and the flowfield displays reasonable symmetry about the centerline. In the region between the jets ($x/R = 2.5$, 3.5), the velocities near the centerline are quite high (as in the isothermal case); in addition, the velocities in the outer flow (near the walls) are substantial. This is likely due to a blockage effect created by penetration of the cold jets to the rapidly expanding reacting flow.

Increased Swirl Air. The common perception of the flowfield in a gas turbine combustor is the presence of an on-axis recirculation zone produced as a result of the interaction between the swirl air and the primary jet flow. Although present in the case of isothermal flow, as described above, the on-axis recirculation is absent in the case of reaction. Exploratory isothermal testing revealed that the backflow produced by the primary jets formed an *off-axis* recirculation zone. By increasing the swirl air, the recirculation zone was transformed to an on-axis configuration. A parametric study was conducted to establish the extent to which the proportion of air directed to the swirler needed to be increased to establish on-axis recirculation for the case of reacting flow. It was found that, for a given flow rate through the swirler, increasing the primary jet air always led to a weakening of the recirculation zone. Except to provide closure to the dome region, a condition was not found for which the primary jet flow played a role in enhancing the recirculation zone strength or size. Increased primary jet flow did however lead to higher levels of rms velocity in the dome region.

Through an iterative process, a flow split in which the swirl air exceeds 45 percent was found to produce a flowfield in the present combustor that represents the flow structure described as representative of a gas turbine combustor (i.e., strong dome region, and on-axis recirculation) (Lefebvre, 1983).

The mean axial velocity field for this condition is shown in Fig. 4(*a*). On-axis recirculation is present at $x/R = 1.13$ and 1.5. A modest asymmetry again appears in the axial velocity profile near the nozzle ($x/R = 0.38$); otherwise, symmetry is maintained throughout the flowfield. The lower percentage of primary air in this case (25 versus 35 percent) results in lower centerline velocities in the region between the jets. The effect of a weaker dilution stream can be seen in the profile at $x/R = 4.5$; in the present case, the velocity profile is essentially uniform.

High rms velocities generated by the penetration, splitting, and resultant velocity gradients produced by the high velocity wall jets are present throughout the flow (Fig. 4*b*).The rms values are generally higher in the region between the jets. The slightly higher rms values near the centerline suggest a strong intermittency flow.

The azimuthal mean flowfield is presented in Fig. 5(*a*). Near the nozzle ($x/R = 0.38$), strong swirl is evident in the velocity profile. The swirl persists until $x/R = 1.13$, where the nonswirling central core created by the jets begins to dominate the flow. A small swirl component remains on the edge of the flow until it is completely dissipated by $x/R = 4.5$. The general upward tendency of the flow on centerline may be due to two possible effects: buoyancy and/or slightly unequal flow distribution to the jets, yielding a general upward flow. The az-

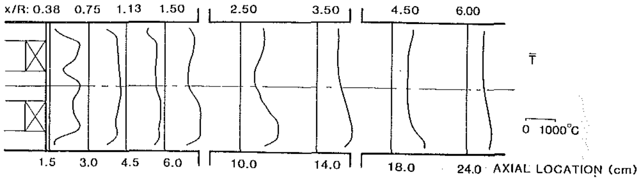

Fig. 6 The mean temperature field for a nozzle air-fuel ratio = 1.5

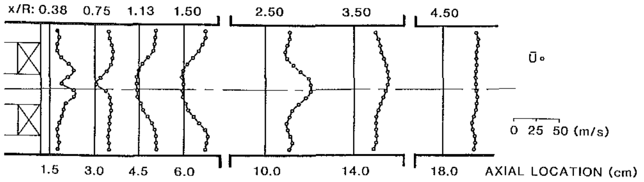

Fig. 7 The mean axial velocity field for a nozzle air fuel ratio = 3.0 (45 percent swirl, 30 percent primary jet air, 25 percent dilution jet air)

imuthal rms velocities are shown in Fig. 5(*b*). As for the axial case, the rms values are higher in the regions where the jet flows dominate, and near the centerline due to the flow intermittency.

The mean temperature field in the WJCC is shown in Fig. 6. Near the nozzle, the spray pattern is evident from the dips in the temperature profile and the correspondingly cooler temperatures on either side of the centerline. Evidence of an asymmetry in the spray distribution can be deduced from the data, namely a greater depression on the positive side of centerline.

Downstream of the nozzle, the temperature profiles are relatively uniform across the combustor until $x/R = 1.5$, where the influence of jet penetration is evident from the colder centerline temperatures. The temperatures remain high downstream of the primary jets; this is evidence of further reaction in the secondary zone. At this point a modest asymmetry in the temperature profile or "hot streak" can be detected on the outer edge of the flow on the negative side of centerline. A probable explanation for the hot streak is the asymmetry in the spray field noted above. The relatively depressed temperature and buildup of carbon on the thermocouple is evidence of a locally high concentration of fuel. This is likely transported downstream in a corkscrew manner within the dome region, and is manifested as a hot streak. The effect is undetected until the reacting fuel streak moves into the measurement plane at this location. The hot streak persists for the rest of the field due to the fact that the swirl is very weak beyond this position and thus transport is primarily in the axial direction. At the final axial position of $x/R = 6.0$, the temperature profile is tending toward uniformity, with some evidence of the hot streak remaining.

Increased Atomization Air. The combustor was also characterized at the baseline air flow splits for a nozzle air-fuel ratio of 3.0. The combustor performance is notably improved for this condition as visually evidenced by the absence of yellow streaks and a more uniform and stable flowfield. Isothermal measurements of the line-of-sight Sauter mean diameter (SMD), via laser diffraction, in the spray field produced by this nozzle showed that 5 cm from the nozzle (corresponding to $x/R = 1.25$), the SMD decreased from 22 μm to 9 μm for nozzle air-fuel ratios of 1.5 and 3.0, respectively.

The mean axial velocity field for this condition is depicted in Fig. 7. The effect of increased atomization air is most evident near the nozzle ($x/R = 0.38$ and 0.75). Although the characteristics of the profiles are similar to those obtained with a nozzle air-fuel ratio of 1.5, the magnitudes of the velocities are much higher, reflecting the increased nozzle air flow. Throughout the remainder of the flowfield ($x/R = 1.13$ to $x/R = 4.5$), this effect has diminished and the velocity profiles for the two cases (nozzle air-fuel ratio = 1.5 and 3.0) are virtually identical.

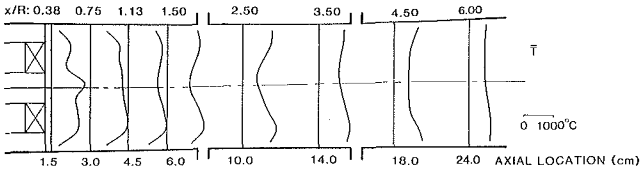

Fig. 8 The mean temperature field for a nozzle air-fuel ratio = 3.0

The average temperature profiles for this condition are shown in Fig. 8. The asymmetry in the temperature profile is again evident near the nozzle. Although there is still evidence of a hot streak, the effect is greatly diminished. The temperature profiles appear relatively symmetric about the centerline. The cold core due to jet penetration appears at $x/R = 1.5$ and persists throughout most of the flow. At $x/R = 6.0$, the temperature profile is relatively uniform.

Summary and Conclusions

In-situ measurements of mean and rms velocities and mean temperature have been performed in the nonreacting and reacting environment of a model gas turbine combustor with wall injection. In the absence of liquid injection and reaction, flow splits typical of practical combustors produce a strong on-axis recirculation zone. The presence of liquid injection and reaction significantly alters the flowfield characteristics. Noteworthy is the absence of on-axis recirculation.

The formation of an on-axis recirculation zone in reacting flow is dominated by the swirl air flow. Except to provide closure to the dome region, the primary jet flow does not appear to interact with the swirl to enhance the strength or size of the mean on-axis recirculation zone. The rms velocity levels are, however, significantly increased with an increase in flow velocity in the region dominated by the primary jets.

The temperature field reveals the location of a primary zone upstream of the first row of jets, a secondary zone between the two jet rows where reaction continues, and a dilution zone downstream of the second row of jets where the gases are cooled. Evidence of a hot streak was identified, most likely associated with a nozzle asymmetry. An increase in the nozzle air-fuel ratio from 1.5 to 3.0 resulted in more symmetric temperature profiles throughout the combustor, and a more uniform exit temperature profile.

This first characterization suggests that the model combustor employed in the present study has attractive features (optical access, wall jet injection, twin fluid atomizer) for studies of gas turbine combustion. Refinements are worthy of exploration, namely: (1) A reduction in the effective area of the swirl vanes should be considered to represent practical designs more accurately; (2) nozzle asymmetries, while a reflection of practical hardware, should be minimized for the acquisition of data for modeling verification and development; and (3) operation at elevated pressures and elevated inlet temperatures should be provided.

Acknowledgments

This study is supported by the Air Force Engineering and Service Center, Research and Development Directorate, Environics Division (Air Force Contract FO-8635-83-0052), and the Naval Air Propulsion Center (Navy Contract N000140-83-C-9151). The United States Government is authorized to reproduce and distribute reprints for governmental purposes notwithstanding any copyright notation hereon. The authors gratefully acknowlege (*i*) the contributions of Scott Drennan and Brian Bissell in the collection and presentation of the data, (*ii*) the cooperation of Hal Simmons and Parker Hannifin in the provision of the liquid fuel injector used in the WJCC, and (*iii*) Janice Johnson for the preparation of the manuscript.

References

Brum, R. D., and Samuelsen, G. S., 1982, "Assessment of a Dilute Swirl Combustor as a Bench Scale, Complex Flow Test Bed for Modeling, Diagnostics, and Fuel Effects Studies," AIAA Paper No. 82-1263.

Brum, R. D., and Samuelsen, G. S., 1987, "Two-Component Laser Anemometry Measurements of Non-reacting and Reacting Complex Flows in a Swirl-Stabilized Model Combustor," *Experiments in Fluids*, Vol. 5, pp. 95-102.

Gouldin, F. C., Depsky, J. S., and Lee, S. L., 1985, "Velocity Field Characteristics of a Swirling Flow Combustor," *AIAA Journal*, Vol. 23, No. 1, p. 95.

LaRue, J. C., Seiler, E. T., and Samuelsen, G. S., 1985, "Momentum and Heat Flux in a Swirl-Stabilized Combustor," *Twentieth Symposium (International) on Combustion*, The Combustion Institute, pp. 277-285.

Lefebvre, A. H., 1983, *Gas Turbine Combustion*, McGraw-Hill, New York.

Lilly, D. G., 1985, "Investigations of Flowfields Found in Typical Combustor Geometries," NASA Contractor Report 3869.

McDonell, V. G., Wood, C. P., and Samuelsen, G. S., 1987, "A Comparison of Spatially-Resolved Drop Size and Drop Velocity Measurements in an Isothermal Chamber and Swirl-Stabilized Combustor," *Twenty-First Symposium (International) on Combustion*, The Combustion Institute (in press).

Rosjford, T. J., and Russell, S., 1987, "Influences on Fuel Spray Circumferential Uniformity," AIAA Paper No. 87-2135.

Rudoff, R. C., 1986, "Design, Evaluation and Characterization of a Gas Turbine Model Laboratory Combustor With Discrete Wall Injection," Master's Thesis, UCI Combustion Laboratory Report UCIR-ARTR-86-1, Department of Mechanical Engineering, University of California, Irvine, CA.

Smith, R. A., Wood, C. P., and Samuelsen, G. S., 1985, "Formation of Soot From Practical and Surrogate Fuels in a Swirl-Stabilized, Spray-Atomized Combustor," AIAA Paper No. 85-1811.

Wood, C. P., and Samuelsen, G. S., 1985, "Optical Measurements of Soot Size and Number Density in a Spray-Atomized, Swirl-Stabilized Combustor," ASME JOURNAL OF ENGINEERING FOR GAS TURBINES AND POWER, Vol. 107, No. 1, pp. 38-47.

Wood, C. P., Smith, R. A., and Samuelsen, G. S., 1985, "Spatially Resolved Measurements of Soot Size and Population in a Swirl-Stabilized Combustor," *Twentieth Symposium (International) on Combustion*, The Combustion Institute, pp. 1083-1094.

A. S. Nejad
Aero Propulsion Laboratory,
Wright-Patterson AFB, OH 45433

S. P. Vanka
Argonne National Laboratory,
Argonne, IL

S. C. Favaloro
Aero Propulsion Laboratory,
Wright-Patterson AFB, OH 45433

M. Samimy

C. Langenfeld

Department of Mechanical Engineering,
Ohio State University,
Columbus, OH 43210

Application of Laser Velocimetry for Characterization of Confined Swirling Flow

A two-component LDV was used in a cold flow dump combustor model to obtain detailed mean and turbulence data for both swirling and nonswirling inlet flows. Large samples were collected to resolve the second and third-order products of turbulent fluctuations with good accuracy. Particle interarrival time weighting was used to remove velocity bias from the data. The swirling flows, with and without vortex breakdown, exhibited significantly different mean flow and turbulent field behavior. A numerical scheme with the k-ϵ *closure model was used to predict the flow fields. Comparison of the numerical and experimental results showed that the* k-ϵ *turbulence model is inadequate in representing the complex turbulent structure of confined swirling flows.*

Introduction

Continuous combustion devices such as furnaces, gas turbines, and ramjet engines are examples of practical applications for confined swirling flows. Swirl is implemented in these systems to provide increased combustion efficiency, enhanced flame stabilization, better fuel air mixing, and improved blow-off limits, and to reduce the formation of pollutants. Due to the variety of applications and combustor geometries, swirling flows have been the subject of extensive research efforts. Different concepts such as free jets (Fujii et al., 1981; Sislian and Cusworth, 1986), co-axial confined jets (Gouldin et al., 1985; Vu and Gouldin, 1982; Habib and Whitelaw, 1980; Ramos and Somer, 1985; Mattingly and Oates, 1985), multijet tangential entries (Kuwatta and Essenhigh, 1975), and a single confined jet expanding into a larger tube (Buckley et al., 1983; Lilley, 1985; Rhode et al., 1983; Janjua and McLaughlin, 1982) have been investigated. Beer and Chigier (1972) and Gupta et al. (1984) have discussed methods of swirl generation and characterization. Buckley et al. (1983) have shown the considerable impact of different swirl profiles (e.g., forced vortex, free vortex and constant angle) on the efficiency and pressure recovery of dump combustors, while Kilik (1985) has illustrated the effects of swirl vane angle curvature on the induced recirculation size.

The majority of the research effort to date has the common goal of increasing the understanding of such complex flow fields and improving the accuracy of computational techniques to reduce the expensive, and somewhat inefficient, cut and try approach to combustor design. However, progress in the realistic simulation and solution of swirling, turbulent recirculating flows has been limited due to the inherent three-dimensional nature of such flows and a lack of detailed experimental data. While predictive codes continue to make various closure assumptions in the solution of the Navier-Stokes equations, computational modelers will require detailed experimental data for improving and refining their closure models.

The accuracy of conventional measuring instruments, such as hot-wire anemometers and pitot probes, is questionable in swirling flows. These measurements suffer from directional ambiguity and flow disturbance. In addition, there is some doubt about the ability of these instruments to cope adequately with high levels of turbulent fluctuations. Of the methods currently available, optical diagnostic techniques would appear to offer the most promise for obtaining detailed and accurate data in highly complex flow fields.

The aim of the current study is twofold. First, to explore the isothermal swirling flow in a dump combustor configuration, which is of particular interest, to assist in understanding the physical processes. Second, to establish a benchmark set of experimental data to assess the accuracy of the predictions, and aid in the improvement, of a recently developed computer program, which uses the k-ϵ closure model. To meet these objectives, a laser Doppler velocimeter was used to measure velocities and fundamental turbulence quantities in a number of different swirling flows.

2 Background

For many flows the laser Doppler velocimeter (LDV) is the ideal instrument for the measurement of flow velocities since it is nonintrusive, calibration free, and has high spatial and tem-

---

Contributed by the International Gas Turbine Institute and presented at the 33rd International Gas Turbine and Aeroengine Congress and Exhibition, Amsterdam, The Netherlands, June 5-9, 1988. Manuscript received by the International Gas Turbine Institute September 10, 1987. Paper No. 88-GT-159.

poral resolution. The technique relies on the detection of the Doppler shift of light scattered from small particles within the flow. However, there are a number of practical problems associated with this technique. Foremost among these is the requirement to seed the measurement region of the flow with sufficient particles to collect a statistically representative sample size in reasonable elapsed time. Other problems include optical aberrations introduced by curvature of test section walls and difficulties in obtaining proper optical access for making measurements in complex geometries. In addition to the above, LDV measurements can suffer from a number of biasing problems that are directly related to the requirement for seeding the flow.

Perhaps the most obvious bias error is that arising from velocity slip between the fluid and the light scattering particle. However, the use of particles small enough to follow the flow virtually eliminates this type of bias. A useful criterion for selecting the particle size is the particle relaxation time—the time required for a seed particle to reach a predetermined level in response to a step change in fluid velocity—or its inverse, the frequency response, which effectively sets the upper limit of turbulent fluctuations that can be accurately measured.

The most significant bias error occurring in highly turbulent flows is velocity bias. This error arises from the fact that counter-type signal processors make discrete velocity measurements from individual realizations of seed particles passing through the measurement volume. In a uniformly seeded flow, the number of particles per unit time passing through the measurement volume is proportional to the flow rate through that volume, and simple arithmetic averaging of an ensemble of particle measurements will therefore produce readings biased toward values greater than the true temporal mean. This problem was first recognized by McLaughlin and Tiederman (1973) and since then has received a great deal of attention, since without the elimination of velocity bias, LDV will provide accurate results only in laminar or low-intensity turbulent flows. Several correction schemes have been proposed for removal of velocity bias. The majority of these schemes assume a uniform distribution of particles throughout the fluid and weight the individual velocity readings by the magnitude of the instantaneous velocity vector. Since a three-component LDV system is required to determine this vector accurately, other assumptions are usually invoked to enable calculation of a weighting function for one and two-component systems. The original McLaughlin and Tiederman (1973) correction assumes one-dimensional flow and equates the measured velocity value to the magnitude of the instantaneous velocity vector, while Durst (1974) suggested that the period of the Doppler burst is inversely proportional to the magnitude of the velocity vector, and that this value may be used to determine the bias correction factor.

More recently, constant time interval sampling based techniques have been used for the removal of velocity bias. This process, first suggested by Simpson and Chew (1979), has been developed and verified by Stevenson et al. (1983), Craig et al. (1984), and Harch and Favaloro (1986). Stevenson's approach was to limit the sampling rate of the LDV processor and to increase the seeding rate until the velocity bias effectively disappeared. Roesler et al. (1980) observed that this occurred when the seeding rate to sampling rate ratio was 100:1. Craig et al. (1984) showed that a ratio of approximately 10:1 reduced the collection time error (the difference between the actual time required to collect the requested number of samples and the ideal time required at the prescribed sampling rate) to roughly one percent. Nejad and Davis (1986) also showed that the velocity bias could be effectively eliminated by using the time between individual velocity realizations (particle interarrival time) as the weighting factor.

In addition to the above difficulties, Durst (1974) has suggested that additional biases may occur due to variations in particle number concentration, which, in a nominally uniform seeded flow, result from turbulent-like fluctuations in fluid density, such as might occur in combusting or unsteady flows. Similar problems occur in the mixing region of two flows of different seed concentration. However, these biases may also be eliminated by the constant sampling techniques described above.

Nejad and Davis (1986) have suggested that coincidence bias, a type of velocity bias resulting from the requirement for near-simultaneous measurements of two or more velocity components, is also of significance. They proposed a general constraint requiring the coincidence seeding rate to be greater than 3000/s for a coincidence time window (the maximum allowable elapsed time between individual realizations from each channel) of 20 μs for local turbulence intensities around 50 percent, which can be relaxed for lower turbulence intensities.

Other biases that can be significant in the flow fields of current interest include directional bias and incomplete signal (fringe) bias. However, these are readily eliminated by frequency shifting one of the input laser beams using an acousto-optic device such as a Bragg cell.

3 Experimental Facility

3.1 Dump Combustor Model. Figure 1 shows a schematic illustration of the sudden expansion combustor (dump combustor) model, which was specifically designed and fabricated to preserve the integrity of the axisymmetric flow field and to provide excellent optical access for two-component laser velocimetry. The modular design consisted of two major sections, the inlet assembly and the combustion chamber. The inlet assembly consisted of the following sections: a 300-mm-diameter settling chamber, an inlet pipe 2850 mm in length and 101.6 mm i.d., a cylindrical Teflon swirler housing 104.5 mm i.d., 152.4 mm o.d., and 154 mm in length. The inlet pipe

Nomenclature

H = step height
k = turbulent kinetic energy
R = radial coordinate
r = radial coordinate
S = swirl number, equation (1)
U, V, W = instantaneous axial, radial, and tangential velocities
$\bar{U}, \bar{V}, \bar{W}$ = time mean axial, radial, and tangential velocities
U_{ref} = inlet pipe centerline velocity
u, v, w = $\bar{U}-U$, $\bar{V}-V$, $\bar{W}-W$ = instantaneous axial, radial, and tangential fluctuating velocities
u', v', w' = axial, radial, and tangential rms turbulent velocities
X = axial coordinate
ϵ = dissipation rate

Subscripts

h = hub of the swirler
i = inlet pipe
in = computational inlet condition
u = axial component
w = tangential component

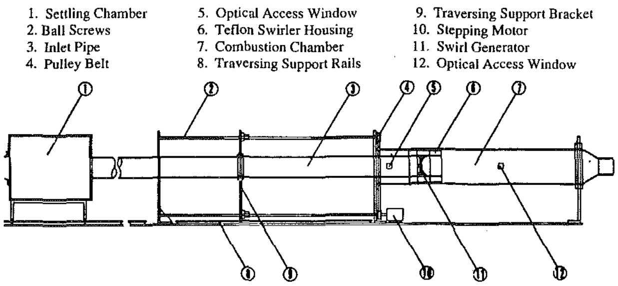

Fig. 1 Schematic of the coaxial dump combustor model

was fastened to the swirler housing with four bolts and provided the option of placing the swirler either at the dump plane or 50.8 mm upstream. Throughout this study, the swirlers were placed 50.8 mm upstream of the dump plane. The combustor chamber section consisted of a Plexiglas cylinder, 1850 mm in length and 152.4 mm i.d., which was connected to a 30 deg contraction nozzle with a 44 percent exit area ratio. To provide optical access, the design incorporated two flat 38 × 38 mm optical quality quartz windows. In order to characterize the inlet flow condition, one window was installed in the inlet pipe 94 mm upstream of the swirler. When measurements in the combustor section were being performed, a plug with the same radius of curvature as the inlet pipe replaced the flat window to remove any upstream flow disturbance. The measurement station in the combustor was held fixed relative to the contraction nozzle by placing the second window 864.7 mm upstream of the nozzle. The unique feature of the design was the capability of readily repositioning the dump plane (swirler housing) relative to the combustion chamber access window. This was accomplished by supporting the settling chamber and the inlet assembly on a traversing mechanism controlled by a stepping motor. The inlet assembly and swirler housing could slide through and traverse the length of the combustion chamber with a resolution of 0.025 mm. Air was pushed through the model by a centrifugal type blower. Throughout the experiments, the inlet centerline velocity was continually monitored with a pitot probe located 360 mm upstream of the swirler housing and kept at 19.2 ± 0.4 m/s, corresponding to a Reynolds number of 125,000 based on combustor inlet diameter.

The effect of the contraction nozzle on the flow field at the measurement station was believed to be insignificant (Lilley, 1985). To confirm this assumption, a series of measurements were taken at $X/H = 2$, 6, and 18. All measurements with the contraction nozzle were taken in the horizontal plane while measurements without the contraction nozzle were performed in the vertical plane. The results shown in Fig. 2 confirm the validity of the above assumption and illustrate the axisymmetry of the combustor flow field.

3.2 Swirler Design. Two constant angle axial flow type swirlers with swirl numbers of 0.3 and 0.5 were designed and used in this study. Swirl number is defined as

$$S = \int_{R_h}^{R_i} \bar{U}\,\bar{W} r^2 dr \Big/ \left(R_i \int_{R_h}^{R_i} \bar{U}^2 r dr \right) \tag{1}$$

Each swirler had 12 circular arc inlet guide vanes welded between a 101.6 mm outer ring and a 19 mm o.d. central hub. The leading edge of each blade was designed to be tangent to the incoming flow and perpendicular to the centerline of the combustor model.

3.3 Particle Generator. A hardened version of the particle generator employed by Craig et al. (1984) was implemented in this study. It has been shown that this chemical seeder is capable of producing spherical, micron size TiO_2 particles in sufficient quantity to enable very high validation rates. In order to approach a uniformly seeded flow, the particles were introduced into the upstream throttling manifold of the centrifugal blower.

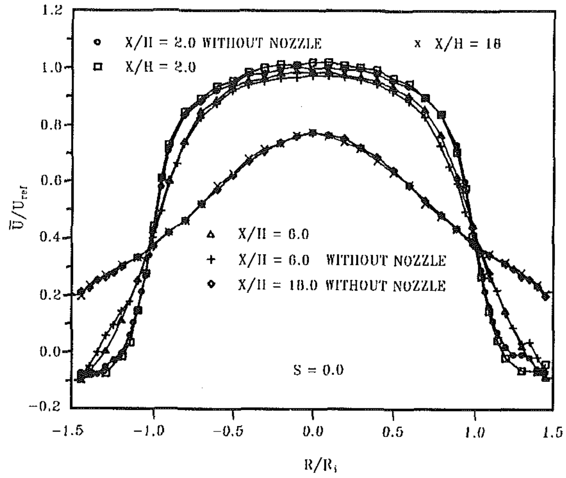

Fig. 2 Contraction nozzle effects

4 Laser Velocimeter

4.1 Optical System. The optical system utilized for these experiments was a two-component TSI Inc. four-beam two-color backscatter system with several in-house modifications. The optics included two Bragg cells, a 3.75X beam expander with a 35 mm entrance beam separation and a final focusing lens of focal length 450 mm. The 514.5 nm (green) and 488 nm (blue) lines of an argon-ion laser operating at 300 mW were used for all measurements. The approximate measurement volume dimensions, based on $1/e^2$ intensity points, were length 600 μm and diameter 80 μm. The system was aligned so that the two nominally orthogonal sets of fringes in the measurement volume were inclined at 45 deg and 135 deg to the combustor centerline. To provide directional sensitivity and to prevent fringe bias both sets of fringes were shifted at 40 MHz, corresponding to fringe velocities of approximately 73 m/s. The entire optical system was placed on a three axis traversing table, allowing the probe volume to be positioned with a resolution of 0.02 mm.

Modifications to the standard TSI system and alignment procedure included micrometer adjustment screws for the field stop lens system and both receiving optic modules. These adjustments enabled full optimization of the system in terms of data rate and Doppler signal quality. A 20 μm aperture was used in the alignment procedure to ensure all four beams crossed at the same point. Since the aperture was appreciably smaller than the measuring volume diameter, Fraunhofer diffraction rings were evident when the beams were passed through the aperture and projected onto a screen. When all projected beams simultaneously showed Fraunhofer rings of equal intensity and symmetry, the crossing point was established. As a further check, the aperture was moved along the optical axis in and out of the probe volume to ensure that the four projected beams appeared and disappeared simultaneously. With the crossing point established, and the distance to the screen measured, the precise fringe inclinations to the combustor centerline were calculated to be 45.667 and 135.167 deg.

4.2 Signal Processing. Two TSI counter-type systems processed the Doppler signals from the photomultipliers. High and low filter limits were set to 100 MHz and 20 MHz on each processor. The comparators were set to one percent and the number of fringe crossings per validation was set to 16.

Depending on the location of the probe volume in the flow, typical data rates in each channel were between 5000 and 10,000/s, which gave coincidence rates of 2000-6000/s with a 20 μs coincidence window. In order to reduce statistical uncertainties, especially for the higher order moments of turbulent fluctuations, a minimum of 27,300 samples/channel were collected at each measurement location in the flow field.

4.3 Data Acquisition and Analysis. A custom-made interface linked the two LDV signal processors to the dedicated computer system (Mod Comp/Classic II/75-5). The interface contained an eight kilobyte FIFO RAM buffer and a 10 MHz clock for each processor. Data transfer to the computer was accomplished in DMA mode at a maximum rate of one megabyte/s. Double precision (48 bit accuracy) calculations of the statistical moments, both biased and unbiased, were made using standard formulae as given in Nejad and Davis (1986). At each measurement location, the upstream flow parameters together with the calculated moments and velocity PDFs were displayed on a Tektronix 4010 graphics terminal. In all but a few instances, the velocity PDFs were virtually noise free, thereby allowing acceptance of all data without imposing cut off limits. This was the final criterion adopted for establishing the performance of the LDV system.

5 Analytical Effort

The above-described experimental program was complemented by an analytical effort to further the development of turbulence models and computational techniques. Several earlier studies (Rhode et al., 1983; Lilley, 1976; Sindir and Harsha, 1982; Srinivasan and Mongia, 1980; Leschziner and Rodi, 1984; Sloan et al., 1986) have numerically solved the partial differential equations governing swirling, recirculating flow fields in conjunction with the k-ϵ turbulence model or the algebraic stress model. Modifications to the k-ϵ model based on a Richardson number correction have also been investigated. In general, the current popularly used turbulence models have been observed to be inadequate in representing the complex turbulent structure of these types of flow fields. Furthermore, the analytical predictions have been observed to be extremely sensitive to the prescription of the inlet conditions.

Research toward the development of these models requires detailed experimental data and efficient grid independent numerical solution of the governing equations. For the flow fields of current interest, the equations are elliptic in space, representing zones of reversed flow that occur in the center (Central Toroidal Zone, CTRZ) and in the corner of an expansion. The solution of these equations has, in the past, required considerable amounts of computing time, thus limiting the number of nodes that can be used without incurring large computational costs.

A significant difference between the current analytical effort and the earlier ones is the development and use of a powerful and efficient numerical procedure for the solution of the equations. This procedure not only converges rapidly, but maintains the same rate of covergence on any grid, however fine it may be. These properties are a consequence of the use of the multigrid technique (BLock Implicit Multigrid Method—BLIMM) and a coupled solution of the momentum and continuity equations. Typically, 20 to 25 iterations are required to obtain an accurate solution, compared with several hundred iterations that have been reported in earlier studies. The details of the BLIMM technique have been reported earlier (Vanka, 1986, 1987) and its extension to the calculation of swirling flows will be published shortly (Vanka, 1988). Therefore, in the present paper only the details of the current calculations and the comparison of the results with the experimental data are given. Figure 3 shows the solution domain considered for the present calculations. The left boundary (inlet) corresponds to the measurement location $X/H = 0.38$ from the dump plane. At this plane, values of the axial, radial, and tangential velocities were prescribed. The inlet turbulence kinetic energy and its dissipation rates were calculated from

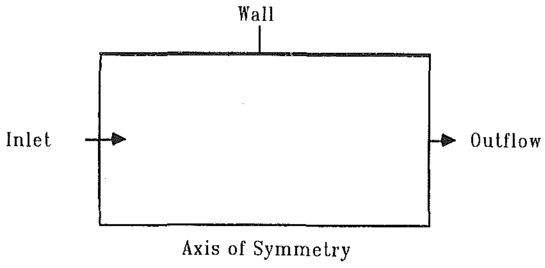

Fig. 3 Computational solution domain

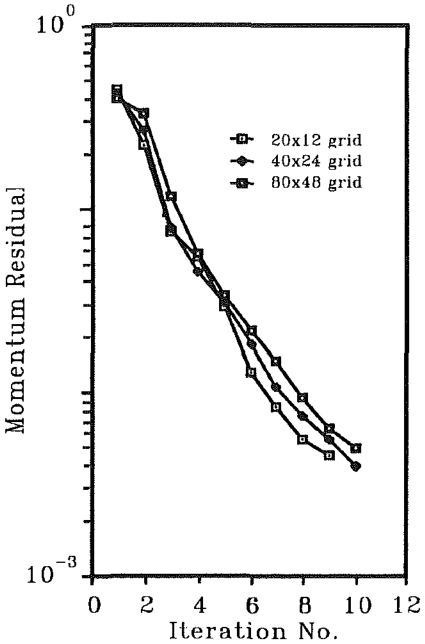

Fig. 4 Convergence rate of numerical technique

$$k = 0.5(u'^2 + v'^2 + w'^2) \tag{2}$$

$$\epsilon = k^{1.5}/0.3\ R_{in} \tag{3}$$

Equation (3) implies that the dissipation length scale was uniform over the cross section. This assumption was necessary because there are currently no means to measure the dissipation rate.

The solution domain was taken to be 20 step heights long and zero derivative boundary conditions were prescribed at the exit. At the top boundary, wall functions (Launder and Spaulding, 1974) were used to model the near-wall turbulence phenomena. The solution was performed only for one half sector of the cross section with the assumption of axisymmetry. The calculations were made for three different finite-difference grids consisting of 20×12, 40×24, 80×48 finite difference cells in the axial and radial directions, respectively. The solution was terminated when the sum of residuals in the x-momentum equation was less than 5×10^{-3} of the inlet momentum. At this level, the maximum successive changes in the U, V, and W velocities were in the order of 10^{-3} of typical inlet values.

Figure 4 shows the rate of convergence of the calculation for the three grids considered. It can be seen that the residual decreased very rapidly with iteration number and good convergence was obtained in less than 15 iterations. The fact that

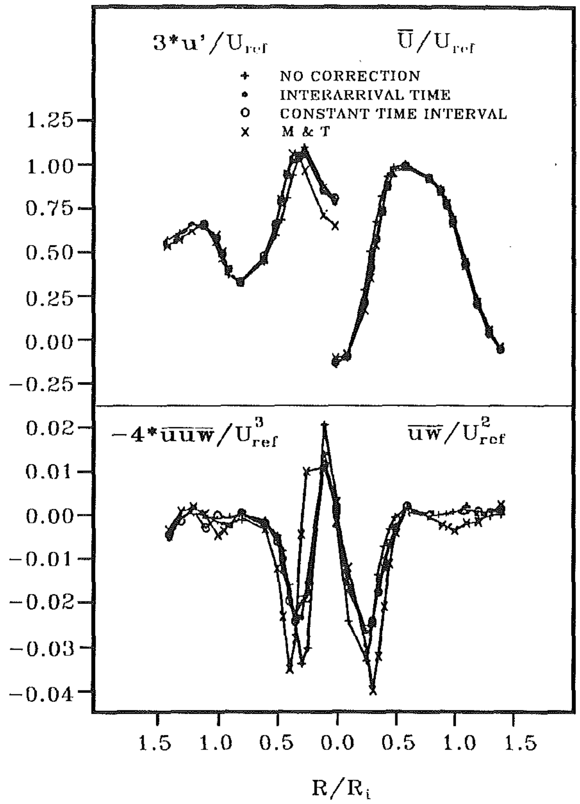

Fig. 5 Comparison of velocity bias correction techniques

the three grids converged at the same rate further illustrates the efficiency of the multigrid cycling procedure and its suitability for computing engineering flows and developing turbulence models.

6 Experimental Results and Discussion

6.1 Assessment of Bias. The extended two-dimensional velocity weighting of McLaughlin and Tiederman, constant time interval sampling, and particle interarrival time weighting were investigated to assess their relative merits in correcting velocity bias. The McLaughlin and Tiederman correction scheme was not expected to be appropriate in the present flow fields, since the existence of simultaneous small velocities in both channels would provide large weighting coefficients and cause the technique to overcompensate for the velocity bias correction factor (Petrie et al., 1988). The criterion for constant time interval sampling was satisfied by ensuring that the sampling frequency was at least an order of magnitude less than the validation rate. Hence, this technique was expected to perform adequately. Particle interarrival time weighting was also expected to be adequate, since the coincident sampling rate was between 2000-6000/s and higher than the expected time scale of large-scale structures in the flow field (Edwards and Jensen, 1983).

Figure 5 shows radial profiles of the mean axial velocity, rms turbulent velocity, Reynolds stress, and one component of third-order mean products of velocity fluctuations for the uncorrected data and the three correction schemes at two step heights downstream of the dump plane for $S=0.5$. The results are normalized with respect to the inlet centerline velocity and for clarity, are plotted on one side of the centerline only.

At this axial location in the flow, there is a large central recirculation zone with small mean axial and tangential velocities. Hence, there is high probability of very large weighting factors in the McLaughlin and Tiederman method. Initially, no upper limit was set for this factor and near zero mean and turbulent velocities from the centerline to 0.5 step heights from the centerline were generated. The maximum weighting factor was then set arbitrarily to 10,000 and produced the results shown in Fig. 5.

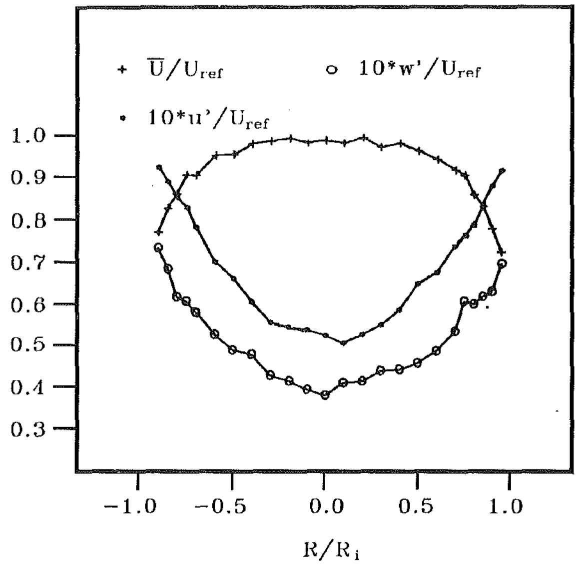

Fig. 6 Upstream flow conditions prior to swirl generator

It is evident that there is excellent agreement between the constant time interval sampling and particle interarrival time weighting methods for mean velocities and turbulence quantities. Nejad and Davis (1986) have shown similar agreement between the shear stress results from these two schemes and analytical results obtained in the self-similar region of a free jet. Hence, the indications are that the two schemes work correctly, but the limitation of both is the requirement for very high data rates, which can be difficult to achieve in combusting and supersonic flow environments (Samimy et al., 1986; Samimy and Addy, 1986).

As expected, the uncorrected mean velocities were higher at all locations with no distinct trend in turbulent velocities. Depending on the measurement location, the values of shear stress and triple products obtained by the uncorrected and McLaughlin and Tiederman methods differed up to 50 percent in magnitude from those of the constant time interval sampling and particle interarrival techniques.

In conclusion, particle interarrival time weighting was chosen to correct velocity bias. This technique was selected over constant time sampling because the available sample size was roughly 10 times larger, 27,300 as compared to 2700 per channel, thereby resulting in a lower statistical uncertainty. To verify the validity of the measurements further, the mean axial velocity profiles at each station were integrated to find the mass flux through the model. On the average, the agreement between upstream and downstream flow rates was 2 percent.

6.2 Incoming Flow. Figure 6 shows the mean axial velocity and the axial and tangential turbulent velocity profiles, normalized with respect to the inlet centerline velocity, 94 mm upstream of the swirler housing.

The turbulent velocity profiles are typical of a fully developed pipe flow: 4 percent tangential and 5 percent axial intensities at the center, increasing to 7 percent tangential and 9 percent axial near the walls. Although the axial turbulent velocities were higher than the tangential turbulent velocities, the anisotropic ratio was almost constant, between 1.3 and 1.4 throughout the inlet pipe.

6.3 Mean Flow Results. Mean and turbulence data were collected at 13 different axial locations for each swirl condition in the dump combustor. The first location was 0.38 step

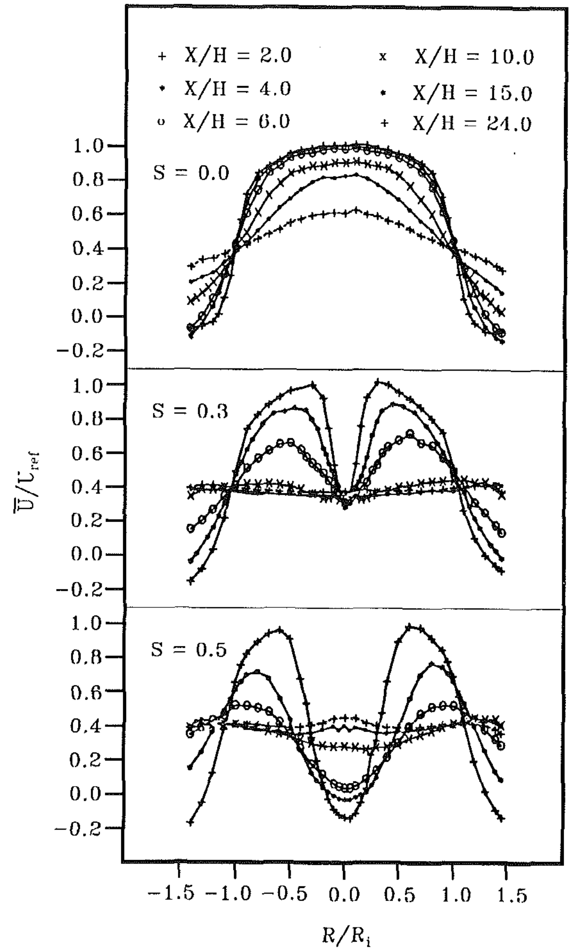

Fig. 7 Axial mean velocity profiles

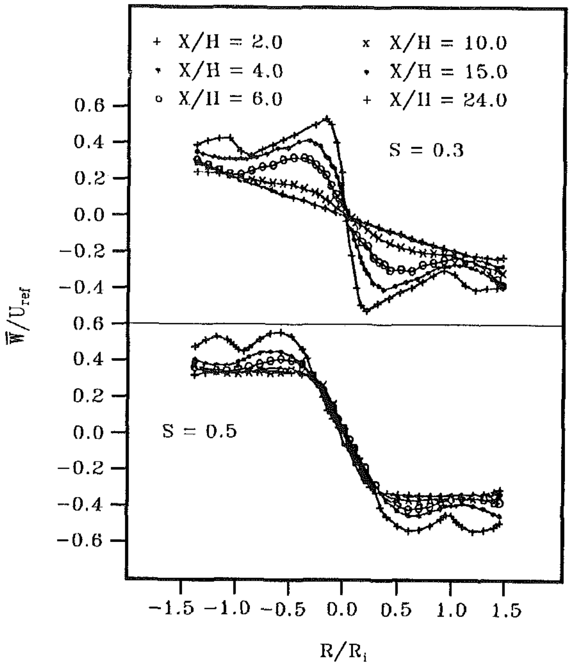

Fig. 8 Tangential mean velocity profiles

heights from the dump plane. This was the location closest to the dump plane where the two-component LDV could be used without the swirler housing intercepting the incident laser beams. Only one half of the profile could be obtained at this location. At all other locations, profiles were obtained on both sides of the combustor centerline.

Figure 7 shows the mean axial velocity profiles at selected streamwise locations for the three swirl levels. The profiles for the flow without swirl are typical of both axisymmetric (Lilley, 1985) and two-dimensional (Smyth, 1979) backstep flows, i.e., very slow decay of the core flow and recirculation in the base region. Re-attachment occurred at approximately 8 step heights downstream of the dump plane, which is in close agreement with similar axisymmetric (Lilley, 1985) and two-dimensional (Eaton and Johnston, 1981) configurations with fully developed inlet flows.

Comparison of the results in Fig. 7 shows the significant impact of swirl on the mean flow field. The length of the corner recirculation zone has decreased from approximately 8 step heights for the nonswirling flow to about 4.3 step heights for $S=0.3$ and to 3.2 step heights for $S=0.5$ swirling flow. This decrease in corner recirculation length, which is caused by the rapid expansion of the flow after separation due to centrifugal forces, has also been reported by Lilley (1985).

Depending on the Reynolds number and vortex strength, vortex breakdown can occur in swirling flows. Vortex breakdown is followed by a flow reversal zone and a region of chaotic flow (Gouldin et al., 1985; Lilley, 1985; Hall, 1972; Leibovich, 1978; Leibovich, 1984). In the present experiments for $S=0.3$, there was a flow deceleration at the core of the central vortex but it was insufficient to cause vortex breakdown. However, for $S=0.5$, vortex breakdown occurred upstream of the dump plane and extended the central recirculating flow to approximately 4.4 step heights downstream of the step. The maximum diameter of the central recirculating region was about 0.8 step heights and was located roughly 3 step heights from the dump plane. Lilley (1985) has shown the significant effects of swirl strength on the size and shape of the recirculation region. In addition, the axial velocity gradient at the centerline was much higher for the stronger swirling flow than for the weaker one.

The tangential velocity profiles for both swirling flows are shown in Fig. 8 (for $S=0.0$, the tangential velocity was almost zero throughout the flow field). While both flow fields initially showed profiles typical of a dump combustor flow (Lilley, 1985), and similarities to lifting surface leading edge or trailing edge vortex flows (Leibovich, 1984; Driver and Seegmiller, 1982), they exhibited totally different behavior farther downstream. The stronger swirling flow retained the strength of its vortex core all the way to the last measurement location, 24 step heights downstream. This is consistent with the earlier results for similar and stronger swirling flows (Lilley, 1985). The weaker swirling flow expanded its vortex core at the expense of losing its strength; the flow became a forced vortex 10 to 12 step heights from the dump plane.

6.4 Turbulence Results. Figure 9 shows the axial turbulent velocities for the three swirl levels. The flow with no swirl revealed local peak values of turbulent velocities in the shear layer generated between the core flow and the corner recirculating flow, which decayed very slowly in the streamwise direction. These results agree well with those of Lilley (1985), and correlate well with the results of similar two-dimensional backstep flows (Smyth, 1979; Eaton and Johnston, 1981). The swirling flows showed two local peaks, one in the aforementioned shear layer and the other in the shear layer at the edge of the vortex core. The decay of turbulent velocities in the streamwise direction was extremely rapid, especially for the stronger swirling flow, which is indicative of high diffusion and dissipation rates. For the three swirl levels, the maximum axial turbulent velocities in the shear layer generated by the corner recirculating flow occurred before re-attachment and decayed very rapidly. This behavior

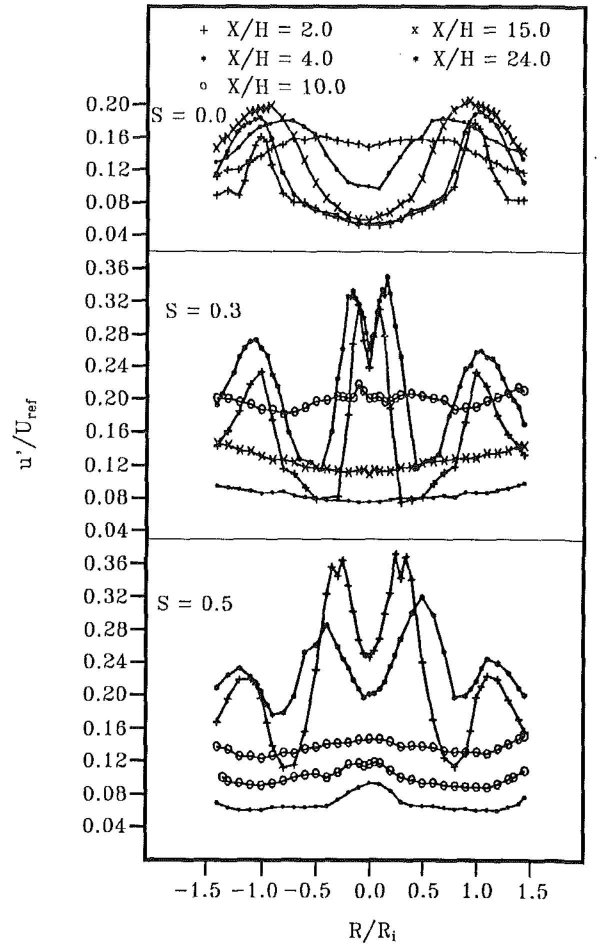

Fig. 9 Axial turbulent velocity profiles

is typical of two-dimensional flows with no swirl (Eaton and Johnston, 1981; Driver and Seegmiller, 1982; Chandrasuda and Bradshaw, 1981). The general consensus is that large-scale structures in the shear flow approaching the wall interact with the wall and break down. Based on the present results, this seems to be the case in swirling flows as well.

Contrary to expectation, the axial turbulent velocities within the shear layer generated by the corner recirculating flow were higher for $S=0.3$ than for $S=0.5$. Both random and organized fluctuations contribute to turbulent velocity levels. With the same experimental apparatus as used in the current study, Samimy et al. (1988) have shown the existence of highly coherent structures within both swirling flows, which contribute significantly to turbulent velocity levels, and that the energy levels associated with these structures were almost an order of magnitude higher for $S=0.3$ than for $S=0.5$.

Figure 10 shows the tangential turbulent velocities for the three swirl levels. For flow with no swirl, the profiles were similar to the axial profiles. The anisotropic ratio varied between 1.1 and 1.5 and consistently peaked around one step height from the centerline. For both swirling flows, the peak turbulent velocities occurred in the core of the vortex. As shown in the mean flow results, the vortex core for $S=0.3$ expanded and finally covered the entire combustor diameter. As a result, the peak turbulent velocities decayed until the levels were uniform across the combustor. For $S=0.5$, the peak turbulent velocities decayed only within the central recirculation region ($X/H=0.38$ to $X/H=6.0$). The anisotropic ratio varied significantly in the flow field, and for the stronger swirling flow dropped to as low as 0.5 in the vortex core downstream of the central recirculation region.

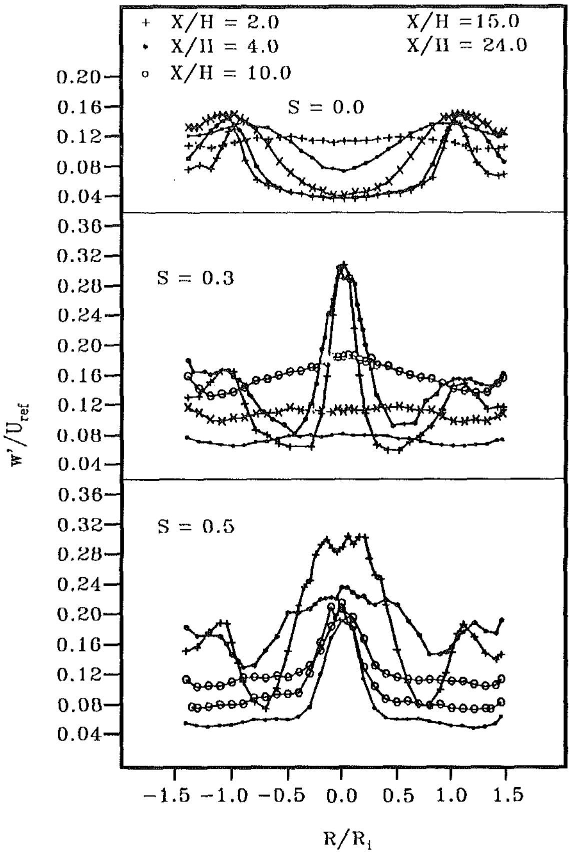

Fig. 10 Tangential turbulent velocity profiles

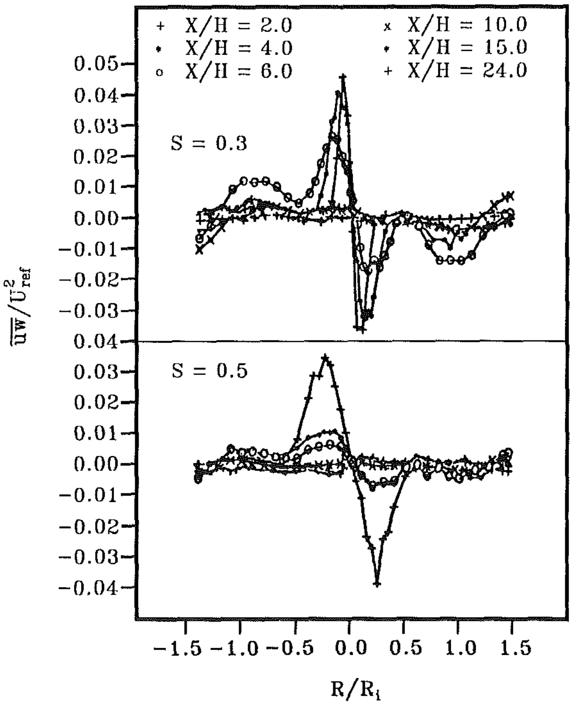

Fig. 11 Reynolds shear stress profiles

Figure 11 shows Reynolds shear stress profiles for both swirling flows (values for the no-swirl case were at least 20 times less than those shown). In both flows, local peaks occurred within the wall boundary layer, the shear layer generated by the recirculating flow, and at the edge of the

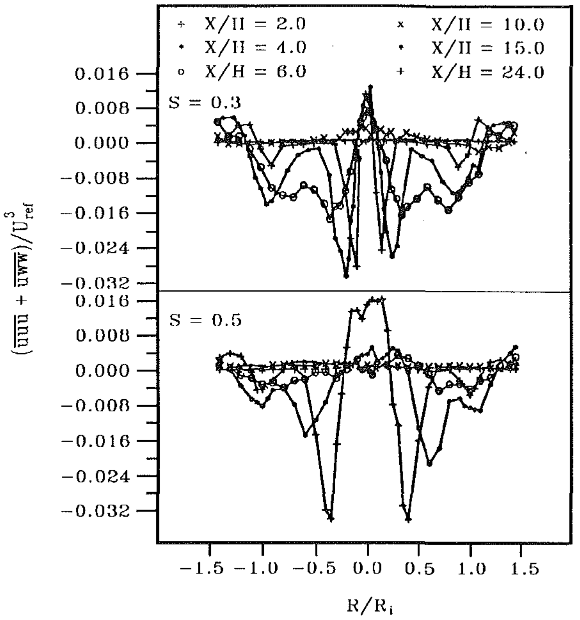

Fig. 12 Axial convection of turbulent kinetic energy

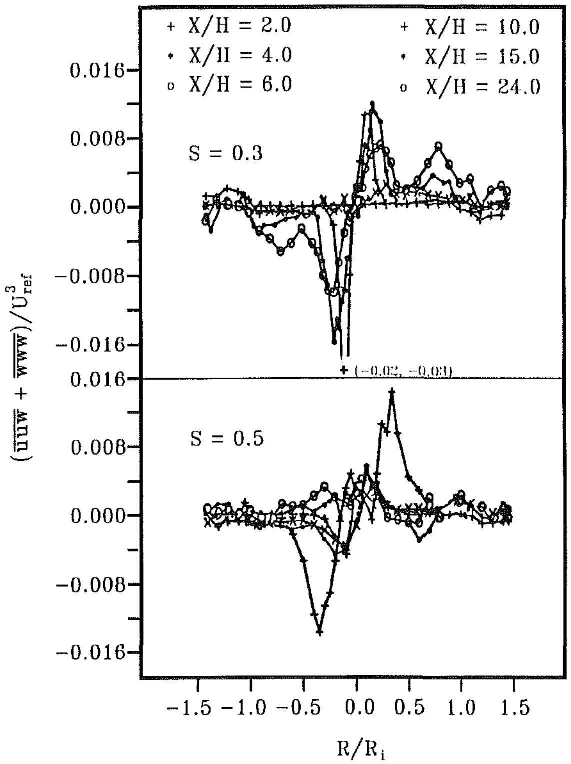

Fig. 13 Tangential convection of turbulent kinetic energy

vortex core. Very high Reynolds stresses at the edge of the vortex core are a reflection of strong shear forces between the vortex core and the outer flow. This has also been shown by Lilley (1985). There are two factors that could contribute to the higher Reynolds stress at the edge of the vortex core for the weaker swirling flow: Firstly, the weaker swirling flow maintained a stronger vortex core up to about 4 step heights downstream of the dump plane as depicted by the larger tangential velocity gradients (see Fig. 8), and secondly, there were well organized large-scale oscillations in the weaker swirling flow as discussed by Samimy et al. (1988).

Radial profiles of triple products of turbulent velocities for both swirling flows are shown in Figs. 12 and 13. The $(\overline{uuu} + \overline{uww})$ and $(\overline{uuw} + \overline{www})$ terms can be interpreted as the convection of turbulent kinetic energy by large-scale structures in the axial and tangential directions, respectively. Extremely large values of these transport terms, especially for $S = 0.3$, confirm the existence of organized structures within these flows.

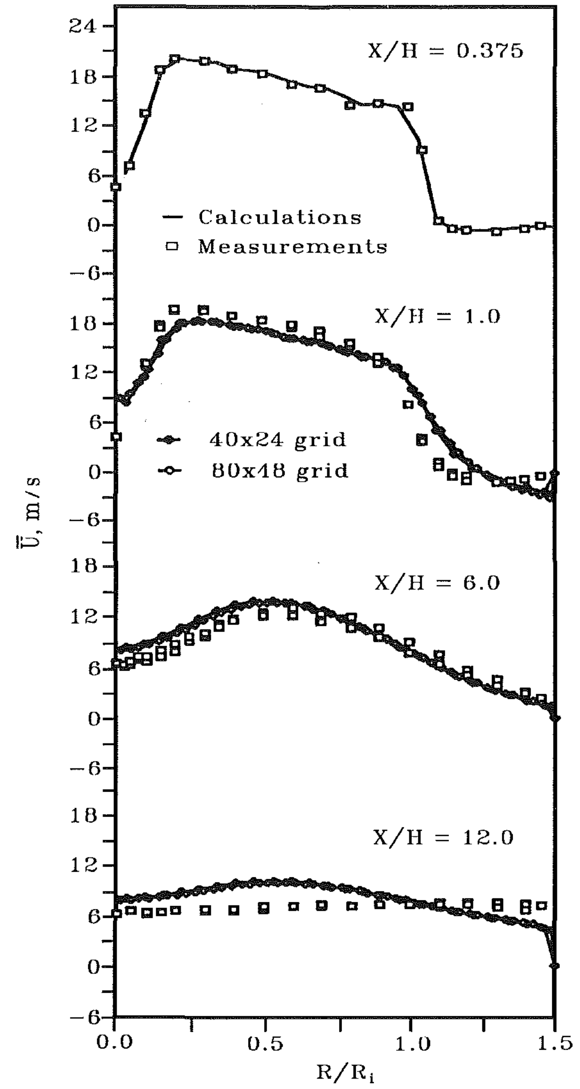

Fig. 14 Computed mean axial velocity profiles

For both flows, the positive and relatively small values of axial convection within the boundaries of the vortex core were in accord with the slow development of the mean axial velocity field at the center, while the negative and relatively large values around the edge of the vortex core were in accord with the fast development of the mean field at the core boundaries. The tangential convection term at the edge of the vortex core for 0.3 swirling flow was initially very high, but decayed to negligible values after about six step heigths. For $S = 0.5$, this term was lower initially, but persisted all the way to 24 step heights. Unfortunately, this does not explain the difference in the mean tangential flow behavior discussed earlier (Fig. 8), since the development of the mean tangential velocity depends primarily on the turbulent mixing in the radial direction.

7 Comparison of Experiments and Calculations

Figure 14 shows profiles of measured and calculated mean axial velocities at a number of axial locations for $S = 0.3$,

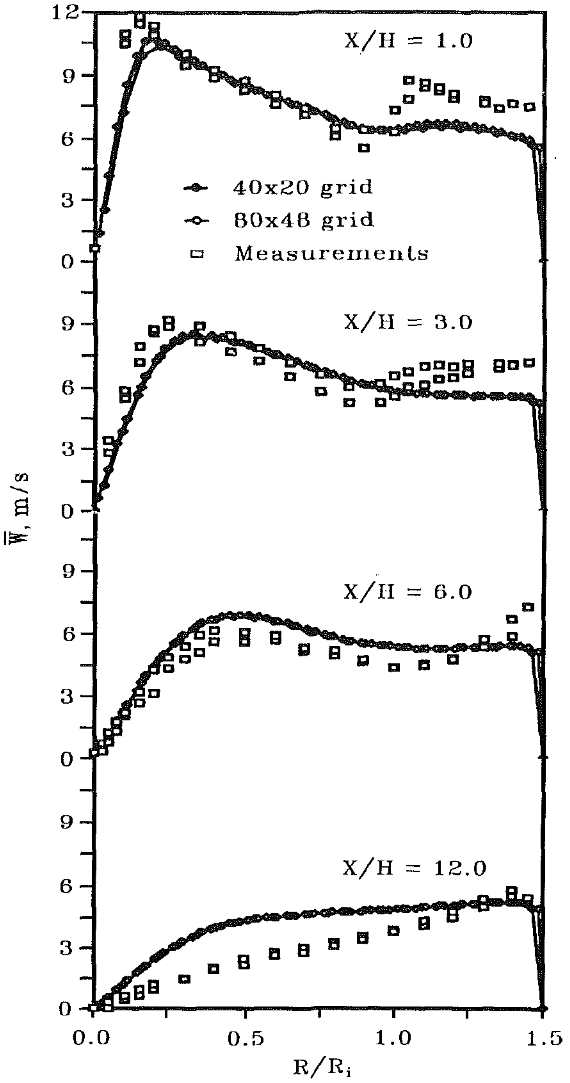

Fig. 15 Computed mean tangential velocity profiles

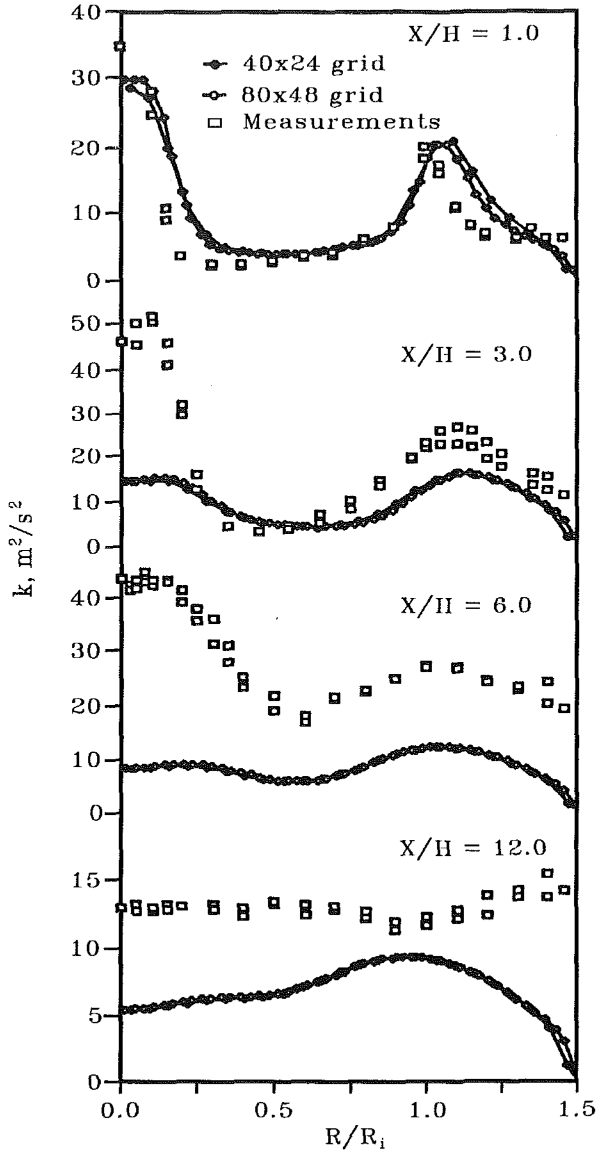

Fig. 16 Computed turbulent kinetic energy profiles

along with the prescribed curve and measured profile at the inlet plane, $X/H = 0.38$. There was some disagreement between the measured and calculated values at $X/H = 1.0$ in the central region and at the edge of the shear layer from the lip of the sudden expansion, but the discrepancies were not large. This pattern continued up to $X/H = 6.0$, but from $X/H = 8.0$ and beyond, the calculations differed significantly from the measured values. The measurements indicated a flatter axial velocity profile than the predictions, which showed higher velocities in the center and lower values toward the wall. The swirl velocity profiles (Fig. 15) presented a similar picture with satisfactory agreement up to $X/H = 6.0$ and significant deviations at $X/H = 8.0$ and onward.

The principal reason for these discrepancies can be inferred from the comparisons of the turbulent kinetic energy, shown in Fig. 16. At $X/H = 1.0$, the flow had not developed very far from the inlet, and as expected, the differences between the measured and calculated turbulent kinetic energies were not significant. However, for stations farther downstream ($X/H = 3.0$ and beyond), it was evident that the large turbulent velocities in the central region were not reproduced by the k-ϵ turbulence model, which instead predicted a sharp decay in the turbulent energy level. The discrepancy near the shear layers was not as pronounced, although the overall energy levels were lower than the observed values. It is worthwhile mentioning that for nonswirling flows, the predicted kinetic energies are in much closer agreement with measured values. This highlights the inability of the k-ϵ model to represent the additional production of turbulent kinetic energy due to azimuthal swirl, and is the principal cause for the smaller amount of turbulent mixing, which results in sharper gradients than those observed in the experiments.

The current calculations appear to display the general trends observed in earlier numerical studies with the k-ϵ model, although many other factors such as the precise turbulence constants, numerical diffusion errors, solution accuracy, specific inlet and boundary conditions used, and any corrections made to the turbulence constants need to be taken into account. Nevertheless, low values of turbulent velocities have been observed previously (Sloan et al., 1986). It is believed that the current results with the finest grid (80 × 48) are nearly free of numerical diffusion errors and demonstrate that the k-ϵ model needs significant modifications before it can be used for calculation of swirling flows.

8 Conclusions

A two-component coincident LDV was used in a novel experimental arrangement to obtain and document detailed experimental data in a dump combustor configuration with and without swirling inlet flow. Particle interarrival time weighting was utilized to remove velocity bias and provide large sample sets to resolve Reynolds stresses and turbulent triple products with good accuracy. The effects of inlet swirl on the dump combustor flow field included the generation of a central vortex, reduced re-attachment lengths, and Reynolds stress and turbulent triple product values up to 25 times higher than nonswirling flows.

The two swirlers investigated showed significantly different behavior. The 0.5 swirling flow experienced centerline flow reversal and maintained the strength of its vortex core throughout the measurement region, while the 0.3 swirling flow showed no vortex breakdown and expanded its vortex core at the expense of losing its strength.

A computational scheme with the k-ϵ model was implemented to predict the swirling flows. The results confirmed conclusions of other researchers that the k-ϵ model requires further modification and improvement before it can be used successfully for the prediction of swirling flows.

References

Beer, J. M., and Chigier, N. A., 1972, *Combustion Aerodynamics*, Wiley, New York.

Buckley, P. L., Craig, R. R., Davis, D. L., and Schwartzkopf, K. G., 1983, "The Design and Combustion Performance of Practical Swirlers for Integral Rocket/Ramjets," *AIAA Journal*, Vol. 21, No. 5, pp. 733–740.

Chandrasuda, C., and Bradshaw, P., 1981, "Turbulence Structure of a Re-attaching Mixing Layer," *Journal of Fluid Mechanics*, Vol. 110, pp. 171–194.

Craig, R. R., Nejad, A. S., Hahn, E. Y., and Schwartzkopf, K. G., 1984, "A General Approach for Obtaining Unbiased LDV Data in Highly Turbulent Non-reacting and Reacting Flows," AIAA Paper No. 84-0366.

Driver, D. M., and Seegmiller, H. L., 1982, "Features of Re-attaching Turbulent Shear Layer Subject to Adverse Pressure Gradients," AIAA Paper No. 82-1029.

Durst, F., 1974, Informal Presentation, *2nd International Workshop on Laser Velocimetry*, Vol. II, pp. 301–306.

Eaton, J. K., and Johnston, J. P., 1981, "A Review of Research on Subsonic Turbulent Flow Re-attachment," *AIAA Journal*, Vol. 19, No. 9, pp. 1093–1100.

Edwards, R. V., and Jensen, A. S., 1983, "Particle-Sampling Statistics in Laser Anemometers: Sample-and-Hold System and Saturable Systems," *Journal of Fluid Mechanics*, Vol. 133, pp. 397–411.

Fujii, S., Eguchi, K., and Gomi, M., 1981, "Swirling Jets With and Without Combustion," *AIAA Journal*, Vol. 19, No. 11, pp. 1438–1442.

Gouldin, F. C., Depsky, J. S., and Lee, S-L, 1985, "Velocity Field Characteristics of a Swirling Flow Combustor," *AIAA Journal*, Vol. 23, No. 1, pp. 95–102.

Gupta, A. K., Lilley, D. G., and Syred, N., 1984, *Swirl Flows*, Abacus Press, Turnbridge Wells, United Kingdom.

Habib, M. A., and Whitelaw, J. H., 1980, "Velocity Characteristics of Confined Coaxial Jets With and Without Swirl," ASME *Journal of Fluids Engineering*, Vol. 102, pp. 47–53.

Hall, M. G., 1972, "The Structure of Vortex Breakdown," *Annual Reviews of Fluid Mechanics*, Vol. 10, pp. 195–218.

Harch, W. H., and Favaloro, S. C., 1986, "A Time Interval Sampling Method for the Removal of Velocity Bias in LDV Measurements in Turbulent Flows," presented at the 9th AFMC, New Zealand.

Janjua, S. I., and McLaughlin, D. K., 1982, "Turbulence Measurements in a Swirling Confined Jet Flowfield Using a Triple Hot-Wire Probe," Dynamics Technology, Inc. Report, DT-8178-02, Torrance, CA.

Kilik, E., 1985, "Better Swirl Generation by Using Curved Vane Swirlers," AIAA Paper No. 85-1087.

Kuwatta, M., and Essenhigh, R. H., 1975, "Correlation of Pollutant Emissions, Noise, and Heat Transfer in a Natural Gas Combustor," AIAA Paper No. 75-1267.

Launder, B. E., and Spalding, D. B., 1974, "The Numerical Computation of Turbulent Flows," *Computer Methods in Applied Mechanics and Engineering*, Vol. 3, pp. 269–289.

Leibovich, S., 1978, "The Structure of Vortex Breakdown," *Annual Reviews of Fluid Mechanics*, Vol. 10, pp. 221–246.

Leibovich, S., 1984, "Vortex Stability and Breakdown: Survey and Extension," *AIAA Journal*, Vol. 22, No. 9, pp. 1192–1206.

Leschziner, M. A., and Rodi, W., 1984, "Computation of Strongly Swirling Axisymmetric Free Jets," *AIAA Journal*, Vol. 22, pp. 1742–1747.

Lilley, D. G., 1976, "Primitive Pressure-Velocity Code for the Computation of Strongly Swirling Flows," *AIAA Journal*, Vol. 14, pp. 749–756.

Lilley, D. G., 1985, "Swirling Flows in Typical Combustor Geometries," AIAA Paper No. 85-0184.

Mattingly, J., and Oates, G., 1985, "An Experimental Investigation of Co-annular Swirling Flows," AIAA Paper No. 85-0186.

McLaughlin, D. K., and Tiederman, W. G., 1973, "Biasing Correction for Individual Realization of Laser Anemometer Measurements in Turbulent Flows," *The Physics of Fluids*, Vol. 16, No. 12, pp. 2082–2088.

Nejad, A. S., and Davis, D. L., 1986, "Velocity Bias in Two-Component Individual Realization Laser Doppler Velocimetry," *Proc. of the 5th International Congress on Application of Laser and Electro Optics*, Arlington, VA.

Petrie, H. L., Samimy, M., and Addy, A. L., 1988, "Laser Doppler Velocity Bias in Separated Turbulent Flows," to be published in *Journal of Experiments in Fluids*.

Ramos, J. I., and Somer, H. T., 1985, "Swirling Flow in a Research Combustor," *AIAA Journal*, Vol. 23, No. 2, pp. 241–248.

Rhode, D. L., Lilley, D. G., and McLaughlin, D. K., 1983, "Mean Flowfields in Axisymmetric Combustor Geometries With Swirl," *AIAA Journal*, Vol. 21, No. 4, pp. 593–600.

Roesler, T. C., Stevenson, W. H., and Thompson, H. D., 1980, "Investigation of Bias Errors in Laser Doppler Velocimeter Measurements," AFWAL-TR-80-2108.

Samimy, M., Petrie, H. L., and Addy, A. L., 1986, "A Study of Compressible Turbulent Re-attaching Free Shear Layers," *AIAA Journal*, Vol. 24, No. 2, pp. 261–267.

Samimy, M., and Addy, A. L., 1986, "Interaction Between Two Compressible Turbulent Free Shear Layers," *AIAA Journal*, Vol. 24, No. 12, pp. 1918–1923.

Samimy, M., Nejad, A. S., Langenfield, C. A., and Favaloro, S. C., 1988, "Oscillatory Behavior of Swirling Flows in a Dump Combustor," AIAA Paper No. 88-0189.

Simpson, R. L., and Chew, Y. T., 1979, "Measurements in Steady and Unsteady Separated Turbulent Boundary Layers," *Laser Velocimetry and Particle Sizing*, H. D. Thompson and W. H. Stevenson, eds., Hemisphere Publishing, Washington, DC.

Sindir, M. M., and Harsha, P. T., 1982, "Assessment of Turbulence Models for Scramjet Flowfields," NASA CR 3643.

Sislian, J. P., and Cusworth, R. A., 1986, "Measurement of Mean Velocity and Turbulent Intensities in a Free Isothermal Jet," *AIAA Journal*, Vol. 24, No. 2, pp. 303–309.

Sloan, D. G., Smith, P. J., and Smoot, L. D., 1986, "Modeling of Swirl in Turbulent Flow Systems," *Progress Energy Combustion Science*, Vol. 12, pp. 163–250.

Smyth, R., 1979, "Turbulent Flow Over a Plane Symmetric Sudden Expansion," ASME *Journal of Fluids Engineering*, Vol. 101, pp. 348–353.

Srinivasan, R., and Mongia, H. C., 1980, "Numerical Computation of Swirling Recirculating Flows," NASA CR 165197.

Stevenson, W. H., Thompson, H. D., Lichick, T. S., and Gould, R. D., 1983, "Laser Velocimeter Measurements in Turbulent Flows With Combustion," AFWAL-TR-82-2076, Parts I & II Sept. 1982, July 1983.

Vanka, S. P., 1986, "Block-Implicit Multigrid Solution of Navier-Stokes Equations in Primitive Variables," *Journal of Computational Physics*, Vol. 65, pp. 138–147.

Vanka, S. P., 1987, "Block-Implicit Calculations of Viscous Internal Flows, Recent Results," AIAA Paper No. 87-0059.

Vanka, S. P., 1988, "Calculation of Swirling Recirculating Flows on Multiple Grids," in preparation.

Vu, B. T., and Gouldin, F. C., 1982, "Flow Measurements in a Model Swirl Combustor," *AIAA Journal*, Vol. 20, No. 5, pp. 642–651.

Thin-Filament Pyrometry: A Novel Thermometric Technique for Combusting Flows

L. P. Goss

V. Vilimpoc

B. Sarka

W. F. Lynn

Systems Research Laboratories,
A Division of Arvin/Calspan,
Dayton, OH 45440-3696

A novel technique is described for making temperature measurements in a combusting flow. The technique, Thin-Filament Pyrometry, is based on the blackbody emission of a small ceramic filament (15 μm), which is introduced into the flow field under study. Because the emission along the entire length of the filament is recorded, the complete spatial temperature distribution is measured. The temporal response of the filament is ~ 700 Hz under ambient conditions. To demonstrate the capabilities of the technique in a combusting flow, a H_2-N_2 jet diffusion flame was studied. The evolution of the large-scale buoyancy-driven structures at low Reynolds numbers was followed by this technique.

Introduction

Over the past decade, significant effort has been expended to develop nonintrusive laser-based diagnostic techniques capable of measuring velocity, temperature, and species concentration in combusting environments. This effort has culminated in the development of techniques such as Laser-Doppler Velocimetry (LDV), Laser-Induced Fluorescence (LIF), Spontaneous Raman Scattering (SRS), and the nonlinear Raman scattering techniques, i.e., Coherent Anti-Stokes Raman Spectroscopy (CARS) [1]. These methods have been most successfully applied to point measurements in flames. Recently, the LIF techniques have been extended to two-dimensional measurements [1]. All of these techniques suffer from the complexity of the optical and laser systems and the sheer cost of building, operating, and maintaining them. The simplicity and low cost of probe techniques such as thermocouples and gas-sampling probes have fostered their continued use. Probes, however, are known to perturb the flow fields in which they are placed, often resulting in anomalous observations. This problem furnished the initial driving force for the development of laser-based techniques. The ideal technique would actually combine the advantages of both types of techniques and be relatively simple, easy to implement, inexpensive, and nonperturbing. This paper describes a technique that offers a majority of these desirable qualities: Thin-Filament Pyrometry (TFP).

TFP combines the advantages of low cost, ease of implementation, and nonperturbing qualities to the measurement of temperature in a combusting environment. The technique has the added advantage that the temperature is measured along a line rather than at a single point, as is the case with most probe techniques. The TFP technique relies upon the blackbody emission of a thin ceramic filament (SiC) in the wavelength range 0.8 to 1.8 μm for measurement of the temperature distribution in a combusting flow field. The emission is recorded spatially along the length of the filament, allowing the radial temperature distribution to be evaluated. The filament is made of ultrafine β-SiC with excess carbon and is available commercially [2]. The filament diameter ranges from 10 to 20 μm (nominally, 15 μm), and the thermal conductivity is relatively low: ~ 10 kcal/m h°C along the filament axis at room temperature. The thermal conductivity of the filament is ~ 40 times lower than that of Pt-PtRh wire, which drastically reduces the spread in the temperature profile along the filament. Because of its small size, the filament can respond quickly to temperature changes in its surroundings. The high emissivity that is constant over the temperature range of interest allows the quantitative conversion of filament intensity to gas temperature.

The TFP technique is similar to a method reported by Ferguson et al. [3], in which the emission from a silica-coated platinum:platinum-13 percent rhodium thermocouple was monitored to determine flame temperature. The major differences between the earlier study and the present one are the use of a β-SiC filament for emission and the fact that line rather than point measurements were made.

Confirmation of the above attributes along with a demonstration of the application of the technique to a H_2-N_2 diffusion flame will be discussed in this paper. Also included will be a detailed analysis of the thermal properties of the filament in a flame environment. This probe should become an important tool in the study of turbulent flame systems.

Theory

In order to relate the emission of the SiC filament to the temperature of the gas, the response of the filament to a temperature change must be calibrated or adequately predicted.

Contributed by the International Gas Turbine Institute and presented at the 33rd International Gas Turbine and Aeroengine Congress and Exhibition, Amsterdam, The Netherlands, June 5-9, 1988. Manuscript received by the International Gas Turbine Institute January 7, 1988. Paper No. 88-GT-28.

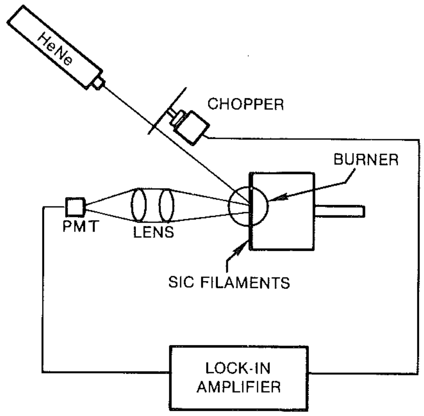

Fig. 1 Experimental arrangement for measuring relative emissivity of SiC filaments by reflectance

The β-SiC is reported in the literature to be a graybody and has a relatively high emissivity (0.88) [4]. The filament behavior is, thus, adequately described by the Planck blackbody equation given by

$$L(\lambda, T) = \frac{\epsilon(\lambda, T)C_1}{\lambda^5[\exp(C_2/\lambda T) - 1]} \quad [\mathrm{W/m}] \qquad (1)$$

where ϵ is the apparent emissivity of the filament, C_1 the first radiation constant, C_2 the second radiation constant. λ the wavelength in a vacuum, and T the filament temperature. If equation (1) is to be used for the quantitative measurement of the temperature of the filament, the emissivity of the filament must be evaluated over the entire wavelength and temperature range of interest. Because it is a graybody, the emissivity does not vary with wavelength. The temperature effect on the emissivity, however, must be evaluated experimentally. The conventional approach to calibrating the emissivity of a material is to heat the material to a known temperature, measure its emittance, and compare the emittance to that of a blackbody at the same temperature. Due to the small size of the filament, this approach is quite difficult. Therefore, the reflectance of the filament was measured instead. The relationship between the reflectance and the emissivity of a material is given by Kirchoff as

$$\begin{aligned}\epsilon(\theta, \phi) &= 1 - \iint \rho(\theta, \phi, \theta', \phi')d\theta' d\phi' \\ &= 1 - \rho_h(\theta, \phi)\end{aligned} \qquad (2)$$

where $\epsilon(\theta, \phi)$ is the directional emissivity, $\rho(\theta, \phi, \theta', \phi')$ the bidirectional reflectance distribution function (BRDF), and $\rho_h(\theta, \phi)$ the directional hemispherical reflectance. In general, the required reflectance accuracy for a desired emissivity accuracy is given by the following relation:

$$\frac{\Delta\rho_h}{\rho_h} = \frac{\epsilon}{1 - \epsilon}\,\frac{\Delta\epsilon}{\epsilon} \qquad (3)$$

where the θ, ϕ index has been dropped. For a highly emissive sample such as the SiC filament, with emissivity of 0.88, the error in the emissivity measurement based on a 1 percent error in the reflectance is 0.13 percent. Thus, reflectance measurements – if conducted properly – can be a very accurate indicator of the emissivity (especially for highly emissive materials). The concern with the SiC filament was not in measuring the absolute emissivity at all temperatures but rather in establishing whether the emissivity remained constant, which reduced the problem to measuring the relative change in the emissivity rather than the absolute value. This was accomplished with the experimental arrangement shown in Fig. 1. The chopped output from a HeNe laser was directed onto a bundle of SiC filaments, the scatter from which was monitored by a PMT and lock-in amplifier. The filaments were then heated by a propane torch to a temperature of ~2200 K. The reflectance was monitored during the heatup of the filament and after it reached its maximum temperature. Several times the reflectance was observed to remain constant throughout this process to within an experimental error of ~1 percent. Assuming that the BRDF of the filament did not vary with temperature, this experiment established an upper bound of ~0.13 percent in the variation of the emissivity of the SiC over the 300-2200 K temperature range. The emissivity is, thus, assumed to be constant for purposes of evaluating the filament temperature from the observed emission.

It should be noted that equation (2) relates the emissivity to the hemispherical reflectance—not the bidirectional reflectance. In the present experiments the bidirectional reflectance rather than the full hemispherical reflectance is measured. It is assumed that the hemispherical is proportional to the directional reflectance and, thus, that the reflectance distribution function does not vary with temperature. Measurements with collection angles at normal and ±45 deg were examined to verify that this was the case.

Because the emissivity is constant with wavelength and temperature, equation (1) can be evaluated for predicting the filament emission characteristics. Experimentally the emission is detected over a limited spectral region with a detector that has a varying response to the wavelength of the emission. Equation (1) must then be multiplied by the detector response and integrated over this region. The detected signal is given by

$$D_{\exp} = k_{\exp}\int_{\lambda_1}^{\lambda_2} L(\lambda, T)R(\lambda)T_r(\lambda) \qquad (4)$$

where $L(\lambda, T)$ is the blackbody response given by equation (1), $R(\lambda)$ the detector response, λ_1 and λ_2 the limits of the detector response, $T_r(\lambda)$ the transmission characteristics of the optics employed in the experiment, and $k_{\exp}$ an experimental constant that takes into account the efficiency of the collection optics and the gain of the detector electronics. The experimental constant $k_{\exp}$ is removed by normalizing the observed signal to the signal at a known temperature. To evaluate equation (4), one must know the detector-response function $R(\lambda)$. The response function for the InGaAs detector employed in these studies is shown in Fig. 2(*a*). By integrating the response function and the blackbody function over the limits of the detector bandwidth, the emission from the filament can be determined. Figure 2(*b*) displays the relative intensity as a function of temperature for the experimental setup. The calculated intensity has been normalized to the emission corresponding to the maximum temperature of a H_2 diffusion flame. Notice that the data have been plotted in this figure with intensity as the independent variable and temperature as the dependent variable. This facilitates the conversion of the measured intensity to a temperature. The curve in Fig. 2(*b*) was fitted by a power-series expansion of I with temperature as the dependent variable. The experimentally measured intensity from an unknown flow field is converted to a temperature by first normalizing the observed intensity to a flame of known temperature such as a stoichiometric propane-air flat flame or pure-hydrogen diffusion flame and then employing the coefficients of the power series with the normalized intensity to determine a temperature.

Because of the nonlinear nature of the Planck equation, the observed filament emission is nonlinear. At the low temperature limit of the curve [Fig. 2(*b*)], the slope is very steep, indicating that a small change in the emittance corresponds to a very large change in the temperature. The experimental detection system, which will be discussed in more detail in a later section, has a dynamic range of 256 to 1. The lowest detectable signal is ~1000 K with the maximum temperature set at 2370 K. Because of the steep slope at low temperature, the precision of the measurement is ~80 K. In contrast, at the high-temperature limit, the change in temperature with intensity is small

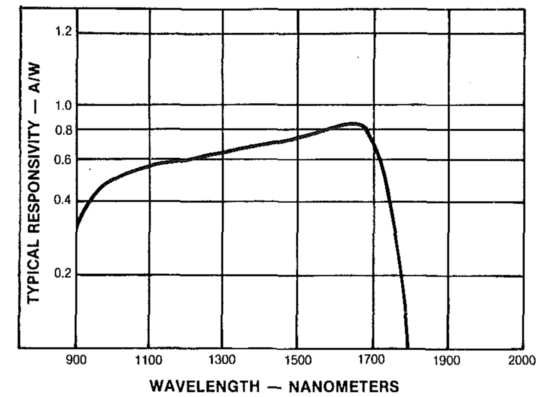

Fig. 2(*a*) **Spectral response of InGaAs detector (from "RCA Technical Publication for C-30980E InGaAs Photodiode")**

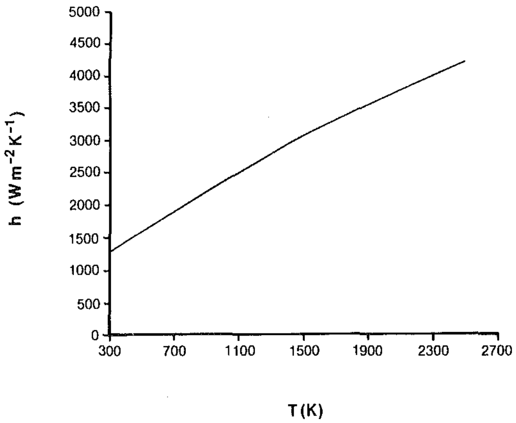

Fig. 3 **Heat transfer coefficient for SiC filament in 2-m/s H_2 flame**

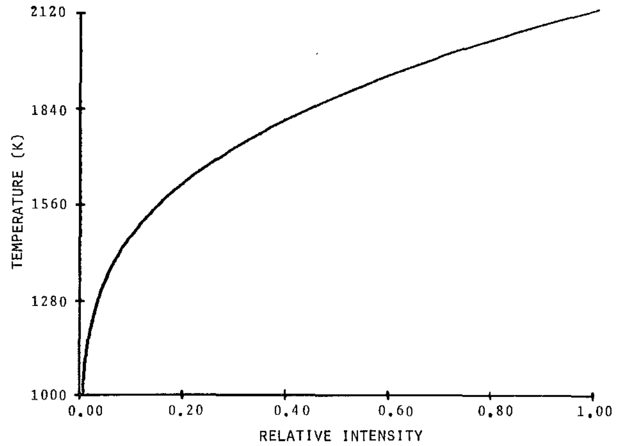

Fig. 2(*b*) **Relative filament emission as a function of temperature**

and the intensity itself is large; thus, the measured precision is improved to ~8 K. The high-temperature limit is determined by the survivability of the filament (~2400 K). The noise in the experimental system was determined to be ~1 percent of full scale.

Throughout the above discussion, it has been assumed that the filament temperature is the same as that of the surrounding gases. At high temperatures a correction to the filament temperature must be made in determining the gas temperature. The source and magnitude of this correction are discussed in the next section.

Thermal Properties of SiC Filament

The discussion on the thermal properties of the SiC filament is divided into four parts, which treat convective heat transfer properties, transient heat response, axial thermal conductivity, and heat-balance and radiation corrections.

Convective Heat Transfer Properties. The convective heat transfer coefficients of the SiC filament are determined from its Nusselt number. For the case of a small filament in a crossflow, the Nusselt number is given by

$$\mathrm{Nu} \equiv \frac{hD}{k} = c(\mathrm{Re})^n \tag{5}$$

where

$$\mathrm{Re} = \frac{vD}{\nu} \tag{6}$$

h is the heat transfer coefficient, D the filament diameter, k the thermal conductivity of the surrounding gases, v the velocity of the gases, ν the kinematic viscosity of the gases, and c and n fitted parameters based upon the Reynolds number

$$h = c(\mathrm{Re})^n \frac{k}{D} \tag{7}$$

Because of the small filament diameter (15 μm), the Reynolds number is small, varying from 0.03 to 1 for the experimental conditions reported in this paper. The generally accepted c and n quantities in this case are 0.80 and 0.280, respectively [5]. The heat transfer coefficient for a 1-m/s hydrogen diffusion flame is shown in Fig. 3, assuming H_2O and air to be the predominant constituents. The thermal conductivity and kinematic viscosity for the flame were taken from [6]. The heat-transfer coefficients are quite large, ranging from a low of ~1300 W m^{-2} K^{-1} to over 4000 W m^{-2} K^{-1}. The large coefficients are primarily due to the small diameter of the filament. Intuitively, because of the large h, the response of the filament to a heat transient should be quite fast.

Transient Heat Response. The response of the filament to a transient heat pulse is determined in a manner similar to that in the case of a small thermocouple. The net change in the internal energy of the filament must be equal to the net heat flow from the filament (neglecting the radiation-loss term), which is written as

$$-C\rho_f V dT = hA_s(T - T_\infty)d\theta \tag{8}$$

where C is the heat capacitance of the filament, ρ_f the density of the filament, V the volume of the filament, A_s the surface area of the filament, and $d\theta$ the change in time. Subject to the initial condition $T(0) = T_0$, equation (8) has the general solution

$$\frac{T - T_\infty}{T_0 - T_\infty} = \exp - \frac{hA_s}{C\rho_f V}\theta \tag{9}$$

The time constant of the filament is given by

$$\tau = \frac{C\rho_f V}{hA_s} \approx 1.59 \times 10^{-3}\ \mathrm{s} \tag{10}$$

for a gas temperature of 2370 K at a velocity of 1 m/s.

To confirm the calculation of the filament temporal response, the response was measured experimentally using a CO_2 laser to heat the filament for a short period of time. The emission of the filament was monitored with an InGaAs detector and recorded. A heat-up and cool-down cycle is shown in Fig. 4. This cycle was recorded under ambient conditions and, thus, represents a lower limit to the filament response time. The $1/e$ value taken from this curve corresponded to ~1.5 ms, in good agreement with the previous calculation. The filament response is ~700 Hz. As the velocity and tem-

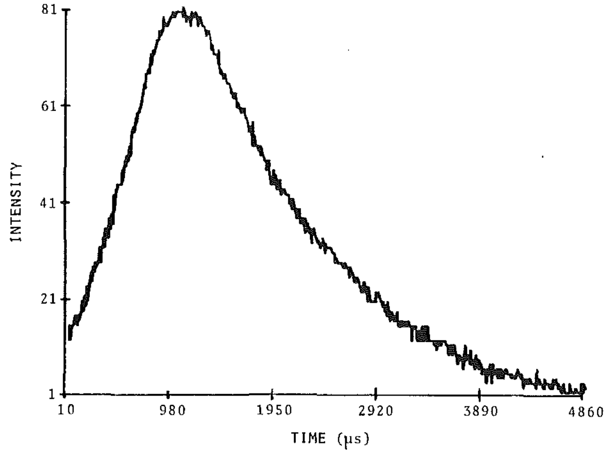

Fig. 4 **Response of SiC filament to CO_2 laser heat pulse**

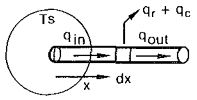

RATE OF HEAT FLOW BY CONDUCTION INTO ELEMENT AT x = RATE OF HEAT FLOW BY CONDUCTION OUT OF ELEMENT (x + dx) + RATE OF HEAT FLOW BY CONVECTION AND RADIATION OUT OF ELEMENT dx

Fig. 5(*a*) **Model for evaluation of axial thermal conductivity of SiC filament**

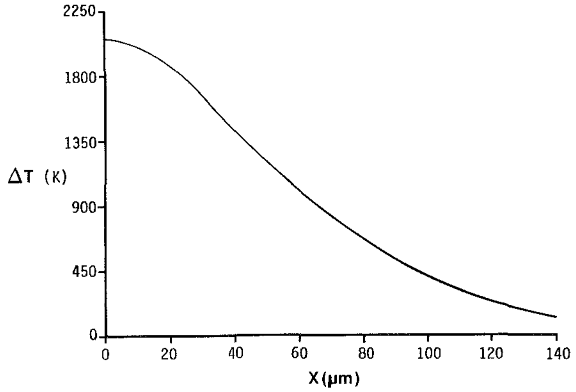

Fig. 5(*b*) **Axial temperature distribution for SiC filament against 2600 K surface**

perature increase, the filament response should improve because of increased heat transfer to the surroundings.

Axial Thermal Conductivity. One of the major advantages of the TFP technique is the ability to measure the temperature distribution along the length of the filament. For the measured temperature distribution to correspond to the real temperature distribution of the gas, the spatial flow of heat along the filament axis must be small. The axial heat flow is evaluated as shown in Fig. 5(*a*). Assuming that the filament is in contact with a flame surface at a temperature T_s, the rate of heat flow by conduction into the element x must be equal to the rate of heat flow out of the element $x + dx$ by conduction, convection, and radiation. Neglecting the radiation term, the heat-balance equation is given by

$$-kA_s\frac{dT}{dx} = -kA_s\frac{dT}{dx} + \frac{d}{dx}\left[-KA_s\frac{dT}{dx}\right]dx + hC_r\,dx\,(T - T_\infty) \quad (11)$$

where C_r is the circumference of the filament. Equation (11) reduces to

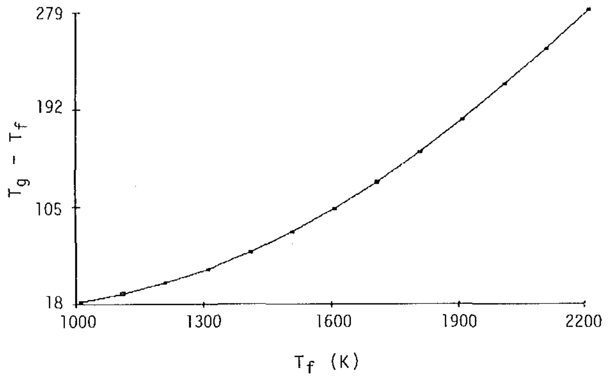

Fig. 6 **Radiation-loss term for 2-m/s H_2 flame: T_f = filament temperature; T_g = gas temperature**

$$\frac{d^2T}{d^2x} = m^2(T - T_\infty) \quad (12)$$

where

$$m = \sqrt{\frac{hC_r}{kA_s}} \quad (13)$$

Equation (12), when subject to the boundary conditions $T = T_0$ at $x = 0$ and $dT/dx = 0$ at $x = \ell$, has the general solution

$$\Delta T = \frac{\cosh m(l - x)}{\cosh ml}\Delta T_i \quad (14)$$

where l is the length of the filament, x the distance from the hot surface, $\Delta T = T - T_\infty$, and $\Delta T_i = T_0 - T_\infty$. Assuming that the initial temperature is 2370 K at the hot flame surface while the filament temperature is 300 K at its end, Fig. 5(*b*) displays the temperature distribution adjacent to the hot flame surface. Because of the low thermal conductivity and the large convective heat transfer at the filament surface, the temperature distribution is restricted to a small region near the hot surface. This thermal conduction along the filament axis is, thus, expected to have only a small effect upon the observed temperature distribution.

Heat Balance and Radiation Corrections. As stated in the theoretical section, the temperature of the filament can be different from that of the surrounding gas. This difference can be obtained from the full heat balance of the filament. The convective heat input from the surrounding gas must equal the radiative heat output due to the filament emission and the conductive heat output along the filament axis, which is written as

$$hA(T_g - T_f) = \sigma\epsilon AT_f^4 + kA\frac{dT}{dx} \quad (15)$$

Because the ratio of the circumferential to cross-sectional surface area is large, the axial heat transfer can be ignored, resulting in

$$hA_s(T_g - T_f) = \sigma\epsilon A_sT_f^4 \quad (16)$$

Rearranging and solving for the gas temperature yields

$$T_g \approx T_f + \frac{\sigma\epsilon T_f^4}{h} \quad (17)$$

The second term on the right-hand side of equation (17) is the correction factor, which relates the measured filament temperature to the surrounding gas temperature. For the experimental conditions reported in this paper, the correction term is plotted in Fig. 6. As the temperature increases the blackbody emission increases as T^4. The convective heat transfer increases only as T; thus, the correction term becomes large as the temperature increases. At 1000 K, the correction is small, ~20

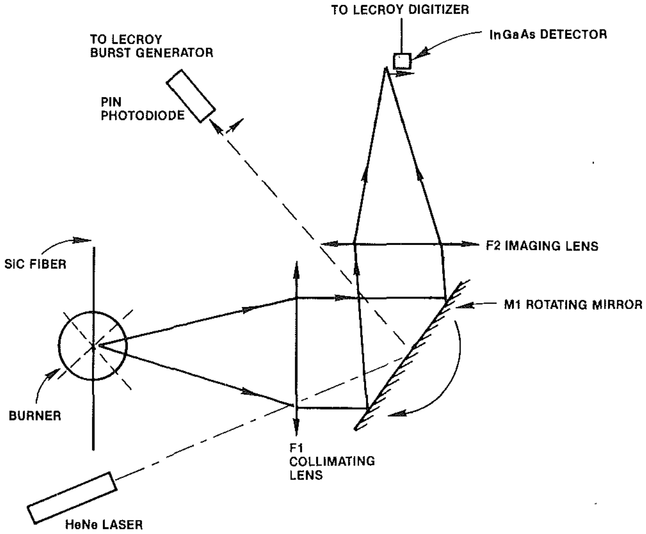

Fig. 7(*a*) Optical layout of filament-imaging system

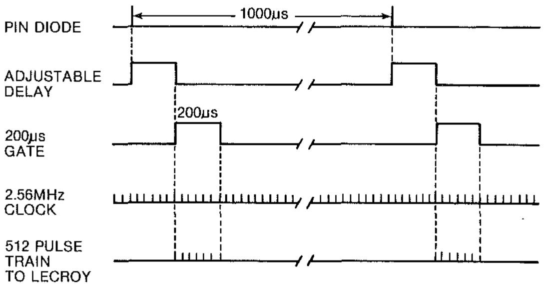

Fig. 7(*b*) Timing diagram of synchronizing and digitizing electronics for filament-imaging system

K; but at 2370 K it is ~276 K. The correction term (or radiation-loss term) is dependent upon the flow conditions and constituents as well as the temperature due to the heat transfer coefficient in the denominator. Thus, the correction term must be evaluated each time the flow conditions or fuel types are changed.

Experimental

The experimental arrangement for the TFP technique is displayed in Fig. 7. The system can be broken out into the optical and electronic subsystems, which will be discussed separately. The optical arrangement is shown in Fig. 7(*a*). The filament is suspended across the flame by a holder, which supplies just enough tension to keep the filament from sagging but not so much as to cause it to break at higher temperatures, where its tensile strength is reduced. The filament emission is collimated by lens fl (f/5, 10-cm-dia) and directed toward a spinning mirror assembly, which consists of a ten-facet wheel rotating at speeds up to 500 Hz. Because each of the ten facets of the wheel acts as an individual mirror (~2 cm^2 area), the effective scan speed of the wheel is ten times its rotating speed (up to 5000 Hz). The reflected radiation from the wheel is swept through a focusing lens f2 (f/2.5, 10-cm-dia) onto a single InGaAs detector (80-μm-dia), which is sensitive to radiation in the spectral bandwidth shown in Fig. 2(*a*). As the wheel rotates, the image of the filament is swept past the detector. The mirror-detector combination thus acts to convert a spatial scan into a temporal one. The combination of high-f-number lenses and the small-area rotating mirror increased the depth of field and field of view. To ensure that the response of the optical system was not angularly dependent, the filament and flame were traversed across the optical axis. No variation in signal was observed in the field of view of interest. The output from a HeNe laser is reflected off the rotating wheel onto a pin diode to produce a pulse that can be used to synchronize the scanning and the digitizing electronics.

A timing diagram of the digitizing electronics is shown in Fig. 7(*b*). The output signal from the InGaAs detector is amplified and fed into a LeCroy TR8818 Transient Recorder. The synchronization pulse from the pin diode is delayed as needed and used to open a 200-μs gate centered on the sweep of the filament image. The delay from the synchronizing pulse allows the image signal to be moved inside the gate for optimum placement. This gate is used in conjunction with a pulse generator to send 512 pulses to the LeCroy digitizer. At the leading edge of each of these pulses, the signal from the InGaAs detector is digitized and stored in the MM8103 ECL Memory Unit. The rate of digitization during the 200-μs gate is 2.56 MHz. The digitization sequence continues with subsequent scans until the memory is completely filled. The data are then transferred through a custom-built interface to a ModComp 7870 Classic Minicomputer for analysis. The digitization rate and gate pulse width are set for a 1000-Hz sweep rate of the filament image. A 6-cm length along the filament is recorded in the 512 discrete samples, translating into an effective spatial resolution of 120 μm per sample point.

The advantages of using a rotating mirror in association with a single detector rather than a scanning array of detectors include the increased flexibility and lower cost of the system. Since a single detector is employed, detectors that are not presently available in array form, i.e., the InGaAs detector, can be used. This is also important for future work where the temperature range will possibly be extended by use of IR detectors.

Analysis of the digitized data consists of unpacking the 8-bit data from the LeCroy into 16-bit data for the ModComp; ratioing the measured intensity to a calibrated intensity at a known temperature; converting the ratioed intensity to temperature employing the fitted, calculated curve shown in Fig. 2(*b*); and correcting the filament temperature for radiation losses. The reduced data can then be plotted either multidimensionally or as contours, as demonstrated in the Results Section. The calibrated intensity usually is determined by measuring a H_2 diffusion flame and noting the maximum intensity corresponding to a temperature of 2382 K.

The LeCroy TR8818 Transient Recorder is a high-speed 8-bit system having a dynamic range of 256 of 1. Experimentally, the filament emission from the flame was surveyed to determine the area of maximum temperature. The signal from this region was then adjusted to the maximum allowed by the digitizer in order to take full advantage of the limited dynamic range. As a result of this limited range and the wavelength response of the InGaAs detector, temperatures below 1000 K are not detected. A wider temperature range is possible by employing IR detectors, but care must be taken to minimize the interference from the hot flame gases in the IR region.

Results and Discussion

Recent studies on the structure of jet diffusion flames have demonstrated the presence of large-scale buoyancy-driven structures (bulges) at relatively low Reynolds numbers [7, 8]. These structures can expand to several jet diameters in width and display an 8–20 Hz repetition. Laser-sheet-lighting visualization techniques, in conjunction with high-speed photography, have added greatly to the understanding of the dynamics of these flames [8]. Temperature measurements in these flames have been made traditionally with thermocouples and, more recently, by means of the CARS technique [9]. In both cases it is complicated to interpret point temperature measurements due to the dynamic nature of these flames. A wealth of in-

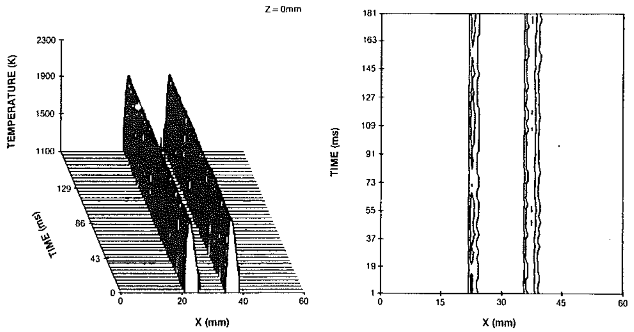

Fig. 8 Imaging scans of SiC filament in H_2-N_2 jet diffusion flame at axial location 0 mm above nozzle exit

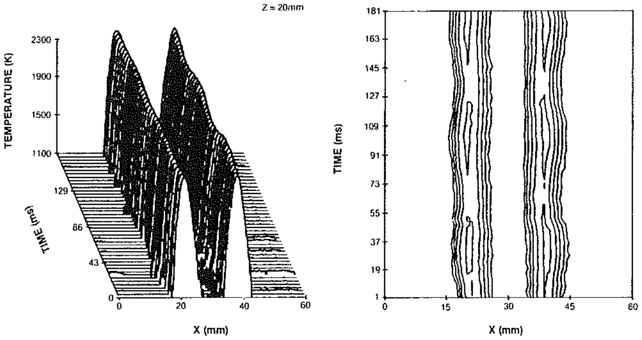

Fig. 9 Imaging scans of SiC filament in H_2-N_2 jet diffusion flame at axial location 20 mm above nozzle exit

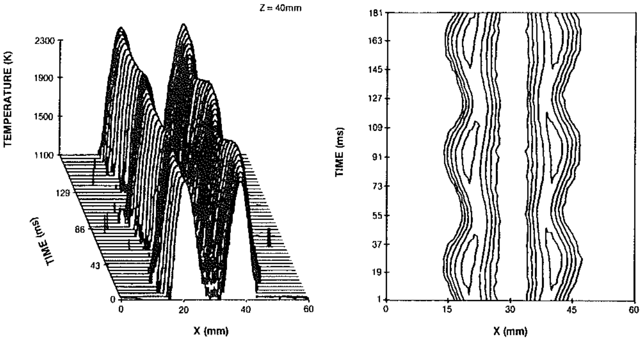

Fig. 10 Imaging scans of SiC filament in H_2-N_2 jet diffusion flame at axial location 40 mm above nozzle exit

formation concerning the temperature field dynamics, however, can be obtained using the TFP technique. Because the temperature measurement is made along the width of the flame and because the filament response is much higher than the variation in the flame, the temporal and spatial temperature field dynamics can be studied.

To demonstrate this point, a H_2-N_2 jet diffusion flame was chosen for study. This flame is ideal for study by the TFP technique due to the dynamics discussed above and the lack of sooting, the emission from which could interfere with the filament emission. The burner consists of a 1-cm contoured jet surrounded by a coannular air jet. The contour of the fuel jet was constructed in such a way as to yield a flat-top velocity profile. The coannular jet is ~25 cm in diameter and is characterized by a low-turbulence flat velocity field ~5 cm/s. The H_2 and N_2 were mixed in the ratio of 8 to 1 by volume and had an exit velocity of ~3 m/s. The adiabatic flame temperature for such a mixture is calculated to be 2320 K. The filament was suspended along the central axis of the axisymmetrical jet flame, and the flame was translated up or down to obtain radial profiles at several axial locations. The filament emission was scanned at the rate of 1000 Hz with a spatial resolution of ~120 μm. The emission was recorded and converted to temperatures, as explained earlier. The temperature data at several axial locations of the jet diffusion flame are shown in Figs. 8-13. The reader should keep in mind that the displayed temperature fields represent the movement of the flame structure past a single axial location as a function of time. The y axis in the plots is time—not space (as in a photograph of the flame).

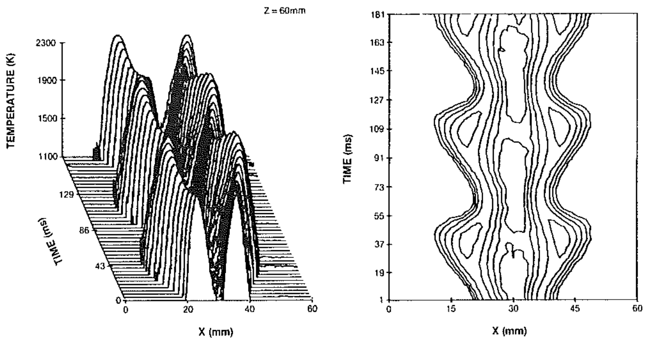

Fig. 11 Imaging scans of SiC filament in H_2-N_2 jet diffusion flame at axial location 60 mm above nozzle exit

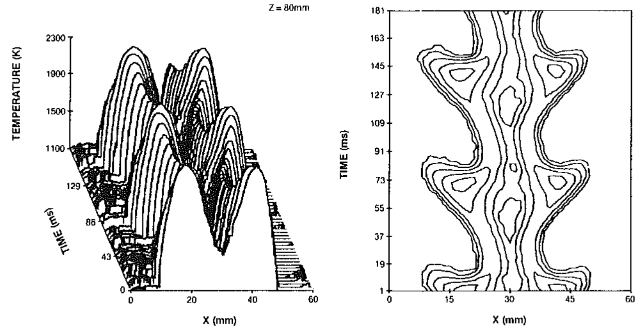

Fig. 12 Imaging scans of SiC filament in H_2-N_2 jet diffusion flame at axial location 80 mm above nozzle exit

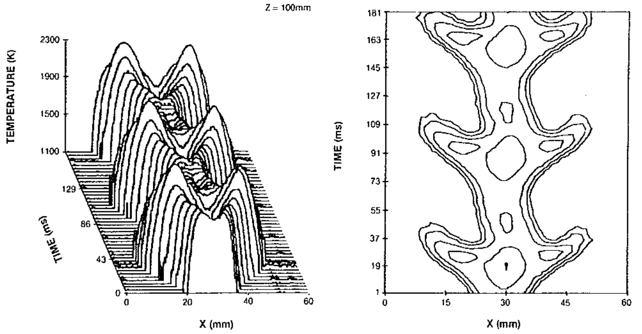

Fig. 13 Imaging scans of SiC filament in H_2-N_2 jet diffusion flame at axial location 100 mm above nozzle exit

The evolution of the large-scale buoyancy-driven structures can be traced from these plots. Near the nozzle exit (Fig. 8), the fuel jet is surrounded by a hot reacting cone, which results from the combustion of fuel and coflowing air. The flame structure is well defined and displays little indication of low-frequency oscillations or flicker. The temperature is below the adiabatic calculated temperature due to heat loss to the nozzle and the small size of the reaction zone.

At the 20-mm axial location (Fig. 9), the flame temperature is very near the calculated adiabatic temperature. The flame has increased in size radially, and the hot temperature zones have increased in size. The increase in hot-zone size is probably due to the high diffusivity of the H_2 molecule and the extremely broad flammability limits. This width has been confirmed by

CARS measurements [10]. Notice at this location that a low-frequency oscillation of the outer flame boundary is occurring. This is the initial development of the large-scale buoyancy-driven structures. At the 40-mm axial location (Fig. 10), the jet has radially expanded further and the flame oscillation has increased markedly in amplitude. Notice that while the outer boundary oscillations are distinct, the inner flame boundary (between the hot temperature zone and the cold jet) exhibits only a small hint of oscillation. The flame or hot zone is acting to dampen the buoyancy-induced oscillations due to the high viscosity of this zone.

At the 60-mm axial location (Fig. 11), the jet flame has more than doubled its width and the oscillations that were nearly sinusoidal at the 40-mm location are now much more complex, having taken on a bell-like shape. The unburnt jet fuel is still present at this height.

At 80 mm (Fig. 12), the expansion of the flame continues, with the bulges showing signs of possibly wrapping and entraining the outside air. Sheet-light studies of this flame at this location indicate that associated with this bulging is a vortex structure in the surrounding air. The vortex tends to grow with the flame bulge and acts to entrain air into the flame. The interplay between the bulge and the coexisting vortex structure is responsible for the flame characteristics observed in these studies.

At the 100-mm axial location (Fig. 13), the temperature field shows the continued evolution of the flame bulge, which strongly displays the massive air entrainment. The flame is three times its original size at the 0-mm location. The cold central jet, which was visible through the 60-mm location, has undergone periodic combustion with the entrained air, coincident with the periodic entrainment of air into the central jet by the outside vortex, as can be seen from the oscillation of temperature in the central part of the jet. Above the 100-mm location, the surrounding coflowing-air jet field has decayed to the point where room disturbance is beginning to affect the flame structure. Thus, higher profiles were not attempted. The start and continued evolution of low-frequency buoyancy-driven structures are clearly evident from the temperature fields measured by the TFP technique. The temporal as well as spatial dynamics of the changing structure are captured by the rotating-mirror imaging system. This technique, in conjunction with laser-sheet-lighting techniques, should greatly enhance the understanding of the dynamics of jet diffusion flames. The advantages of the technique outweigh the disadvantages of restricted temperature range, limitation to low-sooting flames, and limited upper response of ~1000 Hz.

Conclusions

In conclusion, a novel thermometric technique (TFP) has been demonstrated to be capable of measuring the temporal-spatial temperature distributions in nonsooting flames. The technique is characterized by its high spatial resolution of ~200 μm, its fast temporal response of ~1000 Hz, and its ability to measure the radial temperature distribution along a line rather than just at a point. An examination of the thermal properties of the SiC filament employed for the technique indicates that it displays little axial heat conduction but requires that a radiation correction be made at high temperatures. Studies on a H_2–N_2 jet diffusion flame indicate that the evolution of the large-scale buoyancy-driven structures associated with this flame can be studied. Future efforts will be concentrated on combining this technique with dynamic visualization techniques to obtain a more detailed picture of the dynamics of jet diffusion flames.

Acknowledgments

This work was performed under USAF Contract No. F33615-85-C-2562. The authors wish to thank Dr. L. D. Chen for supplying the adiabatic flame calculations, Dr. W. M. Roquemore for encouragement and support, and Dr. R. S. Tankin for discussions on the thermal properties of the filament.

References

1 So, R. M. C., Whitelaw, J. H., and Lapp, M., eds., *Measurements and Techniques in Turbulent Reactive and Non-Reactive Flows*, ASME, New York, 1984, and reference therein.

2 Dow Corning Corporation, Nippon Carbon Company, Ltd., Midland, MI 48686-0994.

3 Ferguson, C. R., and Keck, J. C., "Hot-Wire Pyrometry," *J. Appl. Phys.*, Vol. 49, No. 3031, 1978.

4 "Properties of Silicon Carbide," in: *Thermophysical Properties of High Temperature Solid Materials, Vol. 5—Nonoxides and Their Solutions and Mixtures Including Miscellaneous Ceramic Materials*, Y. S. Touloukian, ed., MacMillan Co., New York, 1967, pp. 118–140.

5 Morgan, V. T., "The Overall Convective Heat Transfer from Circular Cylinder," in: *Advances in Heat Transfer*, T. F. Irvine, Jr., and J. P. Harnett, eds., Academic Press, New York, 1975, Vol. 11, p. 234.

6 Kreith, F., *Principles of Heat Transfer*, 3rd ed., Harper and Row, New York, 1973.

7 Chen, L. D., and Roquemore, W. M., "Visualization of Jet Flames," *Comb. Flame*, Vol. 66, No. 81, 1986.

8 Chen, L. D., and Roquemore, W. M., "Two Dimensional Visualization and Single Point Frequency of Low Reynolds Number Jet Flames," in: *ICALEO '86, Arlington, VA, Vol. 85—Flow and Particle Diagnostics*, Laser Institute of America, Toledo, OH, 1986, pp. 16–23.

9 Roquemore, W. M., Goss, L. P., Lynn, W. F., and Chen, L. D., "Structure of Jet Diffusion Flames," presented at the 1987 Spring Technical Meeting of the Central States Section of the Combustion Institute, May 11, 1987, Argonne, IL.

10 Systems Research Laboratories, Inc., "Combustion Diagnostic Development and Application," SRL R&D Status Report 6890-5 under Contract No. F33615-85-C-2562 covering the period 17 Sept.–16 Dec. 1986, Dayton, OH, 1987.

J. B. McVey

J. B. Kennedy

S. Russell

United Technologies Research Center,
East Hartford, CT 06108

Application of Advanced Diagnostics to Airblast Injector Flows

Experimental data on the characteristics of the spray produced by a gas turbine engine airblast fuel injector are reported. The data acquired include the mass-flux distribution, measured by use of a high-resolution spray patternator; the gas-phase velocity field, measured by use of a two-component laser-Doppler velocimeter; and the liquid droplet size and velocity distributions, measured by use of a single-component phase-Doppler anemometer. The data are intended for use in assessments of two-phase flow computational methods as applied to combustor design procedures.

Introduction

The achievement of a predictable and satisfactory distribution of finely atomized fuel is of importance to the design of well-performing gas turbine engine combustion chambers. The development of nonintrusive laser diagnostics offers the possibility of acquiring detailed point-resolved data on the gas and liquid-phase flow fields and on the droplet size distribution produced by fuel injectors. The availability of such data will aid in the identification of analytic design procedures appropriate to the specification of injector/burner configurations (number of injectors, primary combustion air entrance port location, etc.), and specification of injector/swirler design details (swirler vane angle, filmer diameter, etc.). These analytic design procedures will be based on computational fluid mechanic analyses capable of treating two- and three-dimensional, two-phase, turbulent, reacting flows. Numerous computer codes are under development for this application. The sophistication required for the treatment of the two-phase flow processes will have a major influence on the complexity of the analysis required and, therefore, on the extent of labor and computer resources needed to exercise the design procedures. The objective of this study is to provide experimental data on the behavior of an injector/swirler-produced flow under conditions that more closely approximate those in an engine combustor than do currently available data. These data will be useful in the evaluation of various analytical treatments of the fuel injection process.

For this task, it was required that point-resolved (spatially precise) information on the flow characteristics of both the gas phase and liquid phase be obtained in a representative spray. Work reported to date in this area includes: (1) efforts carried out in order to prove the capability of new instrumentation techniques; (2) efforts to examine simplified, idealized flows under tightly controlled conditions in order to provide benchmark data for the assessment of the physical models to be employed in computational procedures; and (3) efforts to document the behavior of fuel injectors. A summary of recent work is given in Table 1.

The current study is directed at gathering information on the operation of a large-scale airblast nozzle under isothermal conditions in which a strong interaction of a swirling airstream with a liquid spray occurs; the intent is to simulate closely the flow behavior in a combustor. The conditions are more demanding than those of previous studies relative to the capabilities of the instrumentation; of particular impact was the combination of high liquid flow rate, high flow velocity, and high swirl. The approach was to apply three instrumentation techniques that are employed in our laboratory for the characterization of fuel sprays: a high-resolution patternator for establishing the spray mass flux distribution; a two-component laser-Doppler velocimeter (LDV) for documenting the three components of gas flow velocity produced by the injector swirlers in the absence of the spray; and a single-component phase-Doppler particle analyzer (PDA) for obtaining information on the spatial distribution of mean droplet size and the axial component of velocity of both phases.

The information on the behavior of sprays under these conditions should provide a basis for determining which of the processes must be included in analyses in order to generate an adequate description of fuel distribution in engine combustors. The major effect to be considered is, of course, the relative motion between the two phases and the effect of the resulting particle drag on the spray trajectory. Higher-order effects currently under study include: the influence of the gas-phase turbulence on the trajectory of the droplets (Gosman and Ioannedes, 1983); the suppression of the gas-phase turbulence by the droplets (Elghobashi, 1984); droplet-droplet interactions, which can result in coalescence or droplet breakup (Asheim et al., 1987; Ashgriz and Givi, 1987); and the modification of the droplet drag laws due to the influence of neighboring

---

Contributed by the International Gas Turbine Institute and presented at the 33rd International Gas Turbine and Aeroengine Congress and Exhibition, Amsterdam, The Netherlands, June 5–9, 1988. Manuscript received by the International Gas Turbine Institute December 15, 1987. Paper No. 88-GT-12.

Table 1 Two-phase flow investigations employing laser diagnostics

Flow Configuration	Characteristic Velocity (mps)	Swirl	Second Phase	Flow Rate (kg/hr)	Particle Size (Microns)	Loading Ratio	Investigator
Jet	10	None	Glass Beads	10	50,200	0.3-1	Modarress et al (1982, 1983) Modarress and Tan (1983)
Jet	30	None	Sand	12(1)	80,120,200	0.2-0.7	Shuen et al (1983, 1984)
Jet	5	None	Glass Beads	10(1)	100	0.2-1	Mostafa et al (1987)
Jet	15	S=.16, .3	Glass Beads	4(1)	40	0.2	Bulzan et al (1987)
Airblast Injector	150, 40	None	Oil	5	20-200	2-7	Solomon et al (1983, 1984a, 1984b)
Pressure Atomizer	8(2)	None(2)	Water	132	35-350	N/A(2)	Bachalo et al (1987)
Pressure Atomizer	30	None	Water	11.4	30-150	N/R	Rudoff et al (1987)
Hybrid Atomizer	15	Yes	Water	64	150-700	N/R	Kraemer and Bachalo (1986)
Air Assist Nozzle	N/R	Yes	Water	3.2	10-80	0.7	Jackson and Samuelsen (1986)
Air Assist Nozzle	12	Yes	JP-4	3.3	10-50	0.7	McDonnell et al (1986, 1987)
Airblast	100	None	Water	20	20-120	N/R	Wang et al (1987)

N/R - Not reported
N/A - Not applicable
S - Swirl number
(1) - Estimated based on characteristic dimension, velocity, and loading or mass flow
(2) - No significant airflow, velocity is that of the liquid phase
Loading Ratio = Ratio of mass flow of injectant to mass flow of air

droplets (Soo, 1967). The various methods of analysis have been thoroughly reviewed in the literature (e.g., Faeth, 1983).

Test Apparatus and Instrumentation

Fuel Nozzle. An airblast fuel nozzle (Fig. 1) was employed in this study. This atomizer concept is well established (Lefebvre, 1983) and is employed in current high-thrust gas turbine engines. Fuel is supplied at low pressure to a filming surface where the shearing action of a high velocity swirling the airstream acts to atomize the fuel. This nozzle is sized as a 375 kg/h unit.

The configuration embodies inner and outer clockwise (when viewed from the upstream direction) air swirlers. The final turning angle of the 16 helical vanes of the outer swirler is 40 deg. This swirling flow is turned radially inward by the end cap, which imparts a radial-inflow velocity component resulting in a further increase in swirl angle. The flow discharges through a 4-mm gap at a mean angle of 62.5 deg relative to the injector axis. The 14-vane inner swirler employs straight vanes with a turning angle of 45 deg. The resulting annular swirling flow is contracted to a smaller diameter turbular flow, thereby increasing the gas rotational velocity.

The fuel is distributed through an annular channel having a 20-mm gap height. Within this gap is located a blockage ring containing six 7.6-mm-wide slots, which swirl the flow at an angle of 55 deg in the clockwise direction. The fuel supply pressure in this type of nozzle is very low [1.4×10^5 Pa (20 psi) at the test condition used] and serves primarily to distribute the fuel uniformly throughout the annular gap. At the discharge end, the swirling flow is turned radially inward and is discharged through a slightly converging passage (1.0 mm exit gap) having a mean angle of 52.5 deg relative to the injector axis.

The particular combination of components employed was selected in order to produce a spray with a high degree of circumferential uniformity, a representative radial mass flow distribution, and satisfactory atomization. The sensitivity of airblast injector spray uniformity to nozzle component configurations has been reported previously (Rosfjord and Russell, 1987).

Installation. All testing was conducted under unconfined, atmospheric pressure conditions using ambient temperature air. Water was used as the injectant for all tests.

For the patternator tests, the injector was mounted with the flow axis vertical. For the LDV and PDA measurements, the flow axis was horizontal. Patternation tests conducted previously have determined that, under the high flow conditions employed in these tests, the spray characteristics are insensitive to gravitational effects.

For the LDV and PDA tests, the injector was mounted in a fixturing device, which acted as a plenum for the seeded air supply and which also permitted the injector to be rotated about its centerline. This fixture was rigidly attached to the air supply centerline, which was adjacent to and aligned with an optical table on which all the optical instrumentation was mounted (Fig. 2). The air flowing through the injector swirler discharged into the ambient surroundings. At a location approximately 150 cm downstream of the injector, a 46-cm-dia duct, which was under a slight negative pressure produced by the ejector action of a water spray, captured the seeded airflow. The ejector-induced flow velocity on the axis of the test region at the farthest downstream measurement station was less than 1 m/s.

A diagram showing the measurement axes and the definitions of the velocity vectors is given in Fig. 3. Note that in this figure, the flow is viewed from the downstream direction, and hence, the sense of rotation of the flow is counterclockwise.

Spray Patternator. A high-resolution spray patternator

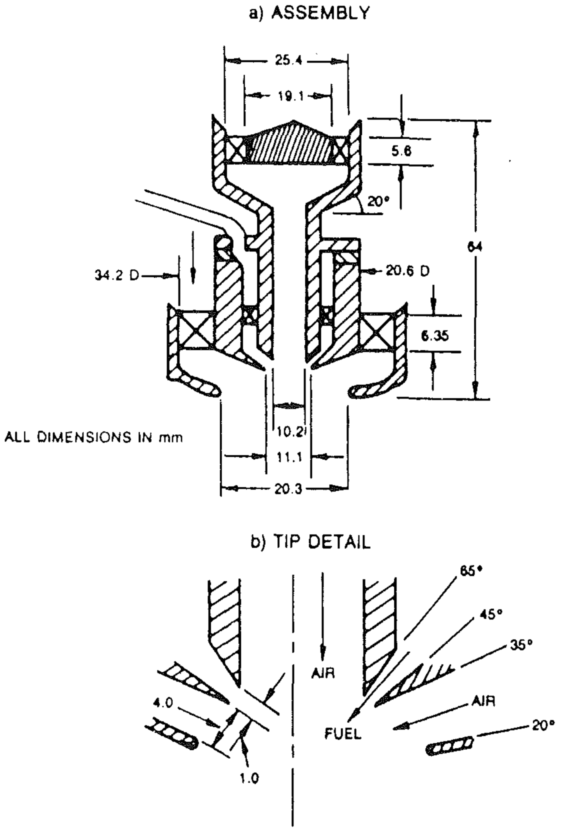

Fig. 1 Airblast fuel nozzle

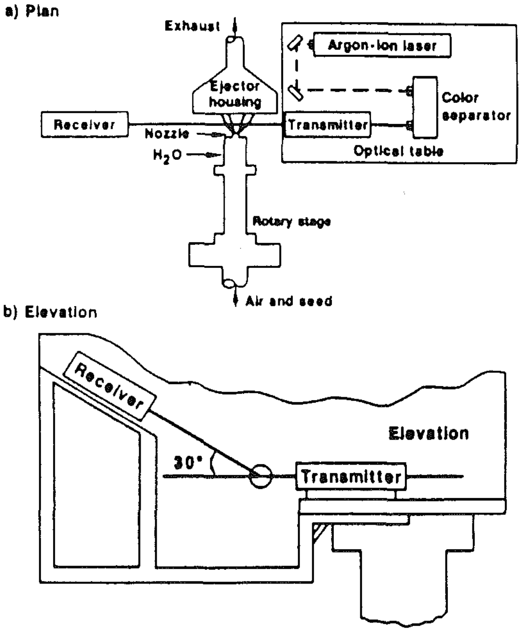

Fig. 2 Laser diagnostics—general arrangement

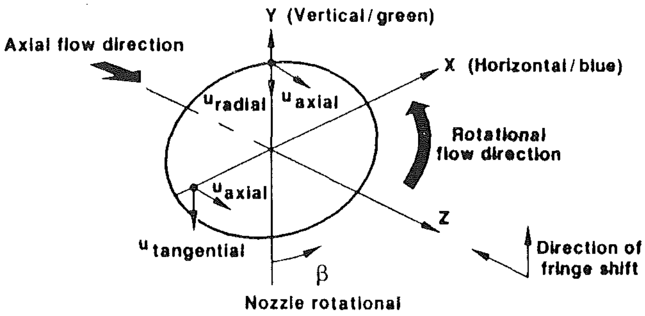

Fig. 3 Coordinate and velocity component definition

(McVey et al., 1987) was used to establish the circumferential uniformity of the fuel spray. The patternator employs extractive probing by use of multiple-point rakes to acquire data on spray mass flux distributions under ambient pressure conditions. Sixty sampling probes with squared, chamfered entrance sections are arranged in linear arrays of ten units each radiating from the patternator axis. The probes are fixed in space while the fuel nozzle fixturing enclosure is positioned azimuthally using a precision rotation stage. For the experiments conducted in this program, a 5-deg angular increment was employed such that 720 data points were used to construct each mass flux distribution contour map. The reported values are the flux values through a plane surface normal to the injector axis (not through a spherical surface).

A Malvern ST1800 Particle Analyzer (Swithenbank et al., 1976; Barth, 1984) was used in conjunction with the patternator. This instrument analyzes the distribution of the intensity of light scattered from a laser beam passing through the entire fuel spray to produce path-averaged SMD values.

Laser Velocimeter. The velocimeter employed was a standard configuration TSI Model 9100-7 two-component system. An argon-ion laser operating at a power output of 2 W was used; frequency shifting by Bragg cells located in both the blue and green incident beams provided the capability for resolving negative velocities. The condition of coincidence between signals detected by the two channels was not imposed; turbulence cross-correlation data were not obtained. The data acquisition mode was effectively a constant time interval mode; no corrections for velocity biasing was used. The seed material used was titanium dioxide having a nominal size of 1 μm. The external flow was not seeded. Standard fluidized bed seeding techniques were used with the seed being introduced far upstream of the test section.

To enable location of the probe volume close to the nozzle in order to provide exit-plane data, a small beam convergence angle in the horizontal beam pair was employed. This resulted in elongation of the probe volume. As a consequence, off-axis collection was required to achieve the desired spatial resolution. A forward-scatter, 30-deg off-axis system with the collection optics rigidly mounted to the velocimeter platform was employed as shown in Fig. 2.

In order to permit the interpretation of the vertical component of velocity as the tangential or as the radial velocity component, it is necessary to establish a reference axis for the flow. In a perfectly axisymmetric flow, the reference axis is the axis of symmetry. In a nearly axisymmetric flow, the axis could be either the geometric axis of the test article or an "aerodynamic center." (The aerodynamic center can be described by the location where the vertical component of velocity vanishes, or the location about which the velocity varies in a symmetric manner.) Space for these tests, the geometric center, based on measurements using fixtures inserted into the core flow passage of the nozzle, was used.

Details concerning the apparatus and techniques employed are given by McVey et al. (1988).

Phase/Doppler Particle Analyzer. A phase/Doppler particle analyzer (PDA) produced by Aerometrics, Inc. was used to obtain spatially resolved information on particle size and velocity (Bachalo et al., 1979; Bachalo and Houser, 1984). The instrument is similar to a laser velocimeter: Crossing laser beams are used to define a probe volume in which interference fringes cause Doppler signals to be generated by moving droplets. Three detectors are employed, using phase differences between signals produced by light refracted from transparent droplets to determine the droplet size. This phase difference is a function of the index of refraction of the liquid phase, the viewing angle, and the characteristics of the incident beams. It is assumed that the droplets are spherical. The instrument was configured to capture forward-scattered light, 30 deg off-axis (Fig. 2). The instrument employed a single data channel; the transmitting optics were oriented in all tests such that the axial component of velocity was detected. Frequency shifting by means of a rotating diffraction grating was available such that negative velocities could be resolved. The 488-mm beam produced by an argon-ion laser operating at a power output of 1 W was used.

The (PDA) instrument provides correlated velocity/size data and therefore can provide a measure of the gas velocity as well as the spray velocity. Two horizontal traverses were conducted at each measurement station. The first traverse, with processor settings optimized to capture the entire range of velocities and particle sizes present, provided information on the droplet spray characteristics. The second traverse, with the instrument configured to obtain detailed information on the smallest particles, provided information on the gas-phase velocity in the presence of the spray. In this case, the velocity size histograms of the small particles were interrogated to determine that the behavior of the velocity smallest particles was regular. That being the case, the data were extrapolated to zero size to yield a value of the gas-phase velocity. Generally, the velocities of the smallest particles (less than 5 μm) varied only weakly with size and this extrapolation could be performed by inspection.

For these tests, the external flow was seeded using a piezoelectric nebulizer; the internal flow was unseeded. See McVey et al. (1987) for further details regarding techniques and instrumentation.

Test Conditions

The objective of this program was to obtain information on the behavior of sprays under engine conditions. Tests were conducted, however, at ambient pressure conditions to avoid the expense of high-pressure testing. It is not possible, however, to preserve simultaneously all of the significant parameters corresponding to engine operation when scaling from high pressure to ambient pressure. The procedure employed was to select the air-side pressure drop so as to produce that air velocity that is generated by the swirler at the selected engine operating condition. The injectant flow is then chosen to preserve the liquid-to-gas momentum ratio. The parameter that is not preserved is the injectant flow rate. As a result, the velocity of the injectant at the discharge plane is lower during testing than during actual engine operation. Also, the loading ratio is lower. TEACH-based calculations have shown that the effect of the initial particle velocity on the spray distribution is small at these conditions. The effect of the loading has not yet been determined.

The conditions selected for this program, which correspond to engine cruise operation, are shown in Table 2. The characteristic velocity is the ideal gas velocity achieved by virtue of the swirler pressure drop. The combination of high velocity and high injection flow rate make performance of the two-phase flow measurements particularly challenging.

Results

The axial stations at which data were obtained by use of the three different instruments are given in Table 3.

Table 2 Test conditions

Injectant flow rate	71.4 kg/h
Swirler pressure drop	70 mm Hg
Loading ratio	0.7
Droplet size range	10-300 μm
Characteristic velocity	125 m/s

Table 3 Test matrix

Station, cm	Patternation	Velocimetry	Phase Doppler
0.114		X	
1.27		X	
2.54	X	X	X
3.81	X	X	X
5.08	X	X	X
6.35	X		
7.62		X	
10.16		X	X

Table 4 Patternator results

Measurement station, cm	2.54	3.81	5.08	6.35
Patternation index	5.5	6.2	7.4	6.7
Spray angle, deg	85	75	69	64
Collection efficiency	1.06	1.06	1.03	0.96
SMD, μm	76	70	63	57

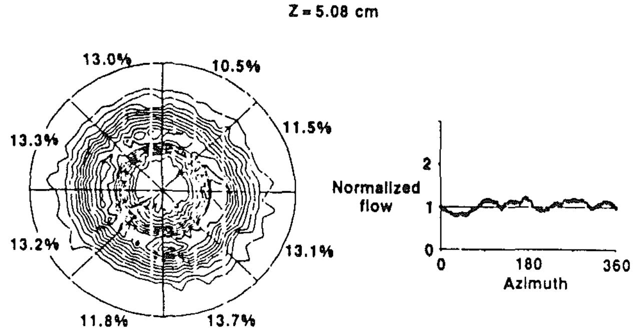

Fig. 4 Spray patternator results

Spray Patternation Data. The results of the spray patternation tests are illustrated by contour plots; data obtained at the 5.08 cm measurement station are shown in Fig. 4. The mass flow in each of eight, 45-deg sectors can be used to calculate the value of the patternation index. (The patternation index is the sum of the absolute differences between the measured flow and the flow produced by ideal nozzle in each of eight pie-shaped sectors; see McVey et al., 1987.) The value of 7.4 obtained at this measurement station is indicative of a highly circumferentially uniform spray. Of course, a perfect nozzle would exhibit circular contours and a patternation index of 0. Values of this parameter and other measured parameters at the four measurement stations are given in Table 4.

A spray angle equal to the included angle of a cone that intercepts both the nozzle filmer lip and the circle encompassing 90 percent of the spray mass flux at the measurement station is given in Table 4. This spray angle varied with axial distance in a manner characteristic of a bell-shaped envelope.

The SMD values reported in Table 4 were measured using the Malvern instrument, and ranged from 76 to 57 μm. The interpretation of the characteristic droplet size obtained using this instrument vis-à-vis point-resolved measurements has been discussed by Dodge (1987).

The collection efficiency of the patternation system varied from 1.06 to 0.96. This value is the ratio of the integrated flow rate to the metered flow rate. The values shown are larger than the range of 0.8 to 0.85 generally obtained (McVey et al., 1987) in this apparatus for Jet-A (not water) sprays probably because the larger droplets reduce losses due to evaporation or to carryover resulting from nonisokinetic conditions.

The radial distribution of mass flux obtained at the four patternator measurement stations is given in Fig. 5. Each plotted data point represents the mean of 72 data points acquired at each of the ten sampling probe radii. The hollow cone nature of the spray is evident.

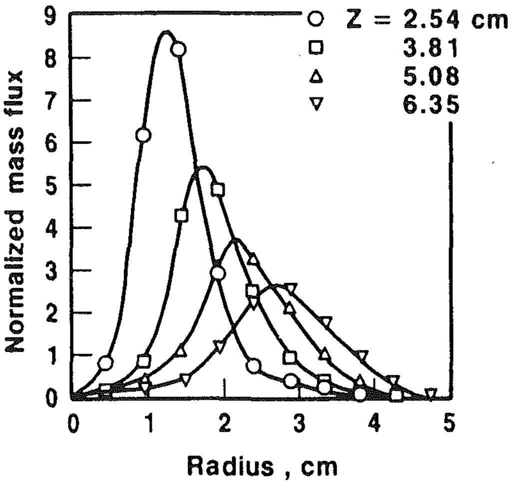

Fig. 5 Radial mass flux distribution

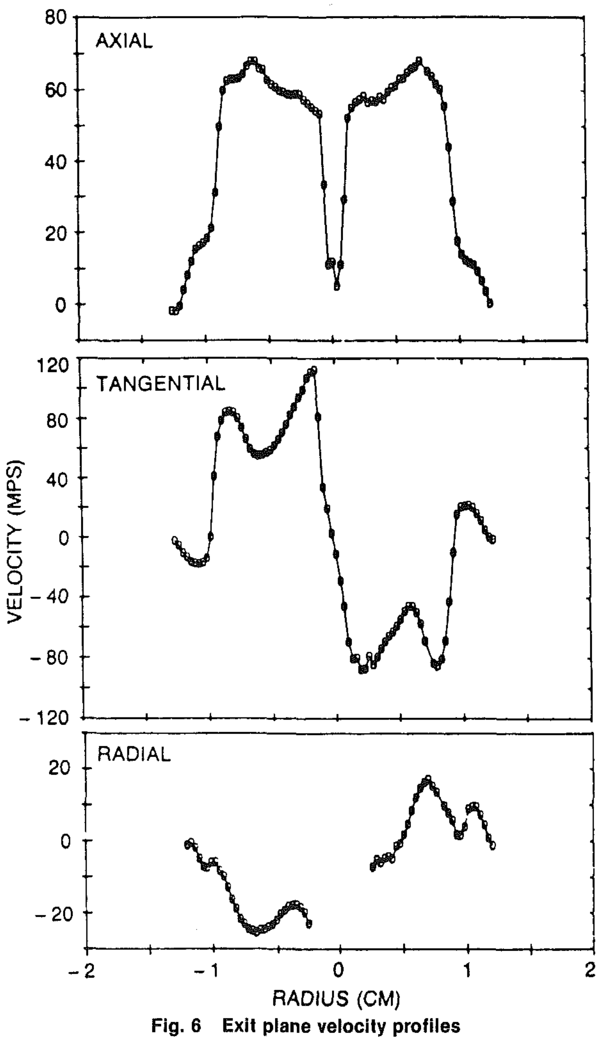

Fig. 6 Exit plane velocity profiles

Laser Velocimeter Data. Velocity profiles of the gas in the absence of the spray at the most upstream measurement station ($Z = 0.114$ cm) are shown in Fig. 6. The existence of a central vortex core region of low velocity is evident from examination of the axial velocity profile. The centrifugal force field established in the central vortex was of such strength that the micron-sized titanium dioxide seed particles were totally centrifuged from this region. In order to obtain information on the nature of the velocity profile in this region, the swirler pressure differential was reduced until the seeding particles were not totally centrifuged. The profiles in this region were found to have a very distinct shoulder that was always located at $r = \pm 0.1$ cm; the velocity profiles measured at the reduced pressure drop (4.67 mm Hg) were multiplied by the ratio of these shoulder velocities to scale the data to the baseline pressure differential level.

The diameter of the high axial flow velocity region (above 60 m/s) is 1.7 cm compared to the end cap diameter of 2.0 cm. This slight convergence of the flow area in the upstream region is consistent with visual observations of the envelope of the fuel spray produced by the type of injector.

The mass flow calculated by integration of the axial velocity distribution is 0.025 kg/s; this value is about 80 percent of the flow delivered to the plenum enclosing the injector in the patternation tests. This 80 percent figure is reasonable, since no attempt was made to seal that plenum fully (the test conditions are set by establishing the swirler pressure differential, not the mass flow).

The measured tangential velocity profile at the exit plane is also shown in Fig. 6. The antisymmetric pattern illustrated in Fig. 6 is the expected profile for a nearly axisymmetric flow. The notable features are the steep velocity gradient in the vortex core, the double-peaked structure in the high-velocity region, and the apparent reversal of the swirl direction in the outer, low-velocity region of the flow. Also evident is a degree of asymmetry in the data, which is most noticeable in the magnitude of the peak tangential velocities at the edge of the vortex core. Such asymmetries in the measurement of tangential component of velocity of a nominally axisymmetric flow can be evidence of biasing in the velocimetry data due to a higher fringe-crossing rate when the gas velocity opposes the direction of fringe motion (imposed by the frequency shift) than when the gas and fringes move in the same direction. To minimize this effect, the frequency shift was maximized (40 MHz compard to a Doppler frequency of 18 MHz) and the number of fringe crossings for data validation was set to the highest possible value (32). The secondary tangential velocity peaks do not exhibit this asymmetry (values of 84.6 and 85.1 m/s being measured).

The apparent reversal of the sense of rotation of flow in the outermost region of the flow displayed by the data is curious. The probability distribution function (pdf) for velocity in the region showed a distinctly bimodal behavior with the average velocity of the major peak being zero. Because this behavior was noted in measurements at the plane closest to the nozzle discharge, signal biasing due to reflections was suspected. However, the magnitude of the Bragg cell velocity offset and the fact that the sign of the velocity associated with the minor peak is different at the near and far boundaries do not support this contention. Given the experimental configuration – a rotating free jet – no external mechanism for establishing a counterrotation in the external flow is apparent.

The radial velocity measured at the exit plane was of a smaller magnitude than the axial and tangential components (Fig. 6). The velocity is directed radially inward (negative velocity at negative values of radius translates to radial inflow; see Fig. 3) as a result of the action of the swirler end cap. It proved to be very difficult to obtain accurate measurements of radial velocity in the region near the vortex core. This was probably associated with the unsteady behavior of a vortex core (Garg and Leibovich, 1979), coupled with the fact that as the center of rotation shifts off the geometric center, the measured vertical component of velocity will contain a component of the large-magnitude tangential velocity. Furthermore, the existence of large velocity gradients, and high turbulence levels (which lead to substantial changes in flow direction relative to

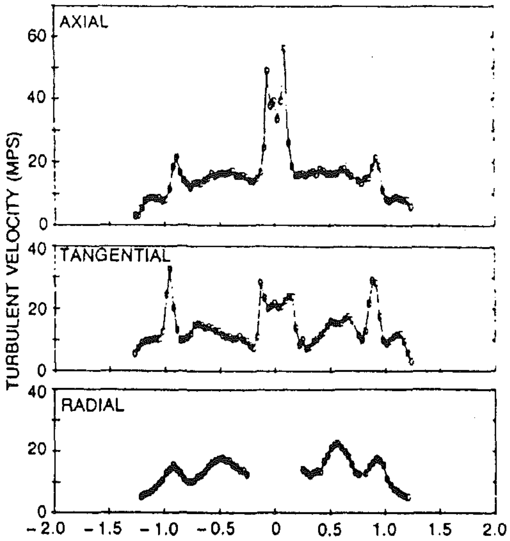

Fig. 7 Exit plane rms velocity profiles

the fringe pattern within the finite probe volume) can be expected to lead to accuracy degradation (Patrick, 1985).

The ratio of the tangential to axial velocity defines the swirl angle, which varies from approximately 45 to 75 deg in the main region of the flow. Indeed, it is expected that the swirl angle would be greater than the 40-deg outer swirler vane exit angle due to the contraction imposed by the swirler end cap. The swirl number, defined as the ratio of the tangential momentum to the product of the axial momentum and the radius of the outermost data point, was calculated to be 0.5. (No accounting was made for the pressure-area term contribution to the axial momentum; the exit plane static pressure distribution was not measured.)

The rms values of the fluctuating velocity components at the exit plane are shown in Fig. 7. As expected, high levels exist in the high shear regions, particularly the vortex core. In the main body of the flow, the fluctuating velocity varies between 10 and 20 m/s.

The axial velocity measurements at successive downstream measurement locations are shown in Fig. 8. At all downstream locations, there was sufficient seed in the central vortex to permit acquisition of data at the full swirler pressure drop of 70 mm Hg. The expected trends are evident with the profiles exhibiting satisfactory symmetry.

The measurements of the tangential velocity distribution in the downstream regions are shown in Fig. 9. The most significant abnormality is the asymmetry, which suggests that the aerodynamic center lies at a value of $r = -0.2$ to -0.3 cm relative to the geometric center. This anomaly was recognized early in the test effort and led to reviews of the equipment alignment procedures; misalignment could not be identified as an error source.

The downstream radial velocity profiles (Fig. 10) show that there is a radial outflow in the downstream region, as opposed to the inflow observed at the discharge plane. This observation is consistent with the decay and flattening of the axial velocity profile and the resultant growth in the jet diameter.

Measurements were also obtained of the mean velocity components at the lateral boundary of the jet. The objective was to obtain information that could be used to establish a boundary condition when modeling this unconfined flow. The geometry of the lateral boundary was that of a conical surface (with a half angle of 21.2 deg) intersecting the coordinates $r=0.45$, $Z=0$ and $r=2.0$, $Z=10.16$. It is recommended that along this boundary the following values of velocity component be assigned:

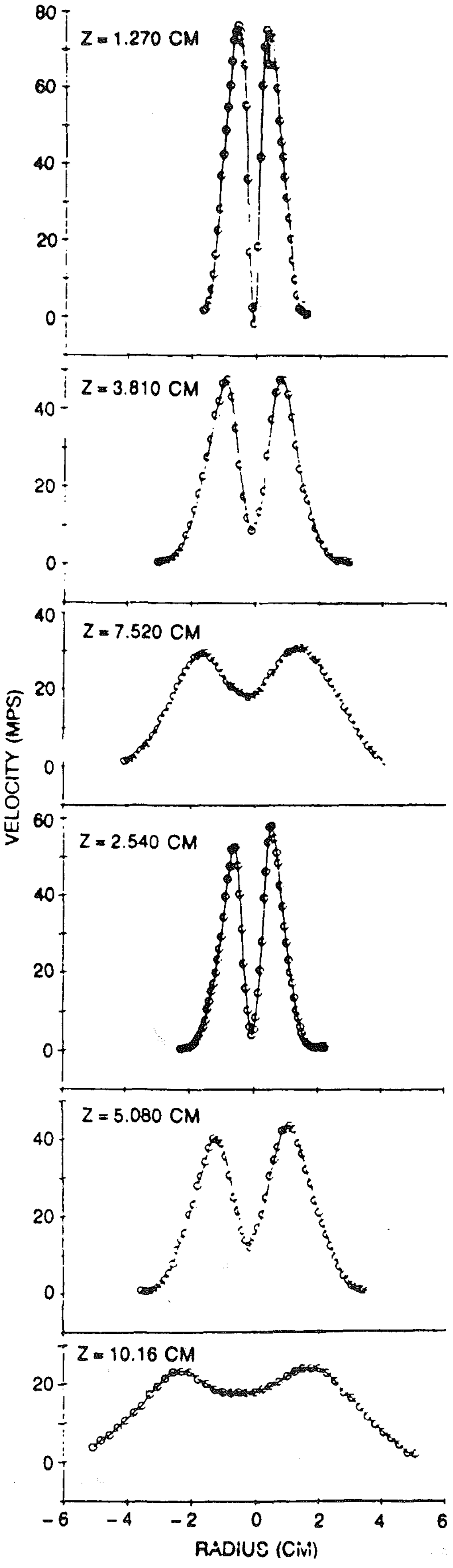

Fig. 8 Downstream swirler flow profiles—axial velocity

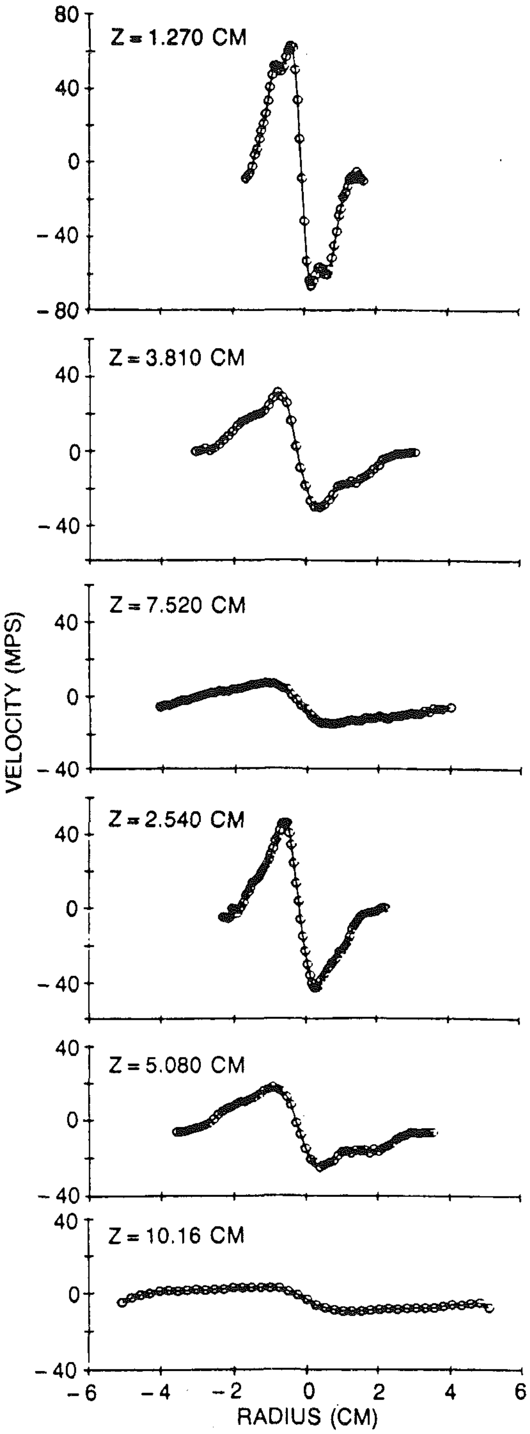

Fig. 9 Downstream swirler flow profiles—tangential

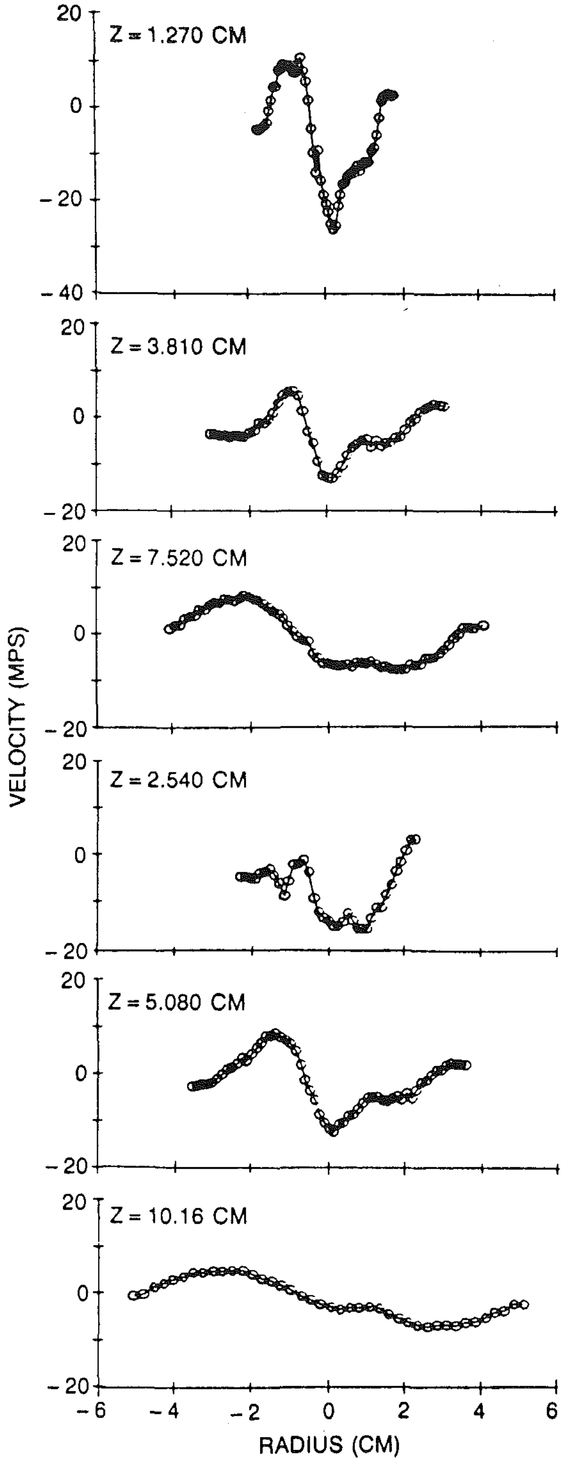

Fig. 10 Downstream swirler flow profiles—radial velocity

Axial velocity = 2 mps
Tangential velocity = 1 mps
Radial velocity = $2 - 0.15 \times Z$ cm

where Z is the distance downstream of the nozzle face and the sense of the radial component is everywhere inward.

Phase-Doppler Anemometer. PDA data were acquired at four downstream stations. Attempts to acquire data at a distance of less than 1.27 cm were unsuccessful due to the very high data rejection rates. The highest indicated droplet number densities for which data were obtained were of the order of 10^4 droplets/cc.

Velocity. The distribution of mean axial velocity is shown in Fig. 11; data acquired using the LDV system for the gas velocity in the absence of the spray are also shown in the figures. Comparison of the gas-only (# symbol) and the gas-phase velocities (X symbol) at the three upstream stations show that, at each station, profiles are virtually identical except in the center of the flow, where the velocity depression associated with the vortex core has been moderated. This feature is consistent with a flow situation in which these central region droplets are accelerated to a high velocity immediately downstream of the nozzle, but thereafter decelerate less rapidly than the gas.

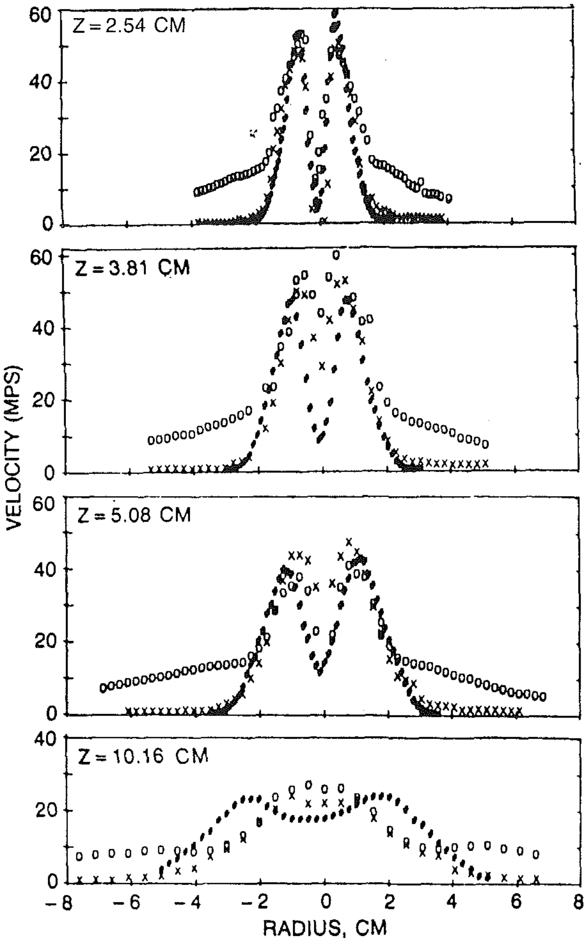

Fig. 11 Spray axial velocity field

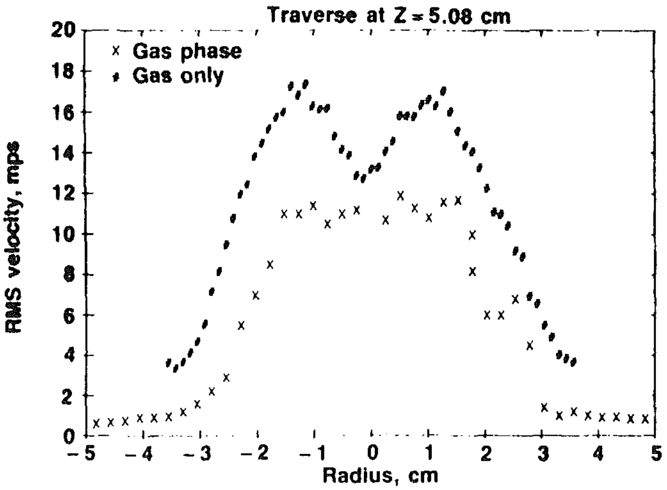

Fig. 12 Axial turbulence

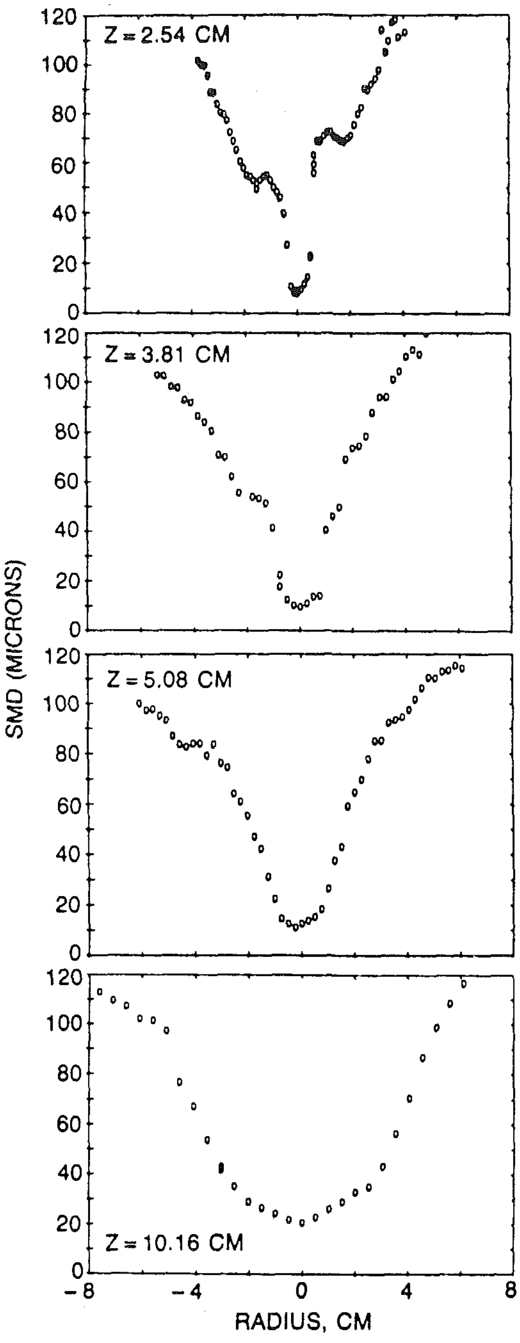

Fig. 13 Droplet size distribution

The liquid phase (0 symbol) is shown to have a nonzero velocity in the outer region of the spray where the gas is essentially quiescent. This is due to the larger droplets being centrifuged to the outer region of the spray. In the interior of the spray the liquid phase velocity is greater than the gas-phase velocity. Between this interior region and the external region, an annular region exists for the three most upstream locations in which the gas and liquid-phase axial velocities are nearly identical. This is not observed at the most downstream location. At that station, a significant difference between the spray-on and spray-off profiles is observed: The breadth of the gas-only jet is greater than in the case of the spray. Whether this is a manifestation of the effect of a reduced jet entrainment rate caused by a moderation of the turbulence levels or is a result that can be explained on the basis of droplet-gas momentum exchange due to velocity lag considerations alone remains to be determined.

A measure of the extent to which the level of the velocity fluctuations can be affected by the presence of the spray is afforded by the PDA information obtained using the seeded spray. In this case the "seed" particles are those produced by the spray itself as well as droplets introduced into the flow by a piezo-electric nebulizer. These particles differ from the titanium dioxide particles used in the LV measurement in their ability to respond to turbulent fluctuations. The indicated droplet sizes in the four smallest-diameter bins (out of 50) ranged from 1.4 to 4.4 μm. A representative value of the rms velocity obtained from inspection of the statistical information

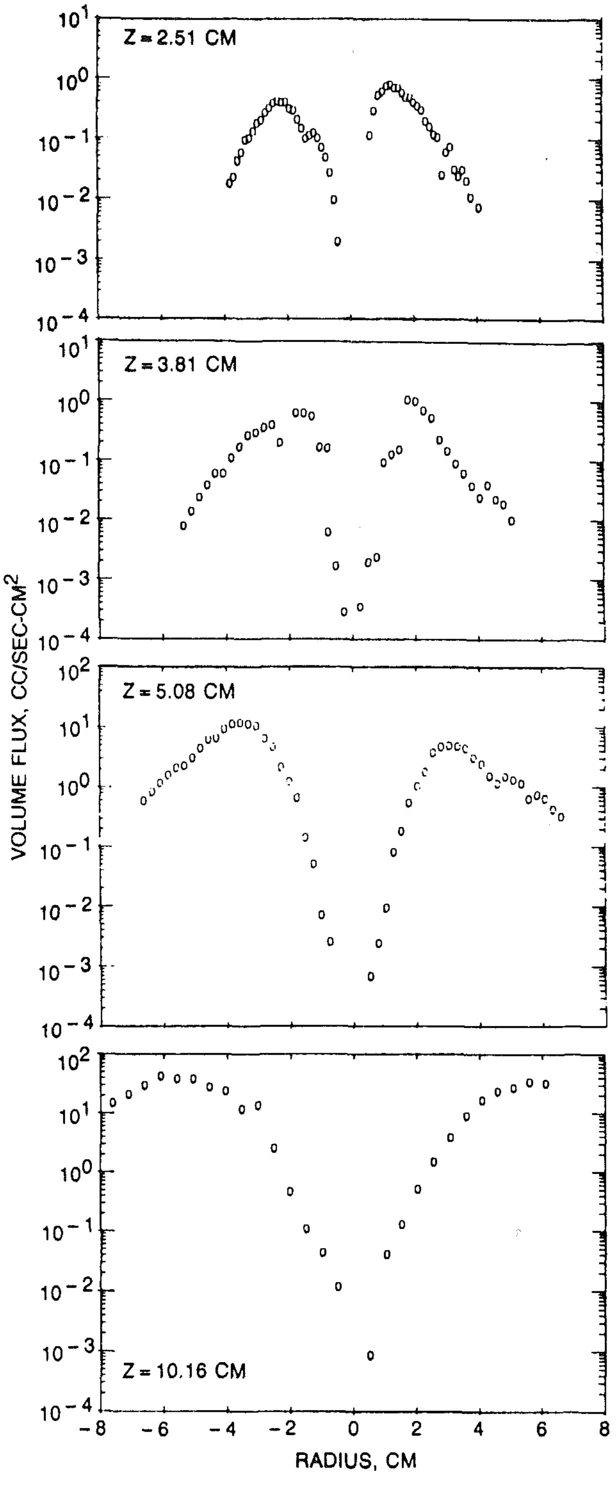

Fig. 14 Volume flux distribution

for these four bins is compared with the rms velocity obtained in the LDV tests for the Z = 5.08 cm station in Fig. 12. As expected, the turbulence level is lower in the case of the spray.

Droplet Size. The Sauter mean droplet size at each radial measurement station is shown in Fig. 13. A substantial range of droplet sizes is observed as is the expected finding that the largest droplets have been centrifuged to the periphery of the spray. In the interior of the flow the mean droplet size is on the order of 10–20 μm. In general, very high radial gradients in SMD exist at all measurement locations.

The irregularities in the data patterns, particularly noticeable at the most upstream station, are manifestations of a clipping of the size distribution due to the inability of the PDA instrument to process all sizes and velocities of droplets with given processor settings. The problem was encountered only in a few instances in regions where there existed both high radial velocity and high radial SMD gradients.

Inspection of the data also shows that measurements of SMD at positive radii are higher than those at negative radii. The discrepancy is most notable at the edges of the spray at upstream regions where droplet number densities are highest. From discussions with the instrument developer, this discrepancy is probably associated with interference of the dense spray with the transmitted beams that form the probe volume, not with interference with the scattered light captured by the receiving optics. This being the case, the values measured at negative values of radius should be the more accurate values.

Volume Flux. The PDA instrument can also provide information on mass (volume) flux distribution in cases where an accurate count of signal rejections can be made (few instances of multiple particles in the sampling volume) and where the flow is nearly undirectional and aligned with the measured velocity component. These benign conditions certainly do not exist in this flow, and therefore, the results (Fig. 14) are only qualitative. The hollow cone nature of the spray is illustrated by the depression of the centerline values and by the profile spreading with increasing downstream distance. The measurements lack quantitative accuracy as illustrated by an increase in the peak concentration values with increasing axial distance, rather than a decrease. Also, integration of the volume flux distribution data at the farthest downstream station yields a total flow rate of 500 kg/h—far in excess of the metered value of 71 kg/h. According to the instrument developer, the overprediction of flow rate is associated with the techniques employed in estimating the size of the sampling volume. This estimate is based on a statistical analysis of the number of fringe crossings detected during the sampling period; a biased result is obtained in flows in which there is a significant component of particle velocity in the plane of the fringes. Improved quantitative measurements of mass flux in high-velocity, swirling flows will require the use of higher-speed processors and a multi-velocity-component system.

Concluding Remarks

Instrumentation techniques currently available are capable of providing significant information on the behavior of airblast injectors operating under high flow conditions: flow rates on the order of 70 kg/h and velocities on the order of 125 m/s. Mass flux, droplet size distribution, and flow velocity data have been acquired.

The data obtained in this effort provide information that can be used to evaluate analytical models. The velocity information possesses significant structure (variation as a function of radius) and that structure undergoes substantial change from measurement station to measurement station. As a result, a useful modeling test can be based on this information.

The SMD data, while possessing significant structure, do not undergo a dramatic change with measurement station location. The most significant change in SMD distribution occurs in the region upstream of the first measurement station—a region too dense for accurate measurements with current instrumentation.

The mass-flux distribution produced by the patternator shows substantial change with measurement station location. Probe interference effects may bias the patternator information, but to date, optical (noninterfering) data do not exist that are known to be of superior quality.

Fluid mechanic analysis of the flow studied herein will establish whether the measurements obtained during this study are sufficient to permit judgments to be made concerning the adequacy of different analytical treatments. It is recognized that certain information required for analysis is lacking, in particular, the initial droplet size distribution. As a result, it will be necessary to evaluate the effect of assumed initial droplet distributions in a parametric manner. From the point of view of developing a practical design procedure, it would be useful to use existing droplet size distribution functions and correlations found in the literature (Lefebvre, 1983) to establish the initial conditions. On the other hand, a best guess regarding an appropriate size distribution is afforded by consideration of the reported PDA mass flux, SMD, and velocity information at a given measurement station. (The assumptions inherent in using such an approach are that the relative mass flux values are accurate, that vaporization is negligible, and that secondary atomization and coalescence are negligible.)

It was recognized at the outset of this effort that use of a confined flow and the simulation of the spray by use of spherical particles of known size would eliminate substantial analytical difficulties. The experimental difficulties in performing extensive optical measurements through curved surfaces (required to avoid the necessity of applying three-dimensional flow procedures) and of providing means of preparing and injecting large quantities of microspheres make such an approach costly and difficult. The results of attempts to match the results of the experiments reported herein with CFD predictions will be useful in establishing the nature of the experiments and analyses to be used in future efforts to develop computational techniques capable of predicting spray behavior. Most significantly, such attempts will serve to establish the level of accuracy that current analysis provides in predicting the spray character within a combustion chamber.

Acknowledgments

This research was sponsored by the National Aeronautics and Space Administration, Contract No. NAS3-24352, under the technical management of D. Bulzan of the Lewis Research Center.

References

Asheim, J. P., Kinwan, J. E., and Peters, J. E., 1987, "Modeling of a Hollow-Cone Liquid Spray Including Droplet Collisions," AIAA Paper No. 87-0135.

Ashgriz, N., and Givi, P., 1987, "Coalescence Collision of Fuel Droplets," AIAA Paper No. 87-0138.

Bachalo, W. D., Hess, C. F., and Hartwell, C. A., 1979, "An Instrument for Spray Droplet Size and Velocity Measurements," ASME Paper No. 79-WA-GT-13.

Bachalo, W. D., and Houser, M. J., 1984, "Development of the Phase/Doppler Spray Analyzer for Liquid Drop Size and Velocity Characterizations," AIAA Paper No. 84-1199.

Bachalo, W. D., Houser, M. J., and Smith, J. N., 1987, "Behavior of Sprays Produced by Pressure Atomizers as Measured Using a Phase/Doppler Instrument," *Atomization and Spray Technology*, Vol. 3, pp. 53–72.

Barth, H. G., ed., 1984, *Modern Methods of Particle Size Analysis, Analytical Chemistry and Its Applications*, Vol. 73, Wiley, New York.

Bulzan, D. L., Shuen, J.-S., and Faeth, G. M., 1987, "Particle-Laden Swirling Free Jets: Measurements and Predictions," AIAA Paper No. 87-0303.

Dodge, L. G., 1987, "Representation of Average Drop Sizes in Sprays," AIAA Paper No. 87-2133.

Elghobashi, S., Abou-Arab, T., Rizk, M., and Mostafa, A., 1984, "Prediction of the Particle-Laden Jet With a Two-Equation Turbulence Model," *Int. Journal of Multiphase Flow*, Vol. 10, pp. 697–710.

Faeth, G. M., 1983, "Evaporation and Combustion of Sprays," *Progress in Energy Combustion Sciences*, Vol. 9, pp. 1–76.

Garg, A. K., and Leibovich, S., 1979, "Spectral Characteristics of Vortex Breakdown Flowfields," *Physics of Fluids*, Vol. 22, pp. 2053–2064.

Gosman, A. D., and Ioannedes, E., 1983, "Aspects of Computer Simulation of Liquid-Fueled Combustors," *Journal of Energy*, Vol. 7, pp. 482–490.

Jackson, T. A., and Samuelsen, G. S., 1986, "Spatially Resolved Droplet Size Measurements," ASME JOURNAL OF ENGINEERING FOR GAS TURBINES AND POWER, Vol. 108, pp. 196–203.

Kraemer, G., and Bachalo, W., 1986, "Evaluation of a Phase/Doppler Particle Analyzer for Measuring Dense Sprays From a Gas Turbine Fuel Injector," AIAA Paper No. 86-1532.

Lefebvre, A., 1983, *Gas Turbine Combustion*, McGraw-Hill, New York, p. 413.

McDonnell, V. G., Wood, C. P., and Samuelsen, G. S., 1986, "A Comparison of Spatially-Resolved Drop Size and Drop Velocity Measurements in an Isothermal Chamber and a Swirl-Stabilized Combustor," *21st Symposium (International) on Combustion*, The Combustion Institute, Pittsburgh, PA.

McDonnell, V. G., Cameron, C. D., and Samuelsen, G. S., 1987, "Symmetry Assessment of a Gas Turbine Air-Blast Atomizer," AIAA Paper No. 87-2136.

McVey, J. B., Russell, S., and Kennedy, J. B., 1987, "High-Resolution Patternator for the Characterization of Fuel Sprays," *Journal of Propulsion*, Vol. 3, pp. 202–209.

McVey, J. B., Kennedy, J. B., and Russell, S., 1988, "Fuel-Injector/Air-Swirl Characterization," NASA Report CR-180864.

Modarress, D., Wuerer, J., and Elghobashi, S., 1982, "An Experimental Study of a Turbulent Round Two-Phase Jet," AIAA Paper No. 82-0964.

Modarress, D., and Tan, H., 1983, "LDA Signal Discrimination in Two-Phase Flows," *Experiments in Fluids*, Vol. 1, pp. 129–134.

Modarress, D., Tan, H., and Elghobashi, S., 1983, "Two-Component LDA Measurement in a Two-Phase Turbulent Jet," AIAA Paper No. 83-0052.

Mostafa, A. A., Mongia, H. C., McDonnell, V. G., and Samuelsen, G. S., 1987, "On the Evaluation of Particle-Laden Jet Flows: A Theoretical and Experimental Study," AIAA Paper No. 87-2181.

Patrick, W. P., 1985, "Error Analysis for Benchmark Fluid Dynamic Experiments," UTRC Report R85-151772.

Rosfjord, T. J., and Russell, S., 1987, "Influences of Fuel Spray Circumferential Uniformity," AIAA Paper No. 87-2135.

Rudoff, R. C., Houser, M. J., and Bachalo, W. D., 1987, "Two-Phase Flow Measurements of a Spray in Turbulent Flow," AIAA Paper No. 87-0062.

Shuen, J. S., Solomon, A. S. P., Zhang, Q.-F., and Faeth, G. M., 1983, "A Theoretical and Experimental Study of Turbulent Particle-Laden Jets," NASA Contractor Report 168293.

Shuen, J. S., Solomon, A. S. P., Zhang, Q.-F., and Faeth, G. M., 1984, "Structure of Particle-Laden Jets: Measurements and Predictions," AIAA Paper No. 84-0038.

Solomon, A. S. P., Shuen, J.-S., Zhang, Q.-F., and Faeth, G. M., 1983, "Measurements and Predictions for Nonevaporating Sprays in a Quiescent Environment," AIAA Paper No. 83-0151.

Solomon, A. S. P., Shuen, J.-S., Zhang, Q.-F., and Faeth, G. M., 1984a, "Structure of Nonevaporating Sprays: Measurement and Predictions," AIAA Paper No. 84-015.

Solomon, A. S. P., Shuen, J.-S., Zhang, Q.-F., and Faeth, G. M., 1984b, "A Theoretical and Experimental Study of Turbulent Nonevaporating Sprays," NASA Contractor Report 174688.

Soo, S. L., 1967, *Fluid Dynamics of Multiphase Systems*, Blaisdell, Waltham, MA.

Swithenbank, J., Beer, J. M., Taylor, D. S., Abbot, D., and McCreath, G. C., 1976, "A Laser Diagnostic Techniques for the Measurement of Droplet and Particle Size Distribution," AIAA Paper No. 76-69.

Wang, G., Mao, C.-P., Dietvorst, J., and Chigier, N., 1987, "An Experimental Investigation of Air-Assist Non-swirl Atomizer Sprays," *Atomization and Spray Technology*, Vol. 3, pp. 13-36.

X. F. Dai
Visiting Scholar.

A. H. Lefebvre
Reilly Professor of Combustion Engineering.

Thermal Science and Propulsion Center,
School of Mechanical Engineering,
Purdue University,
W. Lafayette, IN 47907

J. Rollbuhler
NASA-Lewis Research Center,
Cleveland, OH 44135

Spray Characteristics of a Spill-Return Airblast Atomizer

The spray characteristics of a spill-return airblast atomizer are examined using water as the working fluid. Measurements of mean drop size, drop size distribution, spray cone angle, and circumferential liquid distribution are carried out over wide ranges of liquid injection pressures and atomizing air velocities. Generally it is found that an increase in nozzle bypass ratio worsens the atomization quality and widens the spray cone angle. Increase in airblast air velocity may improve or impair atomization quality depending on whether it increases or decreases the relative velocity between the liquid and the surrounding air. Airblast air can also be used to modify the change in spray cone angle that normally accompanies a change in bypass ratio.

Introduction

A conventional spill-return nozzle is basically a simplex pressure-swirl atomizer, except that the rear wall of the swirl chamber, instead of being solid, contains a passage through which liquid can be "spilled" away from the atomizer. Liquid is always supplied to the swirl chamber at the maximum pressure and flow rate. When the nozzle is operating at its maximum capacity, the valve located in the spill line is fully closed and all the liquid is ejected from the nozzle in the form of a well-atomized spray. Opening the valve allows liquid to be diverted away from the swirl chamber, leaving less to pass through the atomizing orifice. The spill atomizer's constant use of a relatively high pressure means that, even at extremely low flow rates, there is adequate swirl to provide efficient atomization. According to Carey (1954), satisfactory atomization can be achieved even when the flow rate is as low as one percent of its maximum value. Other attractive features include an absence of moving parts and, because the flow passages are designed to handle large flows all the time, freedom from blockage by contaminants in the liquid.

A disadvantage of the spill-return atomizer is that changes in flow rate cause a large variation in spray angle. The effect of a reduction in flow rate is to lower the axial component of velocity without affecting the swirl component; consequently the spray angle widens. The spray angle at minimum flow can be up to 50 deg wider than at maximum flow. Other disadvantages of the spill system include the requirement for a larger capacity pump to handle the large recirculating flows, and a rise in fuel temperature due to recirculating flow. For these reasons interest in the spill-return atomizer for gas turbines has declined in recent years, and its main application has been in large industrial furnaces. However, if the aromatic content of gas turbine fuels continues to rise, this could pose serious problems due to blockage, by gum formation, of the fine passages of conventional pressure atomizers. The spill-return atomizer, having no small passages, is virtually free from this defect. Furthermore, if a conventional spill-return nozzle is incorporated into an airblast shroud, its potential advantages for gas turbine applications become very considerable, as indicated below:

1 Good atomization over the entire fuel flow range. This ensures easy lightoff, good lean blowoff characteristics, and high combustion efficiency at engine idling.
2 Low exhaust smoke and low nitric oxide emissions due to the aeration of the fuel spray provided by the airblast air.
3 Atomizing air passages can be "shaped," if required, to produce an elliptical spray.
4 Large flow passages are much less prone to blockage by contaminants.
5 Carbon buildup on the nozzle tip is eliminated by "washing" with airblast atomizing air.

The purpose of the present investigation is to examine the spray characteristics of a spill-return nozzle when operating both with and without airblast air. Comparisons are made between these two operating modes using measurements of mean drop size, spray angle, and circumferential liquid distribution, obtained over wide ranges of liquid injection pressure, liquid flow rate, and nozzle bypass ratio.

Experimental

The atomizer employed in the research is shown schematically in Fig. 1. It comprises a conventional, spill-return, pressure-swirl nozzle, surrounded by an air shroud. The flow characteristics of this nozzle are typical of those for all types of spill-return nozzle. Figure 2 illustrates the measured variations in nozzle, bypass, and total flow rates, with the nozzle operating at an injection pressure of 0.172 MPa (25 psi).

The airblast portion of the atomizer contains 12 swirl vanes, all of which are set at an angle to the nozzle axis of 60 deg. The purpose of this air is to enhance atomization performance at low liquid injection pressures and to control the spray angle.

The apparatus used to measure spray characteristics is shown schematically in Fig. 3. Water is supplied to the nozzle from

---

Contributed by the International Gas Turbine Institute and presented at the 33rd International Gas Turbine and Aeroengine Congress and Exhibition, Amsterdam, The Netherlands, June 5–9, 1988. Manuscript received by the International Gas Turbine Institute October 1, 1987. Paper No. 88-GT-7.

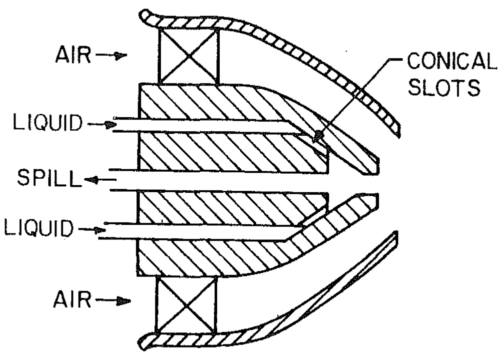

Fig. 1 Schematic diagram of spill-return atomizer fitted with air shroud

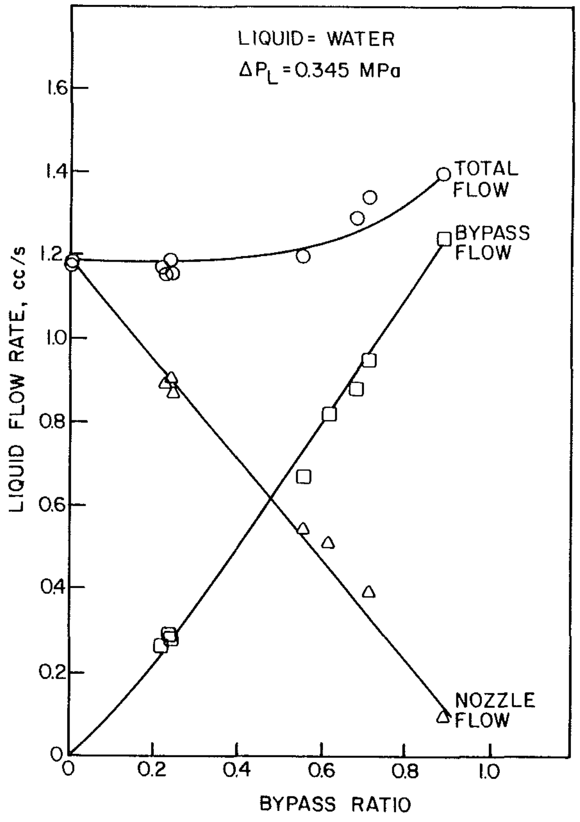

Fig. 2 Flow characteristics of spill-return nozzle

a nitrogen-pressurized tank. The amount of water ejected from the nozzle is controlled by a hand-operated valve located in the bypass line. A number of valves, pressure gages, and flow meters are located in the nozzle feed and bypass lines to provide the desired nozzle operating conditions in terms of liquid injection pressure and bypass ratio. A separate system of valves, flow meters, and pressure gages is also used to supply a controlled amount of shop air to the airblast portion of the nozzle, as shown in Fig. 3.

Mean drop sizes are measured using a Malvern particle size analyzer. This instrument is based on the Fraunhofer diffraction theory of a collimated laser beam scattered by moving drops. The principle of operation of the Malvern has been reviewed by Swithenbank et al. (1977) and Dodge and Cerwin (1984), while the accuracy and limitations of the instrument have been discussed by Hirleman et al. (1984) and Dodge (1984).

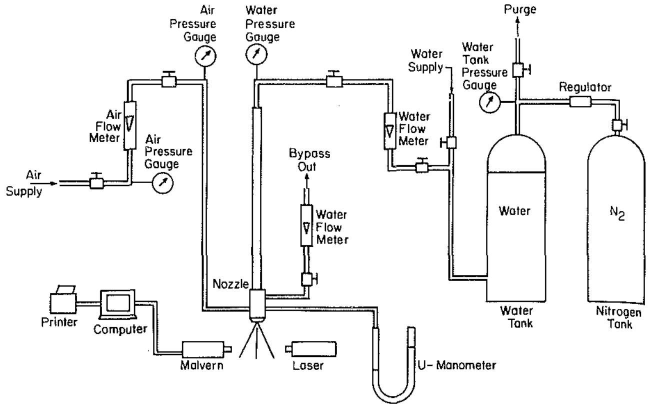

Fig. 3 Basic test facility for atomization and patternation studies

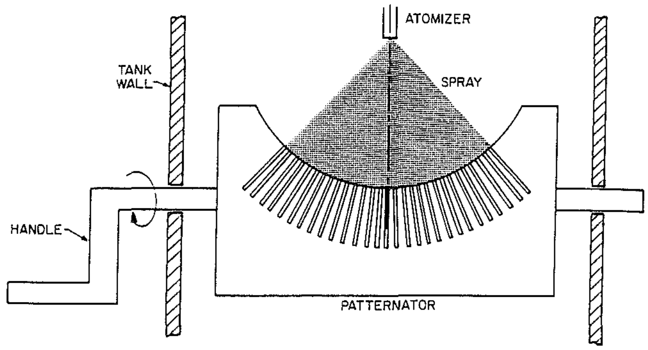

Fig. 4 Schematic diagram of patternator for measuring radial liquid distribution

All measurements are carried out at a distance of 150 mm downstream of the nozzle with the laser beam passing through the centerline of the spray. Centerline measurements ensure that the laser beam encompasses both the smaller drops located at the center of the spray and the larger drops at the spray periphery.

The "effective" or "equivalent" angle of the spray is measured using a patternator of the type shown in Fig. 4, which is 1.27 cm wide and 31.75 cm long. The sampling tubes were formed by cutting slots into the opaque white plastic base over which a clear thin sheet of plastic is glued. The outer edges that form the openings to the tubes are filed to sharp edges so that each tube has a well-defined sampling area. The tubes are almost square in cross section, each tube having an area of 0.504 cm^2. There are a total of 29 sampling tubes, spaced 4.5 deg apart along a radius of curvature of 10 cm.

Before a spray sample is taken, the patternator is inverted to drain away any liquid in the sampling tubes. The liquid flow rate is then adjusted until the nozzle is operating at the desired conditions. The patternator is rotated to the upright position, and the sampling tubes begin to fill. When one of the tubes is about three quarters full, the liquid supply is turned off and the patternator is rotated approximately 30 deg until a thin metal plate attached to the patternator blocks off the spray.

Nomenclature

ALR = mass ratio of atomizing air to nozzle liquid efflux
BPR = bypass ratio; ratio of bypass flow to total liquid flow
FN = flow number, m^2
P_A = ambient air pressure, Pa
ΔP_A = air pressure drop through air shroud, Pa
ΔP_L = liquid pressure differential across nozzle, Pa
q = Rosin-Rammler drop size distribution parameter
SMD = Sauter mean diameter

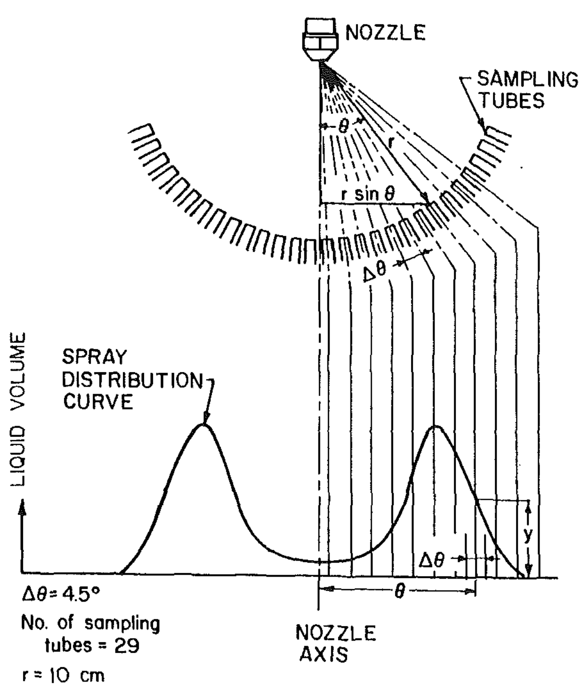

Fig. 5 Measurement of radial liquid distribution

This is necessary due to risk of liquid dribbling after the pump is turned off.

The volume of liquid in each tube is measured by visually locating the meniscus between lines scribed into the clear plastic of the patternator. Liquid distribution curves are made by plotting liquid volume as the ordinate and the corresponding angular location of the sampling tubes as the abscissa, as illustrated in Fig. 5. The method has been fully described by Ortman and Lefebvre (1985).

In order to describe more succinctly the effect of changes in operating parameters on liquid distribution, the curves of liquid volume versus angular position can be reduced to a single numerical value, which DeCorso and Kemeny (1957) called the "equivalent spray angle." The equivalent spray angle is the sum of the two angles, $\phi = \phi_L + \phi_R$, which are calculated using the following equation:

$$\phi_L \text{ (or } \phi_R) = \frac{\Sigma y\theta\Delta\theta \sin\theta}{\Sigma y\Delta\theta \sin\theta} = \frac{\Sigma y\theta \sin\theta}{\Sigma y \sin\theta}$$

L and R represent the left and right lobes of the liquid distribution curve, respectively, θ is the angular location of the sampling tubes, $\Delta\theta$ the angle between the sampling tubes, and y the liquid volume measured at the corresponding tubes. The physical meaning of the equivalent spray angle is that ϕ_L (or ϕ_R) is the value of θ that corresponds to the position of the center of mass of a material system for the left- (or right-) hand lobe of the distribution curve.

Circumferential liquid distribution in the spray is measured by arranging for the nozzle to spray vertically downward into a circular collection tray that is partitioned into 16 pie-shaped sectors. Each sector drains into a separate sampling tube. The height of the nozzle above the collection tray is adjusted to ensure that the entire spray is collected. The duration of each test is determined as the time required for one of the sampling tubes to become nearly full. After the level in each tube is measured and recorded, a plot of liquid height versus angular position can be constructed, as shown in Fig. 14.

Results

In the course of this investigation a large amount of data was collected on the effects of liquid injection pressure, nozzle bypass ratio, air velocity, and air/liquid ratio on mean drop size, drop size distribution, spray cone angle, and circumferential liquid distribution. These various aspects are discussed below in turn.

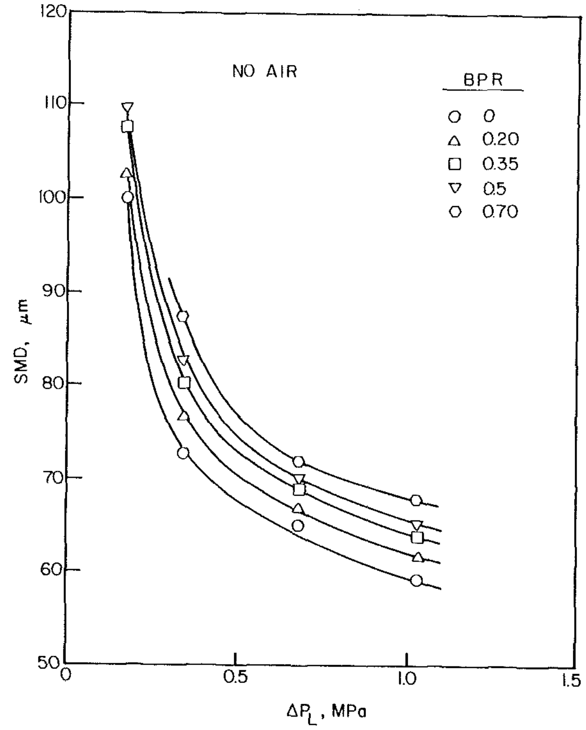

Fig. 6 Influence of injection pressure on mean drop size with no air flow

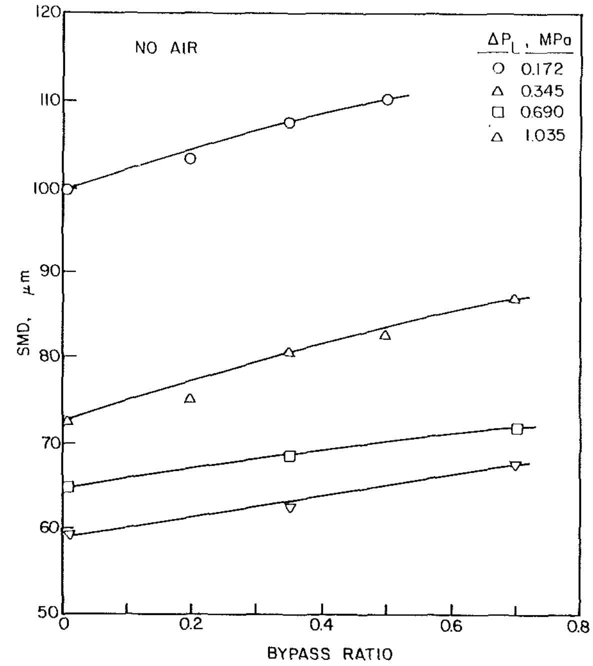

Fig. 7 Influence of nozzle bypass ratio on mean drop size with no air flow

Mean Drop Size. Figure 6 shows the influence of liquid injection pressure (ΔP_L) on mean drop size (SMD) for various values of nozzle bypass ratio (BPR). The results indicate that SMD declines with increasing injection pressure, according to the relationship SMD ∝ $\Delta P_L^{0.3}$. The effect of bypass ratio on mean drop size is shown more directly in Fig. 7. A previous study on the spray characteristics exhibited by spill-return nozzles, carried out by Rizk and Lefebvre (1985), had shown that

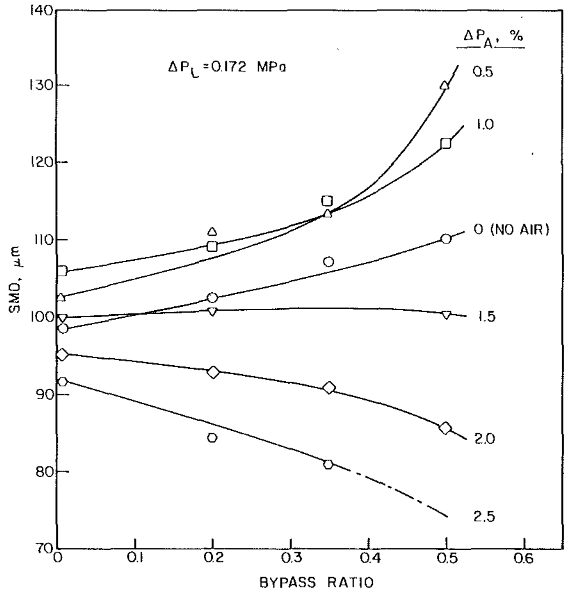

Fig. 8 Influence of atomizing air pressure on mean drop size for different values of bypass ratio

atomization quality was fairly insensitive to variations in nozzle bypass ratio, whereas the data contained in Fig. 7 show a slight increase in SMD with increase in BPR. These apparently differing results can be understood by recognizing that increase in nozzle bypass ratio has two opposing effects on SMD, both of which stem from the corresponding reduction in the axial component of liquid velocity at the nozzle exit. As the liquid discharges from the nozzle, it has two components of velocity, one axial and the other tangential. The tangential velocity component depends only on the liquid injection pressure and is independent of bypass ratio. Thus an increase in bypass ratio, by reducing the axial component of velocity at the nozzle outlet without affecting the swirl component, causes the spray cone angle to increase and the resultant component of velocity (which combines both axial and swirl velocity components) to decline. It is now well established that for pressure-swirl nozzles an increase in spray cone angle produces a finer spray. This is usually attributed to the fact that, from simple geometric considerations, increase in cone angle reduces the thickness of the conical sheet formed at the nozzle exit. As mean drop sizes are roughly proportional to the square root of the thickness of the sheet from which they are formed (Lefebvre, 1983), it follows that the disintegration of a thinner liquid sheet must result in improved atomization. However, it is also well known that a reduction in liquid discharge velocity, by lowering the relative velocity between the liquid and the surrounding air or gas, has an adverse effect on atomization quality. Which of these two opposing effects predominates will depend on many factors, most important of which is the initial spray cone angle. From inspection of the results obtained by Rizk and Lefebvre (1985), it is clear that, for the nozzle designs used in their experiments, these two opposing effects served to cancel each other, so that mean drop size remained virtually independent of bypass ratio. In the present experiments, the adverse effect of reduction in discharge velocity clearly outweighs the beneficial effect of wider cone angle, causing atomization quality to decline with increase in bypass ratio.

Figures 6 and 7 show data obtained with no air flowing, i.e., with the atomizer operating as a conventional spill-return nozzle. The influence of airblast air on mean drop size is illustrated in Fig. 8 for various values of bypass ratio and a constant value of ΔP_L of 0.172 MPa (25 psi). A considerable amount of SMD data was acquired at higher levels of ΔP_L, but special interest is attached to the lowest value tested (0.172 MPa) because the effect of air assistance on spray quality is most pronounced at low liquid injection pressures.

In Fig. 8 the atomizing air pressure differential ΔP_A is expressed as a percentage of the ambient air pressure. The curves drawn in this figure show the SMD increasing with increase in air pressure differential up to a value of ΔP_A of around one percent, beyond which any further increase in ΔP_A causes the SMD to decline. In particular, the results show that air assistance at pressure differentials below around 1.5 percent has a deleterious effect on atomization quality, i.e., SMD values are actually higher than when the nozzle is operating solely in the pressure-swirl mode. Only at values of ΔP_A higher than 1.5 percent does the airblast air successfully augment atomization. This interesting observation can be explained in terms of the relative velocity between the conical sheet of liquid emanating from the spill-return nozzle and the surrounding coflowing air. At low values of ΔP_A, the air velocity is lower than the liquid velocity. Thus, in this regime, any increase in air velocity, i.e., any increase in ΔP_A, will impair atomization quality by reducing the relative velocity between the air and the liquid. For a value of ΔP_A of around one percent, where the SMD values generally attain their highest values, the relative velocity is effectively zero and the interaction between the liquid sheet and the surrounding air is minimal. For all higher values of ΔP_A, the air velocity exceeds the liquid velocity, and any further increase in ΔP_A serves to improve atomization by increasing the relative velocity between the liquid and the air.

This argument suggests that for this type of nozzle there will always be one value of ΔP_L for which the SMD is a maximum. The particular value of ΔP_L at which this condition of worst atomization occurs will be that for which the liquid velocity just equals the air velocity.

It is recognized that in most practical forms of air-assist atomizers the air and liquid flows issuing from the nozzle both have radial and tangential as well as axial components of velocity. In this complex two-phase flow field the term "relative velocity" is clearly very difficult to define. Nevertheless, for any given air velocity there will always be one particular value of liquid velocity at which the level of interaction between the liquid and air is a minimum.

With increases in ΔP_L the condition of zero relative velocity will obviously be reached at higher levels of ΔP_A. Thus one would expect the value of ΔP_L at which SMD attains its maximum value to increase with increase in $\Delta P_A/P_A$, and this is borne out by the data.

When mean drop size is plotted against liquid injection pressure, the effect of air assistance is generally to distort the curves, as shown in Fig. 9. The extent of this distortion may be assessed by comparing Fig. 9 with Fig. 6, which shows corresponding data obtained with no air flowing. The curves drawn in Fig. 9 show that atomization quality generally improves with increase in liquid injection pressure, but there is a range of values of ΔP_L over which the improvement achieved is noticeably less than at lower and higher values of ΔP_L. Based on these and other observations at different operating conditions, it seems reasonably certain that the range of values of ΔP_L over which the influence of ΔP_L on SMD is relatively small corresponds to conditions of minimum relative velocity between the liquid and the atomizing air. The situation is complicated by the fact that any change in ΔP_L produces a change in spray cone angle, which, in turn, affects the degree of interaction between the liquid cone and the swirling air flow.

The influence of bypass ratio on mean drop size with air flowing through the nozzle is illustrated in Fig. 10. The curves drawn in this figure exhibit the same general characteristics as those obtained without air flow (see Fig. 7) with one noticeable difference. At the lowest injection pressure of 0.172 MPa (25 psi), Fig. 7 shows SMD increasing with increase in BPR whereas Fig. 10 shows the opposite trend, namely, SMD decreasing with increase in BPR. This difference occurs because at low

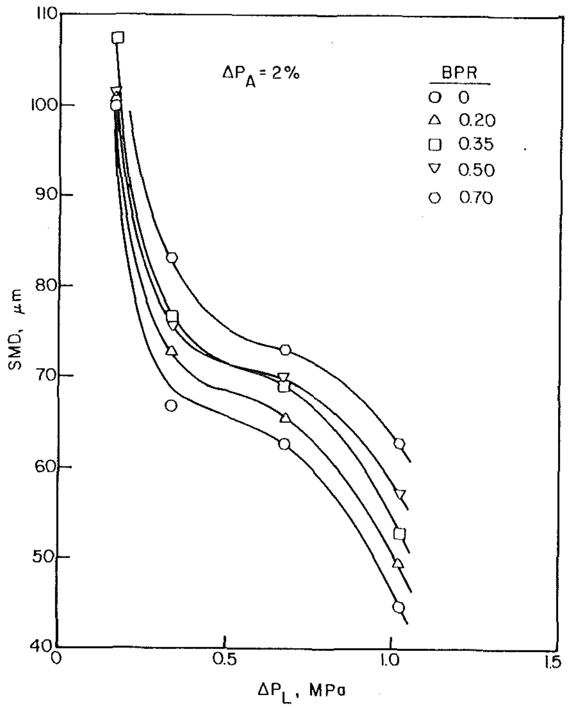

Fig. 9 **Graphs illustrating effect of atomizing air on relationship between mean drop size and liquid injection pressure**

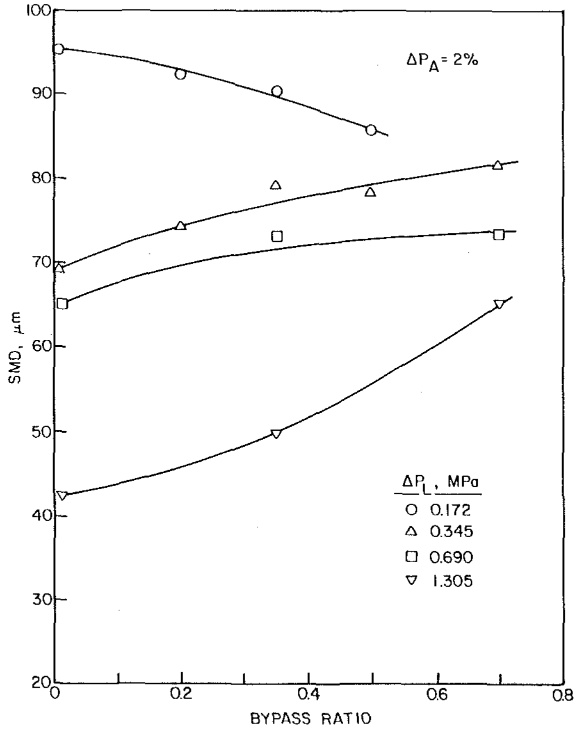

Fig. 10 **Effect of atomizing air on relationship between mean drop size and nozzle bypass ratio**

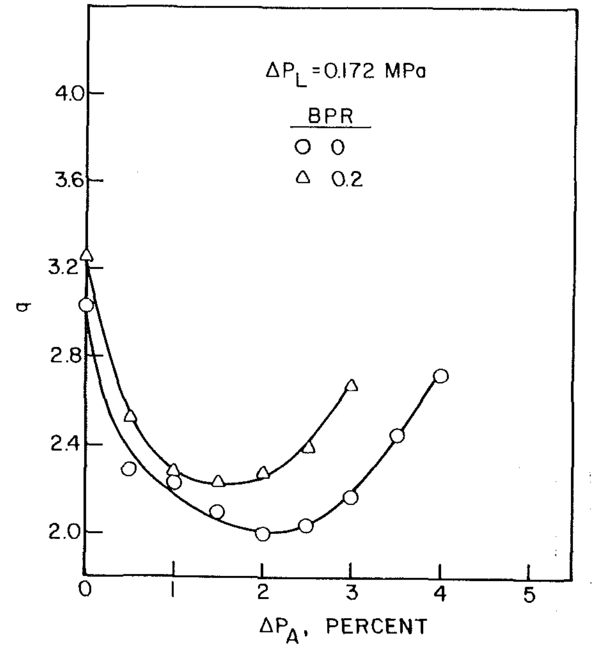

Fig. 11 **Influence of air velocity ratio on Rosin-Rammler drop size distribution parameter**

liquid injection pressures the air velocity corresponding to a pressure drop of 2 percent is sufficient to overwhelm the liquid velocity so that the nozzle operates essentially as an airblast atomizer. For this type of atomizer, atomization quality is always improved by an increase in air/liquid ratio. Thus, at this condition of low liquid velocity and high air velocity, an increase in BPR will improve atomization quality by reducing the liquid flow rate at the nozzle exit, thereby increasing the air/liquid ratio. At higher values of ΔP_L the impact of the airblast air is correspondingly less, and the plots of SMD versus BPR in Fig. 10 exhibit the same general trends as the corresponding curves in Fig. 7, with no air flowing.

Drop-Size Distributions. At the present time the most widely used expression for drop size distribution is one that was originally developed for powders by Rosin and Rammler (1933). It may be expressed in the form

$$1 - Q = \exp - (D/X)^q$$

where Q is the fraction of the total volume contained in drops of diameter less than D, and X and q are constants. Thus, by applying the Rosin-Rammler relationship to sprays, it is possible to describe the drop size distribution in terms of the two parameters X and q. The exponent q provides a measure of the spread of drop sizes. The higher the value of q, the more uniform is the spray. If q is infinite, the drops in the spray are all the same size. For most sprays the value of q lies between 1.5 and 4. However, for rotary atomizers, q can be as high as 7.

Although it assumes an infinite range of drop sizes, the Rosin-Rammler expression has the virtue of simplicity. Moreover, it is obtained as a direct printout from the Malvern particle size analyzer. This instrument can also provide a model independent description of drop size distributions, but the Rosin-Rammler relationship is considered satisfactory for the purposes of the present investigation.

Figure 11 illustrates the manner in which the Rosin-Rammler distribution parameter q varies with air velocity. With no air flowing the spray exhibits a relatively high value of q of around 3. Increase in air velocity from an initial value of zero causes q first to decline and then gradually to rise again. These data suggest that drop-size distributions are relatively narrow when the nozzle is operating in either a pressure or an airblast mode. However, over the range of air velocities where the air is impairing the effectiveness of the pressure nozzle by reducing the relative velocity between the initial liquid sheet and the surrounding air, this interaction leads to a broader distribution of drop sizes in the spray.

Spray Cone Angle. A widening of spray cone angle with increase in nozzle bypass ratio is a well-known characteristic of spill-return atomizers (Lefebvre, 1983). Some of the measurements of equivalent spray angle obtained by the method described above with no air flow are shown in Fig. 12. The

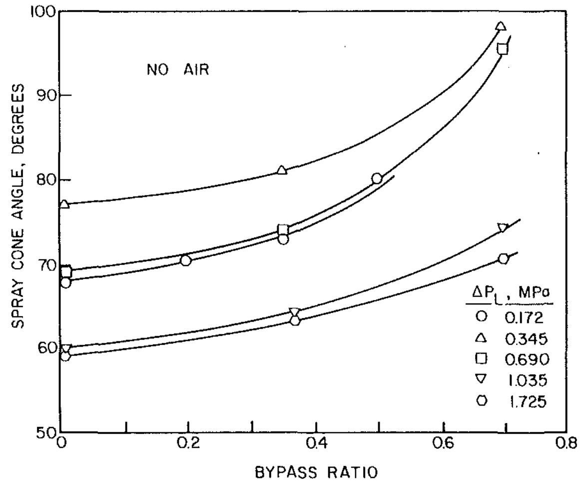

Fig. 12 Effects of changing bypass ratio and liquid pressure differential on equivalent spray angle

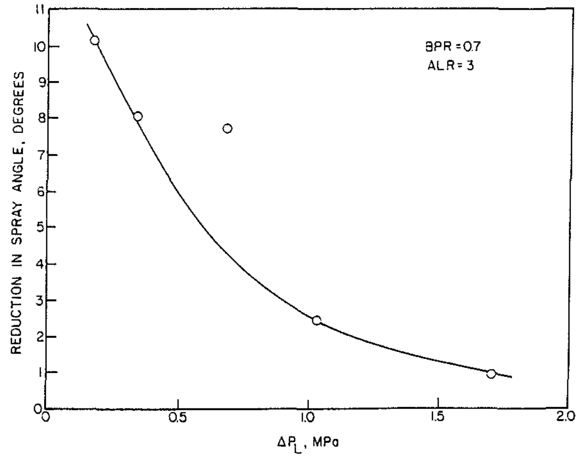

Fig. 13 Variation with liquid pressure differential of reduction in spray cone angle due to airblast air

results demonstrate, as expected, that increase in bypass ratio produces a significant widening of spray cone angle. Inspection of this figure also reveals that, starting from a liquid injection pressure of 0.172 MPa (25 psi), further increase in liquid pressure causes the spray angle to widen and then contract. This phenomenon was also observed by Ortman and Lefebvre (1985) and by Neya and Sato (1963).

If the swirling airblast air has a cone angle that is less than the nozzle cone angle without air, it will tend to lower the equivalent cone angle of the resultant spray. This effect is illustrated in Fig. 13 in which the reduction in equivalent cone angle is plotted against liquid injection pressure for an air/liquid ratio of 3. As would be expected, the influence of airblast air is most pronounced at low values of ΔP_L, where the spray momentum is low, and diminishes with increase in ΔP_L, i.e., with increase in liquid/air momentum ratio. From a gas turbine viewpoint this a most useful characteristic, since small spray angles are usually conducive to good lightup and lean blowout performance, both of which are associated with low fuel flow rates and low values of fuel injection pressure. At the high fuel injection pressures corresponding to high power conditions, a wide spray angle is desirable in order to minimize soot formation and exhaust smoke (Lefebvre, 1983). Figure 13 thus provides a useful demonstration of how airblast air may be used to control spray angle, and, in particular, to counter the widening of spray angle with increase in BPR that detracts from the practical usefulness of conventional spill-return nozzles when operating at low fuel flow rates.

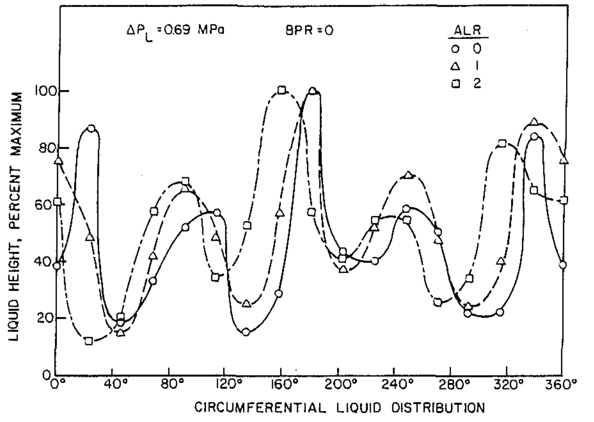

Fig. 14 Influence of atomizing air on circumferential liquid distribution

Circumferential Liquid Distribution. A large number of measurements of circumferential liquid distributions were made, both with and without airblast air. Figure 14 is typical of the results obtained. It shows that airblast air has little influence on circumferential liquid distribution, its main effect being to rotate the spray slightly in the direction of the air swirl.

Conclusions

The airblast spill-return atomizer lends itself to a wide variety of geometric configurations. These include variations in nozzle flow number, nominal liquid spray cone angle, flow area of air shroud, number of air swirl vanes, and swirl vane angle. Thus the test program described in this paper, which employed a single nozzle design, can in no way be regarded as comprehensive. However, many of the results obtained are considered to be characteristic of this type of atomizer, and allow the following conclusions to be drawn:

1 For any given value of liquid injection pressure, increase in airblast air velocity from an initial value of zero causes mean drop size to increase up to a maximum value, beyond which further increase in air velocity leads to finer atomization.

2 The airblast air velocity at which the mean drop size attains its maximum value increases with increase in liquid injection pressure.

3 In general, increase in airblast air velocity may improve or impair atomization quality depending on whether it increases or decreases the relative velocity between the liquid and the surrounding air.

4 Airblast air can be used to prevent or reduce the widening of spray cone angle that normally accompanies an increase in bypass ratio.

5 Airblast air appears to have little effect on circumferential liquid distribution.

References

Carey, F. H., 1954, "The Development of the Spill Flow Burner and Its Control System for Gas Turbine Engines," *Journal of the Royal Aeronautical Society*, Vol. 58, No. 527, pp. 737-753.

DeCorso, S. M., and Kemeny, G. A., 1957, "Effect of Ambient and Fuel Pressure on Nozzle Spray Angle," *ASME Transactions*, Vol. 79, No. 3, pp. 607-615.

Dodge, L. A., and Cerwin, S. A., 1984, "Extending the Applicability of Diffraction-Based Drop Sizing Instruments," in: *Liquid Particle Size Measurement Techniques*, ASTM STP 848, J. M. Tishkoff, R. D. Ingebo, and J. B. Kennedy, eds.

Dodge, L. G., 1984, "Change in Calibration of Diffraction-Based Particle Sizers in Dense Sprays," *Optical Engineering*, Vol. 23, No. 5, pp. 626-630.

Hirleman, E. D., Oechsle, V., and Chigier, N. A., 1984, "Response Characteristics of Laser Diffraction Particle Size Analyzers: Optical Sample Volume Extent and Lens Effects," *Optical Engineering*, Vol. 23, No. 5, pp. 610-619.

Lefebvre, A. H., 1983, *Gas Turbine Combustion*, Hemisphere Publishing Corporation, Washington, DC.

Neya, K., and Sato, S., 1968, "Effect of Ambient Air Pressure on the Spray Characteristics of Swirl Atomizers," Ship Research Institute, Tokyo, Paper No. 27.

Ortman, J., and Lefebvre, A. H., 1985, "Fuel Distributions From Pressure-Swirl Atomizers," *AIAA Journal of Propulsion and Power*, Vol. 1, No. 1, pp. 11-15.

Rizk, N. K., and Lefebvre, A. H., 1985, "Spray Characteristics of Spill-Return Atomizers," *AIAA Journal of Propulsion and Power*, Vol. 1, No. 3, pp. 200-204.

Rosin, P., and Rammler, E., 1933, "The Laws Governing the Fineness of Powdered Coal," *J. Inst. Fuel*, Vol. 7, No. 31, pp. 29-36.

Swithenbank, J., Beer, J. M., Taylor, D. S., Abbot, D., and McCreath, G. C., 1977, "Experimental Diagnostics in Gas Phase Combustion Engines," *Prog. Aeronaut. Astronaut.*, B. T. Zin, ed., AIAA, Vol. 53, p. 421.

N. Abuaf
General Electric Company,
Corporate Research and Development,
Schenectady, NY 12309

N. S. Rasmussen

L. C. Szema

General Electric Company,
Aircraft Engine Business Group,
Evendale, OH 45215

Flow in Liner Holes for Countercurrent Combustion Systems

Heavy-duty gas turbine combustion systems have a "reverse flow" combustion-cooling air network. High-temperature gradients have been observed in some combustion liners around the plain holes, or around the cylindrical inserts welded into the mixing holes. Flow visualization tests were performed in a countercurrent flow facility. Measurements of pressure and velocity distributions in and around the mixing hole jet were taken, and mass flow rates and discharge coefficients were calculated in order to characterize and compare the two geometries. The results with a plain hole (square-edged orifice) and the cylindrical insert show the presence of a sharp separation region at the trailing edge (combustion side) of the liner hole, which may cause the high-temperature gradients observed under operating conditions. The measured discharge coefficients show a dependence on the insert geometry, the flow parameter (K), and the bottom section (combustion side) countercurrent flow velocity.

Introduction

Heavy-duty gas turbine combustion systems have a "reverse flow" combustion-cooling air network. The combustor air supply originates from the compressor discharge and flows in one direction, while the air in the sleeve encircling the combustor liner is countercurrent to the combustion hot gas flow. The cross section of the sleeve varies axially along the liner. The minimum cross section is at the hottest reaction zone, resulting in the highest backside (crossflow) velocities. The countercurrent flow configuration is quite significant for combustor operation since it affects the discharge coefficients of the liner-mixing holes, the flow splits, and the jet penetration and mixing with the combustion air crossflow.

In some field units operating with square-edged holes or with cylindrical inserts, large temperature gradients have been observed between the leading and trailing edges of the liner-mixing hole passage. The overall objective of the present work was to investigate the countercurrent flow in the liner-mixing hole configurations in order to develop useful insight and design information that would improve the life expectancy of the combustor liners. For this purpose a cold countercurrent flow test facility was constructed, flow visualization tests were conducted, and pressure and velocity measurements were performed in and around the liner-mixing hole jets in order to characterize the flow phenomena.

Background

Discharge Coefficients. The flow through a liner hole, which determines the effective flow area and thus the discharge coefficient, is a complex phenomenon and depends on the geometries (relative dimensions) and on the flow conditions (pressure, velocity, swirl) on either side of the hole (Lefebvre, 1983; Dittrich and Graves, 1956). For air admission holes in typical combustors, the flows in the annulus (outside the liner) and inside the combustion chamber can be parallel to the plane of the opening and cocurrent, or parallel and countercurrent (in opposite directions) as in the present case.

The discharge coefficient is defined as

$$C_D = \frac{\dot{m}_a}{\dot{m}_t} \tag{1}$$

where $\dot{m}_a$ is the actual measured mass flow rate through the liner hole and $\dot{m}_t$ is the theoretical mass flow rate expected. The latter can be calculated from the isentropic flow relations using the annulus total pressure (P_{OT}) and temperature (T_{OT}), the jet static pressure in the combustion chamber (P_j), and the hole exit area (A_h) (Shapiro, 1953).

Dittrich and Graves (1956) and Dittrich (1958) investigated the effect of various geometric and flow factors on the discharge coefficients for several hole geometries. The flow in the annulus was parallel to the plane of the hole and discharged into a combustion chamber having zero velocity. The discharge coefficients were correlated with a flow parameter K, incorporating the total and static pressures of the discharge jet and of the parallel-flow stream in the annulus

$$K = \frac{P_{OT} - P_J}{P_{OT} - P_T} \tag{2}$$

where P_T is the static pressure of the annulus. This flow parameter represents the ratio of the jet dynamic pressure to the annulus dynamic pressure.

Contributed by the International Gas Turbine Institute and presented at the 33rd International Gas Turbine and Aeroengine Congress and Exhibition, Amsterdam, The Netherlands, June 5–9, 1988. Manuscript received by the International Gas Turbine Institute August 28, 1987. Paper No. 88-GT-158.

Marshall (1958) and Venneman (1960) extended the results to several scoop geometries and the latter measured the jet penetration angle. Both of these investigations had an annulus flow parallel to the plane of the hole, which was discharged into a zero velocity large reservoir representing the combustion chamber.

Lefebvre (1983) proposes an incompressible flow discharge coefficient calculation with

$$C_D = \frac{\dot{m}_A}{A_h\sqrt{2\rho_3(P_{OT}-P_j)}} \qquad (3)$$

where ρ_3 is a reference density. Since in gas turbines the combustor liner pressure drop does not exceed 5 percent of the total pressure, the maximum jet Mach numbers obtained are usually less than 0.3, thus justifying the incompressible flow assumption. The discharge coefficients for an annulus flow parallel to the plane of the hole, discharging into a zero velocity region, were first shown to depend on

$$C_D = \frac{\alpha}{A_r K^{0.5}} \qquad (4)$$

where α = hole mass flow rate/annulus mass flow rate, A_r = hole area/annulus area, and K is the flow parameter defined in equation (2). Lefebvre concluded that for incompressible, nonswirling flows, the discharge coefficients for circular, oval, and rectangular holes with parallel flow discharging into a zero velocity chamber can be correlated by the following expression:

$$C_D = \frac{1.25(K-1)}{[4K^2-K(2-\alpha)^2]^{0.5}} \qquad (5)$$

For plunged holes, it was found that the data can be correlated with the same expression except that the constant is 1.65 instead of 1.25. When the jet penetrating the combustion chamber is inclined at an angle with respect to the wall, Lefebvre proposed a correction to account for the initial jet angle.

We were unable to locate any information in the open literature that provides data or discharge coefficients for liner hole flows where there are strong cocurrent or countercurrent flows in the annulus and the combustion chamber at either side of the hole.

Jet Flow Field and Jet Penetration. In the combustion chamber a good mixing is essential for efficient combustion and the attainment of a satisfactory temperature distribution in the exhaust gases. This mixing will be affected by the trajectory of the air jets.

Demuren (1986) proposes the following expression for the trajectory of a single circular jet injected normally to a crossflow:

$$\frac{y}{D_h} = aR^b\left[\frac{x}{D_h}\right]^C \qquad 1.4 < R < 50 \qquad (6)$$

The coordinates, y and x, are parallel and perpendicular to the jet inlet velocity, D is the jet diameter, and R is the jet-to-crossflow velocity ratio ($R = U_j/U_g$). The constant a has a value between 0.75 and 1.31, b varies between 0.74 and 1.0, and C varies between 0.33 and 0.39, depending on the experimental conditions. This expression is similar to the following relationship recommended by Lefebvre (1983):

$$\frac{y}{D_h} = 0.82\left[\frac{\rho_j U_j^2}{\rho_g U_g^2}\right]^{0.5}\left[\frac{x}{D_h}\right]^{0.33} \qquad (7)$$

For a single jet injected at an angle θ, the trajectory could be obtained by multiplying h/D_h for 90 deg by sin θ. Lefebvre (1983) proposes the following expression for the maximum penetration of a single round jet injected into a circular duct:

$$\frac{Y_{\max}}{D_h} = 1.15\left[\frac{\rho_j U_j^2}{\rho_g U_g^2}\right]^{0.5} \sin\theta \qquad (8)$$

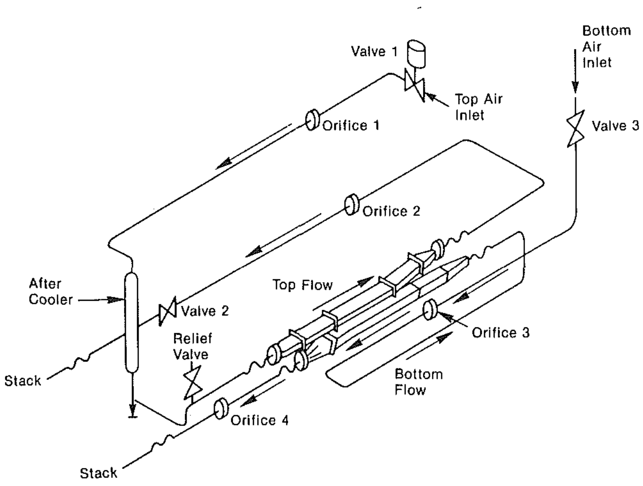

Fig. 1 Flow and piping diagram for the countercurrent test facility

Experimental

Description of the Test Rig. A sketch of the main piping arrangement used in the present study is shown in Fig. 1. The setup consists of two countercurrent flow systems fed by the same centrifugal compressor capable of providing a maximum air flow rate of 4.53 kg/s at a maximum pressure of 1.72 × 10^6 N/m^2. The upper flow is controlled by Valve 1, and its value is determined by a 5.08-cm square-edged orifice 1, positioned in a 10.16-cm nomimal schedule 40 pipe. Some of the air flowing into the upper section of the plexiglass test rig is diverted into the lower section through the liner hole because of the pressure difference existing between the upper and lower sections. The air remaining in the upper section proceeds through orifice 2, 5.08 cm in diameter, located in a 10.16-cm nominal schedule 10 pipe. A hand-operated Valve 2 situated downstream of this second orifice controls the amount of the mass flow diverted through the liner hole. The upper section air is then discharged into the stack.

The counterflow system flowing through the lower section is fed by the same compressor and is controlled by Valve 3. The flow rate of the air entering the lower section is measured by orifice 3 (7.62 cm in diameter) positioned in a nominal 10.16-cm schedule 10 pipe. The flow exiting the lower part of the test section, formed by the flow entering the lower section and by the flow diverted from the upper section, is measured at orifice 4, having a diameter of 8.89 cm and located in a 10.16-cm schedule 10 pipe. The pressures upstream of the orifices are measured by means of Bourdon gauges having a maximum range of 2.07 × 10^5 N/m^2 and an accuracy of 1.38 × 10^3 N/m^2. The pressure drops across the orifices are measured by variable inductance pressure transducers providing 10-V output for a pressure range of 6.895 × 10^4 N/m^2. The air temperatures are measured by copper-constantan thermocouples positioned six diameters downstream of the orifices. The measurement of the inlet and exit air flow rates for both the upper and lower passages of the test section allows a double check on the mass balance of the system and on the air mass flow rate, which is diverted from the upper to the lower section through the interconnecting liner vent hole. A relief valve was included in the upper part of the test section upstream of the plexiglass section.

The details of the plexiglass counterflow test section are presented in Fig. 2. The upper part of the test section consists of a transition piece (No. 1), which goes from a 10.16-cm i.d. circular cross section to a 3.18-cm-high, 17.78-cm-wide rectangular cross section. The 30.48-cm-long flow-straightening section has a perforated plate at the upstream flange connection and a honeycomb flow straightener. The upper flow then proceeds through the 99.06 cm long 3.18×17.78 cm rec-

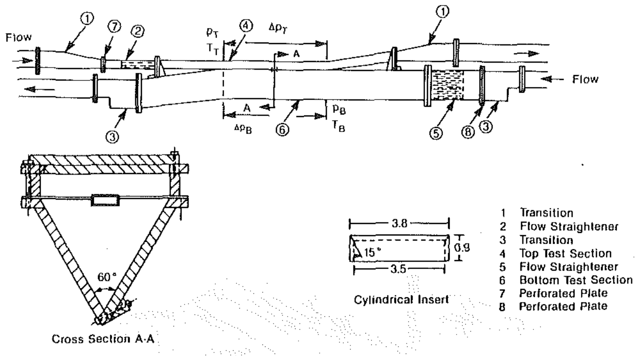

Fig. 2 Details of the plexiglass counterflow test section (dimensions in cm)

tangular section, which accommodates the liner vent hole connecting the upper and lower parts of the test section. The liner vent hole is located 73.66 cm from the inlet of this section No. 4. The flow exiting the upper section goes through a discharge transition section that changes the rectangular cross section into a circular one with a diameter of 10.8 cm. The plexiglass test section is attached to the metal pipes by means of flexible rubber tubing in order to isolate it from the vibrations of the metallic parts.

The lower section air stream flowing in the opposite direction is fed from a 10.16-cm schedule 10 pipe into a transition piece, which changes the circular cross section into an equilateral triangle. The 30.48-cm-long flow-straightening section has a perforated plate at the inlet and a honeycomb flow straightener in the passage. The 121.9-cm-long lower test section is triangular in shape with all three sides equal to 17.78 cm. The air exiting the lower plexiglass section turns slightly downward and flows into a transition piece, which converts the triangular cross section into a circular one.

The details of the upper and lower cross sections of the plexiglass test section are presented in Fig. 2. They represent a 60-deg sector of the flow in the main combustor chamber and in the annulus between the liner and the flow sleeve. For ease of fabrication, the curvature of both the flow sleeve and the liner was eliminated and the circular sector was replaced with a triangular one. A 0.32-cm-thick stainless steel wall separated the upper and lower sections. The liner hole insert could be placed in a removable plate, which is connected to the steel separating wall. The removable plate could be reached through a circular opening cut into the top plexiglass wall of the upper section.

The static pressure at the upper section p_t was measured 30.48 cm upstream of the liner hole center by means of a Heise gage having a range of 0-2.07 × 10^5 N/m^2 and an accuracy of 3.45 × 10^2 N/m^2. Similarly the static pressure of the lower section p_b was monitored by a second Heise gage having a similar range and accuracy. The air temperatures at the upper and lower sections, T_t and T_b, were also measured at the same locations by means of two copper constantan thermocouples. The pressure drop across two points, situated 30.48 cm upstream and 30.48 cm downstream of the liner hole center, Δp_t and Δp_b, was measured by means of two inclined water manometers. Similarly, the pressure drop across the upper and lower sections at the inlet locations, $\Delta p_{t\text{-}b}$, was measured by means of a third water manometer. The uniformity of the velocity distributions at the inlet sections, located 30.48 cm upstream of the liner hole center, both at the upper and lower sections, was measured by means of a cobra-type traversing Pitot tube with a yaw angle zeroing capability.

Tests were run with a square-edged hole, having a diameter of 3.81 cm and a wall thickness of 0.28 cm, and with a cylindrical insert, which was centered in the liner hole (to simulate the real life configuration). The specific geometry of this cylindrical insert is depicted in Fig. 2. It consists of a 3.81-cm o.d. and 3.45-cm i.d. circular insert, 0.92 cm long, and having a rounded inlet. A smoke generator operating with odorless kerosene (Kerosun) was used for flow visualization studies. The smoke injection occurred through a 0.16-cm **L**-shaped stainless steel tube positioned in the upper part of the plexiglass test section, 30.48 cm upstream of the liner hold center. This **L**-shaped tube, through which the smoke discharged into the flowing air stream, could be traversed up or down in the rectangular cross section, thus introducing smoke at several heights upstream of the liner hole. The smoke traces, which were backlighted in darkened surroundings, were recorded photographically with a 35-mm camera in a fixed position with a 50-mm lens and an ASA 200 color print film. A Pitot tube rake was used to measure velocity distributions at fixed points along the discharge area of the liner hole at a distance of 2.54 cm downstream of the liner hole in the lower section. The Pitot rake consists of five 0.16-cm stainless steel tubes bent into **L**-shapes and held together at a distance of 0.82 cm between two consecutive tubes. Each tube of the Pitot rake was connected to the high side of a water manometer bank, with the low common sides connected to a static pressure tap situated along the lower wall 5.08 cm upstream of the liner hole.

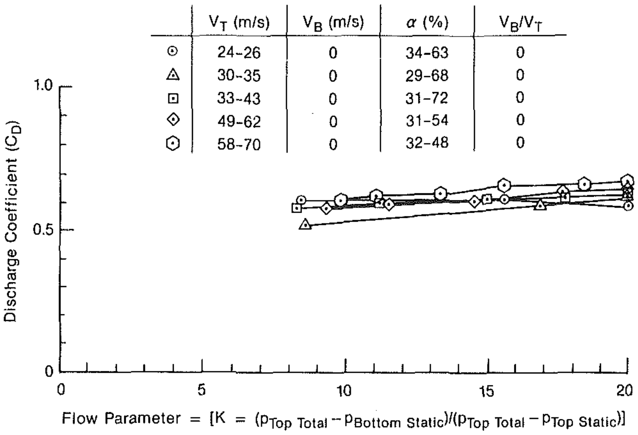

	V_T (m/s)	V_B (m/s)	α (%)	V_B/V_T
⊙	24-26	0	34-63	0
△	30-35	0	29-68	0
⊡	33-43	0	31-72	0
◇	49-62	0	31-54	0
⬡	58-70	0	32-48	0

Fig. 3 *Variation of discharge coefficient with flow parameter (K) for the square-edged hole for zero mainstream (bottom) flow velocity (V_T = top flow velocity, V_B = bottom flow velocity, α = percent of top flow diverted through liner hole)*

Results

Discharge Coefficient Data. For the discharge coefficient calculations, although all the variables such as hole exit area (A_h), total pressure (p_{oT}), and temperature (T_{oT}) of the annulus are well defined for the given configuration, the jet static pressure at the exit area in the main chamber is a quantity that is not well defined. In a counterflowing stream, a strong variation of the static pressure would be expected to occur along the 360-deg periphery of the jet at the exit area. Since we were lacking the information on the complete static pressure distribution around the jet exit, the jet static pressure at the discharge was taken as the static pressure measured 30.48 cm upstream of the hole minus half the pressure drop measured between this location and the static pressure tap located 30.48 cm downstream of the liner hole. To be more rigorous one would need to measure the static pressure distribution around the liner hole and calculate an integrated average.

Figure 3 presents the discharge coefficient data as a function of the dimensionless flow parameter (K), defined by equation (2), for five cases where the bottom incoming air velocity was kept at zero and the top air velocity was increased from 25.3 to 64.0 m/s, while 29 to 72 percent of the top air mass flow rate was diverted through the liner hole into the bottom region. The presented data show that the discharge coefficients vary between 0.55 and 0.6 and there is no obvious trend with varying top airstream velocity. Figure 4, on the other hand, presents the discharge coefficients measured with the bottom air flow velocity of 61.0 m/s, while the top airstream velocity was increased from 28.7 to 52.1 m/s. The discharge coefficients for the small values of *K* (1 to 4) show an increase and then level to a value of 0.7 for the larger values of the flow parameter *K*. This limit is higher than the value of 0.6 quoted for the results presented in Fig. 3, when the bottom air stream velocity was equal to zero. Figure 5, drawn with an amplified ordinate scale covering a discharge coefficient range from 0.5 to 1.0, clearly depicts the dependence of the discharge coefficient on the bottom air stream velocity. During these tests, the top air velocity was kept constant at 30.5 m/s, while the bottom air velocity was increased from 0 to 64.0 m/s. The discharge coefficients for the large values of *K* increase from 0.6 to 0.7 as the bottom inlet air stream velocity increases.

Figure 6 represents the variation of the discharge coefficient with the flow parameter *K*, obtained with the cylindrical insert, while the bottom air velocity is zero and the top air velocity was varied from 17.4 to 43.0 m/s. The results show once again little effect of this parameter and the average value of the discharge coefficient for the large values of *K* is 0.65. Most of the test results presented were repeated more than once in order to check the accuracy of the instrumentation and the repeatability of the results. Figure 7, drawn with an amplified ordinate scale, represents the variation of the discharge coefficient with the flow parameter *K*, for several cases where the top air flow velocity was kept constant at 30.5 m/s and the bottom air velocity was increased from zero to 64.0 m/s, while the ratio of the top air mass flow rate diverted through the hole varied between 5 and 73 percent. The data once again show the dependence of the discharge coefficient on the bottom air velocity. The value of the discharge coefficient at a *K* value of 16 increases from 0.65 to 0.7 as the air velocity at the bottom increases. The plots show that the discharge coefficients do not level off completely to the asymptotic constant value at flow parameters (*K*), which are larger than the ones presented for the square-edged orifice. The present data reach a constant discharge coefficient value when *K* is larger than 10, while those for the square-edged orifice reached the constant discharge coefficient values when *K* was larger than 6.

Jet Penetration Photographs. In the photographs presented, the flow in the top section (not recorded in the photos) is from right to left, while the flow in the bottom triangular section (combustor flow) is from left to right. The photographs depict the liner hole viewed from the bottom with the penetrating jet highlighted by the injected smoke. The jet penetrating into the bottom section through the liner hole is entrained by the crossflow in the bottom section and changes its direction, thus becoming coflowing with the bottom flow.

Figure 8(*a*) presents the photograph of the jet penetration for top and bottom velocities of 34.0 m/s. The static pressure ratio (p_t/p_b) is 1.012, while the flow parameter (*K*) is 2.82 and 21 percent of the top flow is diverted into the bottom through the liner hole orifice. The effect of the top flow, moving from right to left, is clearly observed in the initial region of the jet

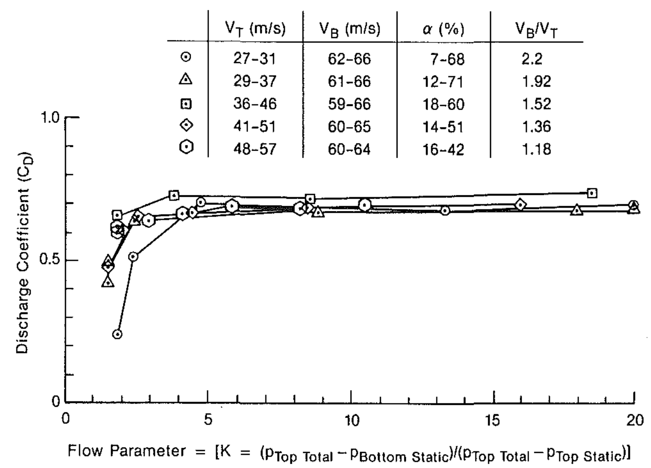

	V_T (m/s)	V_B (m/s)	α (%)	V_B/V_T
⊙	27-31	62-66	7-68	2.2
◬	29-37	61-66	12-71	1.92
⊡	36-46	59-66	18-60	1.52
◈	41-51	60-65	14-51	1.36
⬡	48-57	60-64	16-42	1.18

Fig. 4 Variation of discharge coefficients with flow parameter (*K*) for the square-edged hole for a constant mainstream (bottom) flow velocity of ~ 60 m/s

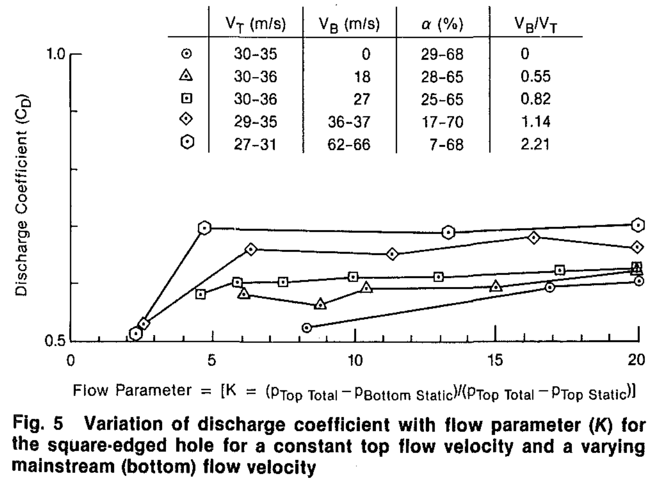

	V_T (m/s)	V_B (m/s)	α (%)	V_B/V_T
⊙	30-35	0	29-68	0
◬	30-36	18	28-65	0.55
⊡	30-36	27	25-65	0.82
◈	29-35	36-37	17-70	1.14
⬡	27-31	62-66	7-68	2.21

Fig. 5 Variation of discharge coefficient with flow parameter (*K*) for the square-edged hole for a constant top flow velocity and a varying mainstream (bottom) flow velocity

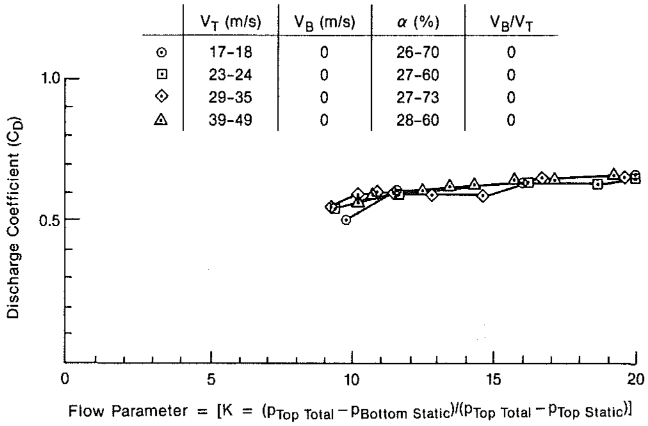

	V_T (m/s)	V_B (m/s)	α (%)	V_B/V_T
⊙	17-18	0	26-70	0
⊡	23-24	0	27-60	0
◈	29-35	0	27-73	0
◬	39-49	0	28-60	0

Fig. 6 Variation of discharge coefficients with flow parameter (*K*) for cylindrical insert for zero mainstream (bottom) flow velocity

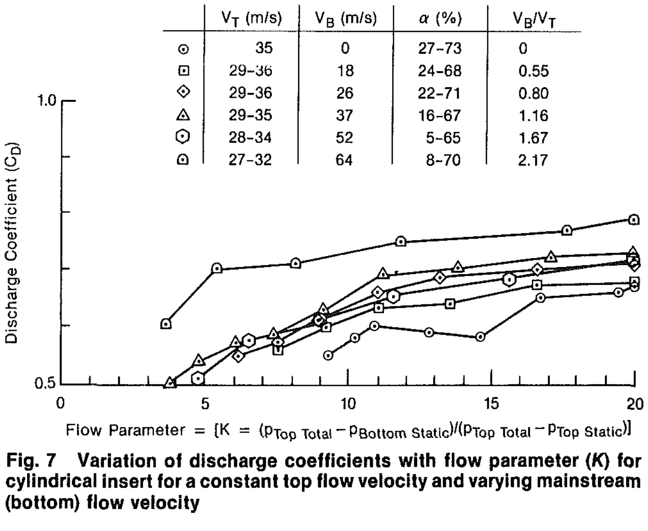

	V_T (m/s)	V_B (m/s)	α (%)	V_B/V_T
⊙	35	0	27-73	0
⊡	29-36	18	24-68	0.55
◈	29-36	26	22-71	0.80
◬	29-35	37	16-67	1.16
⬡	28-34	52	5-65	1.67
⌂	27-32	64	8-70	2.17

Fig. 7 Variation of discharge coefficients with flow parameter (*K*) for cylindrical insert for a constant top flow velocity and varying mainstream (bottom) flow velocity

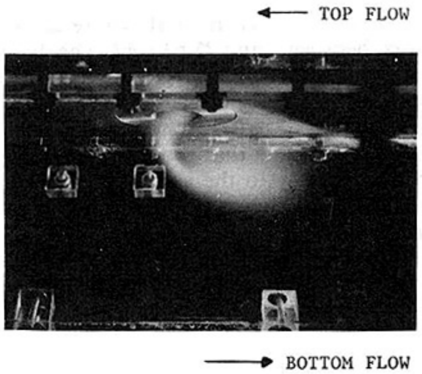

8.a
$V_T = 33$ m/s $V_B = 34$ m/s
$K = 2.82$ $p_T/p_B = 1.012$
$\alpha = 0.21$ $C_D = 0.62$

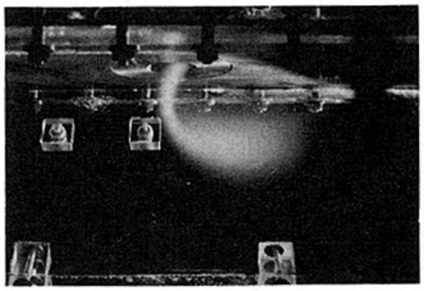

8.b
$V_T = 32$ m/s $V_B = 34$ m/s
$K = 5.56$ $p_T/p_B = 1.029$
$\alpha = 0.32$ $C_D = 0.68$

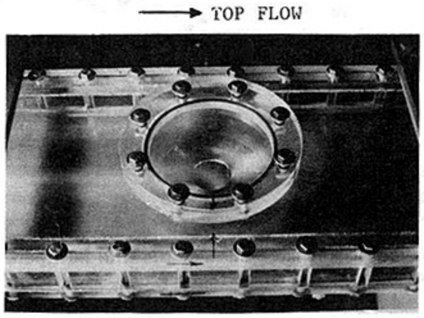

8.c
Top View

Fig. 8 Jet penetration photographs for the square-edged plain

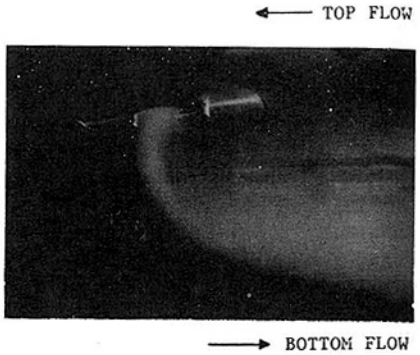

9.a
$V_T = 18$ m/s $V_B = 17$ m/s
$K = 4.2$ $p_T/p_B = 1.006$
$\alpha = 0.22$ $C_D = 0.66$

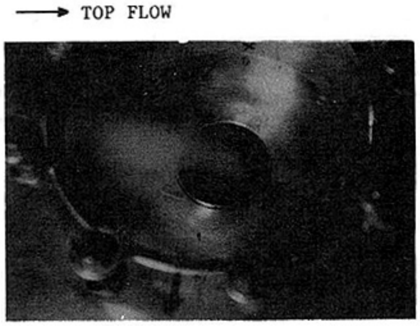

9.b
Top View

Fig. 9 Jet penetration photographs for the cylindrical insert

close to the liner hole exit. The jet enters at an angle opposite to the flow in the bottom section. The flow at the bottom section opposing the jet makes its turn to become first normal and then cocurrent with the bottom flow direction. The photo shows that the jet does not completely fill the physical liner hole cross-sectional area (C_D is 0.62). There is a large recirculation region observed downstream of the jet and near the liner wall. Figure 8(*b*) shows the effect of increasing the fraction of the top mass flow rate, which is diverted into the bottom section (α increasing from 0.21 to 0.32). The top and bottom flow velocities are kept nearly constant at values of approximately 32.6 and 34.1 m/s. The variation in α is made by closing the valve downstream of the top test section and thus increasing the static pressure ratio (p_t/p_b) from 1.012 to 1.029. The flow parameters (*Ks*) for the two photos are 2.82 and 5.56, respectively, while the respective discharge coefficients are 0.62 and 0.68. As the parameter α increases, the jet penetrating into the bottom section appears to center itself in the hole and the penetration angle approaches the normal to the liner wall. Figure 8(*c*) is a view showing the top portion of the test section for the jet depicted in Fig. 8(*a*). The smoke stream is injected from the left of the photo and travels from left to right toward the liner hole entrance. One can see the turning of the flow entering the hole and the separation region between the upstream wall of the hole and the smoke streamlines.

Figure 9(*a*) is a photograph of the jet penetrating into the bottom section obtained with the cylindrical insert at top and bottom velocities of 17.7 and 17.4 m/s, a static pressure ratio (p_t/p_b) of 1.006, a flow parameter (*K*) of 4.21, a discharge coefficient of 0.66, while 22 percent of the top flow is diverted through the hole. The observations imply that the flow being diverted through the field insert impinges first onto the back wall of the insert, changes direction, and appears to penetrate the bottom section crossflow in a more normal direction with respect to the wall than what was observed with the square edge orifice. The photo also shows that the jet attaches to the impingement (back) wall of the insert while the opposite wall is completely free. The limiting streamline originates at this wall, separates from the wall, and crosses the hole somewhere in the middle of the open area. This characteristic description of the flow field is clearly seen in Fig. 9(*b*), which was recorded under the same flow conditions, except that it depicts the top part of the test section with the smoke stream coming from the left and turning toward the liner hole having the field insert in position. During combustion conditions, the wall of the

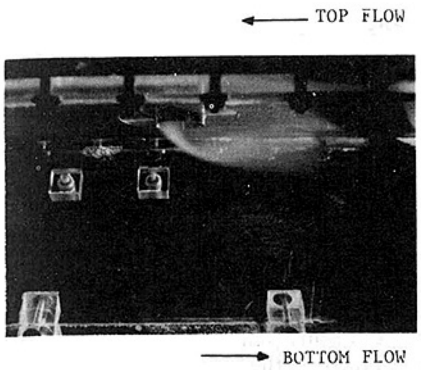

10.a
V_T = 31 m/s
K = 1.47
α = 0.006
V_B = 44 m/s
p_T/p_B = 44 m/s
C_D = 0.3

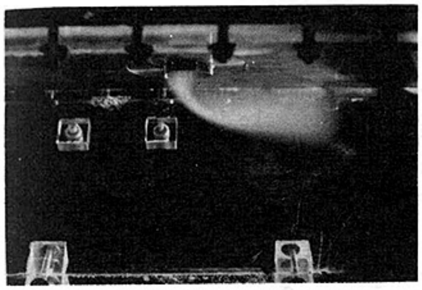

10.b
V_T = 31 m/s
K = 2.55
α = 0.14
V_B = 43 m/s
p_T/p_B = 1.009
C_D = 0.52

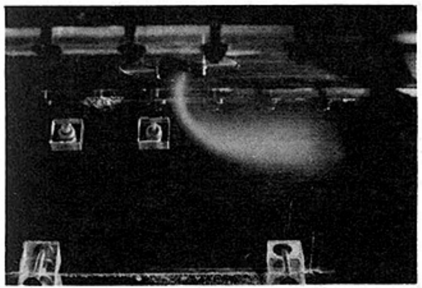

10.c
V_T = 30 m/s
K = 7.02
α = 0.27
V_B = 43 m/s
p_T/p_B = 1.033
C_D = 0.64

Fig. 10 Jet penetration photographs for the cylindrical insert with constant top and mainstream (bottom) flow velocities, while larger amounts of the top flow are directed to the bottom

cylindrical insert where the flow impinges before being diverted into the bottom section will be cooled quite efficiently by the cooler (compressor discharge) air. On the other hand, at the opposite wall of the liner insert, where the streamline separates, the wall will not be affected by the cooler top flow, but the hot combustion gases trapped into the circulation region would penetrate into the wall (see Figs. 8*a* and 9*a*). This will generate a hot spot in contrast to the cold region existing at the opposite wall, thus creating a large temperature gradient along the side-walls of the insert.

Figures 10(*a*), 10(*b*), and 10(*c*) were obtained with a top flow velocity of 30.8 m/s and a bottom section flow velocity of 43.3 m/s. Figure 10(*a*) was recorded with a top-to-bottom-pressure ratio (p_t/p_b) of 1.003, a K value of 1.47, a discharge coefficient of 0.3, while only 6 percent of the top flow was diverted through the hole. Figure 10(*b*), on the other hand, has a pressure ratio (p_t/p_b) of 1.009, a flow parameter K of 2.55, a discharge coefficient of 0.52, and 14 percent of the top flow is diverted through the hole. This increase in the flow provides a jet penetrating deeper into the bottom section. Figure 10(*c*) corresponds to still higher pressure ratios of 1.033, with 27 percent of the top flow being diverted through the liner hole. The flow parameters and discharge coefficients are 7.02 and 0.64. In these last photographs one could once again observe the centering of the jet in the liner insert opening as the air mass diverted from the top to the bottom through the hole increases.

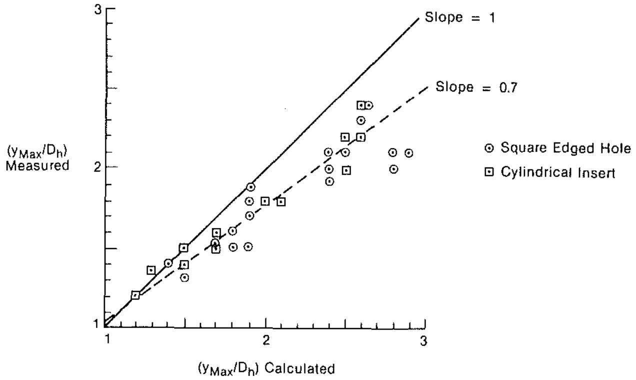

Fig. 11 Comparison of the measured jet penetration with those calculated from equation (8)

Jet Penetration. The photographs depict the limiting streamline separating the jet from the bottom section air flow. This limiting streamline originates at the hole entrance, penetrates into the bottom section, is entrained with the bottom crossflow, and reaches an asymptotic distance from the simulated liner wall. This maximum penetration distance of the streamline below the jet entrance was measured and taken as the representative jet penetration length. These measured penetration distances were compared with those calculated from equation (8) proposed by Lefebvre (1983) for jets with an injection angle of 90 deg. The jet momentum in the numerator was calculated from the measured pressure ratios and the corresponding adiabatic expansion velocities and densities. The bottom cross-flow momentum in the denominator was calculated from the measured bottom section mass flow rate, pressure, and temperature test conditions. The maximum jet penetration distance in equation (8) involves the mid streamline of the jet and not the limiting trajectory as measured in the present work. Since we did not measure detailed velocity distributions, this information is not available at the present time. Thus, our comparison will be qualitative in nature and the equation provides a phenomenological basis for the comparison.

In Fig. 11, the calculated values of the jet penetration are plotted versus the measured ones. The results for the plain hole orifice and the cylindrical insert are close to each other, and a linear regression through all the points shows that they follow a line with a slope of 0.7 (dashed line). The comparison was stopped at a penetration distance of three hole diameters since at larger penetration distances one would expect side-wall effects caused by the test facility's triangular shape of the bottom cross section.

Lefebvre's equation (1983) and all the other jet penetration studies discussed above assume a uniform velocity distribution at the jet inlet. Although qualitative and not very accurate, the above results show that for similar jets to crossflow momentum ratios, the jets discharging with a uniform velocity will penetrate deeper than the jets obtained from the plain hole orifice or the cylindrical inset. The uniform velocity assumption, as will be shown in the next section, may not be justified for the plain hole or for the cylindrical insert.

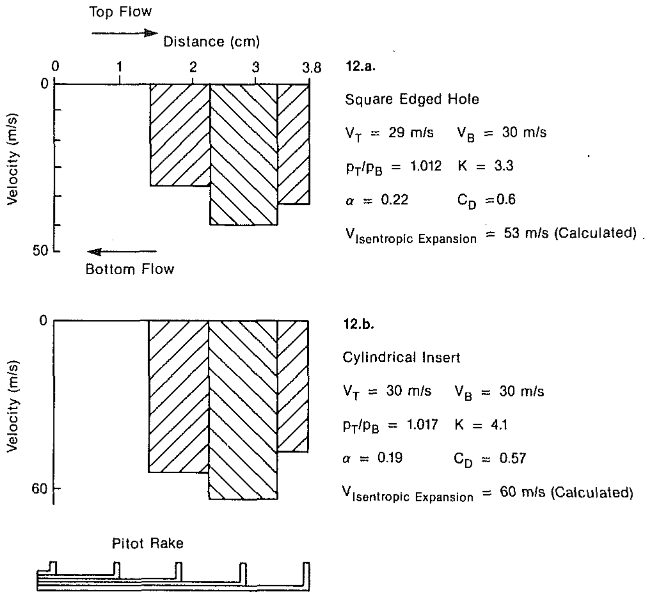

Fig. 12 Velocity distributions measured with the Pitot rake with the square-edged hole and the cylindrical insert

Pitot Rake Data. Figures 12(*a*) and 12(*b*) depict velocity distributions obtained with the plain hole and the cylindrical insert for a top section flow velocity of 29.3 m/s and a bottom flow velocity of 30.2 m/s. The two distributions are very similar in nature. The first two Pitot tubes, facing the upsteam direction of the top flow, do not record any positive velocity, while the three Pitot tubes situated midway and toward the downstream wall show that all the flow penetrates through the downstream half of the mixing hole. The maximum value of the velocity measured agrees quite closely with the velocity calculated assuming an isentropic expansion from the top pressure to the bottom one. This nonuniform characteristic of velocity distributions is consistent with the flow visualization photographs where the smoke jet appears to fill only half of the mixing hole. Similar velocity distributions were also measured with top and bottom section flow velocities of 19.0 and 23.0 m/s. The distributions are similar except that the absolute values are lower.

Detailed local velocity measurements are necessary with controlled jet inlet velocity distributions in order to investigate this hypothesis and to quantify the effect on the jet penetration distances.

Conclusions

The experimental development work, performed and reported above for the two combustor liner hole geometries and the associated flows, has resulted in the following conclusions:

- The discharge coefficients measured with plain hole and the cylindrical insert depend on the insert geometry.
- The discharge coefficients depend on the countercurrent bottom section flow velocity. They increase with the bottom flow velocities.
- This dependence can have important implications on the liner hole performance in real combustor operation under various loads. It means that for a constant pressure ratio, the flow diverted through the liner hole into the combustion chamber will vary with the countercurrent bottom section flow velocity.
- The flow diverted from the top and forming the jet penetrating into the bottom section through the liner hole does not fill the hole completely. The observed flow fields depict a recirculation region, which can explain the large temperature gradients measured across the liner holes while operating under real combustor conditions.
- The jet penetration information (flow visualization photographs) and the Pitot rake data showed that for the same jet-to-crossflow momentum ratios, the jets originating from the plain hole or from the cylindrical insert having a skewed velocity profile penetrate less than the predictions based on a uniform velocity distribution.

Acknowledgments

The authors would like to thank S. P. Urbaetis and O. F. Palmer for designing the test section and helping in the testing and D. Rhodes for typing the manuscript.

References

Demuren, A. O., 1986, "Modeling Turbulent Jets in Crossflow," *Encyclopedia of Fluid Mechanics*, N. P. Cheremisinoff, ed., Gulf Publishing Co., Houston, Vol. 2, Sec. II, Chap. 17, pp. 430-465.

Dittrich, R. T., 1953, "Discharge Coefficients for Combustor Liner Air Entry Holes, II—Flush Rectangular Holes, Step Louvers, and Scoops," NACA TN 3924.

Dittrich, R. T., and Graves, C. C., 1956, "Discharge Coefficients for Combustor Liner Air Entry Holes, I—Circular Holes With Parallel Flow," NACA TN 3663.

Lefebvre, A. H., 1983, *Gas Turbine Combustion*, McGraw-Hill, New York.

Marshall, L. A., 1958, "Aerodynamic Characteristics of Combustion Liner Air Entry Passages," R58AGT558, AGTD, GE, OH.

Shapiro, A. H., 1953, *Compressible Fluid Flow*, The Ronald Press Co., New York.

Venneman, W. F., 1960, "Flow Coefficients and Jet Deflection Angles for Combustor Liner Entry Holes, Part II," 60GL184, GE, General Engineering Lab.

Ö. L. Gülder

B. Glavinčevski

National Research Council of Canada,
Division of Mechanical Engineering,
Ottawa, Ontario K1A 0R6, Canada

S. Das

Engine Laboratory,
Indian Institute of Petroleum,
Dehradun-248005, India

Effect of Molecular Structure on Soot Formation Characteristics of Aviation Turbine Fuels

The smoke point has been shown to be quantitatively related to the molecular structure of hydrocarbon fuels. A fast technique of determining the molecular composition of commercial and experimental fuels, in terms of carbon type structure, by using proton nuclear magnetic resonance (^1H NMR) spectrometry, has been described. By measuring the smoke point soot yields of a laminar diffusion flame with a group of fuels—all having a constant hydrogen-to-carbon ratio—it has been shown that neither the smoke point nor the hydrogen-to-carbon ratio alone can describe the sooting propensity of turbine fuels. Obtained results indicate that smoke points and hydrogen-to-carbon ratio are complementary to each other in describing the sooting propensities of turbine fuels. This has been further tested using the available data in literature obtained from gas turbine combustors and diffusion flames.

Introduction

The contribution of soot particles to the radiative heat transfer in gas turbine combustion chambers has become one of the major concerns in recent years. The subject of soot formation, both in diffusion and premixed flames, is being extensively studied in order to decipher the formation mechanisms. Despite considerable progress in the understanding of soot formation, we still do not have sufficient details of soot formation mechanisms to be able to calculate the sooting tendency of a given hydrocarbon fuel from first principles. The empirical approach of determining the smoke point of the fuel provides an arbitrary measure of sooting tendency of laminar diffusion flames (see, e.g., Schug et al., 1980; Glassman and Yaccarino, 1980; Glassman and Yaccarino, 1981; Markstein, 1985) in which the fuel chemistry dominates the soot formation rate for a given burner geometry. Also, recently reported research results have revealed that soot concentration in diffusion flames can be quantitatively related to the smoke point fuel flow rate (Kent, 1986), and a linear relationship exists between smoke point values and smoke point heat release rates (Markstein, 1987).

The ASTM smoke point, the minimum flame height at which soot just escapes from a laminar diffusion flame tip generated by a standard wick burner, has been used for decades to predict the soot formation tendency of aviation gas turbine fuels. In recent years, hydrogen content has been proposed as a better predictor of the sooting tendency of aviation fuels (Blazowski, 1980; Naegeli and Moses, 1980; Bowden et al., 1984). Also, total aromatic content of the fuel and polycyclic aromatic content have been used by some investigators to describe the soot radiation in combustors (Clark, 1984). Each of these available sooting tendency predictors is being widely criticized because none of them are fully capable of describing the soot radiation encountered in gas turbine combustors. Recently, a new premixed flame technique has been proposed (Carrier and Wetton, 1988) to assess the sooting tendency of aviation turbine fuels.

Although a basic understanding of the effects of fuel hydrocarbon type composition on sooting tendency has evolved as a result of extensive experimental work, there exist two major problems that prevent the establishment of empirical or semi-empirical models for the prediction of sooting tendencies of complex hydrocarbon mixtures from the known sooting tendencies of the individual hydrocarbons contained in the fuel by using a suitable mixing algorithm. The first of these problems is related to the number of components in an aviation fuel. The identification and quantification tasks of several hundreds of components are very arduous and time consuming, if at all possible. The second problem is related to the characteristics of the hydrocarbons. The components in a given complex hydrocarbon mixture can be grouped into a few homologous hydrocarbon series. However, each member of a given homologous series may not have the same sooting tendencies. This means that a reliable data base, which contains the sooting tendencies of all possible components of a complex hydrocarbon mixture, should be established.

In this work, we will show why a single fuel parameter (like smoke point, or hydrogen content, or aromaticity) can not adequately represent the sooting tendency of aviation turbine fuels. Then, a description of the effects of fuel molecular composition, in terms of average carbon type structure, on

---

Contributed by the International Gas Turbine Institute and presented at the 33rd International Gas Turbine and Aeroengine Congress and Exhibition, Amsterdam, The Netherlands, June 5–9, 1988. Manuscript received by the International Gas Turbine Institute September 1987. Paper No. 88-GT-21.

Table 1 Carbon type structural composition and smoke points of the fuels in set 1 with a hydrogen-to-carbon ratio of 1.54. First column gives the components in the blend and the mole fraction of each component. Symbols denoting components in column 1 are listed at the bottom of the table.

Comp. (Mol fract.)	C_a	C_α	C_2	C_3	ψ	S, mm
A/C/G (0.153/0.123/0.724)	52.7	17.6	17.5	12.2	1.54	11.8
C/G (0.26/0.74)	52.1	17.4	24.4	6.1	1.54	12.3
A/F (0.329/0.671)	54.9	9.2	13.5	22.4	1.54	13.2
A/D/F (0.191/0.096/0.713)	53.1	8.9	23.8	14.2	1.54	12.7
A/E (0.363/0.637)	56.8	0.	16.2	27.	1.54	18.8
D/E (0.257/0.743)	52.	0.	42.	6.	1.54	18.8
D/H (0.425/0.574)	43.7	4.4	45.4	6.5	1.54	11.8
A/H (0.55/0.45)	48.1	4.8	17.6	29.5	1.54	10.7
D/F/H (0.321/0.412/0.267)	46.9	6.2	41.	5.9	1.54	13.
A/G/H (0.431/0.326/0.243)	50.2	10.3	14.8	24.7	1.54	11.8
C/E (0.329/0.671)	55.	0.	36.	9.	1.54	21.2
C/F (0.296/0.704)	53.6	8.9	30.	7.5	1.54	15.7
B/E (0.383/0.617)	58.	0.	30.	12.	1.54	20.8
B/F (0.348/0.652)	55.9	9.3	24.9	9.9	1.54	14.5
I (1.)	46.1	7.7	38.5	7.7	1.54	13.3

A = *iso*-octane
B = *n*-heptane
C = *n*-decane
D = *n*-hexadecane
E = benzene
F = toluene
G = xylene
H = 1-methylnaphthalene
I = 1-phenylheptane

Table 2 Carbon type structural composition and smoke points of the fuels in set 2 with hydrogen-to-carbon ratios from 1.513 to 1.905

Comp. (Mol fract.)	C_a	C_α	C_2	C_3	ψ	S, mm
A/C/G (0.257/0.13/0.614)	44.6	14.8	21.9	18.7	1.648	12.8
C/G (0.305/0.695)	48.4	16.1	28.3	7.1	1.587	13.
A/F (0.359/0.641)	52.3	8.7	14.6	24.4	1.575	13.3
A/D/F (0.19/0.192/0.618)	41.6	6.9	36.5	15.	1.668	14.2
A/E (0.432/0568)	49.7	0.	18.9	31.4	1.629	18.2
D/E (0.48/0.52)	28.9	0.	62.2	8.9	1.8	33.7
D/H (0.607/0.393)	28.	2.8	60.5	8.7	1.75	16.8
A/H (0.534/0.466)	49.6	5.0	17.	28.4	1.518	8.8
A/G/H (0.43/0.277/0.293)	51.8	9.5	14.5	24.2	1.513	9.8
C/E (0.451/0.549)	42.2	0.	46.2	11.6	1.693	29.7
C/F (0.376/0.624)	46.1	7.7	37.	9.2	1.632	16.8
B/E (0.421/0.579)	54.2	0.	32.7	13.1	1.59	23.7
B/F (0.347/0.653)	56.	9.3	24.8	9.9	1.54	14.7
A/F (0.492/0.508)	40.7	6.8	19.7	32.8	1.724	14.8
A/F (0.659/0.341)	26.7	4.5	25.8	43.	1.905	20.3
A/C/G (0.149/0.149/0.702)	50.8	16.9	19.8	12.5	1.564	11.7

Symbols for the hydrocarbon components are the same as those of Table 1.

soot formation will be given. Extensive experimental data for complex hydrocarbon mixtures and fuels blended from pure hydrocarbons will be utilized to show the quantitative relationship between sooting tendency and fuel structural features. Also, a very fast and effective technique of determining the carbon type structure of aviation type fuels will be described.

Background

The soot formation rate and mechanism in turbulent diffusion flames are complex and dynamic phenomena not governed by a single property of fuel or fuel–oxidant system, but by the fluid mechanics and thermodynamic conditions of the system as well as the molecular composition of the fuel. Therefore, it is suitable to lump the various effects into two classes: physical and chemical. In a gas turbine combustor, the major physical effects are spray characteristics, swirl/turbulence structure, pressure, and combustor configuration. Molecular constitution of the fuel is responsible for the chemical part for a given temperature and equivalence ratio. This means that, for a given fuel, the response of different engines can be expected to be different (see, e.g., Rudey and Grobman, 1978). But for a given set of engine conditions, any change in soot formation rate will be mainly a function of the molecular structure of the fuel. Therefore, a comprehensive understanding of the effects of fuel molecular structure on soot formation rate and mechanism is essential in order to understand the soot formation in turbulent diffusion flames.

The present practice in gas turbine technology is to represent the fuel molecular composition by one of the following fuel properties: smoke point, hydrogen-to-carbon ratio, aromatic content or carbon aromaticity, and polycyclic aromatic content. In laminar diffusion flames, where physical effects are minimized, it is qualitatively known that soot formation is governed by molecular composition and flame temperature (Glassman and Yaccarino, 1981; Olson et al., 1985). For a given set of initial conditions, flame temperature is dependent on the hydrogen-to-carbon ratio of the fuel (Gülder, 1986). Fuel molecular composition has been shown to be qualitatively represented by the smoke point (Olson et al., 1985; Markstein, 1987). Therefore, smoke point and hydrogen-to-carbon ratio are complementary to each other, rather than alternatives.

Aromatic content, in addition to being an obscure definition, does not tell much about the rest of the fuel composition. The ratio of branched to normal paraffins, for example, can be effective on soot formation for a given aromatic content. The same discussion applies to the polycyclic aromatic content of the fuel.

Table 3 Carbon type structural composition, smoke points, and hydrogen-to-carbon ratios of the fuels in set 3

No.	C_a	C_α	C_2	C_3	ψ	S,mm
1	49.8	14.8	28.2	7.2	1.33	7.9
2	44.1	14.1	32.5	9.2	1.43	6.0
3	38.4	10.3	39.6	11.7	1.54	9.6
4	39.8	13.3	35.5	11.4	1.54	8.7
5	35.8	12.8	39.5	11.9	1.55	10.2
6	37.4	13.8	37.1	11.8	1.60	10.7
7	23.1	10.0	53.3	13.6	1.63	12.8
8	32.7	9.3	43.9	14.1	1.65	11.2
9	27.8	10.5	48.2	13.5	1.65	10.7
10	31.4	10.4	44.4	13.9	1.65	11.6
11	24.3	11.2	50.1	14.4	1.66	12.7
12	31.2	11.3	43.2	14.3	1.67	12.1
13	30.3	10.6	44.7	14.4	1.67	11.3
14	29.6	10.4	46.3	13.7	1.68	11.2
15	25.9	9.9	48.4	15.8	1.70	14.5
16	23.3	7.6	53.2	16.0	1.70	13.9
17	26.6	8.3	48.1	16.9	1.71	13.2
18	25.4	7.7	50.0	17.0	1.72	13.2
19	19.7	8.1	54.5	17.7	1.73	12.0
20	22.5	10.7	50.1	16.6	1.74	15.0
21	26.8	8.5	48.9	15.7	1.75	13.3
22	24.3	10.4	47.6	17.8	1.75	14.8
23	17.4	7.2	56.9	18.6	1.77	15.6
24	20.4	7.7	53.7	18.2	1.78	15.9
25	21.6	9.2	48.9	20.3	1.78	14.8
26	20.2	7.4	53.1	19.2	1.79	15.6
27	20.8	8.0	52.7	18.5	1.79	14.1
28	21.4	9.4	51.1	18.0	1.79	14.5
29	19.7	9.8	52.3	18.2	1.79	14.7
30	21.1	7.3	54.5	17.1	1.79	17.0
31	22.0	9.5	49.3	19.2	1.79	16.9
32	20.7	7.7	52.8	18.8	1.80	16.9
33	18.8	6.5	54.7	20.0	1.80	15.9
34	7.8	3.5	68.8	19.9	1.81	20.1
35	19.9	9.4	51.0	19.8	1.81	14.8
36	18.8	7.7	56.4	17.1	1.81	17.7
37	22.6	7.9	52.3	17.3	1.81	18.2
38	14.1	5.8	59.9	20.1	1.82	15.3
39	15.3	6.5	56.7	21.5	1.82	20.1
40	13.8	5.5	59.5	21.2	1.85	18.7
41	17.7	8.5	56.1	17.7	1.85	18.3
42	14.1	7.2	56.3	22.4	1.87	20.0
43	14.0	5.6	59.4	21.0	1.87	22.0
44	16.1	7.6	56.3	20.1	1.88	19.8
45	21.9	6.8	49.5	21.8	1.90	22.3
46	14.3	5.6	57.5	22.5	1.91	22.8
47	11.7	4.8	59.9	23.6	1.91	23.7
48	11.7	4.9	60.0	23.3	1.91	25.0
49	15.1	6.4	56.2	22.2	1.92	23.4
50	14.4	4.5	57.5	23.5	1.92	24.1
51	16.3	7.1	54.0	22.6	1.92	25.7
52	16.5	5.5	56.4	21.5	1.92	24.3
53	14.5	6.7	56.8	22.0	1.92	22.4
54	15.8	6.3	54.2	23.7	1.93	24.7
55	13.7	5.4	58.4	22.6	1.93	25.0
56	14.4	5.9	56.9	22.8	1.94	25.0
57	14.6	6.3	57.2	21.9	1.94	24.9
58	14.1	5.7	58.2	22.0	1.95	23.7
59	12.1	8.1	59.7	23.0	1.97	26.4
60	15.5	4.7	51.9	27.8	1.99	28.3
61	10.6	4.2	60.3	24.9	2.01	30.9
62	10.2	6.1	58.5	25.2	2.02	31.3

Strategy

In order to differentiate the effects of fuel molecular structure and the flame temperature, a series of experiments has been designed with fuels blended from pure hydrocarbons to get a constant hydrogen-to-carbon ratio for every fuel. Smoke points, mass burning rates, and soot yields of these fuels have been measured on a wick-fed cylindrical burner. A similar set of experiments has been performed with a second set of blended fuels with different hydrogen-to-carbon ratios.

In order to characterize a commercial turbine fuel, for the purpose of obtaining its structural composition, we propose a global fuel characterization scheme in terms of carbon type structure of the fuel. We used a similar approach previously, to describe the ignition quality of diesel type fuels (Gülder and Glavinčevski, 1986a, 1986b). We classify the carbon types in a hydrocarbon molecule as follows: C_a, carbons on mono and condensed aromatic rings; C_α, carbons at α position to aromatic rings; C_2, alkanic CH_2, CH carbons including β — CH_2, CH_3, and γ, δ - CH_2 to aromatic rings; and C_3, alkanic CH_3 carbons including terminal and branched and γ, δ to aromatic rings. In the next section we present the experimental method used to determine these carbon group types from the hydrogen type distribution of aviation turbine fuels.

Experimental Methodology

The fuels used in this study are grouped into three sets. The first set includes 15 fuels blended from pure hydrocarbons, each containing two or three hydrocarbons, such that each blend has a hydrogen-to-carbon ratio of 1.54. The second set has 16 fuels also blended from pure hydrocarbons but the hydrogen-to-carbon ratio varies from 1.51 to 1.91. Hydrogen-to-carbon ratios, carbon type structures, and blend components of the fuels in sets 1 and 2 are listed in Tables 1 and 2, respectively. The third set contains 62 commercial and experimental fuels from various sources, including coal liquids, tar sands, shale oil, hydrotreated fuels, and diesel fuels. Density range is from 0.76 to 0.93 g/cm^3, and the hydrogen-to-carbon ratio ranges from 1.33 to 2.02. Carbon type structures, hydrogen-to-carbon ratios, and smoke points of the fuels in set 3 are given in Table 2.

The smoke points of the fuels in the three sets have been determined using the standard test apparatus. Soot yields have been measured with the fuels in set 1, and mass burning rates have been measured with 13 selected fuels. Smoke point fuel mass burning rates have been measured by weighing the burner/fuel reservoir assembly at suitable intervals. Smoke point soot yields have been determined by passing the exhaust of the flame, burning just above its smoke point, through a fine filter assembly, and measuring the amount of soot deposited over a suitable period of time.

Proton nuclear magnetic resonance (^1H NMR) spectrometry has been used to identify the hydrogen type distribution of the

Table 4 Regions of hydrogen types in proton-1 NMR spectra

hydrogen type	chemical shift,ppm
H_{dar}	9.0-7.05
H_{mar}	7.05-6.5
H_α	4.0-1.8
H_c	1.8-1.06
H_d	1.06-0.5

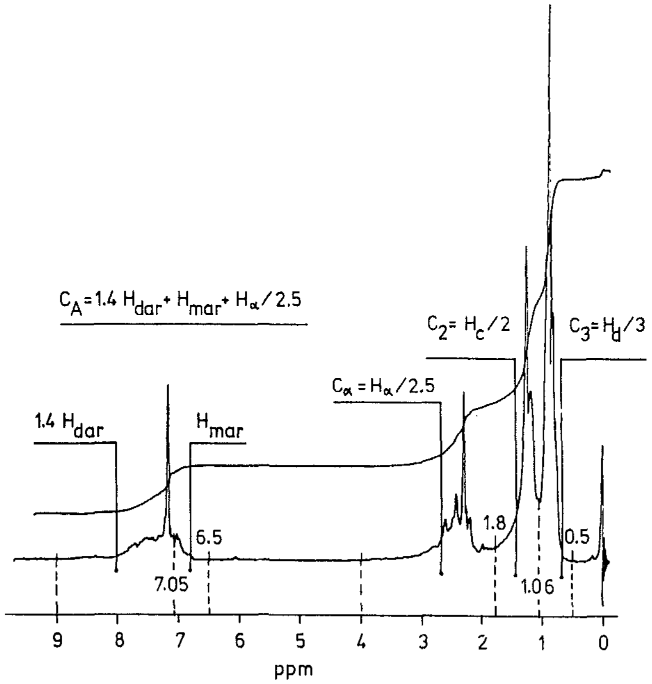

Fig. 1 Regions of five hydrogen types on a typical proton-1 NMR spectrum

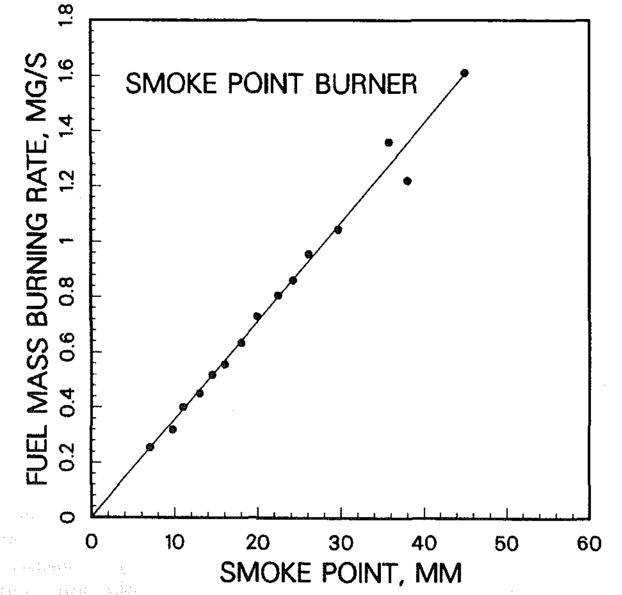

Fig. 2 Fuel mass burning rate at the smoke point for 13 selected fuels

fuels. The ^1H NMR spectra have been obtained at 90 MHz on a Varian EM-390 spectrometer. Concentrations of approximately 50/50 by volume of sample to D-chloroform and 1 percent Me_4Si have been used for recording the spectra. The proton resonance signals of the fuels have been divided into five regions of chemical shift values, and the signals in each region have been assigned to various types of hydrogen relative to Me_4Si (Fig. 1). The relative number of hydrogen atoms in each region can be calculated from the area of the signals of the corresponding region. These regions have been specified in Table 4.

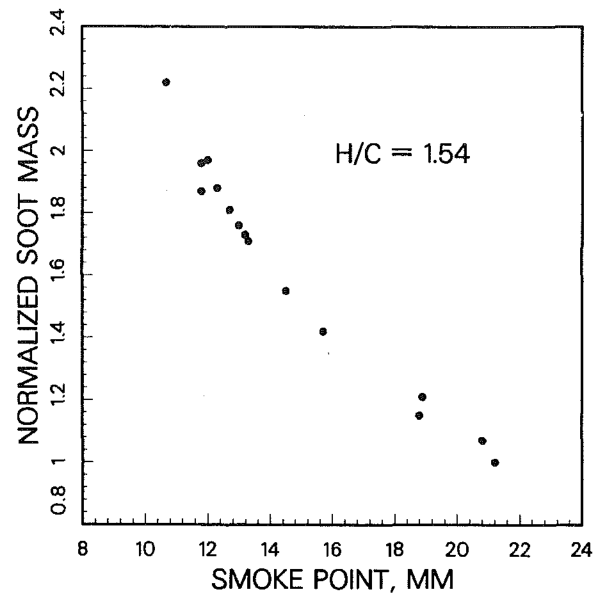

Fig. 3 Normalized smoke point soot yields of the fuels in set 1. Hydrogen-to-carbon ratio of all fuels in this set is 1.54.

The relative number of carbon atoms is calculated from the area ratio of the hydrogen type to the number of hydrogens per carbon atom. To account for the aromatic ring-junction carbons, the hydrogen signal intensity H_{dar} is multiplied by 1.4. The aromatic ring carbons substituted by alkyl groups are equivalent to α-alkyl hydrogen integral divided by 2.5. The sum of [1.4 H_{dar}], H_{mar}, and C_α gives the number of aromatic carbon atoms, C_a. Because of the low concentration of methine and methyl groups in the H_c region, it is assumed that two hydrogen atoms correspond to one carbon atom, C_2, whereas three hydrogen atoms in the area H_d are equivalent to one carbon atom, C_3. The sum of the relative number of carbon atoms of each region is normalized so that $C_a + C_\alpha + C_2 + C_3 = 100$. The calculation procedure is also explained in Fig. 1 on a spectrum of a typical fuel.

Results and Discussion

The smoke point mass burning rate has been found to be linearly dependent on smoke point (Fig. 2). This is in agreement with the findings of Olson et al. (1985).

Measured soot yields, defined as mass of soot per mass of fuel burned normalized with respect to the soot yield at 21.1 mm smoke point, of fuel set 1 are shown in Fig. 3, as a function of smoke point. For constant hydrogen-to-carbon ratio (that is, constant adiabatic flame temperature), soot yields change with the changes in fuel molecular composition measured as the smoke point. A similar graph can be constructed for the constant aromaticity case using some of the data given in Table 1.

Using the normalized carbon types of the 93 fuels in three sets, a functional expression of the following form has been selected to correlate the carbon types to the measured smoke points:

$$S = a_0 + a_1x_1 + a_2x_2 + a_3x_3 + a_4x_4 + a_5x_5 + a_6\psi^3 \quad (1)$$

where $x_1 = C_2/C_a^2$, $x_2 = C_3/C_a^2$, $x_3 = \ln(C_\alpha + 2)$, $x_4 = (C_\alpha + 2)/(C_2 + C_3)$, $x_5 = C_2/C_3$, and ψ is the hydrogen-to-carbon

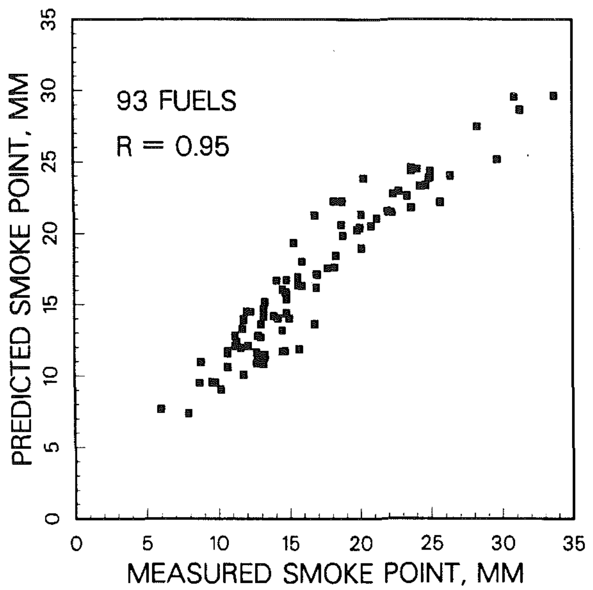

Fig. 4 Predicted smoke points by equation (1) versus observed smoke points for 93 fuels in three sets

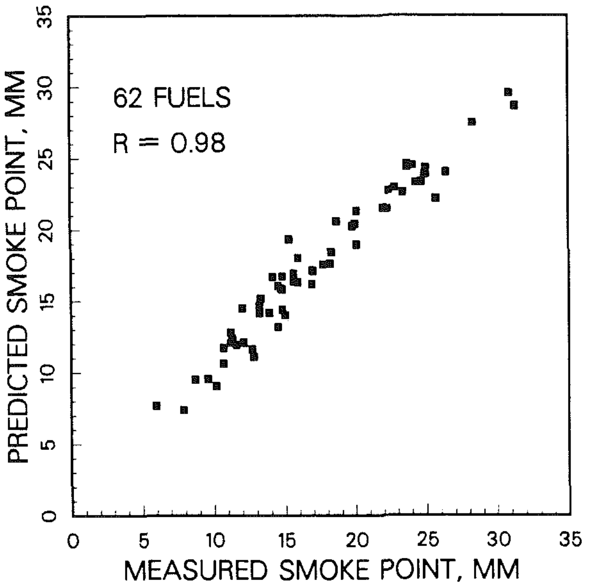

Fig. 5 Predicted smoke points by equation (1) versus observed smoke points for 62 complex hydrocarbon mixtures in set 3

ratio. The following values for the constants a_i have been determined as a result of a multiple regression analysis:

$$a_0 = 11.1$$
$$a_1 = -7.76$$
$$a_2 = 28.86$$
$$a_3 = -8.59$$
$$a_4 = 21.9$$
$$a_5 = 0.429$$
$$a_6 = 3.63$$

A correlation coefficient of 0.95 has been obtained. Standard deviation of the residuals is 1.9 mm.

Smoke points of the 93 fuels predicted by the developed expression are plotted against the observed smoke points in Fig. 4. Considering the experimental errors involved in smoke point measurements, the correlation is very good. The most important implication of this correlation is that smoke point reflects the molecular composition of a hydrocarbon turbine fuel.

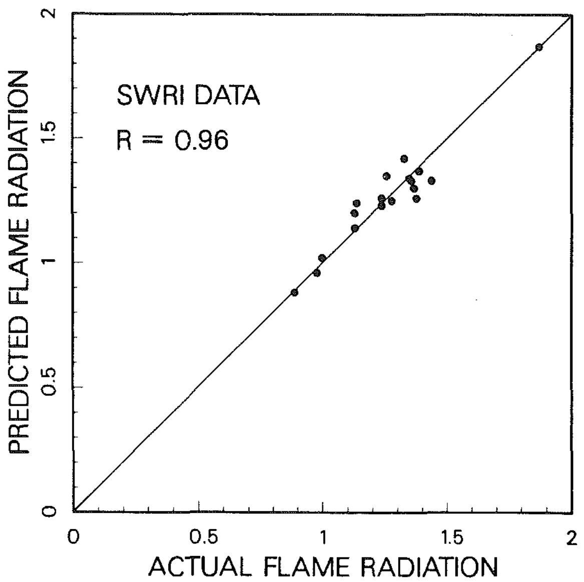

Fig. 6 Predicted normalized flame radiation by equation (2) versus experimental values. The experimental data are from Naegeli and Moses (1980), obtained on a T-63 combustor.

When equation (1) has been used to correlate the smoke points of the fuels in set 3 only, with the same set of constants, the correlation coefficient has improved to 0.98 (Fig. 5). The reason for this is that carbon type structural composition in terms of four carbon groups describes the structure of complex hydrocarbon mixture properly. This type of characterization has been aimed to providing an *average* hypothetical molecule representing the real fuel. For fuels blended from 2 or 3 pure hydrocarbons (fuels in sets 1 and 2), due to a small number of components, characterization of the blend with four carbon groups may produce biased results depending on the component type.

In order to test our proposal (that hydrogen content and smoke point of the fuel should be used together to describe the sooting tendency of a fuel) further, using independent data sets from combustors and laminar diffusion flames, we have performed the following exercises.

Flame radiation data obtained in a T-63 combustor by Naegeli and Moses (1980) have been used to correlate the measured flame radiation to a function, in terms of smoke point and hydrogen-to-carbon ratio, in the following form:

$$F_1 = aS^b \exp[\phi S/\psi^2] \qquad (2)$$

where S is the smoke point, ψ the hydrogen-to-carbon ratio, and a, b, and ϕ are constants. Results are plotted in Fig. 6. A correlation coefficient of 0.96 has been obtained. Equation (2) has also been used to correlate the flame radiation data obtained in a Tyne combustor by Carrier and Wetton (1988). A correlation coefficient of 0.95 has been obtained (Fig. 7). Application of equation (2) to the radiative heat load data of Rosfjord (1984), obtained on a gas turbine combustor, has yielded a correlation coefficient of 0.97 (Fig. 8).

Olson et al. (1985) measured maximum soot volume fractions of a large number of hydrocarbons at half the total smoke point flame heights using a laminar diffusion wick flame. We have used these data to correlate the soot volume fraction to a function, in terms of smoke point and hydrogen-to-carbon ratio, in the following form:

$$F_2 = aS^b \exp[\phi(\psi/S)^2] \qquad (3)$$

The results are shown in Fig. 9. The correlation coefficient is 0.96.

It should be noted here that equations (1) through (3) are

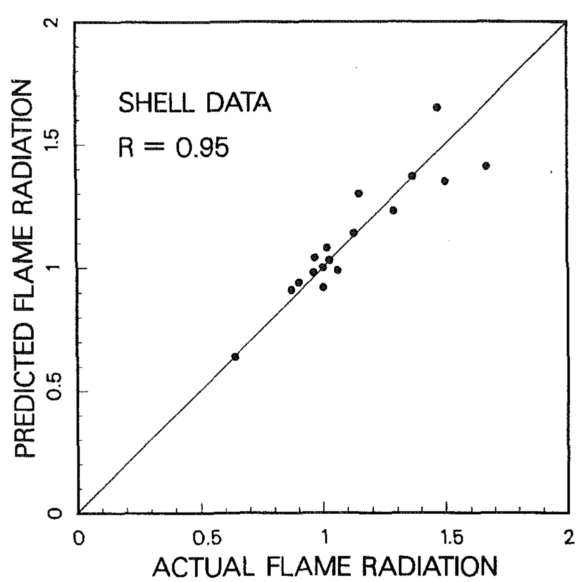

Fig. 7 Predicted normalized flame radiation by equation (2) versus experimental values. Experimental data are from Carrier and Wetton (1988), obtained on a Tyne combustor.

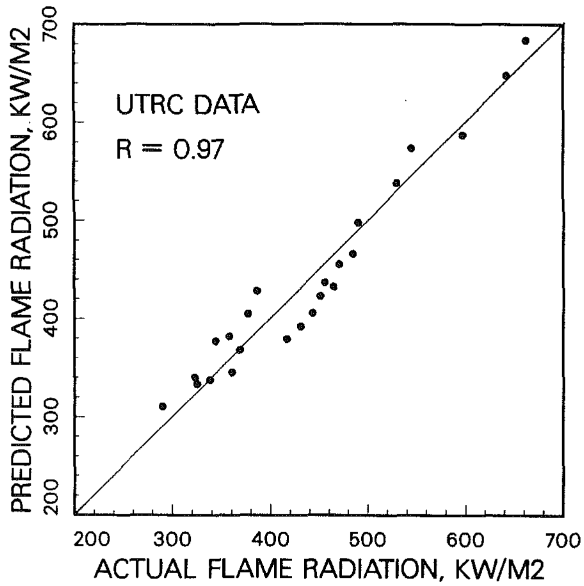

Fig. 8 Predicted normalized flame radiation by equation (2) versus experimental values. The experimental data are from Rosfjord (1984), obtained on a gas turbine combustor.

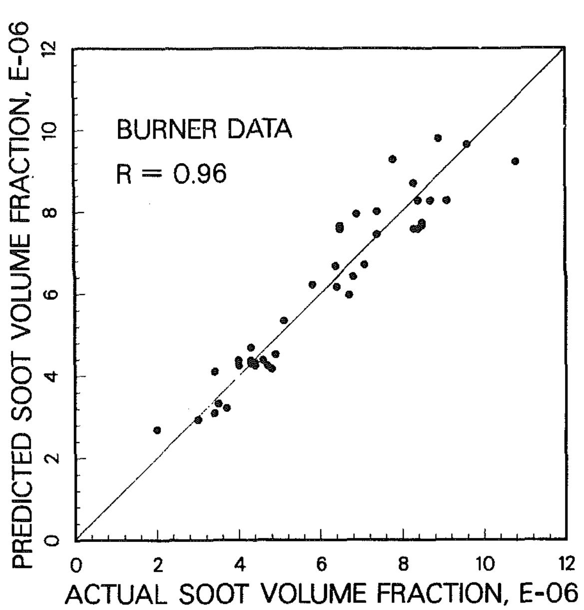

Fig. 9 Predicted maximum soot volume fraction by equation (3) versus experimental values. Experimental data are from Olson et al. (1985), obtained from a laminar diffusion flame using pure hydrocarbons.

empirical, and it will be pure speculation to attach any immediate physical and chemical models to explain the soot formation in diffusion flames. However, equation (1) proves that the smoke point is an indicator of the fuel molecular structure. Equations (2) and (3) show that hydrogen-to-carbon ratio and smoke point of the fuel should be used concomitantly to describe the sooting propensity of a given hydrocarbon fuel. Of course, this point seems to be in sharp contrast to most of previous studies in which the flame properties related to soot have been correlated with either the smoke point or the hydrogen-to-carbon ratio. This stems from the fact that for distillate aviation turbine fuels obtained from conventional sources, hydrogen-to-carbon ratios are generally correlatable to smoke points. This implies that, in terms of fuel carbon type structure, C_α/C_a and C_2/C_3 ratios do not vary much from one fuel to the other. However, for unconventional fuels obtained from tar sands, shale oil, and coal liquids through different processes, including hydrogenation, C_α/C_a and C_2/C_3 ratios vary considerably, to the extent that hydrogen-to-carbon ratios and smoke points display a very poor correlation.

Concluding Remarks

It has been shown that smoke point of a complex hydrocarbon mixture is a lumped measure of the fuel molecular structure. Carbon groups that have a dominant effect on soot formation characteristics of turbine fuels have been identified. A fast and reliable technique of characterizing the fuel molecular structure in terms of these carbon types has been described.

The soot yields of diffusion flames with a group of fuels with a constant hydrogen-to-carbon ratio of 1.54 proved that sooting tendency of the turbine fuels cannot be described by a single fuel property like hydrogen-to-carbon ratio, smoke point, or aromaticity. Smoke point and hydrogen-to-carbon ratio are complementary to each other in describing the sooting propensities of complex hydrocarbon mixtures. This has been further tested successfully by using four sets of independent data obtained by other investigators on gas turbine combustors and diffusion flames. These results strongly support our proposition that in diffusion flames the soot formation rate and soot yields are controlled by the fuel molecular composition indicated by smoke point and hydrogen-to-carbon ratio.

Acknowledgments

The authors thank the United Nations Industrial Development Organization for a UNIDO fellowship granted to S.D. to work as a guest engineer in the National Research Council Laboratories, Canada. The assistance of Mr. G. Burton and Mr. G. Moroz with the experimental work is gratefully acknowledged.

References

Blazowski, W. S., 1980, "Dependence of Soot Production on Fuel Blend Characteristics and Combustion Conditions," ASME JOURNAL OF ENGINEERING FOR POWER, Vol. 102, pp. 403–408.

Bowden, T. T., Pearson, J. H., and Wetton, R. J., 1984, "The Influence of Fuel Hydrogen Content Upon Soot Formation in a Model Gas Turbine Combustor," ASME JOURNAL OF ENGINEERING FOR GAS TURBINES AND POWER, Vol. 106, pp. 789–794.

Carrier, D. M., and Wetton, R. J., 1988, "Prediction of Combustion Performance of Aviation Kerosines Using a Novel Premixed Flame Technique," ASME JOURNAL OF ENGINEERING FOR GAS TURBINES AND POWER, Vol. 110, pp. 100–104.

Clark, J. A., 1984, "The Fuel Property-Flame Radiation Relationship for Gas Turbine Combustors," *AIAA Journal*, Vol. 22, pp. 1828–1830.

Glassman, I., and Yaccarino, P., 1980, "The Effect of Oxygen Concentration on Sooting Diffusion Flames," *Combustion Science and Technology*, Vol. 24, pp. 107–117.

Glassman, I., and Yaccarino, P., 1981, "The Temperature Effect in Sooting Diffusion Flames," *18th Symposium (Int'l) on Combustion*, Vol. 18, pp. 1175–1183.

Gülder, Ö. L., 1986, "Flame Temperature Estimation of Conventional and Future Jet Fuels," ASME JOURNAL OF ENGINEERING FOR GAS TURBINES AND POWER, Vol. 108, pp. 376–380.

Gülder, Ö. L., and Glavinčevski, B., 1986a, "Prediction of Cetane Number of Diesel Fuels From Carbon Type Structural Composition Determined by Proton NMR Spectroscopy," *Industrial and Engineering Chemistry Product Research and Development*, Vol. 25, pp. 153–156.

Gülder, Ö. L., and Glavinčevski, B., 1986b, "Ignition Quality Determination of Diesel Fuels From Hydrogen Type Distribution of Hydrocarbons," *Combustion and Flame*, Vol. 63, pp. 231–238.

Kent, J. H., 1986, "A Quantitative Relationship Between Soot Yield and Smoke Point Measurements," *Combustion and Flame*, Vol. 63, pp. 349–358.

Markstein, G. H., 1985, "Relationship Between Smoke Point and Radiant Emission From Buoyant Turbulent and Laminar Diffusion Flames," *20th Symp. (Int'l) on Combustion*, Vol. 20, pp. 1055–1061.

Markstein, G. H., 1987, "Radiant Emission and Smoke Points for Laminar Diffusion Flames of Fuel Mixtures," *21st Symposium (Int'l) on Combustion*, Vol. 21, pp. 1107–1114.

Naegeli, D. W., and Moses, C. A., 1980, "Effect of Fuel Molecular Structure on Soot Formation in Gas Turbine Engines," ASME Paper No. 80-GT-62.

Olson, D. B., Pickens, J. C., and Gill, R. J., 1985, "The Effects of Molecular Structure on Soot Formation. II. Diffusion Flames," *Combustion and Flame*, Vol. 62, pp. 43–60.

Rosfjord, T. J., 1984, "Role of Fuel Chemical Properties on Combustor Radiative Heat Load," AIAA Paper No. AIAA-84-1493.

Rudey, R. A., and Grobman, J. S., 1978, "Impact of Future Fuel Properties on Aircraft Engines and Fuel Systems," Paper No. 6, *Aircraft Engine Future Fuels and Energy Conservation*, AGARD LS-96.

Schug, K. P., Manheimer-Timnat, Y., Yaccarino, P., and Glassman, I., 1980, "Sooting Behavior of Gaseous Hydrocarbon Diffusion Flames and the Influence of Additives," *Combustion Science and Technology*, Vol. 22, pp. 235–250.

G. A. Richards
Graduate Student.

P. E. Sojka
Assistant Professor of Mechanical Engineering.
Assoc. Mem. ASME

A. H. Lefebvre
Reilly Professor of Combustion Engineering.
Mem. ASME

The Gas Turbine Combustion Laboratory,
Thermal Sciences and Propulsion Center,
School of Mechanical Engineering,
Purdue University,
West Lafayette, IN 47907

Flame Speeds in Fuel Sprays With Hydrogen Addition

The influence of hydrogen addition on the burning rates of kerosine sprays in air is studied experimentally. Flame speeds are measured as a function of fuel drop size, equivalence ratio, and hydrogen concentration. The results obtained show that evaporation rates have a controlling effect on flame speeds over wide ranges of mean drop size. They also demonstrate that the burning rates of liquid kerosine-air mixtures are augmented appreciably by the addition of small quantities of hydrogen to the air flowing into the combustion zone.

Introduction

The efforts now being concentrated on developing air-breathing jet engines capable of propelling aircraft at supersonic speeds have led to renewed interest in the use of hydrogen as a fuel, whether alone or in combination with a more traditional aircraft fuel, such as kerosine. Hydrogen combines high specific energy (four times that of kerosine) with high flame speed (eight times that of kerosine). It also burns far more cleanly than hydrocarbon fuels (including methane), producing no carbon dioxide or soot. The drawbacks to hydrogen include the large tankage volume required, the cryogenic nature of the liquid, and the fire hazard due to its low minimum ignition energy and wide range of flammability.

A number of studies have been carried out in which hydrogen was used to supplement a more conventional gaseous hydrocarbon fuel. For example, Milton and Keck (1984) used a spherical combustor to measure the laminar burning velocities of mixtures of air with hydrogen, acetylene, propane, and methane, while Yu et al. (1986) examined the influence of hydrogen addition on the flame speeds of propane–air and methane–air mixtures. In all cases, it was found that relatively small quantities of hydrogen could greatly enhance burning rates. These previous studies were confined to gaseous hydrogen–hydrocarbon mixtures.

Annushkin and Maslov (1985) measured combustion efficiencies in kerosine sprays burning within an independent hydrogen–air flame. They found an optimum hydrogen concentration for enhancing the overall efficiency of hydrogen–hydrocarbon combustion. The present work reports flame speed measurements carried out under conditions where a liquid hydrocarbon fuel, namely kerosine, is sprayed into flowing hydrogen–air mixtures. Apart from the hydrogen injection, this study closely parallels the work of Mizutani and Nishimoto (1972) and Myers and Lefebvre (1986). Both of these investigations produced evidence to show that flame speeds are limited by evaporation rates over wide ranges of fuel drop sizes. Ballal and Lefebvre (1981) have also demonstrated, both theoretically and experimentally, that evaporation-limited combustion is characterized by a linear relationship between flame speed and the reciprocal of fuel mean drop size.

In this study, flame speeds are measured as a function of fuel drop size, equivalence ratio, and hydrogen concentration. The results obtained confirm the importance of evaporation rates to the overall combustion process, and also demonstrate that the burning rates of liquid kerosine–air mixtures can be augmented appreciably by the addition of small quantities of hydrogen gas to the air stream flowing into the combustion zone.

Experimental

The apparatus employed is shown schematically in Fig. 1. Essentially, it is an upgrade of the facility designed by Myers and Lefebvre (1986). Air is drawn at room temperature through a sound attenuator and butterfly valve to the suction side of a centrifugal blower. At exit, the air enters a flow-metering section and then proceeds into a series of perforated plates, honeycombs, and wire gauzes to flatten the velocity profile, erase any swirl, and eliminate any large-scale eddies. Downstream of this flow-conditioning section, a transition piece converts the ducting from a nominal 15 cm diameter to a 10 cm square cross section, which mates with the test section. The test section comprises a 10 × 30 cm rectangular duct, 50 cm long, milled from stainless steel plates, and equipped with removable quartz windows, 25 cm long and 10 cm wide, which provide optical access to the flame. The use of a rectangular test section allows the two opposing windows to be located at a sufficient distance from the spray to protect them from being fogged by the kerosine mist. The test section is followed by a simple expansion nozzle, which conveys the combustion products outdoors via a large diameter section of water-cooled exhaust ducting.

The flame is ignited and stabilized using a 6.2 mm o.d. stainless steel tube carrying a premixed supply of propane and

---

Contributed by the International Gas Turbine Institute and presented at the 33rd International Gas Turbine and Aeroengine Congress and Exhibition, Amsterdam, The Netherlands, June 5–9, 1988. Manuscript received by the International Gas Turbine Institute November 30, 1987. Paper No. 88-GT-20.

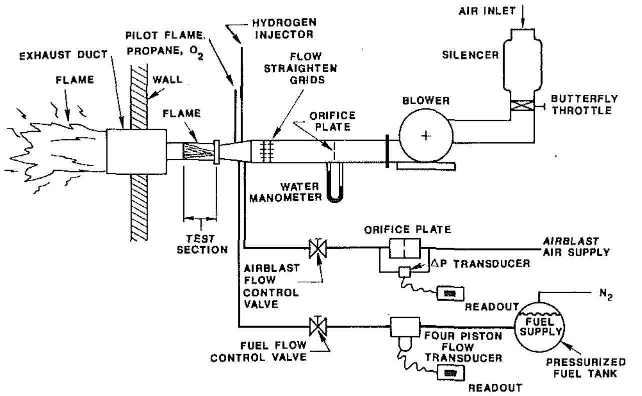

Fig. 1 Schematic diagram of test rig

oxygen. The igniter tube is located at the center of the test section entrance. The pilot flame is ignited by a high-voltage spark. A minimum of oxygen is used because a high flame temperature at the igniter could disturb the schlieren image.

Fuel Injection. The liquid fuel injection system is designed to provide a controllable, metered, filtered supply of fuel and air to the multipoint airblast atomizer. The fuel supply system consists of a nitrogen-pressurized fuel tank, which feeds the atomizer through throttling valves. Fuel metering is accomplished using a four-piston flow transducer in conjunction with a control valve, as shown in Fig. 1. The 36-point airblast atomizer employed in this study was constructed to fit snugly in the transition piece just upstream of the test section. Each plain-jet atomizer consists of a fuel tube of 1.08 mm o.d. and 0.33 mm i.d., surrounded concentrically by an air tube of 1.83 mm o.d. and 1.37 mm i.d. Each individual atomizer is fed by separate supplies of fuel and air.

Mean drop sizes were measured at various downstream positions using a Malvern particle sizer. Analysis of the experimental data yielded an equation for Sauter mean diameter of the form (Richards et al., 1975)

$$\mathrm{SMD} = 365\left(\frac{\rho_L \sigma}{\rho_A^{0.5} U_R^2}\right)^{0.5}\left(1 + \frac{1}{\mathrm{ALR}}\right)^{0.7} \qquad (1)$$

In the above equation, ρ_L and σ are the liquid density and surface tension, respectively; ρ_A is the air density; and U_R is readily calculated using the liquid and atomizing air flow rates, and the dimensions of the liquid and air discharge orifices.

As shown in Fig. 1, a metered supply of hydrogen gas can be added to the airstream via an injector located just downstream of the flow straighteners. The arrangement is shown in more detail in Fig. 2. Note that, for simplicity, this figure shows the liquid fuel injector as a grid of 4 × 4 airblast atomizers, although the actual injector comprises a 6 × 6 array of atomizers.

Measurement of Flame Speed. The system for determining the flame angle for the measurement of burning velocity is based upon a two-mirror schlieren system, whose optical components include a 100 W high-pressure mercury vapor arc, two 2 m focal length parabolic mirrors silvered on the front surface, and a knife edge stop that is adjustable horizontally and vertically. The schlieren image is recorded using a 35 mm camera with the lens removed. The camera is equipped with a horizontal travel focal plane shutter capable of exposure times down to 1/2000 s. In practice, a fairly long exposure time of 8 ms is used to ensure that the wrinkled flame appears as a straight-edged one in the resulting photograph. The camera is mounted on a tripod 25 cm behind the knife edge, producing a rectangular image on the film 1.25 cm wide and 3.4 cm long. Lines are marked directly on an enlarged image of the negative with a fine-point pen, and the angles are measured to the nearest half-degree with a protractor. The flame speed is calculated by multiplying the mainstream velocity by the sine of the corresponding angle. The average flame speed is then

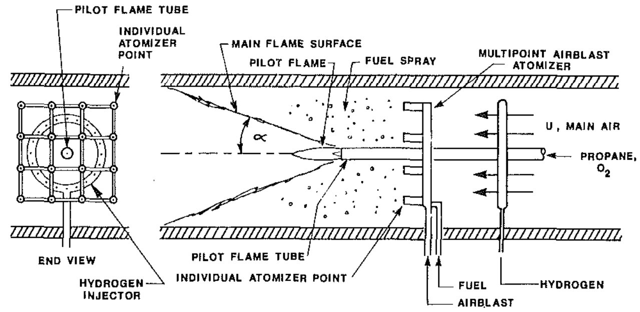

Fig. 2 Main components of test section

$$S_T = 0.5U(\sin \alpha_U + \sin \alpha_L) \qquad (2)$$

where the U and L subscripts represent upper and lower positions, respectively.

Test Conditions. All tests were conducted in flowing air at normal atmospheric temperature and pressure, with a mean velocity through the test section of 20 m/s. Because turbulence can influence flame speeds (Ballal and Lefebvre, 1975), turbulent velocity fluctuations parallel to the flow were measured in the absence of combustion with a hot-wire anemometer. As the main air and the airblast atomizing air both contribute to turbulent fluctuations, by adjusting the main air velocity it was possible to create identical spray conditions (fuel/air ratio and mean drop size) with different values of the rms velocity fluctuation u'. Comparing such conditions, no significant difference in flame speed was observed. Thus, the influence of turbulent velocity fluctuations on flame speed was considered negligible over the small range of u' values included in this study.

Following the practice employed in previous studies on hydrogen flame initiation and propagation, the hydrogen content is expressed as a volume percentage of the air into which it is injected, i.e.,

$$\text{Percentage hydrogen} = \frac{100\ (\text{VFR Hydrogen})}{\text{VFR Hydrogen} + \text{VFR Air}} \qquad (3)$$

where VFR = volume flow rate in m^3/s, at $T = 311$ K and $P = 101.3$ kPa.

The equivalence ratios reported here retain the usual definition, namely, the actual kerosine fuel/air ratio by mass relative to the stoichometric fuel/air ratio by mass. It is emphasized that the presence of hydrogen is accounted for solely in the volume percent mentioned above, as favored by Yu et al. (1986) whose work was published after this research was almost complete.

The values of equivalence ratio indicated in Figs. 4-11

Nomenclature

ALR = air/liquid ratio by mass
C_A = mole fraction of air
C_F = mole fraction of hydrocarbon fuel
C_H = mole fraction of hydrogen

S = flame speed, m/s
S_O = flame speed without hydrogen, m/s
S_T = turbulent flame speed, m/s
SMD = Sauter mean diameter, μm

U = mainstream velocity, m/s
ρ = density, kg/m^3
σ = surface tension, kg/s^2
ϕ = equivalence ratio

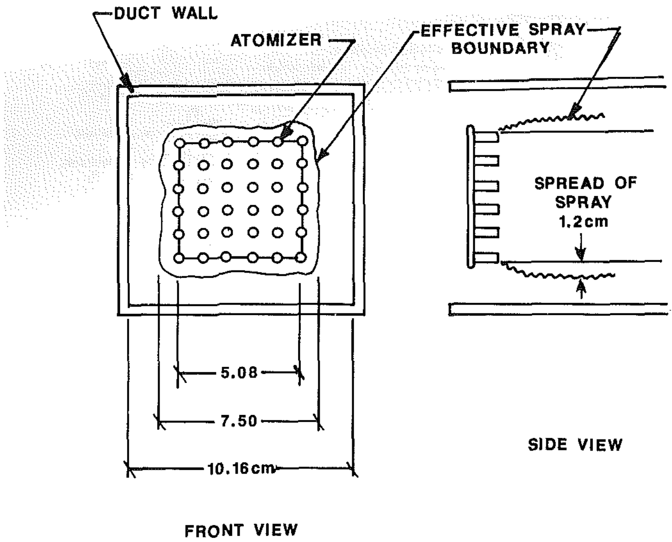

Fig. 3 Diagram illustrating effective spray boundaries

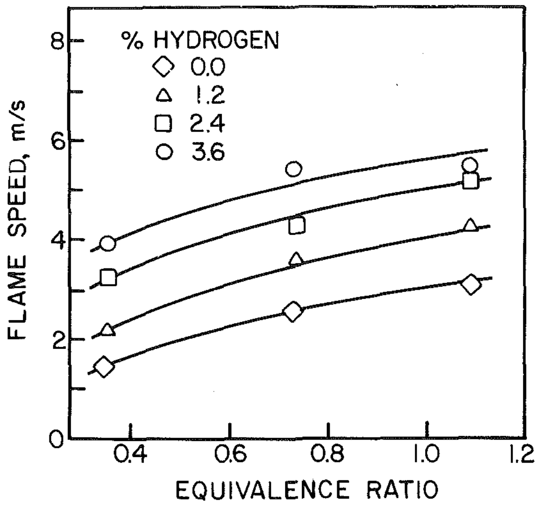

Fig. 5 Influence of equivalence ratio on kerosine/hydrogen flame speeds for an SMD of 50 μm

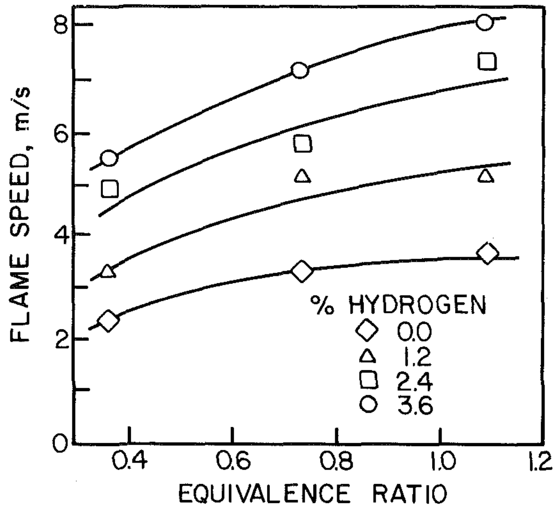

Fig. 4 Influence of equivalence ratio on kerosine/hydrogen flame speeds for an SMD of 30 μm

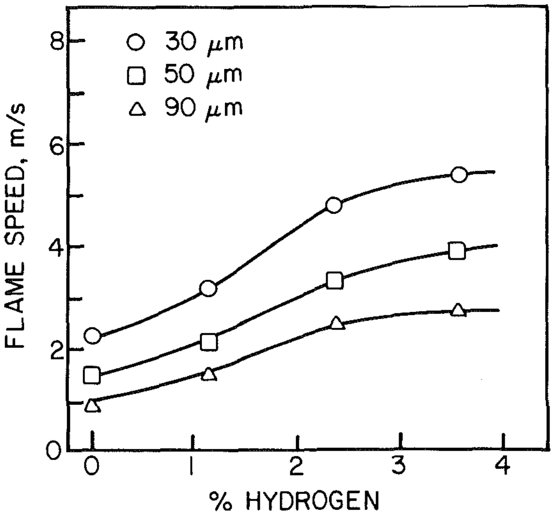

Fig. 6 Flame speed versus hydrogen content for various values of SMD; equivalence ratio = 0.37

represent the mixture strength at the flame front and take full account of the fact that some air (and hydrogen) passes around the boundaries of the spray. Appropriate calculation of the air participating in combustion was first based on visual observation of the effective spray boundary (as shown in Fig. 3) and then confirmed with a simple probe. The probe was fashioned from a 6.35 mm copper tube formed into an **L** shape. With a cold flow water spray (rather than fuel) flowing into the section, this probe was inserted into the spray. The base of the **L** was positioned parallel to the flow, with the open end upstream. The leg of the probe was angled down (outside the spray) into a graduated cylinder. In this manner, the probe end of the tube intercepted the flowing spray and the collected liquid would drip into the graduated cylinder. Based on the local air speed, the quantity of air that arrived at the probe opening could be calculated. From the collected fluid, the quantity of water that arrived at the probe opening could be directly measured and compared with the air flow to give a local mixture strength.

In confirmation of the validity of this simple measurement, combustion of well-atomized kerosine sprays (30 μm SMD) showed that the flame speed peaked at an equivalence ratio of 1.1, as would be expected.

Measurements of flame speeds were carried out at equivalence ratios of 0.37, 0.74, and 1.10. Sauter mean diameters for the kerosine fuel drops were selected at 20, 30, 40, 50, 70, 90, and 110 μm. The hydrogen content was varied in three equal steps from 0 to 3.6 percent. The highest concentration employed was set deliberately below the hydrogen lean flammability limit. Exceeding this limit raised the possibility of establishing an independent hydrogen flame burning ahead of the main spray flame. Furthermore, the highest hydrogen concentrations reported here led to flame cone angles that approached the limitations of the experiment. Under these extreme conditions, the flame cone filled the duct such that additional hydrogen would lead to flashback through the slow-moving boundary layer at the duct walls.

In summary, the apparatus produces a uniform flowing mixture of kerosine fuel drops, hydrogen, and air. This mixture is characterized by known values of pressure, temperature, velocity, equivalence ratio, hydrogen content, and mean fuel drop size. A pilot flame ignites this mixture, which then burns in a cone-shaped flame. The angle of this flame is measured through schlieren photography and used to determine the flame speed.

Flame Speed Data

Figures 4 and 5 show flame speed versus equivalence ratio for 30 and 50 μm SMD, respectively. Data were collected at just three equivalence ratios, but the figures do show that the

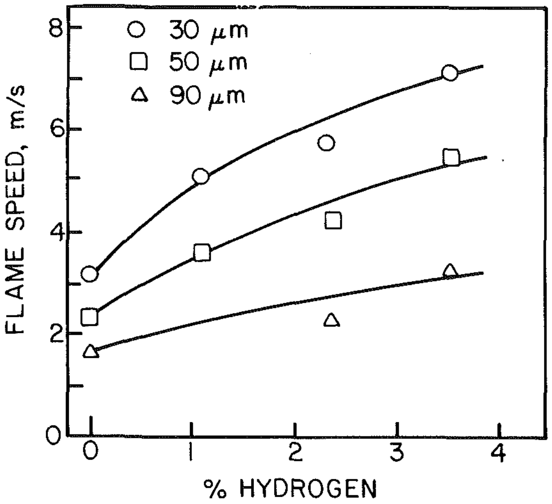

Fig. 7 Flame speed versus hydrogen content for various values of SMD; equivalence ratio = 0.74

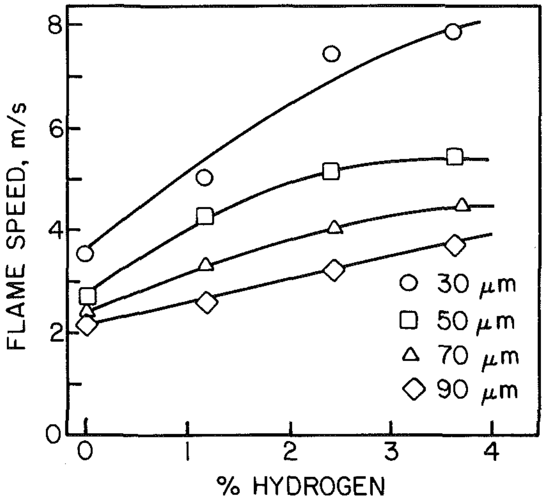

Fig. 8 Flame speed versus hydrogen content for various values of SMD; equivalence ratio = 1.1

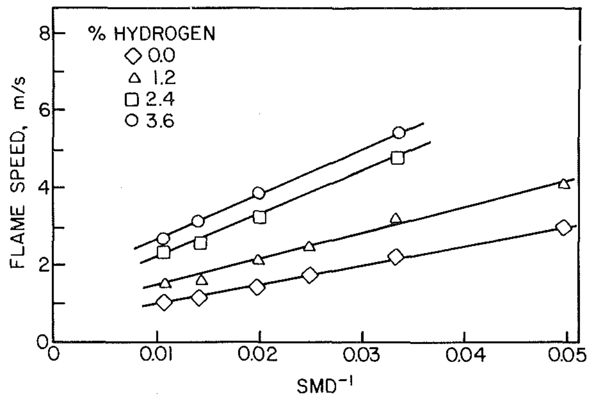

Fig. 9 Influence of fuel drop size on flame speed for various values of hydrogen content; equivalence ratio = 0.37

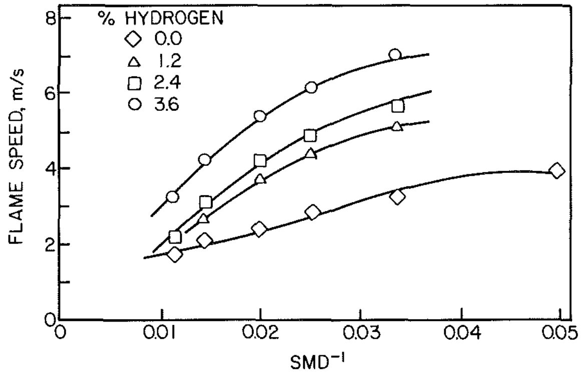

Fig. 10 Influence of fuel drop size on flame speed for various values of hydrogen content; equivalence ratio = 0.74

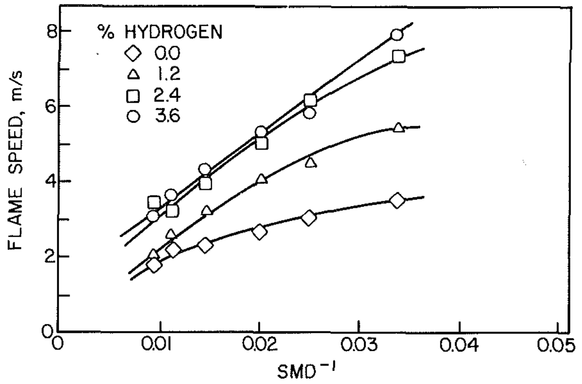

Fig. 11 Influence of fuel drop size on flame speed for various values of hydrogen content; equivalence ratio = 1.1

hydrogen-supplemented flame speed responds to changes in the hydrocarbon equivalence ratio in approximately the same manner as a pure hydrocarbon spray.

Figures 6–8 show flame speed data for various values of equivalence ratio and drop size, with hydrogen content varying from 0 to 3.6 percent. It is of interest to observe that the sensitivity of flame speed to hydrogen content generally declines at the highest hydrogen levels.

The influence of kerosine fuel drop size on flame speed when hydrogen is present is illustrated more directly in Figs. 9–11 in which flame speed data are shown plotted against 1/SMD at liquid fuel equivalence ratios of 0.37, 0.74, and 1.1, respectively. The curves shown in these figures are based on four different values of hydrogen content. Over a wide range of SMD values, they demonstrate a linear relationship between flame speed and 1/SMD. As discussed earlier, this is evidence of evaporation-limited combustion. However, some thought will show that these results cannot be explained solely in terms of a simple evaporative model. Inspection of the data shows that the plot of S versus 1/SMD is "shifted up" as hydrogen is added, with a modest increase in slope. The change in slope is consistent with an increase in evaporation rate, but the fact that the observed increase in flame speed with increase in hydrogen content is dependent on mean fuel drop size requires an alternative explanation.

With the evaporation rate being a direct function of the air thermal conductivity, it is of interest to calculate the thermal transport properties of the gaseous mixture when hydrogen is added. This calculation was carried out for all test conditions using the well-known program of Gordon and McBride (1976). The results show that the low concentrations of hydrogen used in this research produce only small increases in thermal conductivity and diffusivity. In fact, the maximum enhancement to thermal conductivity is 6 percent, while diffusivity increases by 16 percent. As flame speed is proportional to the square root of diffusivity and evaporation rate (Lewis and von Elbe, 1961), these modest changes to transport properties cannot account for the significant enhancements of flame speeds actually observed. The only feasible explanation is that the combustion of hydrogen must, in some manner, change the physical structure of the flame. The nature of this change is discussed below.

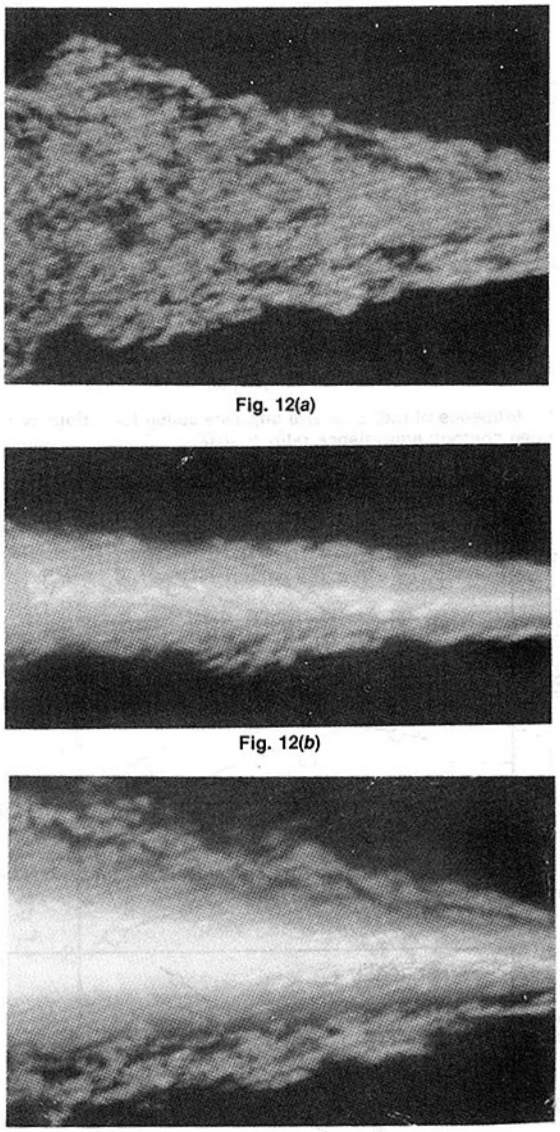

Fig. 12(a)

Fig. 12(b)

Fig. 12(c)

Fig. 12 Schlieren photographs illustrating effect of hydrogen content on flame structure

Discussion

The data presented show that addition of hydrogen gas can play a substantial role in promoting the combustion of liquid fuel sprays that otherwise appear to be limited by evaporation rates. As already mentioned, this observation is somewhat surprising considering that hydrogen produces only modest increases in transport properties and should thus have only a minor effect on fuel drop evaporation. This result suggests that a change in flame structure might accompany hydrogen addition. To investigate this possibility, high-speed flash (0.5 μs) schlieren photos were taken for three burning conditions and are shown in Fig. 12. Figure 12(*a*) shows a gaseous propane flame, which was established in the test section by injecting gaseous propane through the airblast manifold. This photo is included to identify the appearance of purely gas-phase combustion. The mottled surface is the result of hot gas eddies and is obviously not droplet combustion. Figure 12(*b*) is a kerosine spray flame burning under conditions of relatively poor atomization (90 μm SMD). There may be some evidence for single drop combustion near the edge of the flame cone, but the few detectable bright spots could equally well be hot gas eddies, as in Fig. 12(*a*). However, unlike Fig. 12(*a*), the flame cone in this spray is very bright because luminous emissions from the kerosine flame (not present with propane) unavoidably cloud the photographic film. Figure 12(*c*) corresponds to the same spray conditions as in Fig. 12(*b*), but with 3.6 percent hydrogen addition. The increased cone angle is clearly evident, but the flame seems now to have two distinct zones: a region of gas phase reaction (as in Fig. 12*a*) enclosing a highly luminous inner core (as in Fig. 12(*b*)). To the eye, the flame in Fig. 12(*c*) was uniformly brighter than for Fig. 12(*b*), but the photographs indicate that most of the light emerges from the inner core. These photographs suggest that the hydrogen is burning ahead of the main spray flame. Because the hydrogen is below its lean flammability limit, it requires heat from the main kerosene combustion to sustain burning. However, in a synergistic manner, the hydrogen also releases heat to promote the main flame that follows.

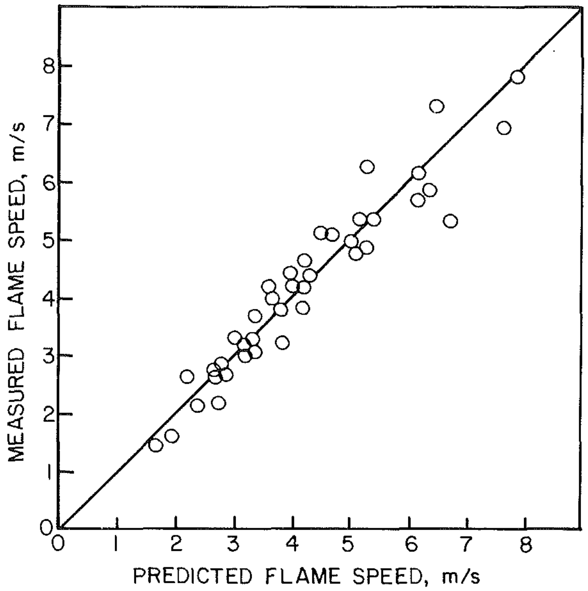

Fig. 13 Comparison of measured flame speeds with values calculated using equation (8)

Yu et al. (1986) have proposed the parameters ϕ_F and R_H to describe the relative hydrogen content as if the hydrogen and hydrocarbon separately consume the available air.

We have

$$\phi_F = \frac{C_F/[C_A - C_H/(C_H/C_A)_{st}]}{(C_F/C_A)_{st}} \tag{4}$$

and

$$R_H = \frac{C_H + C_H/(C_H/C_A)_{st}}{C_F + [C_A - C_H/(C_H/C_A)_{st}]} \tag{5}$$

where C_F, C_A, and C_H are respectively the mole fractions of hydrocarbon fuel, air, and hydrogen. Physically, ϕ_F represents the hydrocarbon fuel concentration relative to the air that is not used for hydrogen combustion. The numerator of the parameter R_H is the amount of hydrogen plus air needed to burn it completely, while the denominator represents the hydrocarbon concentration plus the air available to burn it.

These definitions of ϕ_F and R_H are fully compatible with the photographic evidence on flame structure obtained in the present experiments. Thus, the flame speed data acquired in this investigation might be expected to follow the correlation proposed by Yu et al., namely

$$S_{(\phi_F,R_H)} = S_o + \alpha R_H \tag{6}$$

where

$S_{(\phi_F,R_H)}$ = flame speed at conditions defined by ϕ_F and R_H

ϕ_F = hydrocarbon fuel equivalence ratio, defined above

Table 1

CONVENTIONAL HYDROCARBON EQUIVALENCE RATIO, ϕ	PERCENTAGE HYDROGEN ($\%H_2$)	EFFECTIVE EQUIVALENCE RATIO, ϕ_F	HYDROGEN PARAMETER R_H	$\frac{\%H_2}{R_H}$
0.37	0	0.37	0.00	-
0.37	1.2	0.38	0.042	28.6
0.37	2.4	0.39	0.088	27.3
0.37	3.6	0.40	0.135	26.7
0.74	0	0.74	0.00	-
0.74	1.2	0.75	0.042	28.6
0.74	2.4	0.78	0.087	27.6
0.74	3.6	0.80	0.134	26.9
1.1	0	1.10	0.00	-
1.1	1.2	1.13	0.042	28.6
1.1	2.4	1.17	0.087	27.6
1.1	3.6	1.20	0.133	27.1

R_H = relative hydrogen concentration, defined above
S_o = hydrocarbon (no hydrogen) flame speed at equivalence ratio ϕ_F
α = const

Equation (6) was developed for gaseous hydrocarbon/hydrogen mixtures. It was not available at the start of this research, and the experimental program was based on the conventional equivalence ratio ϕ, and the percentage of hydrocarbon ($\%$ H_2), in the flowing air stream. Table 1 lists values of ϕ_F and R_H that correspond to the conditions of ϕ and $\%$ H_2 studied here. The last column is the quotient of $\%$ H_2 and R_H, and shows that the ratio of these two parameters is almost constant. Neglecting the modest change in ϕ_F, this suggests that for spray combustion equation (6) can be written

$$S_{(\phi,\mathrm{SMD},\%H_2)} = S_o + \beta(\%H_2)/\mathrm{SMD} \tag{7}$$

In this equation, S_o is the flame speed of the kerosine-air mixture with no hydrogen present, at specified values of ϕ and SMD. Equation (7) recognizes that evaporation effects manifest themselves as the reciprocal of SMD. The constant β must be selected to provide the best fit to the experimental data. Analysis of the data over the following range of test conditions:

$$\phi = 0.37\text{-}1.1$$
$$\%\ H_2 = 0\text{-}3.6$$
$$\mathrm{SMD} = 30\text{-}90\ \mu\mathrm{m}$$

yields the following expression for flame speed:

$$S = S_o + 35(\%H_2)/\mathrm{SMD} \tag{8}$$

In this equation, the units of S and SMD are m/s and μm, respectively. Figure 13 shows a plot of measured values of flame speed versus predicted values from equation (8). The correlation achieved is considered satisfactory in view of the inherent errors associated with turbulent flame speed measurements by the angle method.

While equation (8) might prove useful for engineering calculations, it is by no means universal, and could change appreciably with change in fuel type. In particular it predicts a straight line relationship between flame speed and percentage hydrogen, whereas the lines drawn in Figs. 6-8 are slightly curved. Although from an engineering viewpoint these minor subtleties might well be neglected, the curves undoubtedly reflect certain physical aspects ignored by equation (8). For example, the small changes in transport properties created by the presence of hydrogen cannot account for the observed significant increase in flame speed, but they could influence some of the minor mixing and reaction phenomena involved in combustion, and thereby have a small but by no means negligible influence on flame speed.

Conclusions

The experimental data obtained in the present study on the influence of small additions of hydrogen gas on the flame speeds of kerosine sprays burning in air fully confirm the results of previous studies on the effects of hydrogen content on the burning rates of gaseous hydrogen-hydrocarbon-air mixtures.

Over wide ranges of kerosine fuel drop size and equivalence ratio, it is found that the effect on flame speed of small additions of hydrogen gas (below the flammability limit for hydrogen-air mixtures) is adequately described by the relationship

$$S = S_o + 35(\%H_2)/\mathrm{SMD}$$

where S_o is the flame speed of the kerosine-air mixture without hydrogen.

The results obtained suggest that evaporation rates have a controlling effect on flame speeds over wide ranges of kerosine fuel drop size (SMD). However, evaporation effects appear to be modified by the presence of hydrogen gas, which affects flame speeds to an extent that is much larger than would be predicted by examination of the influence of hydrogen on the transport properties governing fuel drop evaporation. The combined combustion of hydrogen gas and kerosine fuel drops appears to produce a synergistic effect. The hydrogen burns ahead of the main kerosine flame at an equivalence ratio that is below its normal lower flammability limit. Its combustion is sustained by the kerosine flame which, in turn, is accelerated to higher than normal values of flame speed by the heat released in the preceding hydrogen flame.

References

Annushkin, Iu. M., and Maslov, G. F., 1985, "Combustion Efficiency of a Hydrogen-Kerosene Fuel in a Straight-Through Channel" [in Russian], *Fizika Goreniia i Vzryva*, Vol. 21, pp. 30-32.

Ballal, D. R., and Lefebvre, A. H., 1975, "The Structure and Propagation of Turbulent Flames," *Proc. Roy. Soc. London*, Vol. 334, Series A, pp. 217-234.

Ballal, D. R., and Lefebvre, A. H., 1981, "Flame Propagation in Heterogeneous Mixtures of Fuel Droplets, Fuel Vapor, and Air," *18th Symposium (International) on Combustion*, The Combustion Institute, pp. 321-328.

Gordon, S., and McBride, B. J., 1976, "Computer Program for Complex Chemical Equilibrium Composition, Incident and Reflected Shocks, and Chapman-Jouget Detonations," NASA SP-273.

Lewis, B., and von Elbe, A., 1961, *Combustion, Flames and Explosions of Gases*, Academic Press, New York.

Milton, B. E., and Keck, J. C., 1984, "Laminar Burning Velocities in Stoichiometric Hydrogen and Hydrogen-Hydrocarbon Gas Mixtures," *Combustion and Flame*, Vol. 58, No. 1, pp. 13-22.

Mizutani, Y., and Nishimoto, T., 1972, "Turbulent Flame Velocities in Premixed Sprays—Part I, Experimental Study," *Combustion Science and Technology*, Vol. 6, pp. 1-10.

Myers, G. D., and Lefebre, A. H., 1986, "Flame Propagation in Heterogeneous Mixtures of Fuel Drops and Air," *Combustion and Flame*, Vol. 66, No. 2, pp. 193-210.

Richards, G. A., Sojka, P. E., and Lefebvre, A. H., 1985, "Drop Size Studies in a Radially Uniform Spray," *SAE Transactions, Fuels and Lubricants*, Vol. 94, No. 7, pp. 570-576.

Yu, G., Law, C. K., and Wu, C. K., 1986, "Laminar Flame Speeds of Hydrocarbon and Air Mixtures With Hydrogen Addition," *Combustion and Flame*, Vol. 63, No. 3, pp. 339-347.

Scalar Characteristics of Combusting Flow in a Model Annular Combustor

A. F. Bicen

M. Senda[1]

J. H. Whitelaw

Imperial College of Science & Technology,
Department of Mechanical Engineering,
Fluids Section,
London SW7 2BX, United Kingdom

Temperature and species concentration measurements have been obtained in a model combustor operating at an inlet temperature of 515 K and atmospheric pressure and are reported and discussed. The model comprises two rectangular sectors representing the primary and upper dilution zones of an annular combustor used in small gas-turbine engines. Natural gas (94 percent CH_4) was used as fuel and was delivered through a T-vaporizer at rates that led to air-fuel ratios of 29 and 50, similar to those of take-off and ground-idle conditions, respectively. Temperatures were obtained at the exit of the combustor using fine-wire thermocouples and mean concentrations of major species were obtained in the primary zone and at the exit on a dry basis by gas sampling and analysis. The results show that the 200 K increase in inlet air temperature reduces the pattern factor from 0.55 to 0.3 and increases the combustion efficiency from 69 to 94 percent with the air-fuel ratio of 29. The higher air-fuel ratio improves the combustion efficiency to 97.6 percent but results in a worse pattern factor of 0.48. The results confirm the need for consideration of the rate-controlled $CO \rightarrow CO_2$ reaction in the dilution zone if CO emission is to be calculated correctly and temperatures are to be within 150 K. Examination of temperatures obtained from a local enthalpy balance shows that they are higher than measurements obtained with preheat, in contrast to a similar comparison without preheat.

Introduction

This investigation is concerned with the scalar characteristics of the combusting flow in a model annular combustor operating with preheat at near-atmospheric pressure. It involves measurements of temperature characteristics and mean concentrations of major species and, when examined in relation to the related measurements of Bicen et al. (1987, 1988), which were obtained without preheat, provides information on the controlling mechanisms. The present flow conditions compare to those of engine practice, except for the use of gaseous fuel and atmospheric pressure. In addition, they provide a testing ground of sufficient accuracy and detail for assessment and development of calculation methods, including those that use numerical methods for the solution of conservation equations in differential form (Jones and Whitelaw, 1984).

The particular model arrangement involves fuel injection through a T-vaporizer, which is in accord with current engine developments (Sotheran, 1984), and makes use of two rectangular sectors representing the primary and upper dilution zones of the annular combustor. The flow is characterized by a primary vortex driven by three film-cooling jets and limited by primary air jets injected normal to the bulk flow with additional film-cooling jets and dilution air jets to ensure adequately cool walls and exit-plane temperatures. The model geometry and the nature of the flow in the combustor are similar to those of Toral and Whitelaw (1982) but with some geometric changes, including the addition of a set of primary holes and vaporizer fueling, which makes the model more in accord with the real combustor.

In a real gas turbine combustor, the inlet air pressure and temperature are substantially higher than atmospheric conditions and, therefore, the combustion process cannot be characterized with the physical processes alone and the thermodynamic state of the gas, in particular its temperature, has to be accounted for. The main purpose of the investigation is, therefore, to provide information with a more realistic geometry than that used by Toral and Whitelaw (1982) and under more realistic flow conditions than those of Bicen et al. (1987, 1988). Here the experiments were carried out with the geometry of Bicen et al. (1987, 1988) and with an inlet air temperature of 200 K above ambient for air-fuel ratios of 29 and 50 corresponding to take-off and ground-idle conditions. Some of the results of Bicen et al. (1988) are reproduced here so as to quantify the effect of preheat on combustion characteristics.

---

[1] Present address: Doshisha University, Department of Mechanical Engineering, Kyoto 602 Japan.

Contributed by the International Gas Turbine Institute and presented at the 33rd International Gas Turbine and Aeroengine Congress and Exhibition, Amsterdam, The Netherlands, June 5–9, 1988. Manuscript received by the International Gas Turbine Institute December 9, 1987. Paper No. 88-GT-14.

Table 1 Geometric details of combustor (Fig. 1 identifies the entrances to the combustor by number)

Cooling slots	Slot height/ mm	No. of holes	Diam/mm	Pitch/mm
2	1.65	21	2.25	5.91
3	1.38	24	2.00	5.20
4	1.38	24	1.65	5.20
5	1.60	18	2.40	6.84
7	1.10	18	1.65	6.84
Primary and dilution holes	Hole diam/ mm	No. of holes	Pitch/mm	
1	6.2	4	28	
6	4.6	5	28	
8	4.6	2	56	
Vaporiser	Exit diam/ mm			
9	5			
10	5			

Table 2 Flow conditions and air split of combustor

Air-fuel ratio	Mass flow rate of air, g/s	Mass flow rate of fuel, g/s	Inlet temperature K
29	26.0	0.90	515
50	26.0	0.52	515
29	33.8	1.17	315

$\dot{m}T^{\frac{1}{2}}/AP$ is constant in all three cases

Combustor entrance (No's as in Figure 1)	1	2	3	4	5	6	7	8
% of mass flow*	27	8	12.3	15	8.2	16	6	7.5

* within $\pm$ 4%

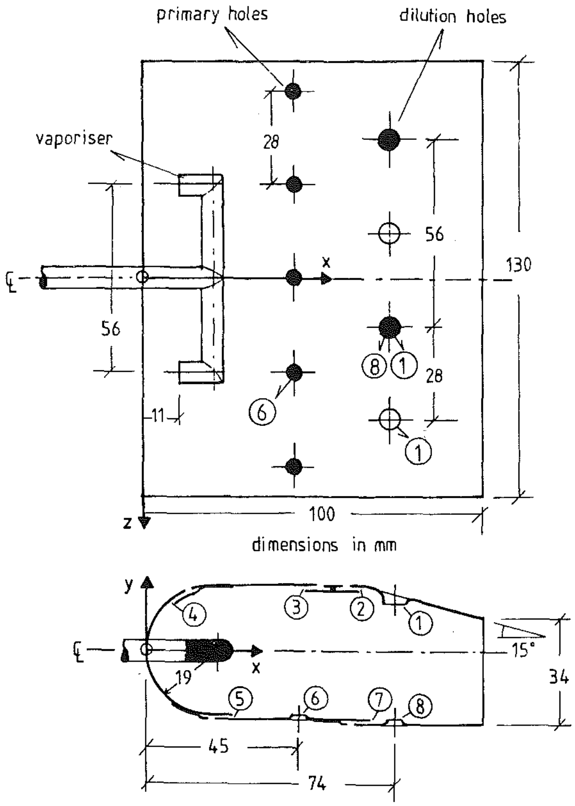

Fig. 1 Combustor geometry

A second purpose of the work is to assess the accuracy of inferring temperatures from a local enthalpy balance and to quantify the extent to which the combustion processes can be characterized by mean flow properties and equilibrium reactions.

The measurement techniques are similar to those of Bicen et al. (1986) and Heitor and Whitelaw (1986). Temperature was obtained by fine wire thermocouples with digital sampling. Concentrations of unburned hydrocarbon (UHC), CO_2, CO, O_2, and H_2 were obtained by a sampling probe with appropriate gas analyzers. The flow configuration and the measurement techniques, together with the associated uncertainties, are described in the following section. Results are presented and discussed in the subsequent sections to address the purposes mentioned in the previous paragraph. The final section summarizes the main findings of the investigation.

Experimental System

The geometry of the model combustor is shown in Fig. 1 and its geometric details provided in Table 1. The combustor is similar to the reverse-flow annular combustor of the Gem-60 engine used in helicopters. It comprises two rectangular sectors representing the primary and upper dilution zones of the annular combustor and makes use of a **T**-vaporizer mounted on the head; the real engine combustor comprises, in addition, a lower dilution zone in the form of a reverse-flow nozzle with additional film-cooling air. The use of the **T**-vaporizer is convenient particularly since, with gaseous fuel used here, questions on the extent of vaporization of liquid fuel are removed. The combustor consists of five film-cooling slots, a set of five primary holes located on the lower wall (two of which are in line with the vaporizer exits), and two sets of dilution holes staggered by a half-pitch with respect to the primary holes. The combustor was mounted in the flow arrangement of Fig. 2, which provided air flow at a constant rate with near-atmospheric pressure and inlet temperature of around 515 K to plenum chambers surrounding the combustor. The plenum chambers replace the reverse-flow casing of the real combustor and allowed the same static pressure on the outer surfaces of the combustor.

Natural gas (94 percent CH_4) was used as fuel and delivered to the **T**-vaporizer by a pump at flow rates which led to air-fuel ratios of 29 and 50, corresponding to the take-off and ground-idle conditions for the Gem-60, when burning kerosene, respectively; the mass flow rates were scaled according to the parameter $mT^{1/2}/AP$, where m is the mass flow rate, T the temperature, and P the pressure at the inlet to the combustor, and A is the cross-sectional area of the combustor. The flow conditions and the air-flow split of the combustor are summarized in Table 2.

Temperature measurements were obtained with thermocouples made from 80 μm platinum/13 percent rhodium and platinum wires. The temperature signal was amplified, digitized, and processed in a microcomputer to determine the mean and rms values of temperature fluctuations, which, as discussed by Heitor et al. (1985), are closely related to the unweighted averages. The uncertainty in the mean value was due mainly to radiation losses and was always less than 8 percent. The maximum uncertainty in the rms value was around 10 percent and was due mainly to uncertainties in the time constant of the thermocouple wire (Bicen et al., 1986).

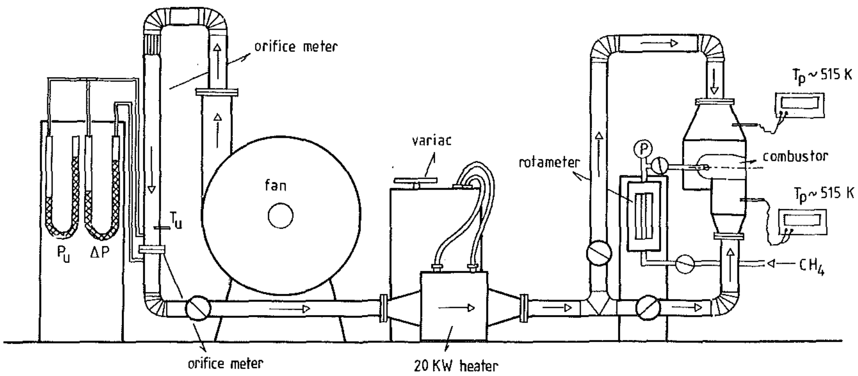

Fig. 2 Schematic of flow arrangement

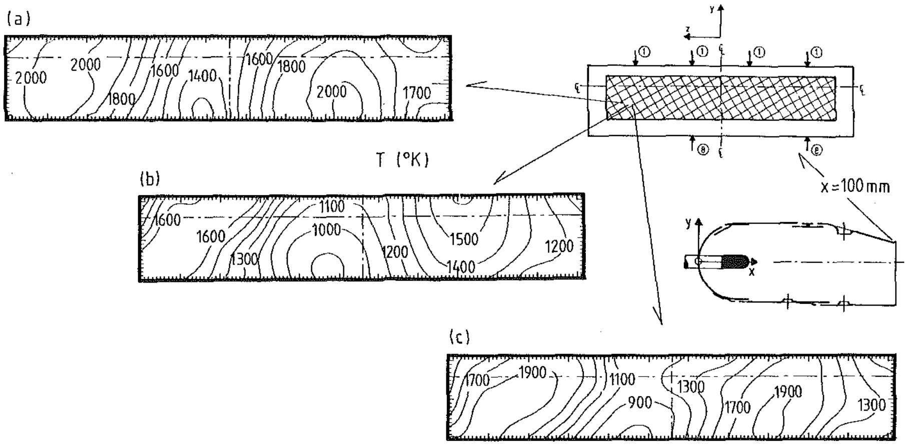

Fig. 3 Mean temperature distributions at exit: (*a*) air-fuel ratio of 29 with preheat; (*b*) air-fuel ratio of 50 with preheat; (*c*) air-fuel ratio of 29 without preheat

Concentration measurements were made by extracting samples of gas through a water-cooled probe inside and at the exit of the combustor and passing the sample to various gas analyzers to determine, on a dry basis, volume concentrations of UHC (by a flame-ionization detector), O_2 (by a paramagnetic analyzer), H_2 (by a gas chromatograph), and CO and CO_2 (by infrared detectors). Uncertainties in gas analysis were less than ±0.5 percent of the full scale of each analyzer, but larger errors are likely to result from the sampling process. The outside and inside diameters of the water-cooled probe were 8.0 and 1.0 mm, respectively, and consequent flow disturbances (Bilger, 1977) can be important, particularly in the primary zone, but cannot readily be quantified. The suction velocity was kept constant at around 20 m/s and was close to that of the gas at the exit of the combustor. It is expected that measured concentrations of major species are close to density-weighted averages and within 10 percent of the maximum value as discussed by Kennedy and Kent (1981).

Results

The measurements of mean temperature and species concentrations are presented in contour form for ease of interpretation. Although the species concentrations were obtained on a dry basis as described in the previous section, they are converted and presented on a wet basis together with the corresponding equivalence ratios, ϕ, calculated from the wet mean concentrations. The results describe in detail the temperature and concentration fields at the exit of the combustor for air-fuel ratio of 29 with preheat and include the temperature measurements for air-fuel ratio of 50 with preheat. Some of the results of Bicen et al. (1988) are also presented here to quantify the effect of a preheat of 200 K on exit combustion characteristics. In the primary zone, measurements are in less detail and were restricted to species concentrations only as it was not possible to make thermocouple measurements due to high temperatures (>2200 K) prevailing in this zone.

Temperature. Exit temperature distributions for air-fuel ratios of 29 and 50 with preheat and for air-fuel ratio of 29 without preheat (Bicen et al., 1988) are shown in Fig. 3. In all three cases, high-temperature regions on either side of the center plane can be observed and temperature distributions are asymmetric about the center plane. Although the hot region on the negative z side is in line with the vaporizer exit, the one on the positive z side has moved farther away from the center plane due to the two lower dilution jets, which are arranged asymmetrically about the center plane (see Fig. 1). There is more dilution air on the negative z side and as a consequence, the temperatures on this side are lower by some 7 percent in all three cases. Increasing the air-fuel ratio from 29 to 50 decreases, as expected, the overall exit temperature from around 1810 K to 1350 K and the maximum value from about 2200 K to 1700 K. Comparison of Fig. 3(*a*) with 3(*c*) quantifies the effect of 200 K preheat on the exit temperature field and shows that the overall exit temperature has been increased by 530 K, which is substantially higher than the expected value of about 120 K, clearly indicating the inferior combustion efficiency achieved in the absence of preheat (Bicen et al., 1988). This observation is verified with concentration measurements presented and discussed in the following subsection.

With preheat, temperature distributions are flatter and this reflects on the exit pattern factor, evaluated from the expression

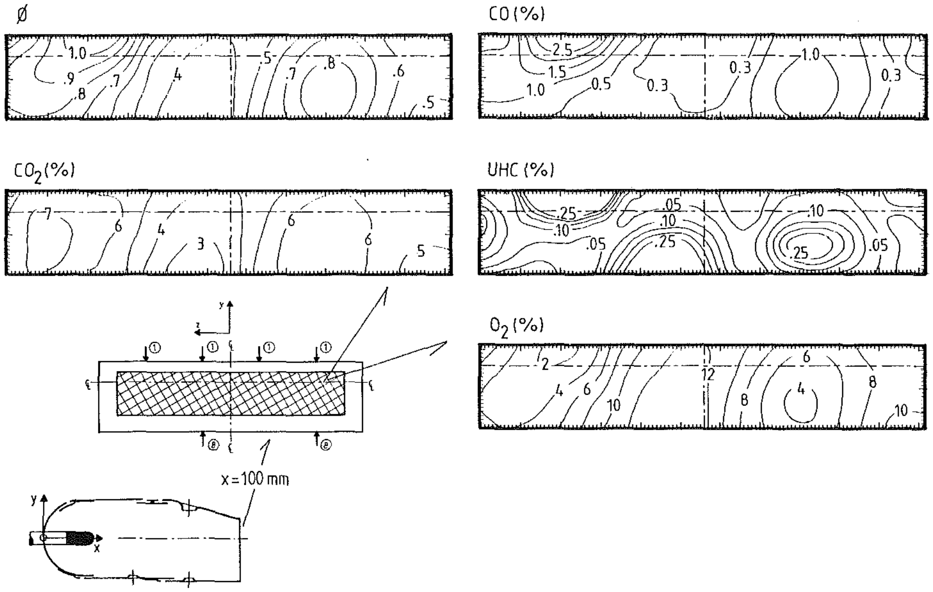

Fig. 4 Distributions of mean species concentrations at exit for air-fuel ratio of 29 with preheat

Table 3 Exit plane characteristics

	Air-fuel ratio	Pattern factor	EI_{CO} (g/kg fuel)	EI_{UHC} (g/kg fuel)	Combustion efficiency (%)
preheat	29	0.29	181	21	94.2
	50	0.48	64	11	97.6
no preheat	29	0.55	228	260	69.0

$$pf = \frac{T_{\max} - T_{\text{mean}}}{T_{\text{mean}} - T_{\text{inlet}}} \tag{1}$$

The pattern factor with preheat is around 0.3, which is very close to that of engine practice (0.3–0.35), compared to 0.55 achieved without preheat. Increasing the air-fuel ratio to 50 has a similar effect to that without preheat, as in both cases the overall temperature decreases, and results in a higher pattern factor of around 0.48.

Species Concentrations. Figure 4 shows the distributions of species concentrations and equivalence ratio at the combustor exit for air-fuel ratio of 29 with preheat. Preliminary measurements of H_2 at the exit showed insignificant levels (<0.5 percent) and, since the chromatography was necessarily a time-consuming technique, H_2 measurements were not made at the combustor exit. The distributions, particularly those of ϕ, CO_2, and O_2, show similar trends to those for temperature in Fig. 3(*a*). It is evident from the UHC distributions that the fuel is still present in the exit plane and that it is distributed along the lower wall and more or less in line with the vaporizer exits. Similar observations were made by Bicen et al. (1988) without preheat but UHC levels were significantly higher with a maximum value in excess of 3 percent.

A quantified summary of these observations can be given in terms of combustion efficiency and emission indices of CO and UHC, as described by Mellor (1976), and these are given, together with the pattern factors, in Table 3. In Table 3 the corresponding results of Bicen et al. (1988) for air-fuel ratio of 29 without preheat and those for air-fuel ratio of 50 with preheat are included to aid comparison. In parallel with the findings of Heitor and Whitelaw (1986) in a can-type combustor, it is clear that the low values of efficiency and high values of pattern factor observed without preheat stem from the limitations imposed by the use of atmospheric conditions. As expected, the higher the average temperature, the lower the emission indices and pattern factor and the higher the efficiency.

On the basis of the flow symmetry observed by Bicen et al. (1987, 1988), the measurements of species concentrations in the primary zone have been obtained in half cross-planes and the corresponding distributions are shown in Fig. 5, for air-fuel ratio of 29. The temperature was evaluated from a local heat balance using measured concentrations, see the following section, and shows a close resemblance to that observed without preheat (Bicen et al., 1988) in that the high-temperature region is in the upper half of the primary zone and in line with the vaporizer exit. The fuel stream, which is close to the lower wall of the combustor, is dispersed to the upper half on impact with the primary jets resulting in equivalence ratios close to stoichiometric and consequently high temperatures in this half. UHC levels are very high, in excess of 25 percent, in the presence of O_2 near the lower wall and indicate that reactions have not proceeded to equilibrium in this fuel-rich region. Maximum levels of CO and H_2 are around 3.5 percent and occur in the plane of primary jet and in line with the vaporizer exit. The CO_2 distribution is similar to that of the temperature and has its highest value of around 7 percent in the upper half of the primary zone.

Discussion

The results of the previous section are discussed here to quantify the extent to which the combustion processes can be characterized by mean flow properties and equilibrium reactions and to assess the accuracy of inferring temperatures from a local enthalpy balance using measured concentrations.

Major species and temperature may be calculated from values of equivalence ratio with the assumption of chemical equilibrium. The corresponding distributions are shown in Figs. 6 and 7 for the primary zone and exit of the combustor, respectively, and may be compared to the corresponding distributions of Figs. 3, 4, and 5 for air-fuel ratio of 29 with preheat. The calculated distributions were obtained by minimizing the free energy as described by Gordon and McBride (1971). In these calculations turbulent fluctuations were neglected and instead of the full-equilibrium assumption, which would result in much higher CO levels than found in practice (Heitor and Whitelaw, 1976), a partial-equilibrium model based on the rich flammability limit restriction of Godoy (1982) was adopted. It was assumed that the mean composition corresponded to chemical equilibrium for mixtures leaner than $\phi = 2.5$ and that for richer mixtures the composition was that of chemical equilibrium at $\phi = 2.5$ diluted with pure fuel.

The measured and equilibrium CO_2 distributions are similar in the primary zone (Figs. 5 and 6), with differences that may be attributed to the neglect of fluctuations. The equilibrium CO and H_2 levels are, however, higher than measured levels by almost an order of magnitude near the lower wall, indicating that even the modified equilibrium assumption is unable to predict reasonable CO and H_2 levels in this region. The comparison suggests that in the fuel-rich primary zone, the CO → CO_2 reaction is fast and controlled more by physical than chemical process and the global fuel breakdown has been inhibited particularly in very fuel-rich regions close to the lower wall. Similar observations were also made by Bicen et al. (1988) and Toral and Whitelaw (1982) and in the primary zone of a can-type combustor by Heitor and Whitelaw (1986).

The measured and equilibrium temperatures have similar trends at the exit of the combustor (Figs. 3*a* and 7), with equilibrium temperatures generally higher in hot regions by around 100 K, which is within the measurement uncertainty. The O_2 levels of Figs. 4 and 7 are also in close agreement but lower-than-equilibrium values of CO_2 and higher CO levels indicate that the CO → CO_2 oxidation is chemical kinetic rate limited. In contrast to the results of Bicen et al. (1988) without preheat, the fuel breakdown is complete and the low level of

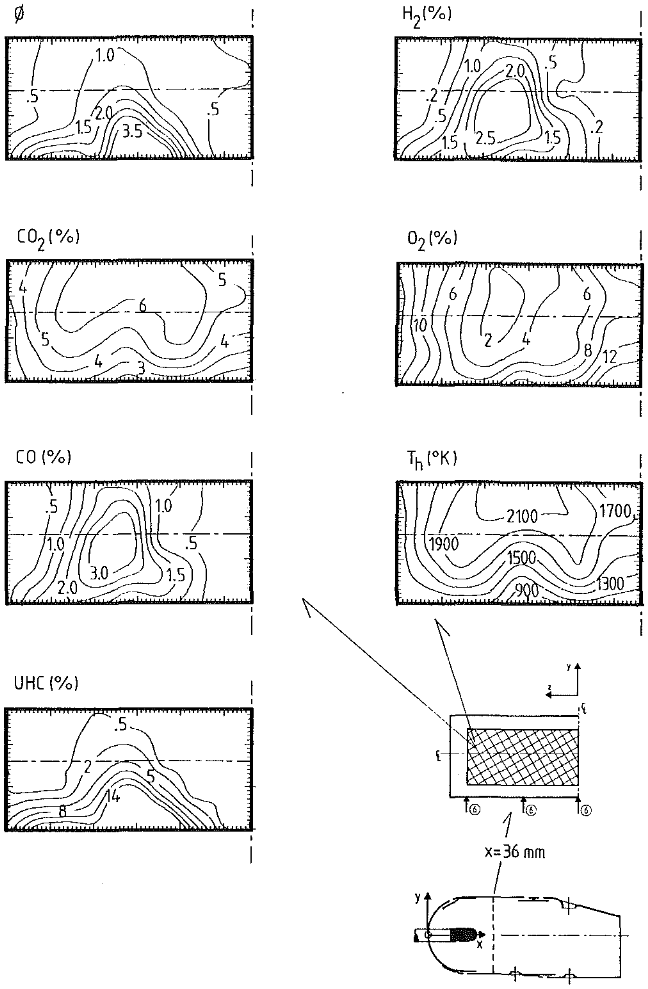

Fig. 5 Distributions of mean species concentrations and enthalpy temperature in primary zone for air-fuel ratio of 29 with preheat

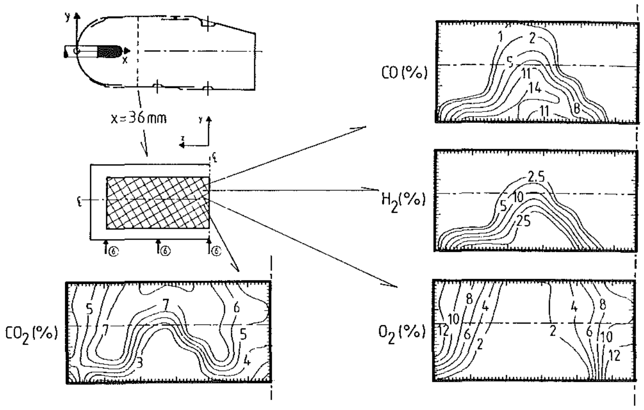

Fig. 6 Equilibrium distributions of mean species concentrations in primary zone for air-fuel ratio of 29 with preheat

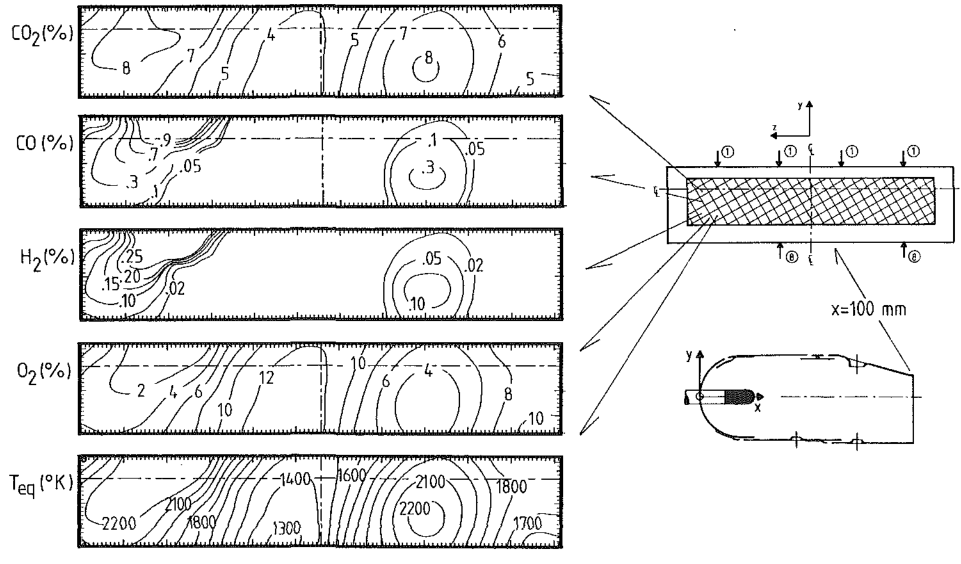

Fig. 7 Equilibrium distributions of mean species concentrations and temperature at exit for air-fuel ratio of 29 with preheat

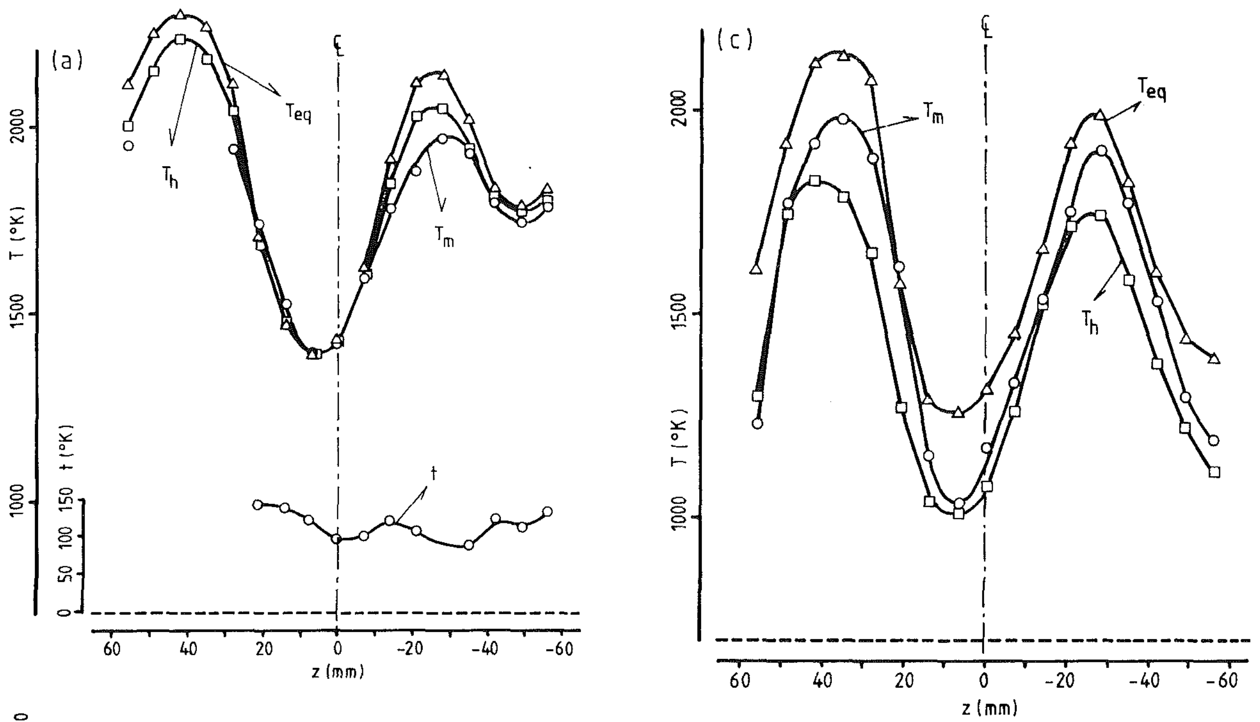

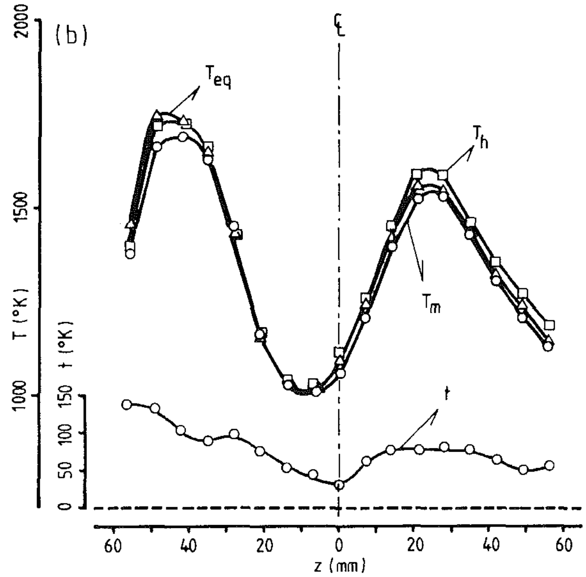

Fig. 8 Calculated and measured temperature profiles at exit (*x* = 100 mm, *y* = 0): (*a*) air-fuel ratio of 29 with preheat; (*b*) air-fuel ratio of 50 with preheat; (c) air-fuel ratio of 29 without preheat

equilibrium H_2 in Fig. 7 supports the choice of not measuring H_2 at the combustor exit.

The measured temperature T_m by a fine-wire thermocouple is close to an unweighted average (Heitor et al., 1985) and the relation between T_m and the density-weighted temperature $\tilde{T}$ can thus be expressed as

$$T_m = \tilde{T} - \frac{\overline{\rho' T'}}{\rho} \tag{2}$$

where the superscript ($\overline{\ }$) represents an unweighted average, ($\tilde{\ }$) a density-weighted average, and (′) fluctuations from an unweighted mean. According to this relation, therefore, $\tilde{T}$ will be less than T_m since the correlation $\overline{\rho' T'}$ is always negative.

Density-weighted temperatures can be evaluated from a local heat balance using measured concentrations, which represent values close to density-weighted averages. Assuming adiabatic conditions, an enthalpy balance gives (Toral and Whitelaw, 1982)

$$\tilde{T} \simeq \frac{\tilde{h} - \Sigma(\tilde{m}_\alpha \Delta h_{f\alpha}) - \Sigma c_{p\alpha} \widetilde{m_\alpha'' T''}}{\Sigma(c_{p\alpha} \tilde{m}_\alpha)} \tag{3}$$

where the superscript (″) represents fluctuations from density-weighted average and $\Delta h_{f\alpha}$ is the standard heat of formation of species, $c_{p\alpha}$ the average specific heat of species, m_α the measured mole fraction of species, and $\tilde{h}$ the enthalpy of the local mixture. Since no information on $\widetilde{m_\alpha'' T''}$ existed, it was assumed to be zero and the temperatures T_h shown in Fig. 8 were calculated according to

$$T_h = \frac{\tilde{h} - \Sigma(\tilde{m}_\alpha \Delta h_{f\alpha})}{\Sigma(c_{p\alpha} \tilde{m}_\alpha)} \tag{4}$$

Since $\widetilde{m_\alpha'' T''}$ is a finite quantity in practice, the relation between T_h and $\tilde{T}$ is thus given by

$$T_h = \tilde{T} + \frac{\Sigma(c_{p\alpha} \widetilde{m_\alpha'' T''})}{\Sigma(c_{p\alpha} \tilde{m}_\alpha)} \tag{5}$$

It is clear from equation (5) that T_h can be higher or lower than $\tilde{T}$ depending on the sign of the last term, which is more likely to be negative in fuel-rich regions.

A comparison between the measured and enthalpy temperatures at the exit with air-fuel ratio of 29 is given in Fig. 8, which includes similar comparisons for air-fuel ratio of 50 and for air-fuel ratio of 29 without preheat. In Fig. 8 corresponding profiles of equilibrium temperatures are also presented for the three cases. With preheat (Figs. 8*a* and 8*b*), the measured temperatures are consistently lower than the enthalpy temperatures and the differences are less with the higher air-fuel ratio and lower temperatures. The observed differences are of the order of the radiation losses of the thermocouple and indicate that the last terms in equations (2) and (5) have an insignificant effect with preheat so that the measured and calculated temperatures agree well at the exit. The measurements of rms temperature fluctuations *t* at the exit are also presented in Figs. 8(*a*) and 8(*b*), and are generally less than 6 percent. In the absence of preheat, however, fluctuations are higher and combustion is incomplete at the exit (Bicen et al., 1988), so that the much higher levels of CO, H_2, and UHC, which are negatively correlated with temperature, cause the last term in equation (5) to become large and negative. The calculated enthalpy temperatures therefore become consistently much lower than the measured temperatures (up to 200 K) at the exit without preheat. In all three cases equilibrium temperatures are higher than measured and enthalpy temperatures and the differences, as expected, become larger by up to 300 K in the absence of preheat, compared to, on average, around 100 K with preheat.

Conclusions

The main findings of the investigation may be summarized as follows:

1 The effect of increasing the combustor inlet air temperature by 200 K was to increase the maximum and average exit temperature by about 35 percent, reduce the pattern factor from 0.55 to around 0.30, and reduce the emission indices of CO and UHC so as to increase the combustion efficiency from 69 percent to 94.2 percent with an air-fuel ratio of 29.

2 Increasing the air-fuel ratio from 29 to 50 with preheat reduced the overall temperature at the exit and resulted in an increased pattern factor of 0.48 and combustion efficiency of 97.6 percent.

3 The comparison of measured results with chemical equilibrium calculations indicated that the $CO \rightarrow CO_2$ reaction was relatively fast in the primary zone and was affected by finite-rate kinetics in the dilution zone. Equilibrium temperatures at the exit were within 8 percent of the measured values, i.e., around 150°C.

4 Exit temperatures calculated on the basis of a local enthalpy balance using measured species concentrations indicated that enthalpy temperatures with preheat were higher than measured temperatures by an amount close to the radiation losses of the thermocouple, but without preheat an opposite trend was observed where enthalpy temperatures were lower by up to 200 K than measured values mainly due to the relatively high fluctuations and high levels of CO, UHC, and H_2 at the exit in the absence of preheat.

Acknowledgments

The authors would like to acknowledge the financial support from Rolls-Royce plc and from the Procurement Executive of the Ministry of Defence. They, and the paper, have benefited from many useful discussions with colleagues at Rolls-Royce plc, The Royal Aircraft Establishment at Pyestock, and Imperial College.

References

Bicen, A. F., Heitor, M. V., and Whitelaw, J. H., 1986, "Velocity and Temperature Measurements in a Can-Type Gas-Turbine Combustor," AGARD-CP-399, Paper 14.

Bicen, A. F., Tse, D., and Whitelaw, J. H., 1987, "Flow Characteristics of a Model Annular Combustor," AGARD-CP-422, Paper 14.

Bicen, A. F., Tse, D., and Whitelaw, J. H., 1988, "Flow and Combustion Characteristics of an Annular Combustor," *Combustion and Flame*, Vol. 72, pp. 175-192.

Bilger, R. W., 1977, "Probe Measurements in Turbulent Combustion," *AIAA Progress in Aeronautics and Astronautics*, Vol. 53, pp. 49-69.

Godoy, S., 1982, "Turbulent Diffusion Flames," Ph.D. Thesis, University of London, United Kingdom.

Gordon, S., and McBride, B. J., 1971, "Computer Programme for Calculation of Complex Chemical Equilibrium Compositions," NASA SP-273.

Heitor, M. V., Taylor, A. M. K. P., and Whitelaw, J. H., 1985, "Simultaneous Velocity and Temperature Measurements in a Premixed Flame," *Experiments in Fluids*, Vol. 3, pp. 323-339.

Heitor, M. V., and Whitelaw, J. H., 1986, "Velocity, Temperature and Species Characteristics of the Flow in a Gas-Turbine Combustor," *Combustor and Flame*, Vol. 64, pp. 1-32.

Jones, W. P., and Whitelaw, J. H., 1984, "Modelling and Measurements in Turbulent Combustion," *20th Symposium (International) on Combustion*, The Combustion Institute, pp. 233-249.

Kennedy, I. M., and Kent, J. H., 1981, "Scalar Measurements in a Co-flowing Turbulent Diffusion Flame," *Comb. Sci. & Tech.*, Vol. 25, pp. 109-119.

Mellor, A. M., 1976, "Gas Turbine Engine Pollution," *Prog. Energy Comb. Sci.*, Vol. 1, pp. 111-133.

Sotheran, A., 1984, "The Rolls-Royce Annular Vaporizer Combustor," ASME JOURNAL OF ENGINEERING FOR GAS TURBINES AND POWER, Vol. 106, pp. 88-95.

Toral, H., and Whitelaw, J. H., 1982, "Velocity and Scalar Characteristics of the Isothermal and Combusting Flows in a Combustor Sector Rig," *Combustion and Flame*, Vol. 45, pp. 251-272.

Fluid Dynamics of a Conical Flame Stabilizer

D. R. Ballal
Senior Research Engineer.
Mem. ASME

T. H. Chen
Associate Research Engineer.

W. J. Schmoll
Assistant Research Physicist.

University of Dayton,
Dayton, OH 45469-0001

Turbulence measurements were performed on a 45 deg conical flame stabilizer with a 31 percent blockage ratio, mounted coaxially at the mouth of a circular pipe and supplied with a turbulent premixed methane-air mixture at a Reynolds number of 2.85×10^4. A two-component LDA system was used in the measurement of mean velocities, turbulence intensities, Reynolds stresses, skewness, and kurtosis. It was found that combustion accelerates mean-flow velocities but damps turbulence intensity via the processes of turbulent dilatation and viscous dissipation due to heat release. Measurements in the axial direction showed that the length of the recirculation zone was nearly doubled as a result of combustion. Also, the region around the downstream stagnation point where streamlines meet and velocities change direction was found to be highly turbulent. Skewness and kurtosis data indicated that large-scale eddies carrying fresh combustible mixture are entrained into the high-shear region surrounding the recirculation zone. Finally, a discussion of turbulence-combustion interaction is presented to explain these experimental results.

Introduction

In practical combustion systems, e.g., afterburners, a widely used method of stabilizing the flame is the introduction of a bluff body such as a cone or a "Vee" gutter in the flowstream. Flow separation takes place around the trailing edge of the bluff body and produces in its near wake a low-velocity recirculatory zone. According to Zukoski and Marble (1955), fresh mixture entering the shear layer is ignited by the hot recirculating combustion products. The burning mixture then flows downstream, in turn igniting neighboring pockets of unburned mixture. Finally, a portion of the fully burned gases leaving the shear layer recirculates back into the wake region and provides a continuous source of ignition to the incoming fresh mixture. In this manner, a stable flame spreads outward from the trailing edge of the bluff body. Numerous studies of vortex shedding from bluff bodies in a turbulent cold flow are available; for example, see Bearman and Morel (1983), Bearman (1984), Calvert (1967), Carmody (1964), Davies and Beer (1971), and Griffin (1985). Typically, these studies have emphasized the determination of mean pressure and velocity fields, eddy-shedding frequency, drag coefficients, Strouhal number correlations, and influence of blockage ratio and bluff-body shape on recirculation zone size. In contrast, very little information is available on the turbulent combustion process. The works of Bovina (1959) and Winterfeld (1965) emphasize the effects of recirculation zone geometry on turbulent exchange coefficients and mean residence time, but do not provide adequate experimental data for turbulence modeling codes. Recent efforts of Heitor and Whitelaw (1986), and Sivasegaram and Whitelaw (1987) have begun to address this deficiency. But, here again, the emphasis has been on testing a gas turbine combustor, measuring stability limits and sound intensity, and suppressing combustion instability, as opposed to fundamental investigations.

The main objectives of the present investigation were (*a*) to perform detailed turbulence measurements, with and without combustion, on a conical flame stabilizer, (*b*) to interpret these data to enhance our understanding of the flame stabilization process, and (*c*) to provide benchmark quality data for evaluating computer modeling codes for turbulent recirculatory combustion.

Experimental Work

1 Test Rig. All measurements were performed on a machined stainless steel conical flame stabilizer of base diameter, d = 4.44 cm (1.75 in.), length = 3.81 cm (1.5 in.), and apex angle θ = 45 deg. As shown in Fig. 1, this conical stabilizer (BR = 30.8 percent) is mounted coaxially at the mouth of a circular pipe 8 cm in diameter. This circular pipe supplies a high-velocity, premixed methane-air mixture from a vertical combustion tunnel mounted on a three-axis traversing platform and described by Ballal et al. (1987). A torch igniter is used to ignite this turbulent combustible mixture. Measurements of turbulence quantities downstream of the conical stabilizer are performed using a laser-Doppler anemometer (LDA) for both noncombusting and combusting situations.

2 Test Conditions. All measurements reported in this paper were carried out for mean velocity past the cone U_a = 10 m/s or $\mathrm{Re}_d = U_a d/\nu = 2.85 \times 10^4$, and approach turbulence level u'/U = 4 percent, and v'/U = 2.8 percent, i.e., conditions of fully developed approach flow turbulence existed. Further, the methane-air mixture equivalence ratio for these tests was ϕ = 0.70, i.e., T_f = 1870 K at room

---

Contributed by the International Gas Turbine Institute and presented at the 33rd International Gas Turbine and Aeroengine Congress and Exhibition, Amsterdam, The Netherlands, June 5-9, 1988. Manuscript received by the International Gas Turbine Institute September 1987. Paper No. 88-GT-13.

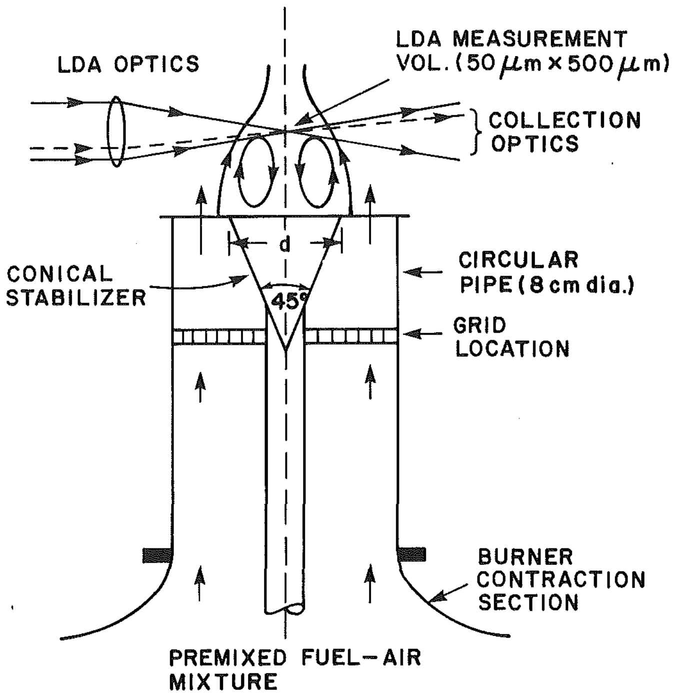

Fig. 1 Schematic diagram of the conical stabilizer flow system

temperature and pressure. The measurement locations in the axial direction ranged between $x/d = 0.05$ to 4.5 (i.e., $x = 2.5$ mm to 200 mm) and in the radial direction were taken between $r/d = -0.9$ and $r/d + 0.9$ (i.e., $r = -40$ mm to 40 mm).

3 LDA Instrumentation. A two-component LDA system was used for all velocity measurements. It uses the green line of a 15-W, argon-ion laser (2 W @ 514.5 nm) as a source, and the two measurement channels are separated by polarization. The design features of our LDA are fully discussed elsewhere by Ballal et al. (1987). Principally, this instrument incorporates Bragg cell frequency shifting for measurements in a recirculatory flow, a unique channel coincidence circuit for rapid acquisition of valid data (a feature that is almost a necessity in integrating LDA with CARS, Raman, or Rayleigh spectroscopic techniques) and a frequency downshifting circuit for measurements of very low velocities (~ 1 cm/s). The scattered signal is collected in a forward direction 10 deg off-axis. This scheme maximizes the signal strength, eliminates any potential crosstalk between the two channels, and preserves the polarization in the scattered radiation. A TSI fluidized bed seeder is used to inject submicron sized Al_2O_3 seed particles into the flowing combustible mixture. The LDA measurement volume dimensions were 50 μm × 500 μm. Scattered signals are processed by TSI Counter Processors (CP) and sent to the LDA interfaces (one for each channel), which also record the time of arrival (32-bit clock, 100-ns resolution) and the number of cycles in the LDA burst. The CP data and the clock data are then sent directly to a MODCOMP computer through a direct memory access (DMA) channel and processed by our custom-designed software to yield intensity, shear stresses, higher moments (skewness and kurtosis), length scales, pdfs, and psdfs. Typical sampling rates for LDA measurements were up to 3 kHz in cold flows and up to 1 kHz in combusting flows.

4 Error Analysis. Both the fuel flow and airflow were monitored by a TYLAN electronic flow control unit to within 1 percent. The output of the TSI LDA seeder had typically 1 μm particle sizes. Durst et al. (1976) have estimated that a 1 μm particle follows flow fluctuations up to 8 kHz with only 1 percent slip velocity. So this error was negligible. It is known that a primary source of error in LDA measurement is the statistical bias of the final measured velocity toward higher mass flux (velocity × density) when number-weighted averages are used to calculate stationary statistics. Chen and Lightman (1985) and Razdan and Stevens (1985) have shown this error to be about 5 percent for highly turbulent flow. For the single-stream seeding, open-flame configuration, and high-sampling rates of our experiments, the error in rms velocity was estimated to be about 5 percent. Near the flame front, where intermittency would be much higher, this error could be greater than 7 percent. But these measurements represented only a small fraction of our total data. Additional sources of error, e.g., effects of beam steering due to variations in refractive index on the movement of the measurement volume in the flame, were found to be negligible because of our unique channel coincidence circuit. During experiments, data were randomly checked for both reproducibility and accuracy. The long-term repeatability of measurements was within 5 percent for turbulence quantities. As for accuracy, mass conservation balance across the mouth of the 8-cm-dia pipe was cross-checked against the flowmeter readings to within 1 percent.

Results and Discussion

An important objective of our investigation was to provide benchmark quality data sets for evaluating and refining turbulence modeling codes of recirculatory combusting flows. To this end, we followed the recommendations of Strahle and Lekoudis (1985).

1 Inlet Boundary Conditions. Modeling codes require the specifications of inlet or starting conditions to initiate calculations of flow development downstream. The importance of inlet boundary conditions to numerical simulation of com-

Nomenclature

BR = blockage ratio
D_r = diameter of the recirculation zone
d = base diameter of conical stabilizer
K = kurtosis
L = length of the recirculation zone
q = turbulent kinetic energy (TKE)
R = radius
r = radial direction
S = skewness
T = temperature
U, V = mean velocities in axial and radial directions, respectively
u, v = fluctuating velocities in axial and radial directions respectively; u', v' = rms components of velocities
$\overline{uv}$ = Reynolds shear stress
x = axial direction
ϵ = viscous dissipation
ν = kinematic viscosity
ρ = density
τ = heat release parameter
τ_{kl}, τ_{lk} = viscous stresses
ϕ = equivalence ratio
ψ = stream function

Superscripts

$\sim$ = Favre (density-weighted) average
$-$ = conventional average
$''$ = fluctuations from Favre average

Subscripts

a = annular flow
f = flame
k, l = Cartesian coordinates
u, b = unburned and burned conditions, respectively

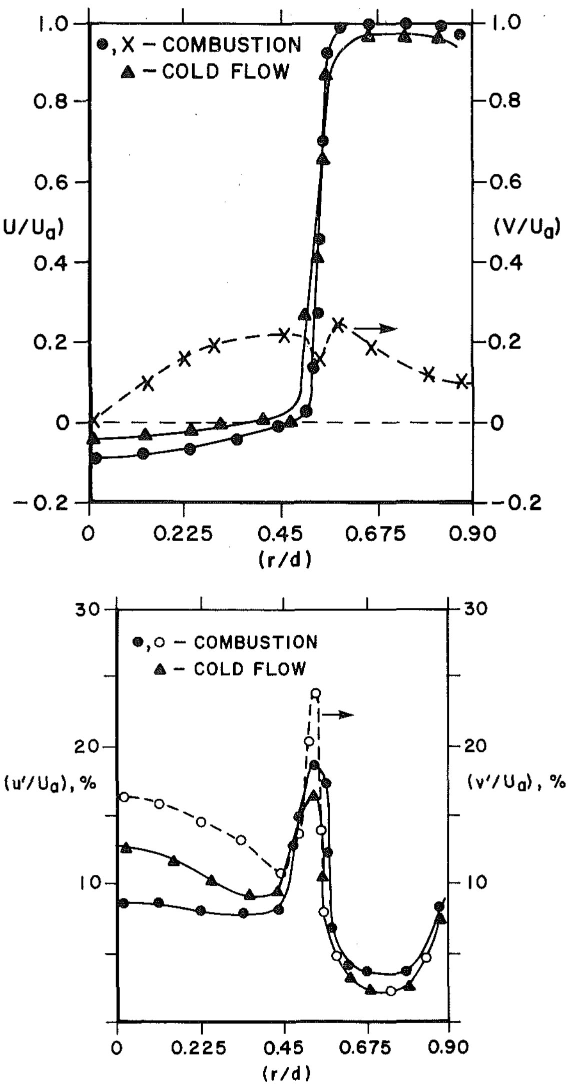

Fig. 2 Measurements of inlet boundary-flow conditions at (x/d) = 0.05: (a) radial profiles of mean axial and mean radial velocities; (b) profiles of axial and radial turbulence intensities

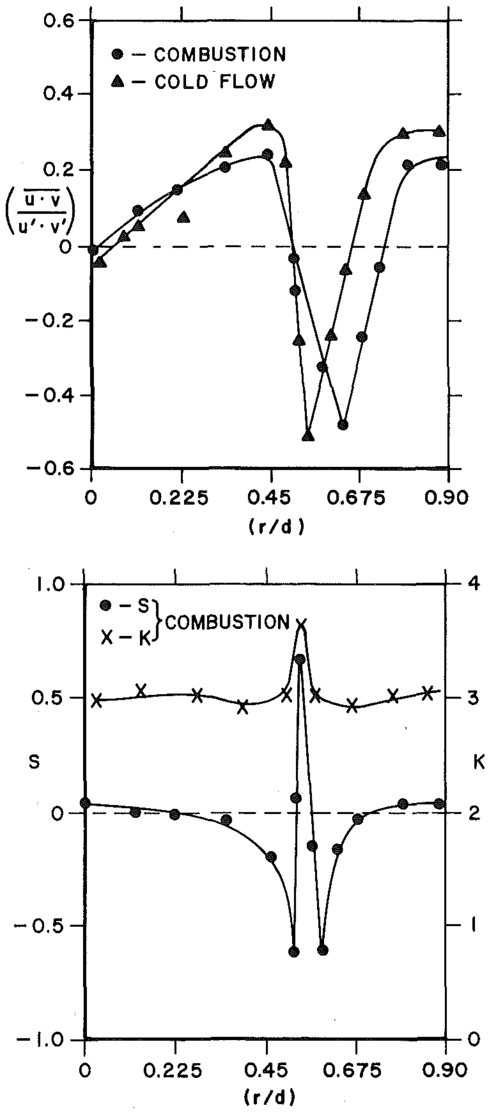

Fig. 3 Measurements of inlet boundary-flow conditions at (x/d) = 0.05: (a) profiles of Reynolds shear stresses; (b) profiles of skewness and kurtosis of axial velocity

bustor flows is very clearly demonstrated by Sturgess et al. (1983). Therefore, in Figs. 2 and 3, we present mean velocity and turbulence data in the axial plane $x/d = 0.056$ ($x = 2.5$ mm) downstream of the face of the conical stabilizer. Since radial measurements showed the flow field to be axisymmetric, only one-half of the profiles are plotted here. Data for both cold-flow and combusting situations are given.

Figures 2(*a*) and 2(*b*) show the mean velocity and turbulence intensity data, respectively. In Fig. 2(*a*), the axial mean velocity U at the center of the cone stabilizer is in the negative direction and approaches zero radially outward toward the edge of the stabilizer. Just past the edge, the axial velocity shoots up rapidly to attain its maximum value $U = U_a = 10$ m/s. In the flame, a similar trend is obvious except that the magnitude in both negative and positive directions is higher. As would be expected in a recirculatory flow, the mean radial velocity has a zero value at the center, gradually increases to a maximum of 20 percent of the annular velocity U_a at the edge, and again drops toward zero in the annular stream. A perturbation in radial mean velocity is evident in the region of high shear around the dividing streamline. Figure 2(*b*) shows data on axial (u'/U_a) and radial (v'/U_a) turbulence intensities in cold and combusting flows. As would be expected, maximum velocity fluctuations (u'/U_a) = 17.5 percent and (v'/U_a) = 24 percent are observed in the high-shear region around $r/d = 0.5$. On either side of this narrow peak, velocity fluctuations are rapidly reduced to (u'/U_a) = 7 percent, and (v'/U_a) = 15 percent within the recirculation zone, and (u'/U_a) = 4 percent and (v'/U_a) = 2.5 percent in the annular flow, respectively. Notice also that in the presence of combustion, turbulent dilatation reduces axial fluctuations from about 11 to 7 percent (i.e., 57 percent suppression) throughout the recirculatory and high-shear regions.

In Fig. 3(*a*) are plotted radial variations of the Reynolds shear stresses with and without combustion. Again turbulent dilatation damps shear stresses in combusting flow though not to the same extent as the normal stresses. Figure 3(*b*) shows data on skewness $S\ (= \overline{u^3}/(\overline{u^2})^{3/2})$ and kurtosis $K\ (= \overline{u^4}/(\overline{u^2})^2)$ of axial velocity fluctuations in a combusting flow. Values of S and K were found to be slightly lower in a cold flow. For a Gaussian pdf distribution associated with random small-scale fluctuations, $S = 0$ and $K = 3$, respectively. Peak values of $S = 0.75$ and $K = 3.5$ were observed in the high-shear regions surrounding the recirculation zone. This suggests a large peak in the velocity pdf associated with the entrainment of large-scale eddies carrying fresh combustible mixture from the annular stream into the high-shear region surrounding the recirculation zone.

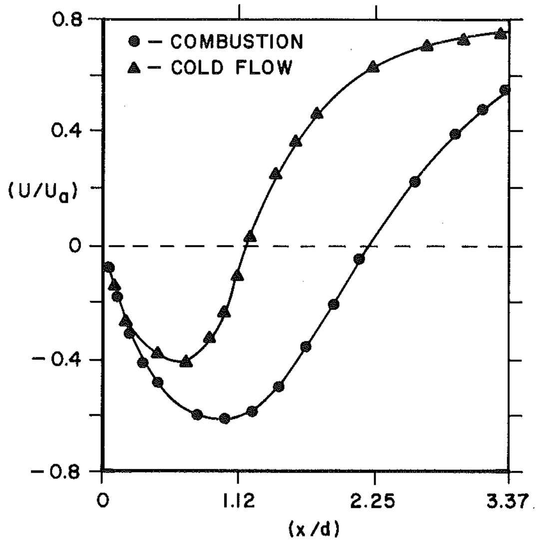

Fig. 4 Development of centerline mean axial velocity profiles downstream of a conical stabilizer

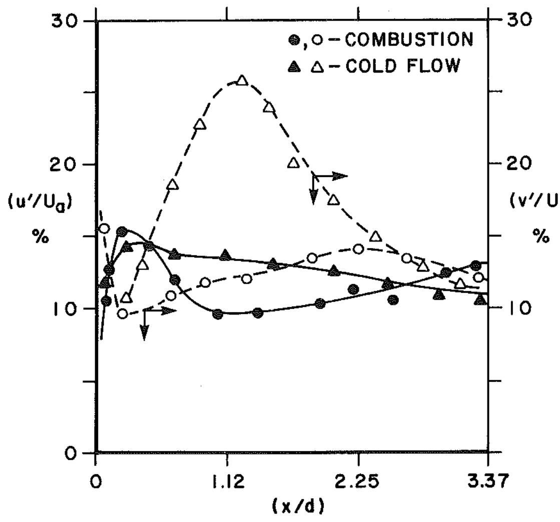

Fig. 6 Centerline axial and radial turbulence intensities downstream of a conical stabilizer

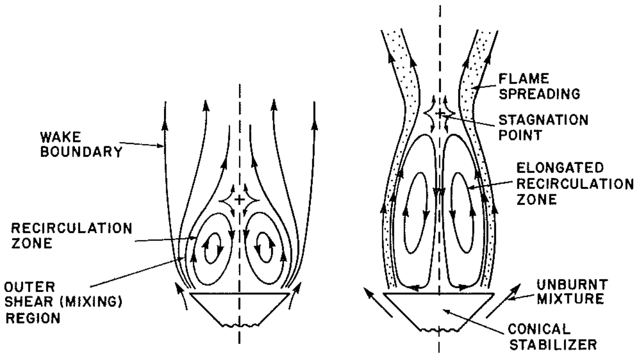

(a) COLD FLOWFIELD (b) COMBUSTING FLOWFIELD

Fig. 5 Structure of the recirculation zone and the flow field downstream of a conical stabilizer without and with combustion

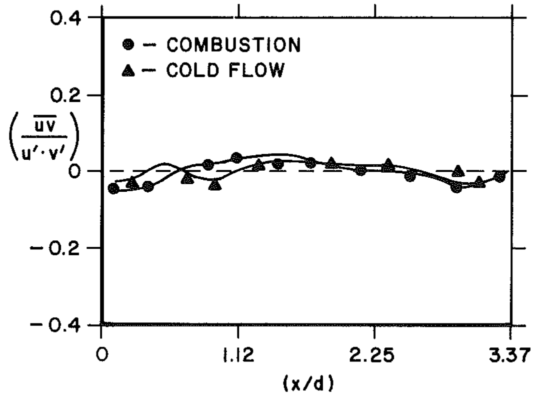

Fig. 7 Development of centerline Reynolds shear stresses downstream of a conical stabilizer

2 Flow Development in Axial Direction. Since the work of Williams et al. (1949), the turbulence properties, size, and geometry of the recirculation zone are of considerable interest in studies of bluff-body flame stabilizers. For example, in the range $10^4 < \mathrm{Re}_d < 10^5$, the recirculation zone $L/D_r \geq 1$ and the location of the stagnation point can be at $L/D_r > 2$. At these high Reynolds numbers, no process of regular vortex shedding was observed by Williams et al. (1949); rather the flow was in a highly turbulent random state. Under these circumstances, mean velocity flow pattern is very meaningful in establishing the size of the recirculation zone.

Accordingly, in Fig. 4, mean axial velocity profiles with and without combustion are given along the axis of the wake for the 45 deg cone. It is observed that combustion elongates the recirculation zone shifting the axial location of its center from $L/d = 0.5$ for the cold flow to $L/d = 1.0$. Similarly, the rear stagnation point moves from $L/d = 1.0$ for the cold flow to $L/d = 2.0$. Now, the spatial distribution of mean stream function ψ may be calculated from

$$\psi = \int_0^\infty \bar{\rho}\, \bar{U}\, r\, dr \qquad (1)$$

These calculations enable the size and shape of the recirculation zone to be sketched. Results of such calculations are plotted in Fig. 5 and clearly illustrate the influence of combustion in elongating the cold-flow recirculation zone downstream. Presumably, the damping of turbulence due to dilatation and due to increased viscosity delays transition to turbulence. This delay results in larger recirculation zone lengths, lower level of turbulence intensity in the combusting case, and increased mean residence time of the mixture. The magnitude of this damping effect is estimated later.

Figures 6 and 7 show the centerline axial profiles of turbulence intensities (i.e., normal stresses) and Reynolds shear stresses, respectively. While in Fig. 7 the Reynolds stresses fluctuate about the zero line (note: these results attest to the high degree of flow symmetry and the good quality of our measurements), appreciable damping of axial (u'/U_a) and radial (v'/U_a) turbulence intensities by the flame is again evident in Fig. 6. For example, (u'/U_a) is reduced from 13 to 10 percent and (v'/U_a) from an average value of 20 to 13 percent. This experimental observation is in line with our earlier discussion.

These results and conclusions were also found to be valid for data obtained along the axial plane located off-centerline at $r/R = 0.5$.

3 Flow Development in Radial Direction. During the course of these experiments radial profiles of turbulence quantities in several axial planes up to $x/d = 4.5$ were measured. Comparisons between data for combusting and cold-flow conditions were made and these revealed most significant and interesting differences in the axial plane of the stagnation point, $x/d \approx 2$. Therefore, Figs. 8 and 9 plot results of turbulence measurements in the axial plane in the vicinity of the stagnation point.

Figure 8(*a*) shows mean axial velocity (U/U_a) profiles. The profile for the combusting case shows the location of the zero axial (or maximum radial) velocity point as being at $r/d = 0.3$ in contrast to being at $r/d = 0.5$ at $x/d \approx 0$. Also at all locations less than $r/d = 0.5$, cold-flow velocities are signif-

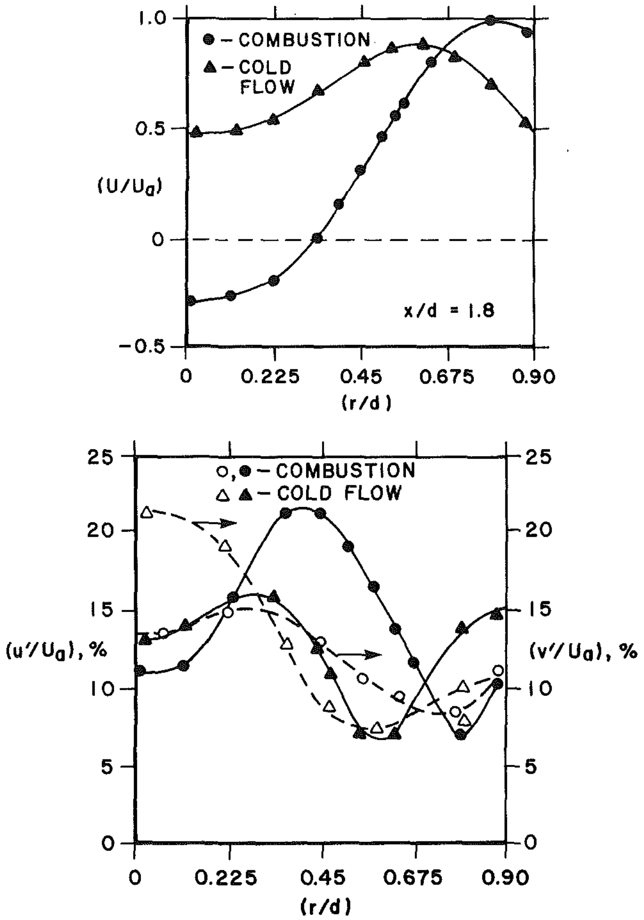

Fig. 8 Flow development in the radial direction in the vicinity of the stagnation point downstream of a conical stabilizer: (*a*) mean axial velocity profiles; (*b*) axial and radial turbulence intensity profiles

icantly higher than those in combusting case. Again, this observation strongly suggests the dilatation of the flow due to heat release.

In Fig. 8(*b*), profiles of axial and radial turbulence intensities (normal stresses) are shown for combusting and cold-flow situations. It is apparent here that the combustion process generates significant additional turbulence over and above the cold-flow turbulence. Visual observations of the stabilized flame showed a necking-down of the flow field (shown in Fig. 5) in the vicinity of the stagnation point. Lewis and von Elbe (1967) have shown that on the outer boundary of the wake where the flame is anchored, the combustion wave propagates in a flow region with high-velocity gradients and flame stretch occurs. It is in this region that shear-generated turbulence is produced. Also, around the stagnation point streamlines meet and velocities change direction. Therefore, this region is always highly turbulent. Finally, in a combusting flow, the axial location $x/d \approx 2$ represents the stagnation point, whereas in the cold flow, the same axial location represents the far-field wake region (i.e., well downstream of the stagnation point) where turbulence has been damped. These observations explain the measured differences between cold-flow and combusting flow results.

Figure 9(*a*) illustrates the radial variation of Reynolds shear stresses in a flame and in a cold-flow test. Again, the shear stresses in a combusting environment are observed to be higher than in a cold-flow environment. Reasons presented above to explain the behavior of normal stresses (i.e., turbulence intensities) are equally applicable here.

In Fig. 9(*b*), radial distribution of skewness and kurtosis of axial velocity fluctuations are shown from combustion and

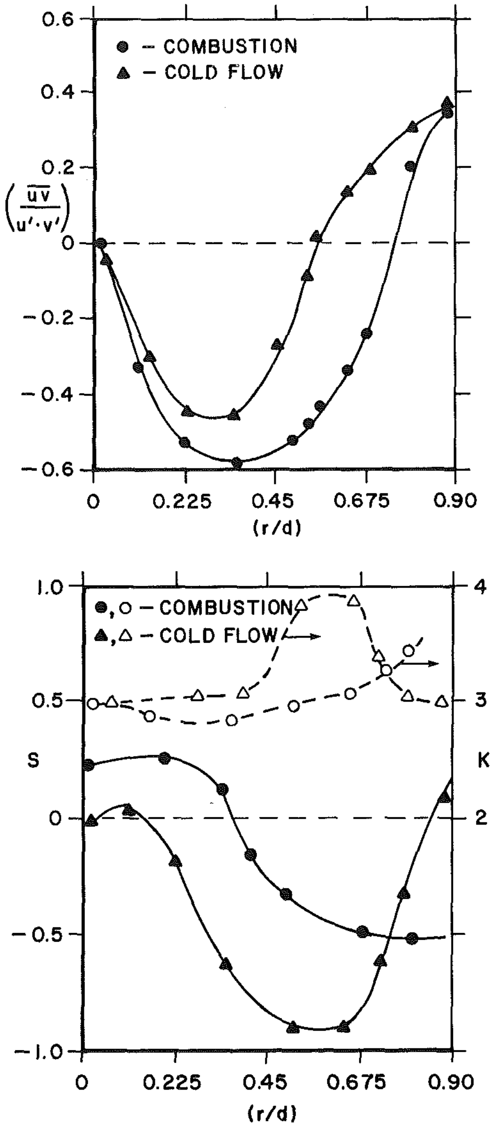

Fig. 9 Turbulence measurements in the vicinity of the stagnation point downstream of a conical stabilizer: (*a*) Reynolds shear stresses; (*b*) skewness and kurtosis of axial velocity fluctuations

cold-flow measurements downstream of the conical flame stabilizer. As explained earlier, for a combusting flow, high values of turbulence intensity are found in the region around the stagnation point. This translates into random, small-scale turbulent fluctuations for which $S \rightarrow 0$ and $K \rightarrow 3$. The results demonstrate this to be approximately the case in the range $r/d = 0$ to 0.5. When $r/d > 0.5$, the skewness values start to fall below $S = -0.5$, signifying a departure from the Gaussian pdf distribution representing random turbulence. In the far-field region of a cold-flow wake, we should expect to observe intermittency and large-scale, roll-up vortices around the outer part of the wake, as has been aptly demonstrated by Townsend (1980). This intermittent nature of the roll-up eddies appears as broad spikes in the skewness and kurtosis distribution in the region, $r/d = 0.5$ to 0.6.

Turbulence-Combustion Interaction

In discussing the results and interpreting the data, reference was often made to the suppression or generation of turbulence by the flame. Therefore, a brief explanation is necessary on the effects of combustion on isothermal turbulence; for details, see Ballal (1986, 1988).

As a turbulent flame propagates through an unburned mixture: (1) it accelerates the hot gases; and if this creates mean fluctuating shear between adjacent streamlines (usually in a confined flame) a shear-generated turbulence is produced; (2) heat release produces expansion of hot gases; velocity divergence and turbulence energy are reduced due to dilatation (usually open flames); (3) the high local viscosity of hot gases damps small-scale turbulence, delays transition to turbulence, or increases viscous dissipation; (4) density gradients and axial pressure gradients (for ducted flames) produce additional turbulence.

Of the above processes, only the second and third mechanisms are dominant in our bluff-body-stabilized conical-wake flame. The Favre-averaged turbulence kinetic energy (TKE) balance equation is

$$\underset{(1)}{\frac{\partial}{\partial x_k}(\bar{\rho}\tilde{u}_k\tilde{q})} = -\underset{(2)}{\overline{\rho u_k'' u_l''}\,\frac{\partial \tilde{u}_l}{\partial x_k}} - \underset{(3)}{\frac{1}{2}\frac{\partial}{\partial x_k}(\overline{\rho u_k'' u_l''^2})} \tag{2}$$

$$+ \underset{(4)}{\frac{\partial}{\partial x_k}(\overline{u_l''\tau_{lk}})} - \underset{(5)}{\overline{\tau_{kl}\frac{\partial u_k''}{\partial x_l}}} - \underset{(6)}{\overline{u_k''\frac{\partial p}{\partial x_k}}}$$

In equation (2), term (1) = convection of TKE in the mean flow; term (2) = TKE production or dilatation for $k = l$ (first and second mechanisms); term (3) = turbulent diffusion of TKE; term (4) = molecular diffusion (negligible at high Re); term (5) = viscous dissipation of TKE (third mechanism); term (6) = pressure-velocity correlation.

For the turbulent dilatation term, Ballal (1986) found that

$$(q_f/q) = 1 - 0.66\,[\tau/(\tau+1)] \tag{3}$$

In our experiments, T_f = 1870 K and T_u = 288 K, so $\tau = (T_f - T_u)/T_u = 5.5$. Therefore $(q_f/q) = 0.44$, i.e., TKE in a combusting flow is only 44 percent of the isothermal flow value or 56 percent of the TKE is damped by turbulent dilatation.

The suppression of turbulence by viscous dissipation is given by Ballal (1986) as

$$(q_f/q) = [\epsilon_f L_f/\epsilon L\,(\tau+1)]^{0.66} \tag{4}$$

This equation is difficult to solve for the present experiment because of lack of measurements on the magnitudes of turbulent dissipation and length scale. But, for $\tau = 5.5$, Ballal (1986) has computed that for open premixed flames $(q_f/q) = 0.73$, i.e., 27 percent of the TKE is damped by viscous dissipation.

The predicted magnitudes of both suppression mechanisms are in the same ballpark as the percentage reduction in turbulence intensities observed in our experiments here (Figs. 2*b* and 6).

Conclusions

Detailed experimental measurements of turbulence quantities were performed downstream of a conical flame stabilizer. These results are presented here for both combusting and cold-flow tests. The following conclusions emerged:

1 It was found that combustion accelerates mean-flow velocities but damps turbulence intensity via the processes of turbulent dilatation and viscous dissipation due to heat release.

2 Skewness and kurtosis measurements showed that large-scale eddies carrying fresh combustible mixture are entrained into the high-shear region surrounding the recirculation zone.

3 Flow measurements in the axial direction demonstrated that the length of the recirculation zone was nearly doubled as a result of combustion.

4 The region around the rearward stagnation point where streamlines meet and velocities change direction was found to be highly turbulent.

5 The predicted magnitudes of turbulent dilatation and viscous dissipation suppression mechanisms are about the same as the observed reduction in turbulence level due to combustion.

Acknowledgments

This research was sponsored by the U. S. Air Force, Wright Aeronautical Laboratories, Aero Propulsion Laboratory, under Contract No. F33615-82-C-2255. The authors are indebted to Dr. W. M. Roquemore, the Air Force Technical Monitor, for his interest and helpful discussions during the course of this work.

References

Ballal, D. R., 1986, "Studies of Turbulent Flow-Flame Interaction," *AIAA Journal*, Vol. 24, pp. 1148-1154.

Ballal, D. R., Lightman, A. J., and Yaney, P. P., 1987, "Development of Test Facility and Optical Instrumentation for Turbulent Combustion Research," AIAA *Journal of Propulsion and Power*, Vol. 3, pp. 97-104.

Ballal, D. R., 1988, "Combustion-Generated Turbulence in Practical Combustors," AIAA *Journal of Propulsion and Power*, Vol. 4, pp. 385-390.

Bearman, P. W., and Morel, T., 1983, "Effect of Free-Stream Turbulence on the Flow Around Bluff Bodies," *Progress in Aerospace Sciences*, Vol. 20, pp. 97-123.

Bearman, P. W., 1984, "Vortex Shedding From Oscillating Bluff Bodies," *Annual Review of Fluid Mechanics*, Vol. 16, pp. 195-222.

Bovina, T. A., 1959, "Studies of Exchange Between Recirculation Zone Behind the Flame Holder and Outer Flow," *Seventh Symposium (International) on Combustion*, The Combustion Institute, Pittsburgh, PA, pp. 692-696.

Calvert, J. R., 1967, "Experiments on the Low-Speed Flow Past Cones," *Journal of Fluid Mechanics*, Vol. 27, pp. 273-289.

Carmody, T., 1964, "Establishment of the Wake Behind a Disk," ASME *Journal of Basic Engineering*, Vol. 86, pp. 869-882.

Chen, T. H., and Lightman, A. J., 1985, "Effects of Particle Arrival Statistics on Laser Anemometer Measurements," ASME FED-Vol. 33, pp. 172-176.

Davies, T. W., and Beer, J. M., 1971, "Flow in the Wake of Bluff-Body Flame Stabilizers," *Thirteenth Symposium (International) on Combustion*, The Combustion Institute, Pittsburgh, PA, pp. 631-638.

Durst, F., Melling, A., and Whitelaw, J. H., 1976, *Principles and Practice of Laser-Doppler Anemometry*, Academic Press, London.

Griffin, O. M., 1985, "Vortex Shedding From Bluff Bodies in a Shear Flow: A Review," ASME *Journal of Fluids Engineering*, Vol. 107, pp. 298-306.

Heitor, M. V., and Whitelaw, J. H., 1986, "Velocity, Temperature, and Species Characteristics of the Flow in a Gas Turbine Combustor," *Combustion and Flame*, Vol. 64, pp. 1-32.

Lewis, B., and von Elbe, G., 1967, *Combustion, Flames, and Explosions of Gases*, Academic Press, New York.

Razdan, M. K., and Stevens, J. G., 1985, "CO/Air Turbulent Diffusion Flame: Measurements and Modeling," *Combustion and Flame*, Vol. 59, pp. 289-296.

Sivasegaram, S., and Whitelaw, J. H., 1987, "Suppression of Oscillations in Confined Disk-Stabilized Flames," AIAA *Journal of Propulsion and Power*, Vol. 3, pp. 291-295.

Strahle, W. C., and Lekoudis, S. G., 1985, "Evaluation of Data on Simple Turbulent Reacting Flows," Technical Report TR-85-0880, Air Force Office of Scientific Research, Bolling Air Force Base, Washington, DC.

Sturgess, G. J., Syed, S. A., and McManus, K. R., 1983, "Importance of Inlet Boundary Conditions for Numerical Simulation of Combustion Flows," AIAA Paper No. 83-1263.

Townsend, A. A., 1980, *The Structure of Turbulent Shear Flows*, Cambridge University Press, London, United Kingdom.

Williams, G. C., Hottle, H. C., and Scurlock, A. C., 1949, "Flame Stabilization and Propagation in High Velocity Gas Streams," *Third Symposium (International) on Combustion*, The Combustion Institute, Pittsburgh, PA, pp. 21-40.

Winterfeld, G., 1965, "On Processes of Turbulent Exchange Behind Flame Holders," *Tenth Symposium (International) on Combustion*, The Combustion Institute, Pittsburgh, PA, pp. 1265-1275.

Zukoski, E. E., and Marble, F. E., 1955, "The Role of Wake Transition in the Process of Flame Stabilization on Bluff Bodies," AGARD *Combustion Researches and Reviews*, A. H. Lefebvre et al., eds., Butterworths Publishing Co., London, pp. 167-180.

Advanced High-Temperature Instrumentation for Hot Section Research Applications

D. R. Englund

R. G. Seasholtz

NASA Lewis Research Center
Cleveland, OH 44135

Programs to develop research instrumentation for use in turbine engine hot sections are described. These programs were initiated to provide improved measurement capability as support for a multidisciplinary effort to establish technology leading to improved hot section durability. Specific measurement systems described here include heat flux sensors, a dynamic gas temperature measuring system, laser anemometry for hot section applications, an optical system for viewing the interior of a combustor during operation, thin film sensors for surface temperature and strain measurements, and high-temperature strain measuring systems. The paper will describe the state of development of these sensors and measuring systems and, in some cases, will show examples of measurements made with this instrumentation. The paper covers work done at the NASA Lewis Research Center and at various contract and grant facilities.

Introduction

The Turbine Engine Hot Section Technology (HOST) Program was started by NASA in the late 1970s in order to develop technology leading to improved hot section durability. The program was a multidisciplinary effort involving structures, surface protection, fatigue, combustion, heat transfer, and instrumentation. The objective of the instrumentation portion of the program was to develop improved measurement capability to measure the environment within the hot section and measure the response of hot section components to that imposed environment. Instrument development programs that resulted including the following:

1 Development of sensors for measuring the heat flux on combustor liners and turbine airfoils.

2 Development of a system to measure the fluctuating component of combustor exit temperature with a frequency response to 1000 Hz.

3 Development of laser anemometer techniques for applications in hot sections.

4 Development of an optical system for viewing the interior of a combustor during operation.

5 Development of high-temperature strain measuring systems.

In addition to this, a major effort was started just prior to the start of HOST to develop thin film sensors for applications in hot sections, particularly for the measurement of turbine airfoil surface temperature.

This paper will describe the state of development of these sensors and measuring systems and, in some cases, will show examples of measurements made with this new instrumentation. The work described was done at the NASA Lewis Research Center and at various contract and grant facilities.

Heat Flux Sensors

One of the important environmental parameters in the hot section is heat flux. The heat flux is a variable in the heat balance equation that establishes the cooling requirements and the anticipated surface temperature of a hot section component. There is not sufficient knowledge of heat transfer coefficients under engine operating conditions to permit prediction of surface temperatures to within acceptable accuracy. This is especially true as heat fluxes approach 1 MW/m^2. Initial work was directed at developing sensors for use in combustor liners (Atkinson et al., 1983, 1985a; Atkinson and Strange, 1982). In later work sensors were mounted into air-cooled blades and vanes (Atkinson et al., 1984, 1985b).

Sensor designs followed conventional concepts in which the temperature difference proportional to heat conduction through the sensor body is measured. Differential thermocouples using the sensor body material as part of the circuit were used to measure the temperature differences. Calibrations (Holanda, 1984) were made of the thermoelectric potential of a number of engineering alloys and these established the validity of this approach, which considerably simplified fabrication.

Figures 1 and 2 show the sensors that were developed for combustor liners. The sensor is built into a Hastelloy X disk 0.8 cm in diameter and the same thickness as the liner. After calibration of the sensor the disk is welded into a hole cut in the liner. Figure 1 shows the embedded thermocouple sensor. The disk is grooved so that 0.25 mm o.d. sheathed, single-conductor thermocouple wire can be laid into the grooves and covered with weld material. The thermocouple wires are ISA

Contributed by the International Gas Turbine Institute and presented at the 33rd International Gas Turbine and Aeroengine Congress and Exhibition, Amsterdam, The Netherlands, June 5–9, 1988. Manuscript received by the International Gas Turbine Institute November 16, 1987.

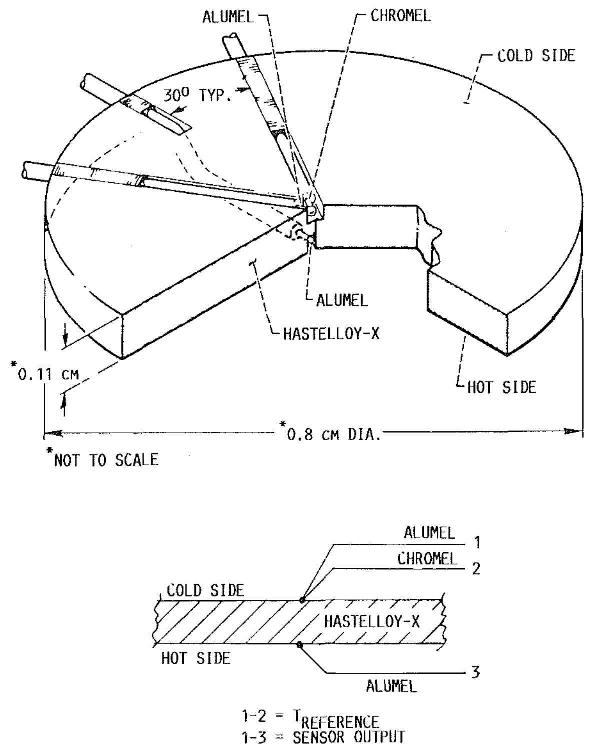

Fig. 1 Embedded thermocouple heat flux sensor

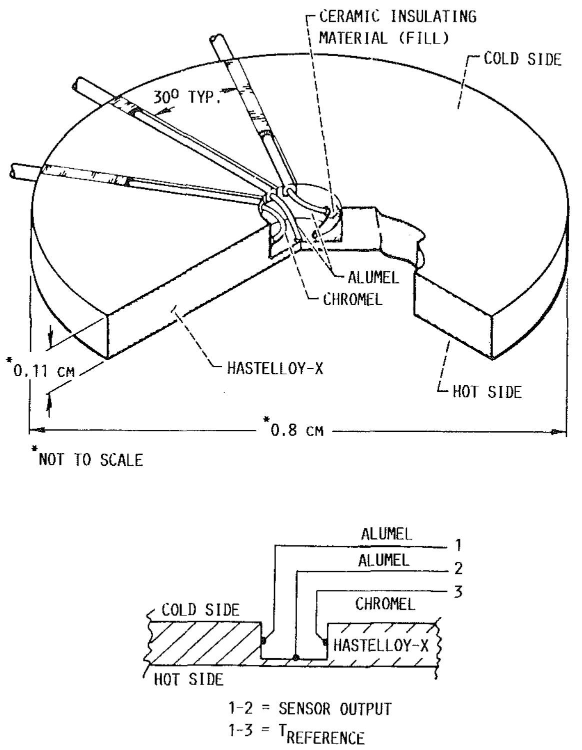

Fig. 2 Gardon gage heat flux sensor

Type K, chromel-alumel, and single conductor leads are used so as to maintain good insulation resistance between the wire and the external metal sheath. Grounded alumel junctions are located on the hot and cold side of the sensor body and a chromel junction is added to the cold side. A voltage measurement between the alumel lead wires (i.e., using the alumel-Hastelloy X-alumel differential thermocouple) provides the hot-to-cold side temperature difference proportional to the one-dimensional heat flow through the sensor body at that point. A measurement using the conventional chromel-alumel thermocouple provides the cold side temperature of the sensor.

Figure 2 shows a Gardon gage sensor. In this case the sensor body has a 1.5-mm-dia cylindrical cavity on the cold side so that a thin membrane of material is left on the hot side. Alumel wires are positioned so the junctions are formed with the Hastelloy X at the center of the membrane and halfway up the side wall of the cavity. A chromel wire junction is also made on the side wall of the cavity. After the thermocouples are installed, the cavity is filled with ceramic cement.

Sensors of the embedded thermocouple and Gardon gage types have also been built into air-cooled blades and vanes. In the case of turbine blades, two-piece blades were used and the sensors were installed from the cooling passage side of the blade. The two blade halves were then joined by brazing. In the case of vanes, sections of the vane wall opposite to the desired sensor sites were removed and the sensors were installed through these "windows." Figure 3 depicts the installation process on a turbine vane.

The heat flux sensors were calibrated over a heat flux range up to 1.7 MW/m^2 and a temperature range to 1250 K. The calibrations were accomplished by imposing a known radiant heat flux on the hot side surface of the sensor and flowing cooling air over the cold side surface. The hot side surface was coated with a high-temperature black paint with a measured absorptance and emittance of 0.89 over the test temperature range. In all cases the reference temperature was measured and used to estimate the hot side surface temperature so that energy being radiated away from the hot surface could be calculated and taken into account. Estimates of the convective heat flow from the hot surface were also made and used in the heat balance.

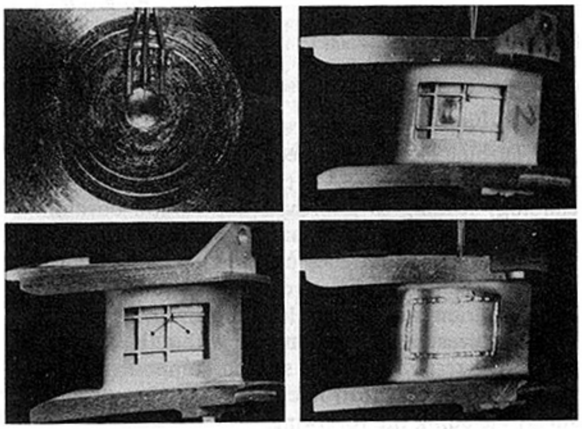

Fig. 3 Heat flux sensors installed in turbine vane

The heat flux sensor calibration systems used banks of tungsten filament lamps enclosed in quartz tubes as heat flux sources; the most powerful of these systems provided heat fluxes up to 1.7 MW/m^2. The quartz lamp rigs were capable of long time and cyclic operation at reduced heat fluxes. Thermal cycling and drift tests were run on these sensors using this capability.

Calibration and performance tests on heat flux sensors have indicated that measurements can be achieved fairly readily on combustor liners, but that accurate measurements on airfoils are difficult to achieve. Combustor liner measurements have been made both at a contractor facility and at NASA Lewis using sensors whose calibration uncertainty is within ±5 percent of a nominal full-scale heat flux of 1 MW/m^2. Figure 4 shows an instrumented combustor liner segment. Figure 5 compares measured values of heat flux conducted through a combustor liner and radiant flux incident on the liner at different combustor pressure levels. The radiant heat flux was measured

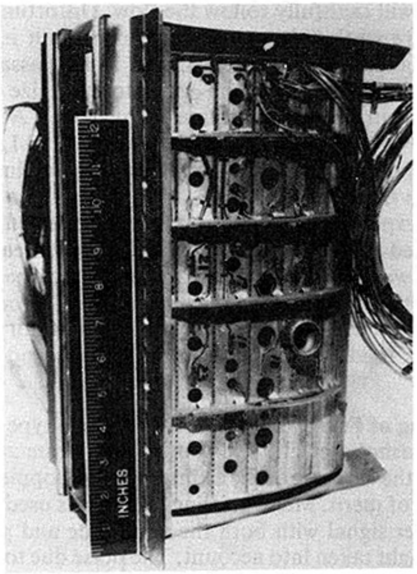

Fig. 4 Combustor segment instrumented with heat flux sensors

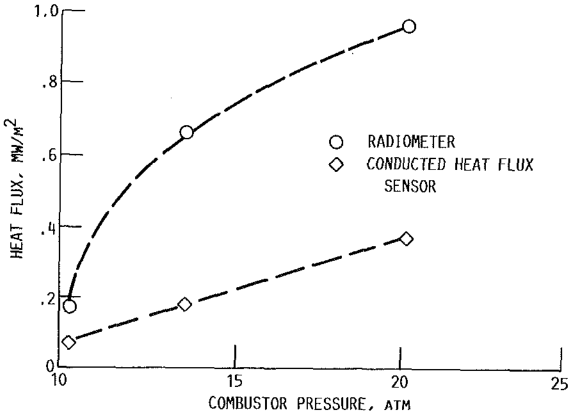

Fig. 5 Comparison of heat flux conducted through the combustor liner and incident radiant heat flux for various levels of combustor pressure; radiant heat flux was measured with a commercial radiometer

with a commercial radiometer. The combustor liner in this test was the type with louver lips and bleed holes to provide film cooling of the hot side surface. The data of Fig. 5 indicate that there is significant convective cooling of the hot side surface of the combustor.

Test results from sensors mounted in turbine airfoils indicate that these sensors are sufficiently sensitive to transverse gradients in the heat flux and temperature that applications in blades and vanes must be carefully evaluated. The greater complexity of the airfoils (e.g., high surface curvature and cooling passage structure) causes more severe gradients than were encountered in combustor liners. Sensitivity to transverse gradients is especially apparent in the Gardon gage sensor because of its lack of symmetry.

Dynamic Gas Temperature Measuring System

Another important environmental parameter in the hot section of a turbine engine is the gas temperature. In general, most attention has been directed at the time-averaged value of gas temperature rather than the fluctuating component of gas temperature. It is generally agreed that there may be significant temperature fluctuation in the gas exiting a combustor due to incomplete mixing of the combustion and dilution gas streams. It is also agreed that thermal cycling of the surfaces of turbine airfoils can result in spalling of oxide films used for corrosion projection and thus shorten the life of the airfoils. Development of a system to measure gas temperature fluctuations was undertaken to aid in modeling combustor flow and in studying the thermal cycling of airfoil surfaces. Combustor modeling requirements set the frequency response goal at 1000 Hz.

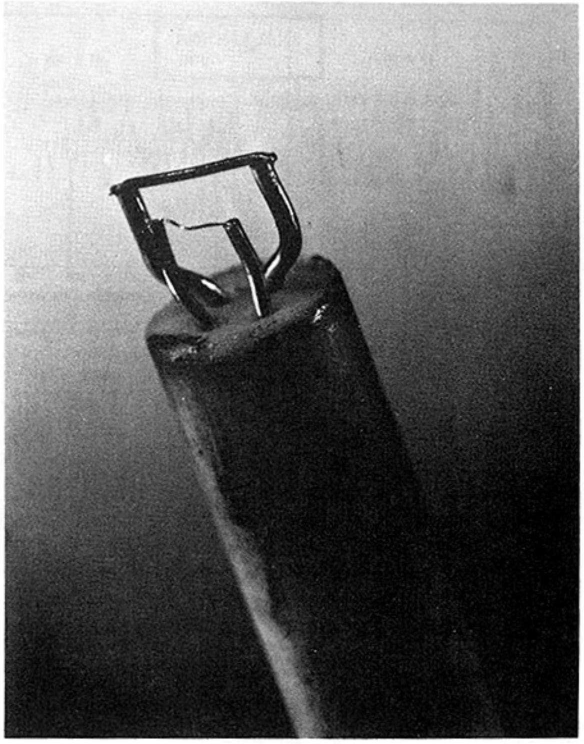

Fig. 6 Dual element thermocouple probe for measuring fluctuating gas temperature

The approach used in this work was to devise a way to determine in situ the compensation spectrum required to correct for the limited frequency response of a thermocouple probe located in the gas stream. Frequency compensation has often been used, especially with hot-wire anemometers, in the measurement of dynamic flow phenomena. The problem with this technique when applied to a thermal element in a flow stream is that the required compensation spectrum is a function of both the thermal mass of the thermocouple and the coefficient for heat transfer between the gas and the thermocouple. This heat transfer coefficient is a function of the gas flow conditions. Each time the flow conditions change, the compensation spectrum must be redetermined. In some cases estimates of the compensation spectrum may be sufficient; in this case it was important to be able to make in situ determinations of the compensation spectrum.

The system that was developed (Elmore et al., 1983, 1984, 1986a, 1986b; Stocks and Elmore, 1986) uses a dual element thermocouple probe such as shown in Fig. 6. Thermocouples are formed with carefully butt welded junctions so that there is no variation in diameter in the region of the junction. These thermocouples are each supported across a pair of support posts so that they are parallel cylinders in cross flow and are in close enough proximity (approx 1 mm) so that they are measuring the same temperature. The thermocouple wires and the support posts are made from Pt–30Rh/Pt–6Rh. The thermocouple junctions are midway between the support posts. The two thermocouples have different diameters, commonly 75 and 250 μm. Neither of these thermocouples has the desired frequency response, but a comparison of their dynamic signals can lead to the needed compensation spectrum. The technique is based on the use of the ratio of the Fourier coefficients of the dynamic signals for frequencies in the range where the

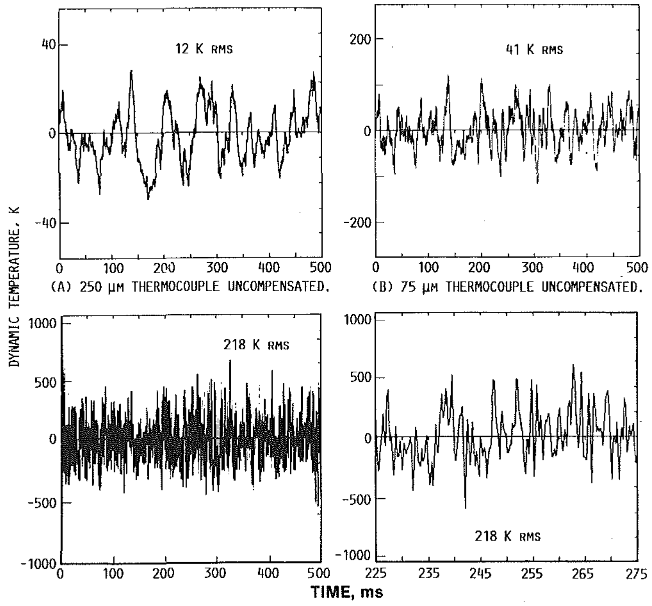

(A) 250 μm THERMOCOUPLE UNCOMPENSATED. (B) 75 μm THERMOCOUPLE UNCOMPENSATED.

(C) 75 μm THERMOCOUPLE COMPENSATED. (D) 75 μm THERMOCOUPLE COMPENSATED.

Fig. 7 Dynamic gas temperature signals from an engine test

signals become attenuated. In the system that has been developed, the signals are recorded on magnetic tape and processed in a general purpose digital computer at a later time. The data reduction process takes approximately 5 min for each flow condition for which a new compensation spectrum must be calculated.

Elmore et al. (1986a, 1986b) describe experiments to demonstrate the frequency response of the system. Measurements were made in a specially designed test rig and in the exhaust of an atmospheric burner. Comparisons were made between the dynamic gas temperature system and very fine wire resistance thermometers (6 and 12 μm wire diameters). At low frequencies (below 250 Hz) with reasonable temperature fluctuations agreements within ±23 percent were obtained. Poorer results were obtained at higher frequencies but here the temperature fluctuations were so small as to make the data questionable.

This system has been used to measure fluctuating temperature both in turbine engines and in combustor test rigs. A sample of data from a turbine engine test is shown in Fig. 7. In this test the probe was located between first-stage turbine vanes. For the data shown in Fig. 7, the engine was operating at an intermediate power level and the average gas temperature was 1200 K. Figure 7 shows four plots of fluctuating temperature versus time. Figures 7(*a*) and 7(*b*) show the uncompensated signals from the 75 and 250 μm thermocouples. Note that the temperature scales on these plots have been adjusted to show the waveforms. Also note that the rms temperature fluctuation is listed on each plot. Figure 7(*c*) shows the compensated temperature fluctuation from the 75 μm thermocouple, and Fig. 7(*d*) shows an expanded time segment of the compensated signal. The rms value of the compensated temperature fluctuation is 218 K and the peak-to-peak fluctuation is approximately ±500 K.

Laser Anemometry

The laser anemometer (LA) has become a valuable tool in turbine engine research, providing data that would be almost impossible to gather using conventional instrumentation. However, the use of LA in turbomachinery has proven to be one of its more difficult applications. Turbomachinery components are typified by small passages and highly accelerated, high-velocity flows. This leads to the need for small seed particles that will faithfully follow the flow. Unfortunately, small particles are weak light scatterers, which result in low signal levels. In addition, measurements in small passages require great care in the design of the optics to minimize the amount of detected surface-scattered laser light (flare). All these considerations must be included in the design of an LA to obtain the maximum amount of accurate data in minimum experimental run times.

HOST experiments where researchers planned to use LA were studied to determine critical technology areas. Research programs were then conducted in several of these areas including optical design, seed generation, signal processing, and data acquisition. An ambient pressure, laboratory-type combustor was used to evaluate optical systems and signal processors.

Modeling of Fringe-Type LA. The fringe-type LA was analyzed (Seasholtz et al., 1984) using the Cramer–Rao lower bound for the variance of the estimate of the Doppler frequency as a figure of merit. Mie scattering theory was used to calculate the Doppler signal with both the amplitude and phase of the scattered light taken into account. The noise due to wall scatter (flare) was calculated using the wall bidirectional reflectance distribution function (BRDF) and the irradiance of the incident beams. A procedure was developed to find the optimum aperture stop shape for the probe volume located a given distance from a wall. Figure 8 shows SNR as a function of probe volume to wall distance for two optical systems with optimum aperture masks.

The BRDF was measured for a number of uncoated materials, finishes, and surface coating. Data were obtained for "as-machined" surfaces, polished surfaces, glossy black coatings, and flat back coatings. Based on these data, the best surface for LA applications appears to be a glossy black coating. Although a black glossy surface has a relatively large specular reflection, the diffusely reflected light, which is usually of greatest concern in LA systems, is substantially less than the diffusely reflected light from a flat black coating.

Seeding. Particle characteristics necessary for hot section LA are primarily the same as low-temperature LA, with the exception that the particles must retain those characteristics at high temperatures. Based on a survey of available materials, a particular grade of aluminum oxide (nominal 1 μm dia) was selected. A commercial, high-volume fluidized bed was chosen to disperse the seed particles.

An experiment was also conducted to determine the feasibility of using chemically formed seed for hot flows. Titanium tetrachloride vapor was injected into the flow where it reacted with the water vapor to form titanium dioxide and hydrochloric acid (HCl). The titanium dioxide is a suitable high-temperature seed material; it has a submicron size, and it is produced in large quantities. However, the HCl, if not neutralized, can cause corrosion, which limits the application of this seeding technique.

Preprocessor for Fringe-Type LA. The quality of data from an LA is critically dependent on a number of control settings of the signal processor. These typically include the optical detection system gain (determined by the photomultiplier tube high voltage and amplifier gain) and the electrical filters used to remove the low-frequency pedestal component and to reduce shot noise. A study was made to quantify the effect of filters on measurement accuracy (Oberle and Seasholtz, 1985). Several common filter designs were examined. It was shown that both the filter type and the cutoff frequencies must be carefully selected to avoid filter-induced errors in counter-type processors. It was shown that these errors are particularly significant for probe volumes containing a small number of fringes and for highly turbulent flow.

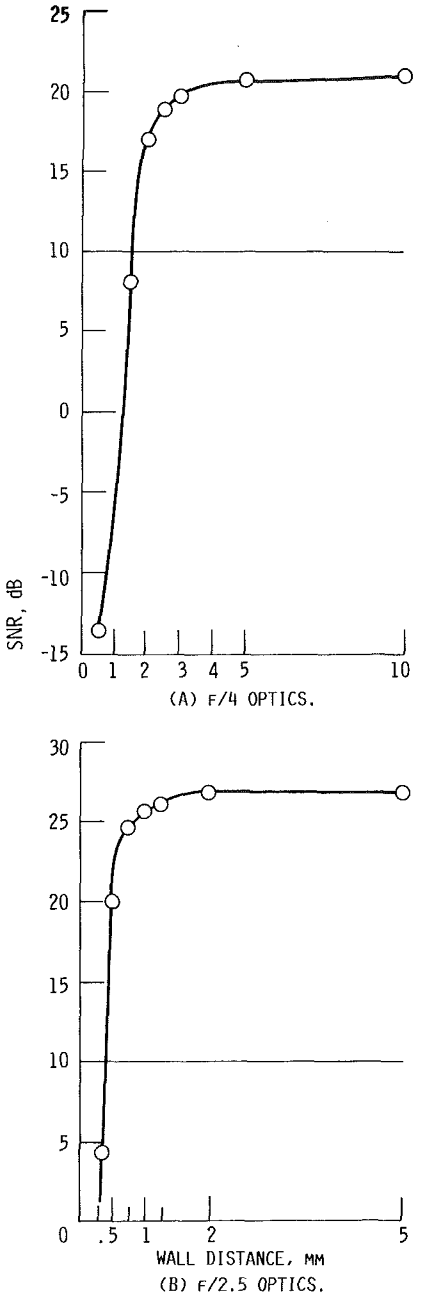

Fig. 8 Signal-to-noise ratio (SNR) for optimum mask versus distance of probe volume from wall

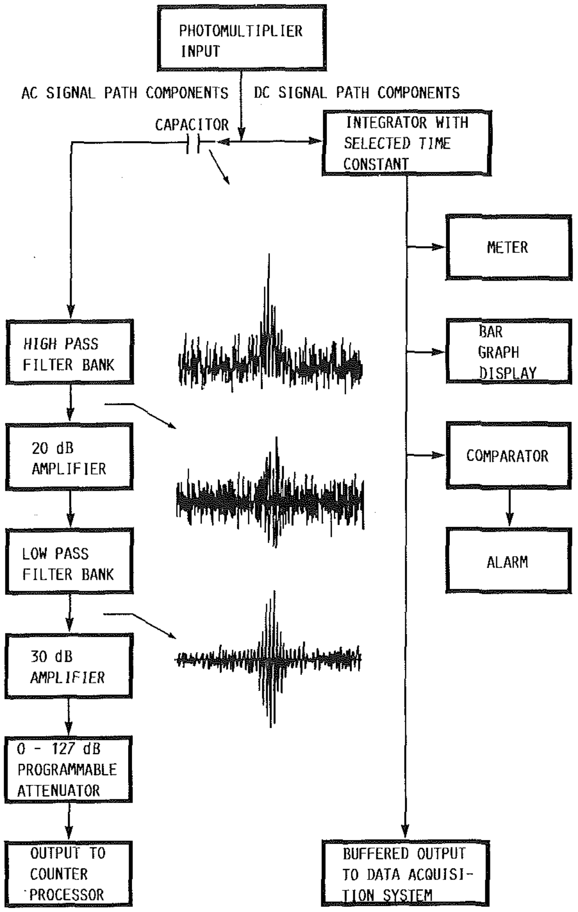

Fig. 9 Laser fringe anemometer preprocessor signal flow diagram showing the Doppler signal in the time domain at three points in the signal flow

Experiments in turbomachinery test facilities usually have high operational costs, so it is necessary to acquire the desired data in a minimum time. Extensive operator interaction with the instrumentation during a test run is usually not desirable. To provide for efficient data acquisition and correct processor settings, a computer-controlled interface (called a preprocessor) was designed, fabricated, and tested (Oberle, 1987). The preprocessor (Fig. 9) amplifies the signal from the photodetector, filters it using both low- and high-pass filters, and then routes it to the counter processor.

The chief virtue of the preprocessor is that it provides direct computer control of the PMT high voltage, the rf gain (50 dB of amplification and a programmable attenuator are used to provide control over the range −77 dB to +50 dB in 1 dB steps), and selection of the low- and high-pass filters (eight low-pass and eight high-pass). In addition, the preprocessor provides computer control of the seed generator and allows computer monitoring of the PMT d-c current. With proper software, the preprocessor will allow the researcher to preprogram the various processor settings based on the expected flow conditions. It will also be possible to use "smart" adaptive software to select the proper settings based current measurement parameters such as the frequency, turbulence intensity, and noise level.

Four-Spot LA. The conventional fringe-type LA has a large acceptance angle (i.e., it can measure velocities having a wide range of flow angles), but it has a relatively large probe volume. This large probe volume limits the closest measurements to about 1 mm from surfaces. The conventional time-of-flight LA (aka two-spot or transit LA) has a much smaller probe volume, which allows it to measure much closer to surfaces. However, the two-spot LA has a very limited acceptance angle, which greatly reduces its capabilities in highly turbulent flows.

The need for an anemometer incorporating the large acceptance angle of the fringe LA and the ability of the two-spot LA to measure close to walls led to the development of a new type of time-of-flight LA (Lading, 1983; Wernet and Edwards, 1986). The new Four-Spot LA, shown in Fig. 10, incorporates two features. One is the use of elliptical rather than circular spots to give a large acceptance angle. (This use of two elliptical spots is also called a two-dash or two-sheet time-of-flight LA.). The other feature, which is unique, is the use of four beams arranged to form two pairs of orthogonally polarized, partially overlapping spots. This allows the use of an optical method to accurately determine the start and stop timing signals. Previously, delay-and-subtract techniques were used to generate the timing signals. The optical method, unlike delay and subtract, is independent of the velocity. This is advantageous in highly turbulent flow or in other flows with a wide range of velocities.

The Four-Spot LA was designed, fabricated, and successfully tested. Measurements were obtained as close as 75 μm from a normal surface (Wernet, 1987). Comparison measurements were also made using the four-spot LA, a two-spot LA, and a fringe-type LA in the vicinity of a single turbine vane mounted in the exhaust of the open jet burner (Wernet and Oberle, 1987).

Windows and Correction Optics. In turbomachinery studies it is highly desirable to obtain measurements without altering the flow being studied. With optical techniques this means that the window contour should match the internal flow passage contour. One Lewis HOST facility was a 508-mm-dia, single-stage, axial flow turbine facility. Two cylindrical windows were designed to allow measurements within the stator and rotor passages. These windows, however, act as cylindrical lenses that introduce aberrations into the LA optical system. If not corrected, these aberrations can greatly degrade the measurements or even prevent any measurements. A monochromatic correction optic (Fig. 11) was designed for this application (Wernet and Seasholtz, 1987). The addition of the correction optic restores the diffraction limited performance of the optical system.

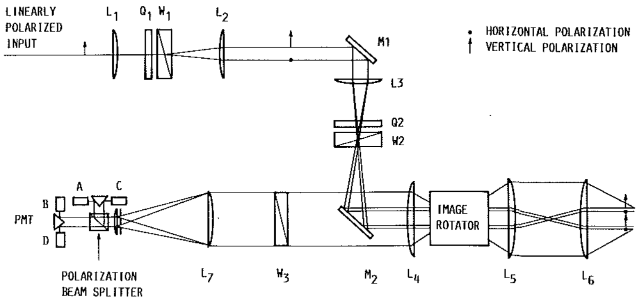

Fig. 10 Schematic view of the transmitting and receiving optics

Combustor Viewing System

Another way to determine the response of a component to the hot section environment is to monitor visual images of the component during operation. This is not likely to produce quantitative data but, in some cases, qualitative data are sufficient or even preferable. A case in point is the Combustor Viewing System (Morey, 1984, 1985). This system was designed to provide recorded images of the interior of a combustor during operation; the objective was to produce a visual record of some of the causes of premature hot section failure.

The Combustor Viewing System consists of a water-cooled optical probe, a probe actuator, an optical interface unit that couples the probe to cameras and to an illumination source, and system controls. The probe with its actuator is designed to mount directly on an engine or a combustor. The probe is 12.7 mm in diameter, small enough to fit into an igniter port. The actuator provides a rotational motion of ±180 deg and radial insertion to a maximum depth of 7.6 cm. Two probes were built to use with the system. The wide field-of-view probe can be fitted with lenses for 90 and 60 deg fields-of-view, with the viewing axis oriented 45 deg to the axis of the probe. The narrow field-of-view probe has lenses for 35 and 13 deg fields-of-view that are oriented 60 deg relative to the probe axis. Both probes are water cooled and gas purged and are capable of operating within the primary combustion zone of a combustor.

Figures 12(*a*) and 12(*b*) show cross-sectional views of the two probes. In each case an image conduit is used to transfer the image through the length of the probe. The image conduit

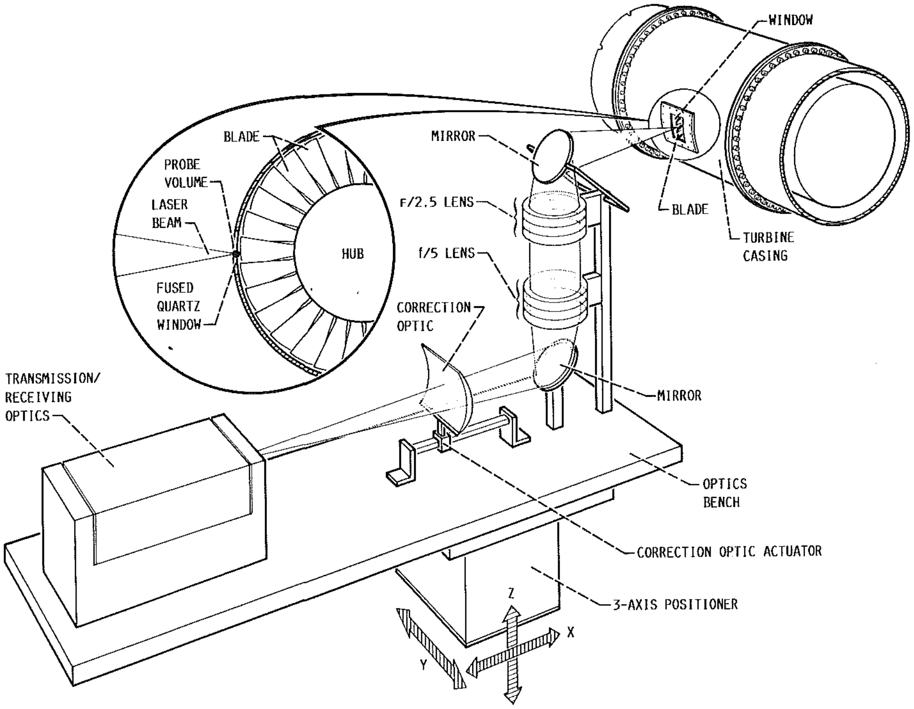

Fig. 11 Schematic view of a laser anemometer system applied to a turbine rig incorporating a curved casing window. The aberrations induced by the turbine window are compensated for by the correction optic. As the three-axis table scans the probe volume through the blade passage, the correction optic position is adjusted by another actuator. In this position, the probe volume is just inside the turbine window, and the actuator is at its farthest position from the f/5 lens.

is a fused bundle of fibers 3 mm in diameter and consists of about 75,000 fibers 10 μm in diameter. Each of these fibers corresponds to a picture element. The image conduit is 33 cm long and is coupled to a flexible fiber bundle, which connects the probe to the optical interface unit. Each probe is also equipped with two 1 mm diameter plastic clad fused quartz fibers used for illumination when required.

The optical interface unit contains cameras, filters, and an illumination source. Either film or video cameras can be remotely selected and up to eight filters can be inserted into the viewing path. The illumination source is a mercury arc lamp focused on the ends of the illumination fibers.

This system has been used in both combustor and full-scale engine tests. Although the original use for the system was in combustor liner durability studies, the system also has capability as a flowpath diagnostic device. It has been used to examine light off and blowout characteristics and appears to have considerable potential for other time-dependent phenomena and for flame radiometry. Subsequent to the initial development program, additional systems were built and put into service in aircraft engine development work and in testing turbine engines used to generate electrical power.

High-Temperature Strain Measuring Systems

The most ambitious instrumentation development effort in this program is the development of high-temperature strain measuring systems. The target goal for this work is to measure strain (approx 2000 microstrain, maximum) at temperatures up to 1250 K with an uncertainty of ±10 percent. This requirement is for relatively short-term testing; a 50 h sensor life is considered sufficient. Spatial resolution of the order of 3 mm is desired and where measurements are required on blades or vanes, large temperature gradients are anticipated. In general, the requirement is for steady-state measurements as differentiated from dynamic (fluctuating component only) measurements.

The principal candidate for making such measurements under similar but lower temperature conditions (less than approx 700 K) is the resistance strain gage. However, at the higher temperatures, strain measurements become increasingly difficult and the commonly used strain gages are marginal at best. As the required temperature range increases, the magnitude of the correction for apparent strain becomes substantially larger than the strain signal and the uncertainty of the correction is excessive. To meet the goals listed above, the uncertainty of the apparent strain correction must be less than ±200 microstrain. This requirement translates to a repeatability of the resistance versus temperature for the mounted strain gage to be well within ±400 parts per million (ppm), based on a gage factor of two.

We made an extensive study of potentially useful high-temperature static strain measurement techniques (Hulse et al., 1987a). As a result of this study, we are pursuing the following to improve our high-temperature strain measuring capability:

1 developing improved high-temperature strain gages
2 learning how better to use available strain gages
3 developing optical strain measuring systems as alternatives to strain gages.

The following section will discuss these three areas of work.

Development of Improved High-Temperature Strain Gages. In attempting to develop improved high-temperature strain gages, we are emphasizing development of alloys with very repeatable resistance versus temperature characteristics (Hulse et al., 1985, 1987b). We tested a number of alloy compositions from five alloy families. These alloy families are FeCrAl, NiCrSi (Nicrosil), PtPdMo, PdCr, and PtW. In all cases except for the thermocouple alloy Nicrosil, we looked at a range of compositions. Alloy samples were cast into rods and then machined into suitable test samples. Measurements were made of resistance versus temperature over a number of cycles in which cooling rates were varied from 50 to 250 K/minute. Additional tests included oxidation (weight gain method) and resistance drift for up to 3 h in air at 1250 K. The results of these tests indicated that two alloys, one in the FeCrAl family and one in the PdCr family, had the best potential for high-temperature strain gage applications.

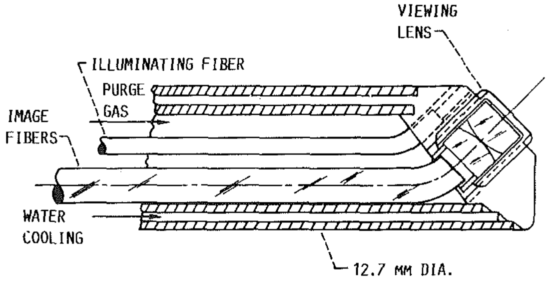

Fig. 12(a) Cross section of wide field of view combustor viewing probe

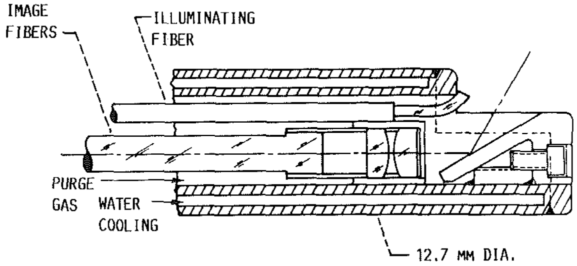

Fig. 12(b) Cross section of narrow field of view combustor viewing probe

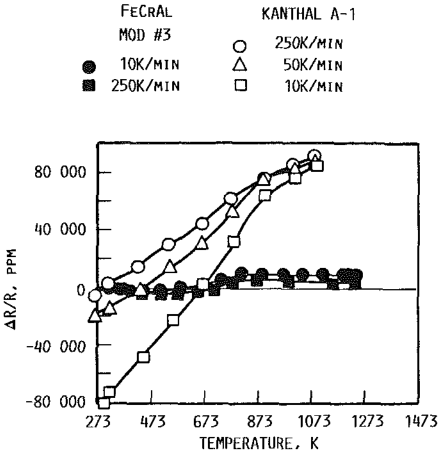

Fig. 13 Fractional resistance change of Kanthal A-1 and FeCrAl mod #3 as a function of temperature

The FeCrAl alloy was designated as "Mod 3." The fractional resistance change with temperature for this alloy at temperatures up to 1250 K is compared with the commercial Kanthal A-1 (also FeCrAl) alloy in Fig. 13. In this case both alloys were annealed for 2 h at 1150 K prior to testing. The resistance change of the Mod 3 alloy is much less than that of the Kanthal A-1 alloy and shows comparatively little change for different cooling rates. This alloy does, however, exhibit different resistance versus temperature characteristics, depending on previous thermal history. Figure 14 illustrates this effect for exposure to 1250 K air for times ranging from 10 to 105 h. Because of this effect, work on this alloy has been de-emphasized in favor of the PdCr alloy.

The PdCr alloy has a resistance versus temperature curve that is characteristic of a solid solution alloy with no phase or internal structure changes being evident. The resistance is es-

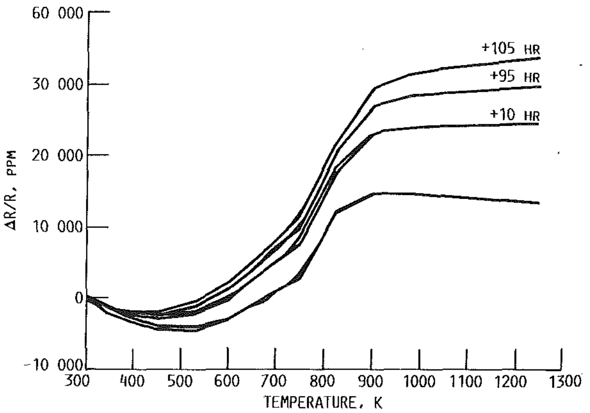

Fig. 14 Effect of soak time at 1250 K on the resistance versus temperature characteristic of FeCrAl mod #3

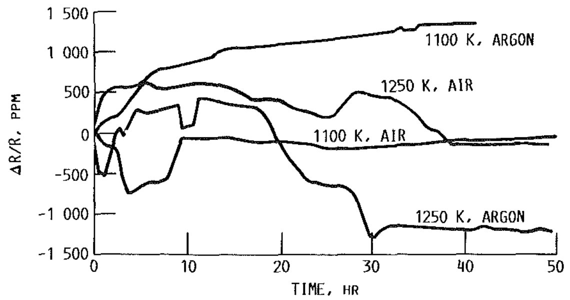

Fig. 15 Long-term resistance drift of PdCr alloy in argon and air

sentially linear with temperature and not affected by changes in cooling rate or previous thermal history. Cycle-to-cycle repeatability of the fractional change in resistance with temperature is excellent. Tests over four thermal cycles showed an average (over the temperature range) standard deviation of 130 ppm. The greatest variation was at approximately 700 K with a standard deviation of 245 ppm. The long-term drift of cast samples of this alloy at 1100 and 1250 K in air and in argon is shown in Fig. 15. It should be noted that these data imply a repeatability in resistance measurement to the order of 100 ppm; it is likely that some of the fluctuation in these curves is attributable to the measuring system rather than the resistance of the alloy samples.

The repeatability of the PdCr alloy is the property that we feel is essential for high-temperature strain gage work. However, there are other properties required for good strain gages and the PdCr alloy may not be ideal considering these properties. The temperature coefficient of resistance is high enough that temperature compensation will be required; the added complication and the larger gage size required for this will have to be accommodated. Other potential problems such as oxidation resistance of high surface-to-volume ratio thin films and fine wires, gage factor changes with temperature, and the elastic/plastic strain properties are still under investigation.

Work With Available Strain Gages. Learning how best to use available strain gages in high-temperature applications requires that considerable experimental work be done to explore strain gage characteristics and devise optimum procedures for specific applications. Such work is very time consuming, especially when tests at many different temperatures are required. Consequently, one of our objectives in this work was to establish a computer-controlled testing capability at NASA Lewis so that testing could be accomplished with minimum operator attention.

The automated strain gage test laboratory has the capability to measure apparent strain and gage factor over a range of

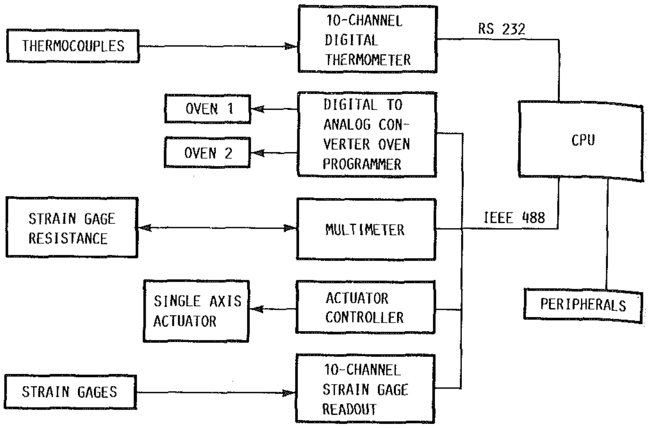

Fig. 16 Block diagram of the high-temperature strain gage testing system

temperatures from 300 to 1370 K. The laboratory has two ovens (one of which contains a test fixture for a constant strain beam), a computer-controlled actuator for deflecting the beam, strain gage and temperature instrumentation, and a personal computer for controlling the tests and collecting the data. Communication between various parts of the system is accomplished using both an IEEE-488 data bus and an RS-232 serial interface. A very versatile control program was developed that allows us to construct a variety of test profiles by entering a series of temperatures and command statements into a data set. Figure 16 shows a block diagram of the system.

One approach to better utilization of available strain gages is outlined by Stetson (1984). In this work using Kanthal A-1 alloy, it was determined that the apparent strain of the gage was strongly affected by the rate at which the gage was cooled from the highest use temperature. Further, the apparent strain for the next thermal cycle followed that established by the cooling part of the previous cycle; a repeatable apparent strain could be obtained if the cooling rate could be reproduced during each thermal cycle. This implies that an accurate apparent strain correction could be obtained by matching the cooling rate during calibration to that which would be impressed on the strain gage during use. It is necessary, of course, that the cooling rates be controllable during use and that is not always possible. But for the work of Stetson (1984), the cooling rates could be matched and, although it took considerable effort, the result was usable static strain measurements at temperatures up to 950 K.

Work based on controlled cooling rates has also been undertaken at NASA Lewis. Hastelloy X plates 13 by 20 cm were instrumented with Kanthal A-1 and Chinese FeCRA1 700°C (Wu et al., 1981) strain gages. A plate-holding fixture was made that permitted cooling gas to flow over the plate uniformly so as to get controlled cooling rates. The Kanthal A-1 gages were mounted using a flame-sprayed alumina and ceramic cement process and the Chinese gages were mounted with a Chinese ceramic cement using directions supplied with the gages. The plates were also instrumented with ten thermocouples so as to measure the temperature distribution at the strain gages. Apparent strain measurements were made over a temperature range from 300 to 950 K with cooling rates controlled at 0.1, 1.0, and 5.6 K/s. Figure 17 shows the resulting resistance versus temperature data. Plotted here are fractional changes in resistance for one each of the Kanthal A-1 and Chinese gages for the three different cooling rates. The data show the Kanthal gage to be strongly dependent on cooling rate but repeatable in resistance at the maximum temperature. The resistance of the Chinese gage is independent of cooling rate at both 300 and 950 K, but at intermediate temperatures the curves deviate depending on cooling rate. The maximum deviations in these curves occur in the temperature

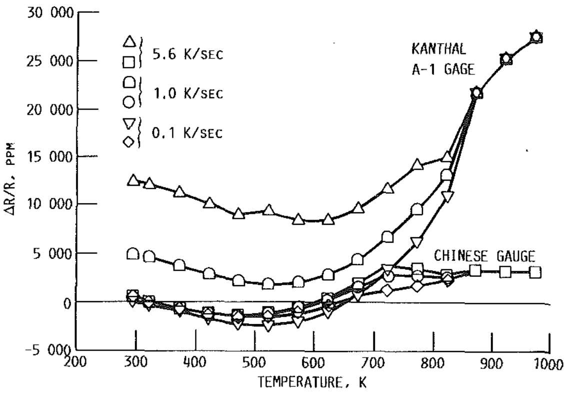

Fig. 17 Fractional resistance change versus temperature for Kanthal A-1 and 700°C Chinese gages with three different cooling rates

range from 650 to 800 K, roughly the same region for which high drift rates have been reported for the Chinese gages (Hobart, 1985).

Optical Strain Measurement. Optical systems may not provide exact alternatives to resistance strain gages for all turbine engine applications, but they appear to have high potential for providing high-temperature, noncontact, two-dimensional strain measuring systems with virtually unlimited strain range. An optical technique that requires no modification to the surface under test uses laser speckle patterns. These patterns are formed by constructive and destructive interference of laser light reflected from a diffuse surface. The source of the pattern is the irregularities in the surface; when the surface is distorted, for example by strain in the plane of the surface, the speckle pattern changes. Precise measurements of changes in recorded speckle patterns can provide information on the strain imposed on the surface. A practical implementation of this technique is a laser speckle photogrammetric system in which speckle patterns are recorded on photographic film (Stetson, 1983). Speckle pattern photographs (called specklegrams) are made at different increments of loading of the test sample and then pairs of specklegrams are examined in an automated interferometric photocomparator. The system uses heterodyne techniques to achieve accurate measurements to a fraction of an interference fringe. No attempt will be made here to describe this system in detail; it has been thoroughly described in the open literature (Stetson, 1983).

The laser speckle photogrammetric system has successfully measured high-temperature surface deformation. Stetson (1983) describes an experiment to measure the thermal expansion of an unrestrained plate of Hastelloy X at temperatures up to 1150 K. The plate was heated in a laboratory furnace to 1150 K and then allowed to cool to 500 K over a period of several hours. Specklegrams were recorded at roughly 200 K intervals during the heating and cooling and succeeding specklegram pairs were used to determine the thermal expansion of the plate. Measured thermal expansion agreed with values calculated from the measured temperature and the thermal expansion coefficient to within 3 percent.

We have attempted to use the laser speckle photogrammetric system in test cell environments. In one attempt we recorded specklegrams of a combustor liner in a high-temperature, high-pressure combustor test rig (Stetson, 1984). The specklegrams were taken through a viewing port in the pressure vessel of the test rig as combustor pressure and temperature were varied. A potential problem in this application is that the high-pressure cooling air flowing over the exterior surface of the combustor liner is in the optical viewing path, and turbulence in the gas flow may cause sufficient optical distortion to prevent correlation of succeeding pairs of specklegrams. Examples of undistorted and distorted specklegrams are shown in Figs. 18(*a*) and 18(*b*). This effect proved to be a fundamental limitation for the measuring system in this application when combustor pressure was higher than approximately 3 atm. We intend to explore further high-temperature applications of optical strain measuring systems.

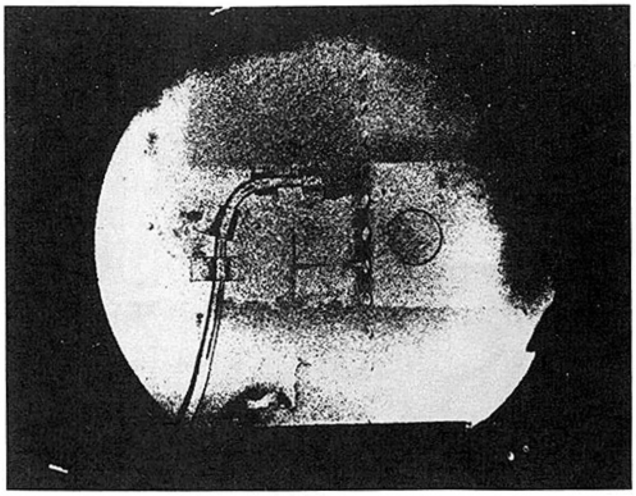

Fig. 18(*a*) Specklegram of combustor liner with no distortion due to flow

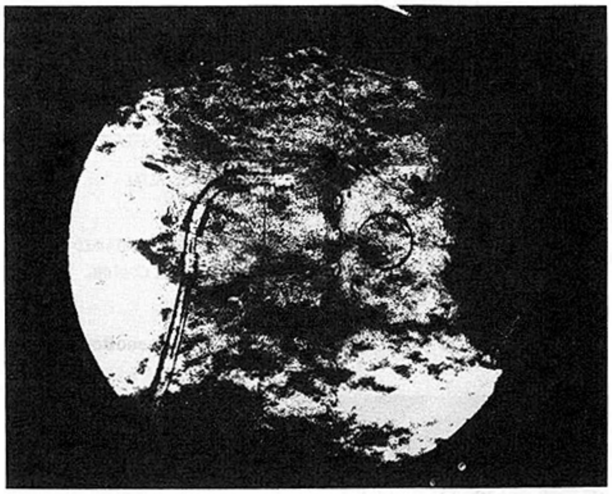

Fig. 18(*b*) Specklegram of combustor liner with distortion from turbulent gas flow

Thin Film Sensors

One of the fundamental precepts of experimentation is that the sensors used to obtain experimental data must not perturb the subject of the experiment from its condition prior to the introduction of the sensors. In turbine engine testing there are many situations in which this precept may be violated. A prime example is the measurement of turbine airfoil surface temperature. Conventional technology involves laying sheathed thermocouple wire into grooves cut into the surface of the airfoil, then covering the installation and smoothing the airfoil contour. Although the airfoil contour is restored, the thermocouple disturbs the temperature distribution, does not give a true measure of the outside surface temperature, and threatens the integrity of the structure of thin walled blades and vanes.

The thin film thermocouple shown in Fig. 19 appears to be an ideal solution for blade and vane surface temperature measurement (Grant and Przybyszewski, 1980; Grant et al., 1981, 1982). As seen in the cross-sectional sketch of the sensor in Fig. 20, the sensor has minimal intrusiveness. In this case the

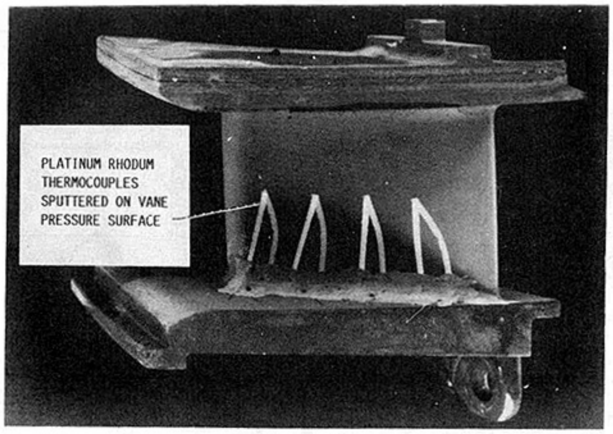

Fig. 19 A turbine vane instrumented with thin film thermocouples

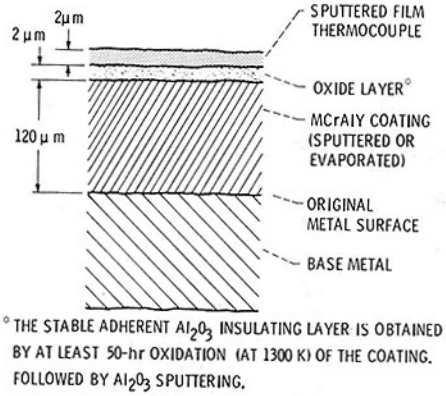

Fig. 20 Thin film thermocouple cross section

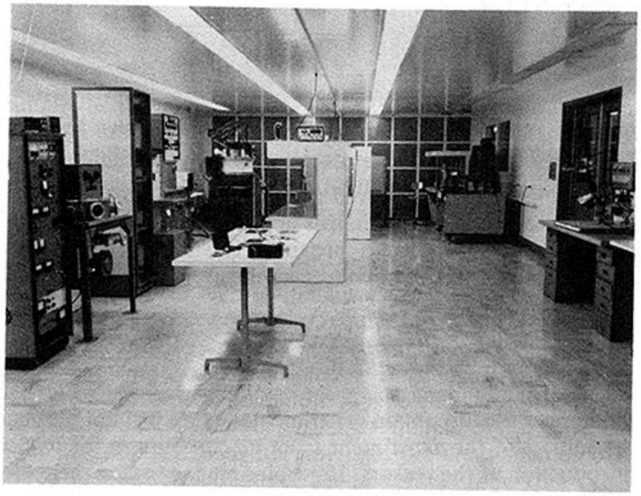

Fig. 21 Thin film sensor laboratory at the Lewis Research Center

blade or vane, coated with an MCrAlY anticorrosion coating, is polished and then oxidized to form an adherent surface coating of aluminum oxide. Additional aluminum oxide is deposited over this film to form an electrically insulating film roughly 2 μm thick. Films of thermocouple alloy (Pt and Pt10%Rh) are sputter deposited through appropriate masks so that the films overlap at one point to form the thermocouple junction. The thermocouple films extend to the root of the vane where connections to conventional lead wires are made. Film-to-lead wire connections are made by parallel-gap welding. The complete installation of insulating film and thermocouple alloy films has a thickness of less than 20 μm. The installation has not changed the contour or the strength of the component and the greatest thermal changes apparent are the different absorptance and emittance of the thermocouple films compared to the oxidized MCrAlY surface. The technology for thin film thermocouples and turbine airfoils has been developed to the extent that instrumented vanes and blades are being used in turbine engine tests at temperatures up to 1250 K.

Thin film sensor development work is going on both at contractor facilities and at NASA Lewis. Figure 21 shows the thin film sensor laboratory at NASA Lewis. The laboratory is housed in a clean room in which both temperature and humidity are controlled. On the left in the photograph are three vacuum sputtering machines for deposition of both insulator and sensor films. In the right-hand corner of the room is equipment for photolithography of sensors; conventional photo-resist techniques are used. At the far right edge of the photograph is a welder for connecting lead wires to sensor films.

Concluding Remarks

This paper has reviewed the state of development of a number of advanced instrumentation projects applicable to the hot sections of turbine engines. Most of these projects are complete and the instrumentation is in use. This is the case for the Combustor Viewing System, the Dynamic Gas Temperature Measuring System, total heat flux sensors, the laser anemometry projects described here, and thin film thermocouples. Work in the general area of thin film sensors is continuing in order to improve the technology further and expand sensor types and applications. The work to improve our high-temperature strain measuring capability is still in progress.

References

Atkinson, W. H., and Strange, R. R., 1982, "Development of Advanced High-Temperature Heat Flux Sensors," NASA CR-165618.

Atkinson, W. H., Hobart, H. F., and Strange, R. R., 1983, "Advanced High Temperature Heat Flux Sensors," *Proceedings of the 38th Instrument Society of America Conference, Advances in Instrumentation*, Vol. 38, Part 2, Instrument Society of America, pp. 1457–1479.

Atkinson, W. H., Cyr, M. A., and Strange, R. R., 1984, "Turbine Blade and Vane Heat Flux Sensor Development, Phase I," NASA CR-168297.

Atkinson, W. H., Cyr, M. A., and Strange, R. R., 1985a, "Development of High-Temperature Heat Flux Sensors, Phase II – Verification Testing," NASA CR-174973.

Atkinson, W. H., Cyr, M. A., and Strange, R. R., 1985b, "Turbine Blade and Vane Heat Flux Sensor Development, Phase II," NASA CR-174995.

Elmore, D. L., Robinson, W. W., and Watkins, W. B., 1983, "Dynamic Gas Temperature Measurement System Final Report, Volume I. Technical Efforts," NASA CR-168267.

Elmore, D. L., Robinson, W. W., and Watkins, W. B., 1984, "Dynamic Gas Temperature Measurement System," *Proceedings of the 30th International Instrumentation Symposium, Instrumentation in the Aerospace Industry*, Vol. 30, *Advances in Test Measurements*, Vol. 21, Instrument Society of America, pp. 289–302.

Elmore, D. L., Robinson, W. W., and Watkins, W. B., 1986a, "Further Development of the Dynamic Gas Temperature Measurement System, Vol. I. Technical Efforts," NASA CR-179513.

Elmore, D. L., Robinson, W. W., and Watkins, W. B., 1986b, "Further Development of the Dynamic Gas Temperature Measurement System," AIAA Paper No. 86-1648.

Grant, H. P., and Przybyszewski, J. S., 1980, "Thin Film Temperature Sensor," NASA CR-159782.

Grant, H. P., Przybyszewski, J. S., and Claing, R. G., 1981, "Turbine Blade Temperature Measurements Using Thin Film Temperature Sensors," NASA CR-165201.

Grant, H. P., Przybyszewski, J. S., Claing, R. G., and Anderson, W. L., 1982, "Thin Film Temperature Sensors, Phase III," NASA CR-165476.

Hobart, H. F., 1985, "Evaluation Results of the 700°C Chinese Strain Gages," NASA TM-86973.

Holanda, R., 1984, "Analysis of Thermoelectric Properties of High-Temperature Complex Alloys of Nickel-Base, Iron-Base, and Cobalt-Base Groups," NASA TP-2278.

Hulse, C. O., Bailey, R. S., and Lemkey, F. D., 1985, "High Temperature Static Strain Gage Alloy Development Program," NASA CR-174833.

Hulse, C. O., et al., 1986, "Advanced High Temperature Static Strain Sensor Development," NASA CR-179520.

Hulse, C. O., Bailey, R. S., Grant, H. P., and Przybyszewski, J. S., 1987, "High Temperature Static Strain Gage Development Contract," NASA CR-180811.

Lading, L., 1983, "Estimating Time and Time-Lag in Time-of-Flight Velocimetry," *Applied Optics*, Vol. 22, No. 22, pp. 3637-3643.

Morey, W. W., 1984, "Hot Section Viewing System," NASA CR-174773.

Morey, W. W., 1985, "Jet Engine Combustor Viewing System," *Conference on Lasers and Electro-Optics*, IEEE, New York, p. 298.

Oberle, L. G., and Seasholtz, R. G., 1985, "Filter Induced Errors in Laser Anemometry Using Counter-Processor," *International Sympsoium on Laser Anemometry*, ASME FED-Vol. 33, A. Dybbs and P. A. Pfund, eds., ASME, New York, pp. 221-230.

Oberle, L. G., 1987, "A Computer Controlled Signal Preprocessor for Laser Fringe Anemometer Applications," NASA TM-88982.

Seasholtz, R. G., Oberle, L. G., and Weikle, D. H., 1984, "Optimization of Fringe-Type Laser Anemometers for Turbine Engine Component Testing," AIAA Paper No. 84-1459 (also NASA TM-83658).

Stetson, K. A., 1983, "The Use of Heterodyne Speckle Photogrammetry to Measure High-Temperature Strain Distributions," *Holographic Data Nondestructive Testing*, D. Vukicevic, ed., Proc. SPIE-370, SPIE, Bellingham, WA, pp. 46-55.

Stetson, K. A., 1984, "Demonstration Test of Burner Liner Strain Measuring System," NASA CR-174743.

Stocks, D. R., and Elmore, D. L., 1986, "Further Development of the Dynamic Gas Temperature Measurement System, Vol. II – Computer Program User's Manual," NASA CR-179513-VOL-2.

Wernet, M. P., and Edwards, R. V., 1986, "Implementation of a New Type of Time-of-Flight Laser Anemometer," *Applied Optics*, Vol. 25, No. 5, pp. 644-648.

Wernet, M. P., 1987, "Four Spot Laser Anemometer and Optical Access Techniques for Turbine Engine Applications," *ICIASF '87, International Congress on Instrumentation in Aerospace Simulation Facilities*, IEEE, New York, pp. 245-254 (also NASA TM-88972).

Wernet, M. P., and Oberle, L. G., 1987, "Laser Anemometry Techniques for Turbine Applications," ASME Paper No. 87-GT-241 (NASA TM-88953).

Wernet, M. P., and Seasholtz, R. G., 1987, "Zoom Lens Compensator for a Cylindrical Window in Laser Anemometer Uses," *Applied Optics*, Vol. 26, No. 21, pp. 4603-4611.

Wu, T. T., Ma, L. C., and Zhao, L. B., 1981, "Development of Temperature Compensated Resistance Strain Gages for Use to 700°C," *Experimental Mechanics*, Vol. 21, No. 3, pp. 117-123.

NNEPEQ—Chemical Equilibrium Version of the Navy/NASA Engine Program

L. H. Fishbach
NASA Lewis Research Center,
Cleveland, OH 44135

S. Gordon
Sanford Gordon & Associates,
Cleveland, OH 44135

The Navy NASA Engine Program, NNEP, developed in 1975, currently is in use at a large number of government agencies, commercial companies, and universities. This computer code has been used extensively to calculate the design and off-design (matched) performance of a broad range of turbine engines, ranging from subsonic turboprops to variable cycle engines for supersonic transports. Recently, there has been increased interest in applications that NNEP was not capable of simulating, namely, high Mach applications, alternate fuels including cryogenics, and cycles such as the gas generator air-turbo-rocket (ATR). In addition, there is interest in cycles employing ejectors such as for military fighters. New engine component models had to be created for incorporation into NNEP, and it was also found necessary to include chemical dissociation effects of high-temperature gases. This paper discusses the incorporation of these extended capabilities of NNEP and illustrates some of the effects of these changes.

Introduction

During the early 1970s, NASA embarked upon the study of technology for the airframe and engines for a supersonic transport—the Supersonic Cruise Research Program SCR. Out of this program emerged a class of engines whose design/off-design performance could not be predicted using any of the existing computational methods. The NASA Lewis Research Center embarked upon a joint program with the Naval Air Development Center to develop a computer code not only capable of simulating these engines, but also having the capability to optimize any variable geometry setting at each operating point. The development was based upon an existing Navy program NEPCOMP (Caddy and Shapiro, 1975) and was reported by Fishbach and Caddy (1975).

This new engine simulation computer program, NNEP, has gained wide acceptance and is currently in use at over 70 institutions. The NNEP computer code does not contain any preset engine cycles that the user can calculate by just issuing a command such as *run turbojet*, etc. Instead, it requires that the user, through a set of inputs, identify the mechanical and thermodynamic connections between the components of the engine. A block diagram is constructed to represent the engine configuration to be studied. The components of the engine can consist of any combination of inlets, ducts (burners), water injectors, compressors (fans), turbines, heat exchangers, flow splitters, mixers, and nozzles. The NNEP program logic uses flow stations and the numbers that are assigned to them to determine the flow path of gases through the engine. Herein lies the versatility of NNEP in that inputs to the code determine the engine to be simulated without the need to build in all the cycles in advance. NNEP can therefore simulate simple engines such as turbojets to highly complicated variable cycle engines with variable geometry. It uses component maps in order to calculate off-design performance.

However, just as NNEP was developed to address shortcomings in the previous methodologies, new areas of interest have arisen that NNEP, with all its versatility, could not handle.

The first area that could not be handled was the use of cryogenic fuels, nonhydrocarbon fuels, and the possibly high resulting temperatures where chemical dissociation of the gas stream might occur. The second area was in a class of engines where flow is introduced into the engine from a source other than an inlet. An example of this type of engine is the gas generator air-turbo-rocket. The third area involved engines incorporating ejectors such as a turbojet engine being used as the primary flow source of an ejector for an Advanced Short Takeoff and Vertical Landing (ASTOVL) aircraft.

This paper will describe the additional capabilities added to NNEP resulting in a new code NNEPEQ, which stands for the Navy NASA Engine Program with EQuilibrium effects.

General Chemistry and Dissociation Effects

In order to extend the NNEP capability to uses other than hydrocarbon fuels and to include dissociation effects that occur at high temperatures, a number of additions and modifications to NNEP were required. These consist primarily of the addition of a number of subroutines to handle chemical equilibrium calculations, and a new subroutine, which serves as an interface between the engine routines and the equilibrium routines.

Chemical equilibrium compositions and thermodynamic

Contributed by the International Gas Turbine Institute and presented at the 33rd International Gas Turbine and Aeroengine Congress and Exhibition, Amsterdam, The Netherlands, June 5–9, 1988. Manuscript received by the International Gas Turbine Institute March 10, 1987. Paper No. 88-GT-314.

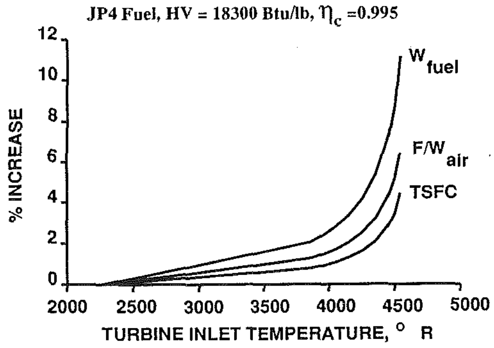

Fig. 1 Effects of dissociation on engine performance

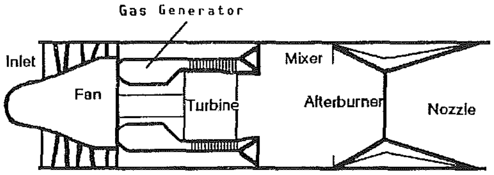

Fig. 2 Schematic of gas generator air-turbo-rocket (ATR)

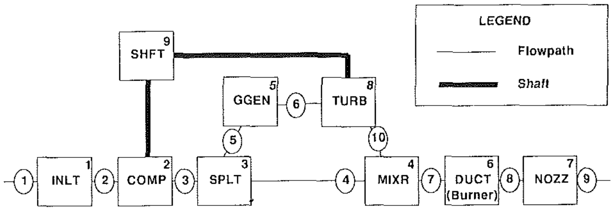

Fig. 3 NNEPEQ schematic of gas generator ATR

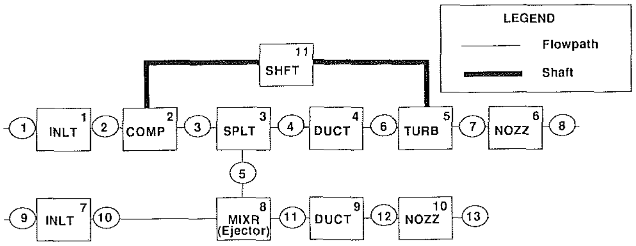

Fig. 4 NNEPEQ schematic of propulsion system for ejector ASTOVL aircraft

mixture properties and derivatives are obtained by means of a modified version of the general chemical equilibirum program (Gordon and McBride, 1976) (currently referred to as CET86). The CET86 program, developed by the NASA Lewis Research Center, has had a wide acceptance (currently used by several hundred institutions) and has been extensively tested. A number of subroutines in CET86 were eliminated (such as those for shock and detonations) and the remainder, with appropriate modifications, were added to NNEP. This new NNEP program, NNEPEQ, is capable of handling any chemical system for which thermodynamic data are available. A library of thermodynamic data, in the form of least-squares coefficient required by CET86, is provided with the program.

For each component that requires reactants to be added, provision has been made for specifying up to six fuels and their corresponding relative fuel weights and, similarly, up to six oxidants and their corresponding relative oxidant weights.

An example of the effect of dissociation on calculated performance is shown in Fig. 1. Shown plotted as a function of turbine inlet temperature is the percent increase due to dissociation in fuel flow, net thrust per unit airflow (F/W_{air}), and total specific fuel consumption TSFC (net thrust per unit fuel flow). This example is for a one-spool turbojet. The JP4 fuel has a lower heat of combustion of 18,300 Btu/lb and a combustion efficiency of 0.995. Computer runs were made for burner-out temperatures in the range of 2260 to 4540 R. As may be seen in Fig. 1, dissociation effects are negligible below about 2300 R. However, at 4540 R (the stoichiometric temperature), dissociation causes an increase of 11.1 percent in fuel flow, a 6.4 percent increase in F/W_{air}, and a 4.4 percent increase in TSFC.

The increase in fuel is due to the higher energy requirements to heat a dissociating gas to a specified temperature. This also results in an increase in the thrust per unit airflow as follows. The increase in fuel increases the mass flow in the engine. This results in an increase in F/W_{air} of 0.6 percent. However, the recombination of the combustion products results in an increase in nozzle total temperature, which therefore yields an increase in jet velocity. This results in an additional increase in F/W_{air} giving the total shown of 6 percent. Thus, approximately 10 percent of the increase is due to additional fuel, and 90 percent due to recombination.

When no dissociation is considered, as in NNEP, the determination of the composition of combustion products is based on mass balance considerations only and is rather trivial. By contrast, the determination of equilibrium compositions, as in NNEPEQ, involves solving nonlinear sets of equations, which generally requires an iteration process. It is not surprising, therefore, that NNEPEQ requires considerably more computer time than NNEP. As an example, computer runs were made on an IBM 370 computer for ten different configurations of a one-spool mixed flow turbofan. The configurations involved both on-design and off-design modes. The total CPU time for NNEP was only 4 seconds as contrasted with 93 seconds for NNEPEQ—a factor of about 24. Work is currently in progress to shorten the NNEPEQ running time by use of several techniques to reduce the number of iterations required for convergence.

Gas Generators

As previously mentioned, the need arose to be able to simulate engine cycles where gas was introduced into the engine other than as flow through an inlet or as fuel in a burner. A typical example of this is the air-turbo-rocket (ATR) shown in Fig. 2. In this engine, air enters the inlet and then passes through a compressor raising both the pressure and temperature. At high Mach number or high pressure ratio, this temperature may be so high that little or no energy can be added by burning fuel without exceeding turbine inlet temperature limits. Therefore, the compressor discharge air does not pass through the turbine; it is ducted around it. Instead, a gas generator is added to the engine. Reactants, such as hydrogen and oxygen, are mixed together and ignited to some temperature less than the allowable turbine inlet temperature. The resulting high temperautre and pressure gas is then expanded through the turbine, which is connected through a shaft to the compressor. The exhaust products of the turbine are then mixed with the air ducted around the turbine and, if desired, more fuel added and burned in an afterburner. This engine has been proposed for operation at Mach numbers as high as five with the turbomachinery still running.

NNEPEQ does not run preconfigured engine cycles and the user, through inputs, connects the components together. The solution to simulating an ATR is to introduce the gas generator component anywhere the user might desire it in the engine cycle. A block diagram is drawn, such as in Figs. 3 and 4, representing the components of the engine. The flow stations that are identified at the entrance and exit of each component (shown in Figs. 3 and 4 as encircled numbers) are then used to construct the gas flow path through the engine. As an example, if the exit flow station number for the inlet of the engine has a value of 2, the next component in the path would be the one that had 2 as the entering station number, etc.

There is only one method available in NNEPEQ to identify multiple gas flow paths in an engine cycle: the use of a splitter. A splitter divides the flow into two streams, a primary and a secondary. The logic in NNEPEQ forces the cycle calculations to proceed along the primary path until either a mixer or a nozzle occurs. When either of these components appears, the program goes back to see if there are any splitters from which the secondary flow path has not been followed or completed. As is the case for the primary flow, the secondary flow must terminate either in a mixer or in a second nozzle. Thus, the use of a splitter provided the key to simulating the ATR cycle.

A NNEPEQ schematic of the ATR cycle (Fig. 2) is shown in Fig. 3. The location of the splitter can be either before or after the compressor. For the cycle shown, air enters the inlet, is compressed, and split into two streams. The primary path air then enters the mixer. Logical coding in NNEPEQ detects the mixer component and looks upstream for a splitter, which of course it finds. The NNEPEQ program logic then follows the splitter secondary path at station 5 into the new gas generator component (GGEN). For this special case, there is no flow at station 5 because the user sets the splitter input specification for this path to zero. Zero flow at station 5 does not interfere with the NNEPEQ program logic. Inputs to the gas generator define the fuel(s) and oxidizer(s) being reacted and their mass flows. In this way, the GGEN component becomes a source of gas flow coming from the splitter secondary outlet and proceeding on to the turbine entrance at station 6.

When generator temperature is specified, the program will determine the corresponding f/o ratio by an iteration process. Other options are available for input to the generator, such as specifying the f/o weight ratio rather than the generator temperature. When f/o is specified, the program will calculate the corresponding generator temperature.

Ejectors

As mentioned in the Introduction, interest has risen in a class of engines incorporating ejectors. An example of this is shown in Fig. 4. This engine is of interest for one version of an ASTOVL aircraft. Compressor discharge air is ducted forward to an ejector while the rest of the compressor air proceeds on back through the main nozzle. The ejector primary air induces additional secondary flow through another inlet and is exhausted vertically toward the front of the vehicle. The main flow is canted slightly downward at the rear of the vehicle. These two exhaust streams are used to provide the short takeoff.

The MIXER component subroutine contained in NNEP was readily modified to simulate an ejector. Referring to Fig. 4, the ejector is shown as the MIXR (component 8). The two flow streams entering the ejector are the primary flow (station 5), which consists of the high-pressure air from the compressor discharge (station 3 from component 2), and the ejector secondary flow from the ramjet inlet (station 10 from component 7). The computer code was changed so that an indicator can be set in the input to show that an ejector is being simulated. Another indicator is set to specify whether subsonic or supersonic (second solution) exit conditions from the mixer exist. The momentum recovery coefficient for both streams, ejector primary exit Mach number, area ratio for the ejector, and primary flow injection angle are all specified.

The continuity, momentum, and energy equations are solved simultaneously for the ejector control volume, and the mixed velocity is obtained. Cycle calculations then proceed on through the remainder of the engine.

Concluding Remarks

The advanced aircraft and their power plants envisioned for the next century represent an enormous challenge to the engineering community. Significant advances in both materials and fuels are being projected in order to achieve the high temperatures needed to develop efficient power plants and vehicles. These high temperatures have presented a challenge to the existing computational methods of predicting engine performance because of the dissociation effects that must be taken into account. The engine cycles envisioned for these vehicles also present a challenge.

The new version of NNEP reported herein has proven capable of meeting these challenges. NNEPEQ can simulate most, if not all, of these engine cycles; be used to study the effects of different fuel types such as cryogenics or slurries; and last, but not least, account for the effects of dissociation at the high temperatures of these cycles. It is believed that NNEPEQ will prove to be even more valuable as a study tool than its predecessor.

Acknowledgments

The authors wish to thank the members of the Advanced Planning and Analysis Office of the NASA Lewis Research Center for their help in developing and testing NNEPEQ.

References

Caddy, Michael J., and Shapiro, Stanley R., 1975, "NEPCOMP—The Navy Engine Performance Computer Program, Version I," NADC-74045-30.

Fishbach, Laurence H., and Caddy, Michael J., 1975, "NNEP—The Navy NASA Engine Program," NASA TM X-71857.

Gordon, Sanford, and McBride, Bonnie J., 1976, "Computer Program for Calculation of Complex Chemical Equilibrium Compositions, Rocket Performance, Incident and Reflected Shocks, and Chapman-Jouguet Detonations," NASA SP-273.

R. T. LeCren

R. E. Gildersleeve

Solar Turbines Incorporated,
San Diego, CA 92138

R. A. Swanek

David Taylor Research Center,
Bethesda, MD 20084

Combustor and Seal System for a Water Piston Propulsor

The Water Piston Propulsor (WPP) is an advanced in-water propulsion system for Marine Corps amphibious vehicles. Significant weight and volume reductions are the primary advantages of the WPP system versus the more conventional propulsion technologies used today. WPP thrust is produced by porting high-pressure combustion gases into the water-filled channels of a rotor. Gas expansion results in the expulsion of water from the downstream end of the rotor channel. Solar Turbines Incorporated, a subsidiary of Caterpillar Inc., is currently under contract to the David Taylor Research Center for the development of the high-temperature, high-pressure combustor and rotor seal systems. Details of combustor and rotor seal design, performance, and development test are discussed.

Introduction

Modern military technology predicates that the Marine Corps amphibious vehicle of the future will be required for assault missions of fortified coasts from 20 or more miles out to sea. Such an assault demands that the vehicles be capable of high in-water speeds for rapid shore approach so that launch ships can be situated a safe distance from adversaries. To obtain high in-water speeds the vehicular power requirements are about four times those for overland operation. Since nearly 80 percent of the operating hours of the vehicle are spent on land, a conventional diesel-driven water power plant is mismatched for most of the vehicle life cycle. The ideal source of in-water propulsive thrust is one that converts a high-energy-density fuel into hydrodynamic thrust while maintaining a small volume and weight. The water piston propulsor (WPP), an advanced propulsive device, is under development to meet this objective. Previous subscale single-channel tests (Krishnamoorthy and Johnson, 1985) have shown the WPP concept to be viable. The objectives of Solar's test program were twofold:

- develop a high-pressure, high-temperature combustor and seal system based on advanced gas turbine technology to meet the stringent design specifications imposed by the WPP system
- develop algorithms for the combustor and the seal control systems

WPP Concept Description

The operation of the water piston propulsor can be better understood by reference to Figs. 1 and 2. The WPP consists of a combustor, a seal system, and a water channel rotor. The combustor and seal systems are used to deliver high-temperature, high-pressure gases to the water channel rotor without significant leakage. The water channel rotor is comprised of 16 trapezoidal cross-section channels. Water enters these channels at the rotor leading edge; these water-filled channels then pass behind a seal plate where they are subsequently exposed to the combustion gases. The gas imparts momentum to the mass of water in the channel by virtue of the gas expansion that occurs. When the channel has rotated to the end of the seal plate the gas pressure has been largely expended. The rotor channel is subsequently exposed to water for the remainder of the rotation where it is filled for the next cycle. Each cycle produces both axial and tangential impulses because of the change in momentum between the incoming and exiting water flows. The tangential impulse, which causes the water channel rotor to rotate, is produced due to the helical water channel configuration.

Combustor Design Requirements

WPP combustion system design requirements were defined for the combustor outlet temperature, overall pressure loss, in-water startup capacity, and system life. From these requirements several derived combustor performance goals such as operating envelope were determined.

Operating Envelope. The prime requirement for the WPP combustion system is that the combustor exit gas temperature be 1922 K (3000°F) at all operating conditions. The combustor air flow is supplied by a compressor driven at variable speeds by the vehicle diesel engine. Therefore the combustor inlet conditions, air flow rate, pressure, and temperature are a function of compressor speed and heat loss in the lines from the compressor to the combustor. Table 1 shows the estimated operating conditions assuming an axial compressor with no variable geometry, intercooling, or heat loss. The operating range of the combustor for the WPP in terms of temperature rise turndown ratio is similar to that of a combustor in a two-shaft gas turbine engine. For the WPP the temperature rise decreases as the compressor speed increases because the combustor outlet temperature is a constant, whereas in a variable

---

Contributed by the International Gas Turbine Institute and presented at the 33rd International Gas Turbine and Aeroengine Congress and Exhibition, Amsterdam, The Netherlands, June 5–9, 1988. Manuscript received by the International Gas Turbine Institute June 2, 1987. Paper No. 88-GT-272.

Table 1 Estimated combustor operating parameters

Speed (%)	Airflow (#/sec)	Pressure (psia)	Temp. (°F)	Temp. Rise (°F)	Fuel Flow (#/hr)
100	1.1	225	800	2200	162
92	0.98	200	762	2238	144
75	0.73	150	657	2343	112
60	0.49	100	522	2478	79
37	0.24	50	323	2677	41

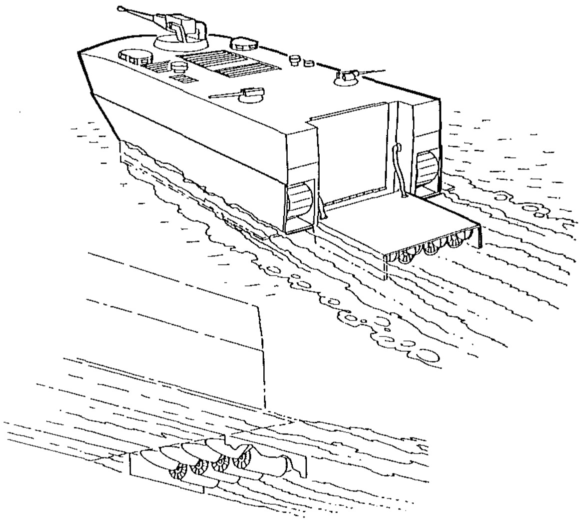

Fig. 1 Water piston propulsor in operation on a marine corps amphibious vehicle

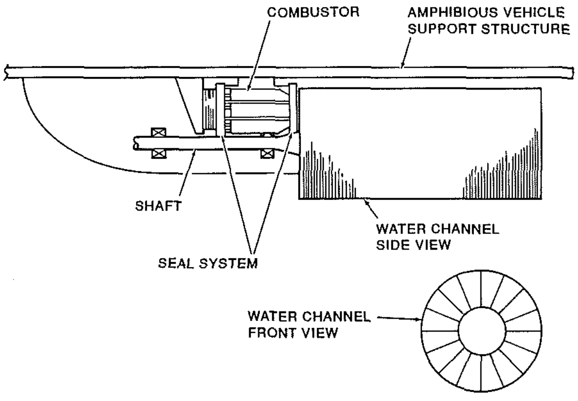

Fig. 2 Water piston propulsor

speed gas turbine the temperature rise increases as compressor speed increases. Because of the probability of heat loss between the compressor and the combustor, the required operating range was extended to include operation at inlet temperatures down to 366 K (200°F). The resulting temperature rise is 1556 K (2800°F). The theoretical fuel/air ratio using the specified fuel, which is Marine diesel fuel per MIL F 16884, is 0.050, which corresponds to an equivalence ratio of 0.70. To accommodate this inlet temperature condition, most of the air must be used for combustion, leaving very little for cooling. The fuel flow turndown ratio ($W_{f\max}/W_{f\min}$) for the no-heat-loss case is approximately 4:1. The low inlet temperature requirement increases this ratio to 5:1.

Overall Pressure Drop. The allowable overall pressure drop was set at a total of 7 percent. As will be discussed in the next section the 7 percent was divided among the inlet line loss, impingement cooling drop, and combustor swirler drop.

In-Water Operation. Since the WPP will be submerged when operating and before startup, the system must be capable of ignition with the combustor and igniter plug wet or damp after water has been purged out of the system by the compressed air. Also, the system must survive an in-water shutdown after which the combustion system is flooded with sea water.

Life. The life requirements for the combustor were set at 180 hours of operation in a 6 year period. Typical operating periods were estimated at a maximum of 1 hour.

Combustor Back Pressure Fluctuations. The back pressure on the combustor varies as the water-filled rotor passages pass the outlet of the combustor. At the design rotor speed of 600 rpm, 160 rotor passages pass behind the combustor outlet each second (160 Hz). One rotor passage is behind the combustor for 0.0063 s. During this time the expulsion of the water begins as the gas expands. The gas expansion and expulsion of water are completed after the rotor passage traverses the combustor outlet. The magnitude of the pressure fluctuation has not been experimentally determined but has been estimated to be as high as ±20 percent of the nominal operational combustor pressure. The combustor design must be tolerant of these fluctuations.

Combustor Aerodynamic and Mechanical Design

A cross-sectional view of the combustor is shown in Fig. 3. The air enters the combustor casing through a single pipe on the top. The flow then passes through an impingement cooling sleeve with 11 rows of orifices. The impingement sleeve is also part of the outlet temperature control system. Approximately 70 percent of the air flows forward and passes through the primary swirler while the remainder flows rearward and is split between the single cooling strip and the exit seal.

Primary Stabilization. The aerodynamic design of the combustor features a strong swirl-stabilized primary zone with all the primary reaction air entering through the swirler. The swirl-stabilized approach provides a strong recirculation of the hot combustion products into the incoming air and fuel, which provides a continuous source of ignition and a high level of combustion stability. This approach was selected to provide tolerance to the pressure fluctuations caused by the passing of the rotor passages.

The recirculation also enhances complete burnout of the fuel to minimize smoke production and liner carbon deposits. This is desirable for this application to avoid fouling of the rotor surfaces and outer liner. The swirler is axial rather than radial to minimize separation at the inner surface. There are 15 swirler vanes set at 45 deg, which results in a swirl number of 0.75. The design was analyzed using the INTERN computer modeling code to determine the velocity profile at the exit. For optimum operation of the WPP concept a uniform velocity profile is desirable. Such a profile can be seen in Fig. 4, which is an output from INTERN.

Combustor Loading. The design specification imposed a maximum external diameter of 10.16 cm (4 in.). An internal diameter of 7.11 cm (2.8 in.) and a length of 11.43 cm (4.5 in.) were selected. The resulting volume of 454 cm^3 (27.7 in.^{3}) gives a combustor loading

$$\frac{\text{LHV} \times \text{Fuel flow}}{\text{Volume} \times (\text{Inlet pressure})^2}$$

of

$$30.9{*}10^6 \text{ kJ/hr m}^3 \text{ atm}^2 \ (0.83{*}10^6 \text{ Btu/hr ft}^3 \text{ atm}^2)$$

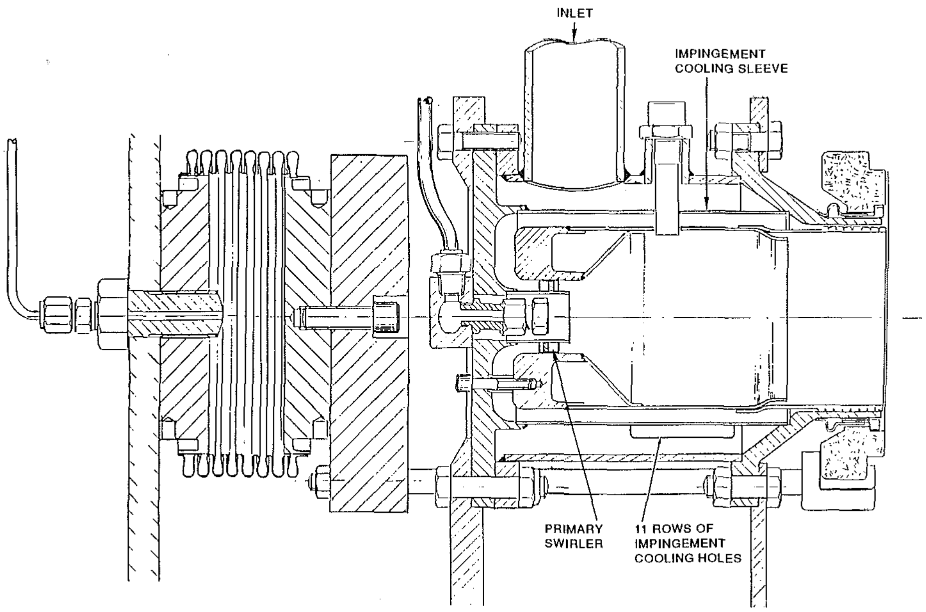

Fig. 3 Combustor cross section

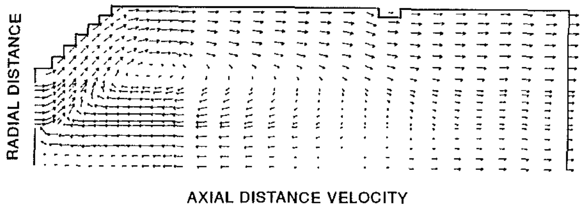

Fig. 4 Combustor velocity profiles

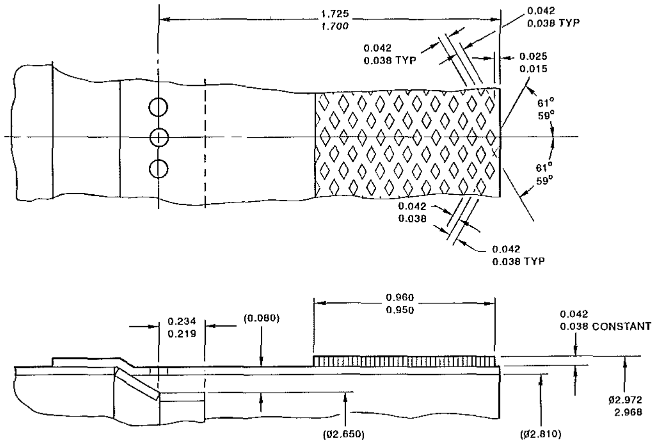

Fig. 5 Combustor aft cooling

or

$$462*10^6 \text{ kJ/hr m}^3 \text{ atm } (12.4*10^6 \text{ Btu/hr ft}^3 \text{ atm})$$

which is not high by gas turbine standards. The θ function loading parameter defined by

$$\theta = P_{in}^{1.75}*\text{VOL}*\exp^{(T_{in}/540)}*(100*f/a)^{0.82}/Wa$$

was also considered.

At the WPP design point, $\theta = 107.5*10^{-5}$, which corresponds to a combustion efficiency of >98 percent.

Cooling Design. The allowable pressure drop was allotted as follows: 1 percent for the supply plumbing, 2.5 percent for impingement cooling, and 3.5 percent across the combustor, which is consistent with current gas turbine design practice.

The initial combustor cooling analysis of the combustor was performed for a totally film-cooled liner with use of a computer code based on a liner combustion side heat transfer correlation developed by Lefebvre and Herbert (1960) and a film-cooling correlation developed at the Lewis Research Center under contract to NASA (Marek and Tacina, 1975). The validity of this code has been experimentally confirmed on Solar gas turbine development programs and has been found to be a useful tool in film-cooled combustor design. The results of the initial film cooling analysis indicated liner hot spot temperatures in excess of 1365 K (2000°F). This result indicated that another type of cooling was required to achieve acceptable liner metal temperatures and hence system life.

A convective impingement cooling system was chosen to provide maximum primary zone cooling heat transfer coefficients. The impingement cooling configuration provides high heat transfer coefficients with the use of the entire combustion air supply. This cooling system also utilized a film-cooling strip and an augmented convective pin fin arrangement at the combustor aft end.

The liner impingement cooling design consists of an outer shroud with 11 rows of impingement holes of different diameters (Fig. 3). The Kercher and Tabakoff (1969) correlation was used for the impingement heat transfer analysis. The impingement cooling was designed to produce maximum heat transfer coefficients in the primary zone (upstream of the film strip) where the combustion heat load is the greatest. The program code used for the impingement analysis determined flow rates for the individual rows of impingement holes and calculated the resultant average heat transfer coefficient for each row of holes.

A single film strip was used near the exit of the combustor (Fig. 3) to augment the impingement cooling and provide secondary zone dilution. The heat transfer correlation used for the film cooling analysis is presented in Marek and Tacina (1975).

The last 2.54 cm (1 in.) of combustor liner is cooled with pin fins in an annular gap between the liner and the combustor case. The pin fins are rectangular in shape (see Fig. 5) and produce augmented convective cooling of the liner. The fins also produce a tightly controlled gap between the hot combustion liner and the combustor case. This passage allows a

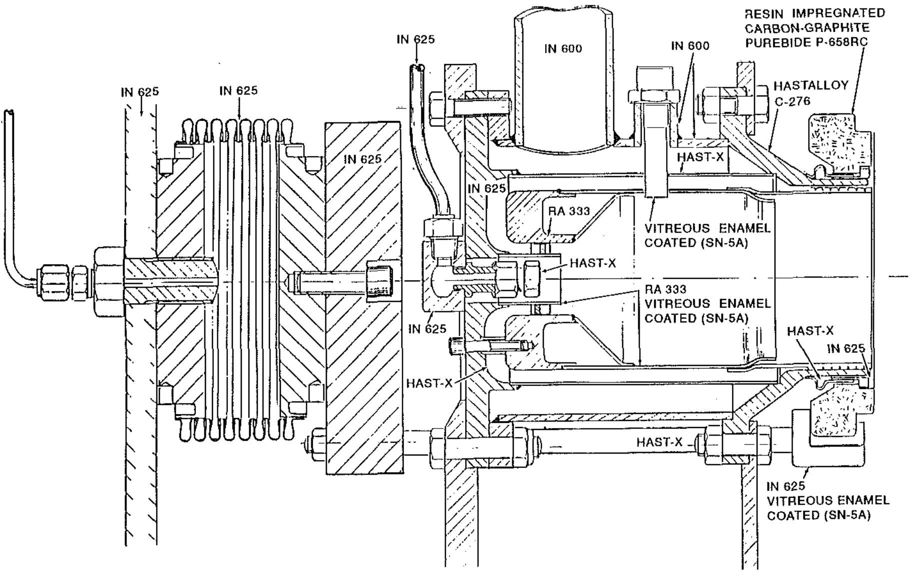

Fig. 6 Materials selection

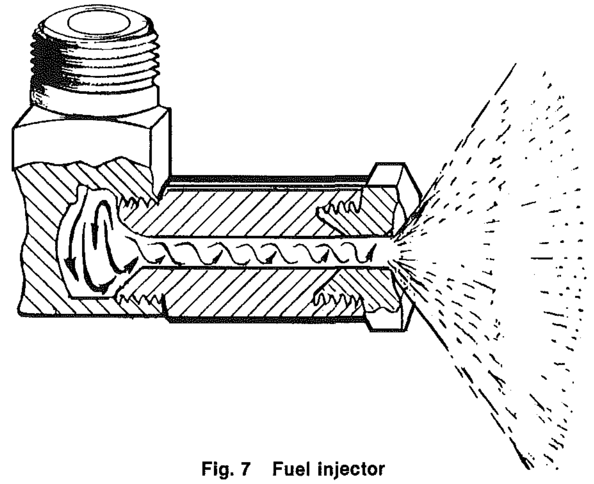

Fig. 7 Fuel injector

slip fit between the hot liner and the cooler outer case to allow for the mismatch in thermal growth.

The results of the final thermal analysis of the combustor line indicated that the maximum liner temperature would not exceed 1172 K (1650°F) based on a maximum predicted heat flux of $5.395 * 10^6$ kJ/h m^2 (475,000 Btu/hr ft^2).

Mechanical Design and Material Selection. Mechanically, the combustor assembly consists of a liner, an impingement sleeve, and the swirler assembly. The liner assembly includes the dome, liner, a film-cooling strip, and the exit seal. The exit seal incorporates a form of pin fin for the augmented convective cooling discussed above. Figure 6 shows the material selection for the various components. The material selection was based on the fact that the combustion system is submerged in sea water when operating and that if an in-water shutdown occurs the hot internal parts will be flooded when the airflow ceases. RA333 was selected for the liner because of its high-temperature strength characteristics. Hot corrosion resistance would ultimately be augmented by coating the liner with a proprietary Solar vitreous coating.

Fuel Injector. The initial fuel injector design is referred to variously as a tangential nozzle, a tanget, or a whirl-jet. It is shown in Fig. 7. The fuel is admitted through a single tangential hole into a swirl chamber. It then flows axially through an extension tube and exits through a final orifice. Spray angles for this type of nozzle are typically greater than 120 deg and can approach 180 deg. The design was chosen because of the relatively large orifices [approximately 0.11 cm (0.045 in.)] and the wide spray angle, which, when combined with the combustor swirler, would provide a form of air atomization. Test results indicated that the spray angle was too large and efforts to reduce it by decreasing the diameter of the final orifice resulted in inadequate atomization quality. An oil burner nozzle of the pressure atomizing swirl type was substituted. The oil burner nozzle used to date has a flow rate of 454 liters/h (12 GPH) at 690 kPa (100 psi), a 90 deg spray angle, and a semisolid spray distribution.

Ignition System. The ignition system selected was a 24 vdc low-tension capacitor discharge system commonly used on gas turbine engines. The discharge voltage of a low tension system is 5000 V maximum. The igniter plug used with a low-tension system has a semiconductor material between the center and ground electrodes whose purpose is to ionize the material in the gap (air, water, or fuel) so that the capacitor can discharge. A low-tension system functions even if the plug tip is wet with fuel or water and this is the optimum approach to satisfy the in-water system startup requirement.

Seal Design

The WPP seal system is required to ensure that air leakage is minimized at the upstream end of the water channel rotor. If a correct seal is not maintained, reductions in WPP thrust occur. The seal can be geometrically approximated as a 110 deg arc section of a circular plate with a circular combustion gas entrance port situated at 40 deg from one edge (Fig. 8). The first 40 deg of the arc are used as the entrance region for the successive rotor water channels. The remaining 70 deg of seal plate are required for combustion gas expansion/water jet expulsion.

The seal material, a graphite compound, is very suitable for the WPP application. It has a low coefficient of friction against the metallic rotor and exhibits a low thermal expansion coefficient. The seal warpage is minimized, even with the high 1922 K (3000°F) combustion gas thermal load. However, since the material has a low modulus of elasticity, the seal must be properly supported so there are no excessive seal plate deformations. This support is accomplished with a stainless steel load plate coupled to the graphite seal plate by 11 steel support

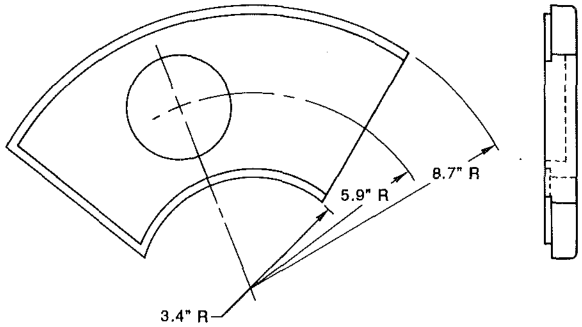

Fig. 8 WPP seal plate

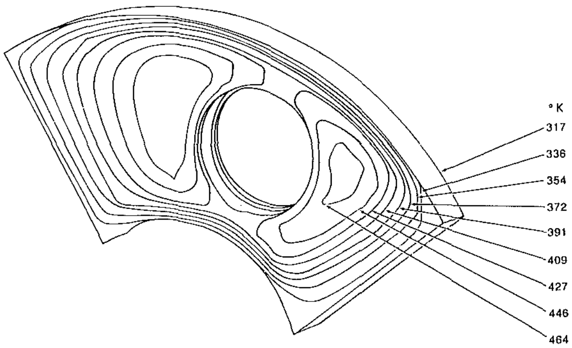

Fig. 9 Thermal profile of seal plate generated with ANSYS

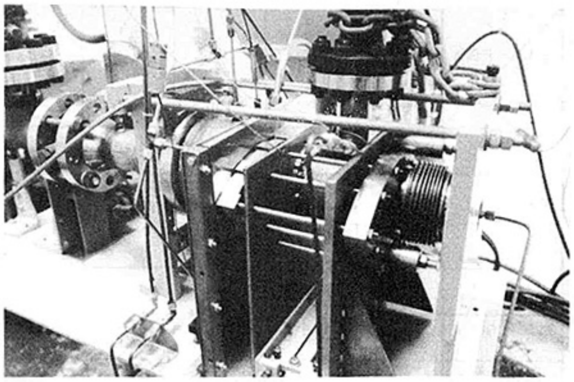

Fig. 10 Test cell installation

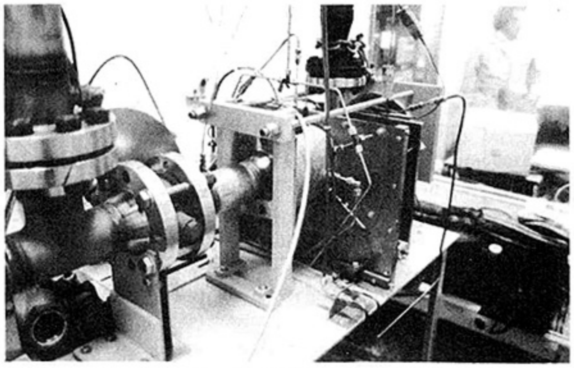

Fig. 11 Test cell installation

rods. The load plate is driven by two pneumatic pressure bellows. The force with which the bellows/plate system must react is due to combustion gases that are injected into the water channel rotor. Since the combustion gases are at pressures up to 1450 kPa gage (210 psig) the reacted load of the bellow/plate system approaches 22,240 N (5000 lb).

A finite element method code (ANSYS) was used to insure that the graphite seal plate thermal and structural loads to be sustained were within the allowable limits of the material. A thermal profile of the graphite plate when operating under normal run conditions is shown in Fig. 9. The seal is seen to reach a maximum temperature of about 464 K (375°F) on the surface adjacent to the combustion gases.

Control Systems

Control systems are required for the WPP combustor and seal systems. The combustion system control loop serves to insure the combustor outlet temperature is maintained at 1922 K (3000°F) over all run conditions. The open loop combustor control algorithm uses the inlet air massflow and temperature as inputs. The fuel flow required for the 1922 K (3000°F) outlet temperature is determined from the following:

$$F/a = (0.1366*\mathrm{CK}*\mathrm{DELT})/[10600-(\mathrm{CK}*\mathrm{DELT})]$$

where

$$\mathrm{CK} = 0.0014*(\text{inlet temperature} - 600) + 1$$

and

$$\mathrm{DELT} = \text{desired outlet temperature} - \text{inlet temperature}$$

This expression gives the fuel-to-air ratio required to achieve a desired outlet temperature when operating on marine diesel fuel. The pressure drop across the impingement sleeve is used to calculate the air flow

$$\text{Fuel flow} = \text{Air flow}*f/a$$

The open loop scheme was selected because of the difficulty in directly measuring the combustor outlet temperature due to the elevated design point (3000°F) and the exit temperature profile.

The second WPP control system is used to insure that the graphite seal plate is positioned leak-free against the water channel rotor without excessive end loads. This closed loop system uses as input rotor angular velocity, vehicular speed, and combustion gas massflow. A variety of seal plate control algorithms have been developed for eventual test and optimization.

Test Program

Combustor Test Facility. The test rig facility was designed to evaluate only combustor performance characteristics and thus did not include a representative rotor system. The combustor, seal, and combustor control system are shown installed in a test cell in Figs. 10 and 11. A slave aluminum seal plate was used in place of the graphite seal plate. A solid plate was used in place of the rotor. Attached to this plate was a water-cooled instrumentation section that incorporates emission probes, pressure taps, thermocouples, and cooling water exit nozzles. This water, used to cool the instrumentation section, is subsequently employed to cool the exit ducting and the pressure raising butterfly valve. This valve, which is positioned by an electric motor, controls the combustor back pressure. Two averaging emission probes situated at right angles to each other were used. The exhaust thermocouples were used during preliminary testing at lower than design outlet temperatures. For full design outlet temperature they were retracted.

Combustor Performance Test Results. Several shakedown runs were made initially to determine operating procedures and to verify the correct relationship between the microprocessor controller output signal and the fuel control-delivered fuel flow. Initially the fuel flow was measured using a turbine flow meter. This meter was subsequently replaced with a Micro

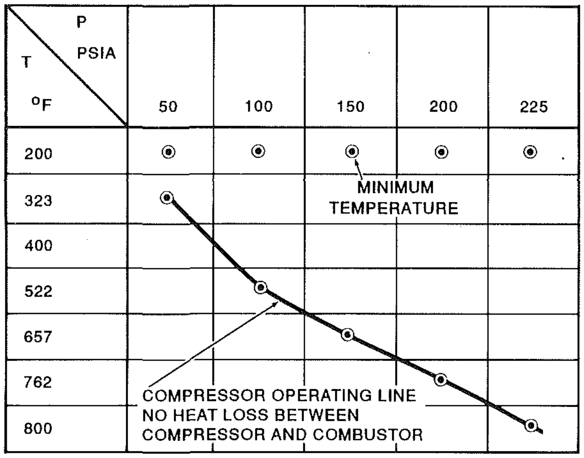

Fig. 12 Combustor operating envelope performance test matrix

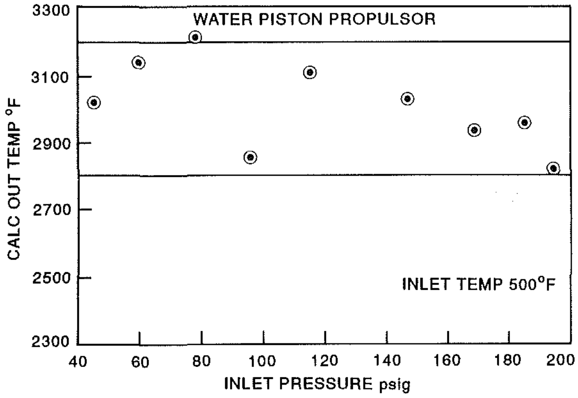

Fig. 13 Combustor system performance

Motion mass flow meter, which simplified the determination of the microprocessor/fuel control relationship. The combustor outlet temperature was determined by measuring the oxygen and carbon dioxide in the exhaust and then calculating the temperature using O_2, CO_2, and fuel properties. This method was used instead of multiple thermocouples for cost, durability and accuracy reasons. The test matrix is shown in Fig. 12. As discussed in the combustor requirements section, this matrix represents the predicted operating envelope. All lightoffs were performed with preheated air and were accomplished with little difficulty. Combustion efficiencies above 98 percent have been demonstrated over the operating range indicated in Fig. 13 based on measured CO and UHC. After a one hour run with an inlet temperature of 533 K (500°F) and outlet, temperature ranging from 1811 K (2800°F) to 2033 K (3200°F), the maximum indicated combustor metal temperature was 977 K (1300°F). The combustor was coated with temperature-indicating paint to determine the metal temperatures.

Combustor Control Results. Figure 13 shows the outlet temperature calculated from exhaust emissions data over a range of inlet pressures from 276 kPa (40 psig) to 1344 kPa (195 psig) at an inlet temperature of 533 K (500°F). The variation in outlet temperature is ±93 K (200°F). This can be corrected with a modification to the control algorithm, which will reduce the variation and make the average outlet temperature more constant over the operating range.

Future Test Program

Program plans call for the integration of the combustor/seal system with a dummy rotor to develop and evaluate seal plate control algorithms. The combustor/seal system will be subsequently assembled into the complete WPP system and installed in a recirculating water channel test facility to evaluate combustor performance fully under pulsating conditions and to verify the seal leakage characteristics. The propulsion performance of the WPP will then be determined and verified by full system tests in a towing basin.

Concluding Remarks

Test results have shown that gas turbine combustor technology can be successfully adapted to the WPP concept. Testing with the full system will demonstrate whether the pressure fluctuations adversely affect combustor performance and stability.

Acknowledgments

The work described in this paper was performed by Solar Turbines Incorporated under Contract No. N00167-85-C-0042 from the David Taylor Research Center, with Richard A. Swanek of the Marine Corps Program Office as Project Manager.

References

Kercher, D. M., and Tabakoff, W., 1969, "Heat Transfer by a Square Array of Round Air Jets Impinging Perpendicular to a Flat Surface Including the Effects of Spent Air," ASME Paper No. 69-GT-4.

Krishnamoorthy, V., and Johnson, V. E., Jr., 1985, "Single Channel Tests of the Water Piston Propulsor," Tracor Hydronautics, Inc.

Lefebvre, A. H., and Herbert, M. H., 1960, "Heat-Transfer Processes in Gas-Turbine Combustion Chambers," *Proc. IMechE*, Vol. 174, No. 12, pp. 463–478.

Marek, Cecil J., and Tacina, Robert R., 1975, "Effects on Free-Stream Turbulence on Film Cooling," NASA TN D-7958.

Tracor Hydronautics, Inc., 1983, "Conceptual Design Study on Unconventional Water Propulsion Systems for Marine Corps Tracked Amphibians," Technical/Management Proposal 32.0041.

Suppressing the Infrared Signatures of Marine Gas Turbines

A. M. Birk
Department of Mechanical Engineering,
Queen's University,
Kingston, Canada

W. R. Davis
W. R. Davis Engineering Limited,
Ottawa, Canada

The exhaust plumes and visible areas of the engine exhaust ducting associated with marine gas turbines are major sources of infrared (IR) radiation on ships. These high-radiance sources make excellent targets for IR-guided threats. In recent years significant efforts have been made to reduce or eliminate these high-radiance sources to increase the survivability of naval and commercial ships when sailing in high-risk areas of the world. Typical IR signature suppression (IRSS) systems incorporate film cooling of visible metal sources, optical blockage to eliminate direct line-of-sight visibility of hot exhaust system parts, and cooling air injection and mixing for plume cooling. Because the metal surfaces radiate as near black bodies, every attempt is made to reduce the temperatures of the visible surfaces to near ambient conditions. The exhaust gases radiate selectively and therefore do not have to be cooled to the same degree as the metal surfaces. The present paper briefly describes the motivation for incorporating IRSS into the exhaust systems of marine power plants. IRSS hardware developed in Canada by the Canadian Department of National Defence and Davis Engineering Limited is presented along with details of their operating principles. A typical installation is presented and discussed. Design impacts on the ship are described with reference to engine back pressure, noise, and weight and center of gravity effects.

Introduction

Naval ships, and in some parts of the world commercial ships, are exposed to the risk of attack by infrared (IR) or partially IR-guided threats. IR as a means of guidance is popular because of its passive nature. That is, an IR-guided threat relies on the electromagnetic radiation emitted by the target, not on the reflection of radiation originating from the threat.

The IR signatures given off by the exhaust uptakes and the exhaust plumes of marine gas turbines make excellent targets for IR-guided threats. Over the last decade, the Canadian Department of National Defence has supported the development of devices for suppressing the IR signatures of marine gas turbines with the ultimate goal of fitting Canadian Navy ships with this hardware. The devices described in this paper are now in the construction phases for the Canadian Patrol Frigate (CPF) program and the update program for the DDH 280 destroyers (TRUMP).

IR Radiation

Thermal radiation is emitted by a body as a result of its temperature. Any body above 0 deg absolute radiates thermal energy. As described by Hudson (1969), thermal radiation lies in the range from about 0.1 to 100 μm in the electromagnetic spectrum. The IR spectrum lies approximately in the range from 0.75 to 1000 μm. Subdivisions of the IR spectrum include the near IR (NIR 0.75–3.0 μm), the middle IR (MIR 3.0–6.0 μm), the far IR (FIR 6.0–15 μm) and the extreme IR (XIR 15.0–1000. μm).

Common engineering materials tend to emit radiation throughout the IR spectrum, that is, they act approximately as gray bodies where the emissivities are constant for all wavelengths. Gases, however, tend to radiate selectively over narrow bands of the electromagnetic spectrum. The exhaust uptake metal surfaces therefore radiate as near gray bodies while the exhaust plume radiates selectively.

High-temperature bodies tend to radiate more energy at lower wavelengths (higher frequencies) and low-temperature bodies radiate at higher wavelengths (lower frequencies). A cool ship hull will radiate thermal energy at longer wavelengths than the hot uptake metal surfaces, which will tend to radiate at shorter wavelengths.

The atmosphere absorbs IR radiation except in certain regions of the electromagnetic spectrum. These regions of the spectrum through which IR radiation can pass are known as atmospheric windows. Two important windows are located at approximately the 3 to 5 μm and the 8 to 12 μm ranges. Low-temperature bodies will radiate more in the 8–12 μm range while hot bodies will tend to radiate more in the 3–5 μm range. Engineering materials, as mentioned earlier, will radiate in both these windows. Exhaust gases containing carbon dioxide and water vapor will radiate primarily in the 3–5 μm range because of their selective radiating characteristics.

The thermal radiation from the exhaust plume is due to the carbon dioxide and water vapor in the plume. As described

---

Contributed by the International Gas Turbine Institute and presented at the 33rd International Gas Turbine and Aeroengine Congress and Exhibition, Amsterdam, The Netherlands, June 5–9, 1988. Manuscript received by the International Gas Turbine Institute October 1987. Paper No. 88-GT-3.

by Hudson (1969), strong emission bands occur in an exhaust plume at 4.4 and 2.7 μm. The 2.7 μm band is caused by both the water vapor and the carbon dioxide, and the 4.4 μm band is due to the carbon dioxide. For detection and tracking, the 4.4 μm band is most useful. Because the carbon dioxide in the plume is at a higher temperature and higher partial pressure than the carbon dioxide in the atmosphere, it radiates outside of the absorption band of the atmospheric carbon dioxide and therefore little of the plume radiation is absorbed by the atmosphere (Hudson, 1969).

Night vision systems use the 8-12 μm range to see items at temperatures very near to the background temperatures. Looking at objects in the 8-12 μm waveband tends to show the entire body and therefore the image is an extended one. IR-guided missiles tend to use the 3-5 μm range so that they can home in on hot spots that appear as point sources.

Detection and Tracking

An IR detector is used to discern an object from its background, while an IR tracking device is used to follow the position of a selected moving object.

For detection purposes the object must appear different from the background it appears in. If an object radiates in a manner similar to the background in which it resides, it will be very difficult to detect. For detection of an extended target, the radiation reaching the detector when it has the target in its field of view must exceed the radiation that the detector receives when it views only the background (Wolfe and Zissis, 1978). In other words, the object radiance as defined below (Hudson, 1969) must be greater than the background radiance:

$$N=\epsilon\,\sigma\,T^4/\pi \qquad (1)$$

where

N = radiance (W/sr m^2)
σ = Stefan-Boltzmann constant
ϵ = emissivity

The radiant power per unit area, or irradiance (W/m^2), reaching the detector depends on the object and background radiance (W/sr m^2), the object and background relative areas in the detectors field of view, the range, and of course the absorbing effects of the intervening atmosphere.

With no atmospheric absorption accounted for, and assuming the target does not fill the field of view of the detector, the irradiance resulting from an extended target in the background scene will be

$$H=(N_t-N_b)\Omega_t+N_b\Omega \qquad (2)$$

where

H = irradiance at detector (W/m^2)
N_t = target radiance (W/sr m^2)
N_b = background radiance (W/sr m^2)
Ω = detector field of view solid angle (sr)
Ω_t = target solid angle = A_t/R^2
A_t = target projected area (m^2)
R = range (m)

From the above expression we see that the irradiance seen by the detector depends on the radiance of the extended source relative to the background radiance. If the target and background have similar radiance then it will be difficult to detect the object. For detection purposes an object radiance should be considered relative to the background radiance.

If the target is a point source then it is difficult to assign a distance and area to it and therefore it is more convenient to use the concept of radiant intensity (W/sr). Radiant intensity is the product of the object radiance and the object surface area. Using the concept of radiant intensity of the target, the above expression can be written as

$$H=(J_t-N_bA_t)/R^2+N_b\Omega \qquad (3)$$

where

J_t = target radiant intensity (W/sr)

As with radiance, radiant intensity of a target should be considered relative to the background radiance effects.

For tracking purposes the same principles apply. The target radiance must be different from the background radiance. However, for trackers it is important to have a signficant contrast between the background and the target. For the same irradiance, a point target is easier to track than an extended target (Wolfe and Zissis, 1978). Trackers designed for point targets usually have degraded performance when confronted by extended targets. Therefore hot spots make good targets for trackers.

Relative Importance of IR Radiation Sources on a Ship

Sources of IR radiation on a ship include the hull (and associated elements), the visible exhaust duct metal, and the exhaust plume. The relative importance of these different sources will be shown with the following approximate analysis.

Consider a hypothetical ship where the hull, plume, and visible uptake surfaces have areas of approximately 1500, 20, and 5 m^2, respectively. These visible areas would apply approximately for a side view of a ship when the plume is flowing straight back from the funnel. The observer's position includes a small downward elevation angle so that part of the hot exhaust uptakes is visible. The plume area of 20 m^2 applies for the 3-5 μm wave band (the plume effective area depends on the waveband of interest because of its selective radiating characteristics).

Let us assume that the background is at a uniform 15°C and the hull average temperature is 5°C above the background temperature. Let us also assume that the effective plume and uptake temperaures are 400°C. This case is, of course, a simplification. Real background effects, solar heating, and nonuniformities in the hull and plume temperatures have not been considered in the analysis. Table 1 shows the assumed properties of the different IR sources on the ship, including the assumed temperatures and areas.

If these different sources of radiation were to radiate as black bodies, a certain percentage of the total radiation would fall within the two atmospheric windows. Table 2 presents the approximate percentages that result.

The hull and the uptake metal surfaces act as gray bodies and for the purposes of the present analysis it has been assumed that the emissivities for both sources are 0.95. For the plume the radiation calculation is based on the assumption that the selective radiation of the carbon dioxide can be approximated

Table 1 Assumed conditions for order of magnitude analysis of different sources of IR radiation on a ship

Source	Temperature, °C	Assumed area, m^2
hull	20	1500
plume	400	20
exhaust duct	400	5

Assumed background temperature = 15°C

Table 2 Approximate percentages of total black body radiation falling within the atmospheric windows for the different sources of IR

Source	Percent black body radiation	
	3-5 μm	8-12 μm
hull	1	26
plume	4*	–
exhaust duct	28	19

*Note: For the plume radiation the percentage of black body radiation is based on the 4.3-4.55 μm waveband.

Table 3 Order of magnitude estimates of radiance and radiant intensity for the different sources (0 K background)

Source	Radiance, W/sr/m²		Radiant intensity, W/sr	
	3-5 μm	8-12 μm	3-5 μm	8-12 μm
hull	1.3	33	1950	49,500
plume	74	–	1480	–
exhaust duct	985	668	4925	3340

Table 4 Order of magnitude estimates of radiance and radiant intensity for the different sources accounting for background at 288 K

Source	Radiance, W/sr/m²		Radiant intensity, W/sr	
	3-5 μm	8-12 μm	3-5 μm	8-12 μm
hull	0.02	2.45	30	3675
plume	73	–	1458	–
exhaust duct	984	638	4920	3188

Table 5 Percentage contribution of sources to overall ship signature (background at 288 K)

Source	Percent contribution of sources to total ship signature	
	3-5 μm	8-12 μm
hull	1	54
plume	23	0
exhaust duct	76	46

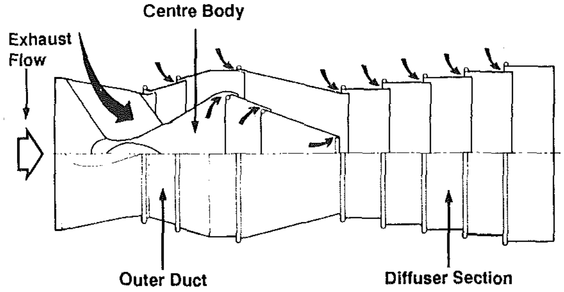

Fig. 1 DRES Ball IR suppression device (marine application)

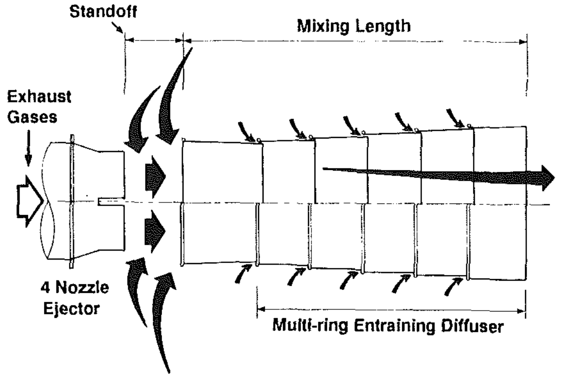

Fig. 2 Eductor/diffuser IR suppression device (marine application)

in the 3-5 μm waveband as a gray gas radiating between 4.3 and 4.55 μm with an effective emissivity of 0.5. This assumption is based on an analysis presented by Hudson (1969) for estimating the IR signature of a jet engine exhaust. Based on these assumptions the radiance and radiant intensities for the various sources have been calculated. Table 3 presents the results of these calculations.

From Table 3 it is evident that for the present hypothetical case the plume and the uptake are by far the highest radiance sources on the ship. In terms of being hot spots, the uptake has a radiance 760 times that of the hull and 13 times that of the plume in the 3-5 μm waveband. In the 8-12 μm waveband the uptake has a radiance 20 times that of the hull. Therefore to eliminate hot spots the first priority is to cool the visible parts of the exhaust duct and the next priority is to cool the plume.

In terms of the radiant intensity all of the sources are significant. In the 8-12 μm waveband the hull appears to be the dominant source. However, this is misleading because the effects of the background have not been accounted for. Table 4 presents the same estimates but with the effects of a 15°C background subtracted out.

For the present hypothetical case, the large hull area compensates for the low hull radiance and therefore the hull becomes the most significant source in terms of radiant intensity in the 8-12 μm waveband. However, in the 3-5 μm waveband all three sources are significant. In this hypothetical case in the 3-5 μm waveband the total ship signature can be reduced by 99 percent if the plume and exhaust duct are cooled. The benefit is not as great in the 8-12 μm range with a reduction of the total signature being about 46 percent if the plume and exhaust duct are cooled. These various percentages are summarized in Table 5 and, of course, apply only for the present hypothetical case.

The above example should be considered as illustrative only. Actual ship signatures of course depend on view angles, background conditions, and many other factors. However, the analysis shows that under certain conditions the plume and exhaust duct surfaces can both be significant sources of IR radiation. Because of their high temperatures the uptakes and the plume make good targets for IR-guided threats.

IR Signature Suppression

The object of IRSS is to reduce or eliminate high radiance sources of thermal radiation. To do this it is necessary to cool the metal surfaces to near ambient temperatures and to cool exhaust plumes to a temperature where its selective radiation in the 3-5 μm band is of the same order as that from the cooled metal surfaces in the same waveband.

If the high radiance sources are eliminated then the ship becomes an extended target with no hot spots that act as point targets to a threat. With the high radiance sources eliminated the effectiveness of decoy countermeasures is significantly increased.

It should be stressed that with today's IR detection technologies it is not possible to eliminate the IR signature and thereby thwart detection. Only a fraction of a degree celsius temperature difference is needed with today's technology to detect an object. The object of IRSS is to eliminate hot spots thereby making the ship an extended target. Once this is done, hot spots can be artificially introduced using decoys.

Typically, engine exhaust IRSS systems involve film and convective cooling of metal surfaces, dilution plume cooling, and optical blockage to eliminate direct line of sight view of hot metal parts. Special finishes are also used to modify the radiating characteristics of surfaces.

Two examples of engine exhaust IRSS devices are the DRES Ball and Eductor/Diffuser (E/D). Figure 1 shows the DRES Ball device and Fig. 2 shows the E/D device.

The DRES Ball device concept originated at the Defence Research Establishment Suffield (DRES) in Alberta, Canada. The device consists of a film-cooled outer duct surrounding a convectively and film-cooled optical block center body and a film-cooled diffuser. The center body or ball is used to block the view down into the exhaust duct, thereby eliminating the direct line of sight of the hot ducting. All visible metal surfaces

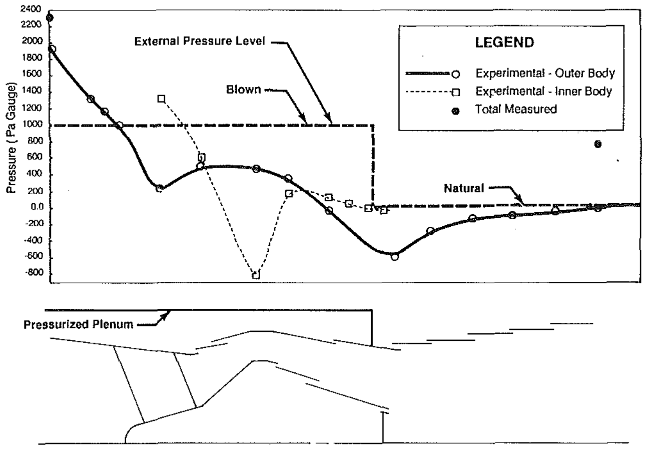

Fig. 3 Flow channel pressure distribution in DRES Ball device (for fan-assisted design)

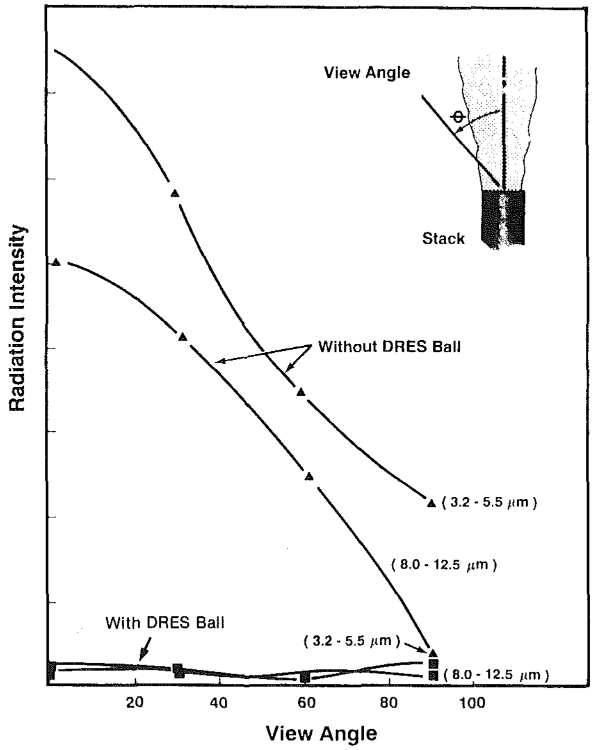

Fig. 4 Measured IR signature for a scale model uncooled stack and a scale model DRES Ball equipped stack (absolute radiant intensity scale removed)

are either convectively cooled or film cooled. The film cooling layers eventually mix with the primary exhaust stream, which results in effective cooling of the plume. Cooling air introduced by the center body results in cooling of the plume core. Cooling air for the center body is brought into the device through the four hollow support struts for the center body. The DRES Ball provides IRSS for all angles of view.

Figure 3 shows the flow channel pressure distribution in a fan-assisted DRES Ball device (DRES Ball can be either passive (no fan) or fan assisted). As can be seen from the figure, the pressure distribution in the device is such that air is induced to flow in through the various cooling air gaps. This flow in through the gaps provides the film cooling layers on the metal surfaces and is the source of cooling air for cooling the plume. The induction of the cooling air results in momentum transfer, which in turn causes an increase in the exhaust system back pressure. Friction losses in the device also result in a small increase in the system back pressure.

Figure 4 presents the results from scale model tests of a DRES Ball device and a simple uptake. The graph shows the measured radiant intensity relative to background versus the angle of view. For security reasons the radiant intensity scale has been removed. As can be seen from the figure, the DRES Ball device results in a dramatic decrease in the exhaust system signature for both atmospheric windows and for all view angles.

The E/D device shown in Fig. 2 consists of an ejector pump for entraining cooling air to cool the plume and a film-cooled diffuser to provide metal surface IRSS for a limited range of view angles. This device is similar to those studied extensively by Pucci (for example, see Ellin and Pucci, 1977) and are similar to systems presently in operation in several Navies. E/D devices have been designed and built to provide metal surface IR suppression for view angles up to 60 deg below the horizontal (looking down from the horizontal into the vertical exhaust duct). Because the cooling air is only introduced at the periphery of the duct, the plume temperature distribution shows a temperature peak at the plume centerline. This type of plume temperature results in a higher plume signature than that from the DRES Ball for the same average plume temperature.

Ship Design Impacts

The DRES Ball and E/D devices are typically installed in the ship's funnel and replace the end section of the exhaust uptake. Figures 5 and 6 show how a typical LM2500 installation might look with either the DRES Ball or the E/D installed.

A typical installation will involve numerous aerothermal and structural considerations. From an initial design standpoint the following are the most important.

1 engine exhaust flow conditions, specifically the mass flow, and temperature (for design power and ambient conditions),
2 allowable back pressure,
3 available space, and allowable weight and location of center of gravity,
4 cooling air supply,
5 allowable noise levels,
6 desired plume exit velocity, and
7 desired plume and metal surface temperatures.

Flow Conditions. The engine exhaust flow conditions are obtained from the engine manufacturer, as is the allowable back pressure. The engine flow conditions are the starting point from which the design begins.

The devices are typically designed for full engine power conditions. Experience to date has shown that at lower engine powers the devices continue to work effectively. As the engine power is reduced, the IR signatures decrease, as does the system back pressure.

Back Pressure. In both devices the cooling air pumping action results in back pressure being applied on the engine. The back pressure penalties depend on the desired IR suppressor performance and are typically in the range of 2000 to 4000 Pag (8 to 16 in. W. G.) total pressure measured at the inlet to the IR suppressor (total pressure being the static pressure plus the exhaust gas dynamic pressure). Note that this back pressure includes the plume dynamic pressure, which is a loss in any exhaust system.

The device back pressure is a function of the volume flow rate through the device. When engine power is reduced the back pressure is reduced because of the combined effect of lower volume flow of exhaust gases and reduced cooling air intake. If the source of cooling air is cut off such that less cooling air is drawn into the device, then the momentum trans-

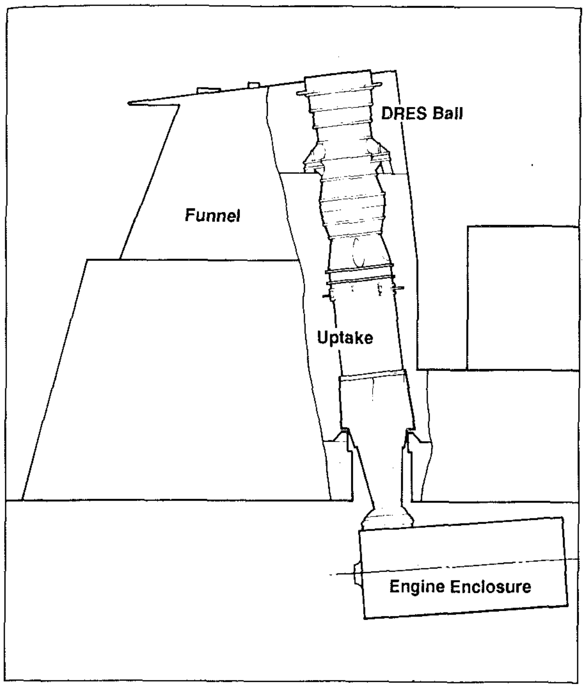

Fig. 5 Typical DRES Ball marine installation

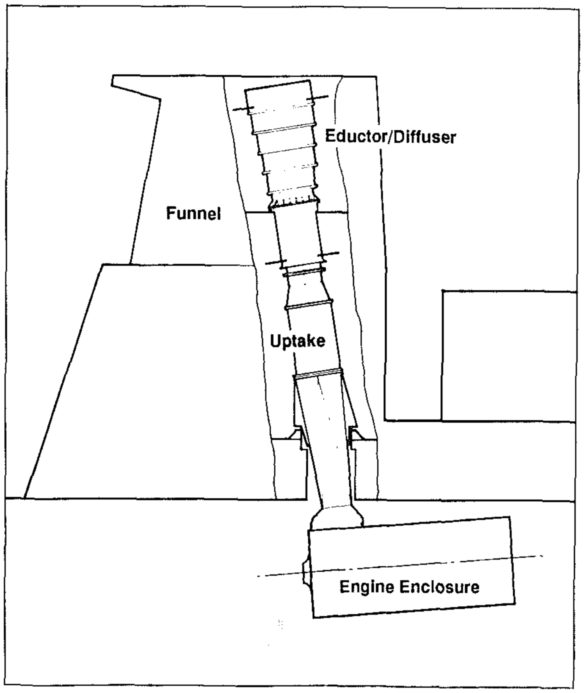

Fig. 6 Typical Eductor/Diffuser marine installation

fer effect is reduced and the system back pressure drops. In other words if the IR suppressor is turned off by stopping cooling air flow then the back pressure penalty effect is reduced.

It should be noted at this time that other IR suppressor designs exist that use slightly different methods of taking in air for surface and plume cooling. However, no magic method exists that gives IR suppression for free; it must be paid for in the form of fan power or back pressure for the same level of surface and plume cooling.

During the initial design activities for an IR suppressor, discussion with the engine manufacturer is necessary to ensure that the exhaust system and IR suppressor design meets the allowable limits for engine back pressure. To date, every design involving either the DRES Ball or the E/D has met the allowable back pressure constraints set by the engine manufacturers.

Table 6 Size, weight, and CofG summaries for DRES Ball, E/D, and simple uptake for a typical LM2500 installation

	Length, m	Maximum diameter, m	Mass, kg	C of G, m
simple uptake	7.4	2.2	4200	3.7
DRES Ball	7.4	2.9	4250	3.4
E/D	8.2	3.0	2800	5.5

Note: The DRES Ball and E/D above are passive designs and therefore do not require fans or sealed plenums.

Space, Weight, and Center of Gravity. Another critical design consideration is the space into which the device is to fit and the acceptable weight. Because the devices are mounted high up in the ship, the weight and center of gravity of the devices is critical, especially in retrofits where much of the weight margin of the ship has been used up over the years.

Table 6 presents a summary of the device dimensions and approximate weights and centers of gravity for the two devices sized for an LM2500 installation, along with the same data for a typical uptake for comparison purposes. As can be seen from the data, the devices require some additional space. In terms of the device weight, the E/D is lighter than the simple uptake by a considerable amount, while the DRES Ball is of similar weight. The weights of the devices have been optimized through extensive structural analysis for the reasons noted above. Note that in all cases the uptake and IR suppressor material is assumed to be stainless steel sheet metal with appropriate stiffening. With use of advanced material the weight effects can be reduced as much as 40 percent at a cost.

Cooling Air Supply. Both the DRES Ball and the E/D device are capable of naturally inducing the required cooling air for cooling the plume and metal surfaces. That is, they are both passive devices and do not require fans.

As can be seen from Figs. 5 and 6, both devices require that air freely enter the ships funnel. Both devices rely on large volumes of cooling air being available at near atmospheric pressure. Pressure losses resulting from the cooling air flow through funnel louvers must be kept to a minimum. Care must be taken to place the funnel louvers such that air flow can efficiently reach the devices. Care must also be taken to position the louvers so that radiation of noise to critical areas is minimized.

In some cases air at above atmospheric pressure may be available, and where possible this air should be used to boost the performance of the device. This air may be exhaust air from an engine room, for example. Fans can also be used to boost performance. For designs incorporating fans the fan intakes must be carefully placed to minimize losses while at the same time considering weight, space, and fan noise effects.

Since the devices are completely housed in the funnel the effects of wind should be at a minimum. However, circumferential pressure variations at the cooling air gaps are inevitable, and therefore some surface temperature variations will be found in the devices. These temperature variations usually have little effect on the overall IR signature. In special cases where local hot spots result, special measures can be taken, such as the introduction of transpiration cooling holes to reduce the effect of the hot spots.

Noise. Both of the devices rely on the entrainment of cooling air by using a venturi effect. The resulting high velocities generate noise. Noise levels given off by these types of devices are an important design consideration because high noise levels in areas where verbal communication is necessary can not be tolerated. From a noise standpoint the DRES Ball with its relatively closed design is superior to the E/D. For the purposes of limiting noise, maximum velocities in the devices are usually limited to 95 m/s. However, it is not always possible to meet other design targets and still meet the maximum flow velocity constraint. In such cases special care is taken to ensure that noise levels meet appropriate specifications. In some cases this will involve the use of acoustic treatment of ducting and other associated surfaces.

Table 7 Approximate noise levels from DRES Ball and E/D

Location	Sound levels (dBA) at locations shown in Fig. 7 A	 B	 C
DRES Ball	91.6	89.9	88.8
E/D	99.0	93.0	91.0

Note: Estimated full-scale levels from 1/4 scale hot flow model tests with no acoustic treatment.

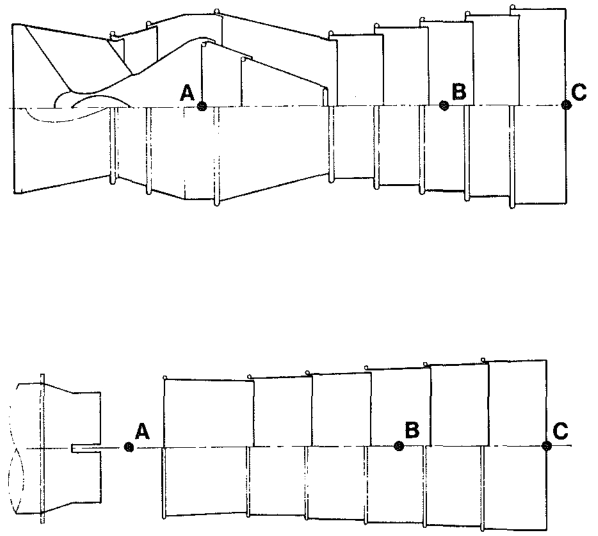

Fig. 7 Location of noise measurements on DRES Ball and Eductor/ Diffuser models

Table 7 presents a summary of estimated noise levels for a typical installation. Figure 7 shows the locations of the noise levels relative to the primary noise sources.

Plume Velocity. In some installations the plume velocity is a design constraint. For the plume to clear the ship boundary layer the plume must have sufficient upward momentum; this will require a minimum plume velocity. The fact that the plume is cooled must also be considered, because a cool plume is of course less buoyant.

Ship boundary layer model tests will show a required minimum plume velocity for the plume to clear the ship, and this minimum velocity has an impact on the design of an IRSS system. The higher the plume velocity, the higher the plume dynamic head, and this relates directly to the exhaust back pressure. Typical plume velocities for LM2500 installations are in the order of 40–45 m/s for full power operation.

The entraining diffuser on both the DRES Ball and E/D is designed to reduce the plume velocity to minimize the total back pressure. For installations where the desired plume velocity and allowable back pressure constraints conflict, a fan-boosted IR suppressor design may be necessary.

Plume and Metal Surface Temperatures. The IR suppressors are designed to reduce the plume and metal surface temperatures. The degree of cooling depends on the types of threat to be countered and on the types of decoy to be used. The desired plume temperature and the engine flow conditions dictate the total amount of cooling air that must be entrained. The device size, the cooling air gap areas, and the resulting flow rates fix the back pressure. The metal surface cooling dictates the placement of cooling air gaps and the shaping of the flow channel.

Figure 8 shows an approximate performance map for the DRES Ball device. The map shown is for a device with uniform gap sizes and applies for a specific device geometry (fixed number and location of gaps, and flow channel shaping). The actual scales have been removed from the map for security

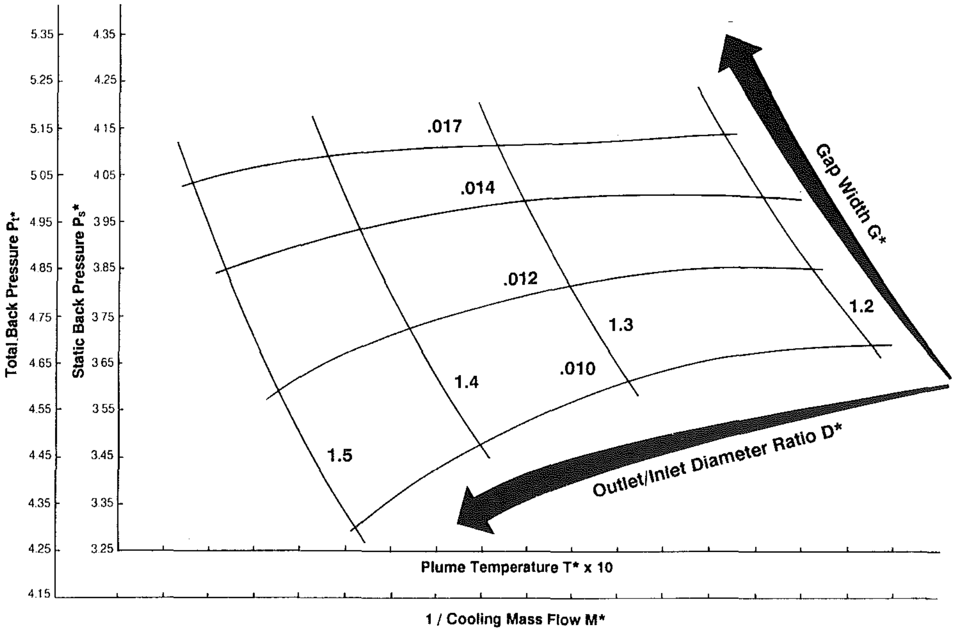

Fig. 8 Approximate performance map for DRES Ball device (temperature and mass flow scales removed)

reasons; the map is intended to show trends for discussion purposes.

The figure shows a nondimensional back pressure versus nondimensional plume temperature and mass flow ratio for different device configurations. The different configurations are created by varying the gap sizes and the ratio of the uptake diameter to the device exit diameter. The various parameters are defined as follows:

Nondimensional plume temperature

$$T^* = (T_p - T_c)/(T_g - T_c) \tag{5}$$

Nondimensional back pressure

$$P^* = P_b/1/2\rho\ U^2 \tag{6}$$

Nondimensional gap size

$$G^* = G/D_i \tag{7}$$

Nondimensional cooling air flow

$$M^* = m_c/m_g \tag{8}$$

Nondimensional size

$$D^* = D_e/D_i \tag{9}$$

where

T_g = exhaust gas temperature, °C
T_c = cooling air temperature, °C
T_p = plume average temperature, °C
P_b = static or total back pressure, Pag
ρ = exhaust gas density, kg/m^3
U = uptake flow velocity, m/s
D_i = inlet (uptake) diameter, m
G = gap size, m
D_e = exit diameter, m
m_g = exhaust gas mass flow, kg/s
m_c = cooling air mass flow, kg/s

To use the map one must select a desired engine mass flow and exhaust temperature, allowable back pressure, ambient temperature, uptake diameter, and desired plume temperature. Based on the above, the nondimensional back pressure and plume temperature can be calculated. The intersection of the vertical line passing through T^* and the horizontal line passing through P^* indicates the required gap area and device size ratio. One can perform tradeoff studies by varying the gap sizes and device size and noting the effect this has on the plume temperature and back pressure.

It must be noted that this map is approximate only and does not include Reynolds number or Mach number effects. The map is presented for discussion purposes only. The above map was generated using a computer code called IRSCOOL. IR suppressor design studies are conducted using this code. A similar map can be generated for the E/D device.

Conclusions

IRSS of marine power plant exhausts, especially gas turbine exhausts, has been shown to have a significant effect on the overall IR signature of a ship. It was shown that the engine exhaust plume and visible metal surfaces are by far the major source of radiance or hot spots on a ship. In terms of radiant intensity the ship hull was shown to be the primary source in the 8–12 μm waveband and therefore the IRSS of the engine exhaust played only a minor role in reducing the signature in this atmospheric window. However, in the 3–5 μm waveband, the suppression of the plume and the hot metal of the exhaust duct had a very significant effect.

Devices incorporating film and convective cooling of metal surfaces and plume dilution for plume cooling were described. These devices replace the last portion of the exhaust uptake and have numerous impacts on the ship including back pressure effects on the engine, weight and center of gravity effects, and noise.

References

Ellin, C. R., and Pucci, P. F., 1977, "Model Tests of Multiple Nozzle Exhaust Gas Eductor Systems for Gas Turbine Powered Ships," Masters Thesis, Naval Postgraduate School, Monterey, CA, June.

Hudson, R. D., 1969, *Infrared System Engineering*, Wiley, New York.

Wolfe, W. L., and Zissis, G. J., eds., 1978, *The Infrared Handbook*, Environmental Research Institute of Michigan for the Office of Naval Research, Department of the Navy, Washington, DC.

Multivariable Turbofan Engine Control for Full Flight Envelope Operation

J. A. Polley

S. Adibhatla

P. J. Hoffman

GE Aircraft Engines,
Cincinnati, OH 45215

The design of a full flight envelope nonlinear multivariable controller is described for a single-bypass variable-cycle jet engine. The nonlinear controller is obtained by using appropriate engine corrected parameters to schedule multivariable linear compensator gains designed at selected operating points of the flight envelope. The KQ (K-matrix compensator, Q-desired response) multivariable control design technique is used to design the compensators using linear state-space models obtained from a detailed nonlinear aerothermo model. The controller is implemented in the detailed nonlinear aerothermo model. The paper describes an example KQ compensator design, the corrected-parameter gain scheduling approach, and controller performance validation by nonlinear simulation. Computer simulations for sea-level static, and supersonic operating points are included to show the closed-loop transient performance in the presence of an acceleration fuel schedule.

Introduction

Integrated flight and propulsion control systems proposed for the next generation of fighter aircraft will require propulsion control systems to vary engine, inlet, and exhaust nozzle variables simultaneously. The technology features of these advanced future aircraft will provide the means to achieve short takeoff and landing, greater maneuverability, and versatile weapons delivery capability. The benefits to the engine will be improved thrust response and engine efficiency, and improved control of critical temperatures and pressures when maintaining fan and compressor stall protection. Brown and Fisk (1983), Joshi et al. (1983), and Skira (1986) have provided detailed descriptions of approaches to achieve several integrated flight and propulsion features.

A control system that can achieve these advanced technology features in the presence of the highly coupled dynamics of advanced aircraft engines lends itself to a multi-input/multi-output (MIMO) or multivariable approach. Doyle and Stein (1981) developed and described a linear multivariable analysis and design methodology that incorporates singular value ideas to ensure good fundamental feedback properties. Several multivariable feedback control design techniques have been used to design control systems for jet engines. A number of methods were demonstrated by Sain et al. (1978). The Linear Quadratic Regulator (LQR) and the Linear Quadratic Gaussian with Loop Transfer Recovery (LQG/LTR) methodologies have been used in several engine control studies, including Kapasouris (1984), Skira (1986), and Pfeil (1986). The KQ (K-matrix compensator, Q-desired response) was described by Edmunds (1979) and in the same publication, he demonstrated the use of this technique to design a compensator for an aircraft jet engine. Polley et al. (1986) described the design of a GE16/J11A6 variable-cycle engine compensator for a single operating point using the KQ technique. The majority of the above research studied the design of a multivariable compensator for a single engine operating point. There have been a limited number of multivariable control designs for full flight envelope operation (for example, Kapasouris, 1984). The emphasis in this paper will be on the use of the KQ technique to design a nonlinear multivariable controller that operates over the entire flight envelope of the GE16/J11A6 engine and also includes power level variations.

Outline of Paper

The paper begins with a description of the GE16/J11A6 variable-cycle engine and its aerothermo model, followed by a brief background of the selection of the measurement and actuation variables for the compensator. An overview of the development of steady-state schedules to be used as demand values for the control precedes the multivariable compensator design section. We show by an example how we evaluated the performance of the KQ linear compensator by the shapes of the singular values of the open-loop and closed-loop transfer function matrices in the frequency domain. We then describe the development of a full flight envelope controller by scheduling the gains of the KQ compensator as functions of measurable corrected parameters of the turbofan engine. The last section presents the results of nonlinear computer simulations of the GE16/J11A6 engine using a detailed nonlinear aerothermo model. The results validate the closed-loop performance of the nonlinear controller for large thrust demands at

---

Contributed by the International Gas Turbine Institute and presented at the 33rd International Gas Turbine and Aeroengine Congress and Exhibition, Amsterdam, The Netherlands, June 5-9, 1988. Manuscript received by the International Gas Turbine Institute January 22, 1988. Paper No. 88-GT-6.

sea level static and supersonic (36,000 feet, Mach 1.2) flight operating points.

Engine Description and Models

This section describes the GE16 engine, and the engine models that were used for controller design and evaluation.

GE16 Variable-Cycle Engine. The GE16/J11 Study A6 engine is a low-bypass, variable-cycle, turbofan engine, depicted schematically in Fig. 1. Air entering the engine is compressed in a two-stage low-pressure-ratio fan. Part of the air exiting the fan bypasses the engine core, goes through the bypass duct and a variable-area ($A16$) bypass injector (VABI), and mixes with the gas exiting the low-pressure turbine. The major portion of the air goes through the core where it is compressed further in a five-stage high-pressure-ratio compressor, and combusted with fuel ($WF36$) in an annular combustor. The combustion products are expanded through a single-stage high-pressure turbine (HPT) and further expanded in a single-stage low-pressure turbine (LPT). The gases from the core stream are mixed with the bypass air and the mixture goes through a final expansion in a converging-diverging nozzle whose area ($A8$) can be varied. The nozzle has variable features to allow for thrust vectoring and thrust reversing capabilities as needed in integrated flight and propulsion control (IFPC).

Nonlinear Aerothermo Transient Model. Two levels of transient aerothermodynamic models of the GE16/J11A6 engine were used for this study. They are:

- A detailed nonlinear aerothermo model
- A simplified real-time component-level model

The general characteristics of each model are discussed in the following sections.

The *detailed nonlinear transient* simulation of the engine is used to obtain the linear models needed for the design of the controller. This model consists of a steady-state model of the engine with the following dynamic effects added in the form of differential equations or transfer functions:

- Low-pressure rotor dynamics (fan and LP turbine)
- High-pressure rotor dynamics (compressor and HP turbine)
- Heat transfer between engine metal and gas
- Actuator dynamics
- Sensor dynamics

For the detailed steady-state model, the engine components (fan, compressor, combustor, turbines, augmentor, and exhaust nozzle) are represented by equations or table lookup. An iterative solution is used to ensure flow continuity between components and energy balance throughout the system so that calculated pressure and temperature changes are consistent with enthalpy and entropy changes of real gases throughout the engine.

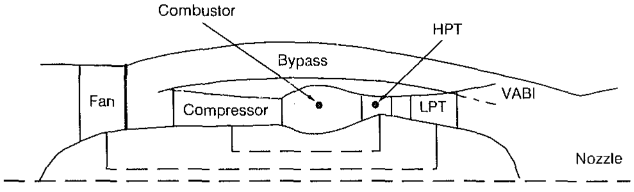

HPT - High Pressure Turbine
LPT - Low Pressure Turbine
VABI - Variable Area Bypass Injector

Fig. 1 Schematic of GE16/J11A6 turbofan engine

The *real-time, component-level*, engine model is a simplified, low-frequency, transient engine simulation. It is coded to run within the control sample time (typically 20 ms or less), and contains all the essential physics required to simulate the engine. The term "component level" refers to the nature of the simulation, that is, each engine component is simulated within the body of the overall model. The dynamic effects listed for the detailed transient model are included in the component-level model. Since it is a low-frequency model, it does not include the rate-of-change of pressures in engine volumes. An appropriate iteration scheme is used with a single pass per time step for improved accuracy.

Control Mode and Structure Analysis

The control configuration selected for this study (Fig. 2) uses core compressor speed ($N25$), fan speed ($N2$), and fan tip discharge Mach number ($XM13$) as sensed variables; and main fuel flow ($WF36$), exhaust nozzle area ($A8$), and rear VABI area ($A16$) as the control actuators. It is therefore a three input/three output multivariable mode. The fan inlet guide vanes and core compressor stators were kept on steady-state schedules by open-loop control.

This configuration was selected after a detailed study of several control modes for new and deteriorated engines. Since the main control performance variables for the turbofan engine cannot be measured, the objective of the control mode study is to select a mode that will indirectly control thrust while maintaining adequate core and fan stall margins and engine temperatures within limits. Control mode analysis was per-

Nomenclature

A = engine open-loop system matrix
$A16$ = variable area bypass injector, in.^{2}
$A8$ = exhaust nozzle throat area, in^2
B = engine open-loop control matrix
C = engine open-loop output matrix relative to state variables
D = engine open-loop output matrix relative to control inputs
e_{N2} = error between demand fan rotor speed and feedback signal
e_{N25} = error between demand core compressor rotor speed and feedback signal
e_{XM13} = error between demand Mach number and feedback signal
FN = net thrust of engine, lb
G = open-loop transfer function of engine, sensors, and actuators
HPT = high-pressure turbine
I_{ij} = integral gain schedule (i-row, j-column)
$K(s)$ = multivariable compensator transfer function matrix
LPT = low-pressure turbine
$N2$ = fan rotor speed, rpm
$N2D$ = demand fan rotor speed for closed-loop control, rpm
$N2R$ = corrected fan speed $= N2/\theta_2^{0.5}$
$N25$ = compressor rotor speed, rpm
$N25D$ = demand compressor rotor speed for closed-loop control, rpm
$N25R$ = corrected compressor speed $= N25/\theta_{25}^{0.5}$
$P2$ = fan rotor inlet pressure, psia
$P6$ = exhaust nozzle inlet pressure, psia

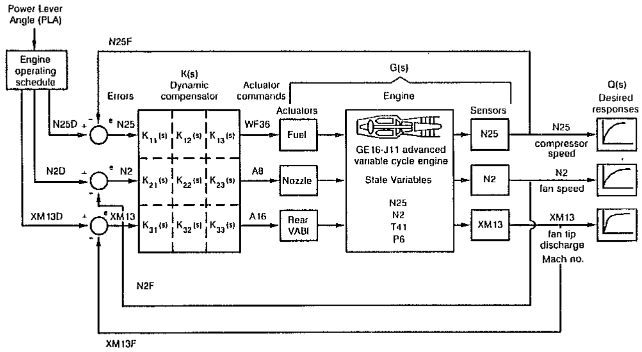

Fig. 2 Schematic of KQ multivariable engine control system

formed by using Control Mode Evaluation of Temperature Margin (COMET), a GE Aircraft Engines computer program, and by Relative Gain Array (RGA) analysis. The COMET procedure has been described in detail by Brown and Elgin (1985) for an aircraft engine. The RGA analysis has been described by McAvoy (1983) and Grosdidier and Morari (1985). The results from these two analyses were used to select the recommended control configuration.

The COMET procedure uses statistical variations between engines due to manufacturing tolerances, actuator and sensor tolerances, and changes in efficiency and flow functions due to engine deterioration with time. The procedure evaluates each potential closed-loop control mode by a Monte Carlo analysis to develop statistical data on the maximum and minimum steady-state variations (from nominal) in thrust, stall margins, turbine temperature, specific fuel consumption and rotor speeds.

The RGA provides a measure of interactions between sensed and manipulated variables in a multivariable control system. It emphasizes what manipulated variables and sensed variables can be paired and what simplified control structure can be used for closed-loop design without significant performance deterioration. It is used for steady-state as well as dynamic analysis.

The control mode used for this paper showed good properties using the analyses described above. Details will not be described here since the emphasis of this paper is on full flight envelope control design and performance. The topic of multivariable control structure and analysis has been discussed by Nett and Spang (1987) and Nett (1987).

Steady-State and Transient Schedules

Steady-State Schedules. Steady-state control schedules specify the values of control variables for every operating condition. These values are then used as reference or demand inputs to the controller to achieve the desired operating condition, or to transition between operating points.

The GE16 engine multivariable control schedules were obtained using a nonlinear constrained optimization algorithm. The algorithm was used to minimize specific fuel consumption (SFC) as a function of the manipulated variables (fuel flow and areas). During the optimization, constraints were placed on engine variables, such as rotor speeds, stall margins, and internal Mach numbers, temperatures, and pressures. This assures that the engine can be operated safely at the optimum found. The nonlinear aerothermo steady-state model was used for the optimization. The optimization process was repeated at several power levels at the sea-level static condition and at other selected operating points. The optimum operating points were used to schedule control variables and other variables of interest as functions of fan inlet temperature (T2) and fan inlet pressure (P2), power lever angle, and corrected rotor speeds.

Transient Accel and Decel Schedules. Since the nominal control schedules are based on steady-state values, the engine may exceed operating limits transiently. To prevent this, fuel flow is limited during throttle burst by the Accel. schedule such that the minimum core compressor stall margin and the maximum turbine inlet temperature remain within their safe limits. The Accel. schedule used for controller validation simulations is a curve of corrected fuel flow ($WF36/PS3$ $(\theta_{25}^{0.688})$) versus corrected percent core speed ($PCN25R$). The transient Decel. schedule provides protection against primary combustor blowout by limiting the fuel flow during throttle chops. The Decel. schedule used for the controller validation simulations was expressed as a function of $PS3$.

Multivariable Compensator Design and Evaluation

As discussed in the Introduction, the KQ design methodology is used for the compensator design. In this section, a multivariable compensator design will be discussed for one operating point to illustrate the design procedure. The next section on full flight envelope control design combines compensators designed by this technique at a selected number of operating points by gain scheduling. For each operating point, it is essential to design a compensator that can achieve the

Nomenclature (cont.)

$P56$ = low pressure turbine discharge pressure, psia
P_{ij} = proportional gain schedule (i = row, j = column)
$PCN25R$ = corrected percent core speed
PLA = power lever angle
$PS3$ = static pressure at compressor discharge, psia
$Q(s)$ = desired closed-loop response transfer function matrix
RGA = relative gain array
s = LaPlace transform operator
SFC = engine specific fuel consumption
$SM2$ = fan stall margin
$SM25$ = compressor stall margin
$T2$ = engine inlet total temperature, R
$T41$ = temperature at high-pressure turbine inlet, R
u = engine control variables
$WF36$ = main fuel flow, lb/hr
x = engine state variables
$XM13$ = fan tip discharge Mach number
$XM13D$ = demand fan tip discharge Mach number for closed-loop control
XPLA = generic parameter to represent engine power level
y = engine output variables
$(\ )D$ = demand, reference, or setpoint variable
$(\ )F$ = feedback variable
δ_2 = corrected fan inlet pressure = $P2/14.7$
δ_{56} = corrected low-pressure turbine discharge pressure = $P56/14.7$
δ_{S3} = corrected compressor discharge static pressure = $PS3/14.7$
θ_2 = corrected fan inlet temperature = $T2/518.7$
θ_{25} = corrected compressor inlet temperature = $T25/518.7$
σ = singular value function

desired requirements in the presence of uncertainties. This is a key step in producing a satisfactory nonlinear controller by gain scheduling. Therefore, the discussion on single-point design that follows includes a description on how singular value (principal gain) plots of appropriate system transfer function matrices are used to evaluate satisfactory feedback control performance and robustness requirements.

The KQ compensator design methodology is a frequency-domain technique, which uses closed-loop Nyquist and Bode plots. The parameters of the dynamic matrix compensator (K) are estimated by minimizing the mean square error between the desired closed-loop response (Q) and the actual closed-loop response. This design method, described by Edmunds (1979), consists of the following steps:

- Specification of desired closed-loop transfer function matrix.
- Selection of the MIMO compensator form (proportional, proportional/integral, etc.)
- Computation of compensator gains.
- Closed-loop performance check.

Use of this method to design a compensator at a single operating point for the GE16/J11A6 turbofan engine is described by Polley et al. (1986). Only the relevant portions of a single point design will be highlighted in this paper.

Linear State-Space Models. Linear state-space models were generated for the engine open-loop dynamic behavior by linearizing the detailed nonlinear aerothermo model at the operating point of interest.

The conventional state-space relationship which follows was used to describe the dynamics of the GE16/J11A6 engine.

$$\dot{x} = Ax + Bu \tag{1}$$

$$y = Cx + Du \tag{2}$$

where

$x =$ (N25, N2, T41, P6)—state variables (3)
$u =$ (WF36, A8, A16)—control variables (4)
$y =$ (N25, N2, XM13)—engine output variables (5)

The state variables used as shown in equation (3) are: core compressor rotor speed ($N25$), fan rotor speed ($N2$), high-pressure turbine inlet temperature ($T41$), and exhaust nozzle inlet pressure ($P6$). The control vector (u) and the output vector (y) are the same as described under control mode and structure analysis. The fan inlet guide vanes ($STP2$) and core compressor stators ($STP25$) are kept on their steady-state schedules by open-loop control and are therefore not used as control variables in equations (1) and (2).

The complete open-loop model used for the compensator design was a combination of the linear state-space model (equations (1) and (2)) with the actuator and sensor models. The actuators and sensors are represented by individual blocks in the schematic in Fig. 2.

Performance Requirements. The performance requirements used for the engine compensator design may be expressed in terms of requirements for good feedback control, which are:

- Low-frequency command following
- Low-frequency disturbance rejection
- Insensitivity to sensor noise
- Robustness to unmodeled high-frequency dynamics
- Insensitivity to low-frequency modeling errors

These performance requirements are met by using the KQ technique to design the compensator and ensuring that the singular value plots satisfy required frequency domain constraints. Doyle and Stein (1981) presented a detailed design perspective on multivariable feedback control with respect to the above fundamental feedback issues. They noted that singular values play a design role in MIMO control design much like classical Bode plots in single-input/single-output (SISO) design. Turbofan engine control specifically requires

- Fast thrust response without overshoot
- Zero steady-state error

The fast response requirement is fulfilled by designing to achieve maximum crossover frequencies for the output variables while producing a thrust transient response with no overshoot. The steady-state error requirement is met by using a multivariable proportional plus integral (PI) controller (the integrators are added to ensure zero steady-state error). The maximum crossover frequency is limited by the capability of the open-loop dynamics of the engine and the level of complexity the design engineer allows for the compensator (P, PI, PID, etc.)

Compensator Design and Performance Evaluation. The compensator transfer function matrix that was used for this design has three inputs and three outputs, as described by equation (6).

$$\begin{bmatrix} WF36 \\ A8 \\ A16 \end{bmatrix} = \begin{bmatrix} \dfrac{P_{11}s+I_{11}}{s} & \dfrac{P_{12}s+I_{12}}{s} & \dfrac{P_{13}s+I_{13}}{s} \\ \dfrac{P_{21}s+I_{21}}{s} & \dfrac{P_{22}s+I_{22}}{s} & \dfrac{P_{23}s+I_{23}}{s} \\ \dfrac{P_{31}s+I_{31}}{s} & \dfrac{P_{32}s+I_{32}}{s} & \dfrac{P_{33}s+I_{33}}{s} \end{bmatrix} \times \begin{bmatrix} e_{N25} \\ e_{N2} \\ e_{XM13} \end{bmatrix} \tag{6}$$

The inputs are errors in demand variables as shown in Fig. 2. The outputs are signals to the specified actuators. Each entry of the dynamic matrix is a proportional plus integral controller to meet the zero steady-state error requirement. The parameters of the compensator were estimated by the KQ technique and several methods were used to evaluate the linear compensator's closed-loop performance using the linear state-space model. Multivariable closed-loop Nyquist array and singular-value plots were used to check for interactions and feedback performance characteristics, respectively. Closed-loop eigenvalues and transient responses were used to check response speed and stability.

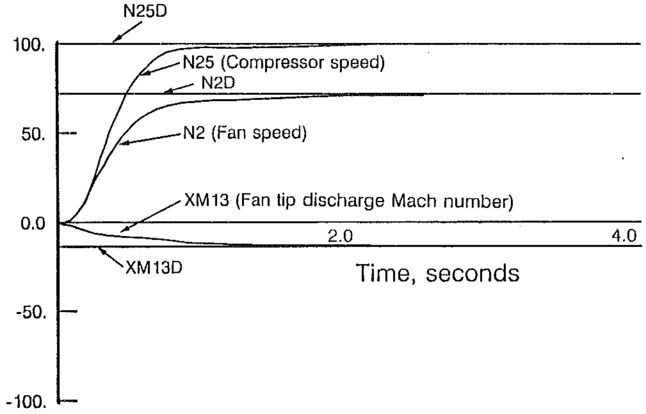

Fig. 3 Closed-loop response of speeds and fan tip discharge Mach number

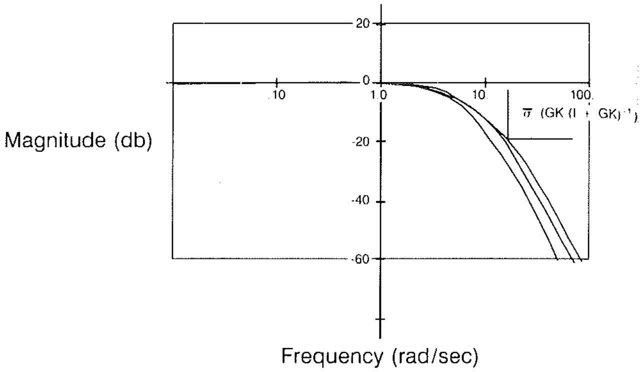

Fig. 5 Singular values of closed-loop transfer function ($GK(I + GK)^{-1}$)

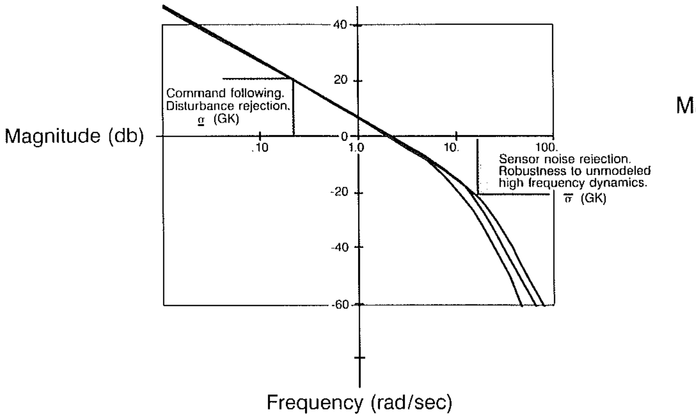

Fig. 4 Singular values of loop tranfer function (GK)

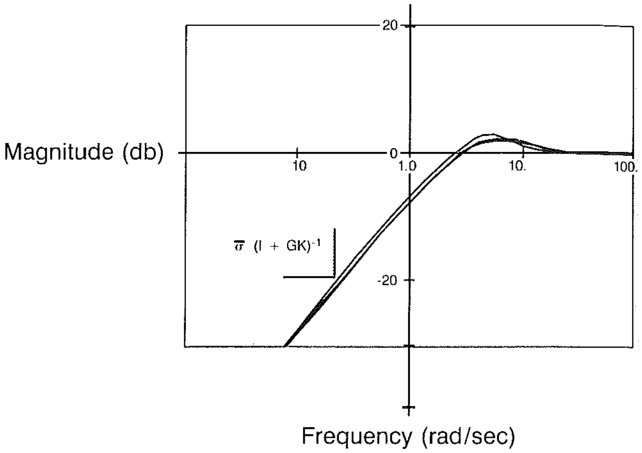

Fig. 6 Singular values of the sensitivity transfer function ($(I + GK)^{-1}$)

The next part of this section will be devoted to the description of a compensator design example. It will illustrate the use of some of the closed-loop performance evaluation techniques. The selected operating point is at sea level, zero Mach number, and at 75 percent of maximum dry thrust.

Figure 3 shows the closed-loop transient response to simultaneous setpoint changes in core compressor speed ($N25D$), fan speed ($N2D$), and fan tip discharge Mach number ($XM13D$). They all indicate response times to 95 percent of setpoint changes of about 1 s. Thrust response, which is not shown here, was also 1 s. These setpoint changes correspond to a small change in power level angle (PLA) at the selected operating point. A scaling matrix was used for the output vector ($N25$, $N2$, $XM13$) to produce the same order of magnitude for the output variables. Controller signals to the actuators were checked during the simulation to ensure internal stability. Figures 4, 5, and 6 show the characteristics of three singular value functions. The singular value plot of the loop transfer function (Fig. 4) demonstrates satisfactory command following and disturbance rejection characteristics since the minimum singular value $\underline{\sigma}$ $[GK]$ is large with respect to unity (or 0 db) at frequencies below desired crossover. For frequencies above crossover, since the maximum singular value $\bar{\sigma}$ $[GK]$ is small with respect to unity (or 0 db), sensor noise can be satisfactorily rejected and the stability of the closed-loop system will be robust to unmodeled high-frequency dynamics. The closed-loop transfer function singular value $\sigma[GK(I+GK)^{-1}]$ plot (Fig. 5) shows similar robustness properties to unmodeled high-frequency dynamics. Figure 6 shows the singular values of the sensitivity transfer function $\sigma[I+GK]^{-1}$. The plot indicates that the closed-loop system will be insensitive to low-frequency engine modeling errors since the maximum singular value is small with respect to unity (or 0 db) at frequencies below crossover.

Full Flight Envelope Design

The objective of a nonlinear controller for a turbofan engine is to control thrust during accelerations and decelerations while ensuring that predetermined limits on stall margins, speeds, pressures, and temperatures are not exceeded. The discussion in this section will cover the approach, the corrected-parameter gain scheduling process, and examples of large transient computer simulations in the presence of an acceleration fuel schedule.

The compensator design and evaluation techniques described in the previous section were used to design compensators at a number of operating points. For a full flight envelope operation, the compensator gains were linked and scheduled by a curve-fitting method using functions of appropriate engine corrected parameters to produce a global nonlinear feedback controller. This is in contrast to conventional gain scheduling involving multiparameter table lookup schemes, which can be memory intensive. Three-input/three-output multivariable compensators were designed for the higher power levels (about 50 to 100 percent of maximum dry power) where they will be effective. For low power levels close to flight idle operation, single-input/single-output (SISO) compensators were designed. The SISO design used fan rotor speed ($N2$) as the sensed variable and fuel flow ($WF36$) as the control variable.

A typical aircraft engine's operating point is represented by its altitude, Mach number, and power level. The differences in the engine's open-loop dynamics are primarily due to changes

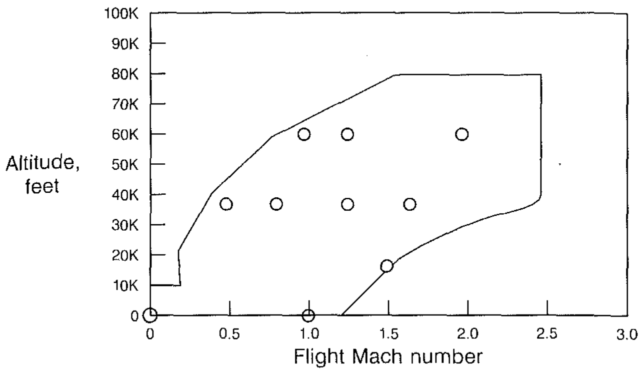

Fig. 7 Sample of compensator design points

in the fan inlet pressure (*P*2) and temperature (*T*2) and the power level (PLA). Ten compensator design points were selected to cover the flight envelope of a typical advanced aircraft engine.

These points, shown in Fig. 7, were used as initial design points for one power level. They provide a sufficient number of points to cover the *P*2 and *T*2 range of the flight envelope. Ten additional design points were chosen at sea level static operating point to cover engine power levels from ground idle to maximum dry power. Before the nonlinear control design was finalized, a few additional design points were identified to provide an improved gain scheduling. These additional compensator designs were needed to meet transient response requirements at potential problem areas in the flight envelope. Additional designs will also be needed to ensure that specific mission requirements are met.

Corrected fan inlet pressure (δ_2) and temperature (θ_2) were used to represent the flight altitude and Mach number. These are described by the following expressions:

$$\delta_2 = \frac{P2}{14.7} \tag{7}$$

$$\theta_2 = \frac{T2}{518.7} \tag{8}$$

There are several alternative corrected parameters to account for changes in power level (XPLA). They include corrected speeds (*N*2*R*, *N*25*R*), corrected compressor discharge pressure (δ_{S3}) and corrected low-pressure turbine discharge pressure (δ_{56}), to list a few. For this study, the following parameters were used where appropriate to account for changes in engine power level:

$$\delta_{S3} = \frac{PS3}{14.7} \tag{9}$$

$$\delta_{56} = \frac{P56}{14.7} \tag{10}$$

For the three-input/three-output controller, the functions used to schedule the proportional gains were

$$P_{ij} = K_P[\delta_2]^a[\theta_2]^b[\text{XPLA}]^c \tag{11}$$

where

P_{ij} = proportional gain schedule
K_p = constant

Similarly the functions used to schedule the integral gains were

$$I_{ij} = K_I[\delta_2]^d[\theta_2]^e[\text{XPLA}]^f \tag{12}$$

where

I_{ij} = integral gain schedule
K_I = constant

A regression analysis computer program was used to determine the exponents of the gain schedules (a, b, c, d, e, f) and the constants (K_p, K_I).

The goodness-of-fit obtained for the controller gains is dependent on the parameters selected to describe variations in the gain, and on the form of the function used in equations (11) and (12). For instance, the parameter used to account for variations in power level, XPLA, is important for scheduling the aircraft engine gains. We have found that selecting parameters that describe the underlying physics of the system being controlled is very critical. If the form of the function used for the curve fit is preselected, some of the elements in the matrix of gains may have poor fits. Two different strategies can be used in such cases. In the first, the form of the function remains unchanged, but the curve fit is biased to produce more accurate results in one region while sacrificing accuracy in another. For instance, the curve can be forced to pass through points in the high-power (PLA) region, where speed of response is critical, while tolerating large errors in the low power region. The alternate strategy involves tailoring the form of function used for the curve fit to better describe the variation in the gain term being curve fit. This might involve using polynomial functions, products or sums of simple functions, or piecewise continuous functions for equations (11) and (12), instead of the power functions used here.

The gain scheduling procedure described above produces 18 gain schedules (9 proportional and 9 integral gains) for the three-input/three-output nonlinear controller. One set of gain schedules will be described in this section as an example. The selected gains (P_{11} and I_{11}) relate the core compressor rotor speed error (e_{N25}) with fuel flow (*WF*36) control signal as follows:

$$WF36 = (P_{11} + I_{11}/s)e_{N25} \tag{13}$$

The regression analysis using equations (11) and (12) produced the following curve fit for the proportional gain:

$$P_{11} = 1.303[\delta_2]^{0.79}[\theta_2]^{0.68}\left[\frac{\delta_{S3}}{10\delta_2}\right]^{0.85} \tag{14}$$

where δ_2, θ_2, and δ_{s3} are defined in equations (7), (8), and (9).

The corresponding integral gain was

$$I_{11} = 3.373[\delta_2]^{1.69}[\theta_2]^{0.1}\left[\frac{\delta_{S3}}{10\delta_2}\right]^{1.66} \tag{15}$$

For these gains (equations (14) and (15)), changes in the power level (XPLA) were represented by the ratio (δ_{s3}/δ_2).

The average difference between the actual data and the curve fit (equations (14) and (15)) was 7 percent for the proportional gains and 4 percent for the integral gains. The maximum difference was 18 percent for the proportional gains and 14 percent for the integral gains. This set is one of the dominant gains in the multivariable controller and it also represents one of the best fits. In general, when a gain varied by several orders of magnitude, this type of function (parameters raised to exponents as described by equations (11) and (12)) exhibited large errors for lower gains.

We have also found that, since each gain in the matrix varies in importance, it is difficult to define an acceptable level of accuracy for the curve fits. It is therefore necessary to evaluate the closed-loop transient performance with the scheduled controller before acceptance. Whenever the responses obtained using the scheduled gains are unacceptable, some or all of the gains may need rescheduling. Occasionally, repeating the regression analysis after adding data in the form of additional compensators (designed for the specific operating points where the responses using the original gain schedules were not good) improves the accuracy of the fit for the entire flight envelope. Failing this, we recommend biasing the fit or using functions other than power functions, as described earlier.

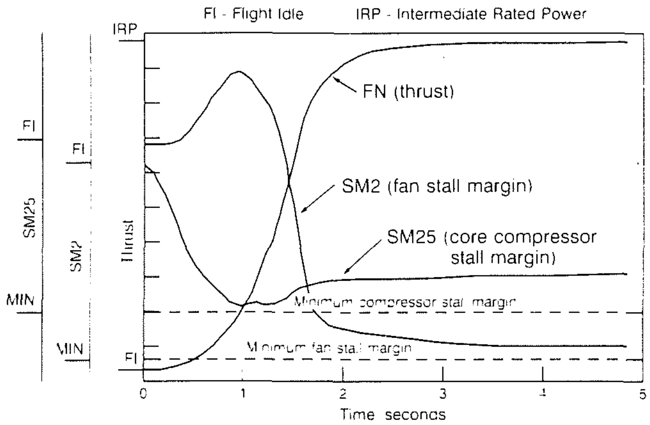

Fig. 8 Closed-loop response of thrust and stall margins (sea level static)

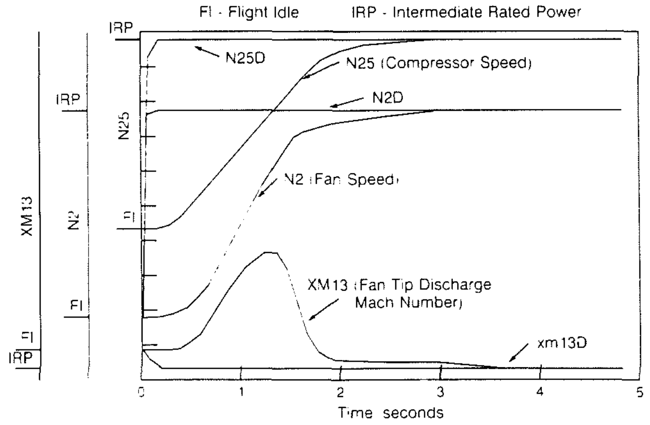

Fig. 9 Closed-loop response of rotor speeds and fan tip discharge Mach number (sea level static)

Controller Performance Validation

The continuous controller design was discretized by using the Tustin (trapezoidal) transformation and implemented with both engine models described previously in the section on engine models. The transient responses shown here were run with the detailed aerothermo model of the GE16/J11A6 engine. A satisfactory full flight envelope controller must retain its regulator response properties at critical flight conditions as well as satisfactory response properties through large ranges of power levels at critical operating points. The transient responses shown in Figs. 8 through 10 were run at sea level static operating point from flight idle to maximum dry power. Thrust response is the most important response, but a fast thrust response must be achieved without exceeding stall margin limits and other engine protection limits. The thrust response shown in Fig. 8 indicates about 2 s to achieve 95 percent of the commanded thrust change. The stall margin responses in the same figure show that the limits were not exceeded. Large power level command inputs show the capabilities of the controller when operating in a nonlinear range. Figure 9 shows the dynamic behavior of the output variables; core compressor rotor speed (*N*25), fan rotor speed (*N*2), and fan tip discharge Mach number (*XM*13). The compressor rotor speed (*N*25) and fan rotor speed (*N*2) show response times of 2.0 s to reach 95 percent of demanded changes while the fan tip discharge Mach number shows 3.0 s response time. Figure 10 shows the controller signals to the fuel flow (*WF*36), exhaust nozzle (*A*8), and rear VABI (*A*16) actuators. The fuel flow is limited by the Acceleration fuel schedule during a good portion of the transient, as shown in Fig. 10.

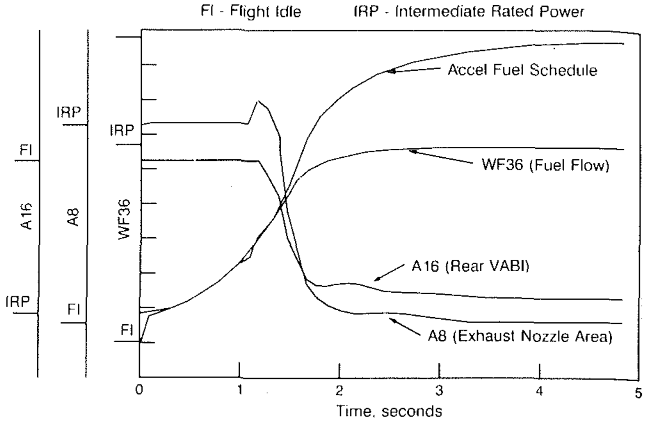

Fig. 10 Controller signals to fuel flow, exhaust nozzle, and rear VABI actuators (sea level static)

Additional computer transient simulations have been shown in Figs. 11 through 13 to demonstrate the performance of the nonlinear multivariable controller at a supersonic (36,000 feet, Mach 1.2) flight condition. The commanded thrust change is from 45 to 100 percent of Intermediate Rated Power (IRP). The nonlinear multivariable controller produced 95 percent of demanded thrust response in about 2.0 s. Closed-loop response times for compressor rotor speed (*N*25), fan rotor speed (*N*2) and Mach number (*XM*13) were approximately 2.8, 2.0, and 1.0 seconds, respectively, to reach 95 percent of demanded values. Figure 13 shows the controller signals to the fuel flow (*WF*36), exhaust nozzle (*A*8) and rear VABI (*A*16) actuators.

The closed-loop transient simulations shown by Figs. 8 through 13 have demonstrated the capability of a multivariable controller obtained by scheduling compensator gains, to produce fast responses for large thrust changes and to control fan and compressor stall margins within limits.

Conclusion

This paper has summarized an approach for designing a robust multivariable nonlinear feedback controller for a turbofan engine. The choice of appropriate engine corrected parameters to schedule compensator gains produces a controller that adapts for flight altitude, Mach number, and the engine power level.

The KQ multivariable control design technique was successfully used to design three-input/three-output perturbational compensators. The combination of the KQ technique with singular value methods provided compensator designs with good feedback properties, namely: good command following, good disturbance rejection, robustness to unmodeled high-frequency dynamics, and rejection of high-frequency sensor noise.

The performance of the nonlinear controller has been demonstrated by large signal transient response of the GE16/J11A6 turbofan engine. Another conclusion that may be deduced from the studies is that as the number of control variables increases with growing complexity of advanced propulsion systems, compensator types become more complex, and controller gain schedules and computations in real time become more demanding. The challenge in future control system design process will be the development of methodologies that can utilize recent advances in multivariable control design techniques with minimum complexity in control structure and controller dynamic order.

Acknowledgments

This work was performed under a GE Independent Research and Development (IR&D) program. We would like to ac-

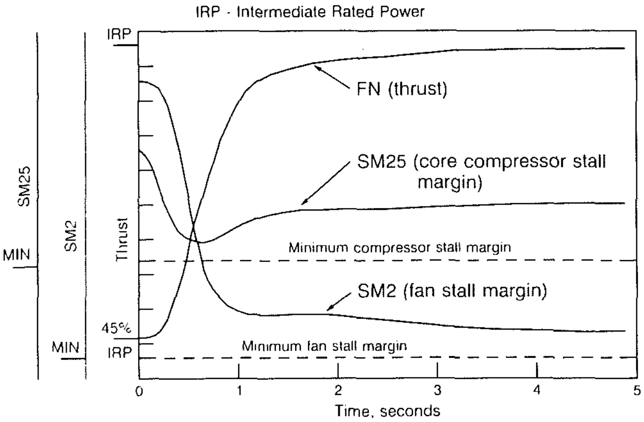

Fig. 11 Closed-loop response of thrust and stall margins (36K ft, Mach 1.2)

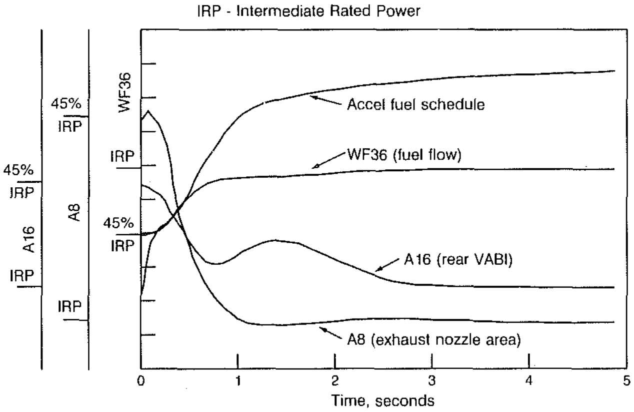

Fig. 13 Controller signals to fuel flow, exhaust nozzle and rear VABI actuators (36k ft, Mach 1.2)

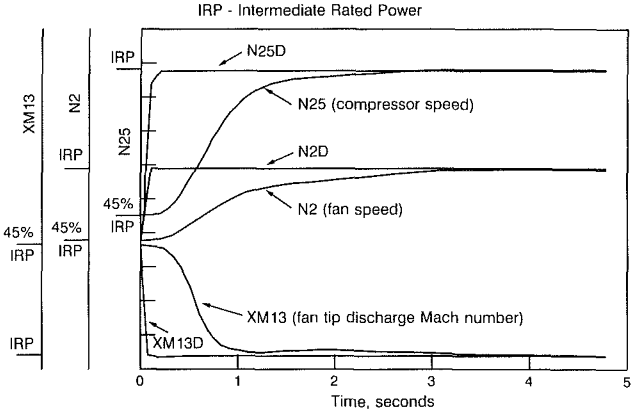

Fig. 12 Closed-loop response of rotor speeds and fan tip discharge Mach number (36k ft, Mach 1.2)

knowledge the assistance of Mr. Harold Brown of GE Aircraft Engines, Cincinnati, OH, and several of our other colleagues, whose criticisms and suggestions were extremely helpful in developing the concepts described in this paper.

References

Brown, H., and Elgin, J. A., 1985, "Aircraft Engine Control Mode Analysis," ASME Journal of Engineering for Gas Turbines and Power, Vol. 107, pp. 838-844.

Brown, H., and Fisk, W. S., 1983, "Integrated Flight and Propulsion Operating Modes for Advanced Fighter Engines," ASME Paper No. 83-GT-194.

Doyle, J. C., and Stein, G., 1981, "Multivariable Feedback Design: Concepts for a Classical/Modern Synthesis," *IEEE Transactions on Automatic Control*, Vol. AC-26, No. 1.

Edmunds, J. M., 1979, "Control System Design and Analysis Using Closed-Loop Nyquist and Bode Arrays," *International Journal of Control*, Vol. 30, No. 5, pp. 773-802.

Grosdidier, P., and Morari, M., 1985, "Closed-Loop Properties from Steady-State Gain Information," *Ind. Eng. Chem. Fund.*, k24, pp. 221-235.

Joshi, D. S., Shaw, P. D., Hodgkinson, J., Rock, S. M., Vincent, J. H., and Fisk, W. S., 1983, "A Design Approach to Integrated Flight and Propulsion Control," SAE Technical Paper No. 831482.

Kapasouris, P., 1984, "Gain-Scheduled Multivariable Control for the GE-21 Turbofan Engine Using the LQR and LQG/LTR Methodologies," S.M. Thesis (LIDS-TH-1380), Massachusetts Institute of Technology, Cambridge, MA.

McAvoy, T. J., 1983, *Interaction Analysis*, Instrument Society of America Monograph Series.

Nett, C. N., 1987, "A Quantitative Theory for Control Structure Design: The Role and Use of Block Relative Gains," presented at the American Control Conference, June.

Nett, C. N., and Spang, H. A., 1987, "Control Structure Analysis and Synthesis: A Missing Link in the Evolution of Modern Control Theories," presented at the American Control Conference, June.

Pfeil, W. H., Athans, M., and Spang, H. A., 1986, "Multivariable Control of the GE T700 Engine Using the LQG/LTR Design Methodology," presented at the American Control Conference, June.

Polley, J. A., Adibhatla, S., and Baheti, K. S., 1986, "Design of Jet Engine Control System by Multivariable Frequency-Domain Method," presented at the American Control Conference, June.

Sain, M. K., Peczkowski, J. L., and Melsa, J. L., 1978, "Alternatives for Linear Multivariable Control," National Engineering Consortium, IL.

Skira, C. A., 1986, "Integrated Flight/Propulsion Control Design Techniques," presented at the IEEE/AIAA Digital Avionics Systems Conference and Technical Display, Oct.

W. Huettner

M. Niggemann

Daimler-Benz Aktiengesellschaft,
Stuttgart, Federal Republic of Germany

Analytical and Numerical Treatment of the Transient Behavior of Rotating Counterflow Regenerators

The transient heat transfer in a rotating counterflow regenerator is analyzed analytically and numerically with the assumption of constant mass flows on both sides of the regenerator. Moreover, first results for the case of temperature-dependent mass flows are presented.

Introduction

The present paper is thought of as a continuation of a previous one (Niggemann, 1986) where we have solved, by means of analytical methods, the coupled system of partial differential equations (PDEs) governing the regenerator problem under classical assumptions.

Among others, these assumptions comprise the condition that the fluid mass flow may be considered as being constant in time and uniformly distributed in space.

In the first part of the present paper we adopt this assumption for treating the transient behavior of the rotating regenerator and we give some numerical results. The results comprise the regenerator response during transition between different operation points and a frequency response.

In the second part we get rid of the abovementioned assumption on the fluid mass flow and allow it to change with temperature. This temperature dependence is induced by the fact of a constant overall pressure drop across the regenerator core (Braig, 1984a). The temperature-dependent mass flow causes the regenerator equations to involve nonlinearities. The nonlinearities, in turn, give rise to difficulties with respect to an analytical solution of the problem.

Therefore, doing a first step, we treat the nonlinear problem for the standing regenerator only. This is performed by means of a perturbation series approach. As a result, we are able to study the effect of the nonlinearity during transients by means of a numerical comparison with the solution of the corresponding linear problem.

The fully coupled nonlinear problem is planned to be studied in a forthcoming paper.

The Linear Problem

The Model Equations. For the physical situation to be considered, we refer to Fig. 1 and the nomenclature. Furthermore, we adopt the physical assumptions of the classical regenerator theory (Braig, 1984a). Under these assumptions, the matrix and fluid-temperature distribution on each side of the regenerator is governed by the system

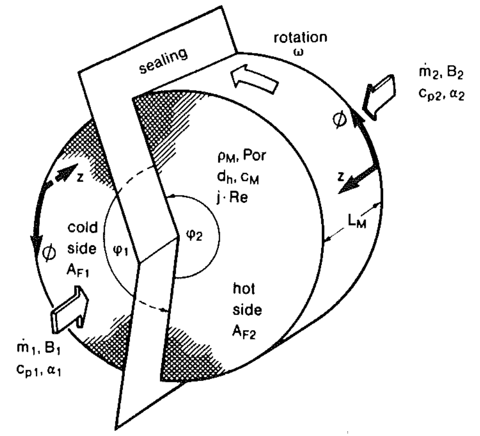

Fig. 1 Scheme of a rotating counterflow regenerator

$$\frac{\partial T}{\partial A} = c_1(T_M - T)$$
$$\frac{\partial T_M}{\partial t} = c_2(T - T_M) \tag{1}$$

which is derived from an unsteady heat balance[1] and completed by an initial condition, i.e., a prescribed function $T_M(t, A)|_{t=0} = g(A)$, and a boundary condition $T(t, A)|_{A=0} = h(t)$.

Contributed by the International Gas Turbine Institute and presented at the 33rd International Gas Turbine and Aeroengine Congress and Exhibition, Amsterdam, The Netherlands, June 5–9, 1988. Manuscript received by the International Gas Turbine Institute December 15, 1987. Paper No. 88-GT-38.

[1] The system equation (1) follows from an unsteady heat balance if one neglects the term $c_p dm\, \partial T/\partial t$. This is possible because of the fact that the heat capacity of the fluid is much less than the capacity of the matrix core. On the other hand it has already been observed by Anzelius (1926) that even if one does not neglect this term, a transformation $t = \tilde{t} + 1/\sigma A_F w \tilde{A}$, $A = \tilde{A}$ (w = mean velocity of the fluid in a matrix pipe) leads to a system $\partial T/\partial \tilde{A} = c_1(T_M - T)$; $\partial T_M/\partial \tilde{t} = c_2(T - T_M)$ of the same type as equation (1).

We have shown that this system is equivalent to a hyperbolic PDE of second order (Niggemann, 1986).

For future use, we state this PDE here in a more general fashion, i.e., for prescribed functions $f(t, A)$, $g(A)$, $h(t)$ we are looking for a solution $T(t, A)$ of the following initial boundary value problem (IBVP)

$$\frac{\partial^2 T}{\partial t \partial A} + c_2 \frac{\partial T}{\partial A} + c_1 \frac{\partial T}{\partial t} = f(t, A)$$

$$\left(\frac{\partial T}{\partial A} + c_1 T \right) \Big|_{t=0} = c_1 g(A) \tag{2}$$

$$T(t, A)|_{A=0} = h(t).$$

In the first part of the paper we have always $f \equiv 0$.

Analytical Solution of the IBVP. Following the same lines as in the approach of Niggemann (1986), we perform a Laplace transform of equation (2) with respect to t, which results in

$$\frac{d\tilde{T}}{dA} + \frac{c_1 s}{s+c_2} \tilde{T} = \frac{c_1 g(A)}{s+c_2} + \frac{\tilde{f}(s, A)}{s+c_2}$$

$$\tilde{T}(s, 0) = \tilde{h}(s) \tag{3}$$

Equation (3) represents an ordinary differential equation (ODE) with respect to A for $\tilde{T}(s, A)$; $\tilde{T}$, $\tilde{f}$, $\tilde{h}$ denote the Laplace transforms with respect to t of the functions T, f, h, respectively; s is a complex parameter. The solution of equation (3) is given by

$$\tilde{T}(s, A) = \tilde{h} e^{-\frac{c_1 s}{s+c_2} A} + \tag{4}$$

$$+ \int_0^A \frac{1}{s+c_2} e^{-\frac{c_1 s}{s+c_2}(A-x)} [c_1 g(x) + \tilde{f}(s, x)] dx$$

Performing the inverse Laplace transform yields the solution of equation (2)

$$T(t,A) = e^{-c_1 A}[h(t) + \int_0^t e^{-c_2(t-\tau)} \sqrt{\frac{c_1 c_2 A}{t-\tau}} \tag{5}$$

$$I_1(2\sqrt{c_1 c_2 A (t-\tau)}) h(\tau) d\tau] +$$

$$+ c_1 e^{-c_2 t} \int_0^A e^{-c_1(A-x)} I_0(2\sqrt{c_1 c_2 t (A-x)}) g(x) dx$$

$$+ \int_0^A \int_0^t e^{-c_1(A-x) - c_2(t-\tau)} I_0(2\sqrt{c_1 c_2 (t-\tau)(A-x)}) f(\tau, x) d\tau dx$$

In deriving equation (5) from equation (4), the only nonstandard inverse Laplace transform is

$$L^{-1}\{e^{-\frac{c_1 s}{s+c_2} A}\}(t) \tag{6}$$

$$= e^{-c_2 t - c_1 A} \left(\frac{\partial}{\partial t} I_0(2\sqrt{c_1 c_2 A t}) + \delta(t) \right),$$

where $\delta(t)$ denotes the Dirac delta distribution. Because of the fact that it enters equation (5) via integrals of convolution type only, we are led back from distributions into some ordinary function space.

For treating the regenerator problem with the fluid mass flow $\dot{m}$ constant on each side of the regenerator, equation (2) has to be solved for $f \equiv 0$ only (considering a nonvanishing function f will be necessary in the section The Nonlinear Problem, where the case $m = m(T)$ will be treated).

Similarly to the above procedure, an explicit formula for the matrix temperature T_M may be derived (Niggemann, 1986), which is (for the case m = const) given by

$$T_M(t, A) = B(1 - G(t, A)) + e^{-c_2 t}[T_M(0, A) \tag{7}$$

$$- \int_0^A e^{-c_1(A-y)} \frac{\partial}{\partial y} I_0(2\sqrt{c_1 c_2 t (A-y)}) T_M(0, y) dy]$$

with

$$G(t, A) = e^{-c_2 t}[e^{-c_1 A} I_0(2\sqrt{c_1 c_2 t A}) \tag{8}$$

$$+ c_1 \int_0^A e^{-c_1 x} I_0(2\sqrt{c_1 c_2 t x}) dx]$$

where h is considered to be constant,

$$h(t) \equiv B = \text{const} \tag{9}$$

So, considering the regenerator as a whole, on each side of the core (hot/cold) the matrix temperature is given according to equation (7) with c_1, c_2, B belonging to the hot and cold side, respectively, and A taken to be in the flow direction on

Nomenclature

A = heat transfer area = $\sigma A_F z$, m^2
$\bar{A}$ = dimensionless heat transfer area
A_F = front area on either side of the matrix, m^2
A_m = maximal available heat transfer area on either side of the regenerator = $\sigma A_F L_M$, m^2
$B(t)$ = inlet temperature, K
c_1 = $\alpha/(c_p m)$, m^{-2}
c_2 = $\sigma\alpha/(\rho_M c_M(1 - Por))$, s^{-1}
$\bar{c_1}$ = defined by equation (15)
c_1^* = $\bar{c_1} T_{M0} A_M$
c_2^* = $c_2 P$
c_k = universal constant in the a priori estimate equation (30)
C^k = function space defined by equation (28)
c_M = specific heat of matrix, J/(kg K)
c_p = specific heat of fluid, J/(kg K)
c_w = pressure loss coefficient
d_H = hydraulic diameter of the matrix pipes, m
f = Fanning friction factor
G = defined by equation (8)
I_ν = modified Bessel function of order ν = 0, 1
j = Colburn factor
L_M = thickness of matrix, m
m = fluid mass contained in the matrix core, kg
$\dot{m}$ = fluid mass flow, kg/s
P = reference time, usually equal to half of the regenerator period, s
p = static fluid pressure, N/m^2
Δp = pressure drop, N/m^2
Por = porosity of the matrix core
R = universal gas constant, J/kg K
R = real numbers
Re = Reynolds number, see equation (12)
s = complex variable
$\underline{t}$ = time variable, s
t = dimensionless time
$\underline{T}$ = fluid temperature, K
$\bar{T}$ = dimensionless fluid temperature
T_M = matrix temperature, K
$\bar{T}_M$ = dimensionless matrix temperature
$T(\phi; t, A)$ = fluid temperature of some individual ele-

each side. The continuity of the matrix temperature across the sealing, which separates the hot side from the cold one (Fig. 1), implies a coupling of the solutions T_{Mi} (i = 1: hot side, i = 2: cold side) (Niggemann, 1986).

The Transient Problem. Treating the "steady-periodic" behavior of the rotating regenerator, the mentioned continuity condition leads to a coupled system of Volterra integral equations, which has been solved using functional analytic methods (Niggemann, 1986).

Here, we want to investigate the transient behavior of the rotating regenerator, e.g., its temperature response to changes in inlet temperatures, mass flows, etc.

For this aim, we have to consider the temperature evolution of every infinitesimal patch of the core, which is located at time $t = 0$ at some well-defined circumferential position ϕ, individually. We follow this element, which we designate by ϕ, on its journey through the hot and cold fluid streams. Let us assume for the moment that $0 < \phi < \phi_1$. Then, for $0 < t < (\phi_1 - \phi)/\omega$, the temperature evolution for the element under consideration is governed by equations (5) and (7) with the settings $c_1 = c_{11}$, $c_2 = c_{21}$, $B = B_1$, $f \equiv 0$. We denote the corresponding temperatures by $T(\phi;\, t,\, A)$ and $T_M(\phi;\, t,\, A)$. When the element passes the sealing (i.e., $t = (\phi_1 - \phi)/\omega$), its temperature evolution will be determined by equations (5) and (7) with the settings $f \equiv 0$, $c_1 = c_{12}$, $c_2 = c_{22}$, $B = B_2$, $g(A) = T_M(\phi;\, (\phi_1 - \phi)/\omega,\, A_M - A)$ (because of the reversion of the fluid direction) and with t being restarted at $t = 0$, i.e., $t = t^* + (\phi_1 - \phi)/\omega$, where t^* has to be used in equations (5) and (7). A similar consideration holds every time, when the element ϕ crosses the sealing. Details of this process are given by Niggemann (1986).

The corresponding fluid temperature may be calculated from equation (5), once the matrix temperature has been determined. The numerical treatment of the above process may be simplified considerably by the observation (Huettner, 1987) that T can be determined from T_M via formula

$$T(\phi;t,\, A) = e^{-c_1 A}\left[B + c_1 \int_0^A e^{c_1 x} T_M(\phi;\, t,\, x)\,dx\right] \qquad (10)$$

which is implied by equation (5) for $f \equiv 0$ replacing $g(A)$ by $T_M(\phi;\, t, A)$ and setting $t = 0$ formally. In this way we calculate $T(\phi;\, t, A)$ from the matrix temperature $T_M(\phi;\, t, A)$ at the same time t (instead of calculating it from the matrix temperature $g(A)$ known at time $t = 0$ only).

Having performed the above analysis for all elements ϕ of the matrix core individually, we take the circumferential average

$$T_{1,2}(t,\, A_m) = \frac{1}{\phi_{1,2}} \int_0^{\phi_{1,2}} T(\phi;\, t,\, A_m)\,d\phi \qquad (11)$$

of the fluid temperature at $A = A_m$ as representing the transient temperature response of the regenerator.

Numerical Procedure. Evaluating the formulae equations (7) and (10) for T_M and T numerically, we have to replace the infinitesimal matrix elements ϕ by a finite number of segments in circumferential direction, each of which covers an arclength $\Delta\phi$. The time evolution of T_M may be treated then by calculating its progress from one segment to another. For this purpose, we have to use the T_M outcome of the previous segment as the input profile for the present segment and need to apply the formula in equation (7) for the time $t = \Delta\phi/\omega$ only. As a result, the convolution integral in equation (7) has to be evaluated on each side of the regenerator for a fixed kernel function only (corresponding to c_1, c_2, $t = \Delta\phi/\omega$) with varying inlet profiles $g(A)$. This fact is of great importance regarding the computation time, because the convolution integral in equation (7) is the only integral, which has to be carried out numerically. For its evaluation we have used the closed Newton–Cotes formulae of higher order (n = 4, 5).

The determination of the corresponding fluid temperature has then been performed by means of equation (10), where we have used a linear interpolation of $T_M(t, A)$ between any successive nodes in the A direction. The resulting integrals with piecewise linear T_M distributions have been evaluated analytically.

Numerical Results. Here we want to apply the numerical scheme outlined above to the case of a rotating counterflow regenerator as used in a small regenerative vehicular gas turbine engine of about 110 kW.

Figures 2 and 3 show the response of the fluid temperature at the outlet of cold (air) and hot (gas) side, respectively, due to a step change at time $t = 0$ with respect to the operation point of the engine (from an operation point 1 to a different operation point 2). This step change comprises transitions

Nomenclature (cont.)

ment being positioned at ϕ for $t = 0$, K

$T_M(\phi;\, t,\, A)$ = matrix temperature of some individual element being positioned at ϕ for $t = 0$, K

$\tilde{T}$ = Laplace transform with respect to t; $\tilde{T}(s, A) = \int_0^\infty e^{-st} T(t, A)\,dt$

T_{M0} = reference temperature, K

α = heat transfer coefficient between fluid and matrix, W/(m^{2}K)

α_n = defined by equation (38)

δ = Dirac function

δ_n = defined by equation (33)

ϵ = defined by equation (22)

η = viscosity, kg/(m s)

Θ = deviation of the dimensionless fluid temperature T from 1

$\tilde{\Theta}$ = majorant series of Θ defined by equation (34)

Θ_n = coefficient function defined by equation (25)

Θ_M = deviation of the dimensionless matrix temperature $\overline{T}_M$ from 1

ν = kinematic viscosity, m^2/s

ν_R = regenerator frequency, 1/s

ρ = density of fluid, kg/m^3

ρ_M = density of the matrix core, kg/m^3

σ = heat transfer area per unit volume, 1/m

ϕ = location of some matrix element in circumferential direction at time $t = 0$

ϕ_1 = angular region covered by the cold side

ϕ_2 = angular region covered by the hot side

ω = $2\pi\nu_R$, 1/s

Subscript

i = index denoting the period (or side) of the regenerator; i = 1: cold side, i = 2: hot side

Special symbols

$\| \;\|_k$ = norm in C^k ([0, 1] × [0, 1])

$|\;|_k$ = norm in C^k ([0, 1])

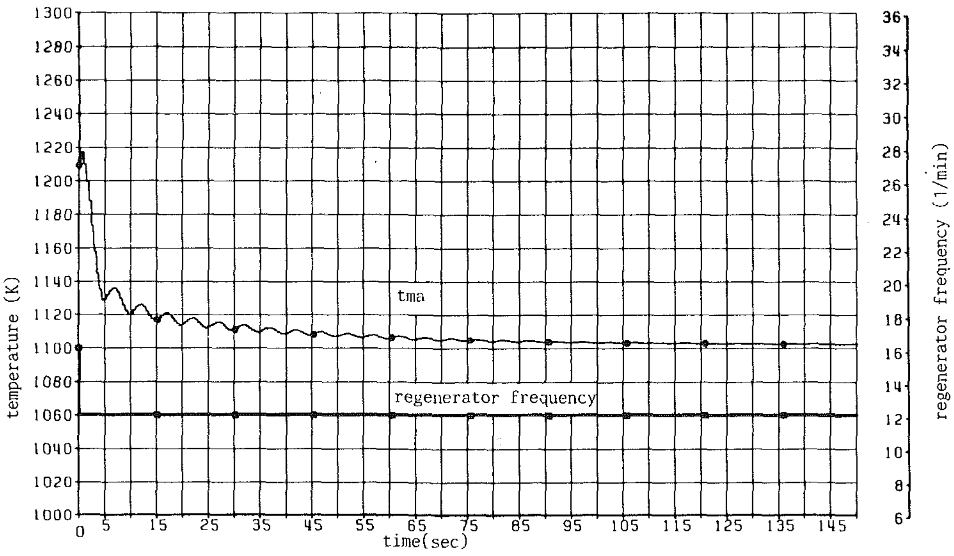

Fig. 2 **Regenerator response to a step change in the operation point of the engine (as indicated by the change of the regenerator frequency). The mean fluid temperature at air exit (tma) is shown.**

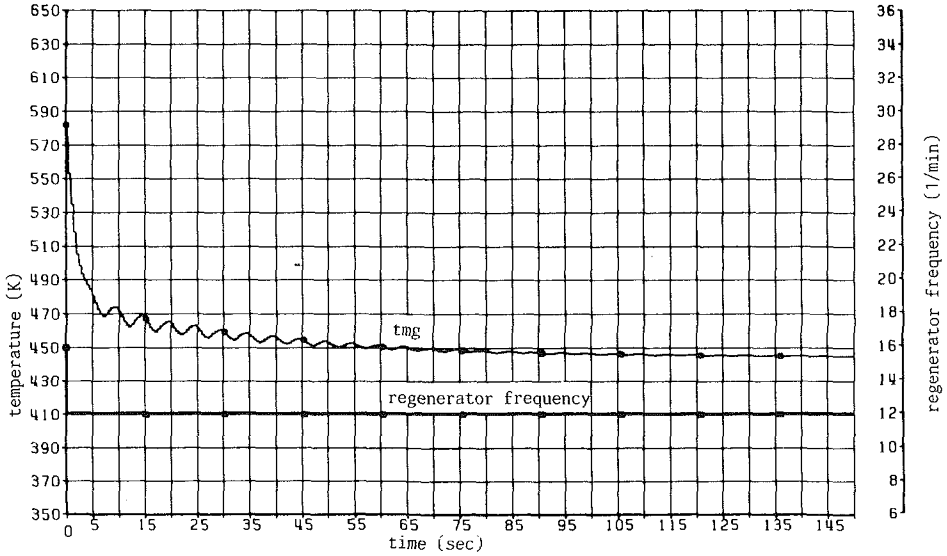

Fig. 3 **Regenerator response to a step change in the operation point of the engine (as indicated by the change of the regenerator frequency). The mean fluid temperature at gas exit (tmg) is shown.**

- of the air inlet temperature from $B = T_1 \simeq 478$ K to $T_1 \simeq 382$ K
- of the gas inlet temperature from $B = T_2 \simeq 1261$ K to $T_2 \simeq 1132$ K
- of the regenerator speed from $\nu_R = 16./\text{min}$ to $\nu_R = 12./\text{min}$ (the regenerator speed is coupled to the engine speed via a fixed transmission)
- of the fluid mass flows, resulting in a change of the heat transfer parameter c_{1i} ($i = 1, 2$) from $c_{11} = 0.8104$ to $c_{11} = 1.3378$, and from $c_{12} = 0.8206$ to $c_{12} = 1.3527$
- of the heat transfer parameter c_{2i} ($i = 1, 2$) from $c_{21} = -3.5419$ to $c_{21} = -3.2016$, and from $c_{22} = -3.8686$ to $c_{22} = -3.3947$

The most significant qualitative features of the temperature evolution with time are the damped oscillations occurring in some neighborhood of the second operation point with a frequency, which equals the corresponding regenerator frequency (a phenomenon that has already been observed by Itoh et al. 1979) and the overshooting of the air exit temperature about 1 s after the step change has taken place. The last phenomenon is of course due to the step change in air flow.

Figure 4 shows the response of the fluid outlet temperature on the air/gas side, respectively, in the case when the transition between the abovementioned operation points of the engine is performed by means of a linear time ramp, which leads in 2 s from one operation point to the other. The first transition corresponds to an acceleration of the engine, the second to a deceleration. Qualitative phenomena similar to those above may be observed. Furthermore, it may be seen that the temperatures belonging to the first operation point have been reached again after nearly 145 s. The steady heat balance is then fulfilled up to 0.1 percent.

The last example, which is depicted in Fig. 5, shows the regenerator response to a harmonic excitation simultaneously with respect to the regenerator frequency, inlet temperatures, and mass flows, where the oscillation occurs between the abovementioned operation points and the frequency of the excitation is given by $\nu_R = 14/\text{min}$. It may be seen at once that there is a phase lag between the fluid temperature evolution

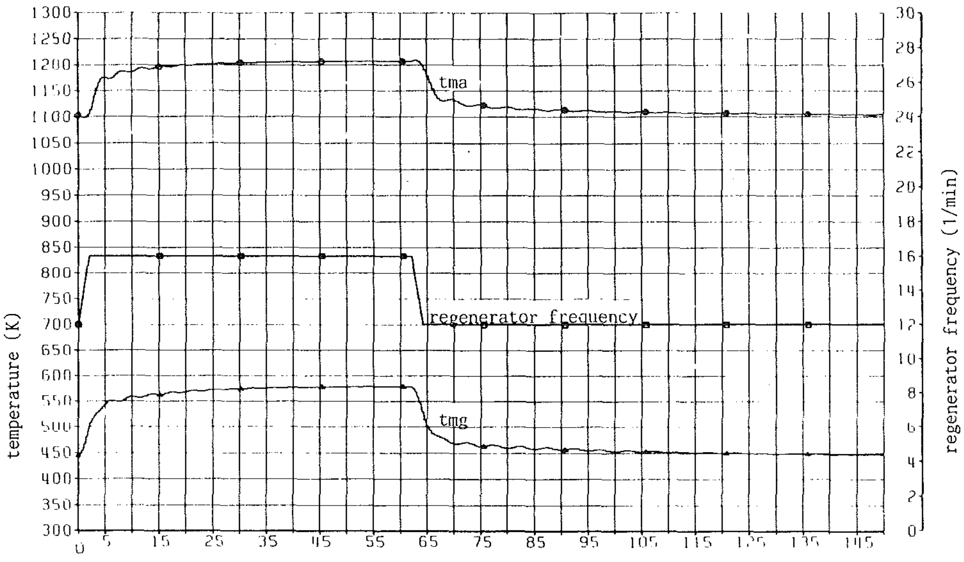

Fig. 4 Regenerator response to an acceleration/deceleration of the engine via a linear time ramp (as indicated by the change of the regenerator frequency). The mean fluid temperature at air exit (tma) and at gas exit (tmg) are depicted.

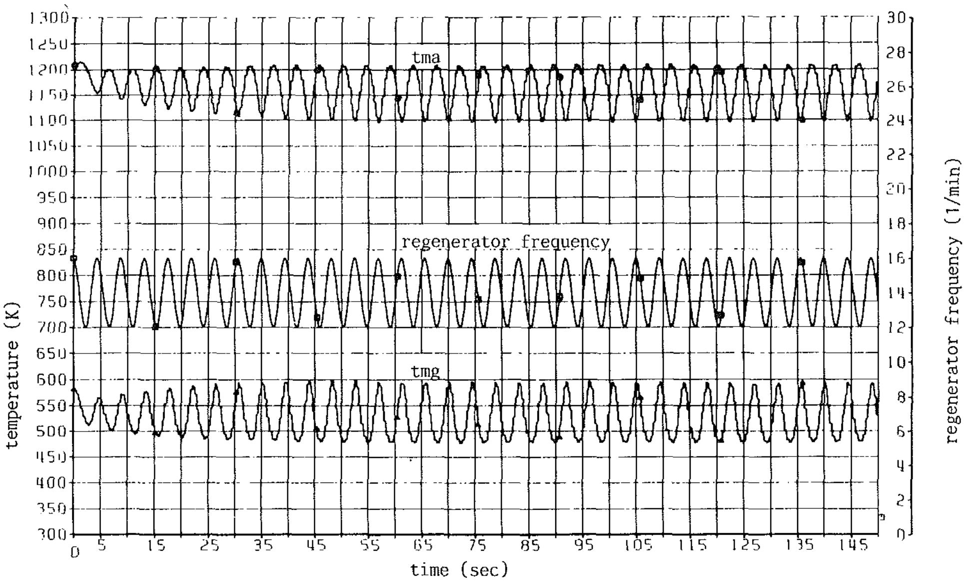

Fig. 5 Regenerator response to harmonic excitation as indicated by the oscillation of the regenerator frequency. The mean fluid temperature at air exit (tma) and at gas exit (tmg) are depicted.

at the air exit and at the gas exit of just half a period of the regenerator.

The Nonlinear Problem

The Physical Model. In the preceding sections the fluid mass flow was regarded as being uniformly distributed in space (with different values on the hot and cold side of the regenerator). In fact, the fluid flow may change in circumferential direction due to the influence of the temperature distribution, an effect, which may be of some significance during transient operations of the regenerator (Braig, 1984a, 1984b).

For deriving a suitable physical model, we start from the observation that the overall pressure drop Δp across the regenerator does not vary in circumferential direction ($\Delta p = p_{\text{inlet}} - p_{\text{exit}}$, with different values on the regenerator's hot and cold side, respectively). On the other hand, we have

$$\begin{aligned} \Delta p &= c_w \frac{\rho}{2} w^2 \\ c_w &= \frac{4f}{\text{Re}} \frac{L_M}{d_H} \\ \text{Re} &= w d_H/\nu \\ \dot{m} &= \rho w A_F \end{aligned} \tag{12}$$

which implies

$$\Delta p = \frac{2 f L_M \nu}{d_H^2 A_F} \dot{m} \tag{13}$$

Because the kinematic viscosity $\nu = \eta/\rho$ is monotonically growing with temperature, $\Delta p \equiv const$ implies that the mass flow $\dot{m}$ decreases with temperature.

In the following, we regard the temperature dependence of

ν as being dominated by the influence of temperature on the fluid density ρ, $\rho = p/(RT)$, i.e., we ignore the temperature dependence of η.

With this assumption, equation (13) may be stated as

$$\dot{m}(T) = \frac{p \Delta p d_H^2 A_F}{2fL_M \eta R} \frac{1}{T} \tag{14}$$

which leads to the following expression for $c_1 = \alpha/(\dot{m}c_p)$:

$$c_1 = \bar{c}_1 T, \qquad \bar{c}_1 = \frac{2fL_M \eta R\alpha}{c_p p \Delta p d_H^2 A_F} \tag{15}$$

So, the nonlinear equations which are to be considered now correspond to equation (1) with the constnt c_1 being replaced by the expression in equation (15).

The Equivalent Hyperbolic PDE. As in the linear case, this system of equations for T, T_M may be shown to be equivalent to

$$\frac{\partial^2 T}{\partial t \partial A} + c_2 \frac{\partial T}{\partial A} + \bar{c}_1 T \frac{\partial T}{\partial t} = 0$$

$$\left(\frac{\partial T}{\partial A} + \bar{c}_1 T^2\right) |_{t=0} = \bar{c}_1 T(0, A) g(A) \tag{16}$$

$$T(t, A) |_{A=0} \equiv B = \text{const}, \qquad g(A) = T_M(0, A)$$

provided $|1/T\, \partial T/\partial t| << 1$ holds. This assumption has been justified by numerical calculations with the scheme proposed by Braig (1984a).

Equation (16) represents a nonlinear IBVP for the fluid temperature T with the initial condition being nonlinear, too. The corresponding matrix temperature T_M may be derived from

$$T_M(t, A) = g(A) - \frac{c_2}{c_1} \int_0^t \frac{1}{T} \frac{\partial T}{\partial A} d\tau \tag{17}$$

Using Dimensionless Variables. In the following analysis it will prove useful to relate every physical variable to some reference value. To be more specific, we use

$$t = \bar{t}P, \quad A = \bar{A}A_m, \quad T = \bar{T}T_{M0}, \quad T_M = \bar{T}_M T_{M0} \tag{18}$$

with

$$T_{M0} = \frac{1}{A_m} \int_0^{A_m} T_M(t, A) |_{t=0} dA \tag{19}$$

denoting the mean matrix temperature at time $t = 0$.

These settings result in an equation for the dimensionless fluid temperature $\bar{T}$ analogous to equation (16) with c_1, c_2, g, B being replaced by $c_1^* = \bar{c}_1 T_{M0} A_m$, $c_2^* = c_2 P$, $\bar{g} = g/T_{M0}$, $\bar{B} = B/T_{M0}$, respectively.

Analytical Solution of the Nonlinear IBVP. In order to solve equation (16) for T, we rewrite the equation by introducing the deviation $\bar{\Theta}(t, A)$ of the dimensionless fluid temperature $\bar{T}$ from 1 (corresponding to the constant reference value T_{M0})

$$\bar{T} = 1 + \bar{\Theta} \tag{20}$$

and similarly for the dimensionless matrix temperature

$$\bar{T}_M = 1 + \bar{\Theta}_M \tag{21}$$

which results in

$$\frac{\partial^2 \bar{\Theta}}{\partial \bar{t} \partial \bar{A}} + c_2^* \frac{\partial \bar{\Theta}}{\partial \bar{A}} + c_1^* \frac{\partial \bar{\Theta}}{\partial \bar{t}} = -c_1^* \bar{\Theta} \frac{\partial \bar{\Theta}}{\partial \bar{t}}$$

$$\left(\frac{\partial \bar{\Theta}}{\partial \bar{A}} + c_1^* \Theta\right) \bigg|_{\bar{t}=0} = c_1^* (\bar{\Theta}_M (1 + \bar{\Theta}) - \bar{\Theta}^2) |_{t=0} \tag{22}$$

$$\bar{\Theta} |_{\bar{A}=0} = \bar{B} - 1 =: \epsilon$$

with $\bar{\Theta}_M |_{t=0}$ given by

$$\bar{\Theta}_M (\bar{t}, A) |_{\bar{t}=0} = 1 - \bar{g}(A) \tag{23}$$

In order to investigate the effect of the nonlinearity in the regenerator equation, we will treat the hot and cold side separately without taking into account the coupling between both sides. The fully coupled nonlinear problem will be studied in a forthcoming paper.

Furthermore, we shall simplify the following analysis by confining ourselves to the situation of the regenerator core being uniformly heated at time $t = 0$, i.e., we assume

$$g(A) \equiv T_{M0} \text{ or } \bar{\Theta}_M |_{t=0} = 0 \tag{24}$$

For simplicity of writing we omit the overbar indicating a dimensionless variable in the following sections, because only dimensionless variables will be used.

With ϵ according to equation (22) (i.e., ϵ measures the difference between the fluid inlet temperature and the mean matrix temperature at $t = 0$) we try a perturbation series development for Θ with respect to ϵ

$$\Theta(t, A) = \sum_{n=0}^{\infty} \Theta_n (t, A) \epsilon^{n+1} \tag{25}$$

Inserting this series into equation (22) results in the following sequence of linear PDEs, which determine the coefficient functions Θ_n recursively and uniquely

$$\frac{\partial^2 \Theta_0}{\partial t \partial \mathrm{A}} + c_2^* \frac{\partial \Theta_0}{\partial A} + c_1^* \frac{\partial \Theta_0}{\partial t} = 0, \quad \left(\frac{\partial \Theta_0}{\partial A} + c_1^* \Theta_0\right) \bigg|_{t=0} = 0$$

$$\Theta_0 |_{A=0} = 1$$

$$\ldots \tag{26}$$

$$\frac{\partial^2 \Theta_n}{\partial t \partial A} + c_2^* \frac{\partial \Theta_n}{\partial A} + c_1^* \frac{\partial \Theta_n}{\partial t} = -c_1^* \sum_{\substack{\nu_1 + \nu_2 = n-1 \\ \nu_i \geq 0}} \Theta_{\nu_1} \frac{\partial \Theta_{\nu_2}}{\partial t}$$

$$\left(\frac{\partial \Theta_n}{\partial A} + c_1^* \Theta_n\right) \bigg|_{t=0} = -c_1^* \sum_{\substack{\nu_1 + \nu_2 = n-1 \\ \nu_i \geq 0}} (\Theta_{\nu_1} \Theta_{\nu_2}) |_{t=0}$$

$$\Theta_n |_{A=0} = 0, \qquad n \geq 1$$

So we have to solve generally a linear IBVP of the type

$$\frac{\partial^2 \Theta}{\partial t \partial \mathrm{A}} + c_2^* \frac{\partial \Theta}{\partial A} + c_1^* \frac{\partial \Theta}{\partial t} = f(t, A)$$

$$\left(\frac{\partial \Theta}{\partial A} + c_1^* \Theta\right) \bigg|_{t=0} = c_1^* g(A) = g^*(A) \tag{27}$$

$$\Theta |_{A=0} = h$$

with prescribed functions f, g^*, h ($h \equiv$ const). The solution of this problem has already been established in the first part of the present paper, it is given by equation (5). So we are able to construct the coefficient functions $\Theta_n(t, A)$ up to an arbitrary order n, which yields the solution Θ via equation (25).

Convergence of the Perturbation Series. For proving the convergence of the series in equation (25) we regard the solution of the general problem (27) as an element in some suitable function space. For example, we may take

$$\Theta \epsilon C^k(\Omega) = \{f: \Omega \to R \mid \frac{\partial^{|\nu|} f}{\partial t^{\nu_1} \partial A^{\nu_2}} \text{ is continuous on } \bar{\Omega},$$

$$\nu = (\nu_1, \nu_2), |\nu| = \nu_1 + \nu_2, 0 \leq |\nu| \leq k\}, \tag{28}$$

$$\bar{\Omega} = [0, 1] \times [0, 1]$$

which is a well-known Banach space with respect to the norm

$$\|f\|_k := \sum_{\substack{\nu_1 + \nu_2 = |\nu| \\ 0 \leq |\nu| \leq k}} \| \frac{\partial^{|\nu|} \mathrm{f}}{\partial t^{\nu_1} \partial A^{\nu_2}} \|_0 \tag{29}$$

$$\|f\|_0 := \sup_{\substack{0 \leq t \leq 1 \\ 0 \leq A \leq 1}} |f(t, A)|$$

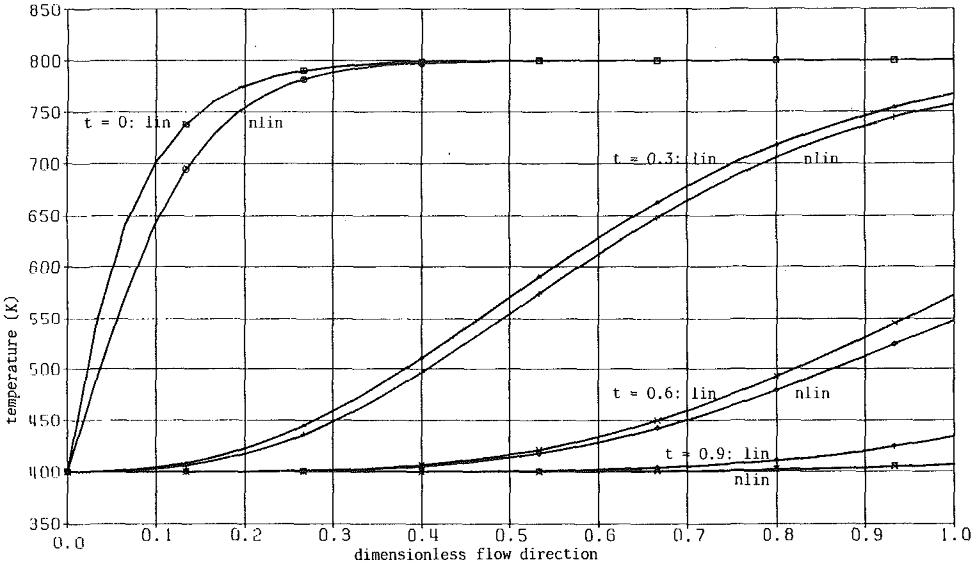

Fig. 6 Single blowup: comparison of the fluid outlet temperature according to the linear (lin) and nonlinear (nlin) theory at different times (t)

Similarly, we define $C^k([0, 1])$ and its norm $|g|_k$.

Because of the fact that our solution of equation (27) is given by an integral representation with holomorphic kernel functions (see equation (5)), we can easily derive the following a priori estimate

$$\|\Theta\|_k \leq c_k(\|f\|_0 + |g^*|_0 + |h|), \tag{30}$$

where Θ is the solution of equation (27) with f, g^*, h the corresponding functions on the right-hand side and $c_k > 0$ is a constant dependent on k but which does not depend on f, g^*, h. Now we are able to prove the convergence of the series $\Sigma\Theta_n(t, A)\epsilon^n$ with respect to an arbitrary C^n norm, i.e., $\|\Sigma\Theta_n\epsilon_n\|_k < \infty$. Let $k \geq 1$ be arbitrary, but fixed.

From equation (30) we get for Θ_0 according to equation (26)

$$\|\theta_0\|_k \leq c_k|h| = c_k =: \delta_0(k) \tag{31}$$

and assuming that we have constructed the estimates

$$\|\Theta_m\|_k \leq \delta_m(\mathrm{k}), \qquad 0 \leq m \leq n-1 \tag{32}$$

already, we get for $n \geq 1$

$$\begin{aligned}\|\Theta_n\|_k \leq c_k\Bigg(c_1^* \sum_{\nu_1+\nu_2=n-1} \Big\|\Theta_{\nu_1}\frac{\partial\Theta_{\nu_2}}{\partial t}\Big\|_0 \\ + c^*{}_1 \sum_{\nu_1+\nu_2=n-1} |\Theta_{\nu_1}\Theta_{\nu_2}|_0\Bigg) \\ \leq c_k c_1^*\Bigg(\sum_{\nu_1+\nu_2=n-1}[\|\Theta_{\nu_1}\|_0\|\Theta_{\nu_2}\|_1 + |\Theta_{\nu_1}|_0|\Theta_{\nu_2}|_0]\Bigg) \\ \leq 2c_k c_1^* \sum_{\nu_1+\nu_2=n-1} \delta_{\nu_1}\delta_{\nu_2} =: \delta_n(k)\end{aligned} \tag{33}$$

We want to show that the series $\Sigma\delta_n\epsilon^n$ is convergent for suitable values of ϵ. Because of equations (31)–(33) we know that it is a majorant of the series $\Sigma\Theta_n(t, A)\epsilon^n$ in any arbitrary C^k norm. Thus convergence of the perturbation series according to equation (25) will be established. Now we consider the quadratic equation

$$\tilde{\Theta} = 2c_k c_1^* \epsilon\tilde{\Theta}^2 + c_k \tag{34}$$

with $\tilde{\Theta}$ being the unknown variable. Equation (34) has a uniquely determined real solution

$$\tilde{\Theta} = \frac{1}{4c_k c_1^* \epsilon}\left(1 - \sqrt{1 - 8c_k^2 c_1^* \epsilon}\right) \tag{35}$$

which depends analytically on ϵ, if

$$|\epsilon| < \frac{1}{8c_k^2 c_1^*} \tag{36}$$

holds. On the other hand, we observe that the coefficients of the power series expansion of $\tilde{\Theta}$ with respect to ϵ

$$\tilde{\Theta} = \sum_{n=0}^{\infty} \alpha_n\epsilon^n \tag{37}$$

(which is convergent if ϵ satisfies equation (36)) may be recursively determined from the relations

$$\begin{aligned}\alpha_0 = c_k = \delta_0 \\ \ldots \\ \alpha_n = 2c_k c_1^* \sum_{\nu_1+\nu_2=n-1} \alpha_{\nu_1}\alpha_{\nu_2}\end{aligned} \tag{38}$$

It follows that we have $\alpha_n = \delta_n$ for all n and thus $\Sigma\alpha_n\epsilon^n$ represents a convergent majorant of our perturbation series $\Sigma\|\Theta_n\|_k|\epsilon|^n$ for values of ϵ satisfying equation (36). This completes the convergence proof.

Numerical Results. The comments that have been made with respect to the numerical procedure in the linear case do also apply here.

In order to investigate the effect of the nonlinearity in the regenerator equation due to the temperature dependence of the mass flow $\dot{m}$, we have studied the following simple test case:

We consider a standing regenerator core being uniformly heated, such that at time $t = 0$ we have $T_{M0} = 800$ K. This heated matrix is exposed to a cold air flow of $B = 400$ K; the heat transfer parameters correspond to some operating point of the engine at part load.

Figure 6 shows a comparison of the fluid temperature as calculated from equation (5) (corresponding to $\dot{m}$ = const) with the result of our nonlinear calculation ($\dot{m} = = \dot{m}(T)$) according to equation (25), where the perturbation series has been carried out up to the order of ϵ^6 ($c_1^* = 14.$, $c_2^* = 28.$, $\epsilon = 0.5$). The fluid temperature profiles in the dimensionless flow direction are depicted with the dimensionless time being a parameter. We see that at the regenerator exit the difference between both calculations is up to nearly 8 percent. So, for more subtle calculations, the effect of the temperature de-

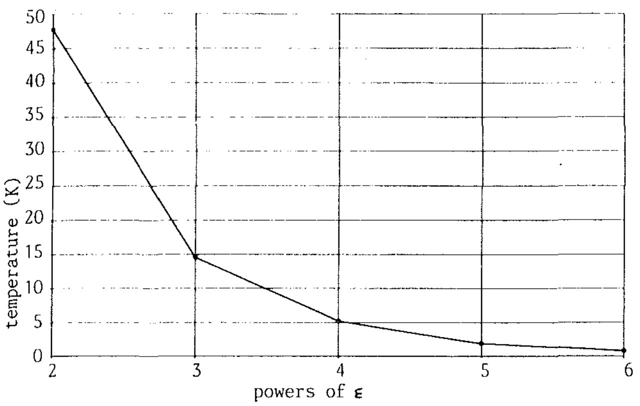

Fig. 7 Convergence of the perturbation series: $\|\Theta_{n-1}\,\epsilon^n\,T_{M0}\|_0$ plotted against *n*

pendence of the mass flow should not be ignored, which confirms a related conjecture stated by Braig (1984a).

In Fig. 7 we show the calculated norm $\|\Theta_{n-1}\epsilon^n T_{M0}\|_0$ in dependence of n, thus indicating numerically the fast convergence of the perturbation series.

Conclusions

- With the assumptions of classical regenerator theory (Braig, 1984a; Niggemann, 1986), which imply especially that the fluid mass flow is constant, an effective numerical scheme for calculating the transient performance of a rotating counterflow regenerator has been developed. The scheme is based on analytical representations of the matrix and fluid temperature, which have been derived by Niggemann (1986). Transient calculations have been performed for transition between different operation points via step changes and time ramps and for some frequency response (Huettner, 1987).
- In a more general setting, which allows the fluid mass flow to change with temperature, the regenerator equations become nonlinear. For the case of a standing regenerator core, these nonlinear PDEs have been solved by a perturbation series method, the convergence of which has been proved. The numerical evaluation of this solution has shown that for a subtle analysis of the regenerator performance the effect of the nonlinearity should not be neglected. The analytical treatment of the fully coupled nonlinear regenerator equations is planned to be covered in a forthcoming paper.

References

Anzelius, A., 1926, "Erwaermung vermittels durchstroemender Medien," *Zeitschr. Angew. Math. Mech.*, Vol. 6, No. 4, pp. 291-294.

Braig, W., 1984a, "Ein numerisches Verfahren zur Berechnung der Waermeuebertragung in rotierenden Speicherwaermetauschern bei instationaerem Betrieb—Teil 1," *Motortechnische Zeitschrift MTZ 45*, Vol. 6, pp. 263-267.

Braig, W., 1984b, "Ein numerisches Verfahren zur Berechnung der Waermeuebertragung in rotierenden Speicherwaermetauschern bei instationaerem Betrieb—Teil 2," *Motortechnische Zeitschrift MTZ 45*, Vol. 7/8.

Brandemuehl, M. J., and Banks, P. J., 1984, "Rotary Heat Exchangers With Time Varying or Nonuniform Inlet Temperatures," ASME *Journal of Heat Transfer*, Vol. 106, pp. 750-758.

Hempel, H., and Schmidt, D., 1983, "Multidimensional Digital Simulation of Rotating Regenerator Flow," ASME Paper No. 83- Tokyo-IGTC, pp. 91-96.

Huettner, W., 1987, "Berechnung des instationaeren Verhaltens eines rotierenden Speicherwaermetauschers," Diplomarbeit Institut fuer Luftfahrtantriebe, Universitaet Stuttgart, unpublished.

Itoh, T., et al., 1979, "Analytical Consideration of Fuel Economy and Dynamic Response of a Regenerative High Temperature Automobile Gas Turbine—Part 1," ASME Paper No. 79-GT-127.

Niggemann, M., 1986, "Analytical Solution for the Matrix- and Fluid-Temperature Distribution in Rotating Regenerators," ASME Paper No. 86-GT-198.

Umeda, A., and Hayama, S., 1977, "The Static and Dynamic Performance of Rotary Regenerators," ASME Paper No. 77-GT-9.

Yosida, K., 1971, *Functional Analysis*, Die Grundlehren der mathematischen Wissenschaften, Vol. 123, Springer, Berlin-Heidelberg-New York.

Ceramic Bearings for Use in Gas Turbine Engines

E. V. Zaretsky
NASA Lewis Research Center,
Cleveland, OH 44135
Fellow ASME

Three decades of research by U.S. industry and government laboratories have produced a vast array of data related to the use of ceramic rolling-element bearings and bearing components for aircraft gas turbine engines. Materials such as alumina, silicon carbide, titanium carbide, silicon nitride, and a crystallized glass ceramic have been investigated. Rolling-element endurance tests and analysis of full-complement bearings have been performed. Materials and bearing design methods have improved continuously over the years. This paper reviews a wide range of data and analyses with emphasis on how early NASA contributions as well as more recent data can enable the engineer or metallurgist to determine just where ceramic bearings are most applicable for gas turbines.

Introduction

Ceramic materials offer some potential advantages for rolling-element bearing components because of their capability of operating over a wide temperature range and their low density relative to rolling-element bearing steels. The low density of ceramics may make them attractive as ball or roller materials for very high-speed bearings. This benefit is due to the fact that the fatigue life of very high-speed ball bearings can be reduced as a result of excessive centrifugal force on the balls and subsequent increased stress at the outer race (Harris, 1968). Lower mass balls can diminish this fatigue life reduction.

Ceramic materials generally maintain their strength and corrosion resistance over a range of temperatures much greater than typical rolling-element bearing steels. Taylor et al. (1963) was the first to evaluate hot-pressed silicon carbide and hot-pressed alumina for rolling-element bearings to temperatures above 811 K (1000°F).

A crystallized glass ceramic was examined in rolling-element fatigue by Carter and Zaretsky (1960) and Zaretsky and Anderson (1961) of NASA Lewis Research Center. The results of these early tests showed that the failure mode of ceramics was similar to that in bearing steels. That is, the failure was cycle dependent and apparently of subsurface origin, occurring at the depth of the maximum shear stress. The failure manifested itself as a spall that was limited to the depth of the maximum shear stress and in diameter to the width of the contact zone. The life of the ceramic material was less than 10 percent that of a typical rolling-element bearing steel under the same conditions of stress. However, the scatter in life (time to failure) was much less than that experienced by bearing steels. Appledoorn and Royle (1965) confirmed these results in a later study.

Parker et al. (1965) of NASA also conducted studies with three ceramics and one cermet for high-temperature, rolling-element bearing applications. The ceramic materials were hot-pressed and cold-pressed alumina, both 99 percent pure, and a two-phase sintered silicon carbide. Endurance tests were also conducted with the hot-pressed alumina to 1367 K (2000°F). The time to failure for the ceramics was found to have less scatter than for bearing steels. The mode of failure was a spall, which was attributed to a surface condition rather than subsurface shear stresses. Hot-pressed alumina performed the best of the four materials. However, the life of this material was only 7 percent that of a typical bearing steel at the same condition of stress. It was concluded that the life of these refractory ceramic materials was related to the porosity, surface finish, and homogeneity of the material (Parker et al., 1965).

Baughman and Bamberger (1963) performed unlubricated high-temperature bearing studies to 922 K (1200°F) in the rolling-contact (R-C) tester and full-scale needle bearings. They tested the following materials: Star-J and Stellite 25 (super alloys) and silicon carbide and alumina ceramics. The silicon carbide was shown to be the most wear-resistant material. However, the silicon carbide material lacked homogeneity, which resulted in nonuniform results.

In 1970, hot-pressed silicon nitride was proposed for rolling-element bearings as well as for journal bearings (Dee, 1970). Rolling-element fatigue testing of hot-pressed silicon nitride has resulted in seemingly contradictory results. Poor results were obtained in the limited tests reported in Scott et al. (1971) and Scott and Blackwell (1973). The results reported in Baumgartner (1973) and Baumgartner et al. (1973) showed the rolling-element fatigue life of hot-pressed silicon nitride to exceed that of a typical rolling-element bearing steel. Extrapolation of the experimental results of Parker and Zaretsky (1975) to contact loads that result in stress levels typical of those in rolling-element bearing applications indicate that hot-pressed silicon nitride running against steel may be expected to yield fatigue lives comparable to or greater than those of bearing quality steel running against steel.

Concurrent with the work of Dee (1970), Scott et al. (1971), Scott and Blackwell (1973), Baumgartner (1973), Baumgartner et al. (1973), and Parker and Zaretsky (1975), hybrid bearings comprising silicon nitride rolling-elements and steel races were

---

Contributed by the International Gas Turbine Institute and presented at the 33rd International Gas Turbine and Aeroengine Congress and Exhibition, Amsterdam, The Netherlands, June 5–9, 1988. Manuscript received by the International Gas Turbine Institute January 15, 1988. Paper No. 88-GT-138.

Table 1 Stress-life exponent and relative dynamic capacity of materials for rolling-element bearing application

Material	Stress-life exponent, n	Dynamic capacity relative to steel
Crystallized glass ceramic[a]	10.5 to 13.8 (Average value, 11.6)	0.07
Hot-pressed alumina[b]	9.4 to 10.8 (Average value, 10.6)	0.07
Cold-pressed alumina[b]	6.0 to 8.1 (Average value, 7)	0.01
Self-bonded silicon carbide[b]	6.9 to 8.6 (Average value, 7.8)	0.01
Nickle-bonded titanium carbide[b]	9.7 to 10.5 (Average value, 10.2)	0.03
Silicon nitride[c]	16 to 16.2 (Average value, 16.1)	0.05 to 0.12
Bearing steel	9 to 10 (Accepted value, 9)	1.00

[a] Carter, et al. (1960); Zaretsky, et al. (1961).
[b] Parker, et al. (1965).
[c] Baumgartner, et al. (1973); Parker, et al. (1975); Parker, et al. (1974).

manufactured and tested (Baumgartner et al., 1973; Baumgartner et al., 1976; Baumgartner and Cowley, 1975; Reddecliff and Valori, 1976; Miner et al., 1981) as well as silicon nitride rolling-elements and rings (Baumgartner et al., 1973; Miner et al., 1981; Hosang, 1987; Bailey, 1983).

In view of the aforementioned it is the objective of the work reported herein to summarize the data and analyses related to ceramic bearings for use in gas turbine engines. Emphasis is placed on how early NASA contributions as well as more recent data can enable the engineer or metallurgist to determine just where ceramic bearings are most applicable for future gas turbine engines.

Effect of Contact Stress

It has long been established that the rolling-element fatigue life $\bar{L}$ of a rolling element is inversely proportional to stress S, to a power n, that is,

$$\bar{L} \sim S^{-n} \qquad (1)$$

For bearing steels the accepted value in the bearing industry for the stress-life exponent is 9 to 10. However, variations in this value have been noted and may be a function of material processing (Parker and Zaretsky, 1972a). A summary of the stress-life exponents for the ceramic and cermet materials tested for rolling-element bearing application, which were compiled from Carter and Zaretsky (1960), Zaretsky and Anderson (1961), Parker et al. (1965), and Baumgartner et al. (1973), are summarized in Table 1.

When steel and other metallic materials are tested at different stress levels, direct comparisons of fatigue lives can be made only by adjusting one of the lives using the proper stress-life exponent for that material (given in Table 1), or by making a comparison on the basis of dynamic load capacity. The dynamic load capacity, contact load, and life are related by the equation (Lundberg and Palmgren, 1947; Lundberg and Palmgren, 1949; Lundberg and Palmgren, 1952)

$$C = P \sqrt[n/3]{\bar{L}} \qquad (2)$$

where

C = dynamic load capacity or load that will produce failure of 10 percent of test specimen in 1 million stress cycles, N (lb)
P = applied or equivalent bearing load, N (lb)
n = exponent relating stress and life, determined experimentally
$\bar{L}$ = life, in millions of stress cycles, that 90 percent of a group of specimens survive or within which time 10 percent fail

For steels, $n/3$ is usually taken as 3 (based on a stress-life exponent of 9). The values of n for each of the materials can be obtained from Table 1. The relative dynamic capacities for each of the ceramic materials are then given based upon typical bearing steels. Knowing the dynamic capacity of an equivalent steel bearing, the value of the steel bearing can be multiplied by the relative dynamic capacity of the selected material from Table 1. Using the resultant value, the applicable stress-life exponent n, and the applied bearing load P, in equation (1), an estimate of the ceramic bearing life $\bar{L}$ in millions of inner-race revolutions can be obtained.

There are conflicting data with regard to the life of the silicon nitride material. Figure 1 (Parker and Zaretsky, 1974) shows a comparison of life data for hot-pressed silicon nitride and for typical bearing steels, consumable-electrode vacuum melted (CVM) AISI 52100 and AISI M-50 (Parker and Zaretsky, 1972b) at a maximum Hertz stress of 5.52×10^9 N/m^2 (800,000 psi). The 10-percent fatigue life of the silicon nitride balls was approximately 1/8 that of the AISI 52100 balls and approximately 1/5 that of the AISI M-50 balls. Figure 2 (Baumgartner et al., 1973) shows results from the rolling-contact fatigue (R-C) tester for silicon nitride and AISI M-50.

Nomenclature

C = dynamic load capacity, N (lb)
$E = \left[\frac{1}{2} + \frac{Ys(1-\delta_c^2)}{2Yc(1-\delta_s^2)}\right]$
e = Weibull slope or modulus
$K_1 = \left[\frac{3P_0R}{8}\right]^{1/3}$, N$^{1/2}M^{1/3}$ (in.$^{1/3}$lb$^{1/3}$)
$K_2 = \frac{3}{8\pi}\left[\frac{P_0}{9R^2}\right]^{1/3}$, N$^{1/3}M^{1/3}$ (psi$^{1/3}$)
$\bar{L}$ = life, h, millions of inner-race revolutions or millions of stress cycles
$\bar{L}_{HR}$ = relative life, hybrid bearing
m = temperature-life exponent
$N = 4(1-\delta^2)/Y$, M^{2}N^{-1} (psi^{-1})
n = stress-life exponent
P = applied or equivalent bearing load, N (lb)
P_0 = normal load, N (lb)
R = radius of a sphere, m (in.)
r = Hertzian contact radius, m (in.)
S = Hertzian contact stress, N/m^2 (psi)
T = temperature, K (R)
V = stressed volume, m^3 (in.^{3})
Y = Young's modulus of elasticity, N/m^2 (psi)
Z = depth to maximum shear stress, m (in.)
δ = Poisson ratio
τ = maximum shear stress, N/m^2 (psi)

Subscripts

a, b = bodies a and b
c = ceramic material
H = hybrid bearing
s = steel material or steel bearing

These results show that the life of the AISI M-50 material was approximately 1/8 the life of the silicon nitride material at a maximum Hertz stress of 4.83×10^9 N/m^2 (700,000 psi). However, the data for Baumgartner et al. (1973) and Parker and Zaretsky (1974) show a stress-life exponent n of 16.2 and 16, respectively. Based upon both sets of data, the dynamic capacity (or load carrying ability) of the silicon nitride material would be significantly less than that of a typical bearing steel. This is shown in Table 1, where relative C values have been calculated and compared to a bearing steel.

Effect of Elastic Properties

The physical and thermal properties of ceramic and cermet materials considered for rolling-element bearing application are given in Table 2. The properties are a compilation (Carter and Zaretsky, 1960; Parker et al., 1965; Parker and Zaretsky, 1974; Parker et al., 1964a; 1964b; Sibley et al., 1960; Bhushan and Sibley, 1982). The elastic modulus of most ceramics is much greater than that of a bearing steel. Consequently, the resultant contact or Hertz stress will be different for a given loading of ceramic on ceramic, a ceramic on steel, or steel on steel. This was first recognized by Carter and Zaretsky (1960) in their work with a crystallized glass ceramic. For the case of a ceramic on steel, it is assumed that the ceramic material will have infinite life and that the steel races will be the element to fail from rolling-element fatigue. Since life is inversely proportional to stress to a power, the life of a hybrid bearing (ceramic rolling element on steel races) will generally be lower than that for a full-complement steel bearing. This can be illustrated as follows:

From Hertz theory for two spheres of radii R_a and R_b in contact (Jones, 1946), the maximum compressive stress is

$$S_{\max} = \frac{3P_0}{2\pi r^2} \tag{3}$$

where P = normal load; r = contact radius. For two spheres in contact the Hertzian contact area is a circle with radius

$$r = \left[\frac{3P_0(N_a + N_b)}{8\left(\dfrac{2}{R_a} + \dfrac{2}{R_b}\right)} \right]^{1/3} \tag{4}$$

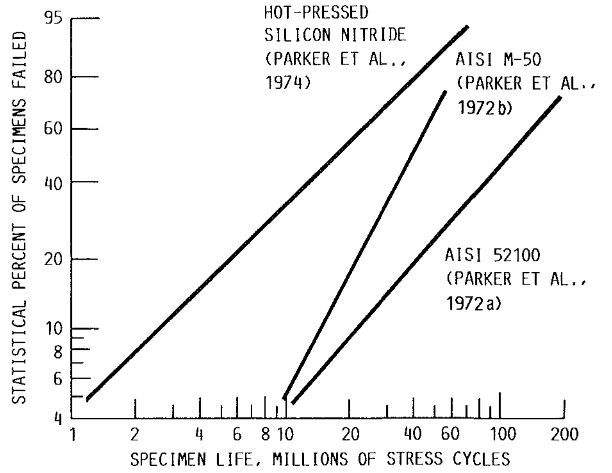

Fig. 1 Rolling-element fatigue life of hot-pressed silicon nitride balls and steel balls in five-ball fatigue tester. Maximum Hertz stress, 5.52×10^9 N/m^2 (800,000 psi); shaft speed, 9400 rpm; race temperature, 328 K (130°F); contact angle, 30 deg; lubricant, super-refined naphthenic mineral oil (Parker et al., 1974).

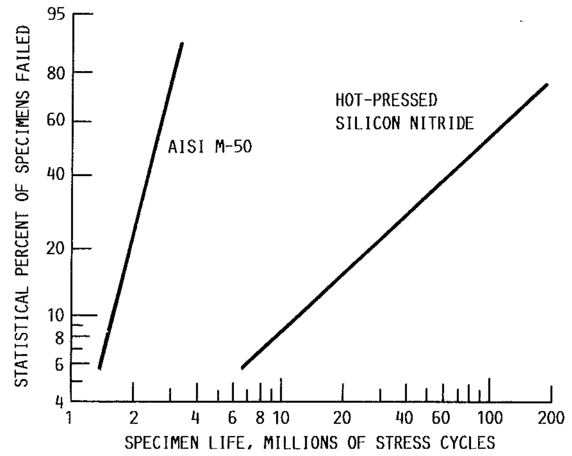

Fig. 2 Rolling-element fatigue life of hot-pressed silicon nitride rollers in rolling-contact (R-C) fatigue tester. Maximum Hertz stress, 4.83×10^9 N/m^2 (700,000 psi); roller speed, 10,000 rpm; temperature, ambient; lubricant, triester (MIL-L-23699B) (Baumgartner et al., 1973).

Table 2 Typical physical and thermal properties of materials for rolling-element bearing application (Carter et al., 1960; Zaretsky et al., 1961; Parker et al., 1965; Baumgartner et al., 1973; Parker et al., 1975; Parker et al., 1974; Parker et al., 1964; Bhushan et al., 1982)

Material	Rockwell C hardness at 294 K (70 °F)	Estimated[a] maximum usable bearing temperature, K (°F)	Density, gm/cc	Elastic modulus at 294 K (70 °F), GPa (10^6 psi), Y	Poisson's ratio, δ	Thermal conductivity, w/mK (BTu ft/hr-ft^2-F) at		Coefficient of thermal expansion, 10^{-6} K (10^{-6}/°F) 273 to 1073 K (32 to 1471 °F)	Weibull[b] slope or modulus, e
						294 K (70 °F)	1073 K (1471 °F)		
Crystallized glass ceramic	53	>644 (700)	2.5	87 (12.5)	0.25	1.6 (0.9)	2.0 (1.2) at 873 K (1112 °F)	0.4 (0.2)	3.3
Alumina	85	~1367 (2000)	3.9	350 (51)	0.25	7.2 (4.2)	1.7 (1.0)	8.5 (4.7)	2.7
Silicon carbide	90	<1367 (2000)	3.2	410 (59)	0.25	35 (20)	12 (6.9)	5.0 (2.8)	2.1
Nickle-bonded titanium carbide	67	<867 (1100)	6.3	390 (57)	0.23	14 (8.1)	6.8 (3.9)	10.7 (5.9)	1.4
Silicon nitride	78	~1367 (2000)	3.11 to 3.24	310 (45)	0.26	7.3 (4.2)	4.7 (2.7)	2.9 (1.6)	1.7
Bearing steel (AISI M-50)	~63	>589 (600)	7.6	190 (28)	0.28	13.4 (7.7)	-----	12.3 (6.8)	1.1

[a] Based primarily on hardness retantion and test experience.
[b] Based upon rolling-element fatigue testing.

Table 3 Relative life and dynamic capacity of hyrbid bearing with various rolling-element materials

Raceway material	Rolling element material	Relative life from Eq. (10),[a] L_{HR}	Relative dynamic capacity to steel from Eq. (2),[a] n = 9
Steel	Crystallized glass ceramic	18	2.6
	Alumina	0.22	0.6
	Silicon carbide	0.16	0.5
	Nickle-bonded titanium carbide	0.18	0.6
	Silicon nitride	0.29	0.7
	Steel	1	1

[a] Based upon failure of steel raceway and assuming no failure of rolling elements.

For two spheres of equal radius

$$R_a = R_b = R$$

Then

$$r = \left[\frac{3P_0 R(N_a + N_b)}{32}\right]^{1/3} \tag{5}$$

where

$$N_a = \frac{4(1-\delta_a^2)}{Y_a}$$

$$N_b = \frac{4(1-\delta_b^2)}{Y_b}$$

and Y = modulus of elasticity; δ = Poisson ratio. Then

$$r = K_1\left[\frac{1-\delta_a^2}{Y_a} + \frac{1-\delta_b^2}{Y_b}\right]^{1/3}$$

$$= K_1\left[\frac{Y_b(1-\delta_a^2) + Y_a(1-\delta_b^2)}{Y_a Y_b}\right]^{1/3} \tag{6}$$

where

$$K_1 = \left[\frac{3P_0 R}{8}\right]^{1/3}$$

Substituting equation (6) into equation (3)

$$S_{\max} = K_2\left[\frac{Y_a Y_b}{Y_b(1-\delta_a^2) + Y_a(1-\delta_b^2)}\right]^{2/3} \tag{7}$$

where

$$K_2 = \frac{3}{8\pi}\left[\frac{P_0}{9R^2}\right]^{1/3}$$

For steel on steel

$$S_{\max_s} = K_2\left[\frac{Y_s}{2(1-\delta_s^2)}\right]^{2/3} \tag{8}$$

The relative life $\bar{L}_{HR}$ for the same load on a steel bearing and a hybrid bearing would be as follows:

$$\frac{\bar{L}_{HR}}{\bar{L}_s} = \left(\frac{S_{\max_s}}{S_{\max_H}}\right)^n \tag{9}$$

Letting $\bar{L}_s = 1$ and $n = 9$ and substituting equation (8) into equation (9)

$$\bar{L}_{HR} = \left[\frac{1}{2} + \frac{Y_s(1-\delta_c^2)}{2Y_c(1-\delta_s^2)}\right]^6 \tag{10}$$

Equation (10) is a stress correction factor based upon a ninth power of the ratio of the Hertz stress in the contact of a ceramic or cermet ball or roller and a steel race to that of a steel rolling element on a steel race for identical contact load and geometry. The factor $\bar{L}_{HR}$ for various rolling-element materials is listed in Table 3. $\bar{L}_{HR}$ can be multiplied by the calculated life of a full-complement or all-steel rolling element bearing to obtain the life of a hybrid bearing using the applicable material in Table 3 as the rolling elements. This simplified correction neglects the effect of stressed volume on fatigue life. However, this effect is found to be small relative to the stress effect. In fact, it is easily shown that the small stressed volume effect is nearly offset by the additional effect of the depth of the maximum shear stress (Parker and Zaretsky, 1975). From the Lundberg–Palmgren analysis (Lundberg and Palmgren, 1947; Lundberg and Palmgren, 1949; Lundberg and Palmgren, 1952)

$$\frac{\bar{L}_{HR}}{\bar{L}_s} = \left(\frac{Z_H}{Z_s}\right)^{2.1}\left(\frac{V_s}{V_H}\right)^{0.9}\left(\frac{\tau_s}{\tau_H}\right)^{9.3} \tag{11}$$

where $\bar{L}$ = contact life; Z = depth to maximum shear stress; V = stressed volume; τ = maximum shear stress.

From the Hertzian equations for line contact (Jones, 1946) where the ellipticity ratio is 0 and from equation (10), letting

$$E = \left[\frac{1}{2} + \frac{Y_c(1-\delta_c^2)}{2Y_c(1-\delta_s^2)}\right] \tag{12}$$

then

$$\frac{Z_H}{Z_s} = E^{2/3} \tag{13}$$

$$\frac{V_s}{V_H} = E^{-2/3} \tag{14}$$

$$\frac{\tau_s}{\tau_H} = E^{2/3} \tag{15}$$

Substituting equations (12) to (15) into equation (11) and letting $\bar{L}_s = 1$, then for line contact,

$$\bar{L}_{HR} = \left[\frac{1}{2} + \frac{Y_s(1-\delta_c^2)}{2Y_c(1-\delta_s^2)}\right]^{6.97} \tag{16}$$

For point contact where the ellipticity ratio is 1 (Jones, 1946),

$$\frac{Z_H}{Z_s} = E^{1/3} \tag{17}$$

$$\frac{V_s}{V_H} = E^{-2/3} \tag{18}$$

$$\frac{\tau_s}{\tau_H} = E^{2/3} \tag{19}$$

Equations (18) and (19) are identical to equations (14) and (15), respectively. Substituting equations (12) and (17) to (19) into equation (11) and letting $\bar{L}_s = 1$, for point contact,

$$\bar{L}_{HR} = \left[\frac{1}{2} + \frac{Y_s(1-\delta_c^2)}{2Y_c(1-\delta_s^2)}\right]^{6.3} \tag{20}$$

Using equation (10) and the elastic properties listed in Table

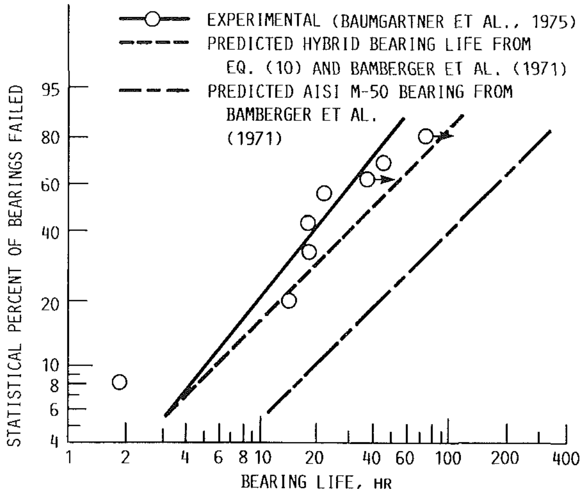

Fig. 3 Comparison of the experimental and predicted lives of hybrid 57-mm bore cylindrical roller bearing. Radial load, 22464 N (5050 lb): maximum Hertz stress, 2.82×10^9 N/m^2 (408,000 psi); shaft speed, 5400 rpm; lubricant triester; outer-race temperature, 380 K (225°F).

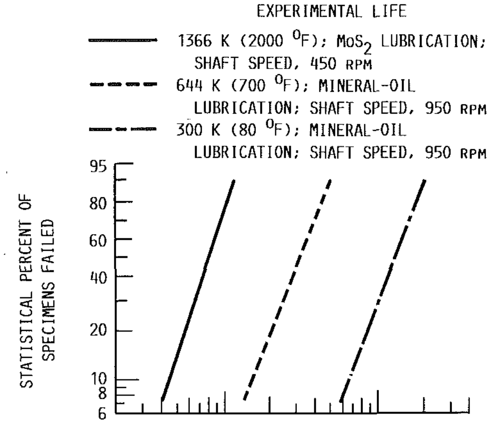

(A) LIFE DISTRIBUTION AT TEMPERATURE.

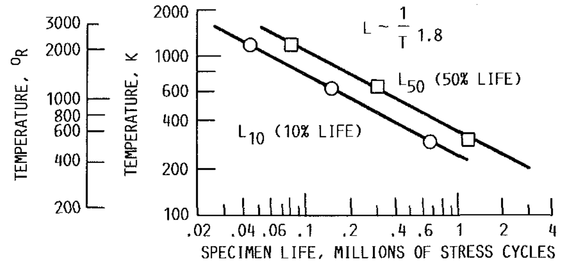

(B) EFFECT OF TEMPERATURE.

Fig. 4 Rolling-element fatigue life of hot-pressed alumina balls in five-ball fatigue tester. Maximum Hertz stress, 3.39×10^9 N/m^2 (550,000 psi); contact angle, 20 deg (Parker et al., 1965).

2, the relative lives and dynamic capacities of a hybrid bearing comprising rolling elements of the materials listed are given in Table 3.

Hybrid 57-mm-bore cylindrical roller bearings each containing 20 crowned, 7.1-mm-dia silicon nitride rollers were endurance tested (Baumgartner and Cowley, 1975). The bearing rings were consumable-electrode vacuum-melted (CVM) AISI M-50. Test conditions were at an outer-race temperature 366 to 380 K (200 to 225°F), a radial load of 22 464 N (5050 lb) producing a maximum Hertz stress of 2.82×10^9 N/m^2 (408,000 psi), a shaft speed of 5400 rpm, and a triester lubricant (MIL-L-23699B). The catalog life of an equivalent steel bearing was calculated to be 21.6 h without any life adjustment factors (Baumgartner and Cowley, 1975). Using the ASME design guide (Bamberger et al., 1971), the following life adjustment factors are obtained: (*a*) material factor, 2; (*b*) processing factor, 3; and (*c*) lubricant factor, 1.5. Combining these factors ($2 \times 3 \times 1.5$), a life adjustment factor of 9 can be used for a CVM AISI M-50 steel bearing under these operating conditions. The adjusted predicted life of an all-steel bearing would equal 194.4 (9×21.6) h at a 90-percent probability of survival. From equation (10) and Table 3 for silicon nitride, the life adjustment factor for the hybrid bearing is 0.29. Hence, the predicted life of the hybrid roller bearing would be 56.4 (0.29×194.4) h. Using equation (16) for line contact, and equation (20) for point contact, the predicted lives would be 46.7 (0.24×194.4) and 53.5 (0.28×194.4) h, respectively. From Fig. 3, the life of the hybrid bearing was approximately 48 h. There were an unusual number of silicon nitride roller failures and roller damage in many of the failed bearings including roller fracture. These results would indicate that the high Hertzian stress at which the bearing was run exceeded the capability of the silicon nitride material.

Effect of Temperature

Lubricated rolling-element tests were conducted in the NASA five-ball fatigue tester with the crystallized glass ceramic, hot-pressed alumina, cold-pressed alumina, self-bonded silicon carbide, and nickle-bonded titanium carbide at temperatures to 1366 K (2000°F) (Carter and Zaretsky, 1960; Zaretsky and Anderson, 1961; Parker et al., 1965; Parker et al., 1964a, 1964b). The crystallized ceramic was only tested to 644 K (700°F) (Carter and Zaretsky, 1960; Zaretsky and Anderson, 1961). There are no fatigue results reported for silicon nitride beyond nominal temperature under lubricated conditions. Shorter lives were exhibited at 644 K (700°F) for these materials. This decrease in life may be accounted for by a change in lubricant viscosity with temperature. As the viscosity of the lubricant decreases any elastohydrodynamic film separating the rolling elements will decrease. The life of a rolling element in addition to its own material properties is a function of the elastohydrodynamic film thickness (Bamberger et al., 1971). Hence, the life of these materials may be affected in a manner similar to steel.

Three materials were run in a modified five-ball fatigue tester to temperatures of 1366 K (2000°F) with molybdenum disulfide-argon mist lubrication (Parker et al., 1965; Parker et al., 1964a, 1964b). The results of these tests indicated that the hot-pressed alumina was capable of operating to temperatures of 1366 K (2000°F). However, tests with the cold-pressed alumina and silicon carbide at 1366 K (2000°F) and maximum Hertz stresses of 1.66×10^9 N/m^2 (270,000 psi) resulted in general track deterioration unlike the failure pits or spalls observed at 300 and 644 K (80 and 700°F). Titanium carbide cermet at temperatures beyond 866 K (1100°F) and a maximum Hertz stress of 1.91×10^9 N/m^2 (310,000 psi) exhibited excess cumulative plastic deformation, which indicated that this material is limited to less severe conditions of temperature and stress.

Surface-failure data with hot-pressed alumina tested at 1366 K (2000°F) and a maximum Hertz stress of 3.39×10^9 N/M^2 (550,000 psi) are given in Fig. 4(*a*) together with the experimental lives at 300 and 644 K (80 and 700°F) (at the same stress) but with a mineral-oil lubricant. Figure 4(*b*) is a plot of the 10- and 50-percent lives of the material as a function of temperature. While the mode of lubrication at the lower temperatures and 1366 K (2000°F) is different, the figure provides not only a relative indication of the life performance of the hot-pressed alumina to 1366 K (2000°F) but also of the other refractory materials with temperature where $\bar{L} \sim 1/T^m$. From Fig. 4(*b*), $m = 1.8$; temperature is in Kelvin or Rankine units.

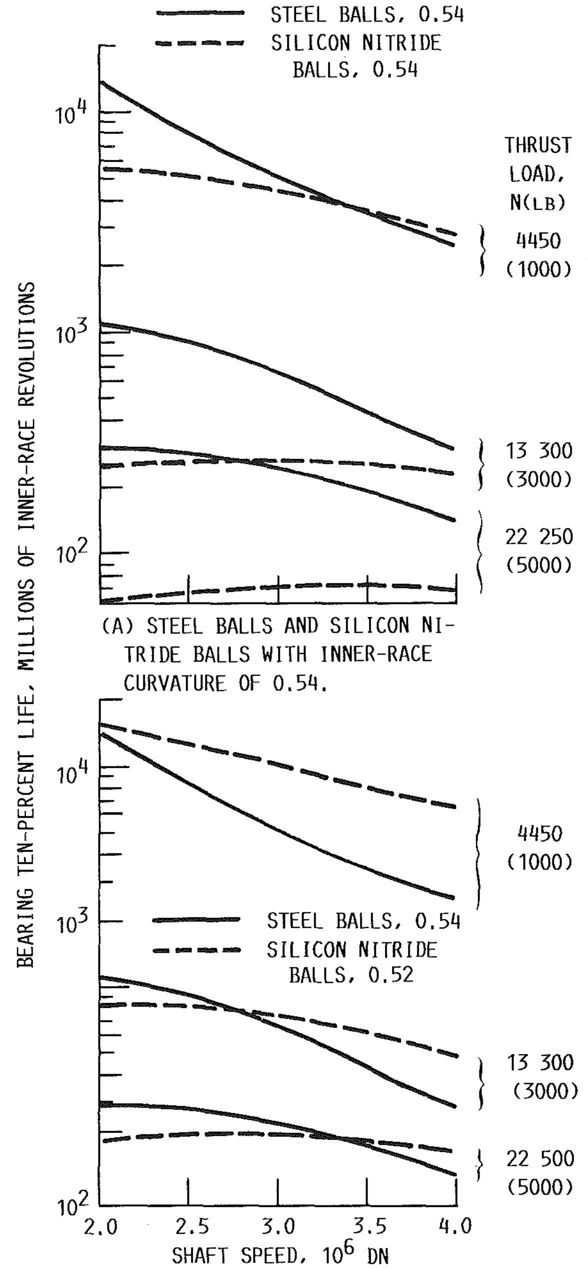

(A) STEEL BALLS AND SILICON NITRIDE BALLS WITH INNER-RACE CURVATURE OF 0.54.

(B) STEEL BALLS AND SILICON NITRIDE BALLS WITH INNER-RACE CURVATURES OF 0.54 AND 0.52, RESPECTIVELY.

Fig. 5 Predicted life of 120 mm bore angular contact ball bearing with silicon nitride balls. Ball diameter, 20.64 mm (0.8125 in.) (Parker et al., 1975).

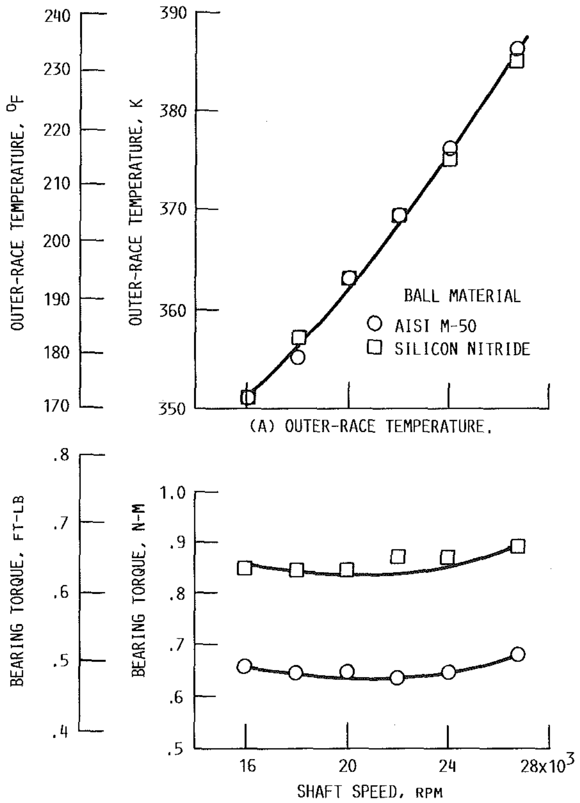

(A) OUTER-RACE TEMPERATURE.

(B) BEARING TORQUE.

Fig. 6 Performance of 75 mm bore angular-contact ball bearing as function of shaft speed. Thrust load, 4400 N (989 lb), oil flow rate, 0.9 kg/min (2 lb/min) oil inlet temperature 316 K (109°F).

Effect of Speed on Life

At high aircraft turbine engine speeds, the effect of centrifugal loading of the rolling elements of a bearing against the bearing outer race becomes extremely important. Theoretical life calculations for a 150-mm bore angular-contact ball bearing operating at 3 million DN (20,000 rpm) (DN is bearing speed in rpm × bearing bore in mm) predict that this bearing has approximately 20 percent AFBMA-calculated life (Scibbe and Zaretsky, 1971). The decrease in predicted life is due to the increased stress in the outer race caused by centrifugal effects. The expected final result is extremely short bearing life at speeds much above 2 million DN both in actual running time (h) and in total bearing inner-race revolutions. In order to reduce the centrifugal force effects, concepts such as hollow and hollowed rolling elements and lightweight ceramic rolling elements have been considered as a substitute for the conventional rolling elements contained within the bearing. Silicon nitride has been one such material.

Computer analysis of the dynamic performance characteristics of ball bearings was used to evaluate the effect of the low-mass silicon nitride balls on 120-mm bore angular-contact ball bearing fatigue life (Parker and Zaretsky, 1975). The analysis was performed with both steel and silicon nitride balls with steel inner and outer races. Figure 5 is a summary of the results for three thrust loads. In general, this analysis indicates that the use of silicon nitride balls to replace steel balls in high-speed bearings will not yield an improvement in fatigue life over the speed range of anticipated advanced air-breathing engine main-shaft ball bearings up to 3 million DN. However, at some conditions of very high speeds and light loads, modest life improvements are indicated, but only if modifications are made in bearing internal geometry (inner-race curvature, for example) (Parker and Zaretsky, 1975).

Bearing life calculations were made with reduced curvature at the inner race (0.52 as opposed to 0.54) (Parker and Zaretsky, 1975). With the exception of very low loads and very high speeds, the life improvements over the steel ball cases are small. For the case of 3 million DN and 13,300 N (3000 lb) thrust load, the life improvement is less than 14 percent (Parker and Zaretsky, 1975).

Heat Generation and Temperature

In a discussion to Reddecliff and Valori (1976), Coe and Zaretsky reported results obtained with a 115 series, 75-mm-bore ball bearing with steel balls operated at a 4400 N (1000 lb) thrust load up to 2.0×10^6 DN at NASA. The steel balls were then replaced with silicon nitride balls and the test repeated.

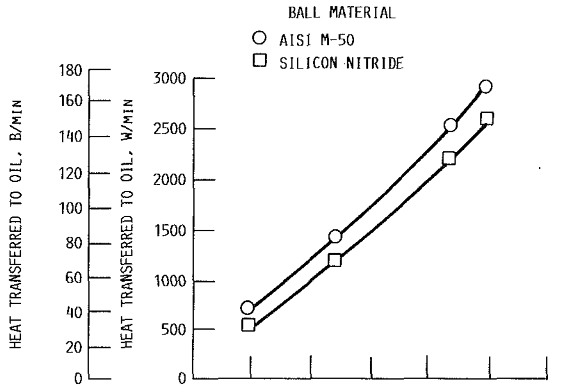

(A) POWER LOSS.

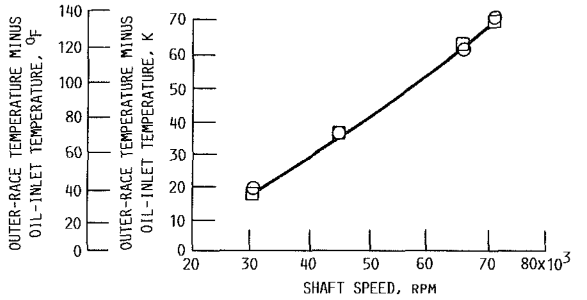

(B) OUTER-RACE TEMPERATURE.

Fig. 7 Performance of 35 mm bore angular-contact ball bearing as a function of shaft speed. Thrust load, 1200 N (270 lb); oil flow rate, 1.1 kg/min (2.5 lb/min); oil inlet temperature, 399 K (150°F) (Reddecliff et al., 1976)

Figure 6(*a*) is a comparison of the outer-race temperature for both bearings over a range of shaft speed. The outer-race temperature was almost the same for both silicon nitride and the steel balls. However, Fig. 6(*b*) is a comparison of the bearing torque over the same speed range. It is apparent that the bearing with silicon nitride balls showed significantly higher torque than the same bearing with steel balls. The torque was measured directly by a force transducer connected to the periphery of the bearing housing. The higher torque with the silicon nitride balls can be explained in part by the fact that the traction coefficient of a lubricant is a function of the viscosity of the oil under the contact pressure (Loewenthal and Zaretsky, 1985). Since for a given load, the contact stress with the silicon nitride balls are higher than with the steel balls, the viscosity of the oil in the contact zone is higher. Because of the higher viscosity, the traction in the contact zone of the bearing must be accordingly higher.

It was reported by Reddecliff and Valori (1976) that a 33-percent reduction in axial preload to prevent skidding in a 35-mm-bore angular-contact ball bearing was achieved by substituting silicon nitride balls for steel balls. This would tend to substantiate that a higher traction force in the bearing may exist with a given load as a result of the higher viscosity with higher contact stress. Higher traction forces should result in higher heat generation with the silicon nitride balls. However, data reported in Reddecliff and Valori (1976) (Fig. 7) show that with the silicon nitride balls in the 35-mm bearing, the heat generation was lower (Fig. 7(*a*) even though the outer-race temperatures were almost identical (Fig. 7*b*).

There are possible explanations for the difference in these results. There could, of course, be an effect due to bearing size. For example, the computer program used in Parker and Zaretsky (1975) indicates that about 60 percent of the calculated heat generation was due to ball spin for a 35-mm-bore bearing, whereas it was about 50 percent for a 120-mm-bore bearing. Further, the oil used for the 75-mm bearing tests was super-refined napthenic mineral oil with undoubtedly different viscosity characteristics from those of the oil used in Reddecliff and Valori (1976). Also, the 75-mm bearings were lubricated directly by oil jet, not through the race, as were those of Reddecliff and Valori (1976). Finally, it should be noted that the diameter of the silicon nitride balls used in the 75-mm bearing differed less than 0.5 μm (20 μin.) from the steel balls, at room temperature. Therefore, at operating temperature, the bearings were slightly different, due to the lower coefficient of expansion of the silicon nitride.

Data were reported for AISI M-50 35-mm roller bearings (Baumgartner et al., 1976) comparing the heat generated in a hybrid roller bearing with the same size bearing having steel rollers and approximately the same radial load. It was concluded in Baumgartner et al. (1976) that the heat generation for the hybrid bearing was comparable to that of the bearing with the steel rollers. It can be concluded that the bearing power loss or heat generation is more a function of the individual bearing design and operation than whether steel or ceramic rolling elements are used within the bearing.

Unlubricated Bearings

It has been proposed that unlubricated ceramic bearings offer an approach toward meeting operating requirements in excess of 578 K (600°F) where both conventional and nonconventional liquid lubricants are not capable of sustaining these higher temperatures nor of providing an elastohydrodynamic film. Tests of full-complement 17-mm-bore silicon nitride cylindrical roller bearings were performed at 644 K (700°F) (Bailey, 1984). The test vehicle used to evaluate these bearings was a modified J402 Turbojet engine. The first test resulted in a catastrophic bearing failure after 11-1/2 min of operation due to fracture of the ceramic. The second test ran for a total time of 2 h and 3 min of which 54 min were run unlubricated. In the unlubricated condition, 30 min were run at shaft speeds between 39,000 and 39,600 rpm or in excess of 660,000 DN. However, residual lubricant may have been present to sustain the bearing for the 54 min. A totally unlubricated endurance test was run with a René 41 gold-plated cage. A catastrophic failure was encountered after 30 min of operation due to fracture of the ceramic.

Solid film lubricants applied in a manner similar to that reported in Parker et al. (1965) may be capable of sustaining full complement ceramic roller bearings at these higher temperatures for longer periods of time. However, extensive work is required both to prove and to develop this concept for practical turbine engine applications.

Bearing Mounting

The use of full complement ceramic rolling-element bearings presents unique mounting problems. Referring to Table 2, the thermal expansions of the refractory materials are less than that of steel. As a result, where a ceramic bearing is mounted on a steel shaft, large hoop stresses can be induced in the bearing inner ring which can result in fracture of the ring. Hosang (1987) proposes the use of a corrugated liner interposed between the journal and the bore of the inner ring. The corrugations run parallel to the bearing and journal axis. This is illustrated in Fig. 8. In principle, the liner diametral thermal expansion is less than that of the shaft journal. The difference is accommodated by stretching of the liner in the circumferential direction. According to Hosang (1987), this action also reduces the envelope outer diameter of the corrugations from that dictated by thermal expansion. The radial stiffness of the liner should also be as high as possible so as not to affect the stiffness of the bearing. An alternate design proposed by Hosang (1987) is the use of the corrugated liner and conical retainers shown in Fig. 8(*a*).

Bailey (1983) reports the use of a collar for the inner ring

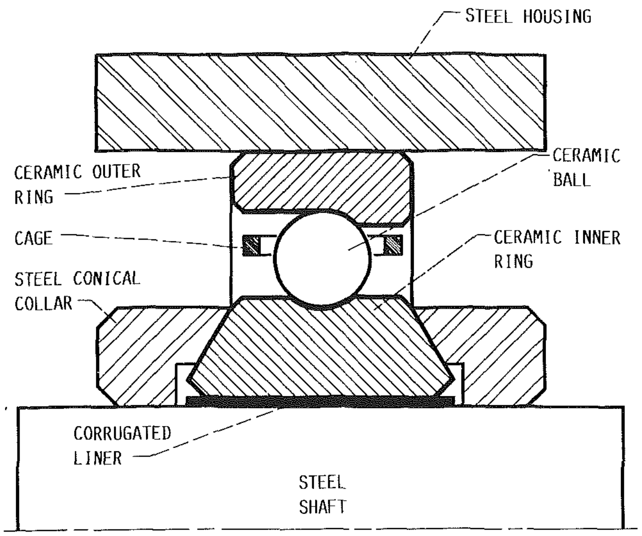

(A) MOUNTING ARRANGEMENT.

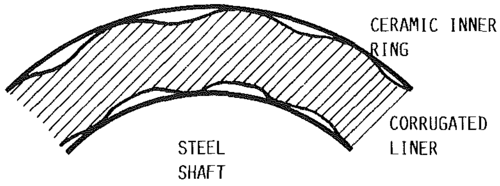

(B) CORRUGATED LINER.

Fig. 8 Mounting arrangement of full-complement ceramic bearing on a steel shaft, using a corrugated liner (Hosang, 1987)

and a spacer for the outer ring to accommodate differences in thermal expansion (Fig. 9).

Baumgartner et al. (1973) use a clamping collar against the inner ring. The axial clamping force is maintained by the clamping collar with an angled face to match the face angle of the inner ring. As the shaft expands axially, the radial expansion forces the collar against the inner ring face, holding it in position.

The use of full complement ceramic bearings requires special mounted design considerations not currently used in turbomachinery. Consequently, these bearings cannot be substituted for steel bearings without extensive design modifications of the rotating shaft and housing.

Manufacturing and Processing

It has long been recognized that voids or surface defects in ceramic or cermet rolling elements can be the source of a subsurface or surface-induced spall (Carter and Zaretsky, 1960; Zaretsky and Anderson, 1961; Parker et al., 1965; Parker and Zaretsky, 1974; Parker et al., 1964a, 1964b). As critical flaw sizes are reduced, it is probable that the values of dynamic capacity summarized in Table 1 and life can be increased. Thus, processing and manufacturing methods can be critical to long life functioning.

In recent years, a relatively large effort has been devoted to the processing manufacture of silicon nitride bearings (Bhushan and Sibley, 1982; Dalal et al., 1977; Baumgartner and Cowley, 1976; Baumgartner and Wheidon, 1973). The most commonly used processing method is hot processing. In hot processing the powder is sized, blended with hot-processing aids, and pressed in graphite dies using temperatures in the 1973 to 2173 K (3091 to 3451°F) range and pressures above 14 MPa. The most common sintering aid is the addition of 1 to 2 percent MgO (Bhushan and Sibley, 1982).

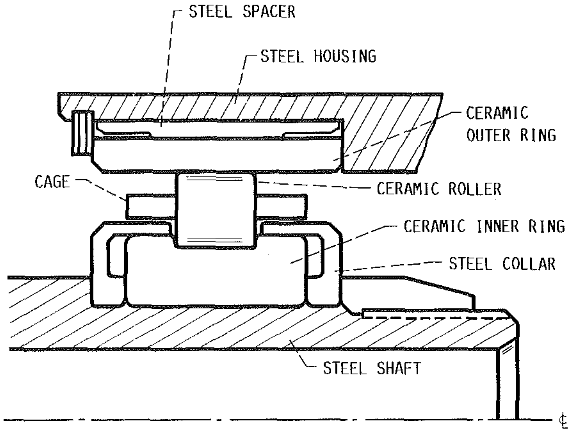

Fig. 9 Mounting arrangement of full-complement ceramic roller bearing on a steel shaft, using a steel collar and spacer (Bailey, 1983)

Other processes include blending of silicon nitride powder with a binder and then cold pressing to near-net shape preforms. The cold-pressed parts are subsequently sintered at high temperature without application of the high pressures present in hot processing (Bhushan and Sibley, 1982). Another processing method is hot isostatic pressing or partial sintering and then hot isostatic pressing (Bhushan and Sibley, 1982). Cold processing silicon and reaction sintering in hot, high-pressure nitrogen called reaction bonding is still another method.

Silicon nitride is hot pressed into billets in the form of plates and then diamond machined. The material can be hot pressed directly into blanks of the required shape for bearing rings, balls, and rollers using suitable multiple cavity graphite molds (Bhushan and Sibley, 1982).

The rolling-element fatigue life of silicon nitride was found to be strongly influenced by finishing procedures (Bhushan and Sibley, 1982; Baumgartner and Cowley, 1976; Baumgartner and Wheidon, 1973). As with steels, improved rolling-element fatigue life was obtained with better surface finishes (Baumgartner and Cowley, 1976; Baumgartner and Wheidon, 1973). The machining of the silicon nitride for bearing application begins with ultrasonic machining, followed by diamond grinding, and then by lapping and polishing (Bhushan and Sibley, 1982). Surface preparation should insure that coarse grit grinding damage is removed during final finish (Baumgartner and Wheidon, 1973).

It was recommended by Baumgartner and Cowley (1976) that, for producing silicon nitride rollers with a straight roller geometry, diamond grinding and honing be used. The use of a formed silicon carbide wheel after initial diamond wheel grinding was recommended for shaping crowned roller geometries (Baumgartner and Cowley, 1976).

Summary

For three decades research has been performed into the use of nonmetallic and refractory materials as rolling-element materials for use in gas turbine engines. Materials and bearing design methods have continuously improved over the years. Materials such as alumina, silicon carbide, titanium carbide, silicon nitride, and a crystallized glass ceramic have been investigated by NASA in the past. Rolling-element endurance tests and analysis of full-complement bearings were performed. The following results were obtained:

1 Silicon nitride material produces the longest life of the materials studied. However, the dynamic capacity of a full complement silicon nitride bearing will be only 5 to 12 percent that of an all-steel bearing of similar geometry.

2 The use of bearings having ceramic rolling elements and

steel races can result in lives less than full complement steel bearings where the elastic modulus of the ceramic is greater than steel, as is the case of most ceramics.

3 Bearing power loss or heat generation is more a function of the individual bearing design and operation than whether steel or ceramic rolling elements are used within the bearing.

4 The lives of ceramic rolling elements are an inverse function of temperature. It is suggested based upon endurance tests with alumina to 1366 K (2000°F) that life is inversely proportional to temperature to the 1.8 power.

5 Unlubricated tests of a full-complement silicon nitride bearing at 644 K (700°F) resulted in catastrophic failure after 30 min, suggesting the need for lubrication at elevated temperatures.

6 Special design and mounting requirements are needed to accommodate a full-complement ceramic bearing into turbomachinery applications. Optimum designs have yet to be developed.

Acknowledgments

The author wishes to acknowledge the technical contributions of Richard J. Parker and Salvatore J. Grisaffe, who with his other colleagues at the NASA Lewis Research Center collaborated with him in conducting the NASA nonmetallic bearing research over the years, which is reported herein. Also, the author wishes to thank Mr. Grisaffe for his technical recommendations and comments, which have been incorporated throughout this paper.

References

Appeldoorn, J. K., and Royle, R. C., 1965, "Lubricant Fatigue Testing With Ceramic Balls," *Lubrication Engineering*, Vol. 21, No. 2, pp. 45-51.

Bailey, T. E., 1984, "Ceramic Roller Bearing Development Program," NAPC-PE-106-C (available NTIS, AD-B086767L).

Bamberger, E. N., et al., 1971, *Life Adjustment Factors for Ball and Roller Bearings—An Engineering Design Guide*, ASME, New York.

Baughman, R. A., and Bamberger, E. N., 1963, "Unlubricated High Temperature Bearing Studies," ASME *Journal of Basic Engineering*, Vol. 85, No. 2, pp. 265-272.

Baumgartner, H. R., and Whieldon, W. M., 1973, "Rolling Contact Fatigue Performance of Hot-Pressed Silicon Nitride versus Surface Preparation Techniques," in: *Surface and Interfaces of Glass and Ceramics*, V. D. Frechette, W. C. LaCourse, and V. L. Burdick, eds., Plenum Press, New York, pp. 179-193.

Baumgartner, H. R., 1973, "Evaluation of Roller Bearings Contacting Hot Pressed Silicon Nitride Rolling Elements," in: *Ceramics for High Performance Applications*, J. J. Burke, A. E. Gorum, and R. N. Katz, eds., Brook Hill Publishing Co., Chestnut Hill, MA, pp. 713-727.

Baumgartner, H. R., Lundberg, D. V., and Whiedon, W. J., 1973, "Silicon Nitride in Rolling Contact Bearings," Norton Co., Worcester, MA (available NTIS, AD-771393).

Baumgartner, H. R., and Cowley, P. E., 1975, "Silicon Nitride in Rolling Contact Bearings," Norton Co., Worcester, MA (available NTIS, AD-A015990).

Baumgartner, H. R., and Cowley, P. E., 1976, "Finishing Techniques for Silicon Nitride Bearings," AMMRC-CTR-76-5 (available NTIS, AD-A025350).

Baumgartner, H. R., Calvert, G. S., and Cowley, P. E., 1976, "Ceramic Materials in Rolling Contact Bearings," Norton Co., Worcester, MA (available NTIS, AD-A031560).

Bhushan, B., and Sibley, L. B., 1982, "Silicon Nitride Rolling Bearings for Extreme Operating Conditions," *ASLE Transactions*, Vol. 25, No. 4, pp. 417-428.

Carter, T. L., and Zaretsky, E. V., 1960, "Rolling Contact Fatigue Life of a Crystallized Glass Ceramic," NASA TN D-259.

Dalal, H. M., Rosenlieb, J. W., and Sibley, L. B., 1977, "Development of Basic Processing Technology for Bearing Quality Silicon Nitride Balls," SKF-AL77T057, SKF Industries, King of Prussia, PA (available NTIS, AD-A053330).

Dee, C. W., 1970, "Silicon Nitride—Tribological Applications of a Ceramic Material," *Tribology*, Vol. 3, No. 2, pp. 89-92.

Harris, T. A., 1968, "On the Effectiveness of Hollow Balls in High-Speed Thrust Bearings," *ASLE Transactions*, Vol. 11, No. 4, pp. 290-294.

Hosang, G. W., 1987, "Results and Design Techniques From the Application of Ceramic Ball Bearings to the MERADCOM 10KW Turbine," AIAA Paper No. 87-1844.

Jones, A. B., 1946, *Analysis of Stresses and Deflections*, Vols. I and II, General Motors, New Departure Division, Bristol, CT.

Loewenthal, S. H., and Zaretsky, E. V., 1985, "Traction Drives," in: *Mechanical Design and Systems Handbook*, 2nd ed., H. A. Rothbart, ed., McGraw-Hill, New York, pp. 34.1-34.56.

Lundberg, G., and Palmgren, A., 1947, "Dynamic Capacity of Rolling Bearings," *Acta Polytechnica*, Mechanical Engineering Series, Vol. 1, No. 3, pp. 1-50.

Lundberg, G., and Palmgren, A., 1949, "Dynamic Capacity of Rolling Bearings," ASME *Journal of Applied Mechanics*, Vol. 16, No. 2, pp. 165-172.

Lundberg, G., and Palmgren, A., 1952, "Dynamic Capacity of Rolling Bearings," *Acta Polytechnica*, Mechanical Engineering Series, Vol. 2, No. 4.

Miner, J. R., Grace, W. A., and Valori, R., 1981, "A Demonstration of High-Speed Gas Turbine Bearings Using Silicon Nitride Rolling Elements," *Lubrication Engineering*, Vol. 37, No. 8, pp. 462-464, 473-478.

Parker, R. J., Grisaffe, S. J., and Zaretsky, E. V., 1964a, "Surface Failure of Alumina Balls Due to Repeated Stresses Applied in Rolling Contact at Temperatures of 2000°F," NASA TN D-2274.

Parker, R. J., Grisaffe, S. J., and Zaretsky, E. V., 1964b, "Surface Failure of Titanium Carbide Cermet and Silicon Carbide Balls in Rolling Contact at Temperatures to 2000°F," NASA TN D-2459.

Parker, R. J., Grisaffe, S. J., and Zaretsky, E. V., 1965, "Rolling-Contact Studies With Four Refractory Materials to 2000°F," *ASLE Transactions*, Vol. 8, No. 3, pp. 208-216.

Parker, R. J., and Zaretsky, E. V., 1972a, "Reevaluation of the Stress-Life Relation in Rolling-Element Bearings," NASA TN D-6745.

Parker, R. J., and Zaretsky, E. V., 1972b, "Rolling-Element Fatigue Lives of Through-Hardened Bearing Materials," ASME *Journal of Lubrication Technology*, Vol. 94, No. 2, pp. 165-173.

Parker, R. J., and Zaretsky, E. V., 1974, "Rolling-Element Fatigue Life of Silicon Nitride Balls," NASA TN D-7794.

Parker, R. J., and Zaretsky, E. V., 1975, "Fatigue Life of High-Speed Ball Bearings With Silicon Nitride Balls," ASME *Journal of Lubrication Technology*, Vol. 97, No. 3, pp. 350-357.

Reddecliff, J. M., and Valori, R., 1976, "The Performance of a High-Speed Ball Thrust Bearing Using Silicon Nitride Balls," ASME *Journal of Lubrication Technology*, Vol. 98, No. 4, pp. 553-563.

Scibbe, H. W., and Zaretsky, E. V., 1971, "Advanced Design Concepts for High Speed Bearings," ASME Paper No. 71-DE-50 (NASA TM X-52958).

Scott, D., Blackwell, J., and McCullagh, P. J., 1971, "Silicon Nitride as a Rolling Bearing Material—A Preliminary Assessment," *Wear*, Vol. 17, No. 1, pp. 73-82.

Scott, D., and Blackwell, J., 1973, "Hot-Pressed Silicon Nitride as a Rolling Bearing Material—A Preliminary Assessment," *Wear*, Vol. 24, No. 1, pp. 61-67.

Sibley, L. B., Mace, A. E., Griesir, D. R., and Allen, C. M., 1960, "Characteristics Governing the Friction and Wear Behavior of Refractory Materials for High-Temperature Seals and Bearings," WADD-TR-60-54.

Taylor, K. M., Sibley, L. B., and Lawrence, J. C., 1963, "Development of a Ceramic Rolling Contact Bearing for High Temperature Use," *Wear*, Vol. 6, No. 3, pp. 226-240.

Zaretsky, E. V., and Anderson, W. J., 1961, "Rolling-Contact Fatigue Studies With Four Tool Steels and a Crystallized Glass Ceramic," ASME *Journal of Basic Engineering*, Vol. 83, No. 4, pp. 603-612.

steel races can result in lives less than full complement steel bearings where the elastic modulus of the ceramic is greater than steel, as is the case of most ceramics.

3 Bearing power loss or heat generation is more a function of the individual bearing design and operation than whether steel or ceramic rolling elements are used within the bearing.

4 The lives of ceramic rolling elements are an inverse function of temperature. It is suggested based upon endurance tests with alumina to 1366 K (2000°F) that life is inversely proportional to temperature to the 1.8 power.

5 Unlubricated tests of a full-complement silicon nitride bearing at 644 K (700°F) resulted in catastrophic failure after 30 min, suggesting the need for lubrication at elevated temperatures.

6 Special design and mounting requirements are needed to accommodate a full-complement ceramic bearing into turbomachinery applications. Optimum designs have yet to be developed.

Acknowledgments

The author wishes to acknowledge the technical contributions of Richard J. Parker and Salvatore J. Grisaffe, who with his other colleagues at the NASA Lewis Research Center collaborated with him in conducting the NASA nonmetallic bearing research over the years, which is reported herein. Also, the author wishes to thank Mr. Grisaffe for his technical recommendations and comments, which have been incorporated throughout this paper.

References

Appeldoorn, J. K., and Royle, R. C., 1965, "Lubricant Fatigue Testing With Ceramic Balls," *Lubrication Engineering*, Vol. 21, No. 2, pp. 45–51.

Bailey, T. E., 1984, "Ceramic Roller Bearing Development Program," NAPC-PE-106-C (available NTIS, AD-B086767L).

Bamberger, E. N., et al., 1971, *Life Adjustment Factors for Ball and Roller Bearings—An Engineering Design Guide*, ASME, New York.

Baughman, R. A., and Bamberger, E. N., 1963, "Unlubricated High Temperature Bearing Studies," ASME *Journal of Basic Engineering*, Vol. 85, No. 2, pp. 265–272.

Baumgartner, H. R., and Whieldon, W. M., 1973, "Rolling Contact Fatigue Performance of Hot-Pressed Silicon Nitride versus Surface Preparation Techniques," in: *Surface and Interfaces of Glass and Ceramics*, V. D. Frechette, W. C. LaCourse, and V. L. Burdick, eds., Plenum Press, New York, pp. 179–193.

Baumgartner, H. R., 1973, "Evaluation of Roller Bearings Contacting Hot Pressed Silicon Nitride Rolling Elements," in: *Ceramics for High Performance Applications*, J. J. Burke, A. E. Gorum, and R. N. Katz, eds., Brook Hill Publishing Co., Chestnut Hill, MA, pp. 713–727.

Baumgartner, H. R., Lundberg, D. V., and Whiedon, W. J., 1973, "Silicon Nitride in Rolling Contact Bearings," Norton Co., Worcester, MA (available NTIS, AD-771393).

Baumgartner, H. R., and Cowley, P. E., 1975, "Silicon Nitride in Rolling Contact Bearings," Norton Co., Worcester, MA (available NTIS, AD-A015990).

Baumgartner, H. R., and Cowley, P. E., 1976, "Finishing Techniques for Silicon Nitride Bearings," AMMRC-CTR-76-5 (available NTIS, AD-A025350).

Baumgartner, H. R., Calvert, G. S., and Cowley, P. E., 1976, "Ceramic Materials in Rolling Contact Bearings," Norton Co., Worcester, MA (available NTIS, AD-A031560).

Bhushan, B., and Sibley, L. B., 1982, "Silicon Nitride Rolling Bearings for Extreme Operating Conditions," *ASLE Transactions*, Vol. 25, No. 4, pp. 417–428.

Carter, T. L., and Zaretsky, E. V., 1960, "Rolling Contact Fatigue Life of a Crystallized Glass Ceramic," NASA TN D-259.

Dalal, H. M., Rosenlieb, J. W., and Sibley, L. B., 1977, "Development of Basic Processing Technology for Bearing Quality Silicon Nitride Balls," SKF-AL77T057, SKF Industries, King of Prussia, PA (available NTIS, AD-A053330).

Dee, C. W., 1970, "Silicon Nitride—Tribological Applications of a Ceramic Material," *Tribology*, Vol. 3, No. 2, pp. 89–92.

Harris, T. A., 1968, "On the Effectiveness of Hollow Balls in High-Speed Thrust Bearings," *ASLE Transactions*, Vol. 11, No. 4, pp. 290–294.

Hosang, G. W., 1987, "Results and Design Techniques From the Application of Ceramic Ball Bearings to the MERADCOM 10KW Turbine," AIAA Paper No. 87-1844.

Jones, A. B., 1946, *Analysis of Stresses and Deflections*, Vols. I and II, General Motors, New Departure Division, Bristol, CT.

Loewenthal, S. H., and Zaretsky, E. V., 1985, "Traction Drives," in: *Mechanical Design and Systems Handbook*, 2nd ed., H. A. Rothbart, ed., McGraw-Hill, New York, pp. 34.1–34.56.

Lundberg, G., and Palmgren, A., 1947, "Dynamic Capacity of Rolling Bearings," *Acta Polytechnica*, Mechanical Engineering Series, Vol. 1, No. 3, pp. 1–50.

Lundberg, G., and Palmgren, A., 1949, "Dynamic Capacity of Rolling Bearings," ASME *Journal of Applied Mechanics*, Vol. 16, No. 2, pp. 165–172.

Lundberg, G., and Palmgren, A., 1952, "Dynamic Capacity of Rolling Bearings," *Acta Polytechnica*, Mechanical Engineering Series, Vol. 2, No. 4.

Miner, J. R., Grace, W. A., and Valori, R., 1981, "A Demonstration of High-Speed Gas Turbine Bearings Using Silicon Nitride Rolling Elements," *Lubrication Engineering*, Vol. 37, No. 8, pp. 462–464, 473–478.

Parker, R. J., Grisaffe, S. J., and Zaretsky, E. V., 1964a, "Surface Failure of Alumina Balls Due to Repeated Stresses Applied in Rolling Contact at Temperatures of 2000°F," NASA TN D-2274.

Parker, R. J., Grisaffe, S. J., and Zaretsky, E. V., 1964b, "Surface Failure of Titanium Carbide Cermet and Silicon Carbide Balls in Rolling Contact at Temperatures to 2000°F," NASA TN D-2459.

Parker, R. J., Grisaffe, S. J., and Zaretsky, E. V., 1965, "Rolling-Contact Studies With Four Refractory Materials to 2000°F," *ASLE Transactions*, Vol. 8, No. 3, pp. 208–216.

Parker, R. J., and Zaretsky, E. V., 1972a, "Reevaluation of the Stress-Life Relation in Rolling-Element Bearings," NASA TN D-6745.

Parker, R. J., and Zaretsky, E. V., 1972b, "Rolling-Element Fatigue Lives of Through-Hardened Bearing Materials," ASME *Journal of Lubrication Technology*, Vol. 94, No. 2, pp. 165–173.

Parker, R. J., and Zaretsky, E. V., 1974, "Rolling-Element Fatigue Life of Silicon Nitride Balls," NASA TN D-7794.

Parker, R. J., and Zaretsky, E. V., 1975, "Fatigue Life of High-Speed Ball Bearings With Silicon Nitride Balls," ASME *Journal of Lubrication Technology*, Vol. 97, No. 3, pp. 350–357.

Reddecliff, J. M., and Valori, R., 1976, "The Performance of a High-Speed Ball Thrust Bearing Using Silicon Nitride Balls," ASME *Journal of Lubrication Technology*, Vol. 98, No. 4, pp. 553–563.

Scibbe, H. W., and Zaretsky, E. V., 1971, "Advanced Design Concepts for High Speed Bearings," ASME Paper No. 71-DE-50 (NASA TM X-52958).

Scott, D., Blackwell, J., and McCullagh, P. J., 1971, "Silicon Nitride as a Rolling Bearing Material—A Preliminary Assessment," *Wear*, Vol. 17, No. 1, pp. 73–82.

Scott, D., and Blackwell, J., 1973, "Hot-Pressed Silicon Nitride as a Rolling Bearing Material—A Preliminary Assessment," *Wear*, Vol. 24, No. 1, pp. 61–67.

Sibley, L. B., Mace, A. E., Griesir, D. R., and Allen, C. M., 1960, "Characteristics Governing the Friction and Wear Behavior of Refractory Materials for High-Temperature Seals and Bearings," WADD-TR-60-54.

Taylor, K. M., Sibley, L. B., and Lawrence, J. C., 1963, "Development of a Ceramic Rolling Contact Bearing for High Temperature Use," *Wear*, Vol. 6, No. 3, pp. 226–240.

Zaretsky, E. V., and Anderson, W. J., 1961, "Rolling-Contact Fatigue Studies With Four Tool Steels and a Crystallized Glass Ceramic," ASME *Journal of Basic Engineering*, Vol. 83, No. 4, pp. 603–612.

DISCUSSION

Y. P. Chiu[1]

Mr. Zaretsky is to be congratulated for his extensive review on research in ceramic rolling element components, in which he has been involved for more than two decades at the NASA Lewis Research Center. While this discusser agrees with most of the statements in the paper about various aspects of ceramic rolling elements, he is somewhat surprised to find in the author's Table 1 that very low load capacity is given to full ceramic bearing, notably silicon nitride. This is contrary to early conclusions by Bhushan and Sibley (1982).

Recognizing the author's keen interest to generate simple factors for use by engineers, this discusser wishes to elaborate on several points regarding the possible limitations on the use of Table 1:

1 Presently, there is lack of endurance test data for all ceramic bearings. Such test data may be desired to assess the load capacity of rolling element bearings.

2 Most of the author's tests were performed prior to 1975,

---

[1] Advanced Technology Center, The Torrington Company, Torrington, CT 06790.

which is about the time Scott et al. (1971, 1973) published their experimental results on silicon nitride rolling elements. The author has correctly pointed out in the paper that the fatigue life of ceramic rolling elements depends on the size of voids and surface defects, but with improved manufacturing methods in recent years, much longer fatigue life should be expected. Based on the author's own argument, it is clear that Table 1 is applicable to silicon nitride rolling elements manufactured in the early 1970s, rather than in the late 1980s.

3 The results reported on the five-ball tests by the author (Fig. 1) contradict the RCF roll-disk test rig data for silicon nitride by Baumgartner (1973) shown in Fig. 2. The latter's test results yield a life about eight times that of the M50 steel rod at the same maximum stress level. Since the author's test and Baumgartner's test were conducted at about the same time and using very similar material, the reason the latter test yields significantly greater relative life than the author's test is a question of interest.

Although experiment shows that a silicon nitride ball (or rod) fails by spalling as with steel rolling elements, there is reason to believe that the spalling mechanism in ceramics is different from that of steel. In general, ceramic is a brittle material weak in tension but strong in compression. Although the process of fracture (or spalling) in ceramic rolling contacts is not well understood, the existence of tensile stress along the edge of the contact area and its effect on Hertzian fracture has been analyzed (Lawn, 1967; Johnson, 1983). Morrison et al. (1984) reported that fatigue spalls on ceramic balls in the hybrid bearings originate at the Hertzian cracks. The load-life exponent of the hybrid bearing is about the mean of the theoretical value of 3 for steel ball bearings and the author's value of approximately 5.4 from a five-ball test rig. Valori (1975) suggests that surface-initiated cracks causing fatigue spalling will not occur below a critical load or Hertz stress level.

In the five-ball test rig, the nominal area of contact is circular with the maximum tensile stress approximately 17 percent of the maximum contact stress. This drops to about 10 percent for an elliptical contact of axis ratio equal to 10. This smaller tensile stress will enable a greater load capacity in a ball (or roller) to race contact. Another possible cause for the conflicting data in five-ball and RCF rigs using ceramic specimens is the existence of spin in the five-ball tester, which can generate tensile stress inside the contact and initiate cracks or spalls.

Recent tests conducted in Japan by Komeya and Kotani (1986) using three 3/8 in. steel balls and silicon nitride disks show at least twice the fatigue life of the same test rig with steel disk under the same load (400 kgf).

Finally, the author has reported conflicting results in frictional loss in ceramic hybrid bearing tested by the authors and by Reddecliff and Valori (1980). The author attributed his finding of higher torque to the higher sliding traction in the steel-ceramic contact than in the steel-steel contact, which has been observed in early ball-disk rolling/sliding experiments (Delal et al., 1975). However, for high-speed ball bearings, the use of lightweight ceramic balls tends to decrease the inner ring contact angle (or less spin) and shorter contact ellipse (lower spin moment); both of these factors can contribute to lower friction loss than in the case where steel balls are used.

It is of interest to point out a recent observation by Aramaki et al. (1988) on testing silicon nitride hybrid ball bearings of two types, i.e., 95 mm bore, 40 deg contact angle, 1000 N axial load, lubricated by grease, and 65 mm bore, 17 deg, 75 N load lubricated with an oil and air mixture. These tests show greater (30-50 percent) reduction in power loss in hybrids than with steel balls when the bearing speed is greater than 3000 rpm.

References

Aramaki, H., et al., 1988, "The Performance of Ball Bearings With Silicon Nitride Ceramic Balls in High Speed Spindles for Machine Tools," presented at the ASME/STLE Joint Tribology Conference, Oct.

Delal, H., Chiu, Y., and Rabinowicz, E., 1975, "Evaluation of Hot Pressed Silicon Nitride as a Rolling Bearing Material," *ASLE Transactions*, Vol. 18, No. 3, pp. 211-221.

Johnson, K. L., 1983, *Contact Mechanics*, Cambridge University Press, p. 94.

Komeya, K., and Kotani, H., 1986, "Development of Ceramic Antifriction Bearing," *JSAE Review*, Vol. 3, No. 3, pp. 72-79.

Lawn, B. R., 1967, "Partial Cone Crack Formation in a Brittle Material Loaded With a Sliding Spherical Indenter," *Proc. Royal Soc. A*, Vol. 299, pp. 307-316.

Morrison, F. R., McCool, J., and Yonushonis, T., 1984, "The Load-Life Relationship for M50 Steel Bearings With Silicon Nitride Ceramic Balls," *Lubrication Engineering*, Vol. 40, No. 3, pp. 153-159.

Valori, R., 1975, Discussion to Parker, R. J., and Zaretsky, E. V., "Fatigue Life of High-Speed Ball Bearings With Silicon Nitride Balls," ASME *Journal of Lubrication Technology*, Vol. 97, No. 3, pp. 350-357.

T. E. Tallian[2]

1 The author rightfully stresses the significance of the high stress levels resulting for a given load from the high elastic modulus of the ceramics. It is not uncommon to see comparisons of the fatigue life of rolling contacts between steel and ceramics, based on identical *stress*, even though, for any practical purpose, the comparison must be based on *identical load*.

However, the disadvantage in stress arising from the high modulus of ceramics is severe only when both the rings and rolling elements are made of ceramic. *Hybrid* bearings (ceramic rolling elements only) suffer much less extra stress from the high modulus of the ceramic. Since hybrids are so much easier to use than full ceramic bearings, they are the design of choice for *high-speed* applications, leaving full ceramic designs for *high-temperature* or *dry lubricated* applications where no other solution serves.

2 While hybrid bearings running in conventional lubricants have undergone sufficient evaluation to be seriously considered where they present a life advantage, the same cannot yet be said about full ceramic bearings in dry lubricant. More than a decade of research has been devoted to this configuration, yet no consistently funded product development is reported by any group that had control over *fabrication and application* of the component, including the lubricant, and was faced with a *continuing major engineering need* that only a full ceramic bearing would solve. As a result, only pilot quantities of dry lubricated ceramic bearings have been made or installed. Neither the ceramic material nor its finishing are fully evolved. As the paper states, we do not even have proven solutions for mounting ceramic rings. All this is the case, since a way has so far always been found to design around the need for a truly high-temperature (over 800°F) rolling bearing (or, for that matter, a long-lived bearing, which must run in a cryogenic liquid).

It is instructive to contrast this situation with the development of aircraft gas turbine mainshaft bearings. The evolution of their material, finishing, and mounting techniques and lubrication methods to the present state has taken about twenty years, during which such bearings were made and used in large numbers. All improvements were incremental and driven by copiously funded major engineering centers at aircraft engine manufacturers and military users. The motivating force was, that turbine engine longevity was largely bearing limited and no design other than rolling bearings worked. If a similar situation were to arise for full ceramic bearings, then we would eventually see them realize their great potential and become a practical machine component.

---

[2] Consultant in Tribology, Tallian Consulting Corp., 36 Dunminning Road, Newtown Square, PA 19073.

Author's Closure

The author would like to thank Dr. Y. P. Chiu and Mr. T. E. Tallian for their respective discussions. Both men have made significant contributions to rolling-element bearing technology over the years and their discussions further add to the author's paper.

Dr. Chiu states that "the results of the author's Table 1 show a very low (relative) load (dynamic) capacity for full ceramic bearings, notably silicon nitride... contrary to early conclusions by Bhushan and Sibley (1982)." Bhushan and Sibley (1982) did not compare the dynamic load capacities of bearing steel and silicon nitride. What they did in their paper was to compare the experimental lives reported in the literature for silicon nitride rolling-element test specimens or hybrid bearings with silicon nitride rolling elements with the predicted lives of steel bearings or test elements using the Lundberg–Palmgren theory (Lundberg and Palmgren, 1947, 1949, 1952) without life adjustment factors (Bamberger et al., 1971). If Bhushan and Sibley had put life adjustment factors into their predictive lives for the steel bearing and test elements, they would have found that the predicted lives would have exceeded the experimental lives obtained with the silicon nitride in nearly all the tests reported. Had Bhushan and Sibley (1982) calculated the dynamic load capacities for the tests reported they would have found that in all the tests the dynamic load capacity of the silicon nitride would have been less than that of bearing steel. Bhushan and Sibley (1982) did not report on other ceramic materials in their paper.

Dr. Chiu is correct in pointing out that the data reported for the silicon nitride in the author's Table 1 were generated in the 1970s. However, the author could not find in the reported literature any other data except those of Morrison et al. (1984). While the author would expect improvement to have been achieved in the 1980s in the performance of silicon nitride and the other ceramic materials reported in the table, it would be reasonable to expect that these improvements, if they exist, would have been reported in the technical literature.

With regard to the comparison of the Baumgartner data (Baumgartner et al., 1973) with AISI M-50 (Fig. 2), the author reviewed data reported by Bamberger and Clark (1982), which were also generated in the rolling-contact (R-C) fatigue tester. The data generated by Baumgartner et al. (1973) were typical but on the low side of CVM AISI M-50 bearing steel fatigue data obtained with the R-C tester. Likewise, the data for CVM AISI M-50 reported in the author's Fig. 1 are consistent with similar data obtained in the NASA five-ball fatigue tester (Zaretsky et al., 1982). This would suggest differences in either manufacturing processes or material quality between the batches of hot-pressed silicon nitride tested by Baumgartner et al. (1973) and Parker et al. (1974). Both batches of material came from a single supplier.

Dr. Chiu states that "the load-life exponent of the hybrid bearing is about the mean of the theoretical value of 3 for steel ball bearings and the author's value of approximately 5.4 (for silicon nitride) from the five-ball test rig." In order to ensure that there is no misunderstanding of the author's data, the stress-life exponent n given in Table 1 would be for a full-complement ceramic bearing and not for a hybrid bearing. For the silicon nitride material, the value for n of 16.1 was independently determined from Parker et al. (1974, 1975) and Baumgartner et al. (1973) in the five-ball rig and the R-C rig, respectively. For the hybrid bearing calculations of Table 3, the author assumed ceramic rolling elements and steel races. The author further assumed that the ceramic rolling elements would not fail. Hence, it was assumed that the life of the bearing was solely dependent on the failure of the steel races. Since the stress-life exponent n of bearing steel is 9, the load-life exponent for a steel bearing would be 3. However, should there be a combination of steel race failures and ceramic rolling-element failures, the apparent load-life relation of the hybrid bearing would fall to between 3 and 5.4. If only the silicon nitride rolling elements failed, then the load-life exponent would be around 5.4. This is illustrated by the work of Morrison et al. (1984).

Morrison et al. (1984) tested four groups of hybrid 45-mm bore angular-contact ball bearings having double-vacuum melted (VIM-VAR) AISI M-50 steel races and silicon nitride balls. There were seven balls in each bearing. The bearings were tested at four thrust loads. These were 4.45, 5.00, 6.45, and 9.56 kN (1000, 1125, 1450, and 2150 lb). These loads produced inner-race maximum Hertz stresses of 1.95×10^9, 2×10^9, 2.17×10^9, and 2.44×10^9 N/m^2 (281, 290, 315, and 354 ksi), respectively. The failure index on the number of bearings failed out of those tested for each load were 5 out of 10, 4 out of 20, 11 out of 20, and 5 out of 10, respectively. All of the failures for each thrust load were spalling of a silicon nitride ball. There were no failures of the steel raceways. The experimental lives obtained by Morrison et al. (1984) are given in Table 4, together with the theoretical lives calculated by the author for full-complement AISI M-50 bearings having the same dimensions. The life and dynamic capacity of the hybrid bearing were less than the theoretical life and capacity of full-complement AISI M-50 steel ball bearings.

Morrison et al. (1984) reported that the load-life exponent for the hybrid bearings was 4.29 with 95 percent confidence limits of 3.16 and 5.42. Based upon a load-life exponent of 4.29, the stress-life exponent n for these bearings is approximately 13, which is solely a function of the failure of the silicon nitride balls. From the experimental data, the actual stress-life exponent was approximately 14. These values are not significantly less than those obtained in the five-ball and R-C rigs previously discussed.

The author has read the paper by Komeya and Kotani (1988). They concluded that "silicon nitride retains a rolling life equivalent to or better than that of a conventional bearing steel." Unfortunately, the information reported in the paper is not sufficient to determine with reasonable certainty whether the steel and ceramic specimens were run under the same load or the same stress.

The work of Aramaki et al. (1988) comparing hybrid bearings with full-complement steel bearings reinforces the author's conclusion that differences in power losses are a function of the individual bearing design. For the same design the operating contact angle on the inner race for the full-complement steel bearing can be higher than with a hybrid bearing. The higher contact angle can result in higher heat generation due to increased spinning relative to the same bearing using lighter weight silicon nitride balls. However, the geometry of a full-complement steel bearing can be optimized to reduce heat generation. Differences in Coulomb friction properties between steel and silicon nitride should not have any effect on rolling-element bearing power losses under reasonable elastohydrodynamic lubrication conditions.

The author agrees with Dr. Chiu's statement that "there is a lack of endurance test data for all (full-complement) ceramic bearings." However, manufacturers of these bearings have been claiming without the benefit of data that these bearings "will last 5 to 100 times longer than high-performance steel bearings in standard operating environments and infinitely longer in hostile operating environments." These same manufacturers further claim that "ceramic bearings run 100 percent faster and 30 percent cooler than steel bearings." Considering that steel bearings have been run to speeds of 3 million DN (DN equals bearing bore in mm multipled by bearing speed in rpm) at lives equivalent to those obtained at lower speeds (Bamberger et al., 1976), it is difficult to imagine the

Table 4 **Comparison of experimental lives obtained with hybrid 7209-size angular-contact ball bearing having silicon nitride balls with theoretical lives of full-complement AISI M-50 angular-contact ball bearings (contact angle, 27 deg; speed, 9700 rpm, lubricant, MIL-L-23699, oil-in temperature, 311 K (100°F)) (Morrison et al., 1984)**

Thrust load, N (lb)	Inner-race stress, N/m^2 (ksi)	L_{10} life, millions of inner race revolutions			Relative hybrid life to AISI M-50		Relative hybrid dynamic capacity to AISI M-50[d]	
		Experimental hybrid[a]	Predicted AISI M-50					
			CVM[b]	VIM-VAR[c]	CVM	VIM-VAR	CVM	VIM-VAR
44 500 (1 000)	1.95×10^9 (281)	404	4698	9396	0.09	0.05	0.24	0.19
50 000 (1 125)	2.00×10^9 (290)	244	3358	6716	0.07	0.04	0.24	0.19
64 500 (1 450)	2.17×10^9 (315)	82.0	1641	3282	0.05	0.03	0.24	0.19
95 600 (2 150)	2.44×10^9 (354)	15.1	548	1096	0.03	0.02	0.23	0.18

[a] Silicon nitride ball failures only, no steel race failures.

[b] Life adjustment factors: material and processing 6; lubricant, 2.9 (Bamberger et al., 1971).

[c] Life adjustment factors: material and processing, 12 (Bamberger et al., 1976); Lubricant, 2.9 (Bamberger et al., 1971).

[d] Load-life exponent: hybrid bearing, 4.29; steel bearing, 3.

basis for the performance claims attributed to the full-complement ceramic bearings.

Ceramic and hybrid bearings have found application in severe chemical and industrial environments where conventional steel bearings are adversely affected by the environment. Hybrid bearings have also found limited application in high-speed machine tool spindles and unmanned missile applications. However, full-complement ceramic rolling-element bearings cannot be retrofitted into an existing design meant for a full-complement steel bearing without redesign of the application. Further, full-complement ceramic rolling-element bearings, and hybrid bearings with today's technology for a given envelope size and load, will not produce longer fatigue lives than an equivalent steel bearing nor necessarily run faster. The problems faced by ceramic bearings are the same as those for other ceramic structures. These are:

1 Fracture toughness
2 Batch-to-batch quality assurance
3 Nondestructive inspection methods
4 Manufacturing technology
5 Design methods and optimization
6 Environmental interaction

As these problems are solved, then as Mr. Tallian states "we would eventually see them (full-complement ceramic bearings) realize their great potential and become a practical machine element."

References

Bamberger, E. N., Zaretsky, E. V., and Signer, H., 1976, "Endurance and Failure Characteristics of Main-Shaft Jet Engine Bearings at 3×10^6DN," ASME *Journal of Lubrication Technology*, Vol. 98, No. 4, pp. 580-585.

Bamberger, E. N., and Clark, J. C., 1982, "Development and Application of the Rolling Contact Fatigue Test Rig," *Rolling Contact Fatigue Testing of Bearing Steels*, J. J. C. Hoo, ed., ASTM STP 771, pp. 85-106.

Zaretsky, E. V., Parker, R. J., and Anderson, W. J., 1982, "NASA Five-Ball Fatigue Tester—Over 20 Years of Research," *Rolling Contact Fatigue Testing of Bearing Steels*, J. J. C. Hoo, ed., ASTM STP 771, pp. 5-45.

AGT101/ATTAP Ceramic Technology Development

G. L. Boyd

D. M. Kreiner

Garrett Auxiliary Power Division,
Allied-Signal Aerospace Company,
Phoenix, AZ 85010

The Garrett Turbine Engine Company/Ford Advanced Gas Turbine Program, designated AGT101, came to an end in June 1987. During this ceramic technology program, ceramic components were exposed to over 250 h of engine test. The 85-h test of the all-ceramic hot section to 1204C (2200F) was a significant accomplishment. However, this AGT101 test program also identified ceramic technology challenges that require continued development. These technology challenges are the basis for the five-year Advanced Turbine Technology Applications Project (ATTAP), which began in Aug. 1987. The objectives of this program include: (1) further development of analytical tools for ceramic component design utilizing the evolving ceramic material properties data base; (2) establishment of improved processes for fabricating advanced ceramic components; (3) development of improved procedures for testing ceramic components and test verification of design methods; and (4) evaluation of ceramic component reliability and durability in an engine environment. These activities are necessary to demonstrate that structural ceramic technology has the potential for competitive automotive engine life cycle cost and life.

Introduction

The Department of Energy (DOE) and NASA-Lewis Research Center, providing project management and administration, have sponsored major technology programs to apply ceramics to automotive gas turbine engines. These activities were authorized under the AGT101 Advanced Gas Turbine Program, NASA Contract DEN3-167, and the recent Advanced Turbine Technology Applications Project (ATTAP), NASA Contract DEN3-335. These programs are directed at providing the United States automobile industry with the high-risk, long range technology necessary to produce gas turbine engines for automobiles that will have reduced fuel consumption and reduced environmental impact.

The AGT101 program began in Oct. 1979 and extended through June 1987, as shown in the schedule in Fig. 1 (Boyd et al., 1987a). Key milestones accomplished included completion of the design review in Jan. 1980, the first set of ceramic structures passing rig test to 1093°C (2000°F) in Aug. 1983, engine test with ceramic structures to 1149°C (2100°F) in Feb. 1984, first ceramic structures rig test to 1371°C (2500°F) in May 1984, and the first all-ceramic engine test in Jan. 1986. Emphasis during the last year of the program revolved around testing of the all-ceramic engine.

The five-year ATTAP effort was initiated in late Aug. 1987 with contract award to Garrett Turbine Engine Company (GTEC). This program is directed at further advancing the development of ceramic technology (see Fig. 2) so that decisions to proceed with commercialization development can be made at the end of ATTAP.

In Jan. 1988, Allied-Signal Aerospace Company (the parent company) reorganized Garrett Turbine Engine Company into two divisions according to product lines. The Garrett Auxiliary Power Division (GAPD) was formed and will conduct the ATTAP contract effort.

AGT101 Design Features. The AGT101 power section, shown in Fig. 3, is a single-shaft, regenerated gas turbine engine utilizing an all-ceramic hot section with symmetric ceramic components, except for one housing that separates the high and low-pressure regenerator flow. The symmetric design provides for more uniform stress distribution and eases manufacturing of the components.

The AGT101 engine is flat rated at 74.5 kW (100 hp) with a specific fuel consumption goal of 0.18 kg/kW-h (0.3 lbm/hp-hr). The single-shaft rotating group is composed of a radial turbine, centrifugal compressor, and output spline. This rotating group is supported by an air-lubricated foil journal

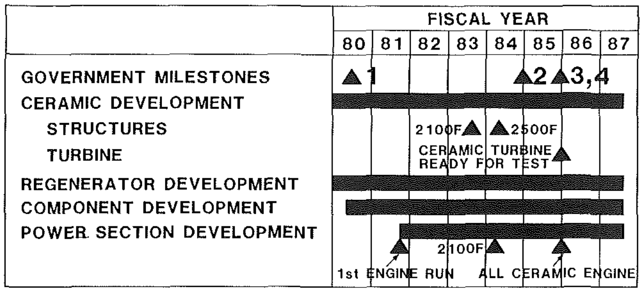

GOVERNMENT MILESTONES
1. DESIGN REVIEW
2. CHARACTERIZE ENGINE - BUILD 1
3. CHARACTERIZE ENGINE WITH CERAMIC STATICS
4. *INITIATE ENGINE TEST WITH CERAMIC ROTOR*

Fig. 1 AGT101 program schedule

Contributed by the International Gas Turbine Institute and presented at the 33rd International Gas Turbine and Aeroengine Congress and Exhibition, Amsterdam, The Netherlands, June 5–9, 1988. Manuscript received by the International Gas Turbine Institute September 12, 1987. Paper No. 88-GT-243.

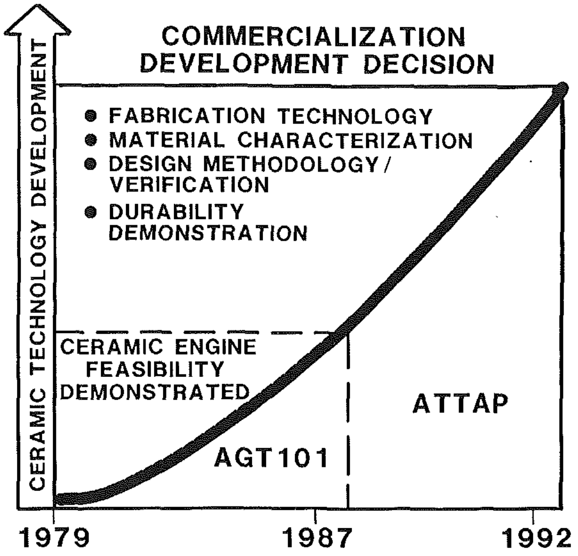

Fig. 2 ATTAP will continue U.S. ceramic technology development

bearing, conventional ball bearing, and an oil film thrust bearing. The maximum (steady state) engine speed is 100,000 rpm.

Ambient air enters the engine through variable inlet guide vanes (IGVs) and passes through the single-stage compressor. The compressed air is routed around the full engine perimeter to the high-pressure side of the ceramic rotary regenerator. The compressed air passes through the regenerator core where it is heated to a maximum of 1060°C (1940°F) (at idle), and then to the combustor.

The combustion system features a fixed-geometry, lean-burn, low-emission combustor. Combustor rig evaluation has demonstrated multifuel operation on JP-4, DF-2, and gasohol. Combustor air discharges the combustor at a maximum temperature of 1371°C (2500°F), then flows through the ceramic stator, and expands across the radial turbine rotor. Turbine exhaust gases [1093°C (2000 F) maximum at idle] are ducted through the low-pressure side of the rotary regenerator and out the engine exhaust.

The AGT101 incorporates several unique design features in the ceramic hot section. Some of the innovative designs shown in Fig. 4 take full advantage of the special capabilities of ceramics. The ceramic turbine forms an ideal journal for a high-temperature foil bearing. This bearing configuration completed 2000 starts in a bearing rig without measurable wear. Also, the gold-plated foil material and silicon nitride journal material survived 500 starts at 649°C (1200°F) in rig evaluation, surpassing other material test combinations. The desire for a journal of ceramic material led to a turbine attachment design utilizing an internal metal collet attached to the tie bolt, which clamps the ceramic turbine journal to a curvic ring that mates with the compressor. The turbine attachment and foil bearing configuration have completed over 90 h of trouble-free operation in the all-ceramic engine.

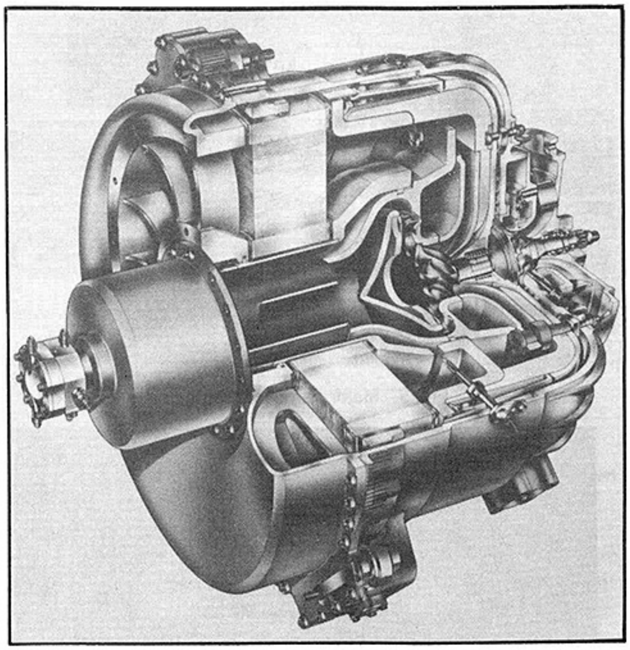

Fig. 3 AGT101 power section

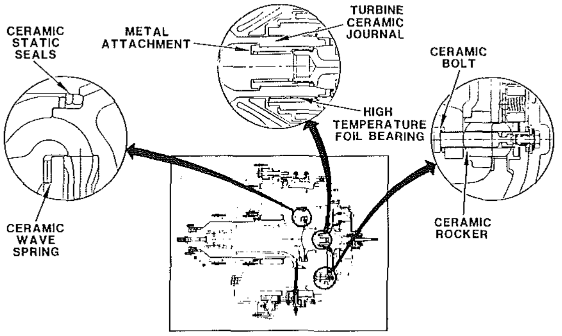

Fig. 4 AGT101 unique design features

The ceramic turbine shroud and inner/outer diffusers are supported by the metal compressor backshroud utilizing three ceramic bolts, ceramic rocker, and spacer assemblies. This

Nomenclature

AGT = advanced gas turbine
AGT101 = Garrett developed ceramic gas turbine engine
ATTAP = advanced turbine technology applications project
DF-2 = diesel fuel, grade 2
DOE = U.S. Department of Energy
EDM = electrical discharge machining
GAPD = Garrett Auxiliary Power Div., Phoenix, AZ
HIP = hot isostatic pressing
HSN = hot isostatic pressed silicon nitride
JP-4 = kerosene-based aviation fuel
ksi = one thousand pounds/inch^2
kW = kilowatt
lbm = pound mass
MPa = mega-Pascal
NDE = nondestructive evaluation
Norton/TRW = high performance ceramics joint venture, Northboro, MA
ORNL = Oak Ridge National Laboratories, TN
RBSN = reaction bonded silicon nitride
SASC = sintered alpha silicon carbide
Si_3N_4 = silicon nitride ceramic material
SSN 250M = silicon nitride material from Kyocera
SSN = sintered silicon nitride
Standard Oil = Standard Oil Engineered Materials Company, Niagara Falls, NY
TiB_2 = titanium diboride additive
TIT = turbine inlet temperature

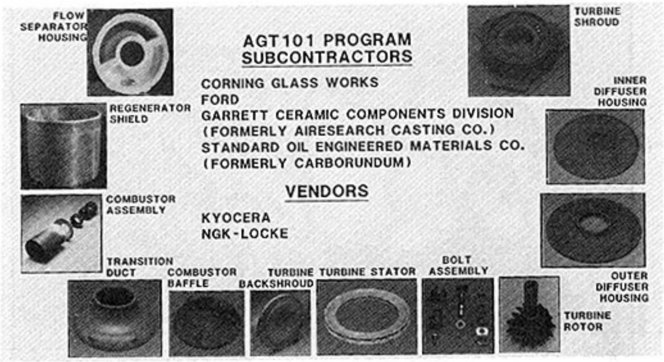

Fig. 5 Major ceramic suppliers

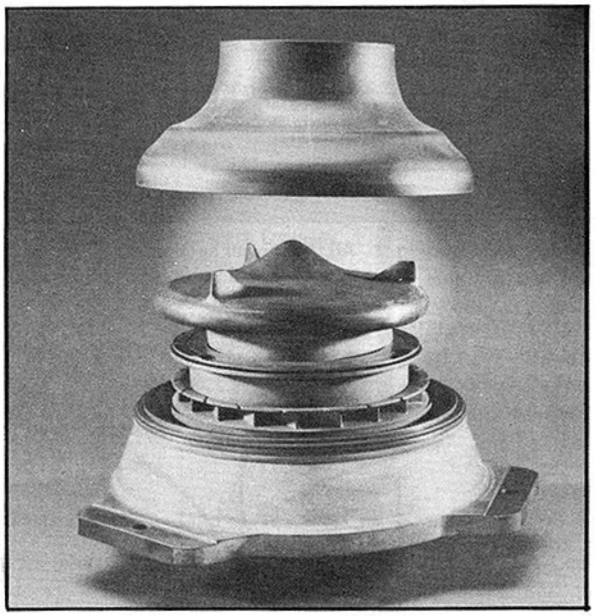

Fig. 6 Ceramic structures test to 2500°F

bolt assembly aligns and supports this assembly of ceramic structures utilizing high contact stress and friction at the ceramic interfaces. As the metal compressor backshroud expands due to higher thermal expansion, the ceramic rockers tilt to maintain alignment of the ceramic structures. This design has passed 10g shock load tests and over 150 h of engine operation while maintaining the critical alignment of the turbine shroud to the turbine rotor.

A ceramic wave spring is utilized to maintain axial load on the ceramic stators, backshroud, and baffle. This spring must maintain this load up to 1371°C (2500°F) operation without creep. This concept allows metal springs, located in the cooler environment of the combustor cap, to place a higher axial load on ceramic static seals in the turbine shroud to reduce leakage.

Ceramic insulation is used to form a portion of the turbine exhaust flow path. The ceramic inner diffuser originally extended around this portion of the flow path. Later, the diffuser was truncated and insulation added; the resultant inner diffuser design is easier to fabricate and the thermal stresses were reduced by a factor of four. The insulation thickness was increased, thus reducing heat loss. These areas are considered important design features critical to the all-ceramic engine operation and cost potential.

Ceramic Gas Turbine Technology Progress in AGT101. Significant progress has been made in ceramic technology since the AGT program inception in 1979. At that time, no usable ceramic parts had been fabricated thicker than 12.7 mm (0.5 in.) and no material existed that would withstand the

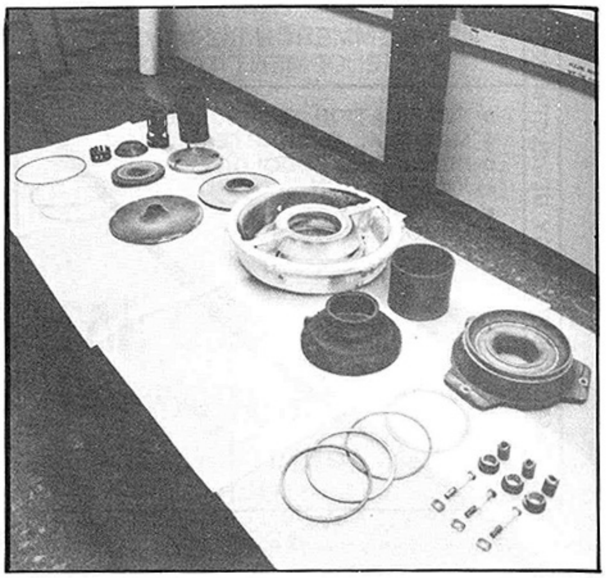

Fig. 7 Ceramic structures following the 85-h, 2200°F test

operational stresses of the AGT101 rotor operating at 100,000 rpm, and 1371°C (2500°F) turbine inlet temperature (TIT). Since that time, the turbine rotor and the complex structures shown in Fig. 5 have been fabricated using near-net shape fabrication processes. Credit should be given to the ceramic suppliers shown in Fig. 5. Their progress in the fabrication of components in silicon nitride, silicon carbide, and lithium aluminum silicate allowed the all-ceramic engine to be assembled and tested.

These ceramic components have undergone an iterative design, fabrication, and test evaluation development loop. This was necessary because the first components fabricated failed during proof test. These proof tests impose a stress 25 percent higher than the peak stress expected in a normal start transient. A normal start transient for the AGT101 engine is lightoff to 1204°C (2200°F) in 5 s. Progress in this component development has been demonstrated by the fact that all-ceramic structural components can now consistently pass screening (proof) tests—over 165 ceramic structures have passed to date.

The capability of the ceramic structures to withstand the harsh environment of the gas turbine at 1371°C (2500°F) TIT is being investigated. The structures shown in Fig. 6 made of reaction-bonded silicon nitride (RBSN), sintered silicon nitride (SSN), and sintered alpha silicon carbide (SASC) have been evaluated. To date, interfacial material degradation has been seen at RBSN-to-RBSN and SASC-to-SASC interfaces. The RBSN to SASC interfaces have shown no interfacial deterioration, which may be due to the thermal expansion differences of the two materials. SSN has shown no tendency to stick to itself such as SASC exhibits. Over 40 hours at 1371°C (2500°F) have been accumulated during tests of these materials, but further testing is needed to understand the environmental and thermal cycle effects.

Engine testing of the ceramic components began in Feb. 1984, and to date, over 250 h have been accumulated on engines with ceramic components. This includes a 100-h test on an engine with ceramic structures and a dual-alloy metal rotor at 1149°C (2100°F), as well as an all-ceramic engine test for 85 h at 1204°C (2200°F). The ceramic turbine rotor has been operated to 100,000 rpm, which produces a turbine tip speed of 701 m/s (2300 ft/sec).

The 85-h, 1204°C (2200°F) test of the all-ceramic engine has provided valuable data. This engine operated in the TIT range of 1049–1204°C (2000–2200°F), and in the speed range of 60,000–70,000 rpm, and accumulated five starts. The test was

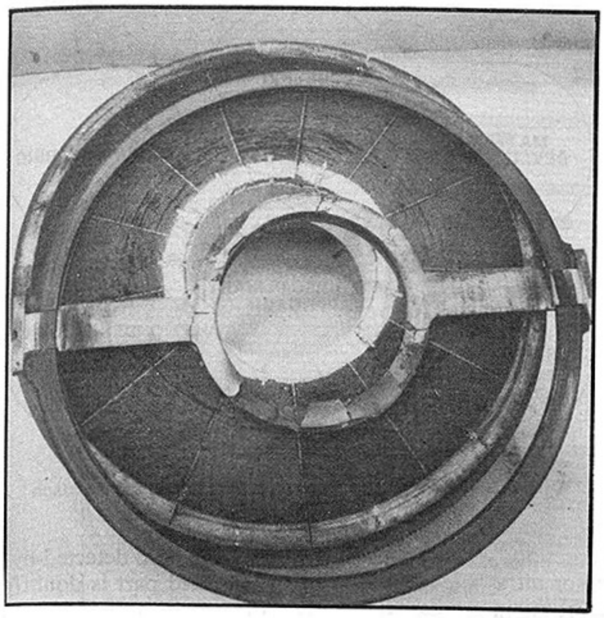

Fig. 8 Regenerator hot seal distorted and I-112 coating delaminated

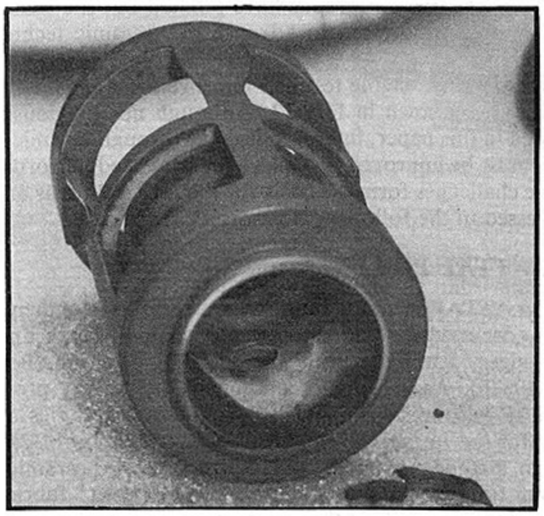

Fig. 9 Carbon deposit formed on combustor

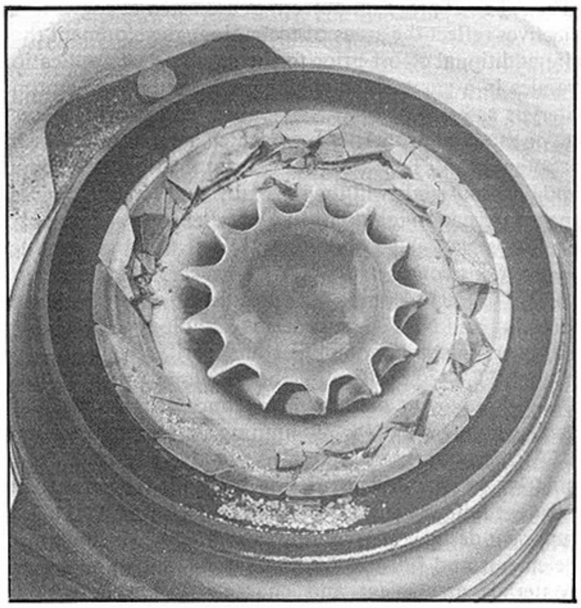

Fig. 10 Impact damage to the turbine and stator

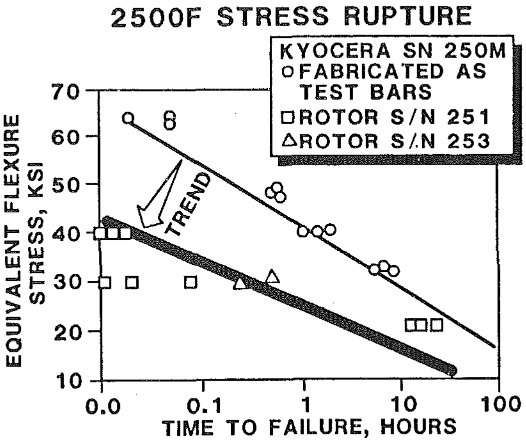

Fig. 11 Rotor material properties inconsistent and lower than specimens made as test bars

stopped due to impact damage to the turbine and stators. The remaining ceramic structures shown in Fig. 7 were in excellent condition. The turbine attachment, foil bearing, and flow path insulation were also in excellent condition.

This test also identified areas where further development is needed. The regenerator hot seal distorted (see Fig. 8) and the I-112 coating (a plasm-sprayed, low-friction ceramic coating) delaminated. Improved seal substrate material and coatings are needed. A hard carbon deposit had formed in the pilot combustor (shown in Fig. 9). The fuel nozzle was found partially plugged after this test and is suspected as being the underlying cause of carbon formations. Further combustor development is needed to eliminate carbon forming conditions, improved combustor efficiency during an engine start, and improved emissions.

Detached carbon deposits from the combustor are believed to be the source of impact damage to the turbine and stator shown in Fig. 10. Although the damage was limited to the turbine and stators, this problem must be solved to assure reliable operation of ceramic gas turbines. Two approaches to solve the impact problem are proposed: (1) investigate a particle separator design to catch particles before entering the turbine stage, and (2) improve toughness of the stator and turbine materials to enhance impact tolerance. Further work is also needed to assess impact damage to the candidate ceramics from a variety of projectiles. Design methods can be developed and correlated to these impact data to form the algorithms for projecting impact damage and impact tolerant designs.

Another turbine rotor of Kyocera's SN 250M silicon nitride (same material used in the 85-h test) was tested in the all-ceramic engine. The rotor experienced an apparent stress rupture failure after operating 12 h at 1204°C (2200°F). Test bars cut from other Kyocera SN 250M rotors were tested in stress rupture and as shown in Fig. 11, the stress rupture properties were lower than SN 250M material fabricated as test bars. Further analysis and testing indicated this material fabricated in turbine rotors was very inconsistent. Although the material data were very limited, the current analysis techniques did not predict the failure at 12 h. This rotor failure pointed out the need for technology advancements in fabrication technology and life prediction methods.

The need for advancements in NDE and proof test are also evident. A ceramic rotor experienced inducer blade fracture during operation in a metal engine. Once fracture origin was found to be a planar flaw perpendicular to the blade surface (see Fig 12). It is not known whether this flaw was the initial cause of the rotor failure or was secondary, but the flaw shown was the origin for that particular inducer blade failure. This rotor had passed the 115 percent cold spin test and visual

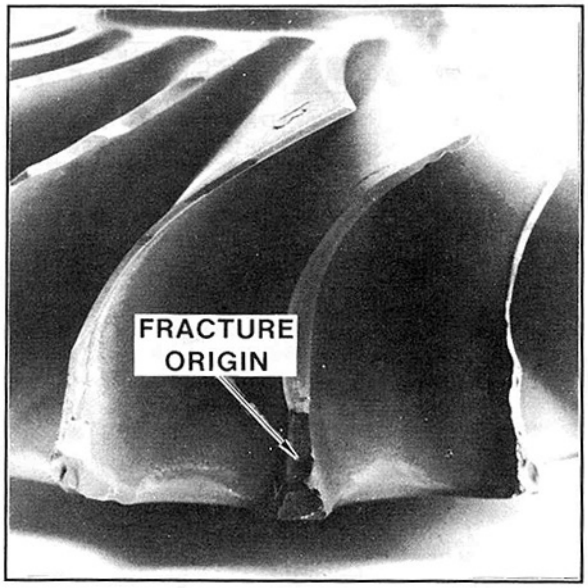

Fig. 12 Turbine inducer blade fractures during engine operation

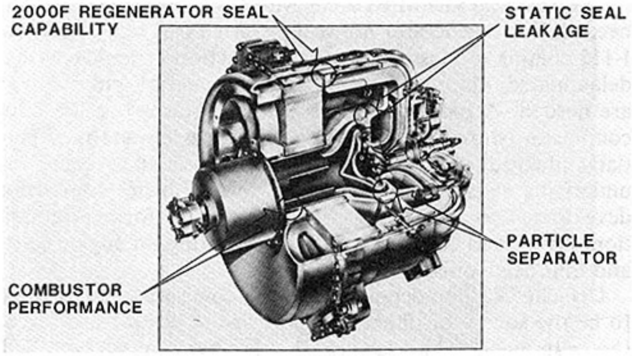

Fig. 13 Engine test bed improvements

U.S. CERAMIC SUPPLIERS

- MATERIALS ASSESSMENT
- CANDIDATE MATERIALS CHARACTERIZATION
- COMPONENT FABRICATION PROCESS DEVELOPMENT
- IN-PROCESS AND FINAL COMPONENT NDE TECHNIQUE DEVELOPMENT
- DESIGN METHODS DEVELOPMENT AND VERIFICATION - ORNL LIFE PREDICTION PROGRAM
- ENGINE TEST BED PERFORMANCE AND COMPONENT DURABILITY
- PUBLICATION OF CERAMIC DESIGN MANUAL

Fig. 14 ATTAP objectives address the AGT101 technology challenges

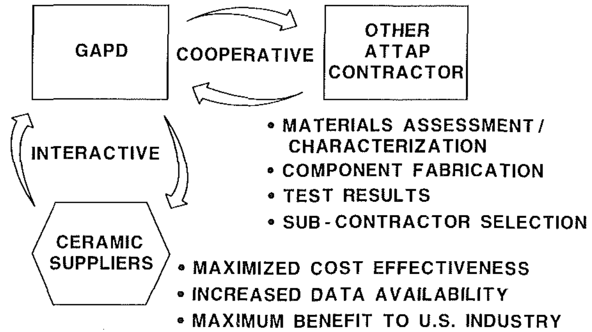

Fig. 15 Duplication of effort eliminated in ATTAP

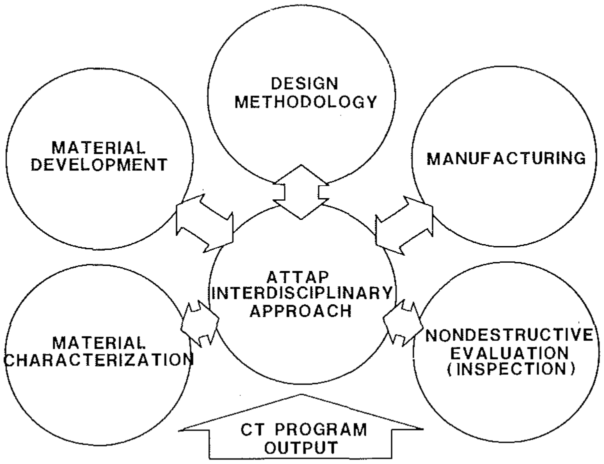

Fig. 16 ATTAP success requires interdisciplinary approach

inspection. Whether this flaw would have been detected by x-ray or ultrasonic inspection of the finished part is doubtful. Improved in-process NDE and proof tests are needed to detect flaws of this nature.

These last few paragraphs have pointed out the challenges that must be addressed to advance this ceramic technology further.

Additionally, engine test bed improvements must be made in the areas shown in Fig. 13. Although not previously addressed in this paper, interpath leakage through ceramic static seals must be improved to achieve the projected performance. These challenges form the basis for the ATTAP focus and are addressed in the following discourse.

The ATTAP Plan

The ATTAP is a 60-month research and development program designed to address ceramic component technology challenges identified during the AGT101 program (Boyd et al., 1987b). As a ceramic component technology program, ATTAP will utilize the AGT101 engine and test rigs as test beds for the further development and verification of ceramic design methods. ATTAP will utilize domestic ceramic suppliers for the development of component fabrication technology and will continually assess new materials and suppliers for potential participation in the program.

The ATTAP program objectives are listed in Fig. 14. These objectives reflect the areas of technology development that require additional effort prior to the commercial application of ceramics in a gas turbine engine environment. A continuous materials assessment of U.S. suppliers will provide necessary data on material properties from which a decision can be made on potential ATTAP component fabrication development. Candidate materials will then be fully characterized and component fabrication initiated. In a parallel contract activity, the Oak Ridge National Laboratory (ORNL) will be conducting two programs considered vital to the successful completion of the ATTAP: (1) Ceramic Life Prediction, and (2) Materials Processing and NDE. The generic technology generated from these programs will be applied and verified in components during ATTAP. Specifically, the development of in-process NDE techniques to define and advance reliable methods of detecting strength and/or life limiting flaws will be utilized by ATTAP component suppliers to aid in Quality Assurance. Similarly, ceramic life prediction methods, specific to time-dependent failures, will be incorporated into ATTAP ceramic component designs with resulting predictions verified through subelements and full size component rig and/or engine tests.

Materials assessment and characterization data coupled with fabricated component "cut-up" material characteriza-

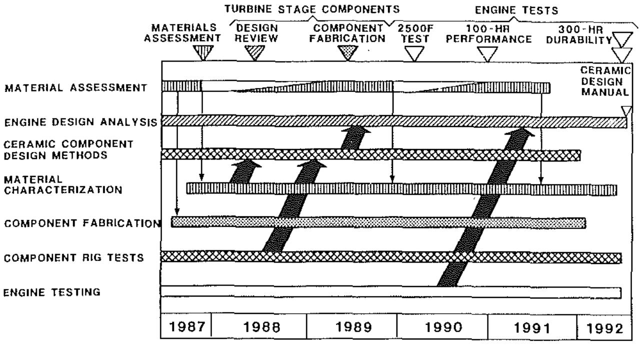

Fig. 17 Technology challenges set ATTAP milestones

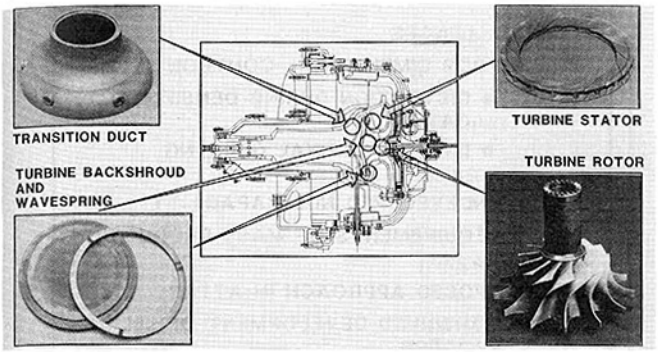

Fig. 18 Five AGT101 components have been identified for initial development

tion will be shared between the ATTAP contractors to preclude a duplication of effort. Figure 15 illustrates this cooperative effort and how it will be utilized to improve program effectiveness. Figure 16 denotes the technical elements of the ATTAP that must be combined in an interdisciplinary manner. The program success strategy revolves around the integration of each element into a final verified design format. Each element is critical to the final program milestone: A Ceramic Design Manual.

The ATTAP program schedule shown in Fig. 17 details the program elements and clearly illustrates the interdisciplinary interaction in a time-phased manner. Major program milestones (shown at the top of the schedule) show the program requirements for materials assessment reviews, turbine stage component design and fabrication, and significant engine tests. The schedule shows the flow of information from materials assessment to materials characterization, and on to component fabrication. Component material characterization is compared with laboratory test specimens to gage the level of process maturity and supplements data required for component probabilistic life prediction method development and verification. Final validation of overall program success will be manifested through intensive steady state and cyclic engine tests to 1371°C (2500°F), 100,000 rpm, and for periods of up to 300 h.

Component fabrication activity will be initiated in the ATTAP on five components selected as critical technology challenges during the AGT101 program. These components, shown in Fig. 18, have demonstrated technology challenges that require further development in either processing and/or design. The components are the turbine rotor, turbine stator segments, transition duct, turbine backshroud, and a ceramic wave spring. Each of these components has unique material property and/or fabrication challenges that relate to life, dimensional control, elevated temperature strength, or fabrication method amenable to high volume production. Each of these components is discussed in detail in the following paragraphs.

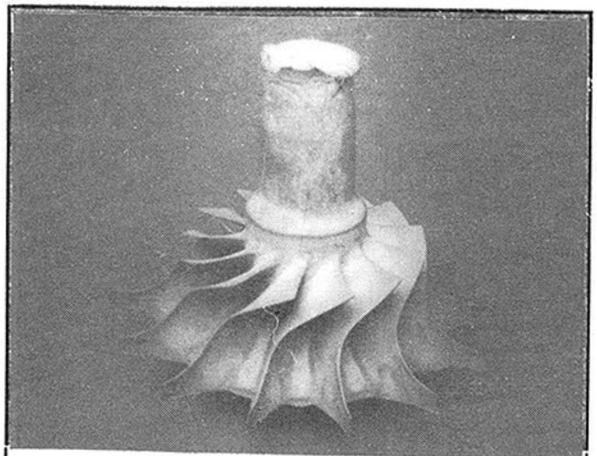

- CHALLENGES
  - INADEQUATE HIGH-TEMPERATURE PROPERTIES
  - LOW FRACTURE TOUGHNESS
  - POOR DIMENSIONAL CONTROL
  - HIGH-VOLUME PRODUCTION TECHNIQUES
  - UNDEVELOPED NDE METHODS
  - NONUNIFORM PROPERTIES IN COMPONENTS
  - PROCESSING FLAWS
- PROPOSED APPROACHES TO RESOLVE ROTOR PROBLEMS:
  - INCORPORATION OF IMPROVED MATERIALS
  - FURTHER DEVELOPMENT OF INJECTION MOLDING AND SLIP CASTING
  - COORDINATED EFFORT TO DEVELOP NDE
  - EXTENSIVE TEST SPECIMEN AND COMPONENT MATERIAL CHARACTERIZATION
  - PARTICLE SEPARATOR (GAPD)

Fig. 19 Norton/TRW initiates plan to solve ceramic turbine rotor challenges

Turbine Rotor. The turbine rotor (see Fig. 19) has, through the duration of the AGT101 program, posed a formidable challenge to domestic ceramic subcontractors. With a rotor hub cross-sectional thickness of 8.89 cm (3.5 in.), complete dewaxing of injection-molded rotor hubs (Si_3N_4) has not been achieved. Further, slip-cast rotors, although successfully formed in the green state, have not retained laboratory furnace-produced material properties following densification. These problems as well as the other challenges shown in Fig. 19 must be solved to produce a quality turbine rotor.

Norton/TRW has been selected to initiate turbine rotor fabrication development in the ATTAP using two fabrication approaches. Both injection molding and slip casting will be evaluated during the first program year resulting in a selection of the most successful process for full-size turbine rotor fabrication. In-process NDE will be used to detect and guide early process modifications to eliminate the defects prior to costly component densification, machining, and proof testing. Extensive component "cut-up" material characterization will be performed to verify fabrication process material properties.

Material toughness or resistance to impact damage in the engine environment has been a major roadblock to AGT101 test bed operation for extended periods of time. An effort both to eliminate damaging particles from the turbine inlet flowpath and to increase the impact resistance of the turbine rotor material is scheduled for the ATTAP. GAPD is pursuing development of a turbine inlet particle separator concept.

- CHALLENGES
  - POOR DIMENSIONAL CONTROL
    - AS-FIRED SURFACES
    - NEAR-NET-SHAPE
  - LOW RESISTANCE TO:
    - THERMAL SHOCK
    - IMPACT
    - OXIDATION
- APPROACHES TO DEVELOPMENT
  - INCORPORATION OF LATEST MATERIAL TECHNOLOGY
  - DEVELOPMENT OF INJECTION MOLDING
  - DESIGN IMPROVEMENTS (GAPD)
  - PARTICLE SEPARATOR (GAPD)

Fig. 20 Turbine stators offer unique problems to Norton/TRW

Turbine Stators. The turbine stator segments shown in Fig. 20 have also demonstrated technical fabrication challenges in the AFT101 program. The contours of the 19 stator segments must be precisely controlled to achieve aerodynamic performance. Net shape fabrication techniques have not been demonstrated by U.S. suppliers in materials that experience shrinkage during densification. Norton/TRW will address these issues in the ATTAP through the use of a HIPed silicon nitride (HSN). It is believed that the required close dimensional control can be achieved in HSN through a thorough understanding of shrinkage rates, residual forming stresses (green ware), and control of densification schedules and hot-zone temperature variation.

Newly revised materials with improved elevated temperature oxidation resistance, impact resistance, and stress rupture properties are to be incorporated into the turbine stator development activity as the respective material technologies mature.

Transition Duct. The transition duct derives the name from the transition of hot gas flow from the combustor discharge to the larger diameter turbine stator inlet. Figure 21 shows the transition duct with several external features; the flow diverter is the thick ring cross section about a third of the axial length from the top of the photograph. This feature extends 180 deg around the component and is designed to redistribute combustor inlet flow profiles. Since the diverter is asymmetric around the part, an added complexity is placed on fabrication and the need for net shape. Additionally, the three combustor discharge thermocouple bosses shown on the bottom third of the photograph also contribute to the need for close dimensional controls.

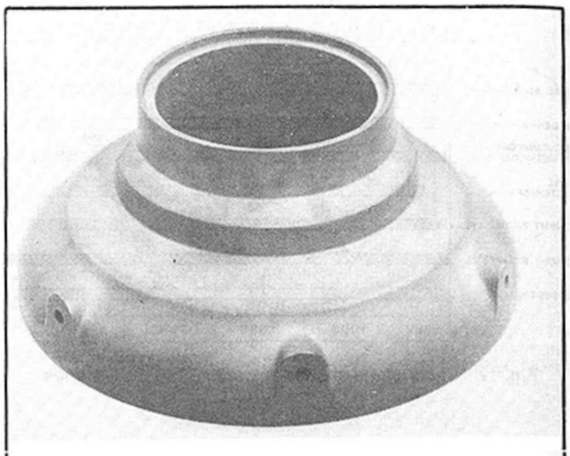

- CHALLENGES
  - POOR DIMENSIONAL CONTROL
    - DISTORTION DURING DENSIFICATION
    - EXCESSIVE FINAL GRINDING
  - UNDEVELOPED NDE CAPABILITY
  - REQUIREMENTS OF MASS PRODUCTION
- PROPOSED APPROACH IN ATTAP
  - CONTINUED DEVELOPMENT OF I.M. PROCESS
  - DEVELOPMENT AND APPLICATION OF ADVANCED NDE

Fig. 21 Standard Oil engineered materials to address net shape of complex structure

The program goal for the transition duct is to demonstrate net shape forming capability with machining only on critical interfaces. Standard Oil initiated injection-molded development of the transition duct during the last two years of the AGT101 program. Fabrication technology challenges encountered include: nonuniform binder distribution in the green-formed component, internal voids along the axial length, and nonuniform shrinkage during densification. The material being used for the transition duct is SASC, which will continue to be used during the optimization of fabrication process parameters in the ATTAP. Quality Assurance requirements will further the use of in-process NDE such that critical defects can be detected prior to densification and the process optimized based on statistically designed experiments.

Turbine Backshroud. The turbine backshroud shown in Fig. 22 forms the turbine rotor backface shroud in the ATTAP/AGT101 engine test bed. During normal engine operation, the backshroud is subjected to a radial thermal gradient from the component centerline to the outside diameter. This gradient distorts the component axially creating a highly stressed 206.8–241.3 MPa (30–35 ksi) area in the center of the component on the turbine side. A stronger material and/or an increased Weibull modulus would improve the component reliability under normal engine operating conditions to 1371°C (2500°F).

Typically, during fabrication (isopressed and green machined, or plastic formed) the backshroud has either distorted out of flat or has drooped in the center conical section during densification. These fabrication issues will be addressed in the ATTAP as the development of a high-volume production

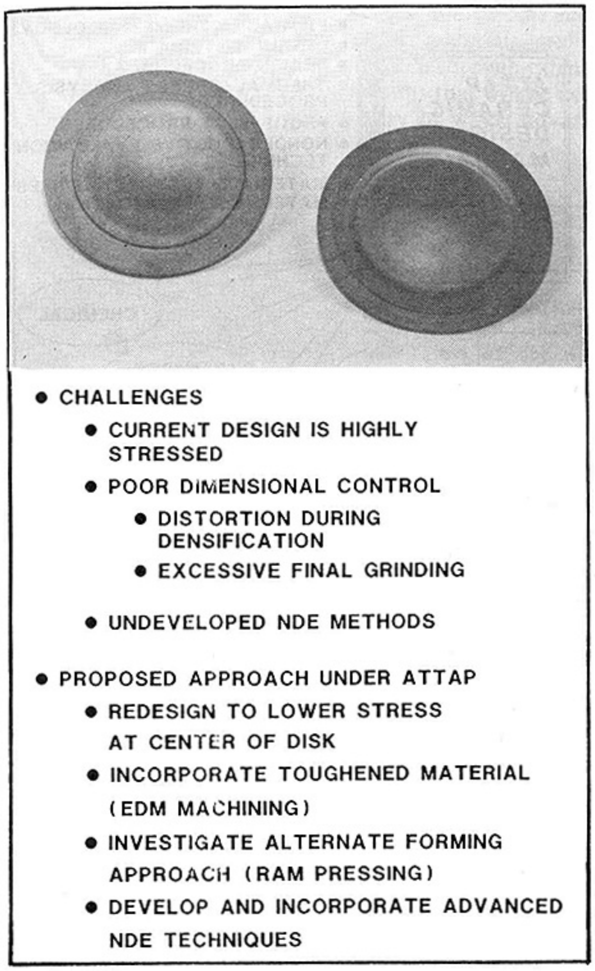

- CHALLENGES
  - CURRENT DESIGN IS HIGHLY STRESSED
  - POOR DIMENSIONAL CONTROL
    - DISTORTION DURING DENSIFICATION
    - EXCESSIVE FINAL GRINDING
  - UNDEVELOPED NDE METHODS
- PROPOSED APPROACH UNDER ATTAP
  - REDESIGN TO LOWER STRESS AT CENTER OF DISK
  - INCORPORATE TOUGHENED MATERIAL (EDM MACHINING)
  - INVESTIGATE ALTERNATE FORMING APPROACH (RAM PRESSING)
  - DEVELOP AND INCORPORATE ADVANCED NDE TECHNIQUES

Fig. 22 Standard Oil proposes ram pressing as high-volume production technique

technique (ram pressing) is pursued. In addition, as revised designs emerge keyed on stress reduction, a new tougher silicon carbide will be implemented, which is toughened by dispersed particles of titanium diboride (TiB_2). A major advantage to the use of TiB_2 and SASC is not only in the improved toughness but also in the capability to machine the material using conventional electrical discharge machining (EDM). This stock removal technique could vastly reduce the cost of a final component when coupled to net shape forming development. In-process NDE must be utilized in all process steps to ensure early flaw detection and elimination through process modifications as described herein.

Ceramic Wave Spring. The ATTAP/AGT101 engine test bed requires the use of a spring loading device within the assembly of ceramic components that mechanically loads static seals and/or components in a 1371°C (2500°F) environment. Figure 23 shows the ceramic wave spring used to establish a spring load on turbine section components. This part was fabricated during the AGT101 from SSN, however for the ATTAP development, creep resistant SASC will be utilized. The wave spring has a 15.2-cm (6-in.) diameter, is approximately 3.18 mm (0.125 in.) thick, and has a sinusoidal wave shape. Typically cam ground or with simple distinct lobes, the wave spring offers a fabrication challenge to Standard Oil.

To meet the program goal to develop a high-volume production technique for fabrication, Standard Oil will pursue two approaches: dry pressing to the desired shape, and extrusion of a thin sheet with subsequent stamping to the desired shape. The waveform will be achieved during the densification step.

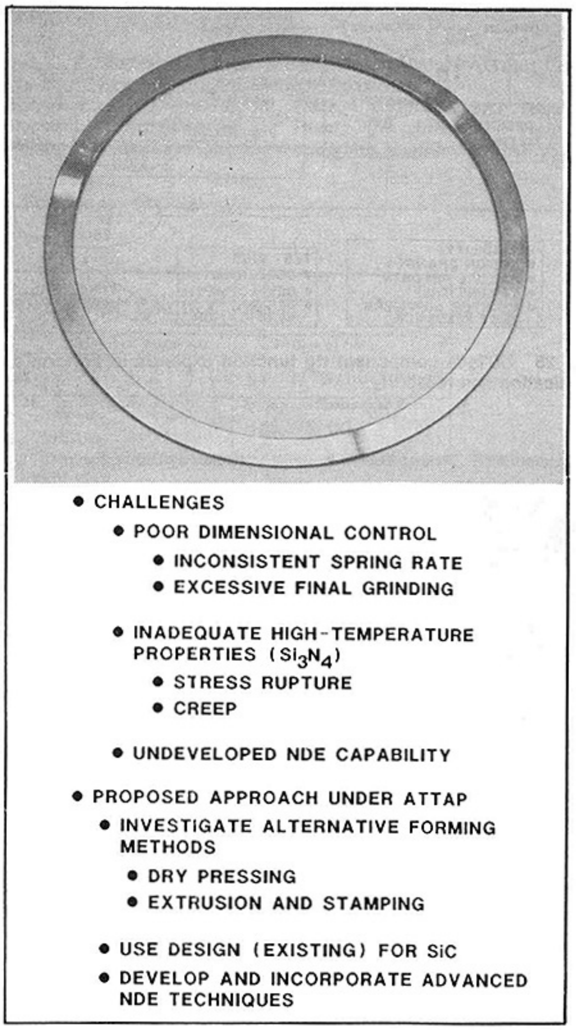

- CHALLENGES
  - POOR DIMENSIONAL CONTROL
    - INCONSISTENT SPRING RATE
    - EXCESSIVE FINAL GRINDING
  - INADEQUATE HIGH-TEMPERATURE PROPERTIES (Si_3N_4)
    - STRESS RUPTURE
    - CREEP
  - UNDEVELOPED NDE CAPABILITY
- PROPOSED APPROACH UNDER ATTAP
  - INVESTIGATE ALTERNATIVE FORMING METHODS
    - DRY PRESSING
    - EXTRUSION AND STAMPING
  - USE DESIGN (EXISTING) FOR SiC
  - DEVELOP AND INCORPORATE ADVANCED NDE TECHNIQUES

Fig. 23 Close tolerance required in high-volume fabrication of wave spring

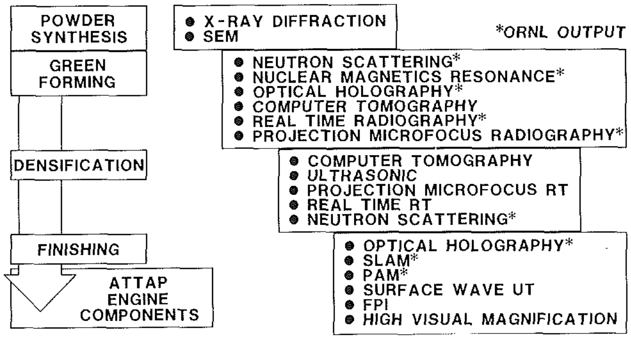

Fig. 24 NDE technique development critical to ceramic volume production

In-process NDE will again assist in improving component quality through early flaw detection and process modification. The major challenge will arise during densification, however, as the green form shrinks to final size and density. Maintaining a circular part and the desired wave form to tight tolerances in this phase will require creative furnace supports and a highly controlled and repeatable hot zone temperature. Control of these factors must be coupled with a homogeneous green density free of minute residual stresses that might occur in green forming. Although the wavespring is a relatively small component, it will require a major engineering effort to achieve success in the ATTAP.

NDE Techniques Development. As indicated in the

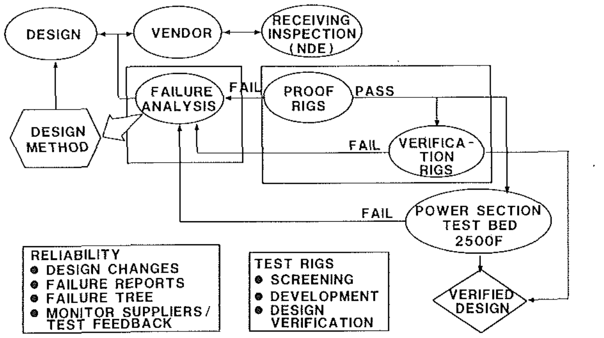

Fig. 25 EGT101 component rig function expands to perform design verification and reliability

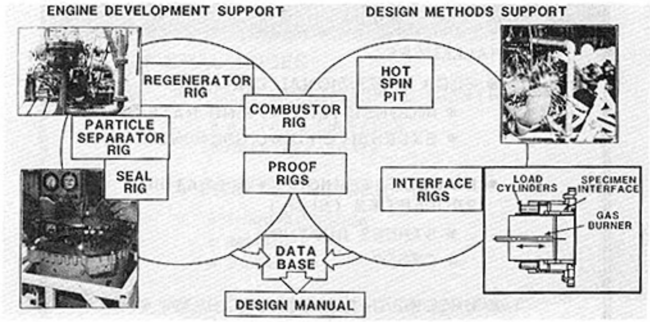

Fig. 26 Component test rigs essential to screening, development, and design method verification

paragraphs above relating to specific ATTAP component fabrication development, NDE must identify potential strength limiting flaws during early processing steps. Figure 24 illustrates some of the the NDE technologies available today and some of those expected to be developed through focused ORNL contracts. Much more work is needed to determine which of these NDE techniques will be most effective in detecting flaws for each phase of the process. Material samples will be deliberately seeded with known defects and detectability limits defined in both green and final densities. NDE methods must be applied to locate and identify type and size of defects with subsequent verification through cut-up visual inspection and modulus of rupture testing. Flaws will be characterized for a given material and fabrication process and a probability of detection calculated for full-size engine components.

Design Methodology and Verification. Design verification in the ATTAP takes on a new perspective from simply proof testing each component as was done in the AGT101 program. With the program scope set on a verified design methodology and life prediction methods, test rigs will be used in part to destructively test components under conditions that are predicted to cause failure. Figure 25 illustrates this test rig role role in design verification and indicates further how a comprehensive reliability plan will assist in improving component quality by performing detailed failure analysis. This analysis will correlate fracture origins with peak stress locations and determine if design modifications and/or fabrication process modifications are required. Feedback to ceramic suppliers will thus assist in improving the component probability of survival in the ATTAP/AGT101 engine test bed environment.

ATTAP test rigs are separated into two major categories: engine development support, and design methods support. Figure 26 illustrates this separation by function and also indicates an overlap in function of the combustor rig and the proof rigs. Rigs that fall under engine development are specific to the ATTAP/AGT101 engine test bed in which performance is the primary goal. These rigs include the hot regenerator rig, combustor rig, seal rigs, and component subassembly thermal/mechanical screening rigs. In design methods development, the rigs shown will be used to develop and/or verify design methods that are not specific to the ATTAP/AGT101 engine but are more generic in nature, i.e., methods to predict life in an impact environment or in high Hertzian stress contact load conditions, etc. The resulting methods can be applied to any ceramic engine utilizing similar materials. The combined data base generated by the test rig program illustrated will feed into the DOE/NASA ceramic design manual shown in Fig. 27. Procedures, methods, criteria, techniques, and specifications that relate to the design and practical use of structural ceramics will be presented. The detail provided in the ceramic design manual will assist U.S. industry in exploiting this new technology in many new and existing product arenas.

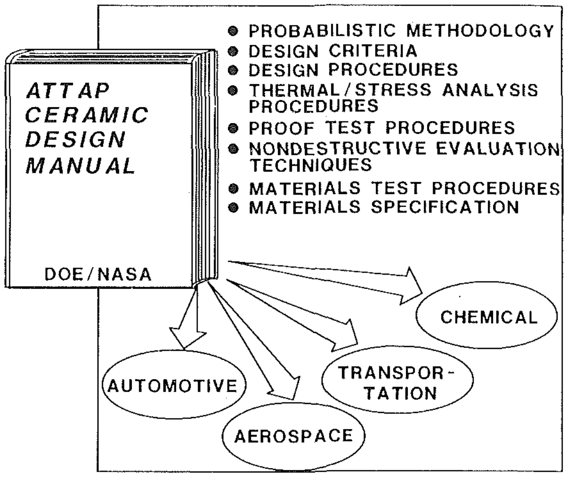

Fig. 27 ATTAP yields critical support for U.S. ceramic industry

Summary

The AGT101 Program ended in June 1987 and the ATTAP was initiated to advance ceramic technology further. Ceramic feasibility in a gas turbine environment was demonstrated in the AGT101 Program in several all-ceramic engine tests to 1204°C (2200°F) TIT and 100,000 rpm operation of the ceramic turbine rotor.

Ceramic technology challenges have been identified through the AGT101 Program that provide the major focus for the ATTAP development activities. These activities include: component fabrication process development with domestic suppliers, NDE technique development, design methods development and verification, improved impact-resistant materials, designs, and high-temperature particle separation technologies. U.S. ceramic suppliers will develop selected critical ceramic components utilizing high volume production fabrication techniques. To verify progress in fabrication development, components will be: (1) cut up and characterized, (2) dimensionally inspected, (3) nondestructively inspected for potentially life-limiting flaws, (4) destructively tested for design method verification in test rigs, (5) proof tested for ceramic engine qualification, and (6) extensively engine tested to 1371°C (2500°F) to demonstrate durability and engine test bed performance. Design methods for predicting component life will be developed under both ATTAP and ORNL programs and will be verified in full-size engine components in engines and highly specialized test rigs.

The total accumulation of technology from both the AGT101 and ATTAP programs will be compiled and published in a DOE/NASA Ceramic Design Manual at the end of the ATTAP contract. The design, NDE, materials, and test methods presented will have been validated through extensive testing to provide statistically sound results that will be useful to all major segments of U.S. industry in which advanced ceramic technology may be applied.

References

Boyd, G. L., Easley, M. L., and Kreiner, D. M., 1987a, "AGT101-Ceramic Gas Turbine Development," ASME Paper No. 87-GT-228.

Boyd, G. L., and Kreiner, D. M., 1987b, "AGT101/ATTAP Technology Development," *Proceedings of the Twenty-Fifth Automotive Technology Development Contractors' Coordination Meeting*, published by SAE.

L. Y. Chao

D. Singh

D. K. Shetty

Department of Materials Science
and Engineering,
University of Utah,
Salt Lake City, UT 84112

Effects of Subcritical Crack Growth on Fracture Toughness of Ceramics Assessed in Chevron-Notched Three-Point Bend Tests

Chevron-notched bend specimens in three-point loading are increasingly used for evaluation of fracture toughness of structural ceramics. Its advantages include stable precracking of the specimen during loading, a simple specimen geometry, and a compressive mode of loading that is convenient for testing ceramics at elevated temperatures. Subcritical crack growth caused by environmental interactions or mass transport phenomena at elevated temperatures, however, can affect the apparent fracture toughness measured. A numerical computational study was carried out to assess the effects of subcritical crack growth on crack stability in the chevron-notched three-point bend specimens. A power-law relationship between the subcritical crack velocity (v) *and the applied stress intensity* (K_I) *was used along with compliance and stress-intensity relationships for the chevron-notched bend specimen to calculate the load response under fixed deflection rate and a machine compliance. The results indicate that the maximum load during the test occurs at the same crack length for all the deflection rates; the maximum load, however, is dependent on the deflection rate for rates below a critical rate. The resulting dependence of the apparent fracture toughness on the deflection rate is compared to experimental results on soda-lime glass and polycrystalline alumina.*

Introduction

The experimental techniques and procedures for evaluating plane strain fracture toughness of metallic materials are well established and they are described in fracture toughness test standards, for example, the ASTM Standard E 399-83 (1984). The test procedures described in this standard, however, cannot be easily employed to measure the fracture toughness of structural ceramics. The limitations are due to the difficulties in precracking the ceramic specimens as well as in applying the test procedures at elevated temperatures that are of interest for structural ceramics. The practice of using machine-notched fracture toughness specimens in place of precracked specimens is all but abandoned since such measurements can give apparent fracture toughness values significantly greater than the true material-characteristic fracture toughness, particularly in fine-grained ceramics (Munz et al., 1980a).

One approach for stable precracking of the fracture toughness specimens of brittle structural materials is through the use of chevron notches, i.e, notches in which the prospective crack-front increases in width from zero to the full thickness of the specimen as the crack length increases in the notch plane. On loading a chevron-notched specimen a crack initiates at the chevron-notch tip at a relatively low load and extends stably with increasing load before becoming unstable at a maximum load corresponding to a critical crack length that is characteristic of the specimen and notch geometry (Newman, 1984). For materials that exhibit a flat crack-growth-resistance behavior, the fracture toughness can be calculated directly from the maximum load using specimen geometry and a stress-intensity coefficient that is dependent only on the chevron-notch geometry. Thus, the main advantages of the chevron-notched specimens are the ease of precracking and avoiding the requirement of measuring the crack lengths.

Chevron notches have now been used with several fracture toughness specimen geometries. Barker (1977, 1979) developed the chevron-notched short-rod and short-bar specimens and measured fracture toughness of both metallic and ceramic materials. The fracture toughness calculations were, however, initially based on an experimental calibration of the maximum load using fracture toughness data on several materials. Munz et al. (1980a, 1980b, 1980c) introduced two approximate methods to calculate the stress-intensity coefficients for chevron-notched four-point bend, short-rod, and short-bar specimens. The first one, now generally referred to as the straight-through-crack assumption (STCA), makes the assumption that the derivative of the compliance with respect to the crack length for a chevron-notched specimen is equal to that of a straight-through crack specimen. In the second method, Munz et al. used a slice synthesis model of Bluhm

---

Contributed by the International Gas Turbine Institute and presented at the 33rd International Gas Turbine and Aeroengine Congress and Exhibition, Amsterdam, The Netherlands, June 5–9, 1988. Manuscript received by the International Gas Turbine Institute December 1, 1987. Paper No. 88-GT-185.

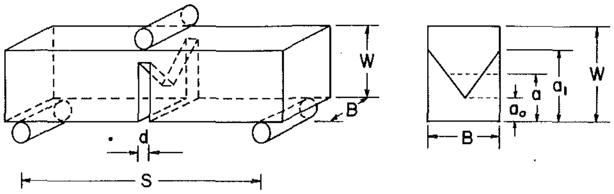

Fig. 1 Geometry of the chevron-notched bend specimen used in the experiments and the numerical calculations

(1975) to evaluate the compliance and stress-intensity factor of a chevron-notched specimen. These methods of analysis have been since employed to assess fracture toughness of brittle materials using chevron-notched three-point bend (Shin, 1981; Wu, 1984) and chevron-notched diametral-compression specimens (Shetty et al., 1985).

Structural ceramics often exhibit subcritical crack growth prior to unstable fast fracture. Subcritical crack growth observed at low temperatures in glasses and ceramics containing a residual glassy phase is believed to be related to interaction with moisture in the environment (Wiederhorn, 1978). At elevated temperatures, subcritical crack growth is caused by diffusional mechanisms, for example, grain-boundary sliding, which in turn is affected by the grain-boundary phases derived from the sintering additives (Evans et al., 1975). Subcritical crack growth can occur during fracture toughness testing and the measured apparent value may be an underestimate of the true fracture toughness of a ceramic. Evans and Wiederhorn (1974) and Chuang et al. (1983) used load-deflection records at different deflection rates to assess subcritical crack growth parameters using precracked double torsion and three-point bend specimens, respectively. Coyle and Buhl (1984) used a computer-assisted technique for measuring subcritical crack growth from the load-deflection records on chevron-notched short-rod specimens. More recently, Troczynski and Nicholson (1987) examined the effects of subcritical crack growth on fracture toughness and work-of-fracture tests using chevron-notched four-point bend tests.

This paper describes the results of a computational and experimental study of the effects of subcritical crack growth on the load-deflection characteristics of chevron-notched three-point bend specimens. A power-law relationship between the subcritical crack velocity (v) and the applied stress intensity (K_I) was used along with compliance and stress-intensity relationships for the chevron-notched bend specimens to calculate the load response under fixed deflection rate and a machine compliance. The results indicate that the maximum load during the test occurs at the same crack length for all the deflection rates; however, the maximum load is dependent on the deflection rate for rates below a critical rate. Experimental results on soda-lime glass and a polycrystalline alumina are in agreement with the results of the numerical computations.

Method of Analysis

The chevron-notched three-point bend specimen investigated in the numerical computations and the experiments is illustrated in Fig. 1. The specimen dimensions and the notch geometry for the two materials used in the calculations and the experiments are listed in Table 1.

Compliance and Stress Intensity for a Chevron-Notched Three-Point Bend Specimen. Application of Irwin's compliance relationship for elastic energy release rate G to a chevron-notched specimen leads to the following equation for the mode I stress-intensity K_I, for a crack in the chevron-notch section (Munz et al., 1980a):

$$K_I = \frac{P}{BW^{1/2}}\left[\frac{1}{2}\,\frac{dC_v(\alpha)}{d\alpha}\,\frac{(\alpha_1-\alpha_0)}{(\alpha-\alpha_0)}\right]^{1/2} \qquad (1)$$

Table 1 Dimensions of the chevron-notched specimens of soda-lime glass and alumina

Ceramic	S (mm)	B (mm)	W (mm)	a_0 (mm)	a_1 (mm)	d (μm)
Soda-Lime Glass	40	5.5	10	3.3	8.06	360
Alumina	40	5.0	10	3.3	7.63	340

where P = load applied in bending, B = specimen thickness, W = specimen width, α = normalized crack length = a/W, α_0 = normalized chevron-notch tip = a_0/W, α_1 = normalized chevron-notch base = a_1/W, and $C_v(\alpha)$ is a nondimensional compliance of the chevron-notched specimen defined by the following equation:

$$C_v(\alpha) = \frac{EB}{(1-\nu^2)}\,C(\alpha) \qquad (2)$$

where E is Young's modulus, ν is Poisson's ratio, and $C(\alpha)$ is the conventional compliance. The compliance of the chevron-notched specimen is independent of the notch width (d) for small values of d.

Two approximations are usually employed to calculate the derivative of the compliance, $dC_v(\alpha)/d\alpha$, for a chevron-notched specimen. In one approximation, it is assumed to be equal to the derivative of the compliance of a straight-through crack specimen. This is referred to as the STCA assumption (Munz et al., 1980). In a second approach, an explicit compliance function $C_v(\alpha)$ is developed for the chevron-notched specimen based on an approximation suggested by Bluhm (1975). In this method, which is referred to as slice synthesis, a chevron-notched specimen is considered to be made up of many slices in the thickness direction with the slices in the central section having the same crack depth, while the slices in the outer chevron-notch sections have crack depths varying according to the notch geometry. The compliance of the composite specimen is developed from the individual compliances of the slices. A correction is introduced to account for the stiffening effects of the interslice shear.

Wu (1984) used a compliance formula for a three-point bend specimen with a straight-through crack reported by Chen Chih et al. (1974) in Bluhm's slice synthesis equation and presented the following analytical expression for the nondimensional compliance of a chevron-notched three-point bend specimen:

$$\frac{1}{C_v(\alpha)} = \frac{\alpha-\alpha_0}{\alpha_1-\alpha_0}\,\frac{1}{\gamma+\beta\tan^2\dfrac{\pi\alpha}{2}} + \frac{k}{(\alpha_1-\alpha_0)(\gamma-\beta)} \times$$

$$(\alpha_1-\alpha) - \frac{2}{\pi}\times\sqrt{\frac{\beta}{\gamma}}\times\left[\tan^{-1}\left(\sqrt{\frac{\beta}{\gamma}}\,\tan\frac{\pi\alpha_1}{2}\right)\right.$$

$$\left. -\tan^{-1}\left(\sqrt{\frac{\beta}{\gamma}}\,\tan\frac{\pi\alpha}{2}\right)\right] \qquad (3)$$

where γ and β are nondimensional constants given by the following equations (Wu, 1984):

$$\gamma = \frac{1}{4}\left(\frac{S}{W}\right)^3\left[1+3(1+\nu)\left(\frac{S}{W}\right)^2\right] \qquad (4)$$

$$\beta = \frac{2}{\pi}\left(\frac{S}{4W}\right)^2\left[7.31+0.21\sqrt{\frac{S}{W}-2.9}\right] \qquad (5)$$

and k in equation (3) is a shear transfer coefficient; according to Bluhm's analysis it is given by

$$k = 1 + 0.444(\alpha_1)^{3.12} \qquad (6)$$

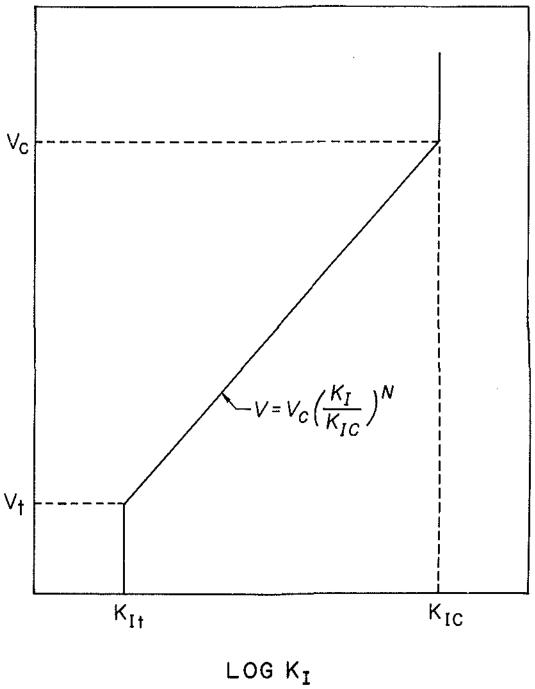

Fig. 2 Schematic of the subcritical crack velocity (v)-stress intensity (K_I) relationship assumed in the numerical calculations

Wu (1984) compared Bluhm's experimental compliance values with the values predicted by equation (3) and found them to agree within 0.5 percent for the case $S/W = 8$, $\alpha_0 = 0$, $\alpha_1 = 1$, and $\alpha = 0.4$. Equation (3) was used in this study to calculate both the specimen deflections as well as stress intensities for the chevron-notched bend specimens at various crack lengths.

Subcritical Crack Growth Behavior. Figure 2 shows the general nature of the subcritical crack growth behavior assumed in the calculations. The subcritical crack growth rate v is zero for applied stress intensities below a threshold value K_{It}. The crack growth rate increases as a power function of the normalized stress intensity for stress intensity values between K_{It} and the critical stress intensity K_{Ic}:

$$v = v_c\left[\frac{K_I}{K_{Ic}}\right]^N \tag{7}$$

where v_c and N are empirical parameters referred to as the critical crack growth rate and the stress-intensity exponent, respectively. v_t is a threshold crack growth rate corresponding to the threshold stress intensity.

The subcritical crack growth behavior shown in Fig. 2 was used in the calculations because experimental measurements on soda-lime glass in water by Wiederhorn and Bolz (1970) and on a 96 percent alumina ceramic in water by Evans (1974) can be closely approximated by the three-stage crack-growth behavior as shown. Further, the subcritical crack growth parameters, K_{It}, v_t, v_c, and N, reported in these studies were used in the calculations since the ceramics and the test conditions employed in this study were very similar. Table 2 lists these parameters and other properties of the ceramics employed in the calculations.

Calculation of Load (P) – Crack Length (α) Relationships for Constant Deflection Rate ($\dot{\delta}$) Testing. Since the subcritical crack growth effects manifest only for $K_I > K_{It}$, a set of initial conditions were first defined based on the value of K_{It} and an arbitrarily selected value of an initial crack length, α_i. The initial load corresponding to this threshold condition can be written as

$$P_i = \frac{K_{It} B W^{1/2}}{Y(\alpha_0, \alpha_1, \alpha_i)} \tag{8}$$

where $Y(\alpha_0, \alpha_1, \alpha_i)$ is a nondimensional stress-intensity coefficient defined from equation (1) as

$$Y(\alpha_0, \alpha_1, \alpha_i) = \left[\frac{1}{2}\,\frac{dC_v(\alpha_i)}{d\alpha}\,\frac{(\alpha_1 - \alpha_0)}{(\alpha_i - \alpha_0)}\right]^{1/2} \tag{9}$$

An initial deflection of the specimen and machine assembly corresponding to the initial load P_i is defined using the following equation:

$$\delta_i = P_i[C(\alpha_i) + C_M] \tag{10}$$

where C_M is a machine compliance. For deflections $\delta > \delta_i$, the load at any crack length is given in terms of the time during slow crack growth as

$$P(\alpha) = \left[\frac{\dot{\delta} t(\alpha) + \delta_i}{C(\alpha) + C_M}\right] \tag{11}$$

The function $t(\alpha)$ is the time taken for the crack to extend subcritically from an initial crack length α_i to a crack length α under the imposed condition of a fixed total deflection rate. It is obtained by integrating the subcritical crack growth equation, equation (7), which can be first rewritten in terms of the normalized crack length and the stress intensity relation for the chevron-notched bend specimen

$$\frac{d\alpha}{dt} = \frac{v_c}{W K_{Ic}^N}\left[\frac{\dot{\delta} t(\alpha) + \delta_i}{C(\alpha) + C_M}\right]^N \left[\frac{Y(\alpha_0, \alpha_1, \alpha)}{B W^{1/2}}\right]^N \tag{12}$$

Rearrangement of equation (12) and integration leads to the following equation for the time for subcritical crack growth, $t(\alpha)$:

$$t(\alpha) = \frac{1}{\dot{\delta}}\left[\left\{\frac{\dot{\delta}(N+1) I(\alpha)}{F} + \delta_i^{N+1}\right\}^{\frac{1}{N+1}} - \delta_i\right] \tag{13}$$

where F and $I(\alpha)$ are, respectively, given by the following equations:

$$F = \frac{v_c}{K_{Ic}^N B^N W^{\frac{N+2}{2}}} \tag{14}$$

$$I(\alpha) = \int_{\alpha_i}^{\alpha}\left[\frac{C(\alpha) + C_M}{Y(\alpha_0, \alpha_1, \alpha)}\right]^N d\alpha \tag{15}$$

The sequence of calculations consisted of first numerically integrating equation (15) for an assumed crack length increment, $\Delta\alpha = \alpha - \alpha_i$; the integral $I(\alpha)$ is then substituted in equation (13) to obtain the time taken for the crack extension $t(\alpha)$, which is then substituted in equation (11) to calculate the load $P(\alpha)$, and finally equation (8) is used to calculate the stress intensity, $K_I(\alpha)$.

The above procedure was used repetitively for a number of specific values of α until the calculated stress intensity equaled K_{Ic}. At this point, the procedure for calculating the load–crack length relationship was changed. For an assumed small increment of deflection $\Delta\delta$, crack lengths and loads were iteratively calculated until the final values simultaneously satisfied both the compliance equation, equation (11), and the stress intensity equation, equation (1), with $K_I = K_{Ic}$. In this manner, the stress intensity remained constant at $K_I = K_{Ic}$ while the crack velocity increased discontinuously according to the log K_I – log v relationship of Fig. 2.

Table 2 Properties of soda-lime glass and alumina ceramics used in the calculations

Ceramic	K_{Ic} (MPam$^{1/2}$)	K_{It} (MPam$^{1/2}$)	N	v_c (mm/s)	E (GPa)	ν
Soda-Lime Glass	0.74	0.26	14.6	14	72.4	0.215
Alumina	3.06	2.0	30.0	10	283	0.21

Test Materials and Experimental Procedures

The ceramics used in the experiments for comparison with the results of the calculations were soda-lime glass and a commercial grade alumina.[1] The primary reason for choosing these specific ceramics was the availability of subcritical crack growth data in the literature on the same (glass) or nearly similar (alumina) materials tested in water. The properties of the two materials are listed in Table 2. The subcritical crack growth parameters were obtained from the literature. Fracture toughness (K_{Ic}) data were obtained in the present study. The alumina ceramic was reported to contain 94 vol percent Al_2O_3 with an average grain size of 6 μm.

Chevron-notched bend specimens of the geometry shown in Fig. 1 were machined by first rough cutting specimen blanks to an approximate size using diamond grit blades. The specimens were machined to the final size by surface grinding with diamond grit wheels. The notching was done with a diamond grit blade nominally 250 μm in thickness. The final notch width (d in Fig. 1) in the specimens was 360 μm in glass and 340 μm in alumina. Following notching the specimens were annealed in air, at 514°C for the glass specimens and at 1000°C for the alumina specimens, to eliminate any residual stresses that may have been introduced during the specimen fabrication.

The constant deflection rate tests were conducted in a universal testing machine.[2] Test fixtures designed to the specifications of MIL-STD-1942 (1983) were used in three-point loading of the chevron-notched bend specimens. Deionized water was used as the environment by containing the water in the notch by using compliant tapes on the sides of the specimens.

Results and Discussion

The results of the numerical calculations and the experiments are presented in two parts. First, the results of the numerical calculations are discussed in terms of the crack length dependence of the loads and the stress intensities for the soda-lime glass and the alumina ceramics. This is then followed by a comparison of the apparent fracture toughness calculated from the maximum loads at different deflection rates with the corresponding experimental results.

Crack Length (α) Dependence of Load (P) and Stress Intensity (K_I). Figure 3 shows the results of the calculations of the effects of subcritical crack growth on the stress-intensity/crack length and load-crack length relationships for chevron-notched bend specimens of soda-lime glass. The load increases monotonically above P_i for deflections greater than δ_i, reaches a maximum load $P_{\max}$ and then decreases at large crack lengths or deflections. The maximum load occurs at the same crack length, $\alpha_c = 0.48$, for different deflection rates at low rates. The corresponding maximum load increases with increasing deflection rates up to a critical deflection rate. Above this critical rate the maximum load occurs at a slightly lower crack length, $\alpha_c = 0.47$, and the maximum load becomes independent of the deflection rate.

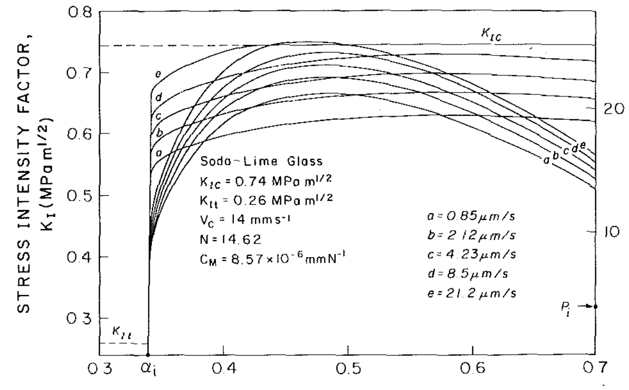

Fig. 3 Calculated load (P)-crack length (α) and stress intensity (K_I)-crack length (α) relationships for chevron-notched bend specimens of soda-lime glass at different deflection rates in water

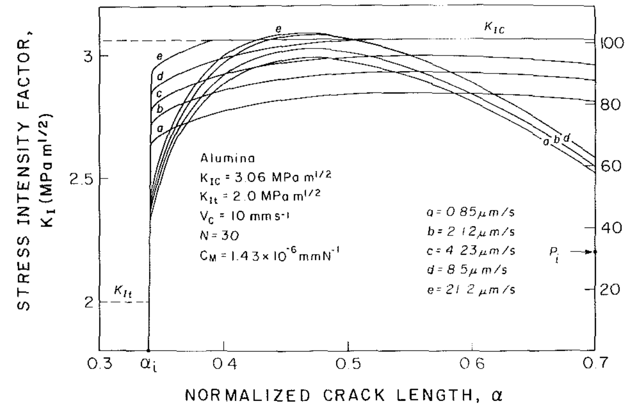

Fig. 4 Calculated load (P)-crack length (α) and stress intensity (K_I)-crack length (α) relationships for chevron-notched bend specimens of alumina at different deflection rates in water

The trend in the variation of the stress intensity with crack length is similar for deflection rates lower than the critical value. The stress intensity increases very rapidly in the early stages of crack growth, then gradually increases to a maximum and then decreases gradually for large crack lengths. The maximum stress intensity occurs at the same crack length ($\alpha = 0.57$ for soda-lime glass and $\alpha = 0.54$ for alumina) for the different deflection rates. For deflection rates above the critical deflection rate, the stress intensity plots show two regimes; at small crack lengths the stress intensity increases in a manner similar to that observed at low deflection rates. The stress intensity, however, reaches K_{Ic} before it reaches a subcritical maximum at a crack length less than α_c. Additional crack growth occurs at constant stress intensity $K_I = K_{Ic}$.

The results of the numerical calculations for the alumina ceramic specimens are shown in Fig. 4. The qualitative trends of the load and the stress intensity with crack growth are similar to the results on soda-lime glass. The critical crack length where maximum loads occur in the subcritical crack growth regime and the critical deflection rate for the transition from the fully subcritical crack growth behavior to the subcritical to critical transition behavior are different because of the quantitative differences in the slow crack growth parameters.

Dependence of the Apparent Fracture Toughness (K_Q) on the Deflection Rates ($\dot{\delta}$). Figure 5 shows a plot of an apparent fracture toughness K_Q for soda-lime glass measured in the chevron-notched bend tests as a function of the deflection

---

[1] Grade AD-94, Coors Ceramics, CO.

[2] Model 1125, Instron Corporation, Canton, MA.

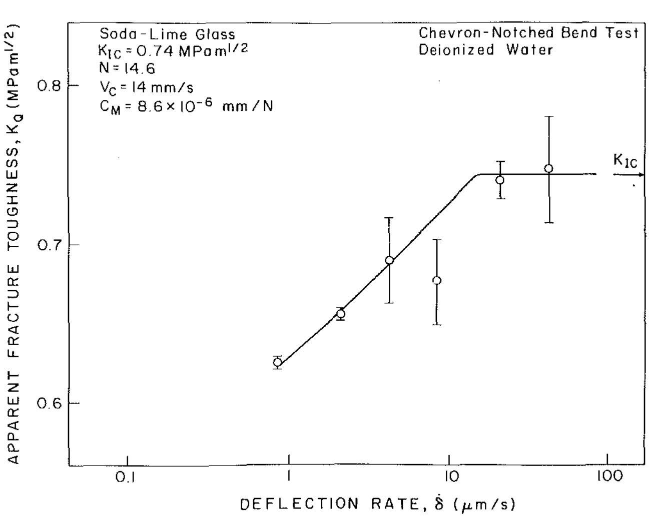

Fig. 5 Deflection rate ($\dot{\delta}$) dependence of apparent fracture toughness for soda-lime glass: ——: numerical calculations; o: experiments

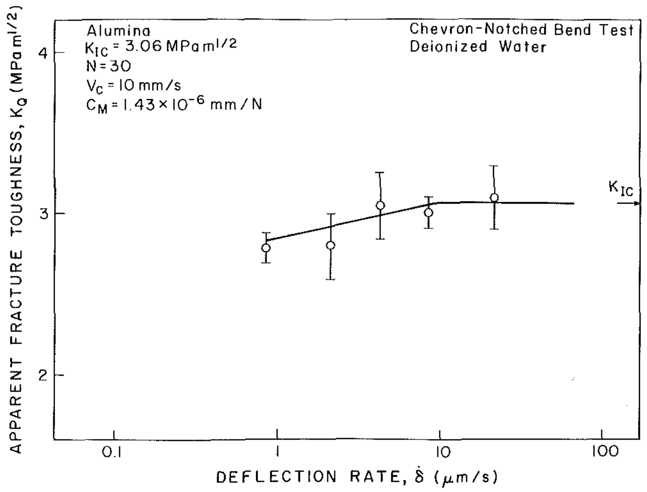

Fig. 6 Deflection rate ($\dot{\delta}$) dependence of apparent fracture toughness for alumina: ——: numerical calculations; o: experiments

rate and compares these experimental results with the predictions of the numerical calculations. For both the experiments and the numerical predictions the apparent fracture toughness was defined by the following equation:

$$K_Q = \frac{P_{\max}}{BW^{1/2}} Y_m \tag{16}$$

where $P_{\max}$ is the maximum load measured in the experiments or obtained in the numerical calculations such as those shown in Figs. 3 and 4. Y_m is the minimum value of the nondimensional stress-intensity coefficient defined in equation (9). Equation (16) is normally used to calculate the fracture toughness K_{Ic} from the maximum loads in chevron-notched bend tests in which subcritical crack growth effects are absent. If inert conditions truly prevail in fracture toughness testing the measured fracture toughness should be independent of the deflection rate and $K_Q = K_{Ic}$. Both the experimental results and the calculations shown in Fig. 5 indicate that in an environment such as water, which promotes subcritical crack growth, the apparent fracture toughness K_Q for soda-lime glass increases with increasing deflection rate up to a critical deflection rate, $\dot{\delta}_c = 21$ μm/s; the apparent fracture toughness $K_Q = K_{Ic}$ and is independent of the deflection rates for higher deflection rates. This critical deflection rate is primarily determined by the velocity parameter v_c, while the deflection rate dependence of the apparent fracture toughness, i.e., slope of the K_Q versus log $\dot{\delta}$ plot for $\dot{\delta} < \dot{\delta}_c$ is mostly determined by the stress-intensity exponent N. A smaller value of N implies a greater susceptibility to subcritical crack growth and the apparent fracture toughness K_Q shows a correspondingly greater dependence on the deflection rate $\dot{\delta}$.

The experimental results and the calculations of the apparent fracture toughness for the alumina ceramic specimens are shown in Fig. 6. The results are qualitatively simliar to those of soda-lime glass. Because of the larger stress-intensity exponent for the alumina (N = 30) as compared to soda-lime glass (N = 14.6) the apparent fracture toughness for the alumina shows much smaller variation with the deflection rate.

Implications of the Results

The results of the numerical calculations and the experiments reported in this paper have important implications for fracture toughness testing of structural ceramics. Many structural ceramics exhibit subcritical crack growth prior to fast fracture and very often the occurrence of this subcritical crack growth cannot be avoided during fracture toughness testing. This is the case, for example, in many ceramics that exhibit subcritical crack growth at elevated temperatures and the subcritical crack growth occurs by an intrinsic diffusion-controlled mechanism that may be independent of the environment. It is important in such cases to ensure that the measured fracture toughness is an intrinsic material property and not an apparent value influenced by subcritical crack growth. Fracture toughness tests at different deflection rates and quantitative calculations of the load-deflection relationships at different rates such as those carried out in this study can provide a useful evaluation of this influence of the subcritical crack growth. For the case of the subcritical crack growth behavior that can be described by the power relationship shown in Fig. 2 the effects of subcritical crack growth can be avoided by conducting the fracture toughness tests at a deflection rate that is greater than a critical value. For the two materials studied here, soda-lime glass and alumina, this critical deflection rate is well within the range that is available in standard universal testing machines.

One important requirement for valid fracture toughness measurements using a chevron-notched specimen is that a stable crack must initiate and propagate through the chevron notch. In purely inert conditions it is often difficult to initiate a sharp crack despite the presence of the chevron notch and an overloaded fast fracture condition may prevail. Results of the present study suggest that subcritical crack growth can in effect be used to advantage for stable precracking of the chevron-notched specimen, and yet valid fracture toughness values can be obtained from such tests, provided the deflection rate is greater than a critical value.

Conclusions

1 Subcritical crack growth accompanying fracture toughness testing of structural ceramics can result in an apparent fracture toughness that is significantly lower than the true value.

2 The magnitude of the effect of subcritical crack growth can be quantitatively assessed for chevron-notched bend specimens using compliance and stress-intensity relationships and an empirical relationship for the subcritical crack growth behavior.

3 For a power-law relationship, effects of subcritical crack growth appear only below a critical deflection rate.

4 Knowledge of the critical deflection rate for a given ceramic/environment system can be used effectively for stable precracking of the chevron-notched specimens.

Acknowledgments

This paper is based on research supported by NASA under grant No. NAG 3-789 at University of Utah. The authors are grateful to Dr. John P. Gyekenyesi, NASA Lewis Research Center, for his encouragement, support, and valuable comments on this paper.

References

ASTM E 399-83, 1984, *Standard Test Method for Plane-Strain Fracture Toughness of Metallic Materials*, American Society for Testing and Materials, Annual Book of ASTM Standards, Section 3, Vol. 03.01.

Bluhm, J. I., 1975, "Slice Synthesis of a Three-Dimensional Work-of-Fracture Specimen," *Engineering Fracture Mechanics*, Vol. 7, pp. 593-604.

Barker, L. M., 1977, "A Simplified Method for Measuring Plane Strain Fracture Toughness," *Engineering Fracture Mechanics*, Vol. 9, pp. 361-369.

Barker, L. M., 1979, "Short Bar Specimens for K_{Ic} Measurements," in: *Fracture Mechanics Applied to Brittle Materials, ASTM STP 678*, S. W. Freiman, ed., American Society for Testing and Materials, Philadelphia, pp. 73-82.

Chen, C., Yao, H., and Chin, C. Y., 1974, "The K_I Calibration of Arc-Shaped, Edge-Cracked Three-Point Bend Specimens," *Kexue Tongbao*, Vol. 19, pp. 41-45.

Chuang, T. J., Chuck, L., Fields, R. J., and Fuller, E. R., 1983, "Effects of Crack Growth on the Load-Displacement Characteristics of Precracked Specimens Under Bending," *Engineering Fracture Mechanics*, Vol. 18, No. 6, pp. 1099-1109.

Coyle, R. T., and Buhl, M. L., 1984, "A Computer-Assisted Technique for Measuring K_I-V Relationships," in: *Chevron-Notched Specimens: Testing and Stress Analysis, ASTM STP 855*, J. H. Underwood, S. W. Freiman, and F. I. Baratta, eds., American Society for Testing and Materials, Philadelphia, pp. 134-151.

Evans, A. G., 1974, "Slow Crack Growth in Brittle Materials Under Dynamic Loading Conditions," *Int. Journal of Fracture*, Vol. 10, No. 2, pp. 251-259.

Evans, A. G., and Wiederhorn, S. M., 1974, "Crack Propagation and Failure Prediction in Silicon Nitride at Elevated Temperatures," *Journal of Materials Science*, Vol. 9, pp. 270-278.

Evans, A. G., Russell, L. R., and Richerson, D. W., 1975, "Slow Crack Growth in Ceramic Materials at Elevated Temperatures," *Metallurgical Trans. A*, Vol. 6A, pp. 707-716.

MIL-STD-1942 (MR), 1983, "Flexural Strength of High Performance Ceramics at Ambient Temperature," Department of Defense, 21 Nov.

Munz, D., Bubsey, R. T., and Shannon, J. L., 1980a, "Fracture Toughness Determination of Al_2O_3 Using Four-Point Bend Specimen With Straight-Through and Chevron Notch," *Journal Am. Ceram. Soc.*, Vol. 63, No. 6, pp. 300-305.

Munz, D., Bubsey, R. T., and Shannon, J. L., 1980b, "Performance of Chevron-Notched Short-Bar Specimens in Determining the Fracture Toughness of Silicon Nitride and Aluminum Oxide," *J. Testing and Evaluation*, Vol. 8, pp. 103-107.

Munz, D., Bubsey, R. T., and Srawley, J. E., 1980c, "Compliance and Stress-Intensity Coefficients for Short-Bar Specimens With Chevron Notch," *Int. Journal of Fracture*, Vol. 16, pp. 359-374.

Newman, J. C., 1984, "A Review of Chevron-Notched Fracture Specimens," in: *Chevron-Notched Specimens: Testing and Stress Analysis, ASTM STP 855*, J. H. Underwood, S. W. Freiman, and F. I. Baratta, eds., American Society for Testing and Materials, Philadelphia, pp. 5-31.

Shetty, D. K., Rosenfield, A. R., and Duckworth, W. H., 1985, "Fracture Toughness of Ceramics Measured by a Chevron-Notched Diametral-Compression Test," *Journal Am. Ceram. Soc.*, Vol. 68, No. 12, pp. C-325-C-327.

Shih, T. T., 1981, "Chevron V-Notched Bend Specimen for K_{Ic} Measurement of Brittle Materials," *J. Testing and Evaluation*, Vol. 9, pp. 50-55.

Troczynski, T. B., and Nicholson, P. S., 1987, "Effect of Subcritical Crack Growth on Fracture Toughness and Work-of-Fracture Tests Using Chevron-Notched Specimens," *Journal Am. Ceram. Soc.*, Vol. 70, No. 2, pp. 78-85.

Wiederhorn, S. M., and Bolz, L. H., 1970, "Stress Corrosion and Static Fatigue of Glass," *Journal Am. Ceram. Soc.*, Vol. 53, No. 10, pp. 543-548.

Wiederhorn, S. M., 1978, "Mechanisms of Subcritical Crack Growth in Glass," in: *Fracture Mechanics of Ceramics*, Vol. 4, Crack Growth and Microstructure, R. C. Bradt, D. P. H. Hasselman, and F. F. Lange, eds., Plenum Press, New York, pp. 549-580.

Wu, S. X., 1984, "Fracture Toughness Determination of Bearing Steel Using Chevron-Notched Three-Point Bend Specimen," *Engineering Fracture Mechanics*, Vol. 19, No. 2, pp. 221-232.

Microstructural Effects on Fracture Toughness of Polycrystalline Ceramics in Combined Mode I and Mode II Loading

D. Singh

D. K. Shetty

Department of Materials Science and
Engineering,
University of Utah,
Salt Lake City, UT 84112

Fracture toughness of polycrystalline alumina and ceria partially stabilized tetragonal zirconia (CeO_2*-TZP) ceramics were assessed in combined mode I and mode II loading using precracked disk specimens in diametral compression. Stress states ranging from pure mode I, combined mode I and mode II, and pure mode II were obtained by aligning the center crack at specific angles relative to the loading diameter. The resulting mixed-mode fracture toughness envelope showed significant deviation to higher fracture toughness in mode II relative to the predictions of the linear elastic fracture mechanics theory. Critical comparison with corresponding results on soda-lime glass and fracture surface observations showed that crack surface resistance arising from grain interlocking and abrasion were the main sources of the increased fracture toughness in mode II loading of the polycrystalline ceramics. The normalized fracture toughness for pure mode II loading,* (K_{II}/K_{Ic})*, increased with increasing grain size for the* CeO_2*-TZP ceramics. Quantitative fractography confirmed an increased percentage of transgranular fracture of the grains in mode II loading.*

Introduction

Mode I fracture toughness, K_{Ic}, is the most widely used material property for characterizing the fracture resistance of structural ceramics. Material development to obtain "tough" structural ceramics as well as their use in structural design are now largely based on mode I fracture toughness. Failure of structural components of ceramics, however, can occur from cracks or flaws arbitrarily oriented with respect to the applied stresses. Reliability analysis of such components must be based on a physically realistic mixed-mode fracture criterion that incorporates the material resistance to fracture in combined mode I, mode II, and mode III loading. Design of a ceramic specimen in which a crack can be subjected to all three modes of loading in a controlled manner is difficult. Recent developments in fracture testing of structural ceramics, however, permit controlled testing in combined mode I and mode II or combined mode I and mode III loading. Shetty (1987) has recently reviewed these test techniques and the limited results obtained to date on structural ceramics.

Three specimen and crack geometries have been used for fracture toughness testing in combined mode I and mode II loading of brittle materials. Panasyuk et al. (1965) and Kordisch et al. (1984) used plate specimens with through-cracks inclined to the direction of applied tension to study mixed-mode fracture of soda-lime glass. The K_I-K_{II} fracture toughness envelope obtained in their experiments generally followed the predictions of linear elastic fracture mechanics theory, but the scatter in the experimental results did not permit a clear discrimination among the different mixed-mode fracture criteria.

Petrovic (1985) tested hollow Si_3N_4 tubes with circumferential notches in combined tension and torsion loading to obtain mode I-mode II fracture toughness. It was difficult to introduce circumferential cracks in the tube specimens and, therefore, the tubes were tested in the as-notched condition. Fracture response of the notched specimens can be significantly different from that of the precracked specimens in mode II and mode III loading because of the absence of crack-face resistance to shear displacements due to grain interlocking or abrasion (Shetty, 1987).

Awaji and Sato (1987) and Yarema et al. (1984) used disk specimens with inclined center notches in diametral compression loading to obtain combined mode I and mode II fracture toughness of graphite and a WC-Co cermet, respectively. This technique is particularly attractive because of the simple specimen and the loading geometry. However, the use of notches instead of cracks in the test specimens in the above studies again resulted in apparently low relative fracture toughness in mode II.

The need for precracking of fracture toughness specimens, especially those tested in predominantly mode II or mode III loading, has become increasingly clear. Ceramic specimens precracked by Knoop microhardness indentation have been used to study mixed-mode fracture of structural ceramics

---

Contributed by the International Gas Turbine Institute and presented at the 33rd International Gas Turbine and Aeroengine Congress and Exhibition, Amsterdam, The Netherlands, June 5–9, 1988. Manuscript received by the International Gas Turbine Institute January 18, 1988. Paper No. 88-GT-208.

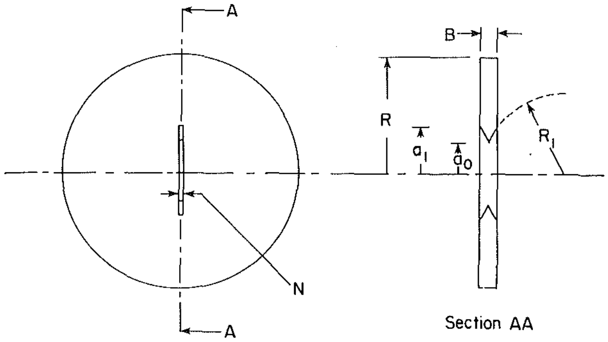

Fig. 1 Geometry of the chevron-notched diametral-compression specimens

(Marshall, 1984; Petrovic, 1985). The surface cracks produced by this technique are difficult to analyze, however, because of the three-dimensional geometry and the consequent variation of K_I, K_{II}, and K_{III} along the crack front. One approach to precracking of ceramic specimens that has been used with some success in recent years is to use specimens with chevron notches. Chevron-notched single-edge-notch-beam (SENB) specimens are now widely used in measurements of mode I fracture toughness of ceramics (Munz et al., 1980). The widening crack front with increasing crack length in the chevron-notched specimens introduces crack stability during the initial precracking. Shetty et al. (1985) have used chevron notches to precrack disk specimens of soda-lime glass, a glass-ceramic, and a polycrystalline alumina prior to testing the disks in diametral-compression for mode I fracture toughness evaluation. Chevron-notched and precracked disk specimens have also been used by these investigators to study mixed-mode fracture in soda-lime glass (Shetty et al. 1987).

Results of combined mode I and mode II fracture toughness measurements on polycrystalline alumina and ceria partially stabilized zirconia (CeO_2-TZP) ceramics using precracked diametral compression specimens are discussed in this paper. The normalized fracture toughness envelopes (plots of K_I/K_{Ic} versus K_{II}/K_{Ic} for fracture) for the polycrystalline ceramics were compared to similar envelopes for soda-lime glass, a model brittle material. The polycrystalline ceramics exhibited significantly higher (normalized) fracture toughness in mode II loading. Fractographic observations suggested that the source of this increased mode II fracture toughness was the crack surface resistance to mode II displacements due to grain interlocking and abrasion. Grain size was found to be an important microstructural variable affecting the normalized mode I-mode II fracture toughness envelope and the fracture toughness in pure mode II loading of polycrystalline ceramics.

Experimental Procedures

Fabricatoin of Disk Specimens With Chevron Notches. In the earlier studies on mode I and mixed-mode fracture in diametral compression, Shetty et al. (1985 and 1987) used disk specimens machined from sintered rods or plates of ceramics obtained from different commercial sources. The chevron notches were machined on fully sintered disks using small-diameter diamond-grit blades. In the present study, the alumina and the CeO_2-TZP ceramic disks were fabricated in house starting with powders. A commercial-grade alumina powder[1] was milled with approximately 3 weight percent polyvinylbuterol as binder and 0.01 weight percent MgO as grain growth inhibitor in acetone with alumina milling media for 24 h. Following drying, the powder was sieved through a 65 μm screen and die pressed at 41.4 MPa (6000 psi) to form nominally 32 mm diameter disks. The disks were subsequently isostatically pressed at 207 MPa (30000 psi) and then presintered at 900 to 1000°C. Chevron notches of the geometry shown in Fig. 1 were machined on the presintered disks using high-speed steel cutting blades 25 mm in diameter and 0.2 mm in thickness. The final sintering of the chevron-notched disk specimens was done at 1600°C for 6 h. The final disk and notch dimensions were as follows: $R = 10.8$ mm, $B = 2.56$ mm, $a_0 = 2.75$ mm, and $a_1 = 5.55$ mm.

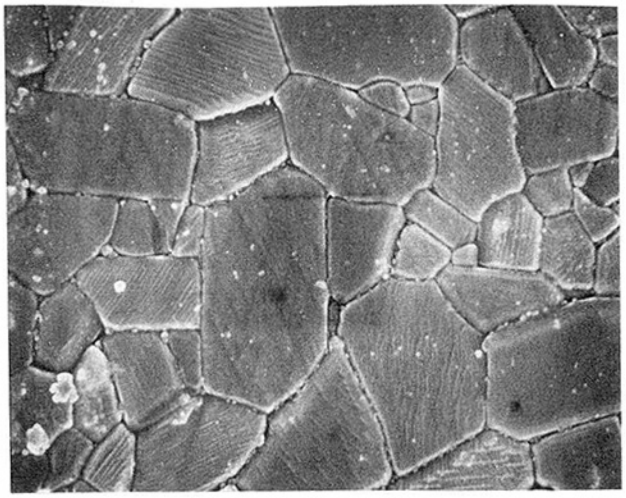

Fig. 2 Microstructure of the polycrystalline alumina used in mixed mode fracture toughness tests

The fabrication procedure for the CeO_2-TZP disks was similar to that used for the alumina. ZrO_2 powder[2] with 12 mole percent CeO_2[3] was milled with ZrO_2 milling media in cyclohexane for 48 h. The dried powder was sieved, die pressed, and isostatically pressed as described above. The presintering was carried out at 900°C. The bisque-fired disks were chevron-notched with the steel cutting blades and final sintered at one of three temperatures selected to vary the grain size of the CeO_2-TZP. The three temperatures chosen in this study were 1450, 1550, and 1625°C. The majority of the fracture toughness measurements on the zirconia were made on the fine-grained (sintered at 1450°C) and the coarse-grained (sintered at 1625°C) ceramics. The intermediate grain size ceramic sintered at 1550°C was used only in a limited number of experiments. The final disk and notch dimensions for the ZrO_2 disks were as follows: $R = 15.5$ mm, $B = 2.2$ mm, $a_0 = 2.6$ mm, and $a_1 = 6$ mm.

The density of the sintered alumina was 3.95 g/cm^3. Figure 2 shows the microstructure of the alumina ceramic. The mean grain size determined by the linear intercept method was 6.7 μm. Figures 3(*a*) and 3(*b*) show the microstructures of the CeO_2-TZP ceramics sintered at 1450 and 1625°C, respectively. The average grain sizes for these two ceramics were 1.6 and 6.7 μm, respectively. The corresponding densities were 6.06 and 6.1 g/cm^3, respectively. Phase analysis of the zirconia ceramics by x-ray diffraction using the calibration of Toraya et al. (1984) indicated 57 vol percent tetragonal phase and 43 vol percent monoclinic phase in the 6.7 μm grain size ceramic and 79 vol percent tetragonal phase and 21 vol percent monoclinic phase in the 1.6 μm grain size ceramic. This difference in the relative contents of the tetragonal and the monoclinic phases in the CeO_2-TZP ceramics is consistent with the particle/grain size effects on phase transformation typically observed in ZrO_2 ceramics (Heuer et al., 1987).

Precracking and Testing of the Disk Specimens. The

---

[1] Grade CR-30, Baikowski, Baikowski International Corp., Charlotte, NC.

[2] Grade DK-1, Daichii, American Vermicullite Corp., Atlanta, GA.

[3] Grade 99.9 weight % Cerium (IV) Oxide, Alpha Products, Danvers, MA.

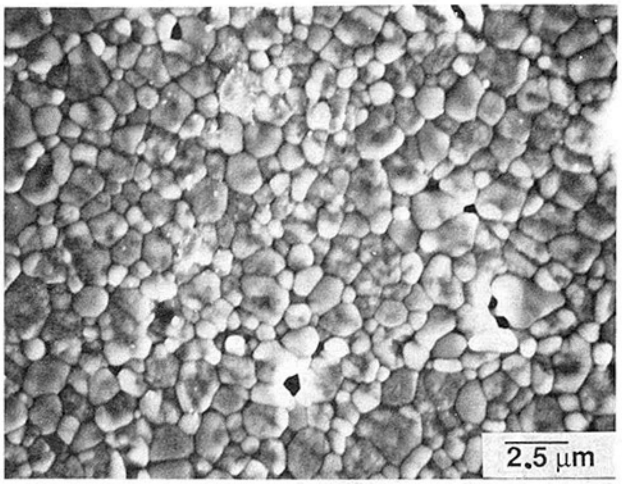

(a)Grain Size = 1.6 μm.

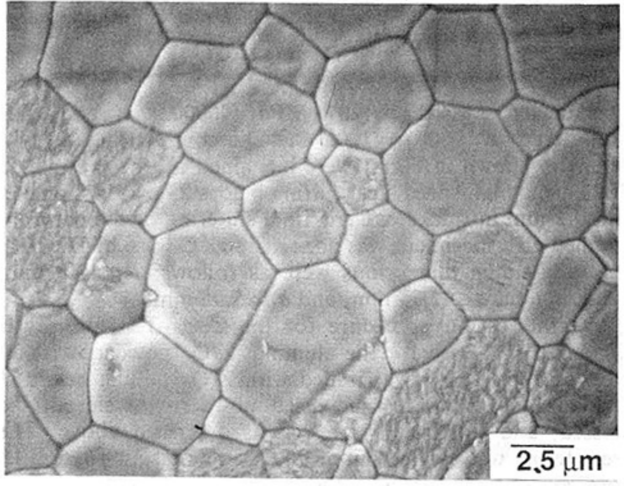

Fig. 3 Microstructures of the CeO_2-TZP ceramics studied in mixed-mode fracture

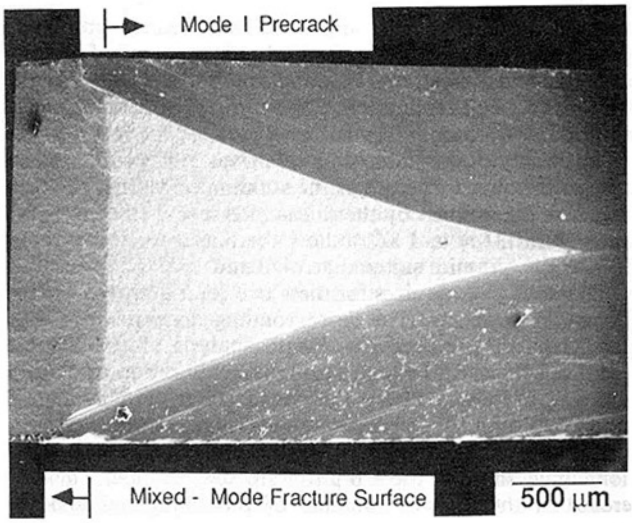

Fig. 4 Fracture surface of a diametral-compression specimen of CeO_2-TZP ceramic precracked in mode I loading and fractured in mixed mode loading

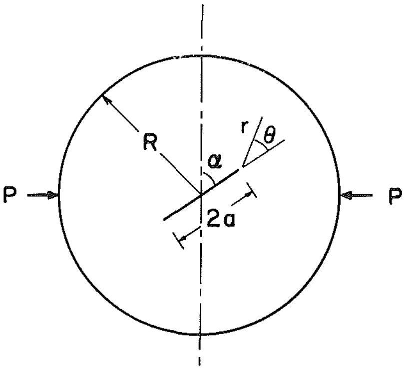

Fig. 5 Inclined crack in a disk specimen and the associated coordinate system

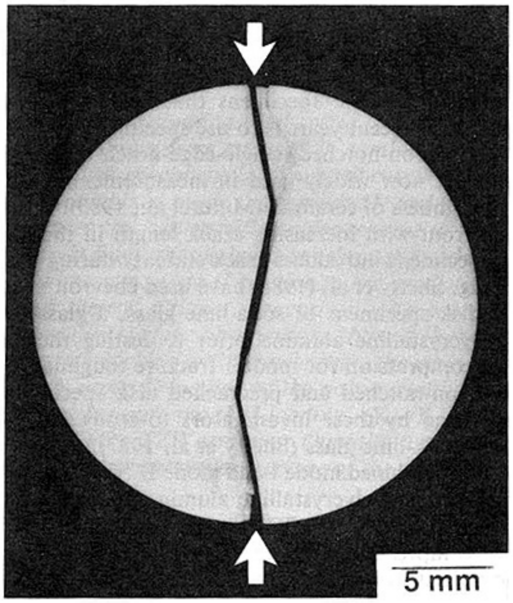

Fig. 6 Fracture pattern in an alumina disk specimen subjected to mixed-mode loading

sintered disk specimens were precracked by loading the disk specimens in mode I, i.e., by loading in compression along a diameter through the chevron notch, to about 90 percent of the critical load. This load was maintained on the specimen for 1 to 2 min and then unloaded. Figure 4 shows typical fracture surface of a diametral-compression specimen of CeO_2-TZP ceramic that was precracked in mode I loading and then fractured in combined mode I and mode II loading. The mode I precracks generally extended to the base of the chevron notch ($a = a_1$).

For combined mode I and mode II fracture testing, the precracked disk specimens were reoriented such that the diameter of compression loading was now at an angle (90-α) with respect to the initial notch and crack plane (see Fig. 5). The crack inclination angle α was varied from 90 deg for pure mode I loading to approximately 60 deg for pure mode II loading in different specimens. The stress-intensity factors for combined mode I (K_I) and mode II (K_{II}) loading were calculated from the initial precrack length a, the fracture load P, and the crack inclination angle α, using the following relationships (Atkinson et al., 1982):

$$K_I = \frac{P\,a^{1/2}}{\pi^{1/2} R\,B} N_I \tag{1}$$

and

$$K_{II} = \frac{P\,a^{1/2}}{\pi^{1/2} R\,B} N_{II} \tag{2}$$

In equations (1) and (2), R and B are the disk radius and thickness, respectively, and N_I and N_{II} are nondimensional

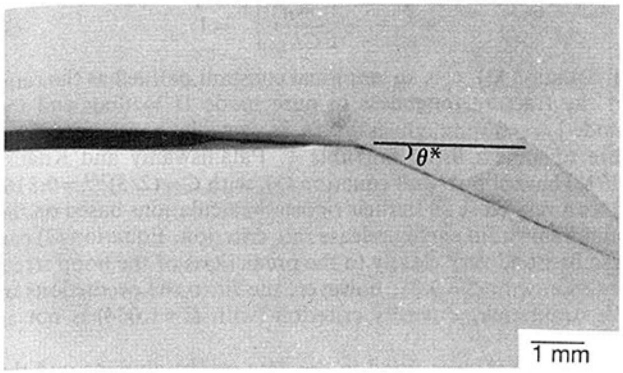

Fig. 7 Noncoplanar crack extension in the vicinity of the original crack tip in an alumina disk specimen

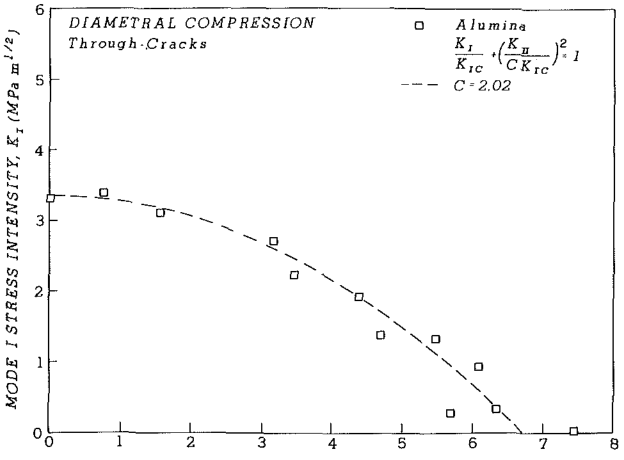

Fig. 8 Mode I and mode II stress-intensity factors for mixed-mode fracture of alumina in diametral-compression tests

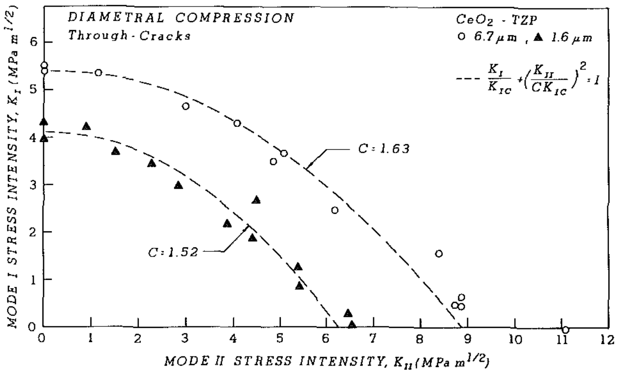

Fig. 9 Mode I and mode II stress-intensity factors for mixed-mode fracture of CeO_2–TZP ceramics in diametral-compression tests

Table 1 Linear elastic fracture mechanics theory predictions and experimental results for pure mode II fracture of ceramics

	Pure Mode II Loading	
	(K_{II}/K_{Ic})	θ*
Theories		
Maximum Hoop Stress	0.866	-70.5
Strain Energy Density	1.054#	-79.2#
Strain Energy Release Rate	0.814	- 77.4
Experiments		
Diametral Compression (Through-Cracks)		
Soda-Lime Glass	1.23	- 66.5
Alumina	2.02	- 45 to -60
Zirconia	1.52,1.63	- 45 to -60
Tension Tests (Through-Cracks)		
Soda-Lime Glass	0.8	- 70.3

for ν = 0.22
θ* : Crack Extension Angle (see Figure 7)

coefficients that are functions of the relative crack length (a/R) and the angle of inclination of the crack relative to the diameter of loading. Atkinson et al. (1982) developed solutions for N_I and N_{II} in the form of series and gave numerical solutions for cracks in the size range $(a/R) = 0.1$ to 0.6 using a five-term approximation. Their solutions were used in the present study by fitting cubic polynomials to the discrete values for purposes of interpolation. Solutions for the stress-intensity factors for inclined cracks in disk specimens have also been independently reported by Yarema et al. (1984). The two solutions agree to a high degree of accuracy.

Extensions of cracks in the disk specimens subjected to combined mode I and mode II loading or those subjected to pure mode II loading were always noncoplanar with the original cracks, i.e., cracks always deviated from their original planes. Figure 6 shows fracture morphology of an alumina specimen subjected to combined mode I and mode II loading. Figure 7 shows the details of the chevron notch, the precrack zone, and the crack extension in the vicinity of the original crack tip. In all the specimens the initial crack extension angle θ^*, as defined in Fig. 7, was measured using a shadowgraph.

Experimental Results

Combined Mode I-Mode II Fracture Toughness of Alumina and Zirconia. Figure 8 shows a plot of mode I stress-intensity factor, K_I, versus mode II stress-intensity factor K_{II}, for combined mode I-mode II fracture of the alumina disks. The critical stress-intensity factor for mode I, K_{Ic}, i.e., mode I fracture toughness, was 3.35 MPam$^{1/2}$. With increasing mode II loading the mode I stress-intensity factor decreased monotonically and for pure mode II loading and mode II stress-intensity factor at fracture was approximately $K_{II} = 6.7$ MPam$^{1/2}$. Thus, the apparent mode II fracture toughness for alumina was twice the mode I fracture toughness.

The disk test results for the fine-grained and the coarse-grained CeO_2–TZP ceramics are summarized in Fig. 9. The critical stress-intensity factor for pure mode I were 4.2 and 5.4 MPam$^{1/2}$, respectively. The fracture toughness envelopes for the zirconia ceramics were similar to that for the alumina with one important difference. The critical mode II stress-intensity factors for pure mode II loading were approximately 6.5 and 9 MPam$^{1/2}$, respectively; thus, the ratios of the apparent mode II fracture toughness to mode I fracture toughness were approximately 1.52 and 1.63 for the two grain sizes. These values are significantly lower than the value of 2.0 observed for the alumina.

Directions of Initial Extensions of Cracks Subjected to Mode I-Mode II Loading. The directions of initial noncoplanar extension of the cracks subjected to combined mode I and mode II loading relative to the notch and the precrack plane θ^* (see Fig. 7) were measured on each disk specimen using a shadowgraph. The crack-extension angle θ^* increased from zero to about 55 deg as the crack-orientation angle α, decreased from 90 deg (pure mode I) to about 65 deg (approximately pure mode II). The crack extension angle showed significant scatter particularly for orientations with large mode II loading. As a result, no significant differences could be detected between the crack-extension directions for the alumina and the zirconia disk specimens.

Comparison With Linear Elastic Fracture Mechanics Theory Predictions. Three different physical criteria have been proposed in linear elastic fracture mechanics theory to predict critical loads and direction of crack extension in mixed-mode fracture of brittle materials (Shetty et al., 1987):

(*a*) Maximum Hoop Stress Criterion (Erdogan and Sih, 1963)
(*b*) Minimum Strain Energy Density Criterion (Sih, 1974)
(*c*) Maximum Strain Energy Release Rate Criterion (Palaniswamy and Knauss, 1978).

Shetty et al. (1987) critically examined the predictions of each of the above criteria with experimental results obtained on soda-lime glass, a model brittle material, using the precracked disk specimens in compression and the angled cracks in tension. A summary of the theoretical predictions and the experimental results, including the present results on alumina and zirconia, is given in Table 1. The table lists the critical value of $K_{\rm II}$ normalized by $K_{\rm Ic}$ for pure mode II loading, i.e., the ratio of the apparent fracture toughness in mode II and mode I fracture toughness and the angle of extension of the cracks subjected to pure mode II loading. The maximum hoop stress and the strain energy release rate criteria predict a lower fracture toughness in mode II than in mode I loading ($K_{\rm II}/K_{\rm Ic}=0.866$ and 0.814, respectively). The strain energy density criterion, on the other hand, predicts comparable fracture toughness values, although the exact value of the fracture toughness ratio is a function of the Poisson's ratio ($K_{\rm II}/K_{\rm Ic}=1.054$ for $\nu=0.22$). The predictions of the angle of crack extension are -70.5, -77.4, and -79.2 with the strain energy density criterion predicting the largest angle.

In relation to the above theoretical predictions, experimental results of combined mode I and mode II fracture show considerable variability. Examination of Table 1 indicates that tension test results on soda-lime glass with the angled through-cracks are the closest to the theoretical predictions. In contrast to this the results of the diametral compression tests with the precracked disk specimens show significantly higher fracture toughness in mode II loading and smaller crack extension angles when compared to the theories. Alumina specimens exhibited the highest toughness value in mode II loading ($K_{\rm II}/K_{\rm Ic}=2.0$) while soda-lime glass showed the lowest value ($K_{\rm II}/K_{\rm Ic}=1.25$). Zirconia showed an intermediate behavior ($K_{\rm II}/K_{\rm Ic}=1.52$ and 1.63).

The trend of the angles of crack extension was similar, i.e., the angle measured on soda-lime glass in tension tests ($\theta^*=-70.3$) was close to the theoretical predictions, while the measurements on the disk specimens were lower. Again, the polycrystalline ceramics showed greater deviation from the theories ($\theta^*=-45$ to -60 for both alumina and zirconia) than soda-lime glass ($\theta^*=-66.5$).

Mode I-Mode II Fracture Toughness Envelopes. In addition to the mode II fracture toughness value and the angle of crack extension for pure mode II loading the mixed-mode fracture criteria in linear elastic fracture mechanics theory also predict combined mode I and mode II fracture toughness envelopes. The mathematical developments for the above three criteria using the elastic stress and displacement solutions for cracks subjected to mode I and mode II loading are tedious and have been discussed recently by Shetty et al. (1987). For the present, it is adequate to note that the following empirical equation, suggested independently by Palaniswamy and Knauss (1987) and, more recently, Richard (1985), gives a good fit to both the theoretical predictions and the experimental results:

$$\frac{K_{\rm I}}{K_{\rm Ic}}+\left[\frac{K_{\rm II}}{CK_{\rm Ic}}\right]^2=1 \tag{3}$$

In equation (3), C is an empirical constant defined as the ratio of the fracture toughness in pure mode II loading and the mode I fracture toughness. C is, in fact, the normalized fracture toughness listed in Table 1. Palaniswamy and Knauss (1978) have shown that equation (3), with $C=(2/3)^{1/2}=0.816$, gives a very close fit to their rigorous calculations based on the minimum strain energy release rate criterion. Equation (3) can also be fitted very closely to the predictions of the hoop stress criterion with $C=0.87$; however, the fit to the predictions of the strain energy density criterion (with $C=1.054$) is not as good.

Equation (3) was fitted to the data on the alumina and the zirconia ceramics by a nonlinear least-square deviation regression analysis of ($K_{\rm II}/K_{\rm Ic}$) on ($K_{\rm I}/K_{\rm Ic}$). The C values obtained by this regression analysis and the fit of equation (3) (shown by the dashed lines) are shown in Figs. 8 and 9. The empirical equation provides reasonably good fits to the data on both alumina and the zirconia ceramics.

Discussion

It is evident from the results of this study that their is no simple and unique mixed-mode fracture criterion that can account for all of the combined mode I and mode II fracture toughness data on ceramics. The data reported in the literature on precracked soda-lime glass (tension specimens of Panasyuk et al., 1965, Kordisch et al., 1984 and diametral compression specimens of Shetty et al., 1987) and the data presented in this study on precracked polycrystalline ceramics show definitively that normalized mode II fracture toughness ($K_{\rm II}/K_{\rm Ic}$) and the mode I-mode II fracture toughness envelope ($K_{\rm I}/K_{\rm Ic}$ versus $K_{\rm II}/K_{\rm Ic}$) show dependence on both specimen and test geometry and nature of the ceramic. As a result, mixed-mode fracture criteria formulated only in terms of the stress-intensity factors $K_{\rm I}$ and $K_{\rm II}$ do not adequately explain combined mode I and mode II fracture toughness of ceramics.

The physical reasons for the observed departure of the experimental results from the predictions of the linear elastic fracture mechanics theory are of interest to gain insight into the mixed-mode fracture behavior of ceramics. The effects of specimen and test geometry on combined mode I and mode II fracture toughness, as exhibited by the results on soda-lime glass in the tension and the disk compression tests, have been discussed in detail by Shetty et al. (1987). The higher values of the mode II fracture toughness measured in the disk tests as compared to the tension tests (see for example, Table 1) have been attributed to the differences in the stress states in the two test specimens. For nominally identical mixed-mode loading in the two test geometries, i.e., for identical combination of $K_{\rm I}$ and $K_{\rm II}$ in the two test geometries, the remote tensile stress normal to the crack plane that defines the mode I stress intensity, $K_{\rm I}$, and the remote shear stress parallel to the crack faces and normal to the crack front and which defines the mode II stress intensity, $K_{\rm II}$, are identical for the two test geometries. However, a third stress component, i.e., the remote normal stress parallel to the cracks, is different in the two test geometries. Specifically, this stress is tensile in the tension test specimen while it is a large compression in the disk specimen. While it is recognized that these stresses do not contribute to the stress singularities, they do modify the stress field in the neighborhood of a crack tip (Eftis and Subramonian, 1978; Smith, 1987). The differences in the mixed-mode results obtained in the two test geometries have been shown to be consistent with this second-order effect on the local crack-tip stress field due to the in-plane normal stresses (Shetty et al., 1987).

In addition to the specimen and loading geometry effects discussed above, the results of the present study also clearly demonstrate a material influence on combined mode I and

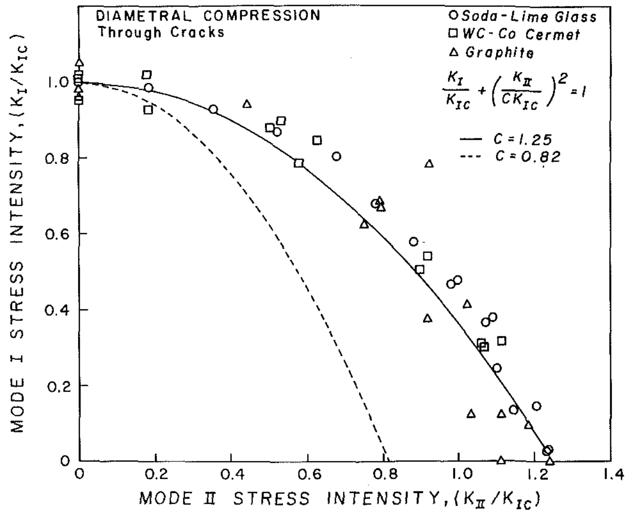

Fig. 10 Normalized mode I-mode II fracture toughness envelopes for graphite and WC-Co in notched disk compression tests compared to the envelope for precracked soda-lime glass

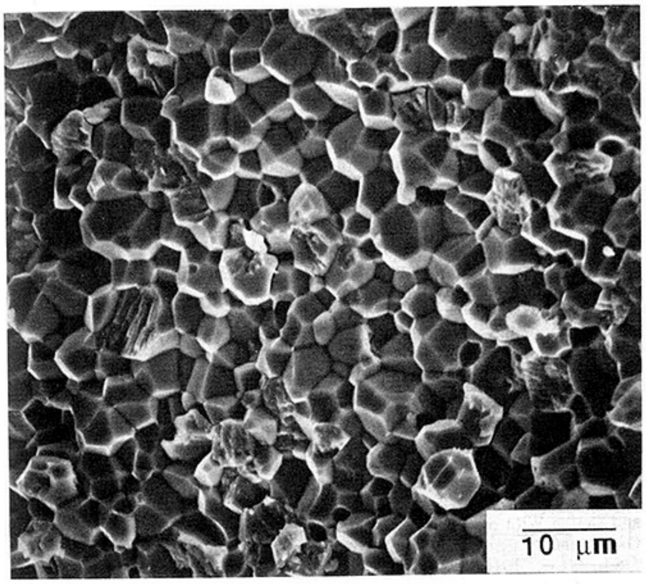

Fig. 11 Intergranular fracture mode in CeO_2-TZP disk specimens subjected to pure mode I loading

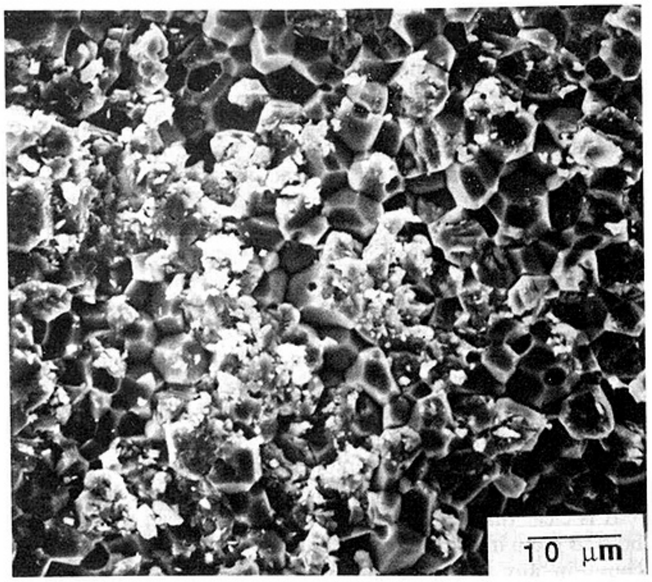

Fig. 12 Debris particles and sheared grains on the fracture surface of CeO_2-TZP disk specimens fractured in mixed-mode loading

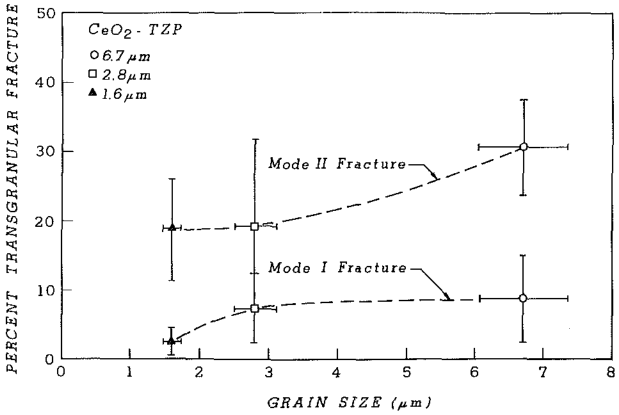

Fig. 13 Variation of percent transgranular fracture with grain size for CeO_2-TZP ceramics tested in pure mode I and pure mode II loading

mode II fracture toughness. For example, in the same disk tests (K_{II}/K_{Ic}) for pure mode II loading was 1.25 for soda-lime glass, 1.52 to 1.63 for CeO_2-TZP, and 2.02 for alumina. The higher normalized mode II fracture toughness of the polycrystalline ceramics relative to soda-lime glass is believed to be due to microstructural asperities and their resistance to shear displacements in predominantly mode II loading (Marshall, 1984).

Two types of experimental evidence directly support the concept of shear resistance to mode II loading. First, when the diametral compresson test results of Shetty et al. (1987) on soda-lime glass are compared with the notched disk test results of Awaji and Sato (1978) on graphite and Yarema et al. (1984) on WC-Co cermet, a good agreement is obtained on a normalized mode I-mode II fracture toughness plot as shown in Fig. 10. In these two latter studies the shear resistance of the microstructural asperities was essentially eliminated by the use of open notches instead of natural cracks. As a result, the polycrystalline ceramics behaved similarly to a model glassy material, i.e., soda-lime glass.

Secondly, examination of the fracture surfaces of the disk specimens revealed significant differences in the micromechanisms of fracture in mode I and mode II loading. Figure 11 shows the fracture surface of a CeO_2-TZP diametral-compression specimen fractured in pure mode I loading. Fracture is essentially intergranular with clean grain facets. Figure 12 shows the fracture surface of a CeO_2-TZP disk specimen fractured in pure mode II loading. The fracture surface shows a significant amount of debris and sheared grains. The percentage of transgranularly fractured grains was estimated by quantitative fractography using a point count method. Measurements on pure mode I and pure mode II specimens of CeO_2-TZP ceramics of three grain sizes are summarized in Fig. 13. The percent transgranular fracture for mode I specimens ranged from 2.5 to 8.5 with increasing grain size; the mode II specimens showed 18.5 to 31 percent of transgranular fracture for zirconia ceramics of increasing grain sizes. Despite the large errors associated with the fractographic measurements, it is clear that the above differences in the percentage of transgranular fracture are significant and reflect intrinsic differences in the micromechanisms of fracture in pure mode I and pure mode II loading. Similar measurements on alumina specimens showed 19.5 and 25 percent transgranular fracture in mode I and mode II specimens, respectively. It is believed that both the debris on the fracture surface and the enhanced transgranular fracture in mode II specimens are direct manifestations of the microstructural effects in mode II fracture. Polycrystalline ceramics that exhibit predominantly intergranular fracture in mode I are susceptible to grain interlocking and grain shear when subsequently loaded in mode II. The grain shearing and abrasion results in the fine debris observed on the fracture surface.

It is interesting to note that on a normalized basis alumina exhibits a higher mode II fracture toughness than does the zirconia ceramic. It is possible that the higher mode II fracture toughness of alumina is due to both its large grain size and its higher hardness. The grain size is important because it determines the asperity size and the relative degree of grain interlocking. This effect of the grain size is indeed noted in Fig. 9. The CeO_2-TZP with the larger grain size does show a slightly higher normalized mode II fracture toughness ($C = 1.63$) as compared to the fine-grained ceramic ($C = 1.52$). Hardness of a ceramic may play a role in mode II fracture because of its influence on wear and abrasion of the precracked surface.

It is clear that the shear tractions on the crack surface due both to grain interlocking and abrasion must be taken into account in any linear elastic fracture mechanics analysis of mixed-mode fracture of polycrystalline ceramics. In the past frictional effects on crack surfaces have been generally taken into account in problems of inclined cracks subjected to compression. Similar treatments must be now extended to combined mode I and mode II fracture with the crack surface tractions closely related to the scale of the microstructural features relative to the crack face displacements.

Conclusions

1 Polycrystalline ceramics exhibit significantly higher normalized mode II fracture toughness as compared to soda-lime glass.

2 The higher mode II fracture toughness of polycrystalline ceramics is related to crack surface resistance from grain interlocking and abrasion.

3 Precracked polycrystalline ceramics subjected to mode II loading exhibit significant abrasion and wear debris and increased percentage of transgranular fracture on the fracture surface.

4 Mixed-mode fracture tests with as-notched test specimens that are not precracked can significantly underestimate fracture toughness in mode II loading.

5 Polycrystalline ceramics do not exhibit unique mode I-mode II fracture toughness envelopes because the crack surface tractions are influenced by microstructural parameters such as grain size and other material properties such as hardness.

Acknowledgments

This paper is based on research supported by NASA under grant No. NAG 3-789 at the University of Utah. The authors are grateful to Dr. John P. Gyekenyesi of NASA Lewis Research Center for the support of this research and valuable comments on the manuscript.

References

Atkinson, C., Smelser, R. E., and Sanchez, J., 1982, "Combined Mode Fracture via the Cracked Brazilian Disk Test," *Int. Journal of Fracture*, Vol. 18, No. 4, pp. 279-291.

Awaji, H., and Sato, S., 1978, "Combined Mode Fracture Toughness Measurement by the Disk Test," ASME *Journal of Engineering Materials Technology*, Vol. 100, No. 4, pp. 175-182.

Eftis, J., and Subramonian, N., 1978, "The Inclined Crack Under Biaxial Load," *Engineering Fracture Mechanics*, Vol. 10, No. 1, pp. 43-67.

Erdogan, F., and Sih, G. C., 1963, "On the Crack Extension in Plates Under Plane Loading and Transverse Shear," ASME *Journal of Basic Engineering*, Vol. 85D, pp. 519-527.

Heuer, A. H., Claussen, N., Kriven, W. M., and Ruhle, M., 1982, "Stability of Tetragonal ZrO_2 Particles in Ceramic Matrices," *Journal of Am. Ceram. Soc.*, Vol. 65, No. 12, pp. 642-650.

Kordisch, H., Riedmuller, J., and Sommer, E., 1984, "The Strain Energy Density Criterion—Investigations for Its Applicability," in: *Proc. Symp. Absorbed Spec. Energy/Strain Energy Density*, G. C. Sih, E. Czoboly, and F. Gillemot, eds., Akademiai Kiado, Budapest, pp. 33-43.

Marshall, D. B., 1984, "Mechanisms of Failure From Surface Flaws in Mixed-Mode Loading," *Journal of Am. Ceram. Soc.*, Vol. 67, No. 2, pp. 110-116.

Munz, D., Bubsey, R. T., and Shannon, J. L., Jr., 1980, "Fracture Toughness Determination of Al_2O_3 Using Four-Point-Bend Specimens With Straight-Through and Chevron Notches," *Journal of Am. Ceram. Soc.*, Vol. 63, No. 5-6, pp. 300-305.

Palaniswamy, K., and Knauss, W. G., 1978, "On the Problem of Crack Extension in Brittle Solids Under General Loading," *Mechanics Today*, Vol. 4, pp. 87-148.

Panasyuk, V. V., Berezhnitskyi, L. T., and Kovchik, S. Ye., 1965, "Propagation of an Arbitrarily Oriented Rectilinear Crack During Extension of a Plate," *Prikladnaya Mekhanika*, Vol. 1, No. 2, pp. 48-55.

Petrovic, J. J., 1985, "Mixed-Mode Fraction of Hot-Pressed Si_3N_4," *Journal of Am. Ceram. Soc.*, Vol. 68, pp. 348-355.

Richard, H. A., 1985, "Fracture Predictions for Cracks Exposed to Superimposed Normal and Shear Stresses," *VDI Forschungsheft*, Vol. 631, pp. 1-60.

Shetty, D. K., Rosenfield, A. R., and Duckworth, W. H., 1985, "Fracture Toughness of Ceramics Measured by a Chevron-Notched Diametral Compression Test," *Journal of Am. Ceram. Soc.*, Vol. 68, No. 12, pp. C-325-C-327.

Shetty, D. K., Rosenfield, A. R., and Duckworth, W. H., 1987, "Mixed-Mode Fracture in Biaxial Stress State: Application of the Diametral-Compression (Brazilian Disk) Test," *Engineering Fracture Mechanics*, Vol. 26, No. 6, pp. 825-840.

Shetty, D. K., 1987, "Mixed-Mode Fracture Criteria for Reliability Analysis and Design With Structural Ceramics," ASME JOURNAL OF ENGINEERING FOR GAS TURBINES AND POWER, Vol. 109, No. 3, pp. 282-289.

Sih, G. C., 1974, "Strain-Energy-Density Factor Applied to Mixed-Mode Crack Problems," *Int. Journal of Fracture*, Vol. 10, No. 3, pp. 305-320.

Smith, R. N. L., 1987, "Second-Order Terms and Strain Energy Density for the Angled Crack Problem," *Engineering Fracture Mechanics*, Vol. 26, No. 3, pp. 463-469.

Toraya, H., Yoshimura, M., and Somiya, S., 1984, "Calibration Curve for Quantitative Analysis of the Monoclinic-Tetragonal ZrO_2 System by X-Ray Diffraction," *Journal of Am. Ceram. Soc.*, Vol. 67, No. 6, pp. C-119-C-121.

Yarema, S. Ya., Ivanitskaya, G. S., Maistrenko, A. L., and Zboromirskii, A. I., 1984, "Crack Development in a Sintered Carbide in Combined Deformation of Types I and II," *Probl. Prochn.*, Vol. 16, No. 8, pp. 1121-1128.

Fiber Metal Acoustic Material for Gas Turbine Exhaust Environments

M. S. Beaton
Brunswick Corporation,
Technetics Division,
Energy Conservation Systems,
DeLand, FL 32724

FELTMETAL® fiber metal acoustic materials function as broad band acoustic absorbers. Their acoustic energy absorbance occurs through viscous flow losses as sound waves pass through the tortuous pore structure of the material. A new FELTMETAL® fiber metal acoustic material has been designed for use in gas turbine auxiliary power unit exhaust environments without supplemental cooling. The physical and acoustic properties of FM 827 are discussed. Exposure tests were conducted under conditions that simulated auxiliary power unit operation. Weight gain and tensile strength data as a function of time of exposure at 650°C (1202°F) are reported. Fabrication of components with fiber metal acoustic materials is easily accomplished using standard roll forming and gas tungsten arc welding practices.

Introduction

FELTMETAL® fiber metal acoustic media (sintered stainless steel fiber structures in thin sheet form) are used to reduce the noise output from gas turbine engines including the auxiliary power units (APUs) on commercial aircraft. Gas turbine exhaust silencers are exposed to the products of combustion of jet fuel. The severity of this environment will vary with the design parameters of each application, with ambient conditions, and with other factors. The temperature limit for the use of a given acoustic medium is primarily determined by the material (alloy) from which the medium is fabricated. New APU installation designs have imposed higher operating temperatures for acoustic media. Higher performance media capable of longer operating life at higher temperatures are required for these applications. This report describes a test program whose objective is to determine the suitability of a new acoustic attenuation material for operation in the 650°C temperature range.

Noise Reduction

The gas turbine engine represents a source of noise of wide frequency range. The jet itself generates noise for several engine diameters downstream from the actual exit. The frequency of the noise decreases with increasing distance from the engine exit point (Franken, 1960). In addition to the jet, noise is created by the fan, both radiating forward from the fan and at the fan bypass exit. The compressor, turbine, and combustors also add their own frequency contributions to the total engine noise spectrum. Efforts to curb the noise generated by gas turbine engines have been exerted since the introduction of jets for commercial aircraft (Kester and Peracchio, 1976).

Acoustic attenuation media may be point reactive or bulk absorbing in nature (Nayfeh et al., 1975). Bulk absorbing media may be physically unwieldy or mechanically unsuitable for use in aircraft engine applications. A typical duct silencer might consist of a thin sheet of porous material with a flat, smooth surface backed by cavities of depth appropriate to the frequency of sound being generated. This arrangement provides noise attenuation over a broad band of frequency with a lightweight structure. The smooth flow surface of the fiber metal sheet keeps self-noise generation low (Bauer, 1976). In the fiber metal structure, the pores are interconnected, with many tortuous flow paths. The energy of an acoustic wave tends to dissipate within a porous material through viscous flow losses as the wave passes through the porous medium. Among the FELTMETAL® fiber metal acoustic materials, layers of screen mesh may be employed to structurally reinforce the material for application (Fisher and Erickson, 1966).

Fiber Metal Acoustic Materials

FELTMETAL® fiber metal acoustic materials are thin sheets of carefully controlled aggregates of metal fibers. The fibers are joined into a contiguous mass by sintering. A given product may incorporate more than one fiber size or type, or layers of screen may be used to reinforce the material structurally and assure product durability. Final product strength and acoustic properties are controlled by the sintering schedule and by compressing the sheet to a predetermined density. The density and fiber diameter control the pore size and determine the specific surface area. These factors have controlling influences on the air flow resistance of the acoustic material.

Most of the FELTMETAL® fiber metal acoustic attenuation materials are fabricated from Type 347 stainless steel. However, any alloy that can be drawn into wire and sintered can be used to produce these materials. The Type 347 materials function well in applications with temperatures up to 540°C (1004°F). FM 134 is a widely used acoustic material with 35 rayl (cgs) flow resistance. Physical properties of this material are listed in Table 1. This material is typically used in exhaust silencers for gas turbine auxiliary power units for commercial aircraft.

A new APU silencer design required a silencing medium of

Contributed by the International Gas Turbine Institute and presented at the 33rd International Gas Turbine and Aeroengine Congress and Exhibition, Amsterdam, The Netherlands, June 5–9, 1988. Manuscript received by the International Gas Turbine Institute September 30, 1987. Paper No. 88-GT-175.

Table 1 Properties of selected fiber metal products

ALLOY	COMPOSITION	CTE, 1/degF x10-6	FIBER DIAM. microns	FM DESIG.
Type 347	Fe18Cr11Ni	10.4	102	FM 134
Type 430	Fe16Cr	6.6	25-85	FM 1304
Hoskins 875	Fe22Cr5.5Al	6.3	142	FM 1401

Table 2 Product properties affected by oxidation in still air

PRODUCT NUMBER	TENSILE STRENGTH (PRETEST) PSI	TENSILE STRENGTH (POST TEST) PSI	STRENGTH CHANGE FROM PRETEST %	OXIDATION WEIGHT GAIN %
FM 134	15,345	13,306	-13.3	4.32
FM 1304	4,893	4,985	+1.9	0.22
FM 1401	4,997	4,680	-6.3	0.04

the same acoustic performance as FM 134, yet capable of operating continuously at 650°C (1202°F). The gas turbine exhaust gases are products of combustion of jet fuel, which are typically oxygen-rich and contain sulfur. Therefore, the design of a material for the new application required consideration of both the temperature and the chemical nature of the environment.

The combustion of fossil fuels presents materials problems mainly due to impurities. Many studies of high-temperature corrosion of engine and power plant components have been carried out. Examples of such studies include Zaigen et al. (1980), Saegusa and Shores (1982), Tiernay and Natesan (1980), Packer and Perkins (1980), and Sorrell (1987). Impurities deposit on operating hardware and can lead to corrosive reaction at the elevated temperatures of operation. Sulfidation is the most studied class of reaction relating to fossil energy conversion applications (Hoffman, 1984). While the corrosion mechanisms vary depending upon the level of sulfur concentration, the oxidation potential of the system, it is generally recognized that greater resistance to the corrosive reactions will be realized as chromium content is increased, and that additions of secondary oxide-forming elements, including aluminum, to high chromium alloys tends to enhance strongly the resistance to hot corrosion.

In selecting an alloy for the new material, consideration was given to corrosion resistance, fabricability, durability in service, cost, and availability. The austenitic stainless steels, which include Type 347, have good corrosion and oxidation resistance at lower temperatures. However, this alloy group exhibits high thermal expansion characteristics. Ferritic stainless steels generally have lower CTEs than austenitics, and also lower ultimate tensile strengths (Gunia et al., 1980). For screening tests, fiber metal materials of three different alloys were selected. Table 1 lists those materials selected along with several important properties.

The Type 347 fiber metal FM 134 was chosen as the control material for the test series. Its extensive field performance is available for comparison against actual operating conditions. The Type 430 fiber metal was selected as a nominal ferritic stainless steel. The configuration of this fiber metal is not optimized for acoustic attenuation service, but the physical properties would allow direct comparison in environmental exposure tests. The Hoskins 875 fiber metal is a material configured for high-temperature oxidation resistance. Its composition includes substantial aluminum, which renders the alloy highly resistant to oxidation, and to sulfidation in a highly oxidizing environment.

The first round of testing consisted of material characterization (ultimate tensile testing and sample weighing) and oxidation in air. The target application temperature of 650°C (1202°F) was chosen for exposure of the specimens. The specimen base weights were recorded after a preoxidation treatment at 650°C for 0.1 h, then weights were determined periodically thereafter. Figure 1 displays the weight gain as a function of time. Each data point is the average for three specimens. Each weight measurement imposed one thermal cycle to room temperature. After 1000 h of exposure and final weight measurement, the tensile strength of each specimen was determined. Table 2 lists the tensile strength and oxidation weight gain properties affected by the oxidation exposure.

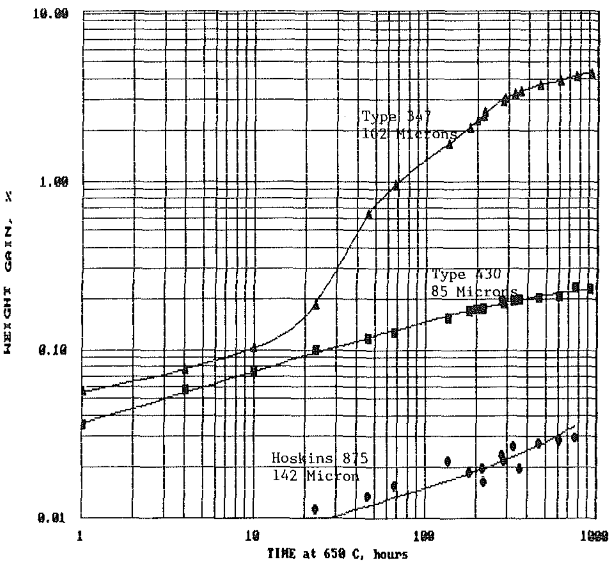

Fig. 1 Oxidation weight gain versus time @ 650°C

Figure 1 shows that the T347 and the T430 fiber metals oxidized at similar rates for about the first day of exposure. However, at about three days of exposure, the rate of oxidation for the T347 fiber metal had increased to almost ten times that of the T430 fiber metal. After the first "breakaway" in the T347 curve, the slope of the oxidation curve for that material leveled out to the same slope as in the initial stage of oxidation. By contrast, the T430 material oxidized at a constant rate throughout the entire 1000 h period. The slope of the H875 curve is also constant, but yet one decade lower than that of the T430. Early data points for this curve are not included as they lie essentially on the abscissa.

The distinction in oxidation behavior between the austenitic product and the ferritic products is related to the coefficients of thermal expansion of the alloys, which are listed in Table 1. The oxide scale that forms on the alloys has a lower CTE than the substrate alloys. The CTE for T430 is 36 percent lower than that for T347. The thermal stress generated in cooling the oxidized fibers is lower for the T430 than for the T347. This thermal stress is sufficient in the T347 material to cause spallation of the protective oxide layer and accelerated oxidation of the underlying fiber. Accelerated oxidation is represented by the "breakaway" section of the oxidation curve for the T347 material. In the case of the T430 material, the thermal stress generated on cooling is below the spallation level and oxidation proceeds without the breakaway behavior. This phenomenon is treated in greater detail by Wood (1962). The CTE for H875 is slightly less than for T430, so the thermal stress generated on cooling would be even less. This alloy's higher chromium and considerable aluminum contents promote the formation of aluminum oxide, or a mixed chromium-aluminum oxide, which greatly retards oxidation in the temperature range of the test.

The data in Table 2 show that the T347 material gained 4.32 percent of its original weight through the 1000 h of oxidation exposure, and incurred a loss of tensile strength of 13.3 percent. In comparison, weight gain for the T430 material was only 0.22 percent, and the oxidized specimens had an average strength greater than the unoxidized control specimens. This apparent anomaly may be due to statistical differences of

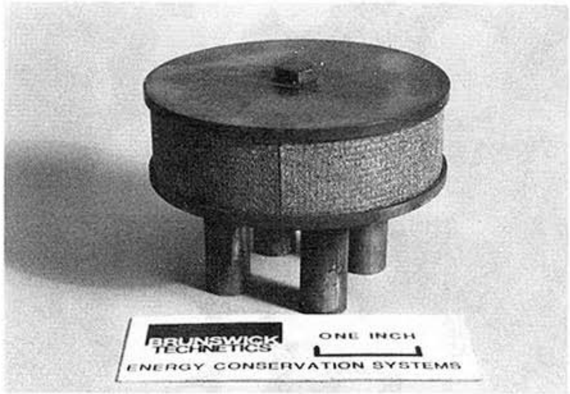

Fig. 2 Test apparatus: specimen holding fixture shown with cylindrical specimen

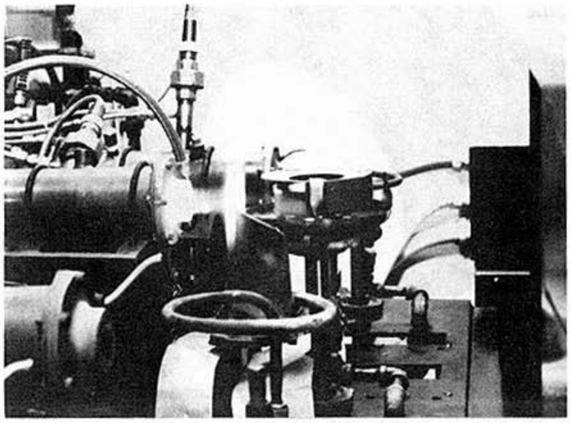

Fig. 3 Flame exposure test in progress

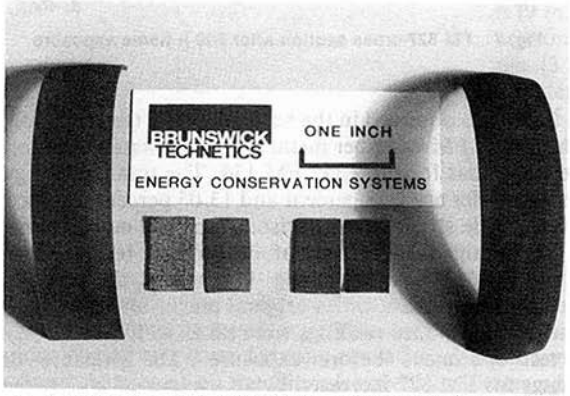

Fig. 4 Specimens after flame test exposure (left to right: FM 827—cylindrical specimen, replacement tab with indirect side shown, intermediate specimen with exposed side shown; FM 134—replacement tab with indirect side shown, intermediate specimen with exposed side shown, cylindrical specimen)

sampling pattern and material variation. The H875 material gained only 0.04 percent of original weight in the 1000 h, with an apparent 6.3 percent strength decrease. A strength variation of ±10 percent is expected among the fiber metal specimens.

Flame Exposure Testing

The screening test results confirmed the initial expectation that the ferritic stainless steels would withstand the rigors of oxidation exposure in the 650°C (1202°F) temperature range better than would the austenitic stainless steel. Based on this indication, a new material was specified. The material would be manufactured to the same acoustic properties as is FM 134 using the same fiber type and size with the exception that the alloy would be Hoskins 875. The new acoustic material was assigned the designation FM 827.

Table 3 Specimen properties as a function of time in flame exposure test

FM 134

time, hours	0	100	200	300	400	500
wt. gain, %	0	4.5154	10.2647	11.2283	12.2246	13.0547
UTS, psi	18,121	-	-	-	-	4,060
oxide thk. (microns)	0	-	12.9*	-	-	37.3*
airflow resistance (in. H2O)	0.65 0.66 0.83 0.86 0.69 0.738	- - - - -	- - - - -	- - - - -	- - - - -	# - 2.25 - - 2.25

*average of 8 readings
#specimen fractured in measurement

FM 827

time, hours	0	100	200	300	400	500
wt. gain, %	0	0.3462	0.7611	0.9348	1.1346	1.3792
UTS, psi	12,903	-	-	-	-	10,746
oxide thk. (microns)	0	-	(!)	-	-	(!)
airflow resistance (in. H2O)	0.77 0.66 0.70 0.65 0.67 0.69	- - - - -	- - - - -	- - - - -	- - - - -	1.02 0.82 0.81 0.74 0.94 0.866

!Oxide layer thickness unresolved at 400x up to 500 hours exposure
Disposition from flame ("soot") on facing side of individual fiber over 24 microns thick.

A test plan was formulated to expose both FM 134 and FM 827 to a simulated gas turbine exhaust environment. The conditions of exposure were selected to represent the operating conditions of an APU. An atmospheric pressure fuel atomizing combustor would burn Jet A fuel with excess air. Combustion could be carried out with a fuel:air ratio up to 1:57, which corresponds to approximately 400 percent theoretical air for combustion. Sulfur level in the fuel was determined to be 0.033 percent by weight.

The specimen test configuration consisted of two half cylinders—one of FM 827 and one of FM 134—mechanically held in a fixture. During exposure, the fixture was positioned within a shroud designed to contain the exhaust and assure uninterrupted immersion of the specimens in the exhaust. Throughout the test the specimen assembly was rotated through the flame. The specimen temperature was controlled by optical pyrometry to the desired set point. Fuel flow to the combustor was controlled based on the signal output from the optical pyrometer.

The exposure schedule consisted of 500 cycles. One cycle consists of one hour heating at 650°C followed by 15 minutes of cooling, without regard to heating or cooling rates. During the first and last heating cycle of each group of 100 cycles, the temperature was raised to 900°C (1652°F) for one minute. At the end of each 100 cycles, the specimens were removed from the fixture and weighed to determine weight gain. After the dry weighing, the specimens were immersed in deionized water and reweighed. The water addition simulates rain and humidity exposure encountered in service. After 300 cycle hours were accumulated specimens were removed for the determination of oxide layer thickness.

Figure 2 shows the specimen holding fixture with a cylindrical specimen in place. With the top plate removed, the specimens can be removed for weighing. Figure 3 is a photo of the test rig during the shakedown run. The shrould is rotated in this photo to show the specimen fixture.

To accommodate the intermediate oxide layer thickness determination, the test procedure calls for four specimens; two larger specimens each comprise slightly less than half of a cylinder, while two smaller specimens are included for removal after 300 cycles. Sectioning of the larger specimens is thus precluded and the progressive accumulation of weight

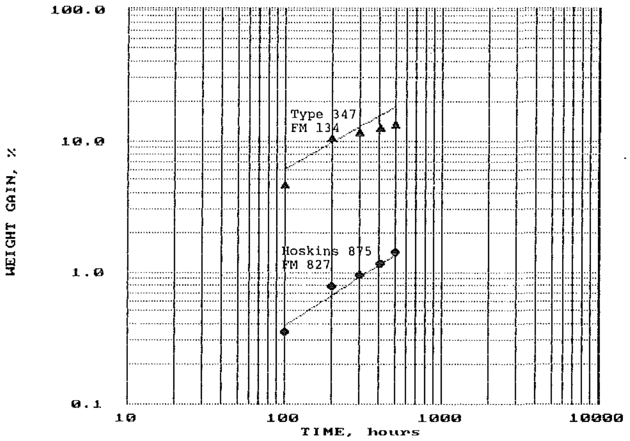

Fig. 5 Weight gain versus time at 650°C

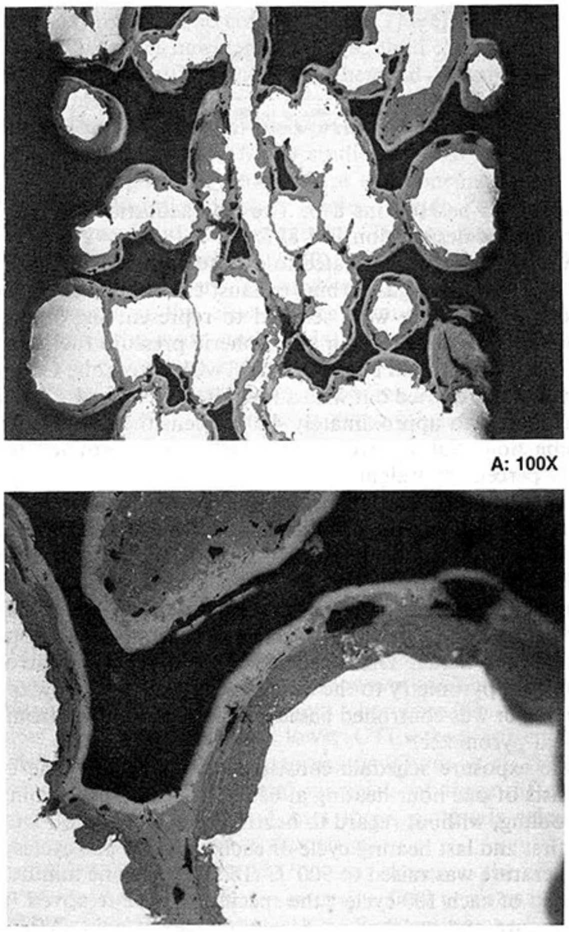
A: 100X

B: 400X

Fig. 6 FM 134 cross section after 500 h flame exposure

gain data is not disturbed. The intermediate specimen was replaced by a duplicate so that temperature measurement was not affected. Prior to the test, ultimate tensile strength of both materials were determined, and air flow resistance on the actual test specimens were measured for post-test comparison.

Flame Exposure Test Results

The specimens after 500 cycles are shown in Fig. 4. The FM 827 specimens exhibit no dimensional distortion. However, the FM 134 specimens have sustained a permanent barreling about the specimen midline. Table 3 contains the specimen property data as a function of time. Weight gain is plotted in Fig. 5. As was observed in the screening test, the curve for the FeCrAl alloy FM 827 fiber metal is approximately one decade lower than that for the T347 FM 134. The total weight gains after 500 cycles are 1.38 percent and 13.05 percent, respectively. The tensile strength comparisons are even more dramatic. FM 827 retained 83 percent of its original tensile strength through the 500 cycles of testing. In contrast, the FM 134 retained only 23 percent of its original tensile strength.

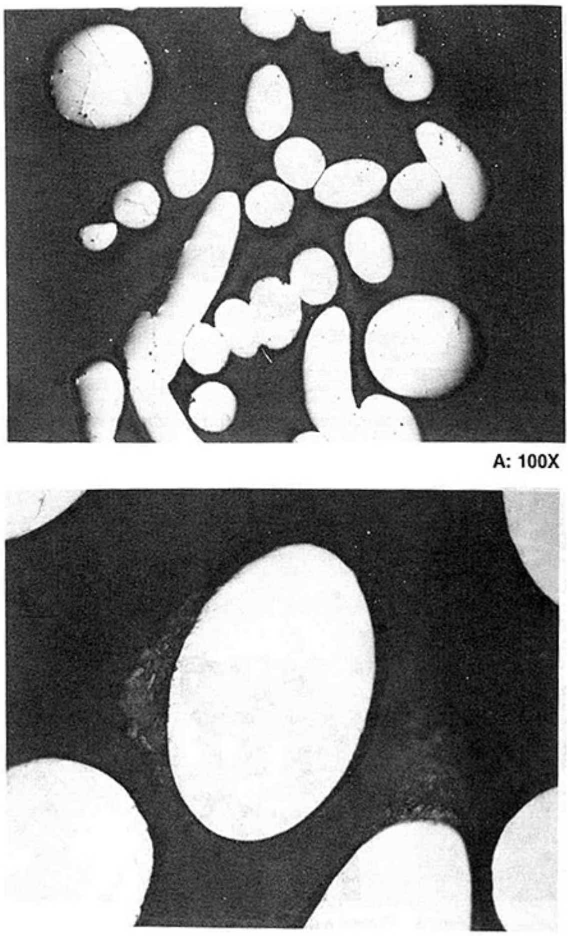
A: 100X

B: 400X

Fig. 7 FM 827 cross section after 500 h flame exposure

Air flow resistance readings were taken in five locations on the test specimens before exposure. The pressure drop readings for FM 827 increased by an average of 20.7 percent. Only one reading was obtained on the FM 134 specimen due to its distortion; the measured pressure drop in that location increased by 270 percent. Attempt to measure air flow in a second location resulted in fracture of the specimen and no further readings could be obtained.

Oxide layer thickness measurements were made from metallographically prepared sections of the exposed specimens. The values listed in Table 2 are the average of eight readings on each cross section. Figure 6 exhibits the microstructure of the T347 fiber metal FM 134 after 500 h of exposure. The entire material thickness is shown in the lower magnification view (Fig. 6A). The light central areas are unoxidized metal; the gray surrounding material is the oxide formed on the fiber surfaces. The large amount of oxide accumulation has decreased the open area of the material, which is reflected in the air flow resistance measurements. The higher magnification view (Fig. 6B) shows the oxide layer on an individual fiber in close detail. Cracks, globular discontinuities, and laminar growth of the oxide are readily visible. Cracking of the oxide layer tends to reduce its protective nature by exposing the base metal to further oxidation. Cracking is promoted by the large difference in thermal expansion rates between the oxide layer and the base metal.

The microstructure of the FeCrAl metal FM 827 after 500 h exposure is exhibited in Fig. 7. The lower magnification view (Fig. 7A) displays the entire material thickness. After this exposure time the open area of the structure remains unobstructed by oxide buildup on the fibers. However, a buildup of material external to the fiber is observed on one side of the fibers in Fig. 7(A), which have a line-of-sight passage to the outer boundary of the structure. As seen in Fig. 7(A), no buildup is present on the opposite side of the fiber. The buildup comprises material carried through the flame and deposited on the fibers and not an oxide generated from the fibers due to heating. Apart from the deposit, no other layer is measurable at the magnification of the photomicrograph.

The presence of an easily discernible deposit on the line-of-sight surfaces in the absence of a significant oxidation layer on other surfaces suggests that the weight gain data collected from the specimens in this test are biased high relative to the actual thermal oxidation response of the materials. As this effect was not anticipated in the test plan, no rigorous attempt was made to separate the contributions of the deposit and of base metal oxidation to the overall weight gain. Since the specimens were exposed to the same flame for the same length of time, the oxidation curves should be merely offset by some constant amount. The oxidation rate for the FeCrAl fiber metal FM 827 is no less than 1/10 that of the austenitic stainless steel fiber metal.

Fabricability

The utilization of the new acoustic fiber metal material requires that it be fabricated into a device for use in actual applications. The usual methods used to fabricate an exhaust silencer include roll forming and welding. A typical exhaust silencer might be a cylinder approximately 230 mm (9 in.) in diameter and 914 mm (36 in.) long. In preparation of specimens for the flame test cylinders of 76.2 mm (3 in.) diameter were roll formed with no damage to the material. Minimum forming limits will be less than 38.1 mm (1.5 in.) radius, although the actual limits have not been determined. The alloy itself has ductility limitations common to ferritic steels slow cooled from elevated temperatures. However, the ductility characteristics of the fiber metal structure itself are such that the alloy ductility only minimally affects the formability of the structure overall. The interwoven and interlocking fibers that comprise the fiber metal structure are individually required to bend or stretch only relatively small amounts during any given forming operation. Yet the sum of the shape changes of all the fibers involved facilitates operations such as roll forming.

Welding of the material is easily accomplished using the Gas Tungsten Arc process. Because of the porous nature of the material, the use of filler metal is recommended. For FM 827 parts longer than approximately 100 mm (4 in.) the filler should be chosen such that thermal expansion coefficient is near that of the base alloy. Excellent weldability was obtained with the parent alloy Hoskins 875, and also with Type 430 stainless steel, Inconel 82, and nickel. For best results in the application for which FM 827 is designed, Hoskins 875 should be chosen. Type 430 or other ferritic stainless steels with at least 16 percent Cr (by weight) can also be used. Filler alloys with nickel should be avoided because of the sulfur content of the exhaust gases.

The technique applied to welding the fiber metal material is similar to that which might be used for sheet metal of the same composition. Weld specimens of an actual application length were produced using the following parameters:

joint preparation: sheared edge, butt joint without gap
weld configuration: longitudinal seam, filler added
work holding: chill fixturing on both sides of weld couple
arc parameters:
voltage—10 V DCSP
current—21A
gas—argon @ 15 cubic ft/hr (7.1 l/min.)
  (also backside shielding gas)
high frequency superimposed to start arc
electrode—2 percent thoriated tungsten
    —1.59 mm (1/16 in.) diameter
    —22° tip angle, sharp point
    —6.5 mm (0.256 in.) tip stickout
    —3 mm (0.125 in.) tip to work

Specimens up to 991 mm (39 in.) long (maximum stock size) were welded for demonstration of capability.

Conclusions

Fiber metal materials are effectively utilized in noise reduction.

Fiber metal acoustic materials made from Type 347 stainless steel function well in applications with temperatures up to 540°C (1004°F).

FM 827, the new fiber metal acoustic material made from Hoskins 875, can operate continuously at 650°C (1202°F) in gas turbine exhaust conditions.

FM 827 can be easily fabricated using standard roll forming and gas tungsten arc welding.

References

Bauer, A., 1976, "Impedance Theory and Measurements of Single- and Multi-Layer Liners in a Duct with Flow," AIAA Paper No. 76-539.

Bradshaw, R. W., and Stoltz, R. E., 1980, "Alloy Selection for Sulfidation-Oxidation Resistance in Coal Gasification Environments," *J. Materials for Energy Systems*, Vol. 2, No. 1, pp. 3-11.

Erickson, A. R., and Fisher, J. I., 1966, "Properties of Fiber Metal Acoustically-Resistive Materials," *Proceedings, Seventy-Second Meeting of the Acoustical Society of America*.

Franken, P. A., 1960, "Jet Noise," in: *Noise Reduction*, Leo L. Beranek, ed., McGraw-Hill, New York, p. 645ff.

Gunia, R. B., et al., 1980, "Wrought Stainless Steels," *Metals Handbook*, 9th ed., Vol. 3, American Society of Metals, Metals Park, OH, pp. 3-40.

Hoffman, E. E., ed., 1984, *Materials and Components in Fossil Energy Applications, a DOE Newsletter*, Special Index Edition II.

Kester, J. D., and Peracchio, A. A., "Noise Technology Requirements for Future Aircraft Powerplants," ASME Paper No. 76-GT-69.

Kaiser, J. E., Nayfeh, A. H., and Telionis, D. P., 1975, "Acoustics of Aircraft Engine-Duct Systems," *AIAA Journal*, Vol. 13, pp. 130-153.

Packer, C. M., and Perkins, R. A., 1980, "The Performance of McrAl Alloys in Complex Coal Conversion Atmospheres," abstracted in *Materials and Components in Fossil Energy Applications, a DOE Newsletter*, No. 28, pp. 5-7.

Saegusa, F., and Shores, D. A., 1982, "Corrosion Resistance of Super-alloys in the Temperature Range 800-1300°F (430-700°C)," *J. Materials for Energy Systems*, Vol. 4, No. 1, pp. 16-27.

Sorell, G., 1987, "Parametric Studies of Erosion-Corrosion of Alloys in High-Temperature Sulfidizing Environmnents," *Materials and Components in Fossil Energy Applications, a DOE Newsletter*, No. 69, pp. 1-6.

Natesan, K., and Tiearney, T. C., Jr., 1980, "Metallic Corrosion in Simulated Low-BTU Coal-Gasification Atmospheres," *J. Materials for Energy Systems*, Vol. 1, No. 4, pp. 13-29.

Wood, G. C., 1962, *Corros. Sci.*, Vol. 2, p. 173.

Zaizen, T., et al., 1980, "Oxidation and Hot-Corrosion Resistant High Aluminum Austenitic Stainless Steel," *J. Materials for Energy Systems*, Vol. 2, No. 2, pp. 21-29.